Gamma-Ray Bursts

Contents

1 Topics

- GRB classification in different families with different progenitor systems.
- GRB empirical correlations
- "Genuine short" GRBs: Possible identifications and selection effects
- A modified spectral energy distribution for highly energetic GRBs
- The observed spectra of the P-GRBs
- GRB prompt emission spectra below 5 keV: challenges for future missions
- Interpretation of the ultra high energy emission from GRBs observed by Fermi and AGILE
- Analysis of different families of progenitors for GRBs with different energetics
- GRBs at redshift $z > 6$
- GRBs originating from a multiple collapse
- Prompt emission: the clumpiness of CBM
- Microphysical description of the interaction between the fireshell and the CBM
- Theoretical interpretation of the "plateau" phase in the X-ray afterglow
- Emission from newly born neutron stars, or "neo neutron stars".
- Induced Gravitational Collapse process for GRBs associated with supernovae.

- Redshift estimators for GRBs with no measured redshift.
- Binary Driven Hypernovae (BdHNe) as progenitor of GRBs via Induced Gravitational Collapse.
- GRB light curves as composed of four different episodes.
- Different kinds of binary systems as GRB progenitors.
- “Cosmic Matrix” for GRBs.
- GRB X-Ray Flares and Gamma-Ray Flares.
- GRB afterglow theory consistent with the mildly relativistic velocities inferred from the observations.
- Gravitational wave emission associated to GRBs of different families.
- Extended thermal emission components in GRBs.
- GRBs from merging white dwarfs.

2 Participants

2.1 ICRANet participants

- David Arnett
- Carlo Luciano Bianco
- Massimo Della Valle
- Marco Muccino
- Giovanni Battista Pisani
- Jorge Armando Rueda Hernandez
- Remo Ruffini
- Narek Sahakyan
- Gregory Vereshchagin
- She-Sheng Xue

2.2 Past collaborators

- Andrey Baranov
- Maria Grazia Bernardini (OAB, Italy)
- Joao Braga (INPE, Brazil)
- Sabrina Casanova (MPIK, Germany)
- Letizia Caito

- Pascal Chardonnet (Université de Savoie, France)
- Guido Chincarini (Università di Milano “Bicocca”, Italy)
- Demetrios Christodoulou (ETH Zurich, Switzerland)
- Alessandra Corsi (INAF-IASF Roma, Italy)
- Valeri Chechetkin
- Maria Giovanna Dainotti
- Thibault Damour (IHES, France)
- Maxime Enderli
- Walter Ferrara
- Federico Fraschetti (CEA Saclay, France)
- Roberto Guida
- Vahe Gurzadyan (Yerevan Physics Institute, Armenia)
- Wen-Biao Han
- Massimiliano Lattanzi (Oxford Astrophysics, UK)
- Vincenzo Liccardo
- Hendrik Ludwig
- Nino Panagia
- Barbara Patricelli (Pisa University, Italy)
- Elena Pian
- Giuliano Preparata (Università di Milano, Italy)
- Jay D. Salmonson (Livermore Lab, USA)
- Vineeth Valsan
- Jim Wilson (Livermore Lab, USA)

2.3 Ongoing collaborations

- Alexey Aksenov (ITEP, Russia)
- Lorenzo Amati (INAF-IASF Bologna, Italy)
- Ulisses Barres de Almeida (CBPF, Brazil)
- Laura Marcela Becerra Bayona (Universidad Industrial de Santander, Colombia)
- Riccardo Belvedere (ICRANet-Rio, Brazil)
- Sandip Kumar Chakrabarti (S.N. Bose National Centre and Indian Centre for Space Physics, India)
- Christian Cherubini (Università Campus Biomedico, Italy)
- Alessandro Chieffi (INAF-IASF Roma, Italy)
- Stefano Covino (OAB, Italy)
- Gustavo de Barros (UFRJ, Brazil)
- Simonetta Filippi (Università Campus Biomedico, Italy)
- Filippo Frontera (Università di Ferrara, Italy)
- Chris Fryer (Los Alamos National Laboratories, USA).
- Dafne Guetta (OAR, Italy)
- Cristiano Guidorzi (OAB, Italy)
- Stanislav Kelner (MEPhI, Russia, and MPIK, Germany)
- Marco Limongi (OAR, Italy)
- Clovis Maia (University of Brasilia, Brazil)
- Vanessa Mangano (INAF-IASF Palermo, Italy)
- Grant Mathews (University of Notre Dame, USA)

- Ana Virginia Penacchioni (INPE, Brazil)
- Luis Juracy Rangel Lemos (Fundação Universidade Federal do Tocantins, Brazil)
- Soroush Shakeri (Isfahan University of Technology, Iran)
- Ivan Siutsou (ICRANet-Rio, Brazil)
- Susanna Vergani (Dunsink Observatory, Ireland)
- Francesco Vissani (INFN, Italy)
- Elena Zaninoni (ICRANet-Rio, Brazil)

2.4 Students

- Yerlan Aimuratov (IRAP PhD, Kazakhstan)
- Yen-Chen Chen (IRAP-PhD, China-Taiwan)
- Mile Karlika (IRAP PhD, Croatia)
- Milos Kovacevic (IRAP PhD, Serbia)
- Ronaldo V. Lobato (IRAP-PhD, Brazil)
- J. David Melon Fuksman (IRAP PhD, Argentina)
- Rahim Moradi (IRAP PhD, Iran)
- Daria Primorac (IRAP PhD, Croatia)
- Jose Fernando Rodriguez Ruiz (IRAP PhD, Colombia)
- Yu Wang (IRAP PhD, China-Mainland)

3 Selected publications before 2005

3.1 Refereed journals

1. D. Christodoulou, R. Ruffini; "Reversible Transformations of a Charged Black Hole"; Physical Review D, 4, 3552 (1971).

   A formula is derived for the mass of a black hole as a function of its "irreducible mass", its angular momentum, and its charge. It is shown that 50% of the mass of an extreme charged black hole can be converted into energy as contrasted with 29% for an extreme rotating black hole.

2. T. Damour, R. Ruffini; "Quantum electrodynamical effects in Kerr-Newman geometries"; Physical Review Letters, 35, 463 (1975).

   Following the classical approach of Sauter, of Heisenberg and Euler and of Schwinger the process of vacuum polarization in the field of a "bare" Kerr-Newman geometry is studied. The value of the critical strength of the electromagnetic fields is given together with an analysis of the feedback of the discharge on the geometry. The relevance of this analysis for current astrophysical observations is mentioned.

3. G. Preparata, R. Ruffini, S.-S. Xue; "The dyadosphere of black holes and gamma-ray bursts"; Astronomy & Astrophysics, 338, L87 (1999).

   The "dyadosphere" has been defined as the region outside the horizon of a black hole endowed with an electromagnetic field (abbreviated to EMBH for "electromagnetic black hole") where the electromagnetic field exceeds the critical value, predicted by Heisenberg & Euler for $e^{\pm}$ pair production. In a very short time ($\sim O(\hbar/mc^2)$) a very large number of pairs is created there. We here give limits on the EMBH parameters leading to a Dyadosphere for $10M_{\odot}$ and $10^5M_{\odot}$ EMBH's, and give as well the pair densities as functions of the radial coordinate. We here assume that the pairs reach thermodynamic equilibrium with a photon gas and estimate the average energy per pair as a function of the EMBH mass. These data give the initial conditions for the analysis of an enormous pair-electromagnetic-pulse or "P.E.M. pulse" which naturally leads to relativistic expansion. Basic energy requirements for gamma ray bursts (GRB), including GRB971214 recently observed at z=3.4, can be accounted for by processes occurring in the dyadosphere. In this letter we do not address the problem of forming either the EMBH or the dyadosphere: we establish some inequalities which must be satisfied during their formation process.

4. R. Ruffini, J.D. Salmonson, J.R. Wilson, S.-S. Xue; "On the pair electromagnetic pulse of a black hole with electromagnetic structure"; Astronomy & Astrophysics, 350, 334 (1999).

   We study the relativistically expanding electron-positron pair plasma formed by the process of vacuum polarization around an electromagnetic black hole (EMBH). Such processes can occur for EMBH's with mass all the way up to $6 \times 10^5 M_\odot$. Beginning with a idealized model of a Reissner-Nordstrom EMBH with charge to mass ratio $\xi = 0.1$, numerical hydrodynamic calculations are made to model the expansion of the pair-electromagnetic pulse (PEM pulse) to the point that the system is transparent to photons. Three idealized special relativistic models have been compared and contrasted with the results of the numerically integrated general relativistic hydrodynamic equations. One of the three models has been validated: a PEM pulse of constant thickness in the laboratory frame is shown to be in excellent agreement with results of the general relativistic hydrodynamic code. It is remarkable that this precise model, starting from the fundamental parameters of the EMBH, leads uniquely to the explicit evaluation of the parameters of the PEM pulse, including the energy spectrum and the astrophysically unprecedented large Lorentz factors (up to 6×10^3 for a $10^3 M_\odot$ EMBH). The observed photon energy at the peak of the photon spectrum at the moment of photon decoupling is shown to range from 0.1 MeV to 4 MeV as a function of the EMBH mass. Correspondingly the total energy in photons is in the range of 10^{52} to 10^{54} ergs, consistent with observed gamma-ray bursts. In these computations we neglect the presence of baryonic matter which will be the subject of forthcoming publications.

5. R. Ruffini, J.D. Salmonson, J.R. Wilson, S.-S. Xue; "On the pair-electro magnetic pulse from an electromagnetic black hole surrounded by a baryonic remnant"; Astronomy & Astrophysics, 359, 855 (2000).

   The interaction of an expanding Pair-Electromagnetic pulse (PEM pulse) with a shell of baryonic matter surrounding a Black Hole with electromagnetic structure (EMBH) is analyzed for selected values of the baryonic mass at selected distances well outside the dyadosphere of an EMBH. The dyadosphere, the region in which a super critical field exists for the creation of e+e- pairs, is here considered in the special case of a Reissner-Nordstrom geometry. The interaction of the PEM pulse with the baryonic matter is described using a simplified model of a slab of constant thickness in the laboratory frame (constant-thickness approximation) as well as performing the integration of the general relativistic hydrodynamical equations. Te validation of the constant-thickness approximation, already presented in a previous paper Ruffini et al. (1999) for a PEM pulse in vacuum, is here generalized to the presence of baryonic matter. It is found that for a baryonic shell of mass-energy less than 1% of the total energy of the dyadosphere, the constant-thickness approximation is in excellent agreement with full general relativistic computations. The approximation breaks down for larger values of the baryonic shell mass, however such cases are of less interest for observed Gamma Ray Bursts (GRBs). On the basis of numerical computations of the slab model for PEM pulses, we describe (i) the properties of relativistic evolution of a PEM pulse colliding with a baryonic shell; (ii) the details of the expected emission energy and observed temperature of the associated GRBs for a given value of the EMBH mass; $10^3 M_\odot$, and for baryonic mass-energies in the range 10^{-8} to 10^{-2} the total energy of the dyadosphere.

6. C.L. Bianco, R. Ruffini, S.-S. Xue; "The elementary spike produced by a pure e+e- pair-electromagnetic pulse from a Black Hole: The PEM Pulse"; Astronomy & Astrophysics, 368, 377 (2001).

   In the framework of the model that uses black holes endowed with electromagnetic structure (EMBH) as the energy source, we study how an elementary spike appears to the detectors. We consider the simplest possible case of a pulse produced by a pure e^+e^- pair-electro-magnetic plasma, the PEM pulse, in the absence of any baryonic matter. The resulting time profiles show a *Fast-Rise-Exponential-Decay* shape, followed by a power-law tail. This is obtained without any special fitting procedure, but only by fixing the energetics of the process taking place in a given EMBH of selected mass, varying in the range from 10 to 10^3 $M_\odot$ and considering the relativistic effects to be expected in an electron-positron plasma gradually reaching transparency. Special attention is given to the contributions from all regimes with Lorentz γ factor varying from $\gamma = 1$ to $\gamma = 10^4$ in a few hundreds of the PEM pulse travel time. Although the main goal of this paper is to obtain the elementary spike intensity as a function of the arrival time, and its observed duration, some qualitative considerations are also presented regarding the expected spectrum and on its departure from the thermal one. The results of this paper will be comparable, when data will become available, with a subfamily of particularly short GRBs not followed by any afterglow. They can also be propedeutical to the study of longer bursts in presence of baryonic matter currently observed in GRBs.

7. R. Ruffini, C.L. Bianco, P. Chardonnet, F. Fraschetti, S.-S. Xue; "Relative spacetime transformations in Gamma-Ray Bursts"; The Astrophysical Journal, 555, L107 (2001).

   The GRB 991216 and its relevant data acquired from the BATSE experiment and RXTE and Chandra satellites are used as a prototypical case to test the theory linking the origin of gamma ray bursts (GRBs) to the process of vacuum polarization occurring during the formation phase of a black hole endowed with electromagnetic structure (EMBH). The relative space-time transformation paradigm (RSTT paradigm) is presented. It relates the observed signals of GRBs to their past light cones, defining the events on the worldline of the source essential for the interpretation of the data. Since GRBs present regimes with unprecedently large Lorentz γ factor, also sharply varying with time, particular attention is given to the constitutive equations relating the four time variables: the comoving time, the laboratory time, the arrival time at the detector, duly corrected by the cosmological effects. This paradigm is at the very foundation of any possible interpretation of the data of GRBs.

8. R. Ruffini, C.L. Bianco, P. Chardonnet, F. Fraschetti, S.-S. Xue; "On the interpretation of the burst structure of Gamma-Ray Bursts"; The Astrophysical Journal, 555, L113 (2001).

   Given the very accurate data from the BATSE experiment and RXTE and Chandra satellites, we use the GRB 991216 as a prototypical case to test the EMBH theory linking the origin of the energy of GRBs to the electromagnetic energy of black holes. The fit of the afterglow fixes the only two free parameters of the model and leads to a new paradigm for the interpretation of the burst structure, the IBS paradigm. It leads as well to a reconsideration of the relative roles of the afterglow and burst in GRBs by defining two new phases in this complex phenomenon: a) the injector phase, giving rise to the proper-GRB (P-GRB), and b) the beam-target phase, giving rise to the extended afterglow peak emission (E-APE) and to the afterglow. Such differentiation leads to a natural possible explanation of the bimodal distribution of GRBs observed by BATSE. The agreement with the observational data in regions extending from the horizon of the EMBH all the way out to the distant observer confirms the uniqueness of the model.

9. R. Ruffini, C.L. Bianco, P. Chardonnet, F. Fraschetti, S.-S. Xue; "On a possible Gamma-Ray Burst-Supernova time sequence"; The Astrophysical Journal, 555, L117 (2001).

   The data from the Chandra satellite on the iron emission lines in the afterglow of GRB 991216 are used to give further support for the EMBH theory, which links the origin of the energy of GRBs to the extractable energy of electromagnetic black holes (EMBHs), leading to an interpretation of the GRB-supernova correlation. Following the relative space-time transformation (RSTT) paradigm and the interpretation of the burst structure (IBS) paradigm, we introduce a paradigm for the correlation between GRBs and supernovae. The following sequence of events is shown as kinematically possible and consistent with the available data: a) the GRB-progenitor star P_1 first collapses to an EMBH, b) the proper GRB (P-GRB) and the peak of the afterglow (E-APE) propagate in interstellar space until the impact on a supernova-progenitor star P_2 at a distance $\leq 2.69 \times 10^{17}$ cm, and they induce the supernova explosion, c) the accelerated baryonic matter (ABM) pulse, originating the afterglow, reaches the supernova remnants 18.5 hours after the supernova explosion and gives rise to the iron emission lines. Some considerations on the dynamical implementation of the paradigm are presented. The concept of induced supernova explosion introduced here specifically for the GRB-supernova correlation may have more general application in relativistic astrophysics.

10. R. Ruffini, C.L. Bianco, P. Chardonnet, F. Fraschetti, S.-S. Xue; "On the physical processes which lie at the bases of time variability of GRBs"; Il Nuovo Cimento B, 116, 99 (2001).

    The relative-space-time-transformation (RSTT) paradigm and the interpretation of the burst-structure (IBS) paradigm are applied to probe the origin of the time variability of GRBs. Again GRB 991216 is used as a prototypical case, thanks to the precise data from the CGRO, RXTE and Chandra satellites. It is found that with the exception of the relatively inconspicuous but scientifically very important signal originating from the initial "proper gamma ray burst" (P-GRB), all the other spikes and time variabilities can be explained by the interaction of the accelerated-baryonic-matter pulse with inhomogeneities in the interstellar matter. This can be demonstrated by using the RSTT paradigm as well as the IBS paradigm, to trace a typical spike observed in arrival time back to the corresponding one in the laboratory time. Using these paradigms, the identification of the physical nature of the time variablity of the GRBs can be made most convincingly. It is made explicit the dependence of a) the intensities of the afterglow, b) the spikes amplitude and c) the actual time structure on the Lorentz gamma factor of the accelerated-baryonic-matter pulse. In principle it is possible to read off from the spike structure the detailed density contrast of the interstellar medium in the host galaxy, even at very high redshift.

11. R. Ruffini, C.L. Bianco, P. Chardonnet, F. Fraschetti, S.-S. Xue; "On the structures in the afterglow peak emission of gamma ray bursts"; The Astrophysical Journal, 581, L19 (2002).

    Using GRB 991216 as a prototype, it is shown that the intensity substructures observed in what is generally called the "prompt emission" in gamma ray bursts (GRBs) do originate in the collision between the accelerated baryonic matter (ABM) pulse with inhomogeneities in the interstellar medium (ISM). The initial phase of such process occurs at a Lorentz factor $\gamma \sim 310$. The crossing of ISM inhomogeneities of sizes $\Delta R \sim 10^{15}$ cm occurs in a detector arrival time interval of ~ 0.4 s implying an apparent superluminal behavior of $\sim 10^5 c$. The long lasting debate between the validity of the external shock model vs. the internal shock model for GRBs is solved in favor of the first.

12. R. Ruffini, C.L. Bianco, P. Chardonnet, F. Fraschetti, S.-S. Xue; "On the structure of the burst and afterglow of Gamma-Ray Bursts I: the radial approximation"; International Journal of Modern Physics D, 12, 173 (2003).

    We have recently proposed three paradigms for the theoretical interpretation of gamma-ray bursts (GRBs). (1) The relative space-time transformation (RSTT) paradigm emphasizes how the knowledge of the entire world-line of the source from the moment of gravitational collapse is a necessary condition in order to interpret GRB data. (2) The interpretation of the burst structure (IBS) paradigm differentiates in all GRBs between an injector phase and a beam-target phase. (3) The GRB-supernova time sequence (GSTS) paradigm introduces the concept of *induced supernova explosion* in the supernovae-GRB association. In the introduction the RSTT and IBS paradigms are enunciated and illustrated using our theory based on the vacuum polarization process occurring around an electromagnetic black hole (EMBH theory). The results are summarized using figures, diagrams and a complete table with the space-time grid, the fundamental parameters and the corresponding values of the Lorentz gamma factor for GRB 991216 used as a prototype. In the following sections the detailed treatment of the EMBH theory needed to understand the results of the three above letters is presented. We start from the considerations on the dyadosphere formation. We then review the basic hydrodynamic and rate equations, the equations leading to the relative space-time transformations as well as the adopted numerical integration techniques. We then illustrate the five fundamental eras of the EMBH theory: the self acceleration of the e^+e^- pair-electromagnetic plasma (PEM pulse), its interaction with the baryonic remnant of the progenitor star, the further self acceleration of the e^+e^- pair-electroma--gnetic radiation and baryon plasma (PEMB pulse). We then study the approach of the PEMB pulse to transparency, the emission of the proper GRB (P-GRB) and its relation to the "short GRBs". Particular attention is given to the free parameters of the theory and to the values of the thermodynamical quantities at transparency. Finally the three different regimes of the afterglow are described within the fully radiative and radial approximations: the ultrarelativistic, the relativistic and the nonrelativistic regimes. The best fit of the theory leads to an unequivocal identification of the "long GRBs" as extended emission occurring at the afterglow peak (E-APE). The relative intensities, the time separation and the hardness ratio of the P-GRB and the E-APE are used as distinctive observational test of the EMBH theory and the excellent agreement between our theoretical predictions and the observations are documented. The afterglow power-law indexes in the EMBH theory are compared and contrasted with the ones in the literature, and no beaming process is found for GRB 991216. Finally, some preliminary results relating the observed time variability of the E-APE to the inhomogeneities in the interstellar medium are presented, as well as some general considerations on the EMBH formation. The issue of the GSTS paradigm will be the object of a forthcoming publication and the relevance of the iron-lines observed in GRB 991216 is shortly reviewed. The general conclusions are then presented based on the three fundamental parameters of the EMBH theory: the dyadosphere energy, the baryonic mass of the remnant, the interstellar medium density. An in depth discussion and comparison of the EMBH theory with alternative theories is presented as well as indications of further developments beyond the radial approximation, which will be the subject of paper II in this series. Future needs for specific GRB observations are outlined.

13. R. Ruffini, C.L. Bianco, P. Chardonnet, F. Fraschetti, V. Gurzadyan, S.-S. Xue; "On the instantaneous spectrum of gamma ray bursts"; International Journal of Modern Physics D, 13, 843 (2004).

    A theoretical attempt to identify the physical process responsible for the afterglow emission of Gamma-Ray Bursts (GRBs) is presented, leading to the occurrence of thermal emission in the comoving frame of the shock wave giving rise to the bursts. The determination of the luminosities and spectra involves integration over an infinite number of Planckian spectra, weighted by appropriate relativistic transformations, each one corresponding to a different viewing angle in the past light cone of the observer. The relativistic transformations have been computed using the equations of motion of GRBs within our theory, giving special attention to the determination of the equitemporal surfaces. The only free parameter of the present theory is the "effective emitting area" in the shock wave front. A self consistent model for the observed hard-to-soft transition in GRBs is also presented. When applied to GRB 991216 a precise fit $\left(\chi^2 \simeq 1.078\right)$ of the observed luminosity in the 2–10 keV band is obtained. Similarly, detailed estimates of the observed luminosity in the 50–300 keV and in the 10–50 keV bands are obtained.

3.2 Conference proceedings

1. R. Ruffini; "Beyond the critical mass: The dyadosphere of black holes"; in "Black Holes and High Energy Astrophysics", H. sato, N. Sugiyama, Editors; p. 167; Universal Academy Press (Tokyo, Japan, 1998).

   The "dyadosphere" (from the Greek word "duas-duados" for pairs) is here defined as the region outside the horizon of a black hole endowed with an electromagnetic field (abbreviated to EMBH for "electromagnetic black hole") where the electromagnetic field exceeds the critical value, predicted by Heisenberg and Euler for e^+e^- pair production. In a very short time ($\sim O(\hbar/mc^2)$), a very large number of pairs is created there. I give limits on the EMBH parameters leading to a Dyadosphere for $10M_\odot$ and $10^5M_\odot$ EMBH's, and give as well the pair densities as functions of the radial coordinate. These data give the initial conditions for the analysis of an enormous pair-electromagnetic-pulse or "PEM-pulse" which naturally leads to relativistic expansion. Basic energy requirements for gamma ray bursts (GRB), including GRB971214 recently observed at $z = 3.4$, can be accounted for by processes occurring in the dyadosphere.

2. R. Ruffini, C.L. Bianco, P. Chardonnet, F. Fraschetti, L. Vitagliano, S.-S. Xue; "New perspectives in physics and astrophysics from the theoretical understanding of Gamma-Ray Bursts"; in "COSMOLOGY AND GRAVITATION: Xth Brazilian School of Cosmology and Gravitation; 25th Anniversary (1977-2002)", Proceedings of the Xth Brazilian School on Cosmology and Gravitation, Mangaratiba, Rio de Janeiro (Brazil), July - August 2002, M. Novello, S.E. Perez Bergliaffa, Editors; AIP Conference Proceedings, 668, 16 (2003).

   If due attention is given in formulating the basic equations for the Gamma-Ray Burst (GRB) phenomenon and in performing the corresponding quantitative analysis, GRBs open a main avenue of inquiring on totally new physical and astrophysical regimes. This program is very likely one of the greatest computational efforts in physics and astrophysics and cannot be actuated using shortcuts. A systematic approach is needed which has been highlighted in three basic new paradigms: the relative space-time transformation (RSTT) paradigm, the interpretation of the burst structure (IBS) paradigm, the GRB-supernova time sequence (GSTS) paradigm. From the point of view of fundamental physics new regimes are explored: (1) the process of energy extraction from black holes; (2) the quantum and general relativistic effects of matter-antimatter creation near the black hole horizon; (3) the physics of ultrarelativisitc shock waves with Lorentz gamma factor $\gamma > 100$. From the point of view of astronomy and astrophysics also new regimes are explored: (i) the occurrence of gravitational collapse to a black hole from a critical mass core of mass $M \gtrsim 10M_{\odot}$, which clearly differs from the values of the critical mass encountered in the study of stars "catalyzed at the endpoint of thermonuclear evolution" (white dwarfs and neutron stars); (ii) the extremely high efficiency of the spherical collapse to a black hole, where almost 99.99% of the core mass collapses leaving negligible remnant; (iii) the necessity of developing a fine tuning in the final phases of thermonuclear evolution of the stars, both for the star collapsing to the black hole and the surrounding ones, in order to explain the possible occurrence of the "induced gravitational collapse". New regimes are as well encountered from the point of view of nature of GRBs: (I) the basic structure of GRBs is uniquely composed by a proper-GRB (P-GRB) and the afterglow; (II) the long bursts are then simply explained as the peak of the afterglow (the E-APE) and their observed time variability is explained in terms of inhomogeneities in the interstellar medium (ISM); (III) the short bursts are identified with the P-GRBs and the crucial information on general relativistic and vacuum polarization effects are encoded in their spectra and intensity time variability. A new class of space missions to acquire information on such extreme new regimes are urgently needed.

3. R. Ruffini, C.L. Bianco, P. Chardonnet, F. Fraschetti, S.-S. Xue; "The EMBH Model in GRB 991216 and GRB 980425"; in Proceedings of "Third Rome Workshop on Gamma-Ray Burst in the Afterglow Era", 17-20 September 2002; M. Feroci, F. Frontera, N. Masetti, L. Piro, Editors; ASP Conference Series, 312, 349 (2004).

   This is a summary of the two talks presented at the Rome GRB meeting by C.L. Bianco and R. Ruffini. It is shown that by respecting the Relative Space-Time Transformation (RSTT) paradigm and the Interpretation of the Burst Structure (IBS) paradigm, important inferences are possible: a) in the new physics occurring in the energy sources of GRBs, b) on the structure of the bursts and c) on the composition of the interstellar matter surrounding the source.

4. M.G. Bernardini, C.L. Bianco, P. Chardonnet, F. Fraschetti, R. Ruffini, S.-S. Xue; "A New Astrophysical 'Triptych': GRB030329/SN2003dh/ URCA-2"; in "GAMMA-RAY BURSTS: 30 YEARS OF DISCOVERY", Proceedings of the Los Alamos "Gamma Ray Burst Symposium", Santa Fe, New Mexico, 8 – 12 September 2003, E.E. Fenimore, M. Galassi, Editors; AIP Conference Proceedings, 727, 312 (2004).

   We analyze the data of the Gamma-Ray Burst/Supernova GRB030329/ SN2003dh system obtained by HETE-2, R-XTE, XMM and VLT within our theory for GRB030329. By fitting the only three free parameters of the EMBH theory, we obtain the luminosity in fixed energy bands for the prompt emission and the afterglow. Since the Gamma-Ray Burst (GRB) analysis is consistent with a spherically symmetric expansion, the energy of GRB030329 is $E = 2.1 \times 10^{52}$ erg, namely $\sim 2 \times 10^{3}$ times larger than the Supernova energy. We conclude that either the GRB is triggering an induced-supernova event or both the GRB and the Supernova are triggered by the same relativistic process. In no way the GRB can be originated from the supernova. We also evidence that the XMM observations, much like in the system GRB980425/SN1998bw, are not part of the GRB afterglow, as interpreted in the literature, but are associated to the Supernova phenomenon. A dedicated campaign of observations is needed to confirm the nature of this XMM source as a newly born neutron star cooling by generalized URCA processes.

5. F. Fraschetti, M.G. Bernardini, C.L. Bianco, P. Chardonnet, R. Ruffini, S.-S. Xue; "The GRB980425-SN1998bw Association in the EMBH Model"; in "GAMMA-RAY BURSTS: 30 YEARS OF DISCOVERY", Proceedings of the Los Alamos "Gamma Ray Burst Symposium", Santa Fe, New Mexico, 8 – 12 September 2003, E.E. Fenimore, M. Galassi, Editors; AIP Conference Proceedings, 727, 424 (2004).

   Our GRB theory, previously developed using GRB 991216 as a prototype, is here applied to GRB 980425. We fit the luminosity observed in the 40–700 keV, 2–26 keV and 2–10 keV bands by the BeppoSAX satellite. In addition the supernova SN1998bw is the outcome of an "induced gravitational collapse" triggered by GRB 980425, in agreement with the GRB-Supernova Time Sequence (GSTS) paradigm. A further outcome of this astrophysically exceptional sequence of events is the formation of a young neutron star generated by the SN1998bw event. A coordinated observational activity is recommended to further enlighten the underlying scenario of this most unique astrophysical system.

6. A. Corsi, M.G. Bernardini, C.L. Bianco, P. Chardonnet, F. Fraschetti, R. Ruffini, S.-S. Xue; "GRB 970228 Within the EMBH Model"; in "GAMMA-RAY BURSTS: 30 YEARS OF DISCOVERY", Proceedings of the Los Alamos "Gamma Ray Burst Symposium", Santa Fe, New Mexico, 8 – 12 September 2003, E.E. Fenimore, M. Galassi, Editors; AIP Conference Proceedings, 727, 428 (2004).

   We consider the gamma-ray burst of 1997 February 28 (GRB 970228) within the ElectroMagnetic Black Hole (EMBH) model. We first determine the value of the two free parameters that characterize energetically the GRB phenomenon in the EMBH model, that is to say the dyadosphere energy, $E_{dya} = 5.1 \times 10^{52}$ ergs, and the baryonic remnant mass M_B in units of E_{dya}, $B = M_B c^2 / E_{dya} = 3.0 \times 10^{-3}$. Having in this way estimated the energy emitted during the beam-target phase, we evaluate the role of the InterStellar Medium (ISM) number density (n_{ISM}) and of the ratio $\mathcal{R}$ between the effective emitting area and the total surface area of the GRB source, in reproducing the observed profiles of the GRB 970228 prompt emission and X-ray (2-10 keV energy band) afterglow. The importance of the ISM distribution three-dimensional treatment around the central black hole is also stressed in this analysis.

4 Publications (2005–2018)

4.1 Refereed journals

1. R. Ruffini, C.L. Bianco, P. Chardonnet, F. Fraschetti, V. Gurzadyan, S.-S. Xue; "Emergence of a filamentary structure in the fireball from GRB spectra"; International Journal of Modern Physics D, 14, 97 (2005).

   It is shown that the concept of a fireball with a definite filamentary structure naturally emerges from the analysis of the spectra of Gamma-Ray Bursts (GRBs). These results, made possible by the recently obtained analytic expressions of the equitemporal surfaces in the GRB afterglow, depend crucially on the single parameter R describing the effective area of the fireball emitting the X-ray and gamma-ray radiation. The X-ray and gamma-ray components of the afterglow radiation are shown to have a thermal spectrum in the co-moving frame of the fireball and originate from a stable shock front described self-consistently by the Rankine-Hugoniot equations. Precise predictions are presented on a correlation between spectral changes and intensity variations in the prompt radiation verifiable, e.g., by the Swift and future missions. The highly variable optical and radio emission depends instead on the parameters of the surrounding medium. The GRB 991216 is used as a prototype for this model.

2. R. Ruffini, M.G. Bernardini, C.L. Bianco, P. Chardonnet, F. Fraschetti, V. Gurzadyan, M. Lattanzi, L. Vitagliano, S.-S. Xue; "Extracting energy from black holes: 'long' and 'short' GRBs and their astrophysical settings"; Il Nuovo Cimento C, 28, 589 (2005).

   The introduction of the three interpretational paradigms for Gamma-Ray Bursts (GRBs) and recent progress in understanding the X- and gamma-ray luminosity in the afterglow allow us to make assessments about the astrophysical settings of GRBs. In particular, we evidence the distinct possibility that some GRBs occur in a binary system. This subclass of GRBs manifests itself in a "tryptich": one component formed by the collapse of a massive star to a black hole, which originates the GRB; a second component by a supernova and a third one by a young neutron star born in the supernova event. Similarly, the understanding of the physics of quantum relativistic processes during the gravitational collapse makes possible precise predictions about the structure of short GRBs.

3. M.G. Bernardini, C.L. Bianco, P. Chardonnet, F. Fraschetti, R. Ruffini, S.-S. Xue; "Theoretical interpretation of luminosity and spectral properties of GRB 031203"; The Astrophysical Journal, 634, L29 (2005).

   The X-ray and gamma-ray observations of the source GRB 031203 by INTEGRAL are interpreted within our theoretical model. In addition to a complete spacetime parameterization of the GRB, we specifically assume that the afterglow emission originates from a thermal spectrum in the comoving frame of the expanding baryonic matter shell. By determining the two free parameters of the model and estimating the density and filamentary structure of the ISM, we reproduce the observed luminosity in the 20-200 keV energy band. As in previous sources, the prompt radiation is shown to coincide with the peak of the afterglow, and the luminosity substructure is shown to originate in the filamentary structure of the ISM. We predict a clear hard-to-soft behavior in the instantaneous spectra. The time-integrated spectrum over 20 s observed by INTEGRAL is well fitted. Despite the fact that this source has been considered "unusual", it appears to us to be a normal low-energy GRB.

4. R. Ruffini, M.G. Bernardini, C.L. Bianco, P. Chardonnet, F. Fraschetti, S.-S. Xue; Evidence for isotropic emission in GRB991216; Advances in Space Research, 38, 1291 (2006).

   The issue of the possible presence or absence of jets in GRBs is here re-examined for GRB991216. We compare and contrast our theoretically predicted afterglow luminosity in the 2–10 keV band for spherically symmetric versus jetted emission. At these wavelengths the jetted emission can be excluded and data analysis confirms spherical symmetry. These theoretical fits are expected to be improved by the forthcoming data of the Swift mission.

5. R. Ruffini, M.G. Bernardini, C.L. Bianco, P. Chardonnet, F. Fraschetti, R. Guida, S.-S. Xue; "GRB 050315: A step toward understanding the uniqueness of the overall GRB structure"; The Astrophysical Journal, 645, L109 (2006).

Using the Swift data of GRB 050315, we are making progress toward understanding the uniqueness of our theoretically predicted gamma-ray burst (GRB) structure, which is composed of a proper GRB (P-GRB), emitted at the transparency of an electron-positron plasma with suitable baryon loading, and an afterglow comprising the so-called prompt emission due to external shocks. Thanks to the Swift observations, the P-GRB is identified, and for the first time we can theoretically fit detailed light curves for selected energy bands on a continuous timescale ranging over 106 s. The theoretically predicted instantaneous spectral distribution over the entire afterglow is presented, confirming a clear hard-to-soft behavior encompassing, continuously, the "prompt emission" all the way to the latest phases of the afterglow.

6. C.L. Bianco, L. Caito, R. Ruffini; "Theoretical interpretation of GRB 011121"; Il Nuovo Cimento B, 121, 1441 (2006).

   GRB011121 is analyzed as a prototype to understand the "flares" recently observed by Swift in the afterglow of many GRB sources. Detailed theoretical computation of the GRB011121 light curves in selected energy bands are presented and compared and contrasted with observational BeppoSAX data.

7. R. Ruffini, M.G. Bernardini, C.L. Bianco, P. Chardonnet, F. Fraschetti, R. Guida, S.-S. Xue; "GRB 050315: A step toward the uniqueness of the overall GRB structure"; Il Nuovo Cimento B, 121, 1367 (2006).

   Using the *Swift* data of GRB 050315, we progress on the uniqueness of our theoretically predicted Gamma-Ray Burst (GRB) structure as composed by a proper-GRB (P-GRB), emitted at the transparency of an electron-positron plasma with suitable baryon loading, and an afterglow comprising the so called "prompt emission" as due to external shocks. Thanks to the *Swift* observations, we can theoretically fit detailed light curves for selected energy bands on a continuous time scale ranging over 10^6 seconds. The theoretically predicted instantaneous spectral distribution over the entire afterglow confirms a clear hard-to-soft behavior encompassing, continuously, the "prompt emission" all the way to the latest phases of the afterglow. Consequences of the instrumental threshold on the definition of "short" and "long" GRBs are discussed.

8. M.G. Bernardini, C.L. Bianco, L. Caito, P. Chardonnet, A. Corsi, M.G. Dainotti, F. Fraschetti, R. Guida, R. Ruffini, S.-S. Xue; GRB970228 as a prototype for short GRBs with afterglow; Il Nuovo Cimento B, 121, 1439 (2006).

GRB970228 is analyzed as a prototype to understand the relative role of short GRBs and their associated afterglows, recently observed by Swift and HETE-II. Detailed theoretical computation of the GRB970228 light curves in selected energy bands are presented and compared with observational BeppoSAX data.

9. M.G. Dainotti, M.G. Bernardini, C.L. Bianco, L. Caito, R. Guida, R. Ruffini; "GRB060218 and GRBs associated with Supernovae Ib/c"; Astronomy & Astrophysics, 471, L29 (2007).

   Context: The *Swift* satellite has given continuous data in the range 0.3–150 keV from 0 s to 10^6 s for GRB060218 associated with SN2006aj. This Gamma-Ray Burst (GRB) which has an unusually long duration ($T_{90} \sim 2100$ s) fulfills the Amati relation. These data offer the opportunity to probe theoretical models for GRBs connected with Supernovae (SNe).
   Aims: We plan to fit the complete γ- and X-ray light curves of this long duration GRB, including the prompt emission, in order to clarify the nature of the progenitors and the astrophysical scenario of the class of GRBs associated with SNe Ib/c.
   Methods: We apply our "fireshell" model based on the formation of a black hole, giving the relevant references. It is characterized by the precise equations of motion and equitemporal surfaces and by the role of thermal emission.
   Results: The initial total energy of the electron-positron plasma $E_{e^\pm}^{tot} = 2.32 \times 10^{50}$ erg has a particularly low value, similar to the other GRBs associated with SNe. For the first time, we observe a baryon loading $B = 10^{-2}$ which coincides with the upper limit for the dynamical stability of the fireshell. The effective CircumBurst Medium (CBM) density shows a radial dependence $n_{cbm} \propto r^{-\alpha}$ with $1.0 \lesssim \alpha \lesssim 1.7$ and monotonically decreases from 1 to 10^{-6} particles/cm^3. This behavior is interpreted as being due to a fragmentation in the fireshell. Analogies with the fragmented density and filling factor characterizing Novae are outlined. The fit presented is particularly significant in view of the complete data set available for GRB060218 and of the fact that it fulfills the Amati relation.
   Conclusions: We fit GRB060218, usually considered as an X-Ray Flash (XRF), as a "canonical GRB" within our theoretical model. The smallest possible black hole, formed by the gravitational collapse of a neutron star in a binary system, is consistent with the especially low energetics of the class of GRBs associated with SNe Ib/c. We provide the first evidence for a fragmentation in the fireshell. This fragmentation is crucial in explaining both the unusually large T_{90} and the consequently inferred abnormally low value of the CBM effective

density.

10. M.G. Bernardini, C.L. Bianco, L. Caito, M.G. Dainotti, R. Guida, R. Ruffini; "GRB970228 and a class of GRBs with an initial spikelike emission"; Astronomy & Astrophysics, 474, L13 (2007).

    Context: The discovery by *Swift* and HETE-2 of an afterglow emission associated possibly with short GRBs opened the new problematic of their nature and classification. This issue has been further enhanced by the observation of GRB060614 and by a new analysis of the BATSE catalog which led to the identification of a new class of GRBs with "an occasional softer extended emission lasting tenths of seconds after an initial spikelike emission".
    Aims: We plan a twofold task: a) to fit this new class of "hybrid" sources within our "canonical GRB" scenario, where all GRBs are generated by a "common engine" (i.e. the gravitational collapse to a black hole); b) to propose GRB970228 as the prototype of the above mentioned class, since it shares the same morphology and observational features.
    Methods: We analyze *Beppo*SAX data on GRB970228 within the "fireshell" model and we determine the parameters describing the source and the CircumBurst Medium (CBM) needed to reproduce its light curves in the 40–700 keV and 2–26 keV energy bands.
    Results: We find that GRB970228 is a "canonical GRB", like e.g. GRB050315, with the main peculiarity of a particularly low average density of the CBM $\langle n_{cbm} \rangle \sim 10^{-3}$ particles/cm^3. We also simulate the light curve corresponding to a rescaled CBM density profile with $\langle n_{cbm} \rangle = 1$ particle/cm^3. From such a comparison it follows that the total time-integrated luminosity is a faithful indicator of the nature of GRBs, contrary to the peak luminosity which is merely a function of the CBM density.
    Conclusions: We call attention on discriminating the short GRBs between the "genuine" and the "fake" ones. The "genuine" ones are intrinsically short, with baryon loading $B \lesssim 10^{-5}$, as stated in our original classification. The "fake" ones, characterized by an initial spikelike emission followed by an extended emission lasting tenths of seconds, have a baryon loading $10^{-4} \lesssim B \leq 10^{-2}$. They are observed as such only due to an underdense CBM consistent with a galactic halo environment which deflates the afterglow intensity.

11. R. Guida, M.G. Bernardini, C.L. Bianco, L. Caito, M.G. Dainotti, R. Ruffini; "The Amati relation in the "fireshell" model"; Astronomy & Astrophysics, 487, L37 (2008).

Context: The cosmological origin of gamma-ray bursts (GRBs) has been firmly established, with redshifts up to $z = 6.29$. They are possible candidates for use as "distance indicators" for testing cosmological models in a redshift range hardly achievable by other cosmological probes. Asserting the validity of the empirical relations among GRB observables is now crucial for their calibration.
Aims: Motivated by the relation proposed by Amati and collaborators, we look within the "fireshell" model for a relation between the peak energy E_p of the νF_ν total time-integrated spectrum of the afterglow and the total energy of the afterglow E_{aft}, which in our model encompasses and extends the prompt emission.
Methods: The fit within the fireshell model, as for the "canonical" GRB050315, uses the complete arrival time coverage given by the Swift satellite. It is performed simultaneously, self-consistently, and recursively in the four BAT energy bands (15–25 keV, 25–50 keV, 50–100 keV, and 100-150 keV), as well as in the XRT one (0.2–10 keV). It uniquely determines the two free parameters characterizing the GRB source, the total energy $E_{tot}^{e^\pm}$ of the $e^\pm$ plasma and its baryon loading B, as well as the effective CircumBurst Medium (CBM) distribution. We can then build two sets of "gedanken" GRBs varying the total energy of the electron-positron plasma $E_{tot}^{e^\pm}$ and keeping the same baryon loading B of GRB050315. The first set assumes the one obtained in the fit of GRB050315 for the effective CBM density. The second set assumes instead a constant CBM density equal to the average value of the GRB050315 prompt phase.
Results: For the first set of "gedanken" GRBs we find a relation $E_p \propto (E_{aft})^a$, with $a = 0.45 \pm 0.01$, whose slope strictly agrees with the Amati one. Such a relation, in the limit $B \to 10^{-2}$, coincides with the Amati one. Instead, no correlation is found in the second set of "gedanken" GRBs.
Conclusions: Our analysis excludes the proper GRB (P-GRB) from the prompt emission, extends all the way to the latest afterglow phases, and is independent of the assumed cosmological model, since all "gedanken" GRBs are at the same redshift. The Amati relation, on the other hand, includes the P-GRB, focuses only on the prompt emission, being therefore influenced by the instrumental threshold that fixes the end of the prompt emission, and depends on the assumed cosmology. This might explain the intrinsic scatter observed in the Amati relation.

12. L. Caito, M.G. Bernardini, C.L. Bianco, M.G. Dainotti, R. Guida, R. Ruffini; "GRB060614: a "fake" short GRB from a merging binary system"; Astronomy & Astrophysics, 489, 501 (2009).

Context: GRB060614 observations by VLT and by Swift have infringed the traditionally accepted gamma-ray burst (GRB) collapsar scenario that purports the origin of all long duration GRBs from supernovae (SN). GRB060614 is the first nearby long duration GRB clearly not associated with a bright Ib/c SN. Moreover, its duration ($T_{90} \sim 100$ s) makes it hardly classifiable as a short GRB. It presents strong similarities with GRB970228, the prototype of a new class of "fake" short GRBs that appear to originate from the coalescence of binary neutron stars or white dwarfs spiraled out into the galactic halo. *Aims*: Within the "canonical" GRB scenario based on the "fireshell" model, we test if GRB060614 can be a "fake" or "disguised" short GRB. We model the traditionally termed "prompt emission" and discriminate the signal originating from the gravitational collapse leading to the GRB from the process occurring in the circumburst medium (CBM). *Methods*: We fit GRB060614 light curves in Swift's BAT ($15 - 150$ keV) and XRT ($0.2 - 10$ keV) energy bands. Within the fireshell model, light curves are formed by two well defined and different components: the proper-GRB (P-GRB), emitted when the fireshell becomes transparent, and the extended afterglow, due to the interaction between the leftover accelerated baryonic and leptonic shell and the CBM. *Results*: We determine the two free parameters describing the GRB source within the fireshell model: the total $e^{\pm}$ plasma energy ($E_{tot}^{e^{\pm}} = 2.94 \times 10^{51}$erg) and baryon loading ($B = 2.8 \times 10^{-3}$). A small average CBM density $\sim 10^{-3}$ particles/cm^3 is inferred, typical of galactic halos. The first spikelike emission is identified with the P-GRB and the following prolonged emission with the extended afterglow peak. We obtain very good agreement in the BAT ($15 - 150$ keV) energy band, in what is traditionally called "prompt emission", and in the XRT ($0.2 - 10$ keV) one. *Conclusions*: The *anomalous* GRB060614 finds a natural interpretation within our canonical GRB scenario: it is a "disguised" short GRB. The total time-integrated extended afterglow luminosity is greater than the P-GRB one, but its peak luminosity is smaller since it is deflated by the peculiarly low average CBM density of galactic halos. This result points to an old binary system, likely formed by a white dwarf and a neutron star, as the progenitor of GRB060614 and well justifies the absence of an associated SN Ib/c. Particularly important for further studies of the final merging process are the temporal structures in the P-GRB down to 0.1 s.

13. M.G. Bernardini, C.L. Bianco, L. Caito, M.G. Dainotti, R. Guida, R. Ruffini; "GRB970228 in the "canonical GRB" scenario"; Journal of the Korean Physical Society, 56, 1575 (2010).

Within the "fireshell" model, we define a "canonical GRB" light curve with two sharply different components: the proper-GRB (P-GRB), emitted when the optically thick fireshell of an electron-positron plasma originating from the phenomenon reaches transparency, and the afterglow, emitted due to the collision between the remaining optically thin fireshell and the circumburst medium (CBM). On the basis of the recent understanding of GRB970228 as the prototype for a new class of GRBs with "an occasional softer extended emission lasting tenths of seconds after an initial spikelike emission", we outline our "canonical GRB" scenario, originating from the gravitational collapse to a black hole, with special emphasis on the discrimination between "genuine" and "fake" short GRBs. Furthermore, we investigate how the GRB970228 analysis provides a theoretical explanation for the apparent absence of such a correlation for the GRBs belonging to this new class.

14. L. Caito, M.G. Bernardini, C.L. Bianco, M.G. Dainotti, R. Guida, R. Ruffini; "GRB060614: a preliminary result"; Journal of the Korean Physical Society, 56, 1579 (2010).

    The explosion of GRB 060614 produced a deep break in the GRB scenario and opened new horizons of investigation because it can't be traced back to any traditional scheme of classification. In fact, it manifests peculiarities both of long bursts and of short bursts, and above all, it is the first case of a long-duration near GRB without any bright Ib/c associated Supernova. We will show that, in our canonical GRB scenario, this "anomalous" situation finds a natural interpretation and allows us to discuss a possible variation in the traditional classification scheme, introducing a distinction between "genuine" and "fake" short bursts.

15. M.G. Dainotti, M.G. Bernardini, C.L. Bianco, L. Caito, R. Guida, R. Ruffini; "The astrophysical trypthic: GRB, SN and URCA can be extended to GRB060218?"; Journal of the Korean Physical Society, 56, 1588 (2010).

    The *Swift* satellite has given continuous data in the range 0.3–150 keV from 0 s to 10^6 s for GRB060218 associated with SN2006aj. This GRB is the fourth GRB spectroscopically associated with SNe after the cases of GRB980425-SN1998bw, GRB031203-SN2003lw, GRB 030329-SN2003dh. It has an unusually long duration ($T_{90} \sim 2100$ s). These data offer the opportunity to probe theoretical models for Gamma-Ray Bursts (GRBs) connected with Supernovae (SNe). We plan to fit the complete γ- and X-ray light curves of this long duration GRB, including the prompt emission, in order to clarify the nature of the progenitors and the astrophysical scenario of the class of GRBs associated to SNe Ib/c. We apply our "fireshell" model based on the formation of a black hole, giving the relevant references. The initial total energy of the electron-positron plasma $E^{tot}_{e^\pm} = 2.32 \times 10^{50}$ erg has a particularly low value similarly to the other GRBs associated with SNe. For the first time we observe a baryon loading $B = 10^{-2}$ which coincides with the upper limit for the dynamical stability of the fireshell. The effective CircumBurst Medium (CBM) density shows a radial dependence $n_{cbm} \propto r^{-\alpha}$ with $1.0 \lesssim \alpha \lesssim 1.7$ and monotonically decreases from 1 to 10^{-6} particles/cm^3. Such a behavior is interpreted as due to a fragmentation in the fireshell. Such a fragmentation is crucial in explaining both the unusually large T_{90} and the consequently inferred abnormal low value of the CBM effective density. We fit GRB060218, usually considered as an X-Ray Flash (XRF), as a "canonical GRB" within our theoretical model. The smallest possible black hole, formed by the gravitational collapse of a neutron star in a binary system, is consistent with the especially low energetics of the class of GRBs associated with SNe Ib/c. We present the URCA process and the connection between the GRBs associated with SNe extended also to the case of GRB060218.

16. L. Izzo, M.G. Bernardini, C.L. Bianco, L. Caito, B. Patricelli, R. Ruffini; "GRB 090423 at Redshift 8.1: a Theoretical Interpretation"; Journal of the Korean Physical Society, 57, 551 (2010).

    GRB 090423 is the farthest gamma ray burst ever observed, with a redshift of about 8.1. We present within the fireshell scenario a complete analysis of this GRB. We model the prompt emission and the first rapid flux decay of the afterglow emission as being to the canonical emission of the interaction in the interval $0 \leq t \leq 440$ s by using accelerated baryonic matter with the circumburst medium. After the data reduction of the Swift data in the BAT (15 - 150 keV) and XRT (0.2 - 10 keV) energy bands, we interpret the light curves and the spectral distribution in the context of the fireshell scenario. We also confirm in this source the existence of a second component, a plateau phase, as being responsible for the late emission in the X-ray light curve. This extra component originates from the fact that the ejecta have a range of the bulk Lorentz Γ factor, which starts to interact each other ejecta at the start of the plateau phase.

17. L. Caito, L. Amati, M.G. Bernardini, C.L. Bianco, G. De Barros, L. Izzo, B. Patricelli, R. Ruffini; "GRB 071227: an additional case of a disguised

short burst"; Astronomy & Astrophysics, 521, A80 (2010).

Context: Observations of gamma-ray bursts (GRBs) have shown an hybridization between the two classes of long and short bursts. In the context of the fireshell model, the GRB light curves are formed by two different components: the *proper* GRB (P-GRB) and the extended afterglow. Their relative intensity is linked to the fireshell baryon loading B. The GRBs with P-GRB predominance are the short ones, the remainders are long. A new family of *disguised* short bursts has been identified: long bursts with a protracted low instantaneous luminosity due to a low density CircumBurst Medium (CBM). In the 15–150 keV energy band GRB 071227 exhibits a short duration (about 1.8s) spike-like emission followed by a very soft extended tail up to one hundred seconds after the trigger. It is a faint ($E_{iso} = 5.8 \times 10^{50}$) nearby GRB ($z = 0.383$) that does not have an associated type Ib/c bright supernova (SN). For these reasons, GRB 071227 has been classified as a short burst not fulfilling the Amati relation holding for long burst. *Aims:* We check the classification of GRB 071227 provided by the fireshell model. In particular, we test whether this burst is another example of a *disguised* short burst, after GRB 970228 and GRB 060614, and, for this reason, whether it fulfills the Amati relation. *Methods:* We simulate GRB 071227 light curves in the *Swift* BAT 15–50 keV bandpass and in the XRT (0.3–10 keV) energy band within the fireshell model. *Results:* We perform simulations of the tail in the 15–50 keV bandpass, as well as of the first part of the X-ray afterglow. This infers that: $E_{tot}^{e^\pm} = 5.04 \times 10^{51}$ erg, $B = 2.0 \times 10^{-4}$, $E_{P-GRB}/E_{aft} \sim 0.25$, and $\langle n_{cbm} \rangle = 3.33$ particles/cm^3. These values are consistent with those of "long duration" GRBs. We interpret the observed energy of the first hard emission by identifying it with the P-GRB emission. The remaining long soft tail indeed fulfills the Amati relation. *Conclusions:* Previously classified as a short burst, GRB 071227 on the basis of our analysis performed in the context of the fireshell scenario represents another example of a *disguised* short burst, after GRB 970228 and GRB 060614. Further confirmation of this result is that the soft tail of GRB 071227 fulfills the Amati relation.

18. M.G. Bernardini, C.L. Bianco, L. Caito, L. Izzo, B. Patricelli, R. Ruffini; "Analysis of GRB060607A within the fireshell model: prompt emission, X-ray flares and late afterglow phase"; Astronomy & Astrophysics, submitted to.

Context: GRB060607A is a very distant ($z = 3.082$) and energetic event ($E_{iso} \sim 10^{53}$ erg). Its main peculiarity is that the peak of the near-infrared (NIR) afterglow has been observed with the REM robotic telescope. This NIR peak has been interpreted as the afterglow onset within the fireball forward shock model, and the initial Lorentz gamma factor of the emitting system has been inferred. *Aims*: We analyze GRB060607A within the fireshell model. We emphasize the central role of the prompt emission in determining the initial Lorentz gamma factor of the extended afterglow and we interpret the X-ray flares as produced by the interaction of the optically thin fireshell with overdense CircumBurst Medium (CBM) clumps. *Methods*: We deal only with the Swift BAT and XRT observations, that are the basic contribution to the GRB emission and that are neglected in the treatment adopted in the current literature. The numerical modeling of the fireshell dynamics allows to calculate all its characteristic quantities, in particular the exact value of the Lorentz gamma factor at the transparency. *Results*: We show that the theoretically computed prompt emission light curves are in good agreement with the observations in all the *Swift* BAT energy bands as well as the spectra integrated over different time intervals. The flares observed in the decaying phase of the X-ray afterglow are also reproduced by the same mechanism, but in a region in which the typical dimensions of the clumps are smaller than the visible area of the fireshell and most energy lies in the X-ray band due to the hard-to-soft evolution. *Conclusions*: We show that it is possible to obtain flares with $\Delta t/t$ compatible with the observations when the three-dimensional structure of the CBM clumps is duly taken into account. We stop our analysis at the beginning of the X-ray plateau phase, since we suppose this originates from the instabilities developed in the collision between different subshells within a structured fireshell.

19. G. de Barros, M. G. Bernardini, C.L. Bianco, L. Caito, L. Izzo, B. Patricelli, R. Ruffini; "On the nature of GRB 050509b: a disguised short GRB"; Astronomy & Astrophyscs, 529, A130 (2011)

    Context: GRB 050509b, detected by the *Swift* satellite, is the first case where an X-ray afterglow has been observed associated with a short gamma-ray burst (GRB). Within the fireshell model, the canonical GRB light curve presents two different components: the proper-GRB (P-GRB) and the extended afterglow. Their relative intensity is a function of the fireshell baryon loading parameter B and of the CircumBurst Medium (CBM) density (n_{CBM}). In particular, the traditionally called short GRBs can be either "genuine" short GRBs (with $B \lesssim 10^{-5}$, where the P-GRB is energetically predominant) or "disguised" short GRBs (with $B \gtrsim 3.0 \times 10^{-4}$ and $n_{CBM} \ll 1$, where the extended afterglow is energetically predominant). *Aims*: We verify whether GRB 050509b can be classified as a "genuine" short or a "disguised" short GRB, in the fireshell model. *Methods*: We investigate two alternative scenarios. In the first, we start from the assumption that this GRB is a "genuine" short burst. In the second attempt, we assume that this GRB is a "disguised" burst. *Results*: If GRB 050509b were a genuine short GRB, there should initially be very hard emission which is ruled out by the observations. The analysis that assumes that this is a disguised short GRB is compatible with the observations. The theoretical model predicts a value of the extended afterglow energy peak that is consistent with the Amati relation. *Conclusions*: GRB 050509b cannot be classified as a "genuine" short GRB. The observational data are consistent with a "disguised" short GRB classification, i.e., a long burst with a weak extended afterglow "deflated" by the low density of the CBM. We expect that all short GRBs with measured redshifts are disguised short GRBs because of a selection effect: if there is enough energy in the afterglow to measure the redshift, then the proper GRB must be less energetic than the afterglow. The Amati relation is found to be fulfilled only by the extended afterglow excluding the P-GRB.

20. L. Caito, M.G. Bernardini, C.L. Bianco, L. Izzo, B. Patricelli, R. Ruffini; "GRB 071227: another disguised short burst"; International Journal of Modern Physics D, 20, 1931 (2011).

Observations of Gamma-ray Bursts (GRBs) put forward in the recent years have revealed, with increasing evidence, that the historical classification between long and short bursts has to be revised. Within the Fireshell scenario, both short and long bursts are canonical bursts, consisting of two different phases. First, a Proper-GRB (P-GRB), that is the emission of photons at the transparency of the fireshell. Then, the Extended Afterglow, multiwavelength emission due to the interacion of the baryonic remnants of the fireshell with the CircumBurst Medium (CBM). We discriminate between long and short bursts by the amount of energy stored in the first phase with respect to the second one. Within the Fireshell scenario, we have introduced a third intermediate class: the disguised GRBs. They appear like short bursts, because their morphology is characterized by a first, short, hard episode and a following deflated tail, but this last part — coincident with the peak of the afterglow — is energetically predominant. The origin of this peculiar kind of sources is inferred to a very low average density of the environment (of the order of 10^{-3}). After GRB 970228 and GRB 060614, we find in GRB 071227 a third example of disguised burst.

21. L. Izzo, M.G. Bernardini, C.L. Bianco, L. Caito, B. Patricelli, L.J. Rangel Lemos, R. Ruffini; "GRB 080916C and the high-energy emission in the fireshell scenario"; International Journal of Modern Physics D, 20, 1949 (2011).

    In this paper we discuss a possible explanation for the high energy emission (up to $\sim$ GeV) seen in GRB 080916C. We propose that the GeV emission is originated by the collision between relativistic baryons in the fireshell after the transparency and the nucleons located in molecular clouds near the burst site. This collision should give rise pion production, whose immediate decay provides high energy photons, neutrinos and leptons. Using a public code (SYBILL) we simulate these relativistic collisions in their simple form, so that we can draw our preliminar results in this paper. We will present moreover our hypothesis that the delayed onset of this emission identifies in a complete way the P-GRB emission.

22. B. Patricelli, M.G. Bernardini, C.L. Bianco, L. Caito, L. Izzo, R. Ruffini, G. Vereshchagin; "A new spectral energy distribution of photons in the fireshell model of GRBs"; International Journal of Modern Physics D, 20, 1983 (2011).

    The analysis of various Gamma-Ray Bursts (GRBs) having a low energetics (an isotropic energy $E_{iso} \lesssim 10^{53}$ ergs) within the fireshell model has shown how the $N(E)$ spectrum of their prompt emission can be reproduced in a satisfactory way by a convolution of thermal spectra. Nevertheless, from the study of very energetic bursts ($E_{iso} \lesssim 10^{54}$ ergs) such as, for example, GRB 080319B, some discrepancies between the numerical simulations and the observational data have been observed. We investigate a different spectrum of photons in the comoving frame of the fireshell in order to better reproduce the spectral properties of GRB prompt emission within the fireshell model. We introduce a phenomenologically modified thermal spectrum: a thermal spectrum characterized by a different asymptotic power-law index in the low energy region. Such an index depends on a free parameter α, so that the pure thermal spectrum corresponds to the case $\alpha = 0$. We test this spectrum by comparing the numerical simulations with the observed prompt emission spectra of various GRBs. From this analysis it has emerged that the observational data can be correctly reproduced by assuming a modified thermal spectrum with $\alpha = -1.8$.

23. A.V. Penacchioni, R. Ruffini, L. Izzo, M. Muccino, C.L. Bianco, L. Caito, B. Patricelli, L. Amati; "Evidence for a proto-black hole and a double

astrophysical component in GRB 101023"; Astronomy & Astrophysics, 538, A58 (2012).

Context: It has been recently shown that GRB 090618, observed by AGILE, Coronas Photon, Fermi, Konus, Suzaku and Swift, is composed of two very different components: episode 1, lasting 50 s, shows a thermal plus power-law spectrum with a characteristic temperature evolving in time as a power law; episode 2 (the remaining 100 s) is a canonical long GRB. We have associated episode 1 to the progenitor of a collapsing bare core leading to the formation of a black hole: what was defined as a "proto black hole". *Aims*: In precise analogy with GRB 090618 we aim to analyze the 89s of the emission of GRB 101023, observed by Fermi, Gemini, Konus and Swift, to see if there are two different episodes: the first one presenting a characteristic black-body temperature evolving in time as a broken power law, and the second one consistent with a canonical GRB. *Methods*: To obtain information on the spectra, we analyzed the data provided by the GBM detector onboard the Fermi satellite, and we used the heasoft package XSPEC and RMFIT to obtain their spectral distribution. We also used the numerical code GRBsim to simulate the emission in the context of the fireshell scenario for episode 2. *Results*: We confirm that the first episode can be well fit by a black body plus power-law spectral model. The temperature changes with time following a broken power law, and the photon index of the power-law component presents a soft-to-hard evolution. We estimate that the radius of this source increases with time with a velocity of $1.5 \times 10^4 km/s$. The second episode appears to be a canonical GRB. By using the Amati and the Atteia relations, we determined the cosmological redshift, $z \sim 0.9 \pm 0.084(stat.) \pm 0.2(sys.)$. The results of GRB 090618 are compared and contrasted with the results of GRB 101023. Particularly striking is the scaling law of the soft X-ray component of the afterglow. *Conclusions*: We identify GRB 090618 and GRB 101023 with a new family of GRBs related to a single core collapse and presenting two astrophysical components: a first one related to the proto-black hole prior to the process of gravitational collapse (episode 1), and a second one, which is the canonical GRB (episode 2) emitted during the formation of the black hole. For the first time we are witnessing the process of a black hole formation from the instants preceding the gravitational collapse up to the GRB emission. This analysis indicates progress towards developing a GRB distance indicator based on understanding the P-GRB and the prompt emission, as well as the soft X-ray behavior of the late afterglow.

24. R. Negreiros, R. Ruffini, C. L. Bianco, J. A. Rueda; "Cooling of young

neutron stars in GRB associated to supernovae"; Astronomy & Astrophysics, 540, A12 (2012).

Context: The traditional study of neutron star cooling has been generally applied to quite old objects such as the Crab Pulsar (957 years) or the central compact object in Cassiopeia A (330 years) with an observed surface temperature $\sim 10^6$ K. However, recent observations of the late ($t = 10^8$–10^9 s) emission of the supernovae (SNe) associated to GRBs (GRB-SN) show a distinctive emission in the X-ray regime consistent with temperatures $\sim 10^7$–10^8 K. Similar features have been also observed in two Type Ic SNe SN 2002ap and SN 1994I that are not associated to GRBs. *Aims*: We advance the possibility that the late X-ray emission observed in GRB-SN and in isolated SN is associated to a hot neutron star just formed in the SN event, here defined as a neo-neutron star. *Methods*: We discuss the thermal evolution of neo-neutron stars in the age regime that spans from ~ 1 minute (just after the proto-neutron star phase) all the way up to ages < 10–100 yr. We examine critically the key factor governing the neo-neutron star cooling with special emphasis on the neutrino emission. We introduce a phenomenological heating source, as well as new boundary conditions, in order to mimic the high temperature of the atmosphere for young neutron stars. In this way we match the neo-neutron star luminosity to the observed late X-ray emission of the GRB-SN events: URCA-1 in GRB980425-SN1998bw, URCA-2 in GRB030329-SN2003dh, and URCA-3 in GRB031203-SN2003lw. *Results*: We identify the major role played by the neutrino emissivity in the thermal evolution of neo-neutron stars. By calibrating our additional heating source at early times to $\sim 10^{12}$–10^{15} erg/g/s, we find a striking agreement of the luminosity obtained from the cooling of a neo-neutron stars with the prolonged ($t = 10^8$–10^9 s) X-ray emission observed in GRB associated with SN. It is therefore appropriate a revision of the boundary conditions usually used in the thermal cooling theory of neutron stars, to match the proper conditions of the atmosphere at young ages. The traditional thermal processes taking place in the crust might be enhanced by the extreme high-temperature conditions of a neo-neutron star. Additional heating processes that are still not studied within this context, such as e^+e^- pair creation by overcritical fields, nuclear fusion, and fission energy release, might also take place under such conditions and deserve further analysis. *Conclusions*: Observation of GRB-SN has shown the possibility of witnessing the thermal evolution of neo-neutron stars. A new campaign of dedicated observations is recommended both of GRB-SN and of isolated Type Ic SN.

25. L. Izzo, R. Ruffini, A.V. Penacchioni, C.L. Bianco, L. Caito, S.K. Chakrabarti, J.A. Rueda, A. Nandi, B. Patricelli; “A double component in GRB 090618: a proto-black hole and a genuinely long gamma-ray burst”; Astronomy & Astrophysics, 543, A10 (2012).

    Context: The joint X-ray and gamma-ray observations of GRB 090618 by very many satellites offer an unprecedented possibility of testing crucial aspects of theoretical models. In particular, they allow us to test (a) in the process of gravitational collapse, the formation of an optically thick e+e.-baryon plasma self-accelerating to Lorentz factors in the range $200 < \Gamma < 3000$; (b) its transparency condition with the emission of a component of 10^{53-54} baryons in the TeV region and (c) the collision of these baryons with the circumburst medium (CBM) clouds, characterized by dimensions of 10^{15-16} cm. In addition, these observations offer the possibility of testing a new understanding of the thermal and power-law components in the early phase of this GRB. *Aims*: We test the fireshell model of GRBs in one of the closest ($z = 0.54$) and most energetic ($E_{iso} = 2.90 \times 10^{53}$ erg) GRBs, namely GRB 090618. It was observed at ideal conditions by several satellites, namely *Fermi*, *Swift*, Konus-WIND, AGILE, RT-2, and Suzaku, as well as from on-ground optical observatories. *Methods*: We analyzed the emission from GRB 090618 using several spectral models, with special attention to the thermal and power-law components. We determined the fundamental parameters of a canonical GRB within the context of the fireshell model, including the identification of the total energy of the e^+e^- plasma, E_{tot}^{e+e-}, the proper GRB (P-GRB), the baryon load, the density and structure of the CBM. *Results*: We find evidence of the existence of two different episodes in GRB 090618. The first episode lasts 50 s and is characterized by a spectrum consisting of a thermal component, which evolves between $kT = 54$ keV and $kT = 12$ keV, and a power law with an average index $\gamma = 1.75 \pm 0.04$. The second episode, which lasts for ~ 100 s, behaves as a canonical long GRB with a Lorentz gamma factor at transparency of $\Gamma = 495$, a temperature at transparency of 29.22 keV and with a characteristic size of the surrounding clouds of $R_{cl} \sim 10^{15-16}$ cm and masses of $\sim 10^{22-24}$ g. *Conclusions*: We support the recently proposed two-component nature of GRB 090618, namely, episode 1 and episode 2, with a specific theoretical analysis.We furthermore illustrate that episode 1 cannot be considered to be either a GRB or a part of a GRB event, but it appears to be related to the progenitor of the collapsing bare core, leading to the formation of the black hole, which we call a “proto-black hole”. Thus, for the first time, we are witnessing the process of formation of a black hole from the phases just preceding the gravitational collapse all the way up to the GRB emission.

26. B. Patricelli, M.G. Bernardini, C.L. Bianco, L. Caito, G. De Barros, L. Izzo, R. Ruffini, G.V. Vereshchagin; "Analysis of GRB 080319B and GRB 050904 within the Fireshell Model: Evidence for a Broader Spectral Energy Distribution"; The Astrophysical Journal, 756, 16 (2012).

    The observation of GRB 080319B, with an isotropic energy $E_{iso} = 1.32 \times 10^{54}$ erg, and GRB 050904, with $E_{iso} = 1.04 \times 10^{54}$ erg, offers the possibility of studying the spectral properties of the prompt radiation of two of the most energetic Gamma Ray Bursts (GRBs). This allows us to probe the validity of the fireshell model for GRBs beyond 10^{54} erg, well outside the energy range where it has been successfully tested up to now (10^{49}–10^{53} erg). We find that in the low energy region, the prompt emission spectra observed by *Swift* BAT reveals more power than theoretically predicted. The opportunities offered by these observations to improve the fireshell model are outlined in this paper. One of the distinguishing features of the fireshell model is that it relates the observed GRB spectra to the spectrum in the comoving frame of the fireshell. Originally, a fully radiative condition and a comoving thermal spectrum were adopted. An additional power-law in the comoving thermal spectrum is required due to the discrepancy of the theoretical and observed light curves and spectra in the fireshell model for GRBs 080319B and 050904. A new phenomenological parameter α is correspondingly introduced in the model. We perform numerical simulations of the prompt emission in the *Swift* BAT bandpass by assuming different values of α within the fireshell model. We compare them with the GRB 080319B and GRB 050904 observed time-resolved spectra, as well as with their time-integrated spectra and light curves. Although GRB 080319B and GRB 050904 are at very different redshifts (z=0.937 and z=6.29 respectively), a value of $\alpha = -1.8$ leads for both of them to a good agreement between the numerical simulations and the observed BAT light curves, time-resolved and time-integrated spectra. Such a modified spectrum is also consistent with the observations of previously analyzed less energetic GRBs and reasons for this additional agreement are given. Perspectives for future low energy missions are outlined.

27. M. Muccino, R. Ruffini, C.L. Bianco, L. Izzo, A.V. Penacchioni; "GRB 090227B: The missing link between the genuine short and long GRBs"; The Astrophysical Journal, 763, 125 (2013).

The time-resolved spectral analysis of GRB 090227B, made possible by the *Fermi*-GBM data, allows to identify in this source the missing link between the genuine short and long GRBs. Within the Fireshell model of the Gamma-Ray Bursts (GRBs) we predict genuine short GRBs: bursts with the same inner engine of the long bursts but endowed with a severely low value of the Baryon load, $B \lesssim 5 \times 10^{-5}$. A first energetically predominant emission occurs at the transparency of the e^+e^- plasma, the Proper-GRB (P-GRB), followed by a softer emission, the extended afterglow. The typical separation between the two emissions is expected to be of the order of 10^{-3} – 10^{-2} s. We identify the P-GRB of GRB 090227B in the first 96 ms of emission, where a thermal component with the temperature $kT = (517 \pm 28)$ keV and a flux comparable with the non thermal part of the spectrum is observed. This non thermal component as well as the subsequent emission, where there is no evidence for a thermal spectrum, is identified with the extended afterglow. We deduce a theoretical cosmological redshift $z = 1.61 \pm 0.14$. We then derive the total energy $E^{tot}_{e^+e^-} = (2.83 \pm 0.15) \times 10^{53}$ ergs, the Baryon load $B = (4.13 \pm 0.05) \times 10^{-5}$, the Lorentz Γ factor at transparency $\Gamma_{tr} = (1.44 \pm 0.01) \times 10^4$, and the intrinsic duration $\Delta t' \sim 0.35$ s. We also determine the average density of the CircumBurst Medium (CBM), $\langle n_{CBM} \rangle = (1.90 \pm 0.20) \times 10^{-5}$ particles/cm^3. There is no evidence of beaming in the system. In view of the energetics and of the Baryon load of the source, as well as of the low interstellar medium and of the intrinsic time scale of the signal, we identify the GRB progenitor as a binary neutron star. From the recent progress in the theory of neutron stars, we obtain masses of the stars $m_1 = m_2 = 1.34 M_\odot$ and their corresponding radii $R_1 = R_2 = 12.24$ km and thickness of their crusts ~ 0.47 km, consistent with the above values of the Baryon load, of the energetics and of the time duration of the event.

28. A.V. Penacchioni, R. Ruffini, C.L. Bianco, L. Izzo, M. Muccino, G.B. Pisani, J.A. Rueda; "GRB 110709B in the induced gravitational collapse paradigm"; Astronomy & Astrophysics, 551, A133 (2013).

    Context: GRB 110709B is the first source for which *Swift* BAT triggered twice, with a time separation of ~ 10 minutes. The first emission (called here Episode 1) goes from 40 s before the first trigger up to 60 s after it. The second emission (hereafter Episode 2) goes from 35 s before the second trigger to 100 s after it. These features reproduce the ones of GRB 090618, which has been recently interpreted within the Induced Gravitational Collapse paradigm (IGC). In line with this paradigm we assume the progenitor to be a close binary system composed of a core of an evolved star and a Neutron Star (NS). The evolved star explodes as a Supernova (SN) and ejects material that is partially accreted by the NS. We identify this process with Episode 1. The accretion process brings the NS over its critical mass, thus gravitationally collapsing to a BH. This process leads to the GRB emission, Episode 2. The double trigger has given for the first time the possibility to have a coverage of the X-ray emission observed by XRT both prior to and during the prompt phase of GRB 110709B. *Aims*: We analyze the spectra and time variability of Episode 1 and 2 and compute the relevant parameters of the binary progenitor, as well as the astrophysical parameters both in the SN and the GRB phase in the IGC paradigm. *Methods*: We perform a time-resolved spectral analysis of Episode 1 by fitting the spectrum with a blackbody (BB) plus a power-law (PL) spectral model. From the BB fluxes and temperatures of Episode 1 and the luminosity distance d_L, we evaluate the evolution with time of the radius of the BB emitter, associated here to the evolution of the SN ejecta. We analyze Episode 2 within the Fireshell model, identifying the Proper-GRB (P-GRB) and simulating the light curve and spectrum. We establish the redshift to be $z = 0.75$, following the phenomenological methods by Amati, by Yonetoku and by Grupe, and our analysis of the late X-ray afterglow. It is most remarkable that the determination of the cosmological redshift on the ground of the scaling of the late X-ray afterglow, already verified in GRB 090618 and GRB 101023, is again verified by this analysis. *Results*: We find for Episode 1 a temperature of the BB component that evolves with time following a broken PL, with the slope of the PL at early times $\alpha = 0$ (constant function) and the slope of the PL at late times $\beta = -4 \pm 2$. The break occurs at $t = 41.21$ s. The total energy of Episode 1 is $E_{iso}^{(1)} = 1.42 \times 10^{53}$ erg. The total energy of Episode 2 is $E_{iso}^{(2)} = 2.43 \times 10^{52}$ erg. We find at transparency a Lorentz factor $\Gamma \sim 1.73 \times 10^2$, laboratory radius of 6.04×10^{13} cm, P-GRB observed temperature $kT_{P-GRB} = 12.36$ keV, baryon load $B = 5.7 \times 10^{-3}$ and P-GRB energy of $E_{P-GRB} = 3.44 \times 10^{50}$ erg. We find a remarkable coincidence of the cosmological redshift by the scaling of the XRT data and with three other phenomenological methods. *Conclusions*: We interpret GRB 110709B as a member of the IGC sources, together with GRB 970828, GRB 090618 and GRB 101023. The existence of the XRT data during the prompt phase of the emission of GRB 110709B (Episode 2) offers an unprecedented tool for improving the diagnostic of GRBs emission.

29. G.B. Pisani, L. Izzo, R. Ruffini, C.L. Bianco, M. Muccino, A.V. Penacchioni, J.A. Rueda, Y. Wang; "Novel distance indicator for gamma-ray bursts associated with supernovae"; Astronomy & Astrophysics, 552,

L5 (2013).

Context: In recent years it has been proposed that the temporal coincidence of a Gamma Ray Burst (GRB) and a type Ib/c supernova (SN) can be explained by the concept of Induced Gravitational Collapse (IGC) of a Neutron Star (NS) to a Black Hole (BH) by accretion of matter ejected by a SN Ib/c. This scenario reveals a possible common behavior in the late time X-ray emission of this subclass of GRBs. *Aims*: We want to test if such a common behavior can actually be present in the sources belonging to this GRB sub-class and if this may lead to a redshift estimator for these sources. *Methods*: We build a sample of GRBs belonging to this sub-class, and we rescale the X-ray light curves of all of them both in time and in flux to a common cosmological redshift. *Results*: We found that the X-ray light curves of all the GRBs of the sample with a measured redshift present a common late time behavior when rescaled to a common redshift $z = 1$. We then use this result to estimate the redshift of the GRBs of the sample with no measured redshift. *Conclusions*: The common behavior in the late decay of the X-ray light curves of the GRBs of the sample points to a common physical mechanism in this particular phase of the GRB emission, possibly related to the SN process. This scenario may represent an invaluable tool to estimate the redshift of GRBs belonging to this sub-class of events. More GRBs are therefore needed in order to enlarge the subclass and to make more stringent constraints on the redshift estimates performed with this method for GRBs pertaining to this class.

30. C.L. Bianco, M. G. Bernardini, L. Caito, G. De Barros, L. Izzo, M. Muccino, B. Patricelli, A.V. Penacchioni, G.B. Pisani, R. Ruffini; "The canonical GRB scenario"; Il Nuovo Cimento C, 36 s01, 21 (2013).

    The canonical GRB scenario implied by the fireshell model is briefly summarized.

31. A.V. Penacchioni, R. Ruffini, L. Izzo, M. Muccino, C.L. Bianco, L. Caito, B. Patricelli; "Evidences for a double component in the emission of GRB 101023"; Il Nuovo Cimento C, 36 s01, 117 (2013).

    In this work we present the results of the analysis of GRB 101023 in the fireshell scenario. Its redshift is not known, so we attempted to infer it from the Amati Relation, obtaining $z = 0.9$. Its light curve presents a double emission, which makes it very similar to the already studied GRB 090618. We called each part Episode 1 and Episode 2. We performed a time-resolved spectral analysis with RMFIT using different spectral models, and fitted the light curve with a numerical code integrating the fireshell equations of motion. We used Fermi GBM data to build the light curve, in particular the second NaI detector, in the range (8.5–1000 keV). We considered different hypotheses regarding which part of the light curve could be the GRB and performed the analysis of all of them. We noticed a great variation of the temperature with time in the first episode, as well as almost no variation of the progenitor radius. We found that the first emission does not match the requirements for a GRB, while the second part perfectly agrees with being a canonical GRB, with a P-GRB lasting 4 s.

32. M. Muccino, R. Ruffini, C.L. Bianco, L. Izzo, A.V. Penacchioni, G.B. Pisani; "GRB 090510: A Disguised Short Gamma-Ray Burst with the Highest Lorentz Factor and Circumburst Medium"; The Astrophysical Journal, 772, 62 (2013).

    GRB 090510, observed both by Fermi and AGILE satellites, is the first bright short-hard Gamma-Ray Burst (GRB) with an emission from the keV up to the GeV energy range. Within the Fireshell model, we interpret the faint precursor in the light curve as the emission at the transparency of the expanding e^+e^- plasma: the Proper-GRB (P-GRB). From the observed isotropic energy we assume a total plasma energy $E^{tot}_{e^+e^-} = (1.10 \pm 0.06) \times 10^{53}$erg and derive a Baryon load $B = (1.45 \pm 0.28) \times 10^{-3}$ and a Lorentz factor at transparency $\Gamma_{tr} = (6.7 \pm 1.6) \times 10^2$. The main emission $\sim$ 0.4s after the initial spike is interpreted as the extended afterglow, due to the interaction of the ultrarelativistic baryons with the CircumBurst Medium (CBM). Using the condition of fully radiative regime, we infer a CBM average spherically symmetric density of $\langle n_{CBM} \rangle = (1.85 \pm 0.14) \times 10^3$ particles/cm^3, one of the highest found in the Fireshell model. The value of the filling factor, $1.5 \times 10^{-10} \leq \mathcal{R} \leq 3.8 \times 10^{-8}$, leads to the estimate of filaments with densities $n_{fil} = n_{CBM}/\mathcal{R} \approx (10^6 - 10^{14})$ particles/cm^3. The sub-MeV and the MeV emissions are well reproduced. When compared to the canonical GRBs with $\langle n_{CBM} \rangle \approx 1$ particles/cm^3 and to the disguised short GRBs with $\langle n_{CBM} \rangle \approx 10^{-3}$ particles/cm^3, the case of GRB 090510 leads to the existence of a new family of bursts exploding in an over-dense galactic region with $\langle n_{CBM} \rangle \approx 10^3$ particles/cm^3. The joint effect of the high Γ_{tr} and the high density compresses in time and "inflates" in intensity the extended afterglow, making it appear as a short burst, which we here define as "disguised short GRB by excess". The determination of the above parameters values may represent an important step towards the explanation of the GeV emission.

33. R. Ruffini, M. Muccino, C.L. Bianco, M. Enderli, L. Izzo, M. Kovacevic, A.V. Penacchioni, G.B. Pisani, J.A. Rueda, Y. Wang; "On Binary Driven Hypernovae and their nested late X-ray emission"; Astronomy & Astrophysics, 565, L10 (2014).

    Context: The induced gravitational collapse (IGC) paradigm addresses the very energetic (10^{52}–10^{54} erg) long gamma-ray bursts (GRBs) associated to supernovae (SNe). Unlike the traditional "collapsar" model, an evolved FeCO core with a companion neutron star (NS) in a tight binary system is considered as the progenitor. This special class of sources, here named "binary driven hypernovae" (BdHNe), presents a composite sequence composed of four different episodes with precise spectral and luminosity features.
    Aims: We first compare and contrast the steep decay, the plateau, and the power-law decay of the X-ray luminosities of three selected BdHNe (GRB 060729, GRB 061121, and GRB 130427A). Second, to explain the different sizes and Lorentz factors of the emitting regions of the four episodes, for definiteness, we use the most complete set of data of GRB 090618. Finally, we show the possible role of r-process, which originates in the binary system of the progenitor.
    Methods: We compare and contrast the late X-ray luminosity of the above three BdHNe. We examine correlations between the time at the starting point of the constant late power-law decay t_a^*, the average prompt luminosity $\langle L_{iso} \rangle$, and the luminosity at the end of the plateau L_a. We analyze a thermal emission ($\sim$ 0.97–0.29 keV), observed during the X-ray steep decay phase of GRB 090618.
    Results: The late X-ray luminosities of the three BdHNe, in the rest-frame energy band 0.3–10 keV, show a precisely constrained "nested" structure. In a space-time diagram, we illustrate the different sizes and Lorentz factors of the emitting regions of the three episodes. For GRB 090618, we infer an initial dimension of the thermal emitter of $\sim 7 \times 10^{12}$ cm, expanding at $\Gamma \approx 2$. We find tighter correlations than the Dainotti-Willingale ones.
    Conclusions: We confirm a constant slope power-law behavior for the late X-ray luminosity in the source rest frame, which may lead to a new distance indicator for BdHNe. These results, as well as the emitter size and Lorentz factor, appear to be inconsistent with the traditional afterglow model based on synchrotron emission from an ultra-relativistic ($\Gamma \sim 10^2$–10^3) collimated jet outflow. We argue, instead, for the possible role of r-process, originating in the binary system, to power the mildly relativistic X-ray source.

34. R. Ruffini, L. Izzo, M. Muccino, G.B. Pisani, J.A. Rueda, Y. Wang, C. Barbarino, C.L. Bianco, M. Enderli, M. Kovacevic; "Induced gravitational collapse at extreme cosmological distances: the case of GRB 090423"; Astronomy & Astrophysics, 569, A39 (2014).

    Context: The induced gravitational collapse (IGC) scenario has been introduced in order to explain the most energetic gamma ray bursts (GRBs), $E_{iso} = 10^{52} - 10^{54}$ erg, associated with type Ib/c supernovae (SNe). It has led to the concept of binary-driven hypernovae (BdHNe) originating in a tight binary system composed by a FeCO core on the verge of a SN explosion and a companion neutron star (NS). Their evolution is characterized by a rapid sequence of events: 1) The SN explodes, giving birth to a new NS (νNS). The accretion of SN ejecta onto the companion NS increases its mass up to the critical value; 2) The consequent gravitational collapse is triggered, leading to the formation of a black hole (BH) with GRB emission; 3) A novel feature responsible for the emission in the GeV, X-ray, and optical energy range occurs and is characterized by specific power-law behavior in their luminosity evolution and total spectrum; 4) The optical observations of the SN then occurs.
    Aims: We investigate whether GRB 090423, one of the farthest observed GRB at $z = 8.2$, is a member of the BdHN family.
    Methods: We compare and contrast the spectra, the luminosity evolution, and the detectability in the observations by *Swift* of GRB 090423 with the corresponding ones of the best known BdHN case, GRB 090618.
    Results: Identification of constant slope power-law behavior in the late X-ray emission of GRB 090423 and its overlapping with the corresponding one in GRB 090618, measured in a common rest frame, represents the main result of this article. This result represents a very significant step on the way to using the scaling law properties, proven in Episode 3 of this BdHN family, as a cosmological standard candle.
    Conclusions: Having identified GRB 090423 as a member of the BdHN family, we can conclude that SN events, leading to NS formation, can already occur already at $z = 8.2$, namely at 650 Myr after the Big Bang. It is then possible that these BdHNe originate stem from 40-60 $M_{\odot}$ binaries. They are probing the Population II stars after the completion and possible disappearance of Population III stars.

35. M. Muccino, C.L. Bianco, L. Izzo, Y. Wang, M. Enderli, M. Kovacevic, G.B. Pisani, A.V. Penacchioni, R. Ruffini; "The Genuine Short GRB 090227B and the Disguised by Excess GRB 090510"; Gravitation and

Cosmology, 20, 197 (2014).

GRB 090227B and GRB 090510, traditionally classified as short gamma-ray Bursts (GRBs), indeed originate from different systems. For GRB 090227B we inferred a total energy of the e^+e^- plasma $E^{tot}_{e^+e^-} = (2.83 \pm 0.15) \times 10^{53}$ erg, a baryon load of $B = (4.1 \pm 0.05) \times 10^{-5}$, and a CircumBurst Medium (CBM) average density $\langle n_{CBM} \rangle = (1.90 \pm 0.20) \times 10^{-5}$ cm^{-3}. From these results we have assumed the progenitor of this burst to be a symmetric neutron stars (NSs) merger with masses $m = 1.34 M_\odot$, radii $R = 12.24$ km. GRB 090510, instead, has $E^{tot}_{e^+e^-} = (1.10 \pm 0.06) \times 10^{53}$ erg, $B = (1.45 \pm 0.28) \times 10^{-3}$, implying a Lorentz factor at transparency of $\Gamma = (6.7 \pm 1.7) \times 10^2$, which are characteristic of the long GRB class, and a very high CBM density, $\langle n_{CBM} \rangle = (1.85 \pm 0.14) \times 10^3$ cm^{-3}. The joint effect of the high values of Γ and of $\langle n_{CBM} \rangle$ compresses in time and "inflates" in intensity in an extended afterglow, making appear GRB 090510 as a short burst, which we here define as "disguised short GRB by excess" occurring an overdense region with 10^3 cm^{-3}.

36. M. Muccino, C.L. Bianco, L. Izzo, Y. Wang, M. Enderli, G.B. Pisani, A.V. Penacchioni, R. Ruffini; "Two short bursts originating from different astrophysical systems: The genuine short GRB 090227B and the disguised short GRB 090510 by excess"; Journal of the Korean Physical Society, 65, 865 (2014).

    GRB 090227B and GRB 090510 are two gamma-ray bursts (GRBs) traditionally classified as short bursts. The major outcome of our analysis is that they indeed originate from different systems. In the case of GRB 090227B, from the inferred values of the total energy of the e^+e^- plasma, $E^{tot}_{e^+e^-} = (2.83 \pm 0.15) \times 10^{53}$ erg, the engulfed baryonic mass M_B, expressed as $B = M_B c^2 / E^{tot}_{e^+e^-} = (4.1 \pm 0.05) \times 10^{-5}$, and the circumburst medium (CBM) average density, $\langle n_{CBM} \rangle = (1.90 \pm 0.20) \times 10^{-5}$ cm^{-3}, we have assumed the progenitor of this burst to be a symmetric neutron star (NS) merger with masses $m = 1.34 M_\odot$, radii $R = 12.24$ km, and crustal thicknesses of ~ 0.47 km. In the case of GRB 090510, we have derived the total plasma energy, $E^{tot}_{e^+e^-} = (1.10 \pm 0.06) \times 10^{53}$ erg, the Baryon load, $B = (1.45 \pm 0.28) \times 10^{-3}$, and the Lorentz factor at transparency, $\Gamma = (6.7 \pm 1.7) \times 10^2$, which are characteristic of the long GRB class, as well as a very high CBM density, $\langle n_{CBM} \rangle = (1.85 \pm 0.14) \times 10^3$ cm^{-3}. The joint effect of the high values of Γ and $\langle n_{CBM} \rangle$ compresses in time and "inflates" in intensity the extended afterglow, making GRB 090510 appear to be a short burst, which we here define as a "disguised short GRB by excess", occurring in an overdense region with 10^3 cm^{-3}.

37. R. Ruffini, Y. Wang, M. Kovacevic, C.L. Bianco, M. Enderli, M. Muccino, A.V. Penacchioni, G.B. Pisani, J. Rueda; "GRB 130427A and SN 2013cq: A Multi-wavelength Analysis of An Induced Gravitational Collapse Event"; The Astrophysical Journal, 798, 10 (2015).

    We have performed our data analysis of the observations by *Swift*, *NuStar* and *Fermi* satellites in order to probe the induced gravitational collapse (IGC) paradigm for GRBs associated with supernovae (SNe), in the "terra incognita" of GRB 130427A. We compare and contrast our data analysis with those in the literature. We have verified that the GRB 130427A conforms to the IGC paradigm by examining the power law behavior of the luminosity in the early 10^4 s of the XRT observations. This has led to the identification of the four different episodes of the "binary driven hypernovae" (BdHNe) and to the prediction, on May 2, 2013, of the occurrence of SN 2013cq, duly observed in the optical band on May 13, 2013. The exceptional quality of the data has allowed the identification of novel features in *Episode 3* including: a) the confirmation and the extension of the existence of the recently discovered "nested structure" in the late X-ray luminosity in GRB 130427A, as well as the identification of a spiky structure at 10^2 s in the cosmological rest-frame of the source; b) a power law emission of the GeV luminosity light curve and its onset at the end of *Episode 2*; c) different Lorentz Γ factors for the emitting regions of the X-ray and GeV emissions in this *Episode 3*. These results make it possible to test the details of the physical and astrophysical regimes at work in the BdHNe: 1) a newly born neutron star and the supernova ejecta, originating in *Episode 1*, 2) a newly formed black hole originating in *Episode 2*, and 3) the possible interaction among these components, observable in the standard features of *Episode 3*.

38. M. Muccino, R. Ruffini, C.L. Bianco, M. Enderli, M. Kovacevic, L. Izzo, A.V. Penacchioni, G.B. Pisani, J.A. Rueda, Y. Wang; "On binary driven hypernovae and their nested late X-ray emission"; Astronomy Reports, 59, 581 (2015).

    The induced gravitational collapse (IGC) paradigm addresses energetic (10^{52}–10^{54} erg), long gamma-ray bursts (GRBs) associated to supernovae (SNe) and proposes as their progenitors tight binary systems composed of an evolved FeCO core and a companion neutron star (NS). Their emission is characterized by four specific episodes: Episode 1, corresponding to the on-set of the FeCO

SN explosion and the accretion of the ejecta onto the companion NS; Episode 2, related the collapse of the companion NS to a black hole (BH) and to the emission of a long GRB; Episode 3, observed in X-rays and characterized by a steep decay, a plateau phase and a late power-law decay; Episode 4, corresponding to the optical SN emission due to the ^{56}Ni decay. We focus on Episode 3 and we show that, from the thermal component observed during the steep decay of the prototype GRB 090618, the emission region has a typical dimension of $\sim 10^{13}$ cm, which is inconsistent with the typical size of the emitting region of GRBs, e.g., $\sim 10^{16}$ cm. We propose, therefore, that the X-ray afterglow emission originates from a spherically symmetric SN ejecta expanding at $\Gamma \sim 2$ or, possibly, from the accretion onto the newly formed black hole, and we name these systems "binary driven hypernovae" (BdHNe). This interpretation is alternative to the traditional afterglow model based on the GRB synchrotron emission from a collimated jet outflow, expanding at ultra-relativistic Lorentz factor of $\Gamma \sim 10^2 - 10^3$ and originating from the collapse of a single object. We show then that the rest-frame energy band 0.3–10 keV X-ray luminosities of three selected BdHNe, GRB 060729, GRB 061121, and GRB 130427A, evidence a precisely constrained "nested" structure and satisfy precise scaling laws between the average prompt luminosity, $< L_{iso} >$, and the luminosity at the end of the plateau, L_a, as functions of the time at the end of the plateau. All these features extend the applicability of the "cosmic candle" nature of Episode 3. The relevance of r-process in fulfilling the demanding scaling laws and the nested structure are indicated.

39. R. Ruffini, J.A. Rueda, C. Barbarino, C. L. Bianco, H. Dereli, M. Enderli, L. Izzo, M. Muccino, A.V. Penacchioni, G.B. Pisani, Y. Wang; "Induced Gravitational Collapse in the BATSE era: the case of GRB 970828"; Astronomy Reports, 59, 626 (2015).

    Following the recently established "Binary-driven HyperNova" (BdHN) paradigm, we here interpret GRB 970828 in terms of the four episodes typical of such a model. The "Episode 1", up to 40 s after the trigger time t_0, with a time varying thermal emission and a total energy of $E_{iso,1st} = 2.60 \times 10^{53}$ erg, is interpreted as due to the onset of an hyper-critical accretion process onto a companion neutron star, triggered by the companion star, an FeCO core approaching a SN explosion. The "Episode 2", observed up t_0+90 s, is interpreted as a canonical gamma ray burst, with an energy of $E_{tot}^{e^+e^-} = 1.60 \times 10^{53}$ erg, a baryon load of $B = 7 \times 10^{-3}$ and a bulk Lorentz factor at transparency of $\Gamma = 142.5$. From this Episode 2, we infer that the GRB exploded in an environment with a large average particle density $\langle n \rangle \approx 10^3$ particles/cm^3 and dense clouds characterized by typical dimensions of $(4 \div 8) \times 10^{14}$ cm and $\delta n/n \sim 10$. The "Episode 3" is identified from t_0+90 s all the way up to 10^{5-6} s: despite the paucity of the early X-ray data, typical in the BATSE, pre-Swift era, we find extremely significant data points in the late X-ray afterglow emission of GRB 970828, which corresponds to the ones observed in all BdHNe sources. The "Episode 4", related to the Supernova emission, does not appear to be observable in this source, due to the presence of darkening from the large density of the GRB environment, also inferred from the analysis of the Episode 2.

40. Y. Wang, R. Ruffini, M. Kovacevic, C.L. Bianco, M. Enderli, M. Muccino, A.V. Penacchioni, G.B. Pisani, J.A. Rueda; "Predicting supernova associated to gamma-ray burst 130427a"; Astronomy Reports, 59, 667 (2015).

    Binary systems constituted by a neutron star and a massive star are not rare in the universe. The Induced Gravitational Gamma-ray Burst (IGC) paradigm interprets Gamma-ray bursts as the outcome of a neutron star that collapses into a black hole due to the accretion of the ejecta coming from its companion massive star that underwent a supernova event. GRB 130427A is one of the most luminous GRBs ever observed, of which isotropic energy exceeds 10^{54} erg. And it is within one of the few GRBs obtained optical, X-ray and GeV spectra simultaneously for hundreds of seconds, which provides an unique opportunity so far to understand the multi-wavelength observation within the IGC paradigm, our data analysis found low Lorentz factor blackbody emission in the Episode 3 and its X-ray light curve overlaps typical IGC Golden Sample, which comply to the IGC mechanisms. We consider these findings as clues of GRB 130427A belonging to the IGC GRBs. We predicted on GCN the emergence of a supernova on May 2, 2013, which was later successfully detected on May 13, 2013.

41. R. Ruffini, M. Muccino, M. Kovacevic, F.G. Oliveira, J.A. Rueda, C.L. Bianco, M. Enderli, A.V. Penacchioni, G.B. Pisani, Y. Wang, E. Zaninoni; "GRB 140619B: a short GRB from a binary neutron star merger leading to black hole formation"; The Astrophysical Journal, 808, 190 (2015).

    We show the existence of two families of short GRBs, both originating from the merger of binary neutron stars (NSs): family-1 with $E_{iso} < 10^{52}$ erg, leading to a massive NS as the merged core, and family-2 with $E_{iso} > 10^{52}$ erg, leading to a black hole (BH). Following the identification of the prototype

GRB 090227B, we present the details of a new example of family-2 short burst: GRB 140619B. From the spectral analysis of the early ~ 0.2 s, we infer an observed temperature $kT = (324 \pm 33)$ keV of the e^+e^--plasma at transparency (P-GRB), a theoretically derived redshift $z = 2.67 \pm 0.37$, a total burst energy $E^{tot}_{e^+e^-} = (6.03 \pm 0.79) \times 10^{52}$ erg, a rest-frame peak energy $E_{p,i} = 4.7$ MeV, and a baryon load $B = (5.52 \pm 0.73) \times 10^{-5}$. We also estimate the corresponding emission of gravitational waves. Two additional examples of family-2 short bursts are identified: GRB 081024B and GRB 090510, remarkable for its well determined cosmological distance. We show that marked differences exist in the nature of the afterglows of these two families of short bursts: family-2 bursts, leading to BH formation, consistently exhibit high energy emission following the P-GRB emission; family-1 bursts, leading to the formation of a massive NS, should never exhibit high energy emission. We also show that both the families fulfill an $E_{p,i}$–E_{iso} relation with slope $\gamma = 0.59 \pm 0.07$ and a normalization constant incompatible with the one for long GRBs. The observed rate of such family-2 events is $\rho_0 = \left(2.1^{+2.8}_{-1.4}\right) \times 10^{-4}\mathrm{Gpc}^{-3}\mathrm{yr}^{-1}$.

42. R. Ruffini, Y. Aimuratov, C.L. Bianco, M. Enderli, M. Kovacevic, R. Moradi, M. Muccino, A.V. Penacchioni, G.B. Pisani, J.A. Rueda, Y. Wang; "Induced gravitational collapse in FeCO Core-Neutron star binaries and Neutron star-Neutron star binary mergers"; International Journal of Modern Physics A, 30, 1545023 (2015).

    We review the recent progress in understanding the nature of gamma-ray bursts (GRBs). The occurrence of GRB is explained by the Induced Gravitational Collapse (IGC) in FeCO Core-Neutron star binaries and Neutron star-Neutron star binary mergers, both processes occur within binary system progenitors. Making use of this most unexpected new paradigm, with the fundamental implications by the neutron star (NS) critical mass, we find that different initial configurations of binary systems lead to different GRB families with specific new physical predictions confirmed by observations.

43. R. Ruffini, M. Muccino, Y. Aimuratov, C.L. Bianco, C. Cherubini, M. Enderli, M. Kovacevic, R. Moradi, A.V. Penacchioni, G.B. Pisani, J.A. Rueda, Y. Wang; "GRB 090510: A genuine short-GRB from a binary neutron star coalescing into a Kerr-Newman black hole"; The Astrophysical Journal, 831, 178 (2016).

    In a new classification of merging binary neutron stars (NSs) we separate short gamma-ray bursts (GRBs) in two sub-classes. The ones with $E_{\rm iso} \lesssim 10^{52}$ erg coalesce to form a massive NS and are indicated as short gamma-ray flashes (S-GRFs). The hardest, with $E_{\rm iso} \gtrsim 10^{52}$ erg, coalesce to form a black hole (BH) and are indicated as genuine short-GRBs (S-GRBs). Within the fireshell model, S-GRBs exhibit three different components: the P-GRB emission, observed at the transparency of a self-accelerating baryon-e^+e^- plasma; the prompt emission, originating from the interaction of the accelerated baryons with the circumburst medium; the high-energy (GeV) emission, observed after the P-GRB and indicating the formation of a BH. GRB 090510 gives the first evidence for the formation of a Kerr BH or, possibly, a Kerr-Newman BH. Its P-GRB spectrum can be fitted by a convolution of thermal spectra whose origin can be traced back to an axially symmetric dyadotorus. A large value of the angular momentum of the newborn BH is consistent with the large energetics of this S-GRB, which reach in the 1–10000 keV range $E_{\rm iso} = (3.95 \pm 0.21) \times 10^{52}$ erg and in the 0.1–100 GeV range $E_{\rm LAT} = (5.78 \pm 0.60) \times 10^{52}$ erg, the most energetic GeV emission ever observed in S-GRBs. The theoretical redshift $z_{\rm th} = 0.75 \pm 0.17$ that we derive from the fireshell theory is consistent with the spectroscopic measurement $z = 0.903 \pm 0.003$, showing the self-consistency of the theoretical approach. All S-GRBs exhibit GeV emission, when inside the *Fermi*-LAT field of view, unlike S-GRFs, which never evidence it. The GeV emission appears to be the discriminant for the formation of a BH in GRBs, confirmed by their observed overall energetics.

44. Ruffini, R.; Rueda, J. A.; Muccino, M.; Aimuratov, Y.; Becerra, L. M.; Bianco, C. L.; Kovacevic, M.; Moradi, R.; Oliveira, F. G.; Pisani, G. B.; Wang, Y.; On the classification of GRBs and their occurrence rates; The Astrophysical Journal, 832, 136 (2016).

    There is mounting evidence for the binary nature of the progenitors of gamma-ray bursts (GRBs). For a long GRB, the induced gravitational collapse (IGC) paradigm proposes as progenitor, or "in-state", a tight binary system composed of a carbon-oxygen core ($CO_{\rm core}$) undergoing a supernova (SN) explosion which triggers hypercritical accretion onto a neutron star (NS) companion. For a short GRB, a NS-NS merger is traditionally adopted as the progenitor. We divide long and short GRBs into two sub-classes, depending on whether or not a black hole (BH) is formed in the merger or in the hypercritical accretion process exceeding the NS critical mass. For long bursts, when no BH is formed we have the sub-class of X-ray flashes (XRFs), with isotropic energy $E_{iso} \lesssim 10^{52}$ erg and rest-frame spectral peak energy $E_{p,i} \lesssim 200$ keV. When a BH is formed we have the sub-class of binary-driven hypernovae (BdHNe), with $E_{iso} \gtrsim 10^{52}$ erg and $E_{p,i} \gtrsim 200$ keV. In analogy, short bursts are similarly divided into two sub-classes. When no BH is formed, short gamma-ray flashes (S-GRFs) occur, with $E_{iso} \lesssim 10^{52}$ erg and $E_{p,i} \lesssim 2$ MeV. When a BH is formed, the authentic short GRBs (S-GRBs) occur, with $E_{iso} \gtrsim 10^{52}$ erg and $E_{p,i} \gtrsim 2$ MeV. We give examples and observational signatures of these four sub-classes and their rate of occurrence. From their respective rates it is possible that "in-states" of S-GRFs and S-GRBs originate from the "out-states" of XRFs. We indicate two additional progenitor systems: white dwarf-NS and BH-NS. These systems have hybrid features between long and short bursts. In the case of S-GRBs and BdHNe evidence is given of the coincidence of the onset of the high energy GeV emission with the birth of a Kerr BH.

45. Becerra, L.; Bianco, C. L.; Fryer, C. L.; Rueda, J. A.; Ruffini, R.; On the induced gravitational collapse scenario of gamma-ray bursts associated with supernovae; The Astrophysical Journal, 833, 107 (2016).

    Following the induced gravitational collapse (IGC) paradigm of gamma-ray bursts (GRBs) associated with type Ib/c supernovae, we present numerical simulations of the explosion of a carbon-oxygen (CO) core in a binary system with a neutron-star (NS) companion. The supernova ejecta trigger a *hypercritical* accretion process onto the NS thanks to a copious neutrino emission and the trapping of photons within the accretion flow. We show that temperatures 1–10 MeV develop near the NS surface, hence electron-positron annihilation into neutrinos becomes the main cooling channel leading to accretion rates 10^{-9}–10^{-1} $M_\odot$ s^{-1} and neutrino luminosities 10^{43}–10^{52} erg s^{-1} (the shorter the orbital period the higher the accretion rate). We estimate the maximum orbital period, $P_{\rm max}$, as a function of the NS initial mass, up to which the NS companion can reach by hypercritical accretion the critical mass for gravitational collapse leading to black-hole (BH) formation. We then estimate the effects of the accreting and orbiting NS companion onto a novel geometry of the supernova ejecta density profile. We present the results of a 1.4×10^7 particle simulation which show that the NS induces accentuated asymmetries in the ejecta density around the orbital plane. We elaborate on the observables associated with the above features of the IGC process. We apply this framework to specific GRBs: we find that X-ray flashes (XRFs) and binary-driven hypernovae (BdHNe) are produced in binaries with $P > P_{\rm max}$ and $P < P_{\rm max}$, respectively. We analyze in detail the case of XRF 060218.

46. Pisani, G. B.; Ruffini, R.; Aimuratov, Y.; Bianco, C. L.; Kovacevic, M.;

Moradi, R.; Muccino, M.; Penacchioni, A. V.; Rueda, J. A.; Shakeri, S.; Wang, Y.; On the universal late X-ray emission of binary-driven hypernovae and its possible collimation; The Astrophysical Journal, 833, 159 (2016).

It has been previously discovered a universal power-law behaviour of the late X-ray emission (LXRE) of a "golden sample" (GS) of six long energetic GRBs, when observed in the rest-frame of the source. This remarkable feature, independent on the different isotropic energy (E_{iso}) of each GRB, has been used to estimate the cosmological redshift of some long GRBs. This analysis is here extended to a new class of 161 long GRBs, all with $E_{iso} > 10^{52}$ erg. These GRBs are indicated as binary-driven hypernovae (BdHNe) in view of their progenitors: a tight binary systems composed of a carbon-oxigen core (CO_{core}) and a neutron star (NS) undergoing an induced gravitational collapse (IGC) to a black hole (BH) triggered by the CO_{core} explosion as a supernova (SN). We confirm the universal behaviour of the LXRE for the "enlarged sample" (ES) of 161 BdHNe observed up to the end of 2015, assuming a double-cone emitting region. We obtain a distribution of half-opening angles peaking at $\theta = 17.62°$, with mean value 30.05°, and a standard deviation 19.65°. This, in turn, leads to the possible establishment of a new cosmological candle. Within the IGC model, such universal LXRE behaviour is only indirectly related to the GRB and originates from the SN ejecta, of a standard constant mass, being shocked by the GRB emission. The fulfillment of the universal relation in the LXRE and its independence of the prompt emission, further confirmed in this article, establishes a crucial test for any viable GRB model.

47. Y. Aimuratov, R. Ruffini, M. Muccino, C.L. Bianco, A.V. Penacchioni, G.B. Pisani, D. Primorac, J.A. Rueda, Y. Wang; GRB 081024B and GRB 140402A: Two Additional Short GRBs from Binary Neutron Star Mergers; The Astrophysical Journal, 844, 83 (2017).

Theoretical and observational evidences have been recently gained for a two-fold classification of short bursts: 1) short gamma-ray flashes (S-GRFs), with isotropic energy $E_{iso} < 10^{52}$ erg and no BH formation, and 2) the authentic short gamma-ray bursts (S-GRBs), with isotropic energy $E_{iso} > 10^{52}$ erg evidencing a BH formation in the binary neutron star merging process. The signature for the BH formation consists in the on-set of the high energy (0.1–100 GeV) emission, coeval to the prompt emission, in all S-GRBs. No GeV emission is expected nor observed in the S-GRFs. In this paper we present two additional S-GRBs, GRB 081024B and GRB 140402A, following the already identified S-GRBs, i.e., GRB 090227B, GRB 090510 and GRB 140619B. We also return on the absence of the GeV emission of the S-GRB 090227B, at an angle of 71° from the *Fermi*-LAT boresight. All the correctly identified S-GRBs correlate to the high energy emission, implying no significant presence of beaming in the GeV emission. The existence of a common power-law behavior in the GeV luminosities, following the BH formation, when measured in the source rest-frame, points to a commonality in the mass and spin of the newly-formed BH in all S-GRBs.

48. J.A. Rueda, Y. Aimuratov, U. Barres de Almeida, L.M. Becerra, C.L. Bianco, C. Cherubini, S. Filippi, M. Karlica, M. Kovacevic, J.D. Melon Fuksman, R. Moradi, M. Muccino, A.V. Penacchioni, G.B. Pisani, D. Primorac, R. Ruffini, N. Sahakyan, S. Shakeri, Y. Wang; The binary systems associated with short and long gamma-ray bursts and their detectability; International Journal of Modern Physics D, 26, 1730016 (2017).

    Short and long-duration gamma-ray bursts (GRBs) have been recently subclassified into seven families according to the binary nature of their progenitors. For short GRBs, mergers of neutron star binaries (NS–NS) or neutron star-black hole binaries (NS-BH) are proposed. For long GRBs, the induced gravitational collapse (IGC) paradigm proposes a tight binary system composed of a carbon–oxygen core (COcore) and a NS companion. The explosion of the COcore as supernova (SN) triggers a hypercritical accretion process onto the NS companion which might reach the critical mass for the gravitational collapse to a BH. Thus, this process can lead either to a NS-BH or to NS–NS depending on whether or not the accretion is sufficient to induce the collapse of the NS into a BH. We shall discuss for the above compact object binaries: (1) the role of the NS structure and the equation-of-state on their final fate; (2) their occurrence rates as inferred from the X and gamma-ray observations; (3) the expected number of detections of their gravitational wave (GW) emission by the Advanced LIGO interferometer.

49. R. Ruffini, Y. Aimuratov, L.M. Becerra, C.L. Bianco, M. Karlica, M. Kovacevic, J.D. Melon Fuksman, R. Moradi, M. Muccino, A.V. Penacchioni, G.B. Pisani, D. Primorac, J.A. Rueda, S. Shakeri, G.V. Vereshchagin, Y. Wang, S.-S. Xue; The cosmic matrix in the 50th anniversary of relativistic astrophysics; International Journal of Modern Physics D, 26, 1730019 (2017).

Our concept of induced gravitational collapse (IGC paradigm) starting from a supernova occurring with a companion neutron star, has unlocked the understanding of seven different families of gamma ray bursts (GRBs), indicating a path for the formation of black holes in the universe. An authentic laboratory of relativistic astrophysics has been unveiled in which new paradigms have been introduced in order to advance knowledge of the most energetic, distant and complex systems in our universe. A novel cosmic matrix paradigm has been introduced at a relativistic cosmic level, which parallels the concept of an S-matrix introduced by Feynmann, Wheeler and Heisenberg in the quantum world of microphysics. Here the "in" states are represented by a neutron star and a supernova, while the "out" states, generated within less than a second, are a new neutron star and a black hole. This novel field of research needs very powerful technological observations in all wavelengths ranging from radio through optical, X-ray and gamma ray radiation all the way up to ultra-high-energy cosmic rays.

50. R. Ruffini, Y. Wang, Y. Aimuratov, U. Barres de Almeida, L.M. Becerra, C.L. Bianco, Y.C. Chen, M. Karlica, M. Kovacevic, L. Li, J.D. Melon Fuksman, R. Moradi, M. Muccino, A.V. Penacchioni, G.B. Pisani, D. Primorac, J.A. Rueda, S. Shakeri, G.V. Vereshchagin, S.-S. Xue; Early X-Ray Flares in GRBs; The Astrophysical Journal, 852, 53 (2018).

    We analyze the early X-ray flares in the GRB "flare-plateau-afterglow" (FPA) phase observed by Swift-XRT. The FPA occurs only in one of the seven GRB subclasses: the binary-driven hypernovae (BdHNe). This subclass consists of long GRBs with a carbon-oxygen core and a neutron star (NS) binary companion as progenitors. The hypercritical accretion of the supernova (SN) ejecta onto the NS can lead to the gravitational collapse of the NS into a black hole. Consequently, one can observe a GRB emission with isotropic energy $E_{iso} \gtrsim 10^{52}$ erg, as well as the associated GeV emission and the FPA phase. Previous work had shown that gamma-ray spikes in the prompt emission occur at $\sim 10^{15}$–10^{17} cm with Lorentz gamma factor $\Gamma \sim 10^2$–10^3. Using a novel data analysis we show that the time of occurrence, duration, luminosity and total energy of the X-ray flares correlate with E_{iso}. A crucial feature is the observation of thermal emission in the X-ray flares that we show occurs at radii $\sim 10^{12}$ cm with $\Gamma \lesssim 4$. These model independent observations cannot be explained by the "fireball" model, which postulates synchrotron and inverse Compton radiation from a single ultra relativistic jetted emission extending from the prompt to the late afterglow and GeV emission phases. We show that in BdHNe a collision between the GRB and the SN ejecta occurs at $\simeq 10^{10}$ cm reaching transparency at $\sim 10^{12}$ cm with $\Gamma \lesssim 4$. The agreement between the thermal emission observations and these theoretically derived values validates our model and opens the possibility of testing each BdHN episode with the corresponding Lorentz gamma factor.

51. R. Ruffini, J. Rodriguez, M. Muccino, J.A. Rueda, Y. Aimuratov, U. Barres de Almeida, L.M. Becerra, C.L. Bianco, C. Cherubini, S. Filippi, D. Gizzi, M. Kovacevic, R. Moradi, F.G. Oliveira, G.B. Pisani, Y. Wang; On the Rate and on the Gravitational Wave Emission of Short and Long GRBs; The Astrophysical Journal, 859, 30 (2018).

    On the ground of the large number of gamma-ray bursts (GRBs) detected with cosmological redshift, we classified GRBs in seven subclasses, all with binary progenitors which emit gravitational waves (GWs). Each binary is composed of combinations of carbon-oxygen cores (COcore), neutron stars (NSs), black holes (BHs), and white dwarfs (WDs). The long bursts, traditionally assumed to originate from a BH with an ultrarelativistic jetted emission, not emitting GWs, have been subclassified as (I) X-ray flashes (XRFs), (II) binary-driven hypernovae (BdHNe), and (III) BH-supernovae (BH-SNe). They are framed within the induced gravitational collapse paradigm with a progenitor COcore-NS/BH binary. The SN explosion of the COcore triggers an accretion process onto the NS/BH. If the accretion does not lead the NS to its critical mass, an XRF occurs, while when the BH is present or formed by accretion, a BdHN occurs. When the binaries are not disrupted, XRFs lead to NS-NS and BdHNe lead to NS-BH. The short bursts, originating in NS-NS, are subclassified as (IV) short gamma-ray flashes (S-GRFs) and (V) short GRBs (S-GRBs), the latter when a BH is formed. There are (VI) ultrashort GRBs (U-GRBs) and (VII) gamma-ray flashes (GRFs) formed in NS-BH and NS-WD, respectively. We use the occurrence rate and GW emission of these subclasses to assess their detectability by Advanced LIGO-Virgo, eLISA, and resonant bars. We discuss the consequences of our results in view of the announcement of the LIGO/Virgo Collaboration of the source GW 170817 as being originated by an NS-NS.

52. J.A. Rueda, R. Ruffini, Y. Wang, Y. Aimuratov, U. Barres de Almeida, C.L. Bianco, Y.-C. Chen, R.V. Lobato, C. Maia, D. Primorac, R. Moradi, J. Rodriguez; GRB 170817A-GW170817-AT 2017gfo and the observations of NS-NS, NS-WD and WD-WD mergers; Journal of Cosmology and Astroparticle Physics, 10, 006 (2018).

The LIGO-Virgo Collaboration has announced the detection of GW170817 and has associated it with GRB 170817A . These signals have been followed after 11 hours by the optical and infrared emission of AT 2017gfo. The origin of this complex phenomenon has been attributed to a neutron star-neutron star (NS-NS) merger. In order to probe this association we confront our current understanding of the gravitational waves and associated electromagnetic radiation with four observed GRBs originating in binaries composed of different combinations NSs and white dwarfs (WDs). We consider 1) GRB 090510 the prototype of NS-NS merger leading to a black hole (BH); 2) GRB 130603B the prototype of a NS-NS merger leading to massive NS (MNS) with an associated kilonova; 3) GRB 060614 the prototype of a NS-WD merger leading to a MNS with an associated kilonova candidate; 4) GRB 170817A the prototype of a WD-WD merger leading to massive WD with an associated AT 2017gfo-like emission. None of these systems support the above mentioned association. The clear association between GRB 170817A and AT 2017gfo has led to introduce a new model based on a new subfamily of GRBs originating from WD-WD mergers. We show how this novel model is in agreement with the exceptional observations in the optical, infrared, X- and gamma-rays of GRB 170817A-AT 2017gfo.

53. R. Ruffini, M. Karlica, N. Sahakyan, J.A. Rueda, Y. Wang, G.W. Mathews, C.L. Bianco, M. Muccino; A GRB Afterglow Model Consistent with Hypernova Observations; The Astrophysical Journal, 869, 101 (2018).

    We describe the afterglows of the long gamma-ray-burst (GRB) 130427A within the context of a binary-driven hypernova. The afterglows originate from the interaction between a newly born neutron star (νNS), created by an Ic supernova (SN), and a mildly relativistic ejecta of a hypernova (HN). Such an HN in turn results from the impact of the GRB on the original SN Ic. The mildly relativistic expansion velocity of the afterglow ($\Gamma \sim 3$) is determined, using our model-independent approach, from the thermal emission between 196 and 461 s. The power law in the optical and X-ray bands of the afterglow is shown to arise from the synchrotron emission of relativistic electrons in the expanding magnetized HN ejecta. Two components contribute to the injected energy: the kinetic energy of the mildly relativistic expanding HN and the rotational energy of the fast-rotating highly magnetized ?NS. We reproduce the afterglow in all wavelengths from the optical (10^{14} Hz) to the X-ray band (10^{19} Hz) over times from 604 s to 5.18×10^6 s relative to the Fermi-GBM trigger. Initially, the emission is dominated by the loss of kinetic energy of the HN component.

After 10^5 s the emission is dominated by the loss of rotational energy of the νNS, for which we adopt an initial rotation period of 2 ms and a dipole plus quadrupole magnetic field of $\lesssim 7 \times 10^{12}$ G or $\sim 10^{14}$ G. This scenario with a progenitor composed of a COcore and an NS companion differs from the traditional ultra-relativistic-jetted treatments of the afterglows originating from a single black hole.

54. R. Ruffini, L.M. Becerra, C.L. Bianco, Y.-C. Chen, M. Karlica, M. Kovacevic, J.D. Melon Fuksman, R. Moradi, M. Muccino, G.B. Pisani, D. Primorac, J.A. Rueda, G.V. Vereshchagin, Y. Wang, S.-S. Xue; On the ultra-relativistic Prompt Emission (UPE), the Hard and Soft X-ray Flares, and the extended thermal emission (ETE) in GRB 151027A; The Astrophysical Journal, 869, 151 (2018).

    We analyze GRB 151027A within the binary-driven hypernova approach, with a progenitor of a carbon–oxygen core on the verge of a supernova (SN) explosion and a binary companion neutron star (NS). The hypercritical accretion of the SN ejecta onto the NS leads to its gravitational collapse into a black hole (BH), to the emission of the gamma-ray burst (GRB), and to a copious e+e- plasma. The impact of this e+e- plasma on the SN ejecta explains the early soft X-ray flare observed in long GRBs. Here, we apply this approach to the ultra-relativistic prompt emission (UPE) and to the hard X-ray flares. We use GRB 151027A as a prototype. From the time-integrated and the time-resolved analysis, we identify a double component in the UPE and confirm its ultra-relativistic nature. We confirm the mildly relativistic nature of the soft X-ray flare, of the hard X-ray flare, and of the extended thermal emission (ETE). We show that the ETE identifies the transition from an SN to a hypernova (HN). We then address the theoretical justification of these observations by integrating the hydrodynamical propagation equations of the e+e- into the SN ejecta, with the latter independently obtained from 3D smoothed particle hydrodynamics simulations. We conclude that the UPE, the hard X-ray flare, and the soft X-ray flare do not form a causally connected sequence. Within our model, they are the manifestation of the same physical process of the BH formation as seen through different viewing angles, implied by the morphology and the ~ 300 s rotation period of the HN ejecta.

55. R. Moradi, R. Ruffini, C.L. Bianco, Y.-C. Chen, M. Karlica, J.D. Melon Fuksman, D. Primorac, J.A. Rueda, S. Shakeri, Y. Wang, S.-S. Xue; Relativistic Behavior and Equitemporal Surfaces in Ultra-Relativistic Prompt

Emission Phase of Gamma-Ray Bursts; Astronomy Reports, 62, 905 (2018).

In this work we study a role of baryon load and interstellar medium density to explain the nature of peaks in the ultra-relativistic prompt emission (UPE) phase of Gamma-ray Bursts (GRBs). We study the behavior of their Γ Lorenz factor fromthe moment of transparency all the way up to interstellar medium. We finally study the characteristic of equitemporal surfaces in the UPE phase.

56. D. Primorac, M. Muccino, R. Moradi, Y. Wang, J.D. Melon Fuksman, R. Ruffini, C.L. Bianco, J.A. Rueda; Structure of the Prompt Emission of GRB 151027A Within the Fireshell Model; Astronomy Reports, 62, 933 (2018).

    Long gamma-ray burst GRB 151027A was observed by all three detectors onboard the Swift spacecraft, and many more, including MAXI, Konus-Wind and Fermi GBM/LAT instruments. This revealed a complex structure of the prompt and afterglow emission, consisting of a double-peak gammaray prompt with a quiescent period and a HRF/SXF within the X-ray afterglow, together with multiple BB components seen within the time-resolved spectral analysis. These features, within the fireshell model, are interpreted as the manifestation of the same physical process viewed at different angles with respect to the HN ejecta. Here we present the time-resolved and time-integrated spectral analysis used to determine the energy of the e-e+ plasma E_{tot} and the baryon load B. These quantities describe the dynamics of the fireshell up to the transparency point. We proceed with the light-curve simulation from which CBM density values and its inhomogeneities are deduced. We also investigate the properties of GRB 140206A, whose prompt emission exhibits a similar structure.

4.2 Conference proceedings

1. R. Ruffini, M.G. Bernardini, C.L. Bianco, P. Chardonnet, F. Fraschetti, V. Gurzadyan, L. Vitagliano, S.-S. Xue; "The Blackholic energy: long and short Gamma-Ray Bursts (New perspectives in physics and astrophysics from the theoretical understanding of Gamma-Ray Bursts, II)"; in Proceedings of the XIth Brazilian School on Cosmology and Gravitation, Mangaratiba, Rio de Janeiro (Brazil), July – August 2004, M. Novello, S.E. Perez Bergliaffa, Editors; AIP Conference Proceedings, 782, 42 (2005).

We outline the confluence of three novel theoretical fields in our modeling of Gamma-Ray Bursts (GRBs): 1) the ultrarelativistic regime of a shock front expanding with a Lorentz gamma factor $\sim$ 300; 2) the quantum vacuum polarization process leading to an electron-positron plasma originating the shock front; and 3) the general relativistic process of energy extraction from a black hole originating the vacuum polarization process. There are two different classes of GRBs: the long GRBs and the short GRBs. We here address the issue of the long GRBs. The theoretical understanding of the long GRBs has led to the detailed description of their luminosities in fixed energy bands, of their spectral features and made also possible to probe the astrophysical scenario in which they originate. We are specially interested, in this report, to a subclass of long GRBs which appear to be accompanied by a supernova explosion. We are considering two specific examples: GRB980425/SN1998bw and GRB030329/SN2003dh. While these supernovae appear to have a standard energetics of 10^{49} ergs, the GRBs are highly variable and can have energetics 10^4 – 10^5 times larger than the ones of the supernovae. Moreover, many long GRBs occurs without the presence of a supernova. It is concluded that in no way a GRB can originate from a supernova. The precise theoretical understanding of the GRB luminosity we present evidence, in both these systems, the existence of an independent component in the X-ray emission, usually interpreted in the current literature as part of the GRB afterglow. This component has been observed by Chandra and XMM to have a strong decay on scale of months. We have named here these two sources respectively URCA-1 and URCA-2, in honor of the work that George Gamow and Mario Shoenberg did in 1939 in this town of Urca identifying the basic mechanism, the Urca processes, leading to the process of gravitational collapse and the formation of a neutron star and a supernova. The further hypothesis is considered to relate this X-ray source to a neutron star, newly born in the Supernova. This hypothesis should be submitted to further theoretical and observational investigation. Some theoretical developments to clarify the astrophysical origin of this new scenario are outlined. We turn then to the theoretical developments in the short GRBs: we first report some progress in the understanding the dynamical phase of collapse, the mass-energy formula and the extraction of blackholic energy which have been motivated by the analysis of the short GRBs. In this context progress has also been accomplished on establishing an absolute lower limit to the irreducible mass of the black hole as well as on some critical considerations about the relations of general relativity and the second law of thermodynamics. We recall how this last issue has been one of the most debated in theoretical physics in the past thirty years due to the work of Bekenstein and Hawking. Following these conceptual progresses we analyze the vacuum polarization process around an overcritical collapsing shell. We evidence the existence of a separatrix and a dyadosphere trapping surface in the dynamics of the electron-positron plasma generated during the process of gravitational collapse. We then analyze, using recent progress in the solution of the Vlasov-Boltzmann-Maxwell system, the oscillation regime in the created electron-positron plasma and their rapid convergence to a thermalized spectrum. We conclude by making precise predictions for the spectra, the energy fluxes and characteristic time-scales of the radiation for short-bursts. If the precise luminosity variation and spectral hardening of the radiation we have predicted will be confirmed by observations of short-bursts, these systems will play a major role as standard candles in cosmology. These considerations will also be relevant for the analysis of the long-bursts when the baryonic matter contribution will be taken into account.

2. R. Ruffini, M.G. Bernardini, C.L. Bianco, P. Chardonnet, F. Fraschetti, V. Gurzadyan, L. Vitagliano, S.-S. Xue; "Black hole physics and astrophysics: The GRB-Supernova connection and URCA-1 – URCA-2"; in Proceedings of the Tenth Marcel Grossmann Meeting on General Relativity, Rio de Janeiro, Brazil, July 2003, M. Novello, S.E. Perez-Bergliaffa, Editors; p. 369; World Scientific, (Singapore, 2006).

   We outline the confluence of three novel theoretical fields in our modeling of Gamma-Ray Bursts (GRBs): 1) the ultrarelativistic regime of a shock front expanding with a Lorentz gamma factor ~ 300; 2) the quantum vacuum polarization process leading to an electron-positron plasma originating the shock front; and 3) the general relativistic process of energy extraction from a black hole originating the vacuum polarization process. There are two different classes of GRBs: the long GRBs and the short GRBs. We here address the issue of the long GRBs. The theoretical understanding of the long GRBs has led to the detailed description of their luminosities in fixed energy bands, of their spectral features and made also possible to probe the astrophysical scenario in which they originate. We are specially interested, in this report, to a subclass of long GRBs which appear to be accompanied by a supernova explosion. We are considering two specific examples: GRB980425/SN1998bw and GRB030329/SN2003dh. While these supernovae appear to have a standard energetics of 10^{49} ergs, the GRBs are highly variable and can have energetics 10^4 – 10^5 times larger than the ones of the supernovae. Moreover, many long GRBs occurs without the presence of a supernova. It is concluded that in no way a GRB can originate from a supernova. The precise theoretical understanding of the GRB luminosity we present evidence, in both these systems, the existence of an independent component in the X-ray emission, usually interpreted in the current literature as part of the GRB afterglow. This component has been observed by Chandra and XMM to have a strong decay on scale of months. We have named here these two sources respectively URCA-1 and URCA-2, in honor of the work that George Gamow and Mario Shoenberg did in 1939 in this town of Urca identifying the basic mechanism, the Urca processes, leading to the process of gravitational collapse and the formation of a neutron star and a supernova. The further hypothesis is considered to relate this X-ray source to a neutron star, newly born in the Supernova. This hypothesis should be submitted to further theoretical and observational investigation. Some theoretical developments to clarify the astrophysical origin of this new scenario are outlined.

3. M.G. Bernardini, C.L. Bianco, P. Chardonnet, F. Fraschetti, R. Ruffini, S.-S. Xue; "General features of GRB 030329 in the EMBH model"; in Proceedings of the Tenth Marcel Grossmann Meeting on General Relativity, Rio de Janeiro, Brazil, July 2003, M. Novello, S.E. Perez-Bergliaffa, Editors; p. 2459; World Scientific, (Singapore, 2006).

   GRB 030329 is considered within the EMBH model. We determine the three free parameters and deduce its luminosity in given energy bands comparing it with the observations. The observed substructures are compared with the predictions of the model: by applying the result that substructures observed in the extended afterglow peak emission (E-APE) do indeed originate in the collision of the accelerated baryonic matter (ABM) pulse with the inhomogeneities in the interstellar medium around the black-hole, masks of density inhomogeneities are considered in order to reproduce the observed temporal substructures. The induced supernova concept is applied to this system and the general consequences that we are witnessing are the formation of a cosmological thriptych of a black hole originating the GRB 030329, the supernova SN2003dh and a young neutron star. Analogies to the system GRB 980425–SN1998bw are outlined.

4. R. Ruffini, M.G. Bernardini, C.L. Bianco, P. Chardonnet, A. Corsi, F. Fraschetti, S.-S. Xue; "GRB 970228 and its associated Supernova in the EMBH model"; in Proceedings of the Tenth Marcel Grossmann Meeting

on General Relativity, Rio de Janeiro, Brazil, July 2003, M. Novello, S.E. Perez-Bergliaffa, Editors; p. 2465; World Scientific, (Singapore, 2006).

The γ-ray burst of 1997 February 28 is analyzed within the Electromagnetic Black Hole model. We first estimate the value of the total energy deposited in the dyadosphere, E_{dya}, and the amount of baryonic matter left over by the EMBH progenitor star, $B = M_B c^2 / E_{dya}$. We then consider the role of the interstellar medium number density n_{ISM} and of the ratio R between the effective emitting area and the total surface area of the γ-ray burst source, in reproducing the prompt emission and the X-ray afterglow of this burst. Some considerations are also done concerning the possibility of explaining, within the theory, the observed evidence for a supernova in the optical afterglow.

5. F. Fraschetti, M.G. Bernardini, C.L. Bianco, P. Chardonnet, R. Ruffini, S.-S. Xue; "Inferences on the ISM structure around GRB980425 and GRB980425-SN1998bw association in the EMBH Model"; in Proceedings of the Tenth Marcel Grossmann Meeting on General Relativity, Rio de Janeiro, Brazil, July 2003, M. Novello, S.E. Perez-Bergliaffa, Editors; p. 2451; World Scientific, (Singapore, 2006).

   We determine the four free parameters within the EMBH model for GRB 980425 and deduce its luminosity in given energy bands, its spectra and its time variability in the prompt radiation. We compute the basic kinematical parameters of GRB 980425. In the extended afterglow peak emission the Lorentz γ factor is lower than the critical value 150 which has been found in Ruffini et al. (2002) to be necessary in order to perform the tomography of the ISM surrounding the GRB as suggested by Dermer & Mitman (1999). The detailed structure of the density inhomogeneities as well as the effects of radial apparent superluminal effects are evaluated within the EMBH model. Under the assumption that the energy distribution of emitted radiation is thermal in the comoving frame, time integrated spectra of EMBH model for prompt emission are computed. The induced supernova concept is applied to this system and general consequences on the astrophysical and cosmological scenario are derived.

6. R. Ruffini, M.G. Bernardini, C.L. Bianco, P. Chardonnet, F. Fraschetti, R. Guida, S.-S. Xue; "GRB 050315: A step in the proof of the uniqueness of the overall GRB structure"; in "GAMMA-RAY BURSTS IN THE SWIFT ERA: Sixteenth Maryland Astrophysics Conference", Washington, DC, USA, November 29th – December 2nd 2005, Stephen S. Holt,

Neil Gehrels, John A. Nousek, Editors; AIP Conference Proceedings, 836, 103 (2006).

Using the Swift data of GRB 050315, we progress in proving the uniqueness of our theoretically predicted Gamma-Ray Burst (GRB) structure as composed by a proper-GRB, emitted at the transparency of an electron-positron plasma with suitable baryon loading, and an afterglow comprising the "prompt radiation" as due to external shocks. Detailed light curves for selected energy bands are theoretically fitted in the entire temporal region of the Swift observations ranging over 10^6 seconds.

7. R. Ruffini, M.G. Bernardini, C.L. Bianco, P. Chardonnet, F. Fraschetti, S.-S. Xue; "Theoretical Interpretation of GRB 031203 and URCA-3"; in "Relativistic Astrophysics and Cosmology - Einstein's Legacy", B. Aschenbach, V. Burwitz, G. Hasinger, B. Leibundgut, Editors; Springer-Verlag (2007).

8. R. Ruffini, M.G. Bernardini, C.L. Bianco, L. Caito, P. Chardonnet, M.G. Dainotti, F. Fraschetti, R. Guida, M. Rotondo, G. Vereshchagin, L. Vitagliano, S.-S. Xue; "The Blackholic energy and the canonical Gamma-Ray Burst"; in Proceedings of the XIIth Brazilian School on Cosmology and Gravitation, Mangaratiba, Rio de Janeiro (Brazil), September 2006, M. Novello, S.E. Perez Bergliaffa, Editors; AIP Conference Proceedings, 910, 55 (2007).

   Gamma-Ray Bursts (GRBs) represent very likely "the" most extensive computational, theoretical and observational effort ever carried out successfully in physics and astrophysics. The extensive campaign of observation from space based X-ray and γ-ray observatory, such as the *Vela*, CGRO, BeppoSAX, HETE-II, INTEGRAL, *Swift*, R-XTE, *Chandra*, XMM satellites, have been matched by complementary observations in the radio wavelength (e.g. by the VLA) and in the optical band (e.g. by VLT, Keck, ROSAT). The net result is unprecedented accuracy in the received data allowing the determination of the energetics, the time variability and the spectral properties of these GRB sources. The very fortunate situation occurs that these data can be confronted with a mature theoretical development. Theoretical interpretation of the above data allows progress in three different frontiers of knowledge: **a)** the ultrarelativistic regimes of a macroscopic source moving at Lorentz gamma factors up to ~ 400; **b)** the occurrence of vacuum polarization process verifying some of the yet untested regimes of ultrarelativistic quantum field theories; and **c)** the first evidence for extracting, during the process of gravitational collapse leading to the formation of a black hole, amounts of energies up to 10^{55} ergs of blackholic energy — a new form of energy in physics and astrophysics. We outline how this progress leads to the confirmation of three interpretation paradigms for GRBs proposed in July 2001. Thanks mainly to the observations by *Swift* and the optical observations by VLT, the outcome of this analysis points to the existence of a "canonical" GRB, originating from a variety of different initial astrophysical scenarios. The communality of these GRBs appears to be that they all are emitted in the process of formation of a black hole with a negligible value of its angular momentum. The following sequence of events appears to be canonical: the vacuum polarization process in the dyadosphere with the creation of the optically thick self accelerating electron-positron plasma; the engulfment of baryonic mass during the plasma expansion; adiabatic expansion of the optically thick "fireshell" of electron-positron-baryon plasma up to the transparency; the interaction of the accelerated baryonic matter with the interstellar medium (ISM). This leads to the canonical GRB composed of a proper GRB (P-GRB), emitted at the moment of transparency, followed by an extended afterglow. The sole parameters in this scenario are the total energy of the dyadosphere E_{dya}, the fireshell baryon loading M_B defined by the dimensionless parameter $B \equiv M_B c^2 / E_{dya}$, and the ISM filamentary distribution around the source. In the limit $B \to 0$ the total energy is radiated in the P-GRB with a vanishing contribution in the afterglow. In this limit, the canonical GRBs explain as well the short GRBs. In these lecture notes we systematically outline the main results of our model comparing and contrasting them with the ones in the current literature. In both cases, we have limited ourselves to review already published results in refereed publications. We emphasize as well the role of GRBs in testing yet unexplored grounds in the foundations of general relativity and relativistic field theories.

9. R. Ruffini, M.G. Bernardini, C.L. Bianco, L. Caito, P. Chardonnet, M.G. Dainotti, F. Fraschetti, R. Guida, G. Vereshchagin, S.-S. Xue; "The role of GRB 031203 in clarifying the astrophysical GRB scenario"; in Proceedings of the 6^{th} Integral Workshop - The Obscured Universe, Moscow, (Russia), July 2006, S. Grebenev, R. Sunyaev, C. Winkler, A. Parmar, L. Ouwehand, Editors; ESA Special Publication, SP-622, 561 (2007).

The luminosity and the spectral distribution of the afterglow of GRB 031203 have been presented within our theoretical framework, which envisages the GRB structure as composed by a proper-GRB, emitted at the transparency of an electron-positron plasma with suitable baryon loading, and an afterglow comprising the "prompt emission" as due to external shocks. In addition to the GRB emission, there appears to be a prolonged soft X-Ray emission lasting for 10^6–10^7 seconds followed by an exponential decay. This additional source has been called by us URCA-3. It is urgent to establish if this component is related to the GRB or to the Supernova (SN). In this second case, there are two possibilities: either the interaction of the SN ejecta with the interstellar medium or, possibly, the cooling of a young neutron star formed in the SN 2003lw process. The analogies and the differences between this triptych GRB 031203 / SN 2003lw / URCA-3 and the corresponding ones GRB 980425 / SN 1998bw / URCA-1 and GRB 030329 / SN 2003dh / URCA-2, as well as GRB 060218 / SN 2006aj are discussed.

10. M.G. Bernardini, C.L. Bianco, L. Caito, M.G. Dainotti, R. Guida, R. Ruffini; "GRB970228 and the class of GRBs with an initial spikelike emission: do they follow the Amati relation?"; in Relativistic Astrophysics – Proceedings of the 4^{th} Italian-Sino Workshop, Pescara (Italy), July 2007, C.L. Bianco, S.-S. Xue, Editors; AIP Conference Proceedings, 966, 7 (2008).

    On the basis of the recent understanding of GRB050315 and GRB060218, we return to GRB970228, the first Gamma-Ray Burst (GRB) with detected afterglow. We proposed it as the prototype for a new class of GRBs with "an occasional softer extended emission lasting tenths of seconds after an initial spikelike emission". Detailed theoretical computation of the GRB970228 light curves in selected energy bands for the prompt emission are presented and compared with observational *Beppo*SAX data. From our analysis we conclude that GRB970228 and likely the ones of the above mentioned new class of GRBs are "canonical GRBs" have only one peculiarity: they exploded in a galactic environment, possibly the halo, with a very low value of CBM density. Here we investigate how GRB970228 unveils another peculiarity of this class of GRBs: they do not fulfill the "Amati relation". We provide a theoretical explanation within the fireshell model for the apparent absence of such correlation for the GRBs belonging to this new class.

11. C.L. Bianco, M.G. Bernardini, L. Caito, M.G. Dainotti, R. Guida, R. Ruffini; "The "Fireshell" Model and the "Canonical" GRB Scenario; in Relativistic Astrophysics – Proceedings of the 4^{th} Italian-Sino Workshop, Pescara (Italy), July 2007, C.L. Bianco, S.-S. Xue, Editors; AIP Conference Proceedings, 966, 12 (2008).

In the "fireshell" model we define a "canonical GRB" light curve with two sharply different components: the Proper-GRB (P-GRB), emitted when the optically thick fireshell of electron-positron plasma originating the phenomenon reaches transparency, and the afterglow, emitted due to the collision between the remaining optically thin fireshell and the CircumBurst Medium (CBM). We outline our "canonical GRB" scenario, originating from the gravitational collapse to a black hole, with a special emphasis on the discrimination between "genuine" and "fake" short GRBs.

12. L. Caito, M.G. Bernardini, C.L. Bianco, M.G. Dainotti, R. Guida, R. Ruffini; "GRB 060614: A Progress Report"; in Relativistic Astrophysics – Proceedings of the 4^{th} Italian-Sino Workshop, Pescara (Italy), July 2007, C.L. Bianco, S.-S. Xue, Editors; AIP Conference Proceedings, 966, 16 (2008).

    The explosion of GRB 060614, detected by the Swift satellite, produced a deep break in the GRB scenario opening new horizons of investigation, because it can't be traced back to any traditional scheme of classification. In fact, it manifests peculiarities both of long bursts and of short bursts. Above all, it is the first case of long duration near GRB without any bright Ib/c associated Supernova. We will show that, in our canonical GRB scenario, this "anomalous" situation finds a natural interpretation and allows us to discuss a possible variation to the traditional classification scheme, introducing the distinction between "genuine" and "fake" short bursts.

13. M.G. Dainotti, M.G. Bernardini, C.L. Bianco, L. Caito, R. Guida, R. Ruffini; "GRB 060218 and the Binaries as Progenitors of GRB-SN Systems"; in Relativistic Astrophysics – Proceedings of the 4^{th} Italian-Sino Workshop, Pescara (Italy), July 2007, C.L. Bianco, S.-S. Xue, Editors; AIP Conference Proceedings, 966, 25 (2008).

    We study the Gamma-Ray Burst (GRB) 060218: a particularly close source at $z = 0.033$ with an extremely long duration, namely $T_{90} \sim 2000$ s, related to SN 2006aj. This source appears to be a very soft burst, with a peak in the spectrum at 4.9 keV, therefore interpreted as an X-Ray Flash (XRF). It fullfills the Amati relation. I present the fitting procedure, which is time consuming. In order to show its sensitivity I also present two examples of fits with the same value of B and different value of $E^{tot}_{e^\pm}$. We fit the X- and γ-ray observations by *Swift* of GRB 060218 in the 0.1–150 keV energy band during the entire time of observations from 0 all the way to 10^6 s within a unified theoretical model. The free parameters of our theory are only three, namely the total energy $E^{tot}_{e\pm}$ of the $e^{\pm}$ plasma, its baryon loading $B \equiv M_B c^2/E^{tot}_{e\pm}$, as well as the CircumBurst Medium (CBM) distribution. We justify the extremely long duration of this GRB by a total energy $E^{tot}_{e\pm} = 2.32 \times 10^{50}$ erg, a very high value of the baryon loading $B = 1.0 \times 10^{-2}$ and the effective CircumBurst Medium (CBM) density which shows a radial dependence $n_{cbm} \propto r^{-\alpha}$ with $1.0 \leq \alpha \leq 1.7$ and monotonically decreases from 1 to 10^{-6} particles/cm^3. We recall that this value of the B parameter is the highest among the sources we have analyzed and it is very close to its absolute upper limit expected. By our fit we show that there is no basic differences between XRFs and more general GRBs. They all originate from the collapse process to a black hole and their difference is due to the variability of the three basic parameters within the range of full applicability of the theory. We also think that the smallest possible black hole, formed by the gravitational collapse of a neutron star in a binary system, is consistent with the especially low energetics of the class of GRBs associated with SNe Ib/c.

14. R. Guida, M.G. Bernardini, C.L. Bianco, L. Caito, M.G. Dainotti, R. Ruffini; "The Amati Relation within the Fireshell Model"; in Relativistic Astrophysics – Proceedings of the 4^{th} Italian-Sino Workshop, Pescara (Italy), July 2007, C.L. Bianco, S.-S. Xue, Editors; AIP Conference Proceedings, 966, 46 (2008).

    In this work we show the existence of a spectral-energy correlation within our "fireshell" model for GRBs. The free parameters of the model are the total energy $E^{e\pm}_{tot}$ of the $e^{\pm}$ plasma and its baryon loading $B \equiv M_B\, c^2/E^{e\pm}_{tot}$, characterizing the source, and the parameters describing the effective CircumBurst medium (CBM) distribution, namely its particle number density ρ and its effective emitting area R. We build a sample of pseudo-GRBs, i.e. a set of theoretically simulated light curves, varying the total energy of the electron-positron plasma $E^{e\pm}_{tot}$ and keeping the same baryon loading; the parametrization used to describe the distribution of the CircumBurst medium is the same as well for all the pseudo-GRBs. The values of these parameters (B, ρ and R) used in this work are equal to the ones assumed to fit GRB050315, a *Swift* burst representing a good example of what in the literature has been addressed as "canonical light curve". For each GRB of the sample we calculate the νF_ν spectrum integrating the theoretically computed light curve over the total time, namely from our T_0, the end of the Proper-GRB (P-GRB), up to the end of our afterglow phase, when the fireshell Lorentz gamma factor is close to unity; we exclude the P-GRB from this spectral computation because, following our "canonical" GRB scenario, this component of the GRB emission is physically different from the other component, that is our afterglow component, so one should take care in no mixing them. We find that the maximum of this spectrum, that is the observed peak energy $E_{p,tot}$, correlates with the initial electron-positron plasma energy $E_{tot}^{e\pm}$ in a way very similar to the Amati one: $E_{p,tot} \propto (E_{tot}^{e\pm})^{0.5}$.

15. R. Guida, M.G. Bernardini, C.L. Bianco, L. Caito, M.G. Dainotti, R. Ruffini; "Theoretical interpretation of the Amati relation within the fireshell model"; in GAMMA-RAY BURSTS 2007: Proceedings of the Santa Fe Conference, Santa Fe (NM, USA), November 2007, M. Galassi, D. Palmer, E. Fenimore, Editors; AIP Conference Proceedings, 1000, 60 (2008).

    We discuss within our theoretical "fireshell" model for Gamma-Ray Bursts (GRBs) the theoretical interpretation of the phenomenological correlation between the isotropic-equivalent radiated energy of the prompt emission E_{iso} and the cosmological rest-frame νF_ν spectrum peak energy E_p observed by Amati and collaborators. Possible reasons for some of the outliers of this relation are given.

16. L. Caito, M.G. Bernardini, C.L. Bianco, M.G. Dainotti, R. Guida, R. Ruffini; "GRB 060614: a Fake Short Gamma-Ray Burst"; in GAMMA-RAY BURSTS 2007: Proceedings of the Santa Fe Conference, Santa Fe (NM, USA), November 2007, M. Galassi, D. Palmer, E. Fenimore, Editors; AIP Conference Proceedings, 1000, 301 (2008).

    The explosion of GRB 060614 produced a deep break in the GRB scenario and opened new horizons of investigation because it can't be traced back to any traditional scheme of classification. In fact, it manifests peculiarities both of long bursts and of short bursts and, above all, it is the first case of long duration near GRB without any bright Ib/c associated Supernova. We will show that, in our canonical GRB scenario, this "anomalous" situation finds a natural interpretation and allows us to discuss a possible variation to the traditional classification scheme, introducing the distinction between "genuine" and "fake" short bursts.

17. C.L. Bianco, M.G. Bernardini, L. Caito, M.G. Dainotti, R. Guida, R. Ruffini; "Short and canonical GRBs"; in GAMMA-RAY BURSTS 2007: Proceedings of the Santa Fe Conference, Santa Fe (NM, USA), November 2007, M. Galassi, D. Palmer, E. Fenimore, Editors; AIP Conference Proceedings, 1000, 305 (2008).

Within the "fireshell" model for the Gamma-Ray Bursts (GRBs) we define a "canonical GRB" light curve with two sharply different components: the Proper-GRB (P-GRB), emitted when the optically thick fireshell of electron-positron plasma originating the phenomenon reaches transparency, and the afterglow, emitted due to the collision between the remaining optically thin fireshell and the CircumBurst Medium (CBM). We outline our "canonical GRB" scenario, with a special emphasis on the discrimination between "genuine" and "fake" short GRBs.

18. C.L. Bianco, M.G. Bernardini, L. Caito, M.G. Dainotti, R. Guida, R. Ruffini, G. Vereshchagin, S.-S. Xue; "The Equations of motion of the "fireshell""; in OBSERVATIONAL EVIDENCE FOR BLACK HOLES IN THE UNIVERSE: Proceedings of the 2^{nd} Kolkata Conference, Kolkata (India), February 2008, S.K. Chakrabarti, A.S. Majumdar, Editors; AIP Conference Proceedings, 1053, 259 (2008).

    The Fireshell originating a Gamma-Ray Burst (GRB) encompasses an optically thick regime followed by an optically thin one. In the first one the fireshell self-accelerates from a Lorentz gamma factor equal to 1 all the way to 200-300. The physics of this system is based on the continuous annihilation of electron-positron pairs in an optically thick e^+e^- plasma with a small baryon loading. In the following regime, the optically thin fireshell, composed by the baryons left over after the transparency point, ballistically expands into the CircumBurst Medium (CBM). The dynamics of the fireshell during both regimes will be analyzed. In particular we will re-examine the validity of the constant-index power-law relation between the fireshell Lorentz gamma factor and its radial coordinate, usually adopted in the current literature on the grounds of an "ultrarelativistic" approximation. Such expressions are found to be mathematically correct but only approximately valid in a very limited range of the physical and astrophysical parameters and in an asymptotic regime which is reached only for a very short time, if any.

19. M.G. Bernardini, C.L. Bianco, L. Caito, M.G. Dainotti, R. Guida, R. Ruffini; "The "Canonical" GRBs within the fireshell model"; in OBSERVATIONAL EVIDENCE FOR BLACK HOLES IN THE UNIVERSE: Proceedings of the 2^{nd} Kolkata Conference, Kolkata (India), February 2008, S.K. Chakrabarti, A.S. Majumdar, Editors; AIP Conference Proceedings, 1053, 267 (2008).

    Within the fireshell model we define a "canonical" GRB light curve with two sharply different components: the Proper-GRB (P-GRB), emitted when the optically thick fireshell of electron-positron plasma originating the phenomenon reaches transparency, and the afterglow, emitted due to the collision between the remaining optically thin fireshell and the CircumBurst Medium (CBM). On the basis of the recent understanding of GRB970228 as the prototype for a new class of GRBs with "an occasional softer extended emission lasting tenths of seconds after an initial spikelike emission" we outline our "canonical" GRB scenario, originating from the gravitational collapse to a black hole, with a special emphasis on the discrimination between short GRBs and the ones appearing as such due to their peculiar astrophysical setting.

20. M.G. Dainotti, M.G. Bernardini, C.L. Bianco, L. Caito, R. Guida, R. Ruffini; "GRB 060218: the density mask and its peculiarity compared to the other sources"; in OBSERVATIONAL EVIDENCE FOR BLACK HOLES IN THE UNIVERSE: Proceedings of the 2^{nd} Kolkata Conference, Kolkata (India), February 2008, S.K. Chakrabarti, A.S. Majumdar, Editors; AIP Conference Proceedings, 1053, 283 (2008).

    The Swift satellite has given continuous data in the range 0.3–150 keV from 0 s to 106 s for GRB060218 associated with SN2006aj. It has an unusually long duration ($T_{90} \sim 2100$ s). We plan to fit the complete γ- and X-ray light curves of this long duration GRB, including the prompt emission and we give peculiar attention to the afterglow lightcurve in order to better constrain the density mask. We apply our "fireshell" model based on the formation of a black hole, giving the relevant references. The initial total energy of the electron-positron plasma $E^{tot}_{e^{\pm}} == 2.32 \times 10^{50}$ erg has a particularly low value similarly to the other GRBs associated with SNe. For the first time we observe a baryon loading $B = 10^{-2}$ which coincides with the upper limit for the dynamical stability of the fireshell. The effective CircumBurst Medium (CBM) density shows a radial dependence $n_{cbm} \propto r^{-a}$ with $1.0 \leq a \leq 1.7$ and monotonically decreases from 1 to 10^{-6} particles/cm^3. Such a behavior is interpreted as due to a fragmentation in the fireshell. Such a fragmentation is crucial in explaining both the unusually large T_{90} and the consequently inferred abnormal low value of the CBM effective density. We present the comparison between the density mask of this source and the ones of a normal GRB 050315 and a fake short, GRB 970228, making some assumptions on the CBM behaviour in the surrounding of the Black hole.

21. L. Caito, M.G. Bernardini, C.L. Bianco, M.G. Dainotti, R. Guida, R. Ruffini; "GRB 060614 in the canonical fireshell model"; in OBSERVATIONAL

EVIDENCE FOR BLACK HOLES IN THE UNIVERSE: Proceedings of the 2^{nd} Kolkata Conference, Kolkata (India), February 2008, S.K. Chakrabarti, A.S. Majumdar, Editors; AIP Conference Proceedings, 1053, 291 (2008).

Gamma-Ray Burst (GRB) 060614 is the first nearby long duration GRB clearly not associated to any bright Ib/c Supernova. The explosion of this burst undermines one of the fundamental assumptions of the standard scenario and opens new horizons and hints of investigation. GRB 060614, hardly classifiable as a short GRB, is not either a "typical" long GRB since it occurs in a low star forming region. Moreover, it presents deep similarities with GRB 970228, which is the prototype of the "fake" short bursts, or better canonical GRBs disguised as short ones. Within the "fireshell" model, we test if this "anomalous" source can be a disguised short GRB.

22. L.J. Rangel Lemos, S. Casanova, R. Ruffini, S.S. Xue; "Fermi's approach to the study of pp interactions"; in OBSERVATIONAL EVIDENCE FOR BLACK HOLES IN THE UNIVERSE: Proceedings of the 2^{nd} Kolkata Conference, Kolkata (India), February 2008, S.K. Chakrabarti, A.S. Majumdar, Editors; AIP Conference Proceedings, 1053, 275 (2008).

    The physics of hadronic interactions found much difficulties for explain the experimental data. In this work we study the approach of Fermi (1950) about the multiplicity of pions emitted in pp interactions and in follow we compare with the modern approach

23. R. Ruffini, A.G. Aksenov, M.G. Bernardini, C.L. Bianco, L. Caito, M.G. Dainotti, G. De Barros, R. Guida, G.V. Vereshchagin, S.-S. Xue; "The canonical Gamma-Ray Bursts and their 'precursors"'; in 2008 NANJING GAMMA-RAY BURST CONFERENCE, Proceedings of the 2008 Nanjing Gamma-Ray Burst Conference, Nanjing (China), June 2008, Y.-F. Huang, Z.-G. Dai, B. Zhang, Editors; AIP Conference Proceedings, 1065, 219 (2008).

    The fireshell model for Gamma-Ray Bursts (GRBs) naturally leads to a canonical GRB composed of a proper-GRB (P-GRB) and an afterglow. P-GRBs, introduced by us in 2001, are sometimes considered "precursors" of the main GRB event in the current literature. We show in this paper how the fireshell model leads to the understanding of the structure of GRBs, with precise estimates of the time sequence and intensities of the P-GRB and the of the afterglow. It leads as well to a natural classification of the canonical GRBs which overcomes the traditional one in short and long GRBs.

24. M.G. Bernardini, C.L. Bianco, L. Caito, M.G. Dainotti, R. Guida, R. Ruffini; "Preliminary analysis of GRB060607A within the fireshell model"; in 2008 NANJING GAMMA-RAY BURST CONFERENCE; Proceedings of the 2008 Nanjing Gamma-Ray Burst Conference, Nanjing (China), June 2008, Y.-F. Huang, Z.-G. Dai, B. Zhang, Editors; AIP Conference Proceedings, 1065, 227 (2008).

    GRB060607A is a very distant ($z = 3.082$) and energetic event ($E_{iso} \sim 10^{53}$ erg). Its main peculiarity is that the peak of the near-infrared afterglow has been observed with the REM robotic telescope, allowing to infer the initial Lorentz gamma factor of the emitting system. We present a preliminary analysis of the spectra and light curves of GRB060607A prompt emission within the fireshell model. We show that the N(E) spectrum of the prompt emission, whose behavior is usually described as "simple power-law", can also be fitted in a satisfactory way by a convolution of thermal spectra as predicted by the model we applied. The theoretical time-integrated spectrum of the prompt emission as well as the light curves in the BAT and XRT energy band are in good agreement with the observations, enforcing the plausibility of our approach. Furthermore, the initial value of Lorentz gamma factor we predict is compatible with the one deduced from the REM observations.

25. C.L. Bianco, M.G. Bernardini, L. Caito, M.G. Dainotti, R. Guida, R. Ruffini; "The "fireshell" model and the "canonical GRB" scenario"; in 2008 NANJING GAMMA-RAY BURST CONFERENCE; Proceedings of the 2008 Nanjing Gamma-Ray Burst Conference, Nanjing (China), June 2008, Y.-F. Huang, Z.-G. Dai, B. Zhang, Editors; AIP Conference Proceedings, 1065, 223 (2008).

    The Swift observation of GRB 060614, as well as the catalog analysis by Norris & Bonnell (2006), opened the door "on a new Gamma-Ray Bursts (GRBs) classification scheme that straddles both long and short bursts" (Gehrels et al. 2006). Within the "fireshell" model for the Gamma-Ray Bursts (GRBs) we define a "canonical GRB" light curve with two sharply different components: the Proper-GRB (P-GRB), emitted when the optically thick fireshell of electron-positron plasma originating the phenomenon reaches transparency, and the afterglow, emitted due to the collision between the remaining optically thin fireshell and the CircumBurst Medium (CBM). We here outline our "canonical GRB" scenario, which implies three different GRB classes: the "genuine" short GRBs, the "fake" or "disguised" short GRBs and the other (so-called "long")

GRBs. We also outline some implications for the theoretical interpretation of the Amati relation.

26. G. De Barros, M.G. Bernardini, C.L. Bianco, L. Caito, M.G. Dainotti, R. Guida, R. Ruffini; "Is GRB 050509b a "genuine" short GRB?"; in 2008 NANJING GAMMA-RAY BURST CONFERENCE; Proceedings of the 2008 Nanjing Gamma-Ray Burst Conference, Nanjing (China), June 2008, Y.-F. Huang, Z.-G. Dai, B. Zhang, Editors; AIP Conference Proceedings, 1065, 231 (2008).

    Within our "fireshell" model we introduced a "canonical" GRB scenario which differentiates physically the "proper GRB" (P-GRB) emission when photons decouple, and the afterglow emission due to interaction of the accelerated baryons with the CircumBurst Medium (CBM). The ratio between energetics of the two components is ruled by the baryon loading of the fireshell. We here analyse the possibility that GRB050509b is the first case of a "genuine" short GRB the ones with smaller baryon loading. In such a case, the GRB050509b "prompt emission" would be dominated by the "proper GRB" and, moreover, the P-GRB total energy would be greater than the afterglow one. Our fit of the afterglow data and of the P-GRB energetics indicates that this source present the smallest baryon loading we ever encountered so far, being on the order of 10^{-4}.

27. G. De Barros, A.G. Aksenov, C.L. Bianco, R. Ruffini, G.V. Vereshchagin; "Fireshell versus Fireball scenarios"; in 2008 NANJING GAMMA-RAY BURST CONFERENCE; Proceedings of the 2008 Nanjing Gamma-Ray Burst Conference, Nanjing (China), June 2008, Y.-F. Huang, Z.-G. Dai, B. Zhang, Editors; AIP Conference Proceedings, 1065, 234 (2008).

    We revisit Cavallo and Rees classification based on the analysis of initial conditions in electron-positron-photon plasma which appears suddenly around compact astrophysical objects and gives origin to GRBs. These initial conditions were recently studied in [1,2] by numerical integration of relativistic Boltzmann equations with collision integrals, including binary and triple interactions between particles. The main conclusion is that the pair plasma in GRB sources quickly reaches thermal equilibrium well before its expansion starts. In light of this work we comment on each of the four scenarios proposed by Cavallo and Rees and discuss their applicability to describe evolution of GRB sources.

28. M.G. Bernardini, C.L. Bianco, L. Caito, M.G. Dainotti, R. Guida, R. Ruffini; "GRB970228 as a prototype for the class of GRBs with an initial spike-like emission"; in Proceedings of the Eleventh Marcel Grossmann Meeting on General Relativity, Berlin, Germany, July 2006, H. Kleinert, R.T. Jantzen, Editors; World Scientific, (Singapore, 2008).

    We interpret GRB970228 prompt emission within our "canonical" GRB scenario, identifying the initial spikelike emission with the Proper-GRB (P-GRB) and the following bumps with the afterglow peak emission. Furthermore, we emphasize the necessity to consider the "canonical" GRB as a whole due to the highly non-linear nature of the model we applied.

29. M.G. Bernardini, C.L. Bianco, L. Caito, M.G. Dainotti, R. Guida, R. Ruffini; "GRB980425 and the puzzling URCA1 emission"; in Proceedings of the Eleventh Marcel Grossmann Meeting on General Relativity, Berlin, Germany, July 2006, H. Kleinert, R.T. Jantzen, Editors; World Scientific, (Singapore, 2008).

    We applied our "fireshell" model to GRB980425 observational data, reproducing very satisfactory its prompt emission. We use the results of our analysis to provide a possible interpretation for the X-ray emission of the source S1. The effect on the GRB analysis of the lack of data in the pre-Swift observations is also outlined.

30. C.L. Bianco, M.G. Bernardini, L. Caito, P. Chardonnet, M.G. Dainotti, F. Fraschetti, R. Guida, R. Ruffini, S.-S. Xue; "Theoretical interpretation of 'long' and 'short' GRBs"; in Proceedings of the Eleventh Marcel Grossmann Meeting on General Relativity, Berlin, Germany, July 2006, H. Kleinert, R.T. Jantzen, Editors; World Scientific, (Singapore, 2008).

    Within the "fireshell" model we define a "canonical GRB" light curve with two sharply different components: the Proper-GRB (P-GRB), emitted when the optically thick fireshell of electron-positron plasma originating the phenomenon reaches transparency, and the afterglow, emitted due to the collision between the remaining optically thin fireshell and the CircumBurst Medium (CBM). We here present the consequences of such a scenario on the theoretical interpretation of the nature of "long" and "short" GRBs.

31. C.L. Bianco, M.G. Bernardini, P. Chardonnet, F. Fraschetti, R. Ruffini, S.-S. Xue; "Theoretical interpretation of luminosity and spectral properties of GRB 031203"; in Proceedings of the Eleventh Marcel Grossmann

Meeting on General Relativity, Berlin, Germany, July 2006, H. Kleinert, R.T. Jantzen, Editors; World Scientific, (Singapore, 2008).

We show how an emission endowed with an instantaneous thermal spectrum in the co-moving frame of the expanding fireshell can reproduce the time-integrated GRB observed non-thermal spectrum. An explicit example in the case of GRB 031203 is presented.

32. C.L. Bianco, R. Ruffini; "The 'Fireshell' model in the Swift era"; in Proceedings of the Eleventh Marcel Grossmann Meeting on General Relativity, Berlin, Germany, July 2006, H. Kleinert, R.T. Jantzen, Editors; World Scientific, (Singapore, 2008).

    We here re-examine the validity of the constant-index power-law relation between the fireshell Lorentz gamma factor and its radial coordinate, usually adopted in the current Gamma-Ray Burst (GRB) literature on the grounds of an "ultrarelativistic" approximation. Such expressions are found to be mathematically correct but only approximately valid in a very limited range of the physical and astrophysical parameters and in an asymptotic regime which is reached only for a very short time, if any.

33. L. Caito, M.G. Bernardini, C.L. Bianco, M.G. Dainotti, R. Guida, R. Ruffini; "Theoretical interpretation of GRB011121"; in Proceedings of the Eleventh Marcel Grossmann Meeting on General Relativity, Berlin, Germany, July 2006, H. Kleinert, R.T. Jantzen, Editors; World Scientific, (Singapore, 2008).

    GRB 011121, detected by the BeppoSAX satellite, is studied as a prototype to understand the presence of flares observed by Swift in the afterglow of many GRB sources. Detailed theoretical analysis of the GRB 011121 light curves in selected energy bands are presented and compared with observational data. An interpretation of the flare of this source is provided by the introduction of the three-dimensional structure of the CircumBurst Medium(CBM).

34. M.G. Dainotti, M.G. Bernardini, C.L. Bianco, L. Caito, R. Guida, R. Ruffini; "On GRB 060218 and the GRBs related to Supernovae Ib/c"; in Proceedings of the Eleventh Marcel Grossmann Meeting on General Relativity, Berlin, Germany, July 2006, H. Kleinert, R.T. Jantzen, Editors; World Scientific, (Singapore, 2008).

    We study the Gamma-Ray Burst (GRB) 060218: a particularly close source at $z = 0.033$ with an extremely long duration, namely $T_{90} \sim 2000$ s, related to SN

2006aj. This source appears to be a very soft burst, with a peak in the spectrum at 4.9 keV, therefore interpreted as an X-Ray Flash (XRF) and it obeys to the Amati relation. We fit the X- and γ-ray observations by Swift of GRB 060218 in the 0.1–150 keV energy band during the entire time of observations from 0 all the way to 106 s within a unified theoretical model. The details of our theoretical analysis have been recently published in a series of articles. The free parameters of the theory are only three, namely the total energy $E_{e\pm}^{tot}$ of the $e^{\pm}$ plasma, its baryon loading $B = M_B c^2 / E_{e\pm}^{tot}$, as well as the CircumBurst Medium (CBM) distribution. We fit the entire light curve, including the prompt emission as an essential part of the afterglow. We recall that this value of the B parameter is the highest among the sources we have analyzed and it is very close to its absolute upper limit expected. We successfully make definite predictions about the spectral distribution in the early part of the light curve, exactly we derive the instantaneous photon number spectrum N(E) and we show that although the spectrum in the co-moving frame of the expanding pulse is thermal, the shape of the final spectrum in the laboratory frame is clearly non thermal. In fact each single instantaneous spectrum is the result of an integration of thousands of thermal spectra over the corresponding EQuiTemporal Surfaces (EQTS). By our fit we show that there is no basic differences between XRFs and more general GRBs. They all originate from the collapse process to a black hole and their difference is due to the variability of the three basic parameters within the range of full applicability of the theory.

35. R. Guida, M.G. Bernardini, C.L. Bianco, L. Caito, M.G. Dainotti, R. Ruffini; "Theoretical interpretation of GRB060124"; in Proceedings of the Eleventh Marcel Grossmann Meeting on General Relativity, Berlin, Germany, July 2006, H. Kleinert, R.T. Jantzen, Editors; World Scientific, (Singapore, 2008).

    We show the preliminary results of the application of our "fireshell" model to GRB060124. This source is very peculiar because it is the first event for which both the prompt and the afterglow emission were observed simultaneously by the three Swift instruments: BAT (15 - 350 keV), XRT (0,2 - 10 keV) and UVOT (170 - 650 nm), due to the presence of a precursor $\sim$ 570 s before the main burst. We analyze GRB060124 within our "canonical" GRB scenario, identifying the precursor with the P-GRB and the prompt emission with the afterglow peak emission. In this way we reproduce correctly the energetics of both these two components. We reproduce also the observed time delay between the precursor (P-GRB) and the main burst. The effect of such a time delay in our model will be discussed.

36. R. Ruffini, M.G. Bernardini, C.L. Bianco, L. Caito, P. Chardonnet, C. Cherubini, M.G. Dainotti, F. fraschetti, A. Geralico, R. Guida, B. Patricelli, M. Rotondo, J. Rueda Hernandez, G. Vereshchagin, S.-S. Xue; "Gamma-Ray Bursts"; in Proceedings of the Eleventh Marcel Grossmann Meeting on General Relativity, Berlin, Germany, July 2006, H. Kleinert, R.T. Jantzen, Editors; World Scientific, (Singapore, 2008).

    We show by example how the uncoding of Gamma-Ray Bursts (GRBs) offers unprecedented possibilities to foster new knowledge in fundamental physics and in astrophysics. After recalling some of the classic work on vacuum polarization in uniform electric fields by Klein, Sauter, Heisenberg, Euler and Schwinger, we summarize some of the efforts to observe these effects in heavy ions and high energy ion collisions. We then turn to the theory of vacuum polarization around a Kerr-Newman black hole, leading to the extraction of the blackholic energy, to the concept of dyadosphere and dyadotorus, and to the creation of an electron-positron-photon plasma. We then present a new theoretical approach encompassing the physics of neutron stars and heavy nuclei. It is shown that configurations of nuclear matter in bulk with global charge neutrality can exist on macroscopic scales and with electric fields close to the critical value near their surfaces. These configurations may represent an initial condition for the process of gravitational collapse, leading to the creation of an electron-positron-photon plasma: the basic self-accelerating system explaining both the energetics and the high energy Lorentz factor observed in GRBs. We then turn to recall the two basic interpretational paradigms of our GRB model: 1) the Relative Space-Time Transformation (RSTT) paradigm and 2) the Interpretation of the Burst Structure (IBS) paradigm. These paradigms lead to a "canonical" GRB light curve formed from two different components: a Proper-GRB (P-GRB) and an extended afterglow comprising a raising part, a peak, and a decaying tail. When the P-GRB is energetically predominant we have a "genuine" short GRB, while when the afterglow is energetically predominant we have a so-called long GRB or a "fake" short GRB. We compare and contrast the description of the relativistic expansion of the electron-positron plasma within our approach and within the other ones in the current literature. We then turn to the special role of the baryon loading in discriminating between "genuine" short and long or "fake" short GRBs and to the special role of GRB 991216 to illustrate for the first time the "canonical" GRB bolometric light curve. We then propose a spectral analysis of GRBs, and proceed to some applications: GRB 031203, the first spectral analysis, GRB 050315, the first complete light curve fitting, GRB 060218, the first evidence for a critical value of the baryon loading, GRB 970228, the appearance of "fake" short GRBs. We finally turn to the GRB-Supernova Time Sequence (GSTS) paradigm: the concept of induced gravitational collapse. We illustrate this paradigm by the systems GRB 980425 / SN 1998bw, GRB 030329 / SN 2003dh, GRB 031203 / SN 2003lw, GRB 060218 / SN 2006aj, and we present the enigma of the URCA sources. We then present some general conclusions.

37. R. Ruffini, A.G. Aksenov, M.G. Bernardini, C.L. Bianco, L. Caito, M.G. Dainotti, G. De Barros, R. Guida, G. Vereshchagin, S.-S. Xue; "The canonical Gamma-Ray Bursts: long, 'fake'-'disguised' and 'genuine' short bursts; in PROBING STELLAR POPULATIONS OUT TO THE DISTANT UNIVERSE: CEFALU 2008, Proceedings of the International Conference; Cefalù (Italy), September 2008, G. Giobbi, A. Tornambe, G. Raimondo, M. Limongi, L. A. Antonelli, N. Menci, E. Brocato, Editors; AIP Conference Proceedings, 1111, 325 (2009).

    The Gamma-Ray Bursts (GRBs) offer the unprecedented opportunity to observe for the first time the blackholic energy extracted by the vacuum polarization during the process of gravitational collapse to a black hole leading to the formation of an electron-positron plasma. The uniqueness of the Kerr-Newman black hole implies that very different processes originating from the gravitational collapse a) of a single star in a binary system induced by the companion, or b) of two neutron stars, or c) of a neutron star and a white dwarf, do lead to the same structure for the observed GRB. The recent progress of the numerical integration of the relativistic Boltzmann equations with collision integrals including 2-body and 3-body interactions between the particles offer a powerful conceptual tool in order to differentiate the traditional "fireball" picture, an expanding hot cavity considered by Cavallo and Rees, as opposed to the "fireshell" model, composed of an internally cold shell of relativistically expanding electron-positron-baryon plasma. The analysis of the fireshell naturally leads to a canonical GRB composed of a proper-GRB and an extended afterglow. By recalling the three interpretational paradigms for GRBs we show how the fireshell model leads to an understanding of the GRB structure and to an alternative classification of short and long GRBs.

38. M.G. Bernardini, M.G. Dainotti, C.L. Bianco, L. Caito, R. Guida, R. Ruffini; "Prompt emission and X-ray flares: the case of GRB 060607 A"; in PROB-

ING STELLAR POPULATIONS OUT TO THE DISTANT UNIVERSE: CEFALU 2008, Proceedings of the International Conference; Cefalù (Italy), September 2008, G. Giobbi, A. Tornambe, G. Raimondo, M. Limongi, L. A. Antonelli, N. Menci, E. Brocato, Editors; AIP Conference Proceedings, 1111, 383 (2009).

GRB 060607A is a very distant and energetic event. Its main peculiarity is that the peak of the near-infrared (NIR) afterglow has been observed with the REM robotic telescope, allowing to estimate the initial Lorentz gamma factor within the fireball forward shock model. We analyze GRB 060607A within the fireshell model. The initial Lorentz gamma factor of the fireshell can be obtained adopting the exact solutions of its equations of motion, dealing only with the BAT and XRT observations, that are the basic contribution to the afterglow emission, up to a distance from the progenitor $r \sim 10^{18}$ cm. According to the "canonical GRB" scenario we interpret the whole prompt emission as the peak of the afterglow emission, and we show that the observed temporal variability of the prompt emission can be produced by the interaction of the fireshell with overdense CircumBurst Medium (CBM) clumps. This is indeed the case also of the X-ray flares which are present in the early phases of the afterglow light curve.

39. C.L. Bianco, M.G. Bernardini, L. Caito, M.G. Dainotti, R. Guida, R. Ruffini; "The 'fireshell' model and the 'canonical GRB' scenario. Implications for the Amati relation"; in PROBING STELLAR POPULATIONS OUT TO THE DISTANT UNIVERSE: CEFALU 2008, Proceedings of the International Conference; Cefalù (Italy), September 2008, G. Giobbi, A. Tornambe, G. Raimondo, M. Limongi, L. A. Antonelli, N. Menci, E. Brocato, Editors; AIP Conference Proceedings, 1111, 587 (2009).

    Within the "fireshell" model for GRBs we define a "canonical GRB" light curve with two sharply different components: the Proper-GRB (P-GRB), emitted when the optically thick fireshell reaches transparency, and the extended afterglow, emitted due to the collision between the remaining optically thin fireshell and the CircumBurst Medium (CBM). We here outline our "canonical GRB" scenario, which implies three different GRB classes: the "genuine" short GRBs, the "fake" or "disguised" short GRBs and the other (so-called "long") GRBs. We will also outline the corresponding implications for the Amati relation, which are opening its use for cosmology.

40. R. Ruffini, A.G. Aksenov, M.G. Bernardini, C.L. Bianco, L. Caito, P.

Chardonnet, M.G. Dainotti, G. De Barros, R. Guida, L. Izzo, B. Patricelli, L.J. Rangel Lemos, M. Rotondo, J.A. Rueda Hernandez, G. Vereshchagin, S.-S. Xue; "The Blackholic energy and the canonical Gamma-Ray Burst IV: the 'long', 'genuine short' and 'fake – disguised short' GRBs"; in Proceedings of the XIIIth Brazilian School on Cosmology and Gravitation, Mangaratiba, Rio de Janeiro (Brazil), July-August 2008, M. Novello, S.E. Perez Bergliaffa, Editors; AIP Conference Proceedings, 1132, 199 (2009).

We report some recent developments in the understanding of GRBs based on the theoretical framework of the "fireshell" model, already presented in the last three editions of the "Brazilian School of Cosmology and Gravitation". After recalling the basic features of the "fireshell model", we emphasize the following novel results: 1) the interpretation of the X-ray flares in GRB afterglows as due to the interaction of the optically thin fireshell with isolated clouds in the CircumBurst Medium (CBM); 2) an interpretation as "fake - disguised" short GRBs of the GRBs belonging to the class identified by Norris & Bonnell; we present two prototypes, GRB 970228 and GRB 060614; both these cases are consistent with an origin from the final coalescence of a binary system in the halo of their host galaxies with particularly low CBM density $n_{cbm} \sim 10^{-3}$ particles/cm^3; 3) the first attempt to study a genuine short GRB with the analysis of GRB 050509B, that reveals indeed still an open question; 4) the interpretation of the GRB-SN association in the case of GRB 060218 via the "induced gravitational collapse" process; 5) a first attempt to understand the nature of the "Amati relation", a phenomenological correlation between the isotropic-equivalent radiated energy of the prompt emission E_{iso} with the cosmological rest-frame νF_ν spectrum peak energy $E_{p,i}$. In addition, recent progress on the thermalization of the electron-positron plasma close to their formation phase, as well as the structure of the electrodynamics of Kerr-Newman Black Holes are presented. An outlook for possible explanation of high-energy phenomena in GRBs to be expected from the AGILE and the Fermi satellites are discussed. As an example of high energy process, the work by Enrico Fermi dealing with ultrarelativistic collisions is examined. It is clear that all the GRB physics points to the existence of overcritical electrodynamical fields. In this sense we present some progresses on a unified approach to heavy nuclei and neutron stars cores, which leads to the existence of overcritical fields under the neutron star crust.

41. A.G. Aksenov, M.G. Bernardini, C.L. Bianco, L. Caito, C. Cherubini,

G. De Barros, A. Geralico, L. Izzo, F.A. Massucci, B. Patricelli, M. Rotondo, J.A. Rueda Hernandez, R. Ruffini, G. Vereshchagin, S.-S. Xue; "The fireshell model for Gamma-Ray Bursts"; in The Shocking Universe, Proceedings of the conference held in Venice (Italy), September 2009, G. Chincarini, P. D'Avanzo, R. Margutti, R. Salvaterra, Editors; SIF Conference Proceedings, 102, 451 (2010).

The fireshell model for GRBs is briefly outlined, and the currently ongoing developments are summarized.

42. M.G. Bernardini, C.L. Bianco, L. Caito, L. Izzo, B. Patricelli, R. Ruffini; "The end of the prompt emission within the fireshell model"; in The Shocking Universe, Proceedings of the conference held in Venice (Italy), September 2009, G. Chincarini, P. D'Avanzo, R. Margutti, R. Salvaterra, Editors; SIF Conference Proceedings, 102, 489 (2010)

    The shallow decay emission, revealed by the Swift satellite in the X-ray afterglow of a good sample of bursts, is a puzzle. Within the fireshell model it has been recently proposed an alternative explanation: if we assume that after the prompt phase the system has a range of Lorentz factors, the plateau phase is simply the product of the injection of slower material into the fireshell. This injection produces a modification both in the dynamics of the fireshell and in the spectrum of the emitted radiation. We postulate that this spread in the fireshell Lorentz factor occurs when the fireshell becomes transparent and do not depend on a prolonged activity of the central engine. The aim of this paper is to characterize dynamically the system in order to understand the nature of that material.

43. L. Izzo, M.G. Bernardini, C.L. Bianco, L. Caito, B. Patricelli, R. Ruffini; "GRB 090423 in the fireshell scenario"; in The Shocking Universe, Proceedings of the conference held in Venice (Italy), September 2009, G. Chincarini, P. D'Avanzo, R. Margutti, R. Salvaterra, Editors; SIF Conference Proceedings, 102, 537 (2010).

44. B. Patricelli, M.G. Bernardini, C.L. Bianco, L. Caito, L. Izzo, R. Ruffini, G. Vereshchagin; "A new spectral energy distribution of photons in the fireshell model of GRBs"; in The Shocking Universe, Proceedings of the conference held in Venice (Italy), September 2009, G. Chincarini, P. D'Avanzo, R. Margutti, R. Salvaterra, Editors; SIF Conference Proceedings, 102, 559 (2010).

The fireshell model of Gamma Ray Bursts (GRBs) postulates that the emission process is thermal in the comoving frame of the fireshell, but this is just a first approximation. We investigate a different spectrum of photons in the comoving frame in order to better reproduce the observed spectral properties of GRB prompt emission. We introduce a modified thermal spectrum whose low energy slope depends on an index α, left as a free parameter. We test it by comparing the numerical simulations with observed BAT spectra integrated over different intervals of time. We find that the observational data can be correctly reproduced by assuming $\alpha = -1.8$.

45. C.L. Bianco, M.G. Bernardini, L. Caito, G. De Barros, L. Izzo, B. Patricelli, R. Ruffini; "Disguised Short Bursts and the Amati Relation"; in Deciphering the ancient universe with Gamma-Ray Bursts, Proceedings of the conference held in Kyoto (Japan), April 2010, N. Kawai, S. Nagataki, Editors; AIP Conference Proceedings, 1279, 299 (2010).

    The class of "Disguised short" GRBs implied by the fireshell scenario is presented, with special emphasis on the implications for the Amati relation.

46. L. Izzo, M.G. Bernardini, C.L. Bianco, L. Caito, B. Patricelli, L.J. Rangel Lemos, R. Ruffini; "On GRB 080916C and GRB 090902B observed by the Fermi satellite"; in Deciphering the ancient universe with Gamma-Ray Bursts, Proceedings of the conference held in Kyoto (Japan), April 2010, N. Kawai, S. Nagataki, Editors; AIP Conference Proceedings, 1279, 343 (2010).

    We propose a possible explanation, in the context of the Fireshell scenario, for the high-energy emission observed in GRB 080916C and GRB 090902B. The physical process underlying this emission consists mainly in the interaction of the baryon in the Fireshell with some high-density region around the burst site. Moreover we associate the observed delay of the onset of the high-energy emission as due to the P-GRB emission.

47. B. Patricelli, M.G. Bernardini, C.L. Bianco, L. Caito, G. De Barros, L. Izzo, R. Ruffini; "Black Holes in Gamma Ray Bursts"; in Deciphering the ancient universe with Gamma-Ray Bursts, Proceedings of the conference held in Kyoto (Japan), April 2010, N. Kawai, S. Nagataki, Editors; AIP Conference Proceedings, 1279, 406 (2010).

    Within the fireshell model, Gamma Ray Bursts (GRBs) originate from an optically thick $e^{\pm}$ plasma created by vacuum polarization process during the formation of a Black Hole (BH). Here we briefly recall the basic features of this model, then we show how it is possible to interpret GRB observational properties within it. In particular we present, as a specific example, the analysis of GRB 050904 observations of the prompt emission light curve and spectrum in the Swift BAT energy band (15-150 keV).

48. M.G. Bernardini, C.L. Bianco, L. Caito, M.G. Dainotti, R. Guida, R. Ruffini; "The GRB classification within the "fireshell" model: short, long and "fake" short GRBs"; in Proceedings of the 3rd Stueckelberg Workshop on Relativistic Field Theories, Pescara, Italy, July 2008, N. Carlevaro, R. Ruffini, G.V. Vereshchagin, Editors; Cambridge Scientific Publishers, (UK, 2011).

49. C.L. Bianco, M.G. Bernardini, L. Caito, M.G. Dainotti, R. Guida, R. Ruffini, G.V. Vereshchagin, S.-S. Xue; "Equations of motion of the "fireshell""; in Proceedings of the 3rd Stueckelberg Workshop on Relativistic Field Theories, Pescara, Italy, July 2008, N. Carlevaro, R. Ruffini, G.V. Vereshchagin, Editors; Cambridge Scientific Publishers, (UK, 2011).

50. L. Caito, M.G. Bernardini, C.L. Bianco, M.G. Dainotti, R. Guida, R. Ruffini; "GRB 060614: another example of "fake" short burst from a merging binary system"; in Proceedings of the 3rd Stueckelberg Workshop on Relativistic Field Theories, Pescara, Italy, July 2008, N. Carlevaro, R. Ruffini, G.V. Vereshchagin, Editors; Cambridge Scientific Publishers, (UK, 2011).

51. G. De Barros, M.G. Bernardini, C.L. Bianco, L. Caito, R. Guida, R. Ruffini; "Analysis of GRB 050509b"; in Proceedings of the 3rd Stueckelberg Workshop on Relativistic Field Theories, Pescara, Italy, July 2008, N. Carlevaro, R. Ruffini, G.V. Vereshchagin, Editors; Cambridge Scientific Publishers, (UK, 2011).

52. R. Ruffini, L. Izzo, A.V. Penacchioni, C.L. Bianco, L. Caito, S.K. Chakrabarti, A. Nandi; "GRB 090618: a possible case of multiple GRB?"; in Proceedings of the 25th Texas Symposium on Relativistic Astrophysics, held in Heidelberg (Germany), December 2010, F.M. Rieger, C. van Eldik, W. Hofmann, Editors; PoS(Texas2010), 101.

53. L.J. Rangel Lemos, C.L. Bianco, H.J. Mosquera Cuesta, J.A. Rueda, R. Ruffini; "Luminosity function of BATSE GRBs dominated by extended

afterglow"; in Proceedings of the 25th Texas Symposium on Relativistic Astrophysics, held in Heidelberg (Germany), December 2010, F.M. Rieger, C. van Eldik, W. Hofmann, Editors; PoS(Texas2010), 204.

54. R. Ruffini, A.G. Aksenov, M.G. Bernardini, C.L. Bianco, L. Caito, P. Chardonnet, M.G. Dainotti, G. De Barros, R. Guida, L. Izzo, B. Patricelli, L.J. Rangel Lemos, M. Rotondo, J.A. Rueda Hernandez, G. Vereshchagin, She-Sheng Xue; "Black Holes Energetics and GRBs"; in The Sun, the Stars, the Universe and General Relativity: Proceedings of Sobral 2009; S.E. Perez Bergliaffa, M. Novello , R. Ruffini, Editors; Cambridge Scientific Publishers (UK, 2011).

55. C.L. Bianco, L. Amati, M.G. Bernardini, L. Caito, G. De Barros, L. Izzo, B. Patricelli, R. Ruffini; "The class of 'disguised' short GRBs and its implications for the Amati relation"; in GRBs as probes - from the progenitors environment to the high redshift Universe, Proceedings of the conference held in Como (Italy), May 2011, S. Campana, P. D'Avanzo, A. Melandri, Editors; Mem. S.A.It. Suppl., 21, 139 (2012).

56. A.V. Penacchioni, R. Ruffini, L. Izzo, M. Muccino, C.L. Bianco, L. Caito, B. Patricelli; "Evidences for a double component in the emission of GRB 101023"; in GRBs as probes - from the progenitors environment to the high redshift Universe, Proceedings of the conference held in Como (Italy), May 2011, S. Campana, P. D'Avanzo, A. Melandri, Editors; Mem. S.A.It. Suppl., 21, 230 (2012).

57. M.G. Bernardini, C.L. Bianco, L. Caito, L. Izzo, B. Patricelli, R. Ruffini; "The X-Ray Flares of GRB 060607A within the Fireshell Model"; in Proceedings of the Twelfth Marcel Grossmann Meeting on General Relativity, Paris, France, July 2009, T. Damour, R.T. Jantzen, R. Ruffini, Editors; World Scientific, (Singapore, 2012).

58. L. Izzo, M.G. Bernardini, C.L. Bianco, L. Caito, B. Patricelli, R. Ruffini; "GRB 090423 in the Fireshell Scenario: A Canonical GRB at Redshift 8.2"; in Proceedings of the Twelfth Marcel Grossmann Meeting on General Relativity, Paris, France, July 2009, T. Damour, R.T. Jantzen, R. Ruffini, Editors; World Scientific, (Singapore, 2012).

59. B. Patricelli, M.G. Bernardini, C.L. Bianco, L. Caito, L. Izzo, R. Ruffini, G.V. Vereshchagin; "A New Spectral Energy Distribution of Photons

in the Fireshell Model of GRBs"; in Proceedings of the Twelfth Marcel Grossmann Meeting on General Relativity, Paris, France, July 2009, T. Damour, R.T. Jantzen, R. Ruffini, Editors; World Scientific, (Singapore, 2012).

60. C.L. Bianco, M.G. Bernardini, L. Caito, G. De Barros, L. Izzo, M. Muccino, B. Patricelli, A.V. Penacchioni, G.B. Pisani, R. Ruffini; "Needs for a new GRB classification following the fireshell model: "genuine short", "disguised short" and "long" GRBs"; in Proceedings of the Gamma-Ray Bursts 2012 Conference, held in Munich (Germany), May 2012, A. Rau, J. Greiner, Editors; PoS(GRB 2012), 043.

61. A.V. Penacchioni, G.B. Pisani, R. Ruffini, C.L. Bianco, L. Izzo, M. Muccino; "The proto-black hole concept in GRB 101023 and its possible extension to GRB 110709B"; in Proceedings of the Gamma-Ray Bursts 2012 Conference, held in Munich (Germany), May 2012, A. Rau, J. Greiner, Editors; PoS(GRB 2012), 042.

62. B. Patricelli, M.G. Bernardini, C.L. Bianco, L. Caito, L. Izzo, R. Ruffini; "GRB 050904: The study of a high redshift GRB within the Fireshell Model"; in Proceedings of the Twelfth Marcel Grossmann Meeting on General Relativity, Paris, France, July 2009, T. Damour, R.T. Jantzen, R. Ruffini, Editors; World Scientific, (Singapore, 2012).

63. L. Izzo, G.B. Pisani, M. Muccino, J.A. Rueda, Y.Wang, C.L. Bianco, A.V. Penacchioni, R. Ruffini; "A common behavior in the late X-ray afterglow of energetic GRB-SN systems"; EAS Publications Series, Volume 61, 595-597 (2013).

64. R. Ruffini; "Black Holes, Supernovae and Gamma Ray Bursts"; in Proceedings of the Thirteenth Marcel Grossmann Meeting on General Relativity, Stockholm, Sweden, July 2012, R.T. Jantzen, K. Rosquist, R. Ruffini, Editors; World Scientific, (Singapore, 2015).

65. M. Muccino, R. Ruffini, C.L. Bianco, L. Izzo, A.V. Penacchioni, G.B. Pisani; "GRB 090227B: The missing link between the genuine short and long GRBs"; in Proceedings of the Thirteenth Marcel Grossmann Meeting on General Relativity, Stockholm, Sweden, July 2012, R.T. Jantzen, K. Rosquist, R. Ruffini, Editors; World Scientific, (Singapore, 2015).

66. A.V. Penacchioni, R. Ruffini, C.L. Bianco, L. Izzo, M. Muccino, G.B. Pisani, J.A. Rueda; "The family of the Induced Gravitational Collapse scenario: The case of GRB 110709B"; in Proceedings of the Thirteenth Marcel Grossmann Meeting on General Relativity, Stockholm, Sweden, July 2012, R.T. Jantzen, K. Rosquist, R. Ruffini, Editors; World Scientific, (Singapore, 2015).

67. A.V. Penacchioni, R. Ruffini, C.L. Bianco, L. Izzo, M. Muccino, G.B. Pisani; "GRB 111228, analysis within the Induced Gravitational Collapse scenario and association with a supernova"; in Proceedings of the Thirteenth Marcel Grossmann Meeting on General Relativity, Stockholm, Sweden, July 2012, R.T. Jantzen, K. Rosquist, R. Ruffini, Editors; World Scientific, (Singapore, 2015).

68. G.B. Pisani, L. Izzo, R. Ruffini, C.L. Bianco, M. Muccino, A.V. Penacchioni, J.A. Rueda, Y. Wang; "On a novel distance indicator for Gamma-Ray Bursts associated with supernovae"; in Proceedings of the Thirteenth Marcel Grossmann Meeting on General Relativity, Stockholm, Sweden, July 2012, R.T. Jantzen, K. Rosquist, R. Ruffini, Editors; World Scientific, (Singapore, 2015).

69. M. Muccino, R. Ruffini, C.L. Bianco, L. Izzo, A.V. Penacchioni, G.B. Pisani; "GRB 090510, explosion of a GRB in the highest circumburst medium even inferred: a disguised short GRB"; in Proceedings of the Thirteenth Marcel Grossmann Meeting on General Relativity, Stockholm, Sweden, July 2012, R.T. Jantzen, K. Rosquist, R. Ruffini, Editors; World Scientific, (Singapore, 2015).

70. L. Izzo, G.B. Pisani, M. Muccino, R. Ruffini, C.L. Bianco, M. Enderli, Y. Wang; "Hints for a physically based GRB distance indicator"; in Proceedings of the Thirteenth Marcel Grossmann Meeting on General Relativity, Stockholm, Sweden, July 2012, R.T. Jantzen, K. Rosquist, R. Ruffini, Editors; World Scientific, (Singapore, 2015).

71. R. Ruffini, Y. Aimuratov, V. Belinski, C.L. Bianco, M. Enderli, L. Izzo, M. Kovacevic, G.J. Mathews, R. Moradi, M. Muccino, A.V. Penacchioni, G.B. Pisani, J.A. Rueda, G.V. Vereshchagin, Y. Wang, S.-S. Xue; Cosmic matrix in the jubilee of relativistic astrophysics; in THE SECOND ICRANET CÉSAR LATTES MEETING: Supernovae, Neutron Stars and

Black Holes, Proceedings of the conference held in Rio de Janeiro – Niterói – João Pessoa – Recife – Fortaleza (Brazil), 13-22 April 2015, U. Barres de Almeida, P. Chardonnet, R. Picanco Negreiros, J. Rueda, R. Ruffini, G. Vereshchagin, C. Zen Vasconcellos, Editors; AIP Conference Proceedings, 1693, 020001 (2015).

72. L. Becerra, C.L. Bianco, F. Cipolletta, M. Enderli, C.L. Fryer, L. Izzo, M. Kovacevic, R. Camargo Rodrigues de Lima, M. Muccino, F.G. de Oliveira, A.V. Penacchioni, G.B. Pisani, J.A. Rueda, R. Ruffini, Y. Wang, E. Zaninoni; Black holes, neutron stars and supernovae within the induced gravitational collapse paradigm for GRBs; in THE SECOND ICRANET CÉSAR LATTES MEETING: Supernovae, Neutron Stars and Black Holes, Proceedings of the conference held in Rio de Janeiro – Niterói – João Pessoa – Recife – Fortaleza (Brazil), 13-22 April 2015, U. Barres de Almeida, P. Chardonnet, R. Picanco Negreiros, J. Rueda, R. Ruffini, G. Vereshchagin, C. Zen Vasconcellos, Editors; AIP Conference Proceedings, 1693, 020002 (2015).

73. L.J. Rangel Lemos, C.L. Bianco, R. Ruffini; Applying the luminosity function statistics in the fireshell model; in THE SECOND ICRANET CÉSAR LATTES MEETING: Supernovae, Neutron Stars and Black Holes, Proceedings of the conference held in Rio de Janeiro – Niterói – João Pessoa – Recife – Fortaleza (Brazil), 13-22 April 2015, U. Barres de Almeida, P. Chardonnet, R. Picanco Negreiros, J. Rueda, R. Ruffini, G. Vereshchagin, C. Zen Vasconcellos, Editors; AIP Conference Proceedings, 1693, 070004 (2015).

74. J.A. Rueda, R. Ruffini, J.F. Rodriguez, M. Muccino, Y. Aimuratov, U. Barres de Almeida, L.M. Becerra, C.L. Bianco, C. Cherubini, S. Filippi, M. Kovacevic, R. Moradi, G.B. Pisani, Y. Wang; The binary progenitors of short and long GRBs and their gravitational-wave emission; EPJ Web of Conferences, 168, 01006 (2018).

75. M. Muccino, R. Ruffini, Y. Aimuratov, L.M. Becerra, C.L. Bianco, M. Karlika, M. Kovacevic, J.D. Melon Fuksman, R. Moradi, A.V. Penacchioni, G.B. Pisani, D. Primorac, J.A. Rueda, S. Shakeri, G.V. Vereshchagin, S.-S. Xue, Y. Wang; What can we learn from GRBs?; EPJ Web of Conferences, 168, 01015 (2018).

76. L.M. Becerra, C.L. Bianco, C. Fryer, J.A. Rueda, R. Ruffini; On the Induced Gravitational Collapse; EPJ Web of Conferences, 168, 02005 (2018).
77. G.B. Pisani, R. Ruffini, Y. Aimuratov, C.L. Bianco, M. Karlika, M. Kovacevic, R. Moradi, M. Muccino, A.V. Penacchioni, D. Primorac, J.A. Rueda, Y. Wang; The first ICRANet catalog of Binary-Driven Hypernovae; EPJ Web of Conferences, 168, 04002 (2018).
78. D. Primorac, R. Ruffini, G.B. Pisani, Y. Aimuratov, C.L. Bianco, M. Karlika, J.D. Melon Fuksman, R. Moradi, M. Muccino, A.V. Penacchioni, J.A. Rueda, Y. Wang; GRB 110731A within the IGC paradgm; EPJ Web of Conferences, 168, 04008 (2018).
79. J.D. Melon Fuksman, L.M. Becerra, C.L. Bianco, M. Karlika, M. Kovacevic, R. Moradi, M. Muccino, G.B. Pisani, D. Primorac, J.A. Rueda, R. Ruffini, G.V. Vereshchagin, Y. Wang; Evolution of an electron-positron plasma produced by induced gravitational collapse in binary-driven hypernovae; EPJ Web of Conferences, 168, 04009 (2018).

The Astrophysical Journal, 852:53 (27pp), 2018 January 1 https://doi.org/10.3847/1538-4357/aa9e8b

Early X-Ray Flares in GRBs

R. Ruffini[1,2,3,4], Y. Wang[1,2], Y. Aimuratov[3,1,2], U. Barres de Almeida[4], L. Becerra[1,2], C. L. Bianco[1,2], Y. C. Chen[1,2], M. Karlica[1,2,3], M. Kovacevic[1,2,3], L. Li[2,5], J. D. Melon Fuksman[1,2], R. Moradi[1,2], M. Muccino[1,2], A. V. Penacchioni[2,6,7], G. B. Pisani[1,2], D. Primorac[1,2], J. A. Rueda[1,2,4], S. Shakeri[2,8], G. V. Vereshchagin[1,2], and S.-S. Xue[1,2]

[1] ICRA and Dipartimento di Fisica, Sapienza Università di Roma, Piazzale Aldo Moro 5, I-00185 Rome, Italy
[2] ICRANet, Piazza della Repubblica 10, I-65122 Pescara, Italy; yu.wang@icranet.org
[3] Université de Nice Sophia Antipolis, CEDEX 2, Grand Château Parc Valrose, Nice, France
[4] ICRANet-Rio, Centro Brasileiro de Pesquisas Físicas, Rua Dr. Xavier Sigaud 150, 22290-180 Rio de Janeiro, Brazil
[5] Department of Physics, Stockholm University, SE-106 91 Stockholm, Sweden
[6] ASI Science Data Center, Via del Politecnico s.n.c., I-00133 Rome, Italy
[7] Dept. of Physical Sciences, Earth and Environment, University of Siena, Via Roma 56, I-53100 Siena, Italy
[8] Department of Physics, Isfahan University of Technology, 84156-83111, Iran
Received 2017 April 8; revised 2017 November 8; accepted 2017 November 23; published 2018 January 5

Abstract

We analyze the early X-ray flares in the GRB "flare–plateau–afterglow" (FPA) phase observed by *Swift*-XRT. The FPA occurs only in one of the seven GRB subclasses: the binary-driven hypernovae (BdHNe). This subclass consists of long GRBs with a carbon–oxygen core and a neutron star (NS) binary companion as progenitors. The hypercritical accretion of the supernova (SN) ejecta onto the NS can lead to the gravitational collapse of the NS into a black hole. Consequently, one can observe a GRB emission with isotropic energy $E_{\rm iso} \gtrsim 10^{52}$ erg, as well as the associated GeV emission and the FPA phase. Previous work had shown that gamma-ray spikes in the prompt emission occur at $\sim 10^{15}$–10^{17} cm with Lorentz Gamma factors $\Gamma \sim 10^2$–10^3. Using a novel data analysis, we show that the time of occurrence, duration, luminosity, and total energy of the X-ray flares correlate with $E_{\rm iso}$. A crucial feature is the observation of thermal emission in the X-ray flares that we show occurs at radii $\sim 10^{12}$ cm with $\Gamma \lesssim 4$. These model-independent observations cannot be explained by the "fireball" model, which postulates synchrotron and inverse-Compton radiation from a single ultrarelativistic jetted emission extending from the prompt to the late afterglow and GeV emission phases. We show that in BdHNe a collision between the GRB and the SN ejecta occurs at $\simeq 10^{10}$ cm, reaching transparency at $\sim 10^{12}$ cm with $\Gamma \lesssim 4$. The agreement between the thermal emission observations and these theoretically derived values validates our model and opens the possibility of testing each BdHN episode with the corresponding Lorentz Gamma factor.

Key words: binaries: general – black hole physics – gamma-ray burst: general – hydrodynamics – stars: neutron – supernovae: general

Supporting material: machine-readable table

1. Introduction

Following the discovery of the gamma-ray bursts (GRBs) by the *Vela* satellites (Klebesadel et al. 1973) and the observations by the BATSE detectors on board the *Compton Gamma-Ray Observatory* (*CGRO*; Gehrels et al. 1993), a theoretical framework for the interpretation of GRBs was established. This materialized into the "traditional" model of GRBs developed in a large number of papers by various groups. They all agree in their general aspects: short GRBs are assumed to originate from the merging of binary neutron stars (NSs; see, e.g., Goodman 1986; Paczynski 1986; Eichler et al. 1989; Narayan et al. 1991, 1992; Mészáros & Rees 1997), and long GRBs are assumed to originate from a "collapsar" (Woosley 1993; Paczyński 1998; MacFadyen & Woosley 1999; Bromberg et al. 2013), which, in turn, originates from the collapse of the core of a single massive star to a black hole (BH) surrounded by a thick massive accretion disk (Piran 2004). In this traditional picture, the GRB dynamics follows the "fireball" model, which assumes the existence of an ultrarelativistic collimated jet (see, e.g., Shemi & Piran 1990; Meszaros et al. 1993; Piran et al. 1993; Mao & Yi 1994). The structures of long GRBs were described by either internal or external shocks (see Rees & Meszaros 1992, 1994). The emission processes were linked to the occurrence of synchrotron and/or inverse-Compton radiation coming from the jetted structure, characterized by Lorentz factors $\Gamma \sim 10^2$–10^3, in what later will become known as the "prompt emission" phase (see Section 3).

The joint X-ray, gamma-ray, and optical observations heralded by *BeppoSAX* and later extended by *Swift* discovered the X-ray "afterglow," which allowed the optical identification and the determination of the GRBs' cosmological distance. The first evidence for the coincidence of a GRB and a supernova (SN; GRB 980425/SN 1998bw) was also announced as well as the first observation of an early X-ray flare (XRT), later greatly extended in number and spectral data by the *Swift* satellite, the subjects of this paper. The launch of the *Fermi* and *AGILE* satellites led to the equally fundamental discovery of GeV emission both in long and short GRBs (see Section 2).

The traditional model was modified in light of these new basic information by extending the description of the "collapsar" model, adopted for the prompt emission, to both the afterglow and GeV emission. This approach, based on the gravitational collapse of a single massive star, which was initially inspired by analogies with the astrophysics of active galactic nuclei, has been adopted with the aim to identify a "standard model" for all long GRBs and vastly accepted by concordance (see, e.g., Piran 1999, 2004; Mészáros 2002, 2006; Gehrels et al. 2009; Berger 2014; Kumar & Zhang 2015).

Attempts to incorporate the occurrence of an SN in the collapsar by considering nickel production in the accretion process around the BH were also proposed (MacFadyen & Woosley 1999). In 1999, a pioneering work by Fryer et al. (1999b) introduced considerations based on population synthesis computations and emphasized the possible relevance of binary progenitors in GRBs.

Since 2001, we have been developing an alternative GRB model based on the concept of induced gravitational collapse (IGC) paradigm, which involves, as progenitors, a binary system with standard components: an evolved carbon–oxygen core (CO_{core}) and a binary companion NS. The CO_{core} undergoes a traditional SN Ic explosion, which produces a new NS (νNS) and a large amount of ejecta. There is a multitude of new physical processes, occurring in selected episodes, associated with this process. The "first episode" (see Section 3) of the binary-driven hypernova (BdHN) is dominated by the hypercritical accretion process of the SN ejecta onto the companion NS. This topic has been developed in, e.g., Ruffini et al. (2001c), Rueda & Ruffini (2012), Fryer et al. (2014), and Becerra et al. (2015, 2016). These processes are not considered in the collapsar model. Our SN is a traditional Type Ic, the creation of the νNS follows standard procedure occurring in pulsar physics (see, e.g., Negreiros et al. 2012), the companion NS is a standard one regularly observed in binaries (see e.g., Rueda & Ruffini 2012; Rueda et al. 2017), and the physics of hypercritical accretion has been developed by us in a series of recent articles (see Section 3.4).

In a BdHN, the BH and a vast amount of e^+e^- plasma are formed only after the accreting NS reaches the critical mass and the "second episode" starts (see Section 3.5). The main new aspect of our model addresses the interaction of the e^+e^- plasma with the SN ejecta. We apply the fireshell model, which makes use of a general relativistic correct spacetime parametrization of the GRBs as well as a new set of relativistic hydrodynamics equation for the dynamics of the e^+e^- plasma. Selected values of the baryon loads are adopted in correspondence with the different time-varying density distributions of the SN ejecta.

In the "third episode" (see Section 3.6), we also mention the perspectives, utilizing the experience gained from both data analysis and theory for the specific understanding of X-ray flares, to further address in forthcoming publications the more comprehensive case of gamma-ray flares, the consistent treatment of the afterglow, and finally the implication of the GeV radiation.

As the model evolved, we soon realized that the discovery of new sources was not leading to a "standard model" of long GRBs but, on the contrary, they were revealing a number of new GRB subclasses with distinct properties characterizing their light curves, spectra, and energetics (see Ruffini et al. 2016b). Moreover, these seven subclasses did not necessarily contain a BH. We soon came to the conclusion that only in the subclass of BdHNe, with an E_{iso} larger than 10^{52} erg, does the hypercritical accretion from the SN onto the NS lead to the creation of a newly born BH with the associated signatures in the long GRB emission (see, e.g., Becerra et al. 2015, 2016).

While our alternative model was progressing, we were supported by new astrophysical observations: the great majority of GRBs are related to SNe Ic, which have no trace of hydrogen and helium in their optical spectra and are spatially correlated with bright star-forming regions in their host galaxies (Fruchter et al. 2006; Svensson et al. 2010). Most massive stars are found in binary systems (Smith 2014) where most SNe Ic occur and which favor the deployment of hydrogen and helium from the SN progenitors (Smith et al. 2011), and the SNe associated with long GRBs are indeed of Type Ic (Della Valle 2011). In addition, these SNe associated with long bursts are broad-lined Ic SNe (hypernovae) showing the occurrence of some energy injection leading to a kinetic energy larger than that of traditional SNe Ic (Lyman et al. 2016).

The present paper addresses the fundamental role of X-ray flares as a separatrix between the two alternative GRB models and leads to the following main results, two obtained by data analysis and one obtained from the comparison of the alternative models:

(1) The discovery of precise correlations between the X-ray flares and the GRB E_{iso}.
(2) The radius of the occurrence of X-ray flares ($\sim 10^{12}$ cm) and the Lorentz Gamma factor ~ 2.
(3) The occurrence of a sharp break between the prompt emission phase and the flare–plateau–afterglow (FPA) phase, not envisaged in the current GRB literature. This transition is evidence of a contradiction in using the ultrarelativistic jetted emission to explain the X-ray flares, the plateau, and the afterglow.

In Section 2, we recall, following the gamma-ray observations by the *Vela* satellites and the *CGRO*, the essential role of *BeppoSAX* and the *Swift* satellite. These satellites provided X-ray observations specifically of the X-ray flares, to which our new data analysis techniques and paradigms have been applied. We also recall that the *Fermi* and *AGILE* satellites announced the existence of GeV emission, which has become essential for establishing the division of GRBs into different subclasses.

In Section 3, we update our classification of GRBs with known redshift into seven different subclasses (see Table 2). For each subclass, we indicate the progenitor "in-states" and the corresponding "out-states." We update the list of BdHNe (see Appendix A): long GRBs with $E_{iso} \gtrsim 10^{52}$ erg, with an associated GeV emission and with the occurrence of the FPA phase. We also recall the role of appropriate time parametrization for GRBs, which properly distinguishes the four time variables that enter into their analysis. Finally, we recall the essential theoretical background needed for the description of the dynamics of BdHNe, the role of neutrino emission in the process of hypercritical accretion of the SN ejecta onto the binary companion NS, the description of the dynamics of the e^+e^-–baryon plasma, and the prompt emission phase endowed with gamma-ray spikes. We then briefly address the new perspectives opened up by the present work, to be further extended to the analysis of gamma-ray flares, to the afterglow, and the essential role of each BdHN component, including the νNS. Having established the essential observational and theoretical backgrounds in Sections 2 and 3, we proceed to the data analysis of the X-ray flares.

In Section 4, we address the procedure used to compare and contrast GRBs at different redshifts, including the description in their cosmological rest frame as well as the consequent K corrections. This procedure has been ignored in the current GRB literature (see, e.g., Chincarini et al. 2010 and references therein as well as Section 11 of this paper). We then identify BdHNe as the only sources where early-time X-ray flares are identifiable. We recall that X-ray flares have neither been found in X-ray flashes nor in short GRBs. We also show that a claim of the existence of X-ray flares in short bursts has been superseded. We recall our 345 classified BdHNe (through the end of 2016). Their T_{90},[9] properly evaluated in the source rest frame, corresponds to the duration of their prompt emission phase, mostly shorter than 100 s. Particular attention has been given to distinguishing X-ray flares from gamma-ray flares and spikes, each characterized by distinct spectral distributions and specific Lorentz Gamma factors. The gamma-ray flares are generally more energetic and with specific spectral signatures (see, e.g., the significant example of GRB 140206A in Section 5 below). In this article we focus on the methodology of studying X-ray flares: we plan to apply this knowledge to the case of the early gamma-ray flares. Out of the 345 BdHNe, there are 211 that have complete *Swift-XRT* observations, and among them, there are 16 BdHNe with a well-determined early X-ray flare structure. They cover a wide range of redshifts as well as the typical range of BdHN isotropic energies ($\sim 10^{52}$–10^{54} erg). The sample includes all identifiable X-ray flares.

In Section 5, we give the X-ray luminosity light curves of the 16 BdHNe in our sample and, when available, the corresponding optical observations. As usual, these quantities have been K-corrected to their rest frame (see Figures 9–24 and Section 4). In order to estimate the global properties of these sources, we also examine data from the *Swift*, Konus-*Wind*, and *Fermi* satellites. The global results of this large statistical analysis are given in Table 3, where the cosmological redshift z, the GRB isotropic energy $E_{\rm iso}$, the flare peak time t_p, peak luminosity L_p, duration Δt, and the corresponding E_f are reproduced. This lengthy analysis has been carried out over the past years, and only the final results are summarized in Table 3.

In Section 6, we present the correlations between t_p, L_p, Δt, E_f, and $E_{\rm iso}$ and give the corresponding parameters in Table 4. In this analysis, we applied the Markov Chain Monte Carlo (MCMC) method, and we also have made public the corresponding numerical codes in https://github.com/YWangScience/AstroNeuron and https://github.com/YWangScience/MCCC.

In Section 7, we discuss the correlations between the energy of the prompt emission, the energy of the FPA phase, and $E_{\rm iso}$ (see Tables 5–6 and Figures 29–31).

In Section 8, we analyze the thermal emission observed during the X-ray flares (see Table 7). We derive, in an appropriate relativistic formalism, the relations between the observed temperature and flux and the corresponding temperature and radius of the thermal emitter in its comoving frame.

In Section 9, we use the results of Section 8 to infer the expansion speed of the thermal emitter associated with the thermal components observed during the flares (see Figure 32 and Table 8). We find that the observational data imply a Lorentz factor $\Gamma \lesssim 4$ and a radius of $\approx 10^{12}$ cm for such a thermal emitter.

In Section 10, we present a theoretical treatment using a new relativistic hydrodynamical code to simulate the interaction of the e^+e^-–baryon plasma with the high-density regions of the SN ejecta. We first test the code in the same low-density domain of validity describing the prompt emission phase, and then we apply it in the high-density regime of the propagation of the plasma inside the SN ejecta, which we use for the theoretical interpretation of the X-ray flares. Most remarkably, the theoretical code leads to a thermal emitter with a Lorentz factor $\Gamma \lesssim 4$ and a radius of $\approx 10^{12}$ cm at transparency. The agreement between these theoretically derived values and the ones obtained from the observed thermal emission validates the model and the binary nature of the BdHN progenitors, in clear contrast with the traditional ultrarelativistic jetted models.

In Section 11, we present our conclusions. We first show how the traditional model, describing GRBs as a single system with ultrarelativistic jetted emission extending from the prompt emission all the way to the final phases of the afterglow and of the GeV emission, is in conflict with the X-ray flare observations. We also present three new main results that illustrate the new perspectives opened up by our alternative approach based on BdHNe.

A standard flat ΛCDM cosmological model with $\Omega_M = 0.27$, $\Omega_\Lambda = 0.73$, and $H_0 = 71$ km s^{-1} Mpc^{-1} is adopted throughout the paper, while Table 1 summarizes the acronyms we have used.

Table 1
Alphabetic Ordered List of the Acronyms Used in this Work

Extended Wording	Acronym
Binary-driven hypernova	BdHN
Black hole	BH
Carbon–oxygen core	$CO_{\rm core}$
Circumburst medium	CBM
Flare–Plateau–Afterglow	FPA
Gamma-ray burst	GRB
Gamma-ray flash	GRF
Induced gravitational collapse	IGC
Massive neutron star	MNS
Neutron star	NS
New neutron star	νNS
Proper gamma-ray burst	P-GRB
Short gamma-ray burst	S-GRB
Short gamma-ray flash	S-GRF
Supernova	SN
Ultrashort gamma-ray burst	U-GRB
White dwarf	WD
X-ray flash	XRF

2. Background for the Observational Identification of the X-Ray Flares

The discovery of GRBs by the *Vela* satellites (Klebesadel et al. 1973) was presented at the AAAS meeting in February 1974 in San Francisco (Gursky & Ruffini 1975). The *Vela* satellites were operating in gamma-rays in the 150–750 keV energy range and only marginally in X-rays (3–12 keV; Cline et al. 1979). Soon after it was hypothesized from first principles that GRBs may originate from an e^+e^- plasma in the gravitational collapse to a Kerr–Newman BH, implying an energy $\sim 10^{54}\, M_{\rm BH}/M_\odot$ erg (Damour & Ruffini 1975; see also Ruffini 1998).

Since 1991, the BATSE detectors on the *CGRO* (see Gehrels et al. 1993) have been leading to the classification of GRBs on the basis of their spectral hardness and of their observed T_{90} duration in the 50–300 keV energy band into short/hard bursts ($T_{90} < 2$ s) and long/soft bursts ($T_{90} > 2$ s (Mazets et al. 1981; Dezalay et al. 1992; Klebesadel 1992; Kouveliotou et al. 1993; Tavani 1998). Such an emission was later called the GRB

[9] T_{90} is the duration of the interval starting (ending) when 5% (95%) of the total energy of the event in gamma-rays has been emitted.

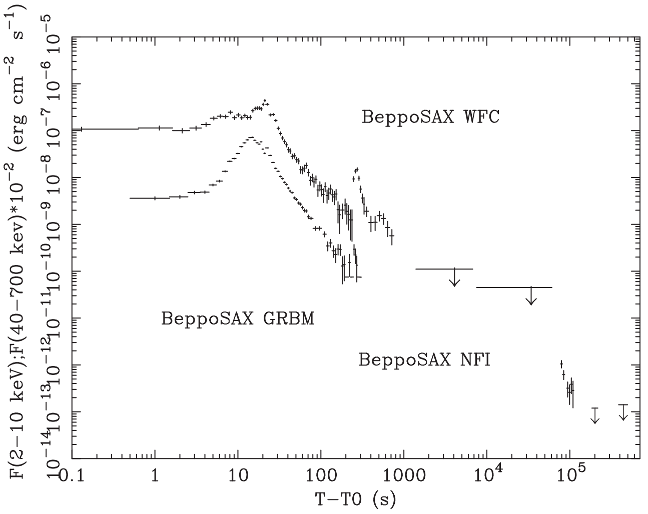

Figure 1. First X-ray flare observed by *BeppoSAX* in GRB 011121. Reproduced from Piro et al. (2005).

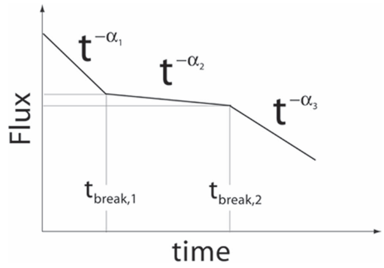

Figure 2. Schematic diagram of the X-ray light- curve composed of three power-law segments with different slopes ($3 \lesssim \alpha_1 \lesssim 5$, $0.5 \lesssim \alpha_2 \lesssim 1.0$, $1 \lesssim \alpha_3 \lesssim 1.5$). Figure taken from Nousek et al. (2006).

"prompt emission." In a first attempt, it was proposed that short GRBs originate from merging binary NSs (see, e.g., Goodman 1986; Paczynski 1986; Eichler et al. 1989; Narayan et al. 1991, 1992; Mészáros & Rees 1997) and long GRBs originate from a single source with ultrarelativistic jetted emission (Woosley 1993; Paczyński 1998; MacFadyen & Woosley 1999; Bromberg et al. 2013).

The *BeppoSAX* satellite, operating since 1996, joined the expertise of the X-ray and gamma-ray communities. Its gamma-ray burst monitor (GRBM) operating in the 40–700 keV energy band determined the trigger of the GRB, and two wide-field cameras operating in the 2–30 keV X-ray energy band allowed the localization of the source within an arcminute resolution. This enabled a follow-up with the narrow-field instruments (NFI) in the 2–10 keV energy band. *BeppoSAX* discovered the X-ray afterglow (Costa et al. 1997), characterized by an X-ray luminosity decreasing with a constant index of ~ -1.3 (see de Pasquale et al. 2006 as well as Pisani et al. 2016). This emission was detected after an "8 hr gap" following the prompt emission identified by BATSE. The consequent determination of the accurate positions by the NFI, transmitted to the optical (van Paradijs et al. 1997) and radio telescopes (Frail et al. 1997), allowed the determination of the GRB cosmological redshifts (Metzger et al. 1997). The derived distances of $\approx$5–10 Gpc confirmed their cosmological origin and their unprecedented energetics, $\approx 10^{50}$–10^{54} erg, thus validating our hypothesis derived from first principles (Damour & Ruffini 1975; Ruffini 1998).

To *BeppoSAX* goes the credit of the discovery of the temporal and spatial coincidence of GRB 980425 with SN 1998bw (Galama et al. 1998), which suggested the connection between GRBs and SNe, soon supported by many additional events (see, e.g., Woosley & Bloom 2006; Della Valle 2011; Hjorth & Bloom 2012). *BeppoSAX* also discovered the first "X-ray flare" in GRB 011121 closely following the prompt emission (Piro et al. 2005); see Figure 1. Our goal in this paper is to show how the X-ray flares, thanks to the observational campaign of the *Swift* satellite, have become the crucial test for understanding the astrophysical nature of the GRB–SN connection.

The *Swift* Burst Alert Telescope (BAT), operating in the 15–150 keV energy band, can detect GRB prompt emissions and accurately determine their position in the sky within 3 arcmin. Within 90 s, *Swift* can re-point the narrow-field X-ray telescope (XRT), operating in the 0.3–10 keV energy range, and relay the burst position to the ground. This overcomes the "8 hr gap" in the *BeppoSAX* data.

Thanks to the *Swift* satellite, the number of detected GRBs increased rapidly to 480 sources with known redshifts. By analyzing the light curve of some long GRBs, including the data in the "8 hr gap" of *BeppoSAX*, Nousek et al. (2006) and Zhang et al. (2006) discovered three power-law segments in the XRT flux light curves of some long GRBs. We refer to these as the "Nousek–Zhang power laws" (see Figure 2). The nature of this feature has been the subject of a long debates, still ongoing, and is finally resolved in this article.

We have used *Swift*-XRT data in differentiating two distinct subclasses of long GRBs: XRFs with $E_{\rm iso} \lesssim 10^{52}$ erg and BdHNe with $E_{\rm iso} \gtrsim 10^{52}$ erg (see Section 3). An additional striking difference appears between the XRT luminosities of these two subclasses when measured in their cosmological rest frames: in the case of BdHNe, the light curves follow a specific behavior that conforms to the Nousek–Zhang power law (see, e.g., Penacchioni et al. 2012, 2013; Pisani et al. 2013, 2016; Ruffini et al. 2014). None of these features are present in the case of XRFs (see Figure 3).

Finally, the *Fermi* satellite (Atwood et al. 2009), launched in 2008, detects ultrahigh energy photons from 20 MeV to 300 GeV with the Large Area Telescope (LAT) and detects photons from 8 keV to 30 MeV with the Gamma-ray Burst Monitor (GBM). For the purposes of this article addressing long GRBs, the *Fermi* observations have been prominent in further distinguishing between XRFs and BdHNe: the *Fermi*-LAT GeV emission has been observed only in BdHNe and never in XRFs.

3. Background for the Theoretical Interpretation of X-Ray Flares and Their Dynamics

3.1. The Classification of GRBs

The very extensive set of observations carried out by the above satellites in coordination with the largest optical and radio telescopes over a period of almost 40 years has led to an impressive set of data on 480 GRBs, all characterized by spectral, luminosity, and time variability information, and each one with a well-established cosmological redshift. By

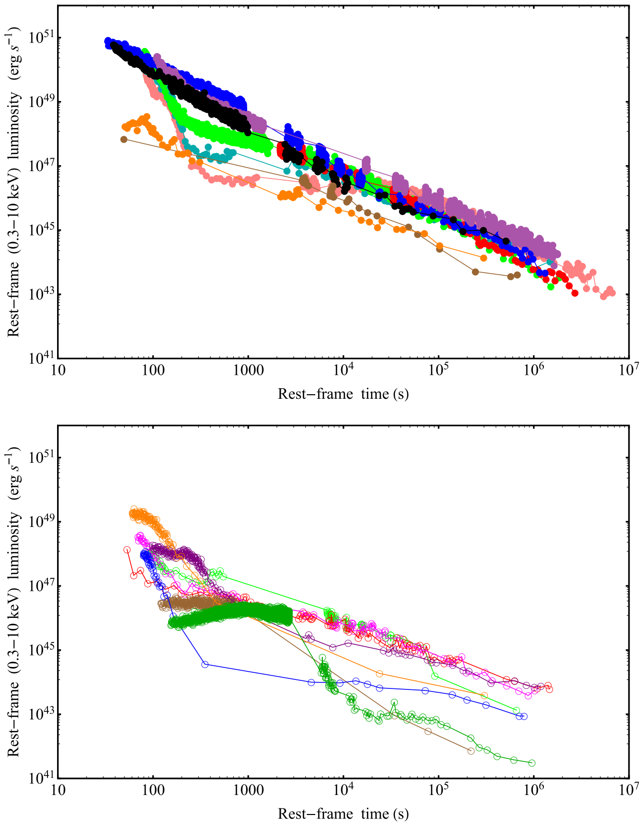

Figure 3. X-ray light curves of long GRBs observed by *Swift*. Top panel: BdHNe 050525 (brown), 060729 (pink), 061007 (black), 080319B (blue), 090618 (green), 091127 (red), 100816A (orange), 111228A (light blue), and 130427A (purple). Bottom panel: XRFs 050416A (red), 060218 (dark green), 070419A (orange), 081007 (magenta), 100316D (brown), 101219B (purple), and 130831A (green). XRFs have generally lower and more scattered light curves. All of these GRBs have known redshifts, and the light curves have been transformed to their cosmological rest frames.

classifying both the commonalities and the differences among all GRBs, it has been possible to create "equivalence relations" and divide GRBs into a number of subclasses, each one identified by a necessary and sufficient number of observables. We recall in Table 2 and Figure 4 the binary nature of all GRB progenitors and their classification into seven different subclasses (see, e.g., Ruffini et al. 2016b). In Table 2, we indicate the number of sources in each subclass, the nature of their progenitors and final outcomes of their evolution, their rest-frame T_{90}, their rest-frame spectral peak energy $E_{\rm p,i}$ and $E_{\rm iso}$ as well as the isotropic energy in X-rays $E_{\rm iso,X}$ and in GeV emission $E_{\rm iso,GeV}$, and finally their local observed number density rate. In Figure 4, we mention the $E_{\rm p,i}$–$E_{\rm iso}$ relations for these sources, including the Amati one for BdHNe and the MuRuWaZha one for the short bursts (see Ruffini et al. 2016a, 2016b), comprising short gamma-ray flashes (S-GRFs) with $E_{\rm iso} \lesssim 10^{52}$ erg, authentic short GRBs (S-GRBs) with $E_{\rm iso} \gtrsim 10^{52}$ erg, and gamma-ray flashes (GRFs), sources with hybrid short/long burst properties in their gamma-ray light curves, i.e., an initial spike-like harder emission followed by a prolonged softer emission observed up to $\sim$100 s, originating from NS–white dwarf binaries (Caito et al. 2009, 2010; Ruffini et al. 2016b). We have no evidence for an $E_{\rm p,i}$ and $E_{\rm iso}$ relation in the XRFs (see Figure 4). The Amati and the MuRuWaZha relations have not yet been theoretically understood, and as such they have no predictive power.

3.2. The Role of Time Parametrization in GRBs

Precise general relativistic rules in the spacetime parameterization of GBRs are needed (Ruffini et al. 2001a). Indeed, there are four time variables entering this discussion, which have to be properly distinguished one from another: (1) the comoving time $t_{\rm com}$, which is the time used to compute the evolution of the thermodynamical quantities (density, pressure, temperature); (2) the laboratory time $t = \Gamma t_{\rm com}$, where as usual the Lorentz Gamma factor is $\Gamma = (1 - \beta^2)^{-1/2}$ and $\beta = v/c$ is the expansion velocity of the source; (3) the arrival time t_a at which each photon emitted by the source reaches an observer in the cosmological rest frame of the source, given by (see also Bianco et al. 2001; Ruffini et al. 2002; Bianco & Ruffini 2005a)

$$t_a = t - \frac{r(t)}{c}\cos\vartheta, \tag{1}$$

where $r(t)$ is the radius of the expanding source in the laboratory frame and ϑ is the displacement angle of the normal to the emission surface from the line of sight; and (4) the arrival time at the detector on the Earth, $t_a^d = t_a(1+z)$, corrected for cosmological effects, where z is the source redshift needed in order to compare GRBs at different redshifts z. As emphasized in Ruffini et al. (2001a, p. L108), "the bookkeeping of these four different times and the corresponding space variables must be done carefully in order to keep the correct causal relation in the time sequence of the events involved." The chain of relations between these four times is given by (see e.g., Bianco et al. 2001; Ruffini et al. 2001a, 2002; Bianco & Ruffini 2005a, and see also Sections 8 and 9 for the dynamics of the flares)

$$\begin{aligned} t_a^d &= (1+z)t_a = (1+z)\left(t - \frac{r(t)}{c}\cos\vartheta\right) \\ &= (1+z)\left(\Gamma t_{\rm com} - \frac{r(\Gamma t_{\rm com})}{c}\cos\vartheta\right). \end{aligned} \tag{2}$$

The proper use of these four time variables is mandatory in modeling GRB sources, especially when we are dealing with a model not based on a single component but on multiple components, each characterized by a different world line and a different Lorentz Gamma factor, as is the case for BdHNe (see Sections 4 and 5).

3.3. The Role of the GRBs' Cosmological Rest Frame

In addition to all of the above, in order to compare the luminosities of different GRBs at different, redshifts we need to express the observational data in the cosmological rest frames of each source (where the arrival time is t_a), and correspondingly apply the K correction to luminosities and spectra (see Section 4). This formalism is at the very foundation of the treatment presented in this paper and has been systematically neglected in the great majority of current GRB models.

3.4. Episode 1: The Hypercritical Accretion Process

In order to describe the dynamics of BdHNe, a number of different episodes involving different physical conditions have

Table 2
Summary of the Seven GRB Subclasses (XRFs, BdHNe, BH–SN, Short Gamma-ray Flashes (S-GRFs), Authentic Short GRBs (S-GRBs), Ultrashort GRBs (U-GRB), and GRFs) and Their Observational Properties

	Subclass	Number	In-state (Progenitor)	Out-state (Final outcome)	T_{90} (s)	$E_{p,i}$ (MeV)	E_{iso} (erg)	$E_{iso,X}$ (erg)	$E_{iso,Gev}$ (erg)	ρ_{GRB} ($Gpc^{-3}yr^{-1}$)
I	XRFs	82	CO_{core}–NS	νNS–NS	$\sim$2–10^3	$\lesssim$0.2	$\sim 10^{48}$–10^{52}	$\sim 10^{48}$–10^{51}	⋯	100^{+45}_{-34}
II	BdHNe	345	CO_{core}–NS	νNS–BH	$\sim$2–10^2	$\sim$0.2–2	$\sim 10^{52}$–10^{54}	$\sim 10^{51}$–10^{52}	$\lesssim 10^{53}$	$0.77^{+0.09}_{-0.08}$
III	BH–SN	⋯	CO_{core}–BH	νNS–BH	$\sim$2–10^2	$\gtrsim$2	$>10^{54}$	$\sim 10^{51}$–10^{52}	$\gtrsim 10^{53}$	$\lesssim 0.77^{+0.09}_{-0.08}$
IV	S-GRFs	33	NS–NS	MNS	$\lesssim$2	$\lesssim$2	$\sim 10^{49}$–10^{52}	$\sim 10^{49}$–10^{51}	⋯	$3.6^{+1.4}_{-1.0}$
V	S-GRBs	7	NS–NS	BH	$\lesssim$2	$\gtrsim$2	$\sim 10^{52}$–10^{53}	$\lesssim 10^{51}$	$\sim 10^{52}$–10^{53}	$(1.9^{+1.8}_{-1.1}) \times 10^{-3}$
VI	U-GRBs	⋯	νNS–BH	BH	$\ll$2	$\gtrsim$2	$>10^{52}$	⋯	⋯	$\gtrsim 0.77^{+0.09}_{-0.08}$
VII	GRFs	13	NS–WD	MNS	$\sim$2–10^2	$\sim$0.2–2	$\sim 10^{51}$–10^{52}	$\sim 10^{49}$–10^{50}	⋯	$1.02^{+0.71}_{-0.46}$

Note. In the first five columns, we indicate the GRB subclasses and their corresponding number of sources with measured z, in-states, and out-states. In the following columns, we list the ranges of T_{90} in the rest frame, the rest-frame spectral peak energies $E_{p,i}$ and E_{iso} (rest frame 1–10^4 keV), the isotropic energy of the X-ray data $E_{iso,X}$ (rest frame 0.3–10 keV), and the isotropic energy of the GeV emission $E_{iso,GeV}$ (rest frame 0.1–100 GeV). In the last column, we list, for each GRB subclass, the local observed number density rate ρ_{GRB} obtained in Ruffini et al. (2016b). For details, see Ruffini et al. (2014, 2015b, 2015c), Fryer et al. (2015), Ruffini et al. (2016a, 2016b), and Becerra et al. (2016).

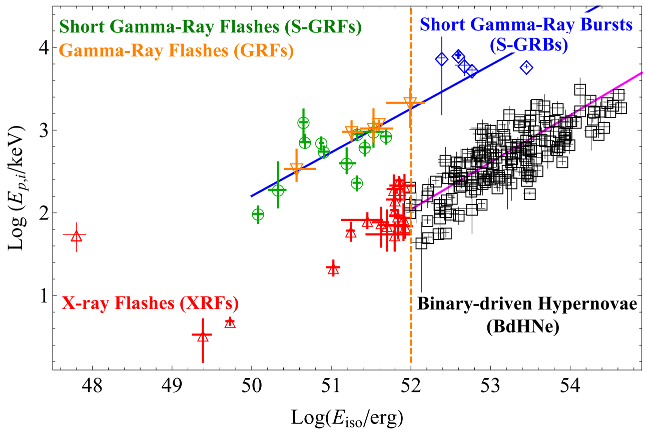

Figure 4. Updated $E_{p,i}$–E_{iso} plane for the subclasses defined in Ruffini et al. (2016b): XRF (red triangles) cluster in the region defined by $E_{p,i} \lesssim 200$ keV and $E_{iso} \lesssim 10^{52}$ erg. BdHN (black squares) cluster in the region defined by $E_{p,i} \gtrsim 200$ keV and $E_{iso} \gtrsim 10^{52}$ erg and fulfilling the Amati relation (solid magenta line with slope $\alpha = 0.57 \pm 0.06$ and extra scatter $\sigma = 0.25$; see, e.g., Amati & Della Valle 2013; Calderone et al. 2015). S-GRFs (green circles) and the initial spike-like emission of the GRFs (orange reverse triangles) are concentrated in the region defined by $E_{p,i} \lesssim 2$ MeV and $E_{iso} \lesssim 10^{52}$ erg, while S-GRBs (blue diamonds) are concentrated in the region defined by $E_{p,i} \gtrsim 2$ MeV and $E_{iso} \gtrsim 10^{52}$ erg. Short bursts and GRFs fulfill the MuRuWaZha relation (blue solid line with slope $\alpha = 0.53 \pm 0.07$ and extra scatter $\sigma = 0.24$; see, e.g., Zhang et al. 2012; Calderone et al. 2015; Ruffini et al. 2015b, 2016a). The BH–SN and U-GRB subclasses (see Table 2 in Ruffini et al. 2016b for details) are not in the plot since their observational identifications are still pending. The crucial difference between BdHNe and XRFs, and S-GRBs and S-GRFs, is that BdHNe and S-GRBs form a BH, their energy is $\gtrsim 10^{52}$ erg, and they exhibit GeV emission.

to be described. Episode 1 is dominated by the IGC paradigm: the hypercritical accretion of an SN ejecta onto the companion binary NS (see, e.g., Fryer et al. 2014, 2015; Becerra et al. 2015, 2016). Weak interactions and neutrinos (see, e.g., Fermi 1934), which play a fundamental role in SNe through the URCA process (Gamow & Schoenberg 1940, 1941), are also needed in the case of hypercritical accretion processes onto an NS in an SN fallback (Colgate 1971; Zel'dovich et al. 1972; Ruffini & Wilson 1973). They are especially relevant in the case of BdHNe where the accretion rate onto the NS companion from CO_{core} can reach up to $\dot{M} = 0.1\, M_\odot$ s^{-1} (Rueda & Ruffini 2012; Fryer et al. 2014; Becerra et al. 2015, 2016). Due to weak interactions, e^+e^- pairs annihilate to $\nu\bar{\nu}$ pairs with a cross-section $\sigma \sim G_F \langle E_e \rangle^2$ (Munakata et al. 1985; Itoh et al. 1989). In the thermal system of e^+e^- pairs at large temperature $kT > m_e c^2$ and density $n_e \sim T^3$, the neutrino emissivity of the e^+e^- annihilation is $\epsilon_{e^+e^-} \sim n_e^2 \langle \sigma v_e \rangle \langle E_e \rangle \sim 10^{25} (kT/\mathrm{MeV})^9$ erg s^{-1} cm^{-3}, leading to neutrino luminosities $L_\nu \sim R_{NS}^3 \epsilon_{e^+e^-} \sim 10^{52}$ erg s^{-1}, which dominate over other microscopic processes for cooling (Becerra et al. 2016). Thus, e^+e^- pair annihilation to $\nu\bar{\nu}$ is the main process for cooling, allowing the process of hypercritical accretion to convert gravitational energy into thermal energy, to build up high temperature, and consequently to form an e^+e^- plasma. Only at the end of Episode 1, as the critical mass of the companion NS is reached, is a BH is formed with the additional e^+e^- pairs linked to the BH electrodynamical process (Damour & Ruffini 1975; Cherubini et al. 2009).

3.5. Episode 2: e^+e^- Pairs Colliding with the SN Ejecta

Episode 2 is dominated by the new phenomenon of the impact of e^+e^- pairs generated in the GRB on the SN ejecta. We describe this process within the fireshell model. Two main differences exist between the fireshell and the fireball models. In the fireshell model, the e^+e^- plasma is initially in thermal equilibrium and undergoes ultrarelativistic expansion, keeping this condition of thermal equilibrium all the way to reaching transparency (Ruffini 1998; see also Aksenov et al. 2007; Ruffini et al. 2010 and references therein), while in the fireball model (Cavallo & Rees 1978), the e^+e^- pairs undergo an initial annihilation process that produces the photons driving the fireball. An additional basic difference is that the evolution of the e^+e^- plasma is not imposed by a given asymptotic solution but integrated following the relativistic fluid dynamics equations. The plasma, with energy $E_{e^+e^-}$, first goes through an initial acceleration phase (Ruffini et al. 1999). After colliding with the baryons (of total mass M_B), characterized by the baryon load parameter $B = M_B c^2/E_{e^+e^-}$, the optically thick plasma keeps accelerating until it reaches transparency and emits a proper gamma-ray burst (P-GRB; see Ruffini et al. 2000). The accelerated baryons then interact with the circumburst medium (CBM) clouds (Ruffini et al. 2001b); the equation of motion of the plasma has been integrated, leading to results that differ from the ones in Blandford & McKee's (1976) self-similar solution (see Bianco & Ruffini 2004, 2005a, 2005b, 2006). By using Equation (2), which defines "equitemporal surfaces" (see Bianco et al. 2001; Bianco & Ruffini 2004, 2005a, 2005b, 2006), it has been possible to infer the structure of the gamma-ray spikes in the prompt emission, which for the most part has been applied to the case of BdHNe (see, e.g., Ruffini et al. 2002, 2016a; Bernardini et al. 2005; Izzo et al. 2012; Patricelli et al. 2012; Penacchioni et al. 2012, 2013). For typical baryon loads of $10^{-4} \lesssim B \lesssim 10^{-2}$ leading to Lorentz Gamma factors $\Gamma \approx 10^2$–10^3 at transparency for the e^+e^-–baryon plasma, characteristic distances from the BH of $\approx 10^{15}$–10^{17} cm have been derived (see, e.g., Ruffini et al. 2016b and references therein). Those procedures are further generalized in this paper to compute the propagation of e^+e^- through the SN ejecta (see Section 10), after computing their density profiles (see Figure 35) and the corresponding baryon load (see Figure 34). The equations have been integrated all the way up to the condition of transparency (see Figures 36 and 37).

3.6. Episode 3: Ongoing Research on the Gamma-Ray Flares, Afterglow, and GeV Emission

We have exemplified the necessary steps in the analysis of each episode, which include determining the physical nature of each episode and the corresponding world line with the specific time-dependent Lorentz Gamma factor and so determining, using Equation (2), the arrival time at the detector, which has to agree, for consistency, with the one obtained from the observations. This program is applied in this article specifically for the analysis of early X-ray flares (see Sections 8 and 9). We will follow the same procedures for (1) the more complex analysis of gamma-ray flares, (2) the analysis of the afterglow consistent with the constraints on the X-ray flares observations, and (3) the properties of the GeV emission, common to BdHNe and S-GRBs (Ruffini et al. 2015c, 2016a). Having established the essential observational and theoretical background in Sections 2 and 3, we proceed to the data analysis of the early X-ray flares (see Sections 4–10).

4. The Early Flares and Sample Selection

With the increase in the number of observed GRBs, an attempt was made to analyze the X-ray flares and other processes considered to be similar in the observer reference frame, independent of the nature of the GRB type and of the value of their cosmological redshift or the absence of such a value. The goal of this attempt was to identify their "standard" properties, following a statistical analysis methodology often applied in classical astronomy (see Chincarini et al. 2007; Falcone et al. 2007; Margutti et al. 2010 as well as the review articles by Piran 1999, 2004; Mészáros 2002, 2006; Berger 2014; Kumar & Zhang 2015). We now summarize our alternative approach, having already given in the introduction and in Sections 2 and 3 the background for the observational identification and the theoretical interpretation of the X-ray flares.

As a first step, we only consider GRBs with an observed cosmological redshift. Having ourselves proposed the classification of all GRBs into seven different subclasses (see Section 3), we have given preliminary attention to verifying whether X-ray flares actually occur preferentially in some of these subclasses and if so, identifying the physical reasons determining such a correlation. We have analyzed all X-ray flares and found, a posteriori, that X-ray flares only occur in BdHNe. No X-ray flare has been identified in any other GRB subclass, either long or short. A claim of their existence in short bursts (Barthelmy et al. 2005; Fan et al. 2005; Dai et al. 2006) has been superseded: GRB 050724 with $T_{90} \sim 100$ s is not a short GRB, but actually a GRF, expected to originate in the merging of an NS and a white dwarf (see Figure 4); the X-ray data for this source from XRT are sufficient to assert that there is no evidence of an X-ray flare as defined in this section. GRB 050709 is indeed a short burst. It has been classified as an S-GRF (Aimuratov et al. 2017) and has been observed by *HETE* with very sparse X-ray data (Butler et al. 2005), and no presence of an X-ray flare can be inferred; the *Swift* satellite pointed at this source too late, 38.5 hr after the *HETE* trigger (Morgan et al. 2005).

As a second step, since all GRBs have a different redshift z, in order to compare them we need a description of each of them in its own cosmological rest frame. The luminosities have to be estimated after doing the necessary K corrections and the time coordinate in the observer frame has to be corrected by the cosmological redshift $t_a^d = (1 + z)t_a$. This also affects the determination of the T_{90} of each source (see, e.g., Figure 38 in Section 11 where the traditional approach by Kouveliotou et al. 1993 and Bromberg et al. 2013 has been superseded by ours).

As a third step, we recall an equally important distinction from the traditional fireball approach with a single ultrarelativistic jetted emission. Our GRB analysis envisages the existence of different episodes within each GRB, each one characterized by a different physical process and needing the definition of its own world line and corresponding Gamma factors, essential for estimating the time parametrization in the rest frame of the observer (see Section 2).

These three steps are applied in the present article, which specifically addresses the study of early X-ray flares and their fundamental role in establishing the physical and astrophysical nature of BdHNe and in distinguishing our binary model from the traditional one.

Before proceeding, let us recall the basic point of the K correction. All of the observed GRBs have a different redshift. In order to compare them, it is necessary to refer to each of them in its cosmological rest frame. This step has often been ignored in the current literature (Chincarini et al. 2007; Falcone et al. 2007; Margutti et al. 2010). Similarly, for the flux observed by the above satellites in Section 2, each instrument is characterized by its fixed energy window $[\epsilon_{\mathrm{obs},1}; \epsilon_{\mathrm{obs},2}]$. The observed flux f_{obs}, defined as the energy per unit area and time in a fixed instrumental energy window $[\epsilon_{\mathrm{obs},1}; \epsilon_{\mathrm{obs},2}]$, is expressed in terms of the observed photon number spectrum n_{obs} (i.e., the number of observed photons per unit energy, area, and time) as

$$f_{\mathrm{obs},[\epsilon_{\mathrm{obs},1};\epsilon_{\mathrm{obs},2}]} = \int_{\epsilon_{\mathrm{obs},1}}^{\epsilon_{\mathrm{obs},2}} \epsilon\, n_{\mathrm{obs}}(\epsilon) d\epsilon. \tag{3}$$

It then follows that the luminosity L of the source (i.e., the total emitted energy per unit time in a given bandwidth), expressed by definition in the source cosmological rest frame, is related to f_{obs} through the luminosity distance $D_L(z)$:

$$L_{[\epsilon_{\mathrm{obs},1}(1+z);\epsilon_{\mathrm{obs},2}(1+z)]} = 4\pi D_L^2(z) f_{\mathrm{obs},[\epsilon_{\mathrm{obs},1};\epsilon_{\mathrm{obs},2}]}. \tag{4}$$

The above Equation (4) gives the luminosities in different cosmological rest-frame energy bands, depending on the source

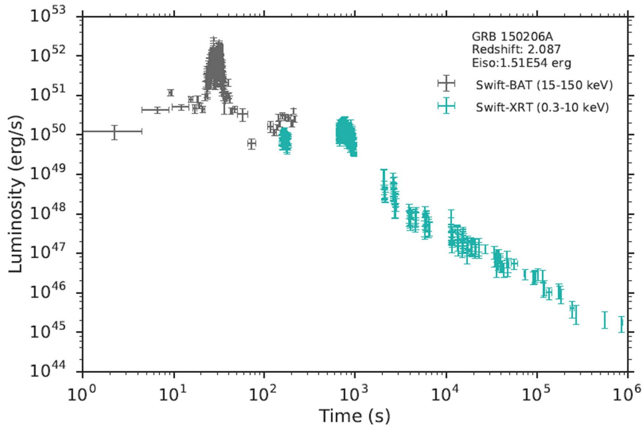

Figure 5. GRB 150206A is an example of a GRB with incomplete data, which therefore must be excluded. It only has 30 s *Swift-XRT* observations in the early 300 s. Flare determination is not possible under these conditions.

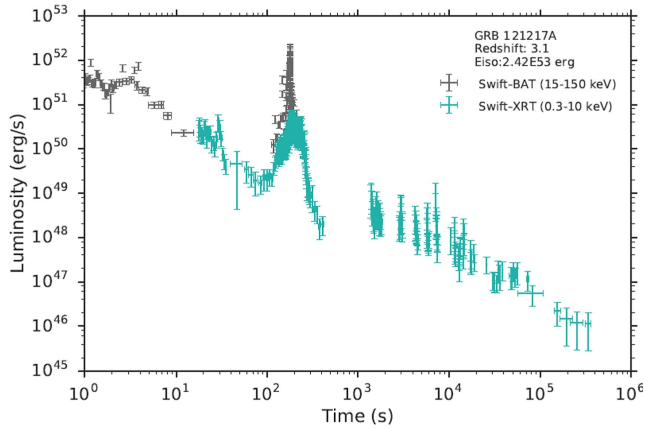

Figure 6. GRB 121217A clearly shows a gamma-ray flare observed by *Swift*-BAT, which coincides with a soft X-ray component observed by *Swift*-XRT. From the spectral analysis, it has a soft power-law photon index, and most of the energy is deposited in high-energy gamma-rays. This is an indication that the soft X-ray component is likely the low-energy part of a gamma-ray flare. For these reasons, we exclude it from our sample.

redshift. To express the luminosity L in a fixed cosmological rest-frame energy band, e.g., $[E_1; E_2]$, common to all sources, we can rewrite Equation (4) as

$$L_{[E_1;E_2]} = 4\pi D_L^2 f_{\mathrm{obs},\left[\frac{E_1}{1+z};\frac{E_2}{1+z}\right]} = 4\pi D_L^2 k[\epsilon_{\mathrm{obs},1};\ \epsilon_{\mathrm{obs},2};\ E_1;\ E_2;\ z] f_{\mathrm{obs},[\epsilon_{\mathrm{obs},1};\epsilon_{\mathrm{obs},2}]}, \quad (5)$$

where we have defined the K-correction factor:

$$k[\epsilon_{\mathrm{obs},1};\ \epsilon_{\mathrm{obs},2};\ E_1;\ E_2;\ z] = \frac{f_{\mathrm{obs},\left[\frac{E_1}{1+z};\frac{E_2}{1+z}\right]}}{f_{\mathrm{obs},[\epsilon_{\mathrm{obs},1};\epsilon_{\mathrm{obs},2}]}} = \frac{\int_{E_1/(1+z)}^{E_2/(1+z)} \epsilon\ n_{\mathrm{obs}}(\epsilon) d\epsilon}{\int_{\epsilon_{\mathrm{obs},1}}^{\epsilon_{\mathrm{obs},2}} \epsilon\ n_{\mathrm{obs}}(\epsilon) d\epsilon}. \quad (6)$$

If the energy range $[\frac{E_1}{1+z};\ \frac{E_2}{1+z}]$ is not fully inside the instrumental energy band $[\epsilon_{\mathrm{obs},1};\ \epsilon_{\mathrm{obs},2}]$, it may well happen that we will need to extrapolate n_{obs} within the integration boundaries $[\frac{E_1}{1+z};\ \frac{E_2}{1+z}]$.

Finally, we express each luminosity in a rest-frame energy band that coincides with the energy window of each specific instrument.

We turn now to the selection procedure for early X-ray flares. We take the soft X-ray flux light curves of each source with known redshift from the *Swift-XRT* repository (Evans et al. 2007, 2009). We then apply the above K correction to obtain the corresponding luminosity light curves in the rest frame 0.3–10 keV energy band. Starting from 421 *Swift*-XRT light curves, we found in 50 sources X-ray flare structures in the early 200 s. Remarkably, all of them are in BdHNe. We further filter our sample by applying the following criteria:

1. We exclude GRBs with flares having a low (<20) signal-to-noise ratio or with an incomplete data coverage of the early X-ray light curve—14 GRBs are excluded (see e.g., Figure 5).
2. We consider only X-ray flares and do not address here the gamma-ray flares, which will be studied in a forthcoming article—eight GRBs having only gamma-ray flares are temporarily excluded (see, e.g., Figure 6). In Figure 7, we show an illustrative example of the possible co-existence of an X-ray flare and a gamma-ray flare, and a way to distinguish them.
3. We also ignore here the late X-ray flare, including the ultralong GRB, which will be discussed in a forthcoming paper—six GRBs are consequently excluded.
4. We ignore the GRBs for which the soft X-ray energy observed by *Swift*-XRT (0.3–10 keV) before the plateau phase is higher than the gamma-ray energy observed by *Swift*-BAT (15–150 keV) during the entire valid *Swift*-BAT observation. This *Swift*-BAT anomaly points to an incomplete coverage of the prompt emission—six GRBs are excluded (see, e.g., Figure 8).

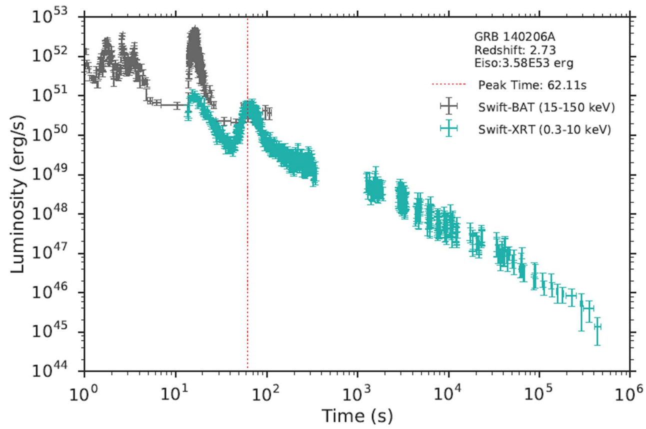

Figure 7. GRB 140206A has two flares. A gamma-ray flare coincides with the first flare while it is dim in the second one. The spectral analysis, using both *Swift*-XRT and *Swift*-BAT data, indicates a power-law index -0.88 ± 0.03 for the first flare. While the second flare requires an additional blackbody component; its power-law index is -1.73 ± 0.06 and its blackbody temperature is 0.54 ± 0.07 keV. Clearly, the energy of the first flare is contributed mainly by gamma-ray photons—it is a gamma-ray flare, and the second flare is an X-ray flare that we consider in this article.

Finally, we have found 16 BdHNe satisfying all of the criteria to be included in our sample. Among them, seven

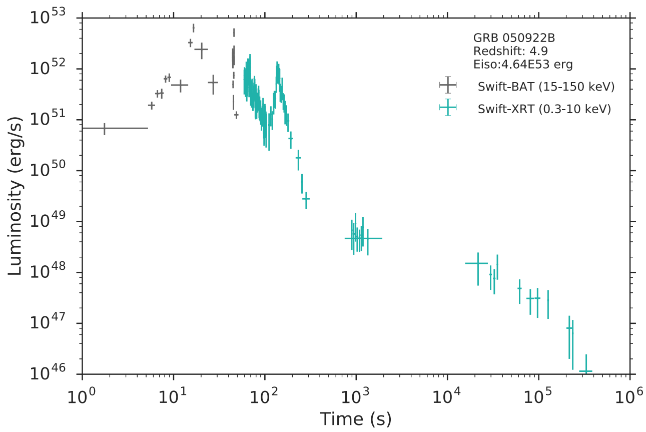

Figure 8. The *Swift*-BAT data of GRB 050922B has poor resolution—it cannot provide valid information after 50 s. The energy observed in its energy band, 15–150 keV, during this 50 s duration is 1.19×10^{53} erg. The energy observed by *Swift*-XRT is higher; the energy of the flares (60–200 s) in the *Swift*-XRT band 0.3–10 keV is 3.90×10^{53} erg. These results imply that the *Swift*-BAT observations may not cover the entire prompt emission phase; the isotropic energy computed from the *Swift*-BAT data is not reliable, and consequently the *Swift*-XRT observed partial prompt emission, which brings complexity to the X-ray light curve, makes the identification of the authentic X-ray flare more difficult.

BdHNe show a single flare. The other nine BdHNe contain two flares: generally, we exclude the first one, which appears to be a component from the gamma-ray spike or gamma-ray flare, and therefore select the second one for analysis (see, e.g., Figure 7).

These 16 selected BdHNe cover a wide range of redshifts. The closest one is GRB 070318 with redshift $z = 0.84$, and the farthest one is GRB 090516A with redshift $z = 4.11$. Their isotropic energy is also distributed over a large range: five GRBs have energies of the order of 10^{52} erg, nine GRBs of the order of 10^{53} erg, and two GRBs have extremely high isotropic energies $E_{\rm iso} > 10^{54}$ erg. Therefore, this sample is well-constructed although the total number is limited.

5. The XRT Luminosity Light Curves of the 16 BdHN Sample

We now turn to the light curves of each of these 16 GRBs composing our sample (see Figures 9–24). The blue curves represent the X-rays observed by *Swift*-XRT, and the green curves are the corresponding optical observations when available. All of the values are in the rest frame and the X-ray luminosities have been K-corrected. The red vertical lines indicate the peak time of the X-ray flares. The rest-frame luminosity light curves of some GRBs show different flare structures compared to the observed count flux light curves. An obvious example is GRB 090516A, which follows from comparing Figure 18 in this paper with Figure 1 in Troja et al. (2015). The details of the FPA, as well as their correlations or the absence of correlation with $E_{\rm iso}$, are given in the next section.

We then conclude that in our sample, there are *Swift* data for all GRBs: Konus-*Wind* observed GRBs 080607, 080810, 090516A, 131030A, 140419A, 141221A, and 151027A, while *Fermi* detected GRBs 090516A, 140206, 141221A, and 151027A. The energy coverage of the available satellites is limited, as mentioned in Section 2: *Fermi* detects the widest photon energy band, from 8 keV to 300 GeV, Konus-*Wind*

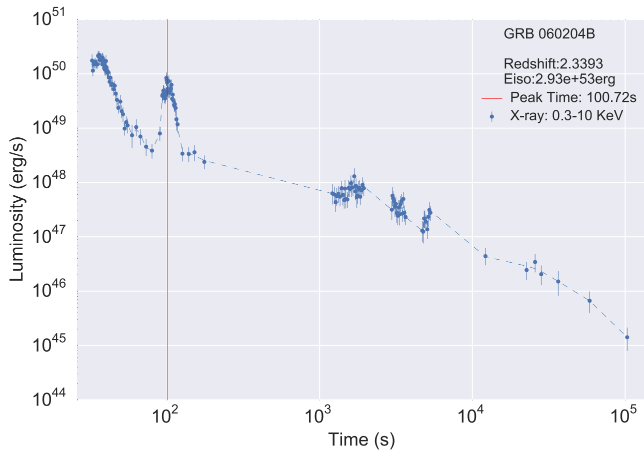

Figure 9. 060204B: this GRB triggered *Swift*-BAT (Falcone et al. 2006); *Swift*-XRT began observing 28.29 s after the BAT trigger. There is no observation from the *Fermi* satellite. X-shooter found its redshift at 2.3393 based on the host galaxy (Perley et al. 2016). The isotropic energy of this GRB reaches 2.93×10^{53} erg, computed from *Swift*-BAT data.

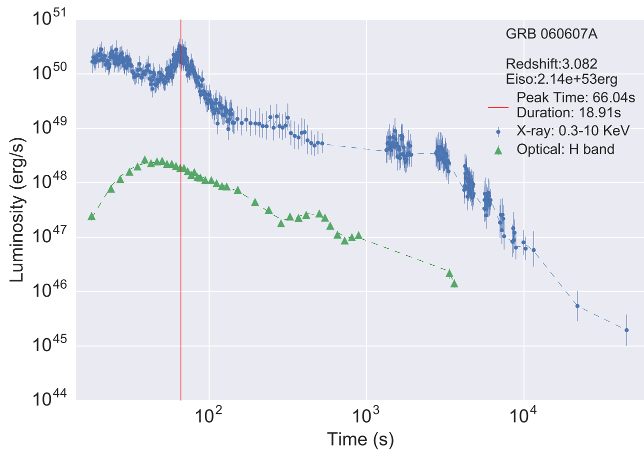

Figure 10. 060607A: this source was detected by the *Swift* satellite (Ziaeepour et al. 2006). It has a bright optical counterpart (Ziaeepour et al. 2006). It is located at a redshift $z = 3.082$ (Ledoux et al. 2006). The prompt light curve presents a doubled-peaked emission that lasts around 10 s, plus a second emission at $\sim$25 s of 2.5 s duration. The isotropic energy is $E_{\rm iso} = 2.14 \times 10^{53}$ erg. Optical data are from Nysewander et al. (2009).

observes from 20 keV to 15 MeV, and *Swift*-BAT has a narrow coverage from 15 keV to 150 keV. No GeV photons were observed, though GRB 090516A and 151027 were in the *Fermi*-LAT field of view. This contrasts with the observations of S-GRBs for which, in all of the sources so far identified and within the *Fermi*-LAT field of view, GeV photons were always observed (Ruffini et al. 2016a, 2016b) and can always freely reach a distant observer. These observational facts suggest that NS–NS (or NS–BH) mergers leading to the formation of a BH leave the surrounding environment poorly contaminated with the material ejected in the merging process ($\lesssim 10^{-2}$–$10^{-3}\,M_\odot$) and therefore the GeV emission, originating from the accretion on the BH formed in the merger process (Ruffini et al. 2016a) can be observed. On the other hand, BdHNe originate in $CO_{\rm core}$–NS binaries in which the material ejected from the $CO_{\rm core}$ explosion ($\approx M_\odot$) greatly pollutes the environment where the GeV emission has to propagate to reach the observer (see Section 3). This, together with the asymmetries of the SN

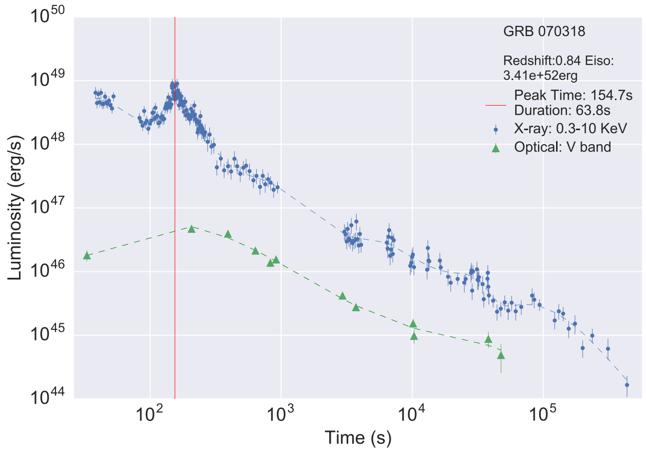

Figure 11. 070318: this source was detected by the *Swift* satellite (Cummings et al. 2007). It has a spectroscopic redshift of $z = 0.836$ (Jaunsen et al. 2007). The prompt light curve shows a peak with a typical fast-rise exponential-decay (FRED) behavior lasting about 55 s. XRT began observing the field 35 s after the BAT trigger. The isotropic energy is $E_{\rm iso} = 3.64 \times 10^{52}$ erg. From the optical observation at ∼20 days, no source or host galaxy is detected at the position of the optical afterglow, indicating that the decay rate of the afterglow must have steepened after some hours (Cobb 2007). Its optical data are from Chester et al. (2008).

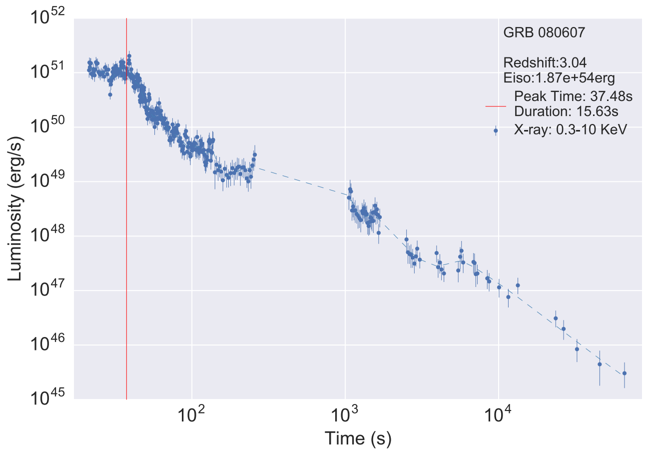

Figure 12. 080607: this source has been observed by *AGILE* (Marisaldi et al. 2008), Konus-*Wind* (Golenetskii et al. 2008), and *Swift* (Mangano et al. 2008). UVOT detected only a faint afterglow, since the source is located at a redshift $z = 3.04$. The isotropic energy is $E_{\rm iso} = 1.87 \times 10^{54}$ erg. The BAT prompt light curve shows a very pronounced peak that lasts ∼10 s, followed by several shallow peaks until 25 s. The *Swift* localization is at about 113° off-axis with respect to the *AGILE* pointing, so well out of the field of view of the *AGILE* gamma-ray imaging detector (GRID), which does not show any detection. The Konus-*Wind* light curve in the 50–200 keV range shows a multiple-peak emission lasting 15 s.

ejecta (see Section 3 and Becerra et al. 2016), lead to the possibility that the GeV emission in BdHNe can be "obscured" by the material of the SN ejecta, explaining the absence of GeV photons in the above cases of GRBs 090516A and 151027.

We derive the isotropic energy $E_{\rm iso}$ by assuming the prompt emission to be isotropic and by integrating the prompt photons in the rest-frame energy range from 1 keV to 10 MeV (Bloom et al. 2001). None of the satellites is able to cover the entire energy band of $E_{\rm iso}$, so we need to fit the spectrum and find the best-fit function, then extrapolate the integration of energy by using this function. This method is relatively safe for GRBs observed by *Fermi* and Konus-*Wind*, but six GRBs in our

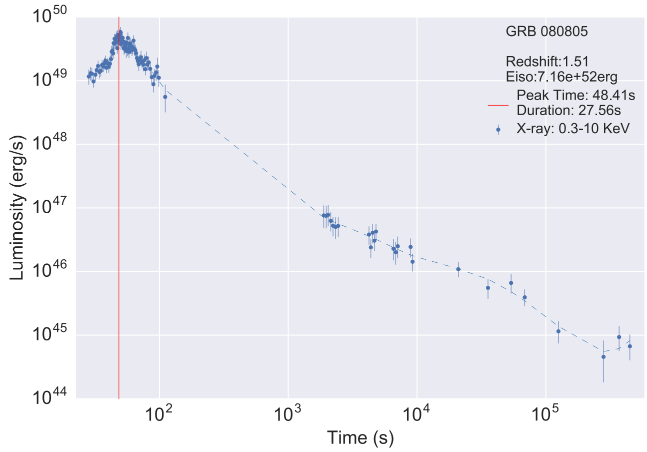

Figure 13. 080805: this source was detected by *Swift* (Pagani et al. 2008). The prompt light curve shows a peak with a FRED behavior lasting about 32 s. The redshift is $z = 1.51$, as reported by VLT (Jakobsson et al. 2008), and the isotropic energy is $E_{\rm iso} = 7.16 \times 10^{52}$ erg.

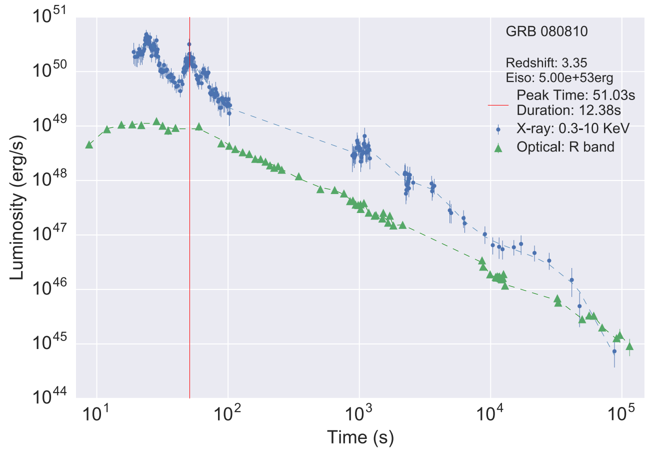

Figure 14. 080810: this source was detected by *Swift* (Golenetskii et al. 2008). The BAT light curve shows a multiple-peaked structure lasting about 23 s. XRT began observing the field 76 s after the BAT trigger. The source is located at a redshift of $z = 3.35$ and has an isotropic energy $E_{\rm iso} = 3.55 \times 10^{53}$ erg. Optical data are taken from Page et al. (2009).

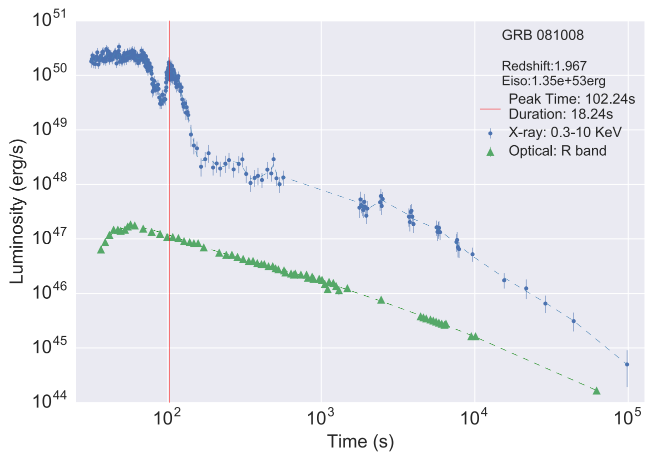

Figure 15. 081008: this source was detected by *Swift* (Racusin et al. 2008). The prompt emission lasts about 60 s and shows two peaks separated by 13 s. It is located at $z = 1.967$, as reported by VLT (D'Avanzo et al. 2008), and has an isotropic energy $E_{\rm iso} = 1.07 \times 10^{53}$ erg. Optical data are from Yuan et al. (2010).

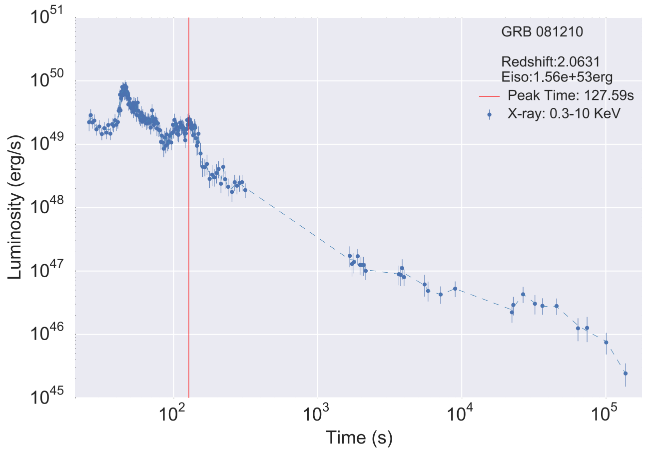

Figure 16. 081210: this GRB was detected by *Swift*-BAT (Krimm et al. 2008), *Swift*-XRT began observing 23.49 s after the BAT trigger. The BAT light curve begins with two spikes with a total duration of about 10 s and an additional spike at 45.75 s. There is no observation from the *Fermi* satellite. X-shooter found its redshift to be 2.0631 (Perley et al. 2016). The isotropic energy of this GRB is 1.56×10^{53} erg.

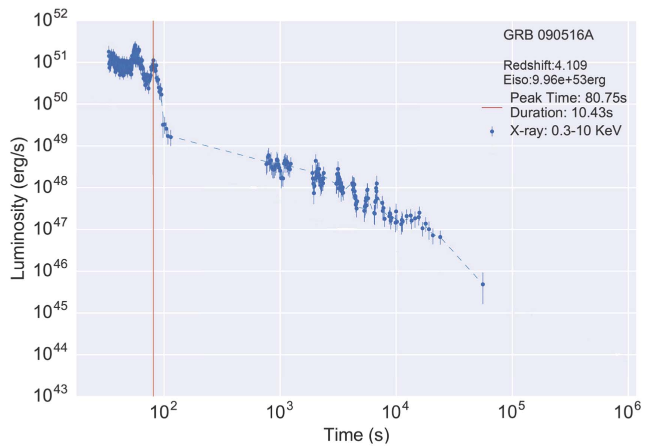

Figure 17. 090516A: this source was detected by *Swift* (Rowlinson et al. 2009), Konus-*Wind*, and *Fermi*/GBM (McBreen 2009). The BAT prompt light curve is composed of two episodes, the first starting 2 s before the trigger and lasting up to 10 s after the trigger, while the second episode starts at 17 s and lasts approximately 2 s. The GBM light curve consists of about five overlapping pulses from $T_{F,0} - 10$ s to $T_{F,0} + 21$ s (where $T_{F,0}$ is the trigger time of the *Fermi*/GBM). Konus-*Wind* observed this GRB in the waiting mode. VLT identified the redshift of the afterglow as $z = 4.109$ (de Ugarte Postigo et al. 2012), in agreement with the photometric redshift obtained with GROND (Rossi et al. 2009). *Fermi*-LAT was inside the field of view, following the standard *Fermi*-LAT likelihood analysis in https://fermi.gsfc.nasa.gov/ssc/data/analysis/scitools/likelihood_tutorial.html, the upper limit of the observed count flux is 4.76×10^{-6} photons $\mathrm{cm}^{-2}\,\mathrm{s}^{-1}$, and no GeV photon was found for this high redshift and low observed fluence GRB. The isotropic energy is $E_{\mathrm{iso}} = 6.5 \times 10^{53}$ erg.

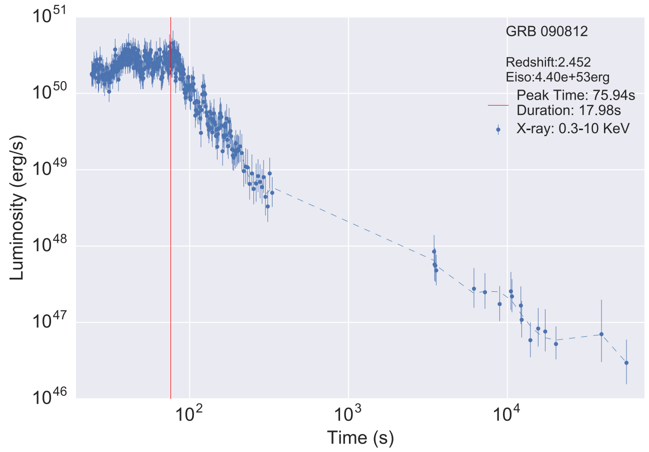

Figure 18. 090812: this source was detected by *Swift* (Stamatikos et al. 2009). It has a redshift $z = 2.452$ as confirmed by VLT (de Ugarte Postigo et al. 2012) and an isotropic energy $E_{\mathrm{iso}} = 4.75 \times 10^{53}$ erg. The BAT light curve shows three successive bumps lasting $\sim$20 s in total. XRT began observing the field 22 s after the BAT trigger (Stamatikos et al. 2009). The BAT light curve shows a simple power-law behavior.

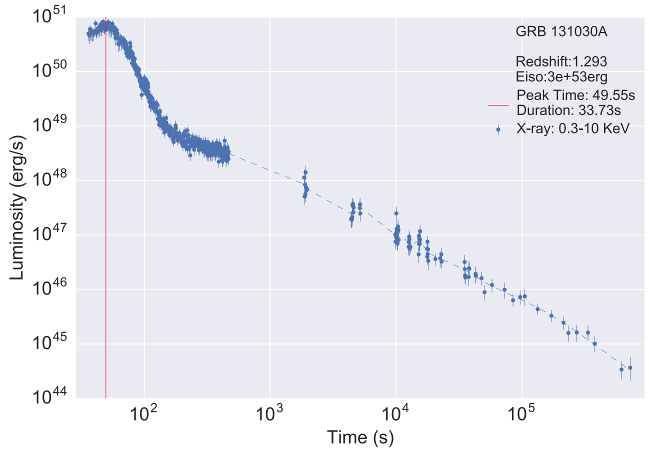

Figure 19. 131030A: this source was observed by *Swift* (Troja et al. 2013) and Konus-*Wind* (Golenetskii et al. 2013). The BAT light curve shows two overlapping peaks starting, with respect to the *Swift*-BAT trigger $T_{B,0}$, at $\sim T_{B,0} - 3.5$ s and peaking at $\sim T_{B,0} + 4.4$ s (Barthelmy et al. 2013). The duration is 18 s in the 15–350 keV band. The Konus-*Wind* light curve shows a multipeaked pulse from $\sim T_{KW,0} - 1.3$ s until $\sim T_{KW,0} + 11$ s (where $T_{KW,0}$ is the Konus-*Wind* trigger time). The redshift of this source is $z = 1.293$, as determined by NOT (Xu et al. 2013). The isotropic energy is $E_{\mathrm{iso}} = 3 \times 10^{53}$ erg.

sample have been observed only by *Swift*, so we uniformly fit and extrapolate these six GRBs by power laws and cutoff power laws; we then take the average value as E_{iso}. In general, our priority in computing E_{iso} is *Fermi*, Konus-*Wind*, then *Swift*. In order to take into account the expansion of the universe, all of our computations consider the K correction. The formula of K correction for E_{iso} varies depending on the best-fit function. The energy in the X-ray afterglow is computed in the cosmological rest-frame energy band from 0.3 to 10 keV. We smoothly fit the luminosity light curve using an algorithm named locally weighted regression (Cleveland & Devlin 1988), which provides a sequence of power-law functions. The corresponding energy in a fixed time interval is obtained by summing up all of the integrals of the power laws within it. This method is applied to estimate the energy of the flare E_f as well as the energy of the FPA phase up to 10^9 s, E_{FPA}. An interesting alternative procedure was used in Swenson & Roming (2014) to fit the light curve and determine the flaring structure with a Bayesian Information method. On this specific aspect, the two treatments are equally valid and give compatible results.

Table 3 contains the relevant energy and time information of the 16 BdHNe of the sample: the cosmological redshift z, E_{iso}, the flare peak time t_p, the corresponding peak luminosity L_p, the flare duration Δt, and the energy of the flare E_f. To determine t_p, we apply a locally weighted regression, which results in a

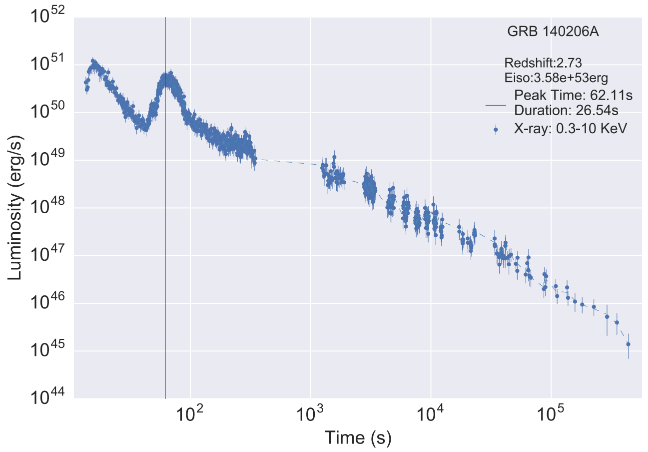

Figure 20. 140206A: this source was detected by all instruments on board *Swift* (Lien et al. 2014) and by *Fermi*/GBM (von Kienlin & Bhat 2014). The GBM light curve shows a single pulse with a duration of ∼7 s (50–300 keV). The source was outside the field of view, 123° from the LAT boresight at the time of the trigger. The BAT light curve shows a multipeaked structure with roughly three main pulses (Sakamoto et al. 2014). The source duration in the 15–350 keV band is 25 s. The redshift, as observed by NOT (Malesani et al. 2014), is $z = 2.73$, and the isotropic energy is $E_{\rm iso} = 4.3 \times 10^{53}$ erg.

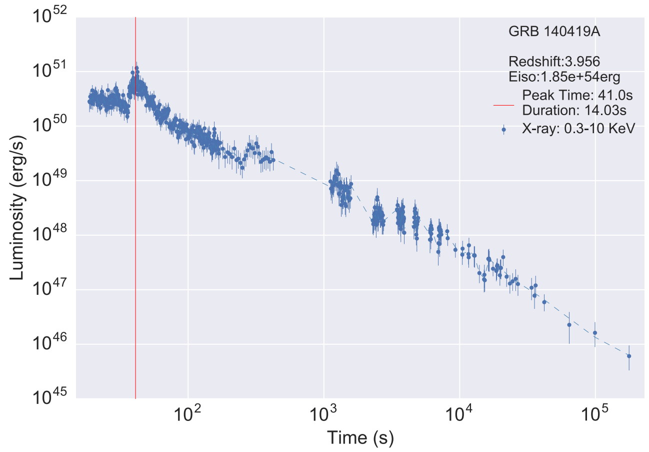

Figure 22. 140419A: this source was detected by Konus-*Wind* (Golenetskii et al. 2014) and *Swift* (Marshall et al. 2014). The Konus-*Wind* light curve shows a broad pulse from $\sim T_{\rm KW,0} - 2$ s to $\sim T_{\rm KW,0} + 8$ s, followed by softer pulses around $\sim T_{\rm KW,0} + 10$ s. The total duration of the burst is ∼16 s. The BAT light curve shows two slightly overlapping clusters of peaks, starting at $\sim T_{\rm B,0} - 2$ s, peaking at $\sim T_{\rm B,0} + 2$ s and $\sim T_{\rm B,0} + 10$ s, and ending at $\sim T_{\rm B,0} + 44$ s (Baumgartner et al. 2014). The total duration (in 15–350 keV) is 19 s. The redshift of this source, as determined by Gemini, is $z = 3.956$ (Tanvir et al. 2014), and its isotropic energy is $E_{\rm iso} = 1.85 \times 10^{54}$ erg.

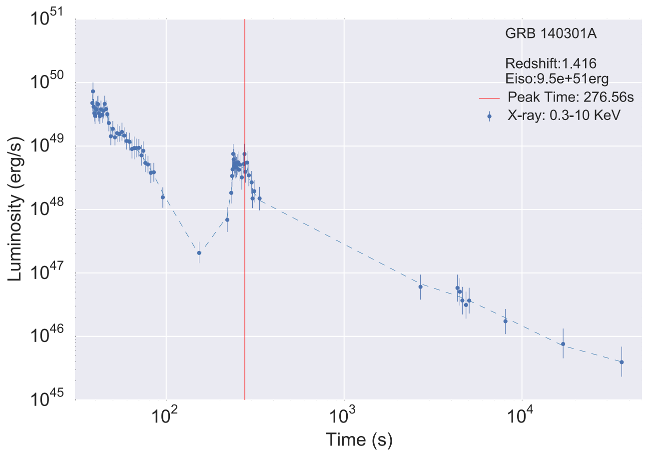

Figure 21. 140301A: this GRB triggered *Swift*-BAT (Page et al. 2014); the BAT light curve has a single spike with a duration of about 4 s. XRT started to observe 35.63 s after the BAT trigger. There is no observation from the *Fermi* satellite. From the X-shooter spectrum analysis, the redshift was revealed at 1.416 (Kruehler et al. 2014). The isotropic energy of this GRB is 9.5×10^{51} erg.

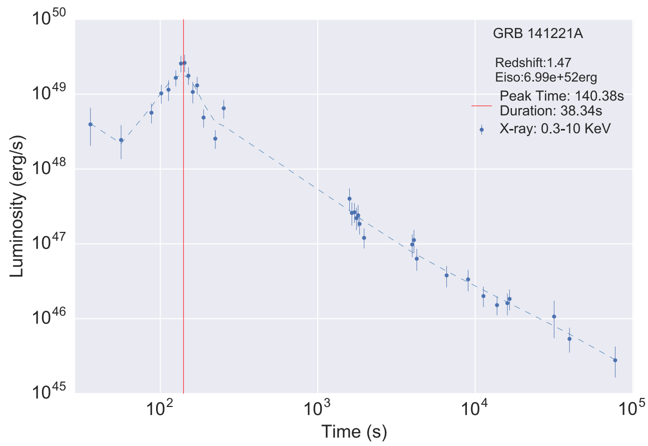

Figure 23. 141221A: this source is located at a spectroscopic redshift $z = 1.47$, as determined by Keck (Perley et al. 2014). Its isotropic energy is $E_{\rm iso} = 1.91 \times 10^{52}$ erg. The emission was detected by all of the instruments on board *Swift* (Sonbas et al. 2014) and by *Fermi*/GBM (Yu 2014). The GBM light curve consists of two pulses with a duration of about 10 s (50–300 keV). The source was 76° from the LAT boresight at the time of the trigger, out of the field of view. The BAT light curve showed a double-peaked structure with a duration of about 8 s. XRT began observing the field 32 s after the BAT trigger.

smoothed light curve composed of power-law functions: the flare peak is localized where the power-law index is zero. Therefore, t_p is defined as the time interval between the flare peak and the trigger time of *Swift*-BAT.[10] Correspondingly, we find the peak luminosity L_p at t_p and its duration Δt, which is defined as the time interval between a start time and an end time where the luminosity is half of L_p. We have made public the entire details including the codes online.[11]

6. Statistical Correlation

We then establish correlations between the above quantities characterizing each luminosity light curve of the sample with the $E_{\rm iso}$ of the corresponding BdHN. We have relied heavily on the MCMC method and iterated 10^5 times to obtain the best fit of the power law and their correlation coefficient. The main results are summarized in Figures 25–28. All of the codes are publicly available online.[12] We conclude that the peak time and

[10] In reality, the GRB occurs earlier than the trigger time, since there is a short period when the flux intensity is lower than the satellite trigger threshold (Fenimore et al. 2003).

[11] https://github.com/YWangScience/AstroNeuron

[12] https://github.com/YWangScience/MCCC

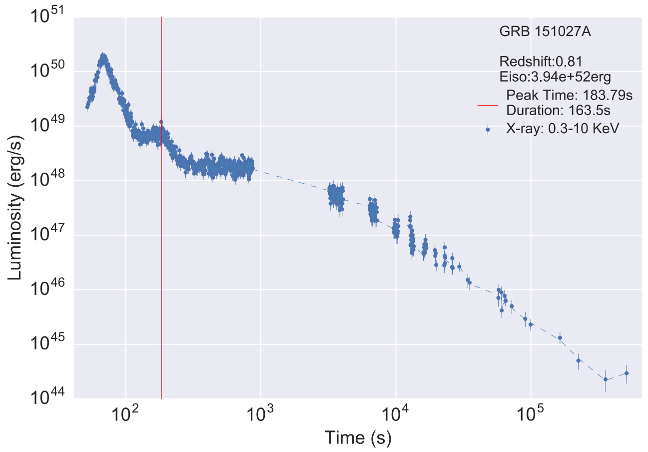

Figure 24. 151027A: this source was detected by MAXI (Masumitsu et al. 2015), Konus-*Wind* (Golenetskii et al. 2015), *Swift* (Maselli et al. 2015), and *Fermi*/GBM (Toelge et al. 2015). It is located at a redshift $z = 0.81$, as determined by Keck/HIRES (Perley et al. 2015), and the isotropic energy is $E_{\rm iso} = 3.94 \times 10^{52}$ erg. The LAT boresight of the source was 10° at the time of the trigger, and there are no clear associated high-energy photons; an upper limit of the observed count flux is computed to be 9.24×10^{-6} photons cm^{-2} s^{-1} following the standard *Fermi*-LAT likelihood analysis. The BAT light curve showed a complex peaked structure lasting at least 83 s. XRT began observing the field 48 s after the BAT trigger. The GBM light curve consists of three pulses with a duration of about 68 s in the 50–300 keV band. The Konus-*Wind* light curve consists of at least three pulses with a total duration of ~66 s. The MAXI detection is not significant, but the flux is consistent with the interpolation from the *Swift*/XRT light curve.

the duration of the flare, as well as the peak luminosity and the total energy of flare, are highly correlated with $E_{\rm iso}$, with correlation coefficients larger than 0.6 (or smaller than −0.6). The average values and the 1σ uncertainties are shown in Table 4.

7. The Partition of the Electron–Positron Plasma Energy Between the Prompt Emission and the FPA

The energy of the prompt emission is proportional to $E_{\rm iso}$ if and only if spherical symmetry is assumed: this clearly follows from the prompt emission time-integrated luminosity. We are now confronted with a new situation: the total energy of the FPA emission up to 10^9 s ($E_{\rm FPA}$) is also proportional to $E_{\rm iso}$, following the correlation given in Tables 5 and 6, and Figure 29. What is clear is that there are two very different components where the energy of the dyadosphere $E_{e^+e^-}$ is utilized: the energy $E_{\rm prompt}$ of the prompt emission and the energy $E_{\rm FPA}$ of the FPA, i.e., $E_{e^+e^-} = E_{\rm iso} = E_{\rm prompt} + E_{\rm FPA}$. Figures 30 and 31 show the distribution of $E_{e^+e^-} = E_{\rm iso}$ between these two components.

As a consequence of the above, in view of the presence of the companion SN remnant ejecta (see Becerra et al. 2016 for more details), we assume here that the spherical symmetry of the prompt emission is broken. Part of the energy due to the impact of the e^+e^- plasma on the SN is captured by the SN ejecta, and gives rise to the FPA emission as originally proposed by Ruffini (2015). We shall return to the study of the impact between the plasma and the SN ejecta in Section 10 after studying the motion of the matter composing the FPA in the next few sections.

It can also be seen that the relative partition between $E_{\rm prompt}$ and $E_{\rm FPA}$ strongly depends on the value of $E_{e^+e^-}$: the lower the GRB energy, the higher the FPA energy percentage, and consequently the lower the prompt energy percentage (see Figure 31).

In Becerra et al. (2016), we indicate that both the value of $E_{e^+e^-}$ and the relative ratio of the above two components can in principle be explained in terms of the geometry of the binary nature of the system: the smaller the distance is between the $CO_{\rm core}$ and the companion NS, the shorter the binary period of the system, and the larger the value of $E_{e^+e^-}$.

8. On the Flare Thermal Emission, Its Temperature, and Dynamics

We discuss now the profound difference between the prompt emission, which we recall is emitted at distances of the order of 10^{16} cm away from the newly born BH with $\Gamma \approx 10^2$–10^3, and the FPA phase. We focus on a further fundamental set of data, which originates from a thermal emission associated with the flares.[13] Only in some cases is this emission so clear and prominent that it allows the estimation of the flare expansion speed and the determination of its mildly relativistic Lorentz factor $\Gamma \lesssim 4$, which creates a drastic separatrix both in the energy and in the Gamma factor between the astrophysical nature of the prompt emission and of the flares.

Following the standard data reduction procedure of *Swift*-XRT (Romano et al. 2006; Evans et al. 2007, 2009), X-ray data within the duration of flare are retrieved from the United Kingdom *Swift* Science Data Centre (UKSSDC)[14] and analyzed by Heasoft.[15] Table 7 shows the fit of the spectrum within the duration Δt of the flare for each BdHN of the sample. As a first approximation, in computing the radius, we have assumed a constant expansion velocity of 0.8c indicated for some BdHNe, such as GRB 090618 (Ruffini et al. 2014) and GRB 130427A (Ruffini et al. 2015c). Out of 16 sources, seven BdHNe have highly confident thermal components (significance >0.95; see boldfaced entries in Table 7), which means that the addition of a blackbody spectrum improves a single power-law fit (which is, conversely, excluded at the 2σ confidence level). These blackbodies have fluxes in a range from 1% to 30% of the total flux and share a similar order of magnitude radii, i.e., ~10^{11}–10^{12} cm. In order to have a highly significant thermal component, the blackbody radiation itself should be prominent as well as its ratio to the nonthermal part. Another critical reason is that the observable temperature must be compatible with the satellite bandpass. For example, *Swift*-XRT observes in the 0.3–10 keV photon energy band, but the hydrogen absorption affects the lower energy part (~0.5 keV), and data are not always adequate beyond 5 keV, due to the low effective area of satellite for high-energy photons. The reliable temperature only ranges from 0.15 keV to 1.5 keV (since the peak photon energy is equal to the temperature times 2.82), so the remaining nine GRBs may contain a thermal component in the flare but outside the satellite bandpass.

We now attempt to perform a more refined analysis to infer the value of β from the observations. We assume that during the flare, the blackbody emitter has spherical symmetry and expands with a constant Lorentz Gamma factor. Therefore, the expansion velocity β is also constant during the flare. The relations between the comoving time $t_{\rm com}$, the laboratory time t,

[13] The late afterglow phases have been already discussed in Pisani et al. (2013, 2016).
[14] http://www.swift.ac.uk
[15] http://heasarc.gsfc.nasa.gov/lheasoft/

Table 3
GRB Sample Properties of the Prompt and Flare Phases

GRB	z	T_{90} (s)	$E_{\rm iso}$ (erg)	t_p (s)	L_p (erg s^{-1})	Δt (s)	E_f (erg)	α_f
060204B	2.3393	40.12	$2.93(\pm0.60)\times10^{53}$	100.72 ± 6.31	$7.35(\pm2.05)\times10^{49}$	17.34 ± 6.83	$8.56(\pm0.82)\times10^{50}$	2.73
060607A	3.082	24.49	$2.14(\pm1.19)\times10^{53}$	66.04 ± 4.98	$2.28(\pm0.48)\times10^{50}$	18.91 ± 3.84	$3.33(\pm0.32)\times10^{51}$	1.72
070318	0.84	28.80	$3.41(\pm2.14)\times10^{52}$	154.7 ± 12.80	$6.28(\pm1.30)\times10^{48}$	63.80 ± 19.82	$3.17(\pm0.37)\times10^{50}$	1.84
080607	3.04	21.04	$1.87(\pm0.11)\times10^{54}$	37.48 ± 3.60	$1.14(\pm0.27)\times10^{51}$	15.63 ± 4.32	$1.54(\pm0.24)\times10^{52}$	2.08
080805	1.51	31.08	$7.16(\pm1.90)\times10^{52}$	48.41 ± 5.46	$4.66(\pm0.59)\times10^{49}$	27.56 ± 9.33	$9.68(\pm1.24)\times10^{50}$	1.25
080810	3.35	18.25	$5.00(\pm0.44)\times10^{53}$	51.03 ± 6.49	$1.85(\pm0.53)\times10^{50}$	12.38 ± 4.00	$1.80(\pm0.17)\times10^{51}$	2.37
081008	1.967	62.52	$1.35(\pm0.66)\times10^{53}$	102.24 ± 5.66	$1.36(\pm0.33)\times10^{50}$	18.24 ± 3.63	$1.93(\pm0.16)\times10^{51}$	2.46
081210	2.0631	47.66	$1.56(\pm0.54)\times10^{53}$	127.59 ± 13.68	$2.23(\pm0.21)\times10^{49}$	49.05 ± 6.49	$8.86(\pm0.54)\times10^{50}$	2.28
090516A	4.109	68.51	$9.96(\pm1.67)\times10^{53}$	80.75 ± 2.20	$9.10(\pm2.26)\times10^{50}$	10.43 ± 2.44	$7.74(\pm0.63)\times10^{51}$	3.66
090812	2.452	18.77	$4.40(\pm0.65)\times10^{53}$	77.43 ± 16.6	$3.13(\pm1.38)\times10^{50}$	17.98 ± 4.51	$5.18(\pm0.61)\times10^{51}$	2.20
131030A	1.293	12.21	$3.00(\pm0.20)\times10^{53}$	49.55 ± 7.88	$6.63(\pm1.12)\times10^{50}$	33.73 ± 6.55	$3.15(\pm0.57)\times10^{52}$	2.22
140206A	2.73	7.24	$3.58(\pm0.79)\times10^{53}$	62.11 ± 12.26	$4.62(\pm0.99)\times10^{50}$	26.54 ± 4.31	$1.04(\pm0.59)\times10^{51}$	1.73
140301A	1.416	12.83	$9.50(\pm1.75)\times10^{51}$	276.56 ± 15.50	$5.14(\pm1.84)\times10^{48}$	64.52 ± 10.94	$3.08(\pm0.22)\times10^{50}$	2.30
140419A	3.956	16.14	$1.85(\pm0.77)\times10^{54}$	41.00 ± 4.68	$6.23(\pm1.45)\times10^{50}$	14.03 ± 5.74	$7.22(\pm0.88)\times10^{51}$	2.32
141221A	1.47	9.64	$6.99(\pm1.98)\times10^{52}$	140.38 ± 5.64	$2.60(\pm0.64)\times10^{49}$	38.34 ± 9.26	$7.70(\pm0.78)\times10^{50}$	1.79
151027A	0.81	68.51	$3.94(\pm1.33)\times10^{52}$	183.79 ± 16.43	$7.10(\pm1.75)\times10^{48}$	163.5 ± 30.39	$4.39(\pm2.91)\times10^{51}$	2.26

Note. This table contains the redshift z, the T_{90} in the rest frame, the isotropic energy $E_{\rm iso}$, the flare peak time t_p in the rest frame, the flare peak luminosity L_p, the flare duration where the starting and ending time correspond to half of the peak luminosity Δt, the flare energy E_f within the time interval Δt, and α_f the power-law index from the fitting of the flare's spectrum.

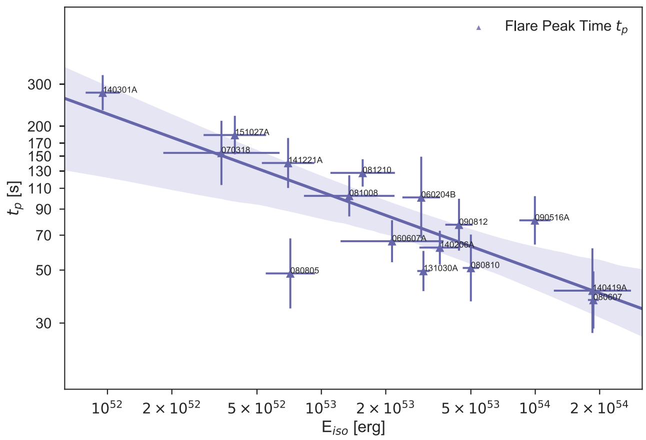

Figure 25. Relation between $E_{\rm iso}$ and t_p fit by a power law. The shaded area indicates the 95% confidence level.

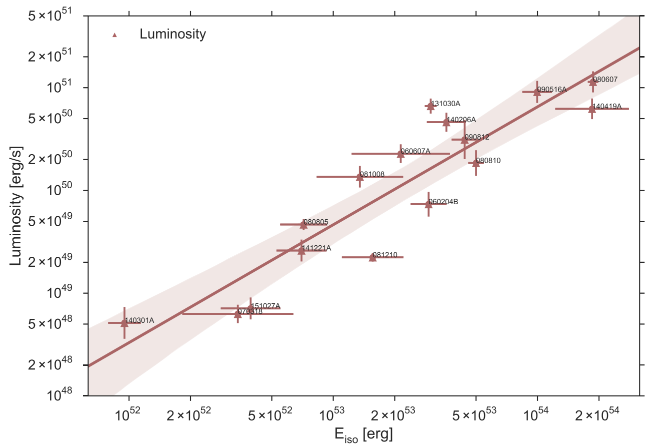

Figure 27. Relation between $E_{\rm iso}$ and L_p fit by a power law. The shaded area indicates the 95% confidence level.

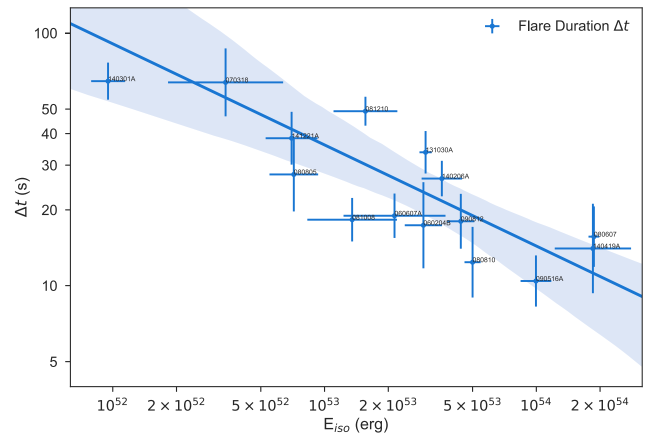

Figure 26. Relation between $E_{\rm iso}$ and Δt fit by a power law. The shaded area indicates the 95% confidence level.

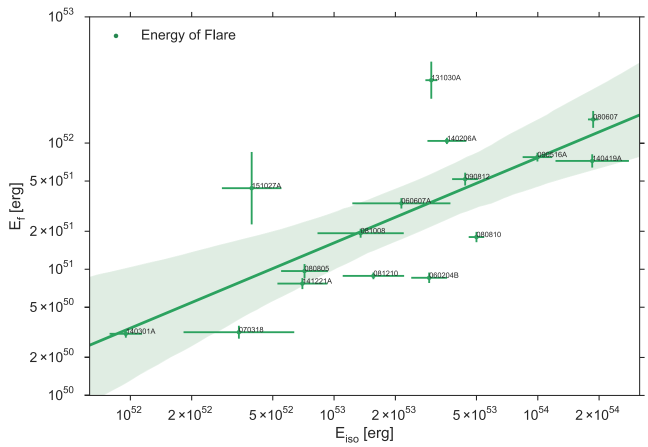

Figure 28. Relation between $E_{\rm iso}$ and E_f fit by a power law. The shaded area indicates the 95% confidence level.

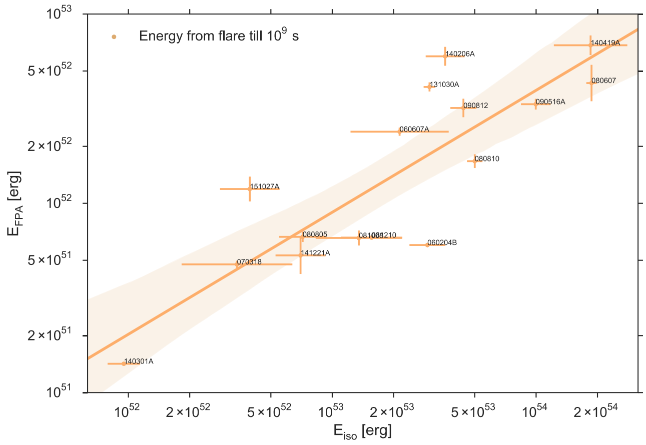

Figure 29. Relation between E_{iso} and E_{FPA} fit by a power law. The shaded area indicates the 95% confidence level.

Table 4
Power-law Correlations Among the Quantities in Table 3

Correlation	Power-law Index	Coefficient
$E_{\text{iso}} - t_p$	$-0.290(\pm 0.010)$	$-0.764(\pm 0.123)$
$E_{\text{iso}} - \Delta t$	$-0.461(\pm 0.042)$	$-0.760(\pm 0.138)$
$E_{\text{iso}} - L_p$	$1.186(\pm 0.037)$	$0.883(\pm 0.070)$
$E_{\text{iso}} - E_f$	$0.631(\pm 0.117)$	$0.699(\pm 0.145)$

Note. The values and uncertainties (at the 1σ confidence level) of the power-law index and of the correlation coefficient are obtained from 10^5 MCMC iterations. All relations are highly correlated.

Table 5
GRB Sample Properties of the Prompt and FPA Phases

GRB	z	E_{iso} (erg)	E_{FPA} (erg)
060204B	2.3393	$2.93(\pm 0.60) \times 10^{53}$	$6.02(\pm 0.20) \times 10^{51}$
060607A	3.082	$2.14(\pm 1.19) \times 10^{53}$	$2.39(\pm 0.12) \times 10^{52}$
070318	0.84	$3.41(\pm 2.14) \times 10^{52}$	$4.76(\pm 0.21) \times 10^{51}$
080607	3.04	$1.87(\pm 0.11) \times 10^{54}$	$4.32(\pm 0.96) \times 10^{52}$
080805	1.51	$7.16(\pm 1.90) \times 10^{52}$	$6.65(\pm 0.42) \times 10^{51}$
080810	3.35	$5.00(\pm 0.44) \times 10^{53}$	$1.67(\pm 0.14) \times 10^{52}$
081008	1.967	$1.35(\pm 0.66) \times 10^{53}$	$6.56(\pm 0.60) \times 10^{51}$
081210	2.0631	$1.56(\pm 0.54) \times 10^{53}$	$6.59(\pm 0.60) \times 10^{51}$
090516A	4.109	$9.96(\pm 1.67) \times 10^{53}$	$3.34(\pm 0.22) \times 10^{52}$
090812	2.452	$4.40(\pm 0.65) \times 10^{53}$	$3.19(\pm 0.36) \times 10^{52}$
131030A	1.293	$3.00(\pm 0.20) \times 10^{53}$	$4.12(\pm 0.23) \times 10^{52}$
140206A	2.73	$3.58(\pm 0.79) \times 10^{53}$	$5.98(\pm 0.69) \times 10^{52}$
140301A	1.416	$9.50(\pm 1.75) \times 10^{51}$	$1.42(\pm 0.14) \times 10^{50}$
140419A	3.956	$1.85(\pm 0.77) \times 10^{54}$	$6.84(\pm 0.82) \times 10^{52}$
141221A	1.47	$6.99(\pm 1.98) \times 10^{52}$	$5.31(\pm 1.21) \times 10^{51}$
151027A	0.81	$3.94(\pm 1.33) \times 10^{52}$	$1.19(\pm 0.18) \times 10^{52}$

Note. This table lists z, E_{iso}, and the FPA energy E_{FPA} from the flare until 10^9 s.

the arrival time t_a, and the arrival time t_a^d at the detector, given in Equation (2), in this case become

$$t_a^d = t_a(1+z) = t(1 - \beta\cos\vartheta)(1+z) \\ = \Gamma t_{\text{com}}(1 - \beta\cos\vartheta)(1+z). \tag{7}$$

We can infer an effective radius R of the blackbody emitter from (1) the observed blackbody temperature T_{obs}, which comes from the spectral fit of the data during the flare; (2) the observed bolometric blackbody flux $F_{\text{bb,obs}}$, computed from T_{obs} and the normalization of the blackbody spectral fit; and (3) the cosmological redshift z of the source (see also Izzo et al. 2012). We recall that $F_{\text{bb,obs}}$ by definition is given by

$$F_{\text{bb,obs}} = \frac{L}{4\pi D_L(z)^2}, \tag{8}$$

where $D_L(z)$ is the luminosity distance of the source, which in turn is a function of the cosmological redshift z, and L is the source bolometric luminosity (i.e., the total emitted energy per unit time). L is Lorentz invariant, so we can compute it in the comoving frame of the emitter using the usual blackbody expression,

$$L = 4\pi {R_{\text{com}}}^2 \sigma {T_{\text{com}}}^4, \tag{9}$$

where R_{com} and T_{com} are the comoving radius and the comoving temperature of the emitter, respectively, and σ is the Stefan–Boltzmann constant. We recall that T_{com} is constant over the entire shell due to our assumption of spherical symmetry. From Equations (8) and (9), we then have

$$F_{\text{bb,obs}} = \frac{{R_{\text{com}}}^2 \sigma {T_{\text{com}}}^4}{D_L(z)^2}. \tag{10}$$

We now need the relation between T_{com} and the observed blackbody temperature T_{obs}. Considering both the cosmological redshift and the Doppler effect due to the velocity of the

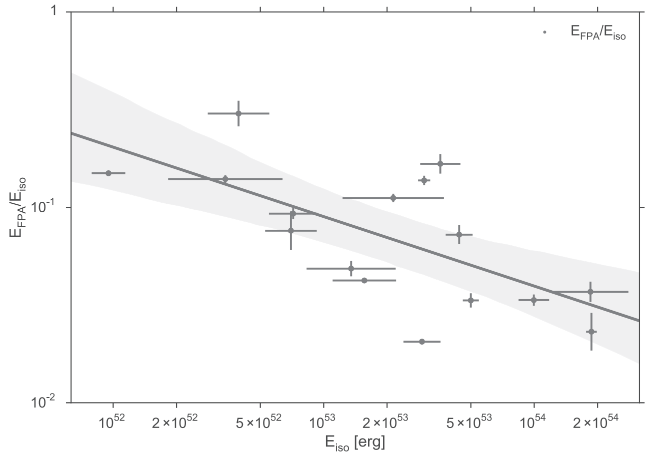

Figure 30. Relation between the percentage of $E_{e^+e^-}$ going to the SN ejecta and accounting for the energy in FPA, i.e., $E_{\text{FPA}}/E_{\text{iso}} \times 100\%$, and E_{iso} fit by a power law. The shaded area indicates the 95% confidence level.

Table 6
Power-law Correlations Among the Quantities in Table 5

Correlation	Power-law Index	Coefficient
E_{iso}–E_{FPA}	$0.613(\pm 0.041)$	$0.791(\pm 0.103)$
E_{iso}–$E_{\text{FPA}}/E_{\text{iso}}$	$-0.005(\pm 0.002)$	$0.572(\pm 0.178)$

Note. The statistical considerations of Table 4 are valid here as well.

Figure 31. Distribution of the GRB total energy $E_{e^+e^-} = E_{\rm iso}$ into prompt and FPA energies. The percentage of $E_{e^+e^-}$ going to the SN ejecta accounting for the energy in the FPA phase appears in red, i.e., $E_{\rm FPA}/E_{\rm iso} \times 100\%$. The green part is therefore the percentage of $E_{e^+e^-}$ used in the prompt emission, i.e., $E_{\rm prompt}/E_{\rm iso} \times 100\%$. It can be seen that the lower the GRB energy $E_{e^+e^-} = E_{\rm iso}$, the higher the FPA energy percentage, and consequently the lower the prompt energy percentage.

emitting surface, we have

$$T_{\rm obs}(T_{\rm com}, z, \Gamma, \cos\vartheta) = \frac{T_{\rm com}}{(1+z)\Gamma(1-\beta\cos\vartheta)} = \frac{T_{\rm com}\mathcal{D}(\cos\vartheta)}{1+z}, \quad (11)$$

where we have defined the Doppler factor $\mathcal{D}(\cos\vartheta)$ as

$$\mathcal{D}(\cos\vartheta) \equiv \frac{1}{\Gamma(1-\beta\cos\vartheta)}. \quad (12)$$

Equation (11) gives us the observed blackbody temperature of the radiation coming from different points of the emitter surface, corresponding to different values of $\cos\vartheta$. However, since the emitter is at a cosmological distance, we are not able to resolve spatially the source with our detectors. Therefore, the temperature that we actually observe corresponds to an average of Equation (11) computed over the emitter surface:[16]

$$\begin{aligned} T_{\rm obs}(T_{\rm com}, z, \Gamma) &= \frac{1}{1+z}\frac{\int_\beta^1 \mathcal{D}(\cos\vartheta)T_{\rm com}\cos\vartheta d\cos\vartheta}{\int_\beta^1 \cos\vartheta d\cos\vartheta} \\ &= \frac{2}{1+z}\frac{\beta(\beta-1)+\ln(1+\beta)}{\Gamma\beta^2(1-\beta^2)}T_{\rm com} \\ &= \Theta(\beta)\frac{\Gamma}{1+z}T_{\rm com}, \end{aligned} \quad (13)$$

where we defined

$$\Theta(\beta) \equiv 2\frac{\beta(\beta-1)+\ln(1+\beta)}{\beta^2}. \quad (14)$$

[16] From the point of view of the observer, the spectrum is not a perfect blackbody, coming from a convolution of blackbody spectra at different temperatures. The blackbody component we obtain from the spectral fit of the observed data is an effective blackbody of temperature $T_{\rm obs}$, analogous to other cases of effective temperatures in cosmology (see, e.g., Ruffini et al. 1983).

Table 7
Radii and Temperatures of the Thermal Components Detected Within the Flare Duration Δt

GRB	Radius (cm)	$kT_{\rm obs}$ (keV)	Significance
060204B	$\mathbf{1.80(\pm1.11)\times10^{11}}$	$\mathbf{0.60(\pm0.15)}$	**0.986**
060607A	$\mathbf{1.67(\pm1.01)\times10^{11}}$	$\mathbf{0.92(\pm0.24)}$	**0.991**
070318	*unconstrained*	$1.79(\pm1.14)$	0.651
080607	$\mathbf{1.52(\pm0.72)\times10^{12}}$	$\mathbf{0.49(\pm0.10)}$	**0.998**
080805	$1.12(\pm1.34)\times10^{11}$	$1.31(\pm0.59)$	0.809
080810	$\mathbf{2.34(\pm4.84)\times10^{11}}$	$\mathbf{0.61(\pm0.57)}$	**0.999**
081008	$\mathbf{1.84(\pm0.68)\times10^{12}}$	$\mathbf{0.32(\pm0.03)}$	**0.999**
081210	*unconstrained*	$0.80(\pm0.51)$	0.295
090516A	*unconstrained*	$1.30(\pm1.30)$	0.663
090812	$1.66(\pm1.84)\times10^{12}$	$0.24(\pm0.12)$	0.503
131030A	$\mathbf{3.67(\pm1.02)\times10^{12}}$	$\mathbf{0.55(\pm0.06)}$	**0.999**
140206A	$\mathbf{9.02(\pm2.84)\times10^{11}}$	$\mathbf{0.54(\pm0.07)}$	**0.999**
140301A	*unconstrained*	*unconstrained*	0.00
140419A	$1.85(\pm1.17)\times10^{12}$	$0.23(\pm0.05)$	0.88
141221A	$1.34(\pm2.82)\times10^{12}$	$0.24(\pm0.24)$	0.141
151027A	$1.18(\pm0.67)\times10^{12}$	$0.29(\pm0.06)$	0.941

Note. The observed temperatures $kT_{\rm obs}$ are inferred from fitting with a power-law plus blackbody spectral model. The significance of a blackbody is computed by the maximum likelihood ratio for comparing nested models and its addition improves a fit when the significance is >0.95. The radii are calculated assuming mildly relativistic motion ($\beta = 0.8$) and isotropic radiation. The GRBs listed in boldface have prominent blackbodies, with radii of the order of $\sim10^{11}$–10^{12} cm. Uncertainties are given at the 1σ confidence level.

We have used the fact that due to relativistic beaming, we observe only a portion of the surface of the emitter defined by

$$\beta \leqslant \cos\vartheta \leqslant 1, \quad (15)$$

and we used the definition of Γ given in Section 3. Therefore, inverting Equation (13), the comoving blackbody temperature $T_{\rm com}$ can be computed from the observed blackbody temperature $T_{\rm obs}$, the source cosmological redshift z. and the emitter Lorentz Gamma factor as follows:

$$T_{\rm com}(T_{\rm obs}, z, \Gamma) = \frac{1+z}{\Theta(\beta)\Gamma}T_{\rm obs}. \quad (16)$$

We can now insert Equation (16) into Equation (10) to obtain

$$F_{\rm bb,obs} = \frac{{R_{\rm com}}^2}{D_L(z)^2}\sigma T_{\rm com}^4 = \frac{{R_{\rm com}}^2}{D_L(z)^2}\sigma\left[\frac{1+z}{\Theta(\beta)\Gamma}T_{\rm obs}\right]^4. \tag{17}$$

Since the radius $R_{\rm lab}$ of the emitter in the laboratory frame is related to $R_{\rm com}$ by

$$R_{\rm com} = \Gamma R_{\rm lab}, \tag{18}$$

we can insert Equation (18) into Equation (17) and obtain

$$F_{\rm bb,obs} = \frac{(1+z)^4}{\Gamma^2}\left(\frac{R_{\rm lab}}{D_L(z)}\right)^2\sigma\left[\frac{T_{\rm obs}}{\Theta(\beta)}\right]^4. \tag{19}$$

Solving Equation (19) for $R_{\rm lab}$, we finally obtain the thermal emitter's effective radius in the laboratory frame:

$$R_{\rm lab} = \Theta(\beta)^2\Gamma\frac{D_L(z)}{(1+z)^2}\sqrt{\frac{F_{\rm bb,obs}}{\sigma T_{\rm obs}^4}} = \Theta(\beta)^2\Gamma\phi_0, \tag{20}$$

where we have defined ϕ_0,

$$\phi_0 \equiv \frac{D_L(z)}{(1+z)^2}\sqrt{\frac{F_{\rm bb,obs}}{\sigma T_{\rm obs}^4}}. \tag{21}$$

In astronomy, the quantity ϕ_0 is usually identified with the radius of the emitter. However, in relativistic astrophysics, this identity cannot be straightforwardly applied, because the estimate of the effective emitter radius $R_{\rm lab}$ in Equation (20) crucially depends on the knowledge of its expansion velocity β (and, correspondingly, of Γ).

It must be noted that Equation (20) above gives the correct value of $R_{\rm lab}$ for all values of $0 \leqslant \beta \leqslant 1$ by taking all of the relativistic transformations properly into account. In the non-relativistic limit ($\beta \to 0$, $\Gamma \to 1$), we have, respectively:

$$\Theta \underset{\beta\to 0}{\longrightarrow} 1, \qquad \Theta^2 \underset{\beta\to 0}{\longrightarrow} 1, \tag{22}$$

$$T_{\rm com} \underset{\beta\to 0}{\longrightarrow} T_{\rm obs}(1+z), \qquad R_{\rm lab} \underset{\beta\to 0}{\longrightarrow} \phi_0, \tag{23}$$

as expected.

9. Implications on the Dynamics of the Flares from Their Thermal Emission

An estimate of the expansion velocity β can be deduced from the ratio between the variation of the emitter effective radius $\Delta R_{\rm lab}$ and the emission duration in laboratory frame Δt, i.e.,

$$\beta = \frac{\Delta R_{\rm lab}}{c\Delta t} = \Theta(\beta)^2\Gamma(1-\beta\cos\vartheta)(1+z)\frac{\Delta\phi_0}{c\Delta t_a^d}, \tag{24}$$

where we have used Equation (20) and the relation between Δt and Δt_a^d given in Equation (7). We then have

$$\beta = \Theta(\beta)^2\frac{1-\beta\cos\vartheta}{\sqrt{1-\beta^2}}(1+z)\frac{\Delta\phi_0}{c\Delta t_a^d}, \tag{25}$$

where we used the definition of Γ given in Section 3.

For example, in GRB 081008, we observe a temperature of $T_{\rm obs} = (0.44 \pm 0.12)$ keV between $t_a^d = 280$ s and $t_a^d = 300$ s (i.e., 20 s before the flare peak time), and a temperature of $T_{\rm obs} = (0.31 \pm 0.05)$ keV between $t_a^d = 300$ s and $t_a^d = 320$ s (i.e., 20 s after the flare peak time, see the corresponding spectra in Figure 32). In these two time intervals, we can infer ϕ_0, and by solving Equation (25) and taking the errors of the parameters properly into account, get the value of $\langle\beta\rangle$ corresponding to the average expansion speed of the emitter from the beginning of its expansion up to the upper bound of the time interval considered. The results so obtained are listed in Table 8. Moreover, we can also compute the value of $\langle\beta\rangle$ between the two time intervals considered above. For $\cos\vartheta = 1$, namely along the line of sight, we obtain $\langle\beta\rangle = 0.90^{+0.06}_{-0.31}$ and $\langle\Gamma\rangle = 2.34^{+1.29}_{-1.10}$. In conclusion, no matter what the details of the approximation adopted, the Lorentz Gamma factor is always moderate, i.e., $\Gamma \lesssim 4$.

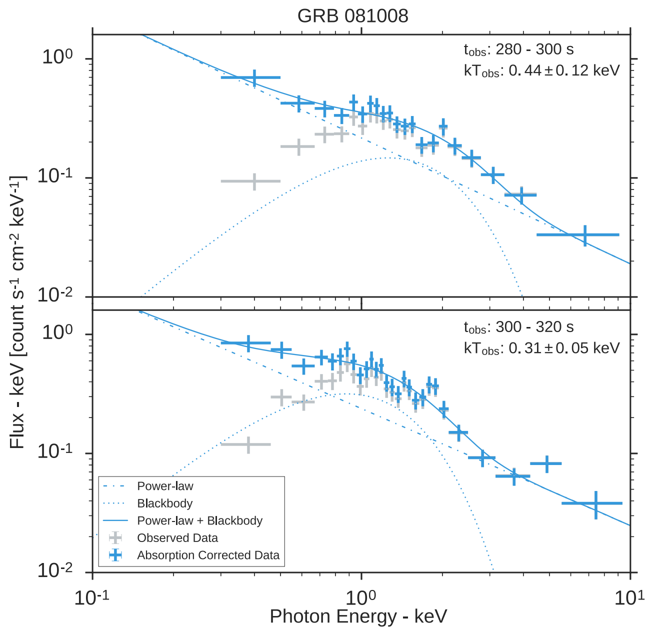

Figure 32. Thermal evolution of GRB 081008 ($z = 1.967$) in the observer frame. The X-ray flare of this GRB peaks at 304($\pm$17) s. Upper panel: *Swift-XRT* spectrum from 280 s to 300 s. Lower panel: *Swift-XRT* spectrum from 300 to 320 s. The gray points are the observed data markedly absorbed at low energies, while the blue points are absorption-corrected ones. The data are fit with a combination of power-law (dotted–dashed lines) and blackbody (dotted lines) spectra. The power-law + blackbody spectra are shown as solid curves. Clearly, the temperature decreases with time from ~0.44 keV to ~0.31 keV, but the ratio of the thermal component goes up from ~20% to ~30%. This is a remarkably high percentage of our sample.

Table 8
List of the Physical Quantities Inferred from the Thermal Components Observed During the Flare of GRB 081008

Time Interval	280 s $\leqslant t_a^d \leqslant$ 300 s	300 s $\leqslant t_a^d \leqslant$ 320 s
$T_{\rm obs}$ (keV)	0.44 $\pm$ 0.12	0.31 $\pm$ 0.05
ϕ_0 (cm)	(5.6 $\pm$ 3.2) $\times$ 10^{11}	(1.44 $\pm$ 0.48) $\times$ 10^{12}
$\langle\beta\rangle_{(\cos\vartheta=1)}$	$0.19^{+0.10}_{-0.11}$	$0.42^{+0.10}_{-0.12}$
$\langle\Gamma\rangle$	$1.02^{+0.03}_{-0.02}$	$1.10^{+0.07}_{-0.05}$
$R_{\rm lab}$ (cm)	(7.1 $\pm$ 4.1) $\times$ 10^{11}	(2.34 $\pm$ 0.78) $\times$ 10^{12}

Note. For each time interval, we summarize the observed temperature $T_{\rm obs}$, ϕ_0, the average expansion speed $\langle\beta\rangle$ computed from the beginning up to the upper bound of the considered time interval, and the corresponding average Lorentz factor $\langle\Gamma\rangle$ and laboratory radius $R_{\rm lab}$.

10. The Electron–Positron Plasma as the Common Origin of the Prompt Emission and the X-Ray Flares

10.1. Necessity for a New Hydrodynamic Code for $10 \leqslant B \leqslant 10^2$

As stated above, there are many different components of BdHNe: following episode 1 of the hypercritical accretion of the SN ejecta onto the NS, the prompt emission occurs with $\Gamma \approx 10^2$–10^3, which represents the most energetic component accelerated by the e^+e^- plasma; a third component, which encompasses the X-ray flare with $\Gamma \lesssim 4$ and represents only a fraction of $E_{e^+e^-}$ ranging from 2% to 20% (see Figure 31); finally, there are in addition the gamma-ray flare and the late X-ray flares, which will be addressed in a forthcoming publication, as well as the late afterglow phases, which have been already addressed in Pisani et al. (2013, 2016) but whose dynamics will be discussed elsewhere. As already mentioned, for definiteness, we address here the case of X-ray flares.

In Section 3.5, we showed that our model successfully explains the entire prompt emission as originating from the transparency of an initially optically thick e^+e^- plasma with a baryon load $B < 10^{-2}$ reaching $\Gamma \approx 10^2$–10^3 and the accelerated baryons interacting with the clouds of the CBM. The fundamental equations describing the dynamics of the optically thick plasma, its self-acceleration to ultrarelativistic velocities, and its interaction with the baryon load have been described in Ruffini et al. (1999, 2000). A semi-analytic approximate numerical code was developed, which assumed that the plasma expanded as a shell with a constant thickness in the laboratory frame (the so-called "slab" approximation; see Ruffini et al. 1999). This semi-analytic approximate code was validated by comparing its results with the ones obtained by numerically integrating the complete system of equations for selected values of the initial conditions. It turns out that the semi-analytic code is an excellent approximation to the complete system of equations for $B < 10^{-2}$, which is the relevant regime for the prompt emission, but this approximation is not valid beyond this limit (see Ruffini et al. 1999, 2000 for details).

We examine here the possibility that the energy of the X-ray flare component also originates from a fraction of the e^+e^- plasma energy (see Figure 31) interacting with the much denser medium of the SN ejecta with $10 \lesssim B \lesssim 10^2$. The above-mentioned semi-analytic approximate code cannot be used for this purpose, since it is valid only for $B < 10^{-2}$, and therefore, thanks to the more powerful computers we have at present, we move on here to a new numerical code to integrate the complete system of equations.

We investigate if indeed the dynamics to be expected from an initially pure e^+e^- plasma with a negligible baryon load relativistically expanding in the fireshell model, with an initial Lorentz factor $\Gamma \sim 100$, and then impacting such an SN ejecta can lead, reaching transparency, to the Lorentz factor $\Gamma \lesssim 4$ inferred from the thermal emission observed in the flares (see Tables 7 and 8, and Figure 32).

We have performed hydrodynamical simulations of such a process using the one-dimensional relativistic hydrodynamical (RHD) module included in the freely available PLUTO[17] code (Mignone et al. 2011). In the spherically symmetric case considered here, only the radial coordinate is used and the code integrates partial differential equations with two variables: radius and time. This permits the study of the evolution of the plasma along one selected radial direction at a time. The code integrates the equations of an ideal relativistic fluid in the absence of gravity, which can be written as follows:

$$\frac{\partial(\rho\Gamma)}{\partial t} + \nabla.(\rho\Gamma\boldsymbol{v}) = 0, \tag{26}$$

$$\frac{\partial m_r}{\partial t} + \nabla.(m_r\boldsymbol{v}) + \frac{\partial p}{\partial r} = 0, \tag{27}$$

$$\frac{\partial \mathcal{E}}{\partial t} + \nabla.(\boldsymbol{m} - \rho\Gamma\boldsymbol{v}) = 0, \tag{28}$$

where ρ and p are, respectively, the comoving fluid density and pressure, $\boldsymbol{v}$ is the coordinate velocity in natural units ($c = 1$), $\Gamma = (1 - \boldsymbol{v}^2)^{-\frac{1}{2}}$ is the Lorentz Gamma factor, $\boldsymbol{m} = h\Gamma^2\boldsymbol{v}$ is the fluid momentum, m_r its radial component, $\mathcal{E}$ is the internal energy density, and h is the comoving enthalpy density, which is defined by $h = \rho + \epsilon + p$. In this last definition, ϵ is equal to $\mathcal{E}$ measured in the comoving frame. We define $\mathcal{E}$ as follows:

$$\mathcal{E} = h\Gamma^2 - p - \rho\Gamma. \tag{29}$$

The first two terms on the right-hand side of this equation coincide with the T^{00} component of the fluid energy–momentum tensor $T^{\mu\nu}$, and the last one is the mass density in the laboratory frame.

Under the conditions discussed in Appendix B, the plasma satisfies the equation of state of an ideal relativistic gas, which can be expressed in terms of its enthalpy as

$$h = \rho + \frac{\gamma p}{\gamma - 1}, \tag{30}$$

with $\gamma = 4/3$. Fixing this equation of state completely defines the system, leaving the choice of the boundary conditions as the only remaining freedom. To compute the evolution of these quantities in the chosen setup, the code uses the Harten–Lax–van Leer-contact Riemann solver. Time integration is performed by means of a second-order Runge–Kutta algorithm, and a second-order total variation diminishing scheme is used for spatial reconstruction (Mignone et al. 2011). Before each integration step, the grid is updated according to an adaptive mesh refinement algorithm, provided by the CHOMBO library (Colella et al. 2003).

It must be emphasized that the above equations are equivalent (although written in a different form) to the complete system of equations used in Ruffini et al. (1999, 2000). To validate this new numerical code, we compare its results with the ones obtained with the old semi-analytic "slab" approximate code in the domain of its validity (i.e., for $B < 10^{-2}$), finding excellent agreement. As an example, in Figure 33 we show the comparison between the Lorentz Gamma factors computed with the two codes for one particular value of $E_{e^+e^-}$ and B.

We can then conclude that for $B < 10^{-2}$, the new RHD code is consistent with the old semi-analytic "slab" approximate one, which in turn is consistent with the treatment done in Ruffini et al. (1999, 2000). This is not surprising, since we already stated that the above system of equations is equivalent to the one considered in Ruffini et al. (1999, 2000).

Having validated the new RHD code in the region of parameter space where the old semi-analytic one can also be

[17] http://plutocode.ph.unito.it/

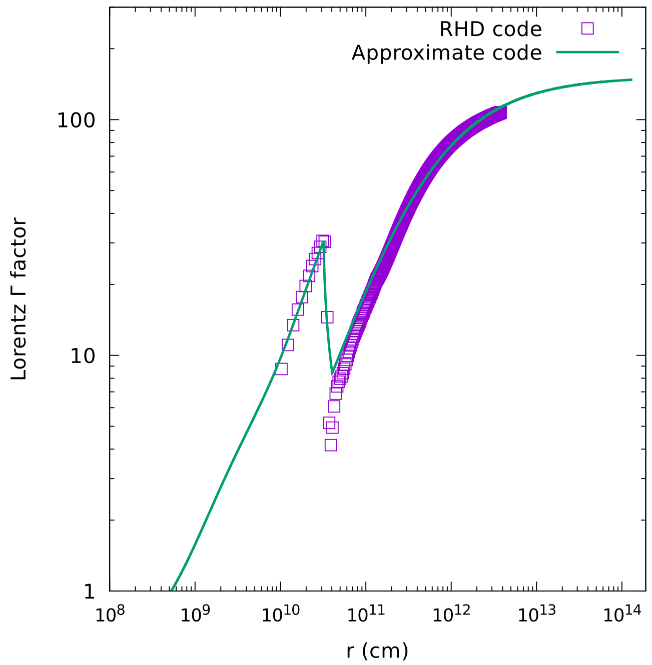

Figure 33. Lorentz Gamma factor computed with the new RHD code compared with the one computed with the old semi-analytic approximate code. This plot is for $E_{e^+e^-} = 1.0 \times 10^{53}$ erg and $B = 6.61 \times 10^{-3}$. Similar agreement is found for other values of $E_{e^+e^-}$ and B as long as $B < 10^{-2}$.

used, we now explore the region of $B > 10^{-2}$, which is relevant for the interaction of the plasma with the SN ejecta.

10.2. Inference from the IGC Scenario for the Ejecta Mass Profile

We start with the shape of the SN ejecta, following the results of the numerical simulations in Becerra et al. (2016).

The first simulations of the IGC process were presented in Fryer et al. (2014) including (1) detailed SN explosions of the CO_{core} obtained from a 1D core-collapse SN code code of Los Alamos (Fryer et al. 1999a); (2) the hydrodynamic details of the hypercritical accretion process; and (3) the evolution of the SN ejecta material entering the Bondi–Hoyle region all the way up to its incorporation into the NS in a spherically symmetric approximation. Then, in Becerra et al. (2015), estimates of the angular momentum carried by the SN ejecta and transferred to the NS via accretion were presented. The effects of such angular momentum transfer on the evolution and fate of the system were examined there. These calculations followed the following procedure: first, the accretion rate onto the NS is computed by adopting a homologous expansion of the SN ejecta and introducing the pre-SN density profile of the CO_{core} envelope from numerical simulations. Then, the angular momentum that the SN material might transfer to the NS is estimated: it turns out that the ejecta have enough angular momentum to circularize for a short time and form a disk-like structure around the NS. Then, the evolution of the NS central density and rotation angular velocity is followed by computing the equilibrium configurations from the numerical solution of the axisymmetric Einstein equations in full rotation, until the critical point of collapse of the NS to a BH is reached, accounting for the stability limits given by mass shedding and the secular axisymmetric instability. In Becerra et al. (2016), an improved simulation of all of the above processes leading to a BdHN was recently presented. In particular:

1. The accretion rate estimate includes the effects of the finite size/thickness of the ejecta density profile.
2. Different CO_{core} progenitors leading to different SN ejecta masses were also considered.
3. The maximum orbital period, P_{max}, up to which the accretion onto the NS companion is high enough to bring it to the critical mass for gravitational collapse to a BH, first estimated in Becerra et al. (2015), was computed for allpossible initial values of the mass of the NS companion. Various values of the angular momentum transfer efficiency parameter were also explored there.
4. It was shown there how the presence of the NS companion gives rise to large asymmetries in the SN ejecta. As we show here, such a density of the SN ejecta modified by the presence of the NS companion plays a crucial role in the physical explanation for the occurrence of X-ray flares.
5. The evolution of the SN material and its consequent accretion onto the NS companion is followed via a smoothed-particle-hydrodynamic-like code in which point-like particles describe the SN ejecta. The trajectory of each particle is computed by solving the Newtonian equations of motion including the effects of the gravitational field of the NS on the SN ejecta, including the orbital motion as well as the changes in the NS gravitational mass owing to the accretion process via the Bondi–Hoyle formalism. The initial conditions of the SN are obtained from the Los Alamos core-collapse SN code (Fryer et al. 1999a). The initial power-law density profile of the CO envelope is simulated by populating the inner layers with more particles. The particles crossing the Bondi–Hoyle radius are captured and accreted by the NS so we remove them from the system. We adopted a total number of 16 million particles in this simulation.

For further details, we refer the reader to Becerra et al. (2016) and references therein.

10.3. The Density Profile of the Ejecta and the Reaching of Transparency

We now use the results of a simulation with the following binary parameters: the NS has an initial mass of 2.0 $M_\odot$; the CO_{core} obtained from a progenitor with a zero-age main-sequence mass $M_{ZAMS} = 30\, M_\odot$ leads to a total ejecta mass of 7.94 $M_\odot$ and follows an approximate power-law profile $\rho^0_{ej} \approx 3.1 \times 10^8 (8.3 \times 10^7/r)^{2.8}$ g cm^{-3}. The orbital period is $P \approx 5$ minutes, i.e., a binary separation $a \approx 1.5 \times 10^{10}$ cm. For these parameters, the NS reaches the critical mass and collapses to form a BH.

Figure 34 shows the SN ejecta mass that is enclosed within a cone of 5° of the semi-aperture angle, whose vertex is at the position of the BH at the moment of its formation (see the lower-left panel of Figure 6 in Becerra et al. 2016), and whose axis is along various directions measured counterclockwise with respect to the line of sight. Figure 35 shows instead the cumulative radial mass profiles within a selected number of the aforementioned cones. We can see from these plots how the e^+e^- plasma engulfs different amounts of baryonic mass

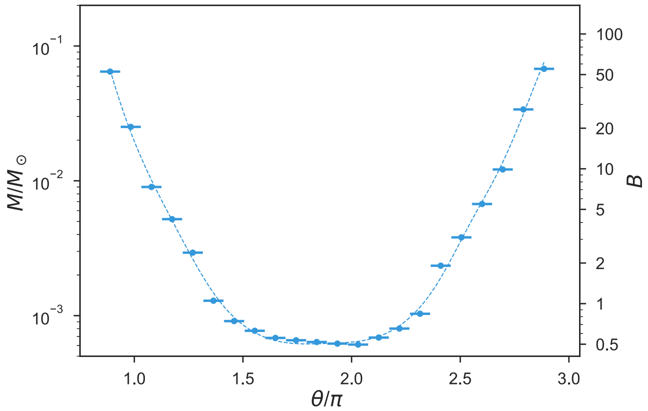

Figure 34. SN ejecta mass enclosed within a cone of 5° of semi-aperture angle, whose vertex is at the position of the BH at the moment of its formation (see the lower-left panel of Figure 6 in Becerra et al. 2016), and whose axis is along various directions measured counterclockwise with respect to the line of sight. The binary parameters of this simulations are the following: the NS has an initial mass of 2.0 $M_\odot$; the CO_{core} obtained from a progenitor with a zero-age -main-sequence mass $M_{ZAMS} = 30\,M_\odot$ leads to a total ejecta mass 7.94 $M_\odot$, and the orbital period is $P \approx 5$ minutes, i.e., a binary separation $a \approx 1.5 \times 10^{10}$ cm. The vertical axis on the right side gives, as an example, the corresponding value of the baryon loading B assuming a plasma energy of $E_{e^+e^-} = 3.16 \times 10^{53}$ erg.

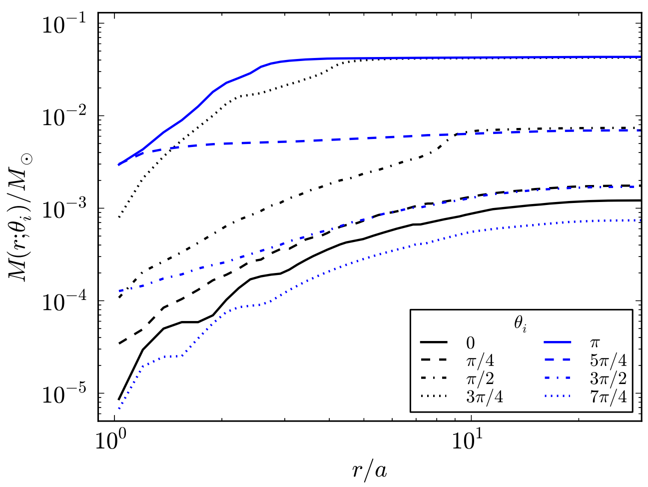

Figure 35. Cumulative radial mass profiles within selected cones among the ones used in Figure 34. We note that the final value for the cumulative mass reached at the end of each direction, namely the value when each curve flattens, is consistent with the total integrated mass value of the corresponding direction shown in Figure 34. The binary parameters of these simulations are the following: the NS has an initial mass of 2.0 $M_\odot$; the CO_{core} obtained from a progenitor with a zero-age main-sequence mass $M_{ZAMS} = 30\,M_\odot$ leads to a total ejecta mass 7.94 $M_\odot$, and the orbital period is $P \approx 5$ minutes, i.e., a binary separation $a \approx 1.5 \times 10^{10}$ cm.

along different directions due to the asymmetry of the SN ejecta created by the presence of the NS binary companion and the accretion process onto it (see Becerra et al. 2016).

In these calculations, we have chosen initial conditions consistent with those of the BdHNe. At the initial time, the e^+e^- plasma has $E_{e^+e^-} = 3.16 \times 10^{53}$ erg, a negligible baryon load, and is distributed homogeneously within a region of radii on the order of 10^8–10^9 cm. The surrounding SN ejecta, whose pressure has been assumed to be negligible, has a mass density

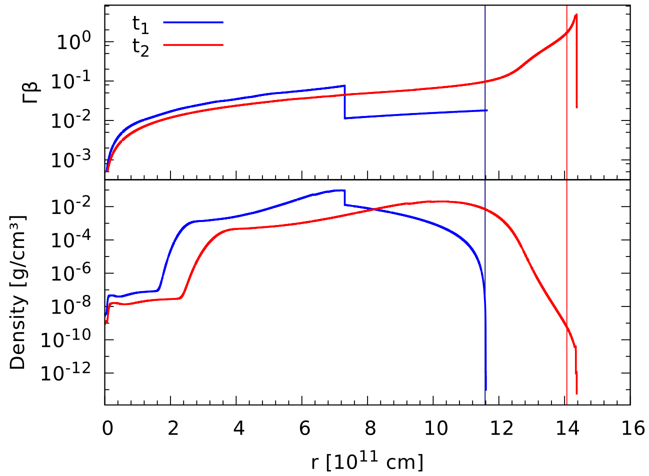

Figure 36. Top panel: distribution of the velocity inside the SN ejecta at the two fixed values of the laboratory times t_1 (before the plasma reaches the external surface of the ejecta) and t_2 (the moment at which the plasma, after having crossed the entire SN ejecta, reaches the external surface). We plotted the quantity $\Gamma\beta$, recalling that we have $\Gamma\beta \sim \beta$ when $\beta < 1$, and $\Gamma\beta \sim \Gamma$ when $\beta \sim 1$. Bottom panel: corresponding distribution of the mass density of the SN ejecta in the laboratory frame ρ_{lab}. These particular profiles are made using a baryon load $B = 200$. The dashed vertical lines corresponds to the two values of the transparency radius R_{ph}; see Figure 37 and Equation (32). In particular, we see that at t_1, the shock front has not yet reached R_{ph} and the system is optically thick.

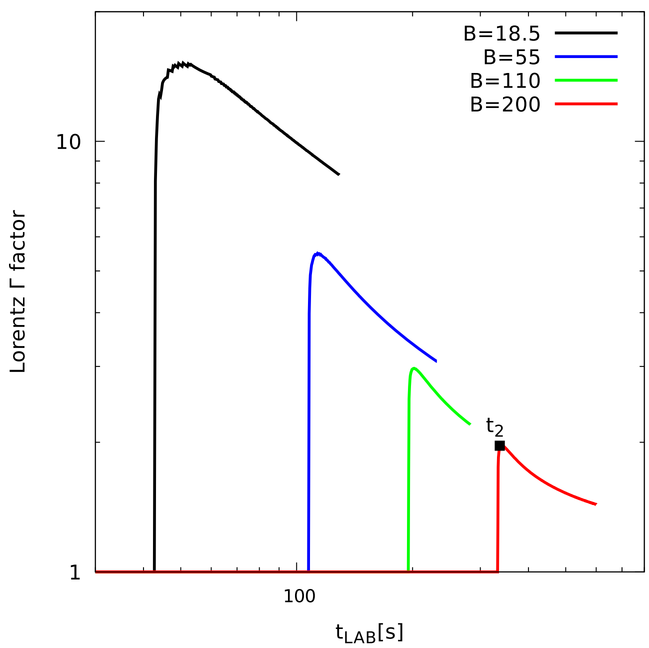

Figure 37. Lorentz Γ factor at the transparency radius R_{ph} as a function of the laboratory time for $E_{e^+e^-} = 3.16 \times 10^{53}$ erg and various selected values of the B parameter. Such B values correspond to the expansion of the e^+e^- plasma along various selected directions inside the remnant (see Figures 34 and 35). Along the red curve, corresponding to $B = 200$, the laboratory time instant t_2 represented in Figure 36 (at t_1 the plasma has not yet reached R_{ph}) is marked. We see that these results are in agreement with the Lorentz Gamma factor $\Gamma \lesssim 4$ inferred from the thermal emission observed in the flare (see Section 9).

radial profile given by

$$\rho \propto (R_0 - r)^\alpha, \tag{31}$$

where the parameters R_0 and α, with $2 < \alpha < 3$, as well as the normalization constant, are chosen to fit the profiles obtained in

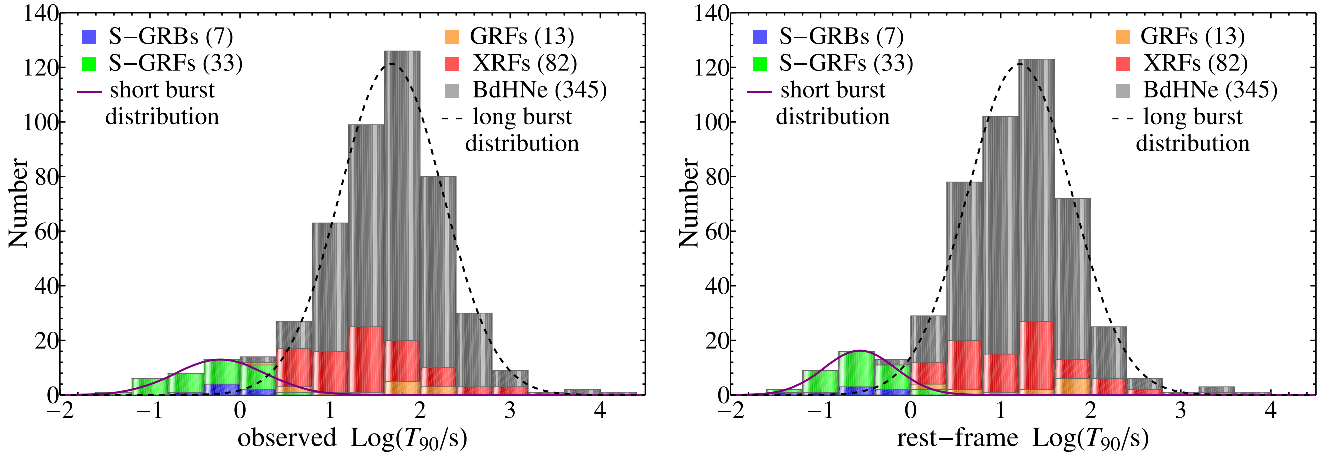

Figure 38. Histograms of T_{90} distributions in the (left panel) observer frame (which is the traditional treatment widely adopted in many previous articles; left panel; see, e.g., Kouveliotou et al. 1993; Bromberg et al. 2013, and references therein) and (right panel) in the cosmological rest frame (which is the approach adopted in the present paper). Both histograms are built using the total number of GRBs with known redshift. The contribution to the total distributions and the number of sources of each subclass are highlighted in the legend (the choice of colors is the same as in Figure 4). The short burst (solid purple curve) and the long burst (dashed black curve) distributions are also shown. In the observer frame, we obtain $T_{90}^{\rm short} = 0.60^{+1.31}_{-0.41}$ s and $T_{90}^{\rm long} = 48^{+133}_{-35}$ s; in the cosmological rest frame, we have $T_{90}^{\rm short} = 0.27^{+0.41}_{-0.16}$ s and $T_{90}^{\rm long} = 16^{+46}_{-12}$ s. The T_{90} value discriminating between short and long bursts shifts from ≈2 s in the observer frame to ≈0.75 s in the cosmological rest frame. The existence of BdHNe with $T_{90} \gtrsim 10^2$ s indicates the origin of the possible contamination between the prompt emission spikes and the X-ray flares, which is indeed observed in some cases (see Section 4 for details).

Becerra et al. (2016) and represented in Figure 35. The initial radial velocity is taken to be $v_r \propto r$ in order to reproduce the homologous expansion of the SN ejecta before its interaction with the plasma. Every choice of these parameters corresponds to studying the evolution along a single given direction.

The evolution from these initial conditions leads to the formation of a shock and to its subsequent expansion until reaching the outermost part of the SN. In Figure 36, we show the radial distribution profiles of the velocity and mass density $\rho_{\rm lab}$ in the laboratory frame inside the SN ejecta as a function of r for $B = 200$ at two selected values of the laboratory time. The velocity distribution peaks at the shock front (with a Lorentz Gamma factor $\Gamma \lesssim 4$), and behind the front it forms a broad tail of accelerated material with $0.1 \lesssim \beta \lesssim 1$.

Figure 37 shows the Lorentz Γ factor at the transparency radius $R_{\rm ph}$, namely the radius at which the optical depth τ, calculated from the observer's line of sight, is equal to 1. If we assume a constant cross-section, τ becomes Lorentz invariant, and therefore we can compute it in laboratory coordinates in the following way:

$$\tau = \int_{R_{\rm ph}}^{\infty} dr\ \sigma_T\ n_{e^-}(r), \tag{32}$$

where $\sigma_T = 6.65 \times 10^{-25}$ cm^2 is the Thomson cross-section, and the electron density is related to the baryon mass density by means of the formula $n_{e^-} = \rho\ \Gamma/m_P$, where m_P is the proton mass, the mass of the electrons and positrons is considered to be negligible with respect to that of the baryons, and we have assumed one electron per nucleon on average. The values of Γ at $r = R_{\rm ph}$ computed in this way are shown in Figure 37, as a function of the time measured in the laboratory frame, for several values of $B > 10^{-2}$ corresponding to the expansion of the e^+e^- plasma along several different directions inside the SN ejecta (see Figures 34 and 35).

We conclude that the relativistic expansion of an initially pure e^+e^- plasma (see Figure 33), interacting with an SN ejecta with the above-described induced asymmetries (see Figures 39–40), leads to the formation of a shock that reaches the outermost part of the ejecta with Lorentz Gamma factors at the transparency radius $\Gamma(R_{\rm ph}) \lesssim 4$. This is in striking agreement with the one inferred from the thermal component observed in the flares (see Section 9). The spacetime diagram of the global scenario is represented in Figure 39. Clearly in this approach neither ultrarelativistic jetted emission nor synchrotron or inverse-Compton processes play any role.

11. Summary, Conclusions and Perspectives

11.1. Summary

In the last 25 years, the number of observed GRBs has exponentially increased, thanks to unprecedented technological developments in all ranges of wavelengths, going from the X-ray to the gamma-ray, to GeV radiation as well as to the radio and the optical. In spite of this progress, the traditional GRB approach has continued to follow the paradigm of a single system (the "collapsar" paradigm; see Woosley 1993), where accretion onto an already formed BH occurs (see, e.g., Piran 2004 and references therein). Following the fireball model, synchrotron and inverse-Compton emission processes, related to an ultrarelativistic jetted emission described by the Blandford & McKee (1976) solution, have been assumed to occur (see, e.g., Troja et al. 2015 for one of the latest example where this approach is further extended to the GeV emission component). The quest for a "standard" GRB model has been pursued even recently (see, e.g., Chincarini et al. 2007; Margutti et al. 2010), ignoring differences among GRB subclasses and/or neglecting all relativistic corrections in the time parameterizations presented in Section 3. Under these conditions, it is not surprising that the correlations we have found here have been missed.

It is appropriate to recall that a "standard" GRB energy of 10^{51} erg (Frail et al. 2001) was considered, assuming the collimation of GRBs and the existence of a light-curve break in

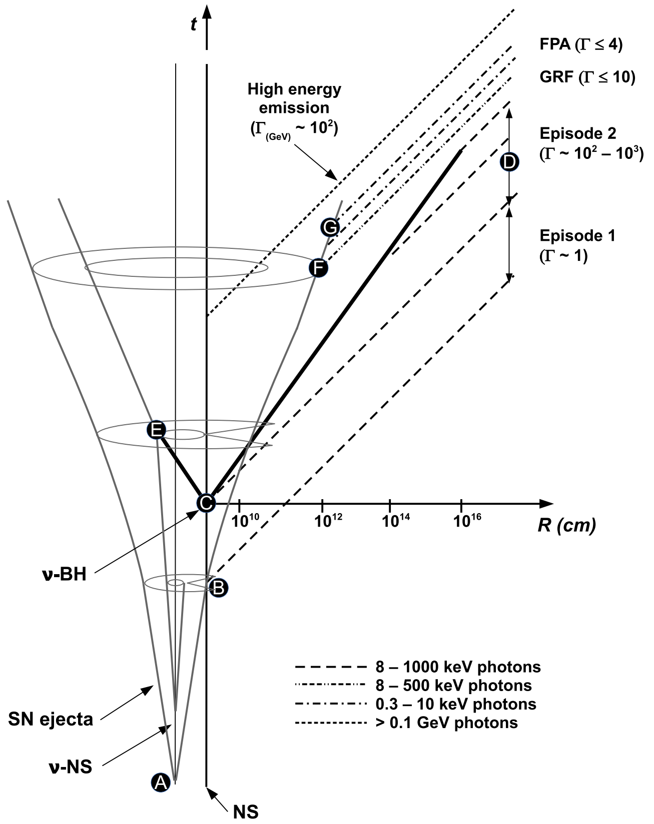

Figure 39. Spacetime diagram (not to scale) of a BdHN. The CO_{core} explodes as an SN at point A and forms a new NS (νNS). The companion NS (bottom-right line) accretes the SN ejecta starting from point B, giving rise to the non-relativistic episode 1 emission (with Lorentz factor $\Gamma \approx 1$). At point C, the NS companion collapses into a BH, and an e^+e^- plasma—the dyadosphere—is formed (Ruffini et al. 1999). The following self-acceleration process occurs in a spherically symmetric manner (thick black lines). A large portion of plasma propagates in the direction of the line of sight, where the environment is cleared by the previous accretion into the NS companion, finding a baryon load $B \lesssim 10^{-2}$ and leading to the GRB prompt gamma-ray spikes (GRSs; episode 2, point D) with $\Gamma \sim 10^2$–10^3. The remaining part of the plasma impacts the high-density portion of the SN ejecta (point E), propagates inside the ejecta encountering a baryon load $B \sim 10^1$–10^2, and finally reaches transparency, leading to the gamma-ray flare emission (point F) in gamma-rays with an effective Lorentz factor $\Gamma \lesssim 10$ and to the FPA emission (point G) corresponding to the X-ray flares with an effective $\Gamma \lesssim 4$ (see Sections 9 and 10). In the meantime, accretion over the newly formed BH produces the high-energy GeV emission with $\Gamma \sim 10^2$. For simplicity, this diagram is 2D and static and does not attempt to show the 3D rotation of the ejecta.

the GRB afterglows. This possibility followed from the traditional approach expecting the ultrarelativistic component to extend all the way from the prompt emission to the last phases of the afterglow (Mao & Yi 1994; Panaitescu & Mészáros 1999; Sari et al. 1999). This “traditional” approach to GRBs has appeared in a large number of papers over recent decades and is well summarized in a series of review papers (see, e.g., Piran 1999, 2004; Mészáros 2002, 2006; Berger 2014; Kumar & Zhang 2015), whichare disproved by the data presented here in which the upper limit for the Lorentz factor $\Gamma \lesssim 4$ is established in the FPA phase.

Since 2001, we have followed an alternative approach, introducing three paradigms: the spacetime parametrization of GRBs (Ruffini et al. 2001a), the field equations of the prompt emission phase (Ruffini et al. 2002), and the IGC paradigm (Rueda & Ruffini 2012; Penacchioni et al. 2013; Ruffini et al. 2015c); see Section 3. Since then,

(a) we have demonstrated that all GRBs originate in binary systems: the short GRBs in binary NSs or in binaries composed of an NS and a BH (Fryer et al. 2015; Ruffini et al. 2016b); the long GRBs in binary systems composed of CO_{core} and a, NS, or alternatively a BH and a CO_{core}, or also a white dwarf and an NS;

(b) we have divided GRBs into seven different subclasses (Ruffini et al. 2016b), each characterized by specific signatures in their spectra and luminosities in the various energy bands;

(c) we have addressed the new physical and astrophysical processes in the ultrarelativistic regimes made possible by the vast amount of gravitational and rotational energies in such binaries.

As we recalled in Sections 1–3, we have confirmed the binary nature of the GRB progenitors (see, e.g., Fryer et al. 2014, 2015; Becerra et al. 2015, 2016; Ruffini et al. 2016a; Aimuratov et al. 2017). We have obtained the first evidence of the formation of a BH in the hypercritical accretion process of the SN ejecta onto the binary NS companion: the BdHN (Ruffini et al. 2014, 2015c, 2016b), which is clearly different from the single-star collapsar model. Finally, in this paper, we have addressed the interaction that occurs in a BdHN of the GRB on the SN ejecta considered as the origin of the X-ray flares. We use this process and the mildly relativistic region in which it occurs as a discriminant between the traditional approach and our binary system approach: we use the X-ray flare properties as a discriminant between our BdHN and the “fireball” GRB models.

11.2. Conclusions

We have reached three major results.

(1) We have searched X-ray flares in all GRBs and identified 16 of them with excellent data. After examining the seven GRB subclasses (Ruffini et al. 2016b), we conclude that they all occur in BdHNe, and no X-ray flares are observed in other GRB sources. This indicates a link between the occurrence of the flare and the formation of a black hole in long GRBs. In Section 4, we have shown how the previously proposed association of X-ray flares with the short GRBs 050724 and 050709 has been superseded.

By a statistical analysis, we correlate the time of occurrence of their peak luminosity in the cosmological rest frame, their duration, their energy, and their X-ray luminosity to the corresponding GRB E_{iso}. We also correlate the energy of the FPA phase, E_{FPA}, as well as the relative ratio E_{FPA}/E_{iso}, to E_{iso}.

(2) Using the data from the associated thermal emission, the relativistic relation between the comoving time, the arrival time at the detector, and the cosmological and Doppler corrections, we determine the thermal emitter effective radii as a function of the rest-frame time. We determine the expansion velocity of the emitter β as the ratio between the variation of the emitter effective radius ΔR_{lab} and the emission duration in laboratory time; see Equation (25). We obtain a radius of 10^{12} cm for the effective radius of the emitter, moving with $\Gamma \lesssim 4$ at a time $\sim$100 s in the rest frame (see Table 8). These results show the clear rupture between the processes in the prompt emission phase, occurring prior to the flares at radii of the order of 10^{16} cm and $\Gamma = 10^2$–10^3, and the ones in the X-ray flares.

(3) We have modeled the X-ray flares by considering the impact of the GRB on the SN ejecta, introducing a new set of

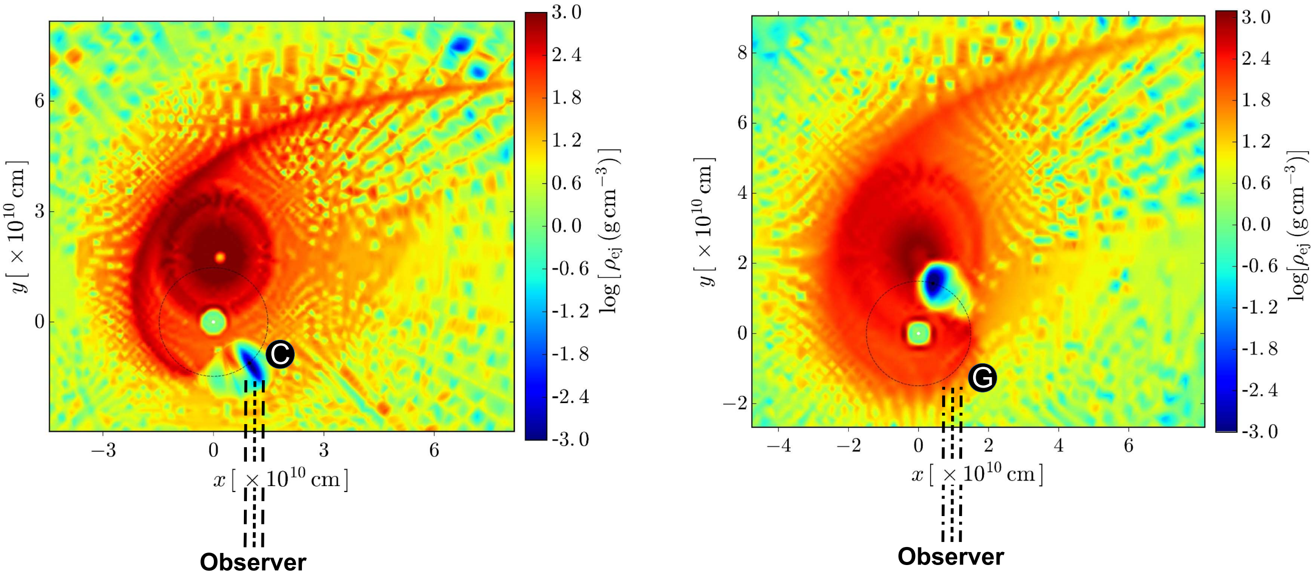

Figure 40. Two snapshots of the distribution of matter in the equatorial plane of the progenitor's binary system. The one on the right side corresponds to point C, when the BH is formed and a large portion of the e^+e^- plasma starts to self-accelerate in a low-density environment ($B \lesssim 10^{-2}$) toward the observer producing the GRB prompt emission. The one on the left side corresponds to point G, when the remaining part of the plasma, after propagating inside the high-density SN ejecta ($B \sim 10^2$–10^3), reaches transparency and produces the FPA emission in the X-rays, which is directed toward the observer due to the rotation of the ejecta in the equatorial plane. The simulations of the matter distributions in the three snapshots are from Becerra et al. (2016).

relativistic hydrodynamic equations for the expansion of the optically thick e^+e^- plasma into a medium with baryon load in the range 10–10^2. The matter density and velocity profiles of the ejecta are obtained from the 1D core-collapse code developed at Los Alamos (Fryer et al. 1999a). With this we generate the initial conditions for our smoothed-particle-hydrodynamics-like simulation (Becerra et al. 2016), which follows the evolution of the ejecta matter and the accretion rate at the position of the Bondi–Hoyle surface of the NS binary companion. In our simulations, we have adopted 16 million particles (see Section 10 for further details). We start the simulation of the interaction of the e^+e^- plasma with such ejecta at 10^{10} cm and continue all the way to 10^{12} cm, where transparency is reached. We found full agreement between the radius of the emitter at transparency and the one derived from the observations, as well as between the time of the peak energy emission and the observed time of arrival of the flare, derived following Equation (2) using the computed Lorentz Γ factor of the world line of the process.

We can now conclude the following.

The existence of such mildly relativistic Lorentz Gamma factors in the FPA phase rules out the traditional GRB model, including the claims of the existence of GRB beaming, collimation, and break in the luminosity (see, e.g., Piran 1999, 2004; Frail et al. 2001; Mészáros 2002, 2006; Berger 2014; Kumar & Zhang 2015). In these models, the common underlying assumption is the existence of a single ultrarelativistic component extending from the prompt radiation, through the FPA phase, all the way to the late afterglow and to the GeV emission, assuming a common dynamics solely described by the Blandford & McKee (1976) solution; see, however, Bianco & Ruffini (2005b, 2006). These assumptions were made without ever looking for observational support. It is not surprising that all GRB models in the current literature purport the existence of an ultrarelativistic Lorentz Gamma factor extending into the afterglow, among many others; see, e.g., Jin et al. (2010) and Yi et al. (2015). All these claims have been disproven by the present article, where a drastic break from ultrarelativistic physics with $\Gamma \sim 10^2$–10^3, occurring in the prompt emission, is already indicated at times $\sim$100 s, when the Lorentz Gamma factor is limited to $\Gamma \leqslant 4$.

In our approach, a multi-episode structure for each GRB is necessary. Each episode, being characterized by a different physical process, leads to a different world line with a specific Lorentz Gamma factor at each event. The knowledge of the world line is essential, following Equation (2) in Section 3, to compute the arrival time of the signals in the observer frame and to compare it with the observations. This procedure, previously routinely adopted in the prompt emission phase of a BdHN, has for the first time been introduced here for X-ray flares. As a byproduct, we have confirmed both the binarity and the nature of the progenitors of the BdHNe, composed of a $CO_{\rm core}$ undergoing an SN explosion and accreting onto a close-by binary NS, and the impact of the GRB on the hypernova ejecta.

11.3. Perspectives

Far from representing solely a criticism of the traditional approach, in this paper, (1) we exemplify new procedures in data analysis—see Sections 4 to 7, (2) we open up the topic to an alternative style of conceptual analysis which adopts procedures well-tested in high-energy physics and not yet appreciated in the astrophysical community—see Sections 8–10, and (3) we introduce new tools for simulation techniques affordable with present-day large computer facilities—see figures in Section 11, which, if properly guided by a correct theoretical understanding, can be particularly helpful in the visualization of these phenomena.

We give three specific examples of our new approach and indicate as well, when necessary, some disagreements with current approaches:

(A) The first step in any research on GRBs is to represent the histogram of T_{90} for the GRB subclasses. We report in

Figure 38 the T_{90} values for all of the GRB subclasses we have introduced (see Ruffini et al. 2016b). The values reported are both in the observer frame (left panel; see, e.g., Kouveliotou et al. 1993; Bromberg et al. 2013) and properly converted to the cosmological rest frame of the sources (right panel). The large majority of papers on GRBs have been neglecting the cosmological corrections and subdivision in the subclasses, making impossible the comparison of T_{90} among different GRBs (see, e.g., Falcone et al. 2007; Chincarini et al. 2010).

(B) For the first time, we present a simplified spacetime diagram of BdHNe (see Figure 39). This spacetime diagram emphasizes the many different emission episodes, each one with distinct corresponding Lorentz Gamma factors and consequently leading through Equation (2) to a specific value of their distinct times of occurrence in the cosmological rest frame of the GRB (see Figure 39). In all episodes we analyzed for the X-ray flares, and more generally for the entire FPA phase, there is no need for collapsar-related concepts. Nevertheless, in view of the richness of the new scenario in Figure 39, we have been examining the possibility that such concepts can play a role in additional episodes, either in BdHNe or in any of the additional six GRB subclasses, e.g., in S-GRBs. These results are being submitted for publication. The use of spacetime diagrams in the description of GRBs is indeed essential in order to illustrate the causal relation between the source in each episode, the place of occurrence, and the time at detection. Those procedures have been introduced long ago in the study of high-energy particle physics processes and codified in textbooks. Our group, since the basic papers (Ruffini et al. 2001a, 2001b, 2001c), has widely shared these spacetime formulations (see, e.g., in Taylor & Wheeler 1992) and also extended the concept of the quantum S-Matrix (Wheeler 1937; Heisenberg 1943) to the classic astrophysical regime of the many components of a BdHN, introducing the concept of the cosmic matrix (Ruffini et al. 2015c). The majority of astrophysicists today make wide use of the results of nuclear physics in the study of stellar evolution (Bethe 1991) and also of Fermi statistics in general relativity (Oppenheimer & Volkoff 1939). They have not yet been ready, however, to approach these additional concepts more typical of relativistic astrophysics and relativistic field theories, which are necessary for the study of GRBs and active galactic nuclei.

(C) The visual representation of our result (see Figure 40) has been made possible thanks to the simulations of SN explosions with the core-collapse SN code developed at Los Alamos (see, e.g., Fryer et al. 1999a, 2014; Frey et al. 2013), the smoothed-particle-hydrodynamics-like simulations of the evolution of the SN ejecta accounting for the presence of an NS companion (Ruffini et al. 2016b), and the possibility of varying the parameters of the NS, of the SN, and of the distance between the two to explore all possibilities (Becerra et al. 2015; Ruffini et al. 2016b). We recall that these signals occur in each galaxy every ~hundred million years, but with their luminosity of $\sim 10^{54}$ erg, they can be detected in all 10^9 galaxies. The product of these two factors gives the "once per day" rate. They are not visualizable in any other way, but analyzing the spectra and time of arrival of the photons now, and simulating these data on the computer, we see that they indeed already occurred billions of years ago in our past light cone, and they are revived by scientific procedures today.

We are happy to acknowledge fruitful discussions with Fulvio Melia, Tsvi Piran, and Bing Zhang in our attempt to make these new results clearer for a broader audience, and with Roy Kerr on the implication of the GRB GeV emission for the Kerr–Newman solution. We also thank the second referee for important suggestions. We acknowledge the continuous support of the MAECI. This work made use of data supplied by the UK *Swift* Science Data Center at the University of Leicester. M.Ka. and Y.A. are supported by the Erasmus Mundus Joint Doctorate Program Grant N. 2014–0707 from EACEA of the European Commission. M.M. and J.A.R. acknowledge the partial support of the project N 3101/GF4 IPC-11 and the target program F.0679 0073-6/PTsF of the Ministry of Education and Science of the Republic of Kazakhstan.

Appendix A
The Complete List of BdHNe

We present here in Table 9 the complete list of the 345 BdHNe observed through the end of 2016, which includes the 161 BdHNe already presented in Pisani et al. (2016).

Appendix B
Parameters of the Equation of State

We give here details concerning the determination of the value of the index γ and verify the accuracy of our assumption $\gamma = 4/3$ adopted in the equation of state of the plasma (30). This index is defined as

$$\gamma \equiv 1 + \frac{p}{\epsilon}. \tag{33}$$

The total internal energy density and pressure are computed as

$$\epsilon = \epsilon_{e^-} + \epsilon_{e^+} + \epsilon_\gamma + \epsilon_B \tag{34}$$

$$p = p_{e^-} + p_{e^+} + p_\gamma + p_B, \tag{35}$$

where the subscript B indicates the contributions of the baryons in the fluid. The number and energy densities, as well as the pressure of the different particles, can be computed in natural units ($c = \hbar = k_B = 1$) using the following expressions (see, e.g., Landau & Lifshitz 1980):

$$n_{e^-} = A\, T^3 \int_0^\infty f(z, T, m_e, \mu_{e^-}) z^2\, dz \tag{36}$$

$$n_{e^+} = A\, T^3 \int_0^\infty f(z, T, m_e, \mu_{e^+}) z^2\, dz \tag{37}$$

$$\epsilon_{e^-} = A\, T^4 \int_0^\infty f(z, T, m_e, \mu_{e^-}) \times \sqrt{z^2 + (m_e/T)^2}\, z^2\, dz - m_e\, n_{e^-} \tag{38}$$

$$\epsilon_{e^+} = A\, T^4 \int_0^\infty f(z, T, m_e, \mu_{e^+}) \times \sqrt{z^2 + (m_e/T)^2}\, z^2\, dz - m_e\, n_{e^+} \tag{39}$$

Table 9
List of the BdHNe Considered in This Work

GRB	z	E_{iso}[a]	LX[b]	Early Flare[c]	UL[d]	T_{90}[e]	Instrument[f]	Reference[g]
970228	0.695	1.65 ± 0.16				80	B-SAX	(1)
970828	0.958	30.4 ± 3.6				90	BATSE	(2)
971214	3.42	22.1 ± 2.7				40	BATSE	IAUC 6789
980329	3.5	267 ± 53				54	B-SAX	(3)
980703	0.966	7.42 ± 0.74				400	BATSE	GCN 143
990123	1.6	241 ± 39				63.3	BATSE	GCN 224
990506	1.3	98.1 ± 9.9				131.33	BATSE	GCN 306
990510	1.619	18.1 ± 2.7				75	BATSE	GCN 322
990705	0.842	18.7 ± 2.7				42	B-SAX	(4)
991208	0.706	23.0 ± 2.3				68	Ulysses	(5)

Notes. It is composed of 345 sources spanning 12 years of *Swift*/XRT observation activity. In the table, we report important observational features: the redshift z, the isotropic energy E_{iso}, the observing instrument in the gamma-ray band, and the corresponding reference from which we take the gamma-ray spectral parameters in order to estimate E_{iso}.
[a] In units of 10^{52} erg.
[b] "LX" marks the sources with *Swift*/XRT data observed up to times larger than 10^4 s in the rest frame after the initial explosion.
[c] "C" and "E" mark the sources showing an early flare in *Swift*/XRT, and they stand for "confirmed" and "excluded," respectively. The 16 "C" sources compose the sample considered in the present paper.
[d] "UL" stands for ultralong, indicating sources with $T_{90} \gtrsim 1000$ s.
[e] Observed T_{90} (s).
[f] "B-SAX" stands for *BeppoSAX*/GRBM; "BATSE" stands for *Compton-GRO*/BATSE; "Ulysses" stands for *Ulysses*/GRB; "KW" stands for Konus/*WIND*; "HETE" stands for *HETE*-2/FREGATE; "*Swift*" standss for *Swift*/BAT; "*Fermi*" stands for *Fermi*/GBM.
[g] (1) Frontera et al. (1998), (2) Ruffini et al. (2015a), (3) in 't Zand et al. (1998), (4) Amati et al. (2000), (5) Hurley et al. (2000), (6) in't Zand et al. (2001), (7) Barraud et al. (2003), (8) Shirasaki et al. (2008), (9) Cenko et al. (2006).

(This table is available in its entirety in machine-readable form.)

$$p_{e^-} = A\,\frac{T^4}{3}\int_0^\infty f(z, T, m_e, \mu_{e^-})\frac{z^4}{\sqrt{z^2 + (m_e/T)^2}}\,dz \quad (40)$$

$$p_{e^+} = A\,\frac{T^4}{3}\int_0^\infty f(z, T, m_e, \mu_{e^+})\frac{z^4}{\sqrt{z^2 + (m_e/T)^2}}\,dz \quad (41)$$

$$\epsilon_\gamma = a\,T^4 \quad (42)$$

$$p_\gamma = \frac{a\,T^4}{3} \quad (43)$$

$$\epsilon_B = \frac{3}{2} n_N\,T \quad (44)$$

$$p_B = n_N\,T, \quad (45)$$

where

$$f(z, T, m, \mu) = \frac{1}{e^{\sqrt{z^2+(m/T)^2}-\mu/T} + 1} \quad (46)$$

is the Fermi–Dirac distribution, m_e is the electron mass, n_N the nuclei number density, $a = 8\pi^5 k_B^4/15h^3c^3 = 7.5657 \times 10^{-15}$ erg cm^{-3} K^{-4} the radiation constant, and $A = 15a/\pi^4$. If the pair annihilation rate is zero, i.e., if the reaction $e^- + e^+ \leftrightarrows 2\gamma$ is in equilibrium, then the equality $\mu_{e^-} = -\mu_{e^+} \equiv \mu$ holds, since the equilibrium photons have zero chemical potential. Besides, charge neutrality implies that the difference in the number of electrons and positrons is equal to the number of protons in the baryonic matter, which can be expressed as

$$n_{e^-}(\mu, T) - n_{e^+}(\mu, T) = Z\,n_B, \quad (47)$$

where n_B is the baryon number density and $1/2 < Z < 1$ is the average number of electrons per nucleon. The number density n_B is related to the other quantities as

$$\rho = m_p\,n_B + m_e(n_{e^-} + n_{e^+}), \quad (48)$$

where m_p is the proton mass. If the baryons are only protons, then $Z = 1$ and $n_N = n_B$. Together with Equation (47), this completely defines the mass density as a function of (μ, T). The equation of state that relates the pressure with the mass and internal energy densities is thus defined implicitly as the parametric surface

$$\{(\rho(\mu, T), \epsilon(\mu, T), p(\mu, T)):\ T > 0,\ \mu \geqslant 0\} \quad (49)$$

that satisfies all of the above relations.

In the cases relevant for the simulations performed in Section 10, we indeed have that the index γ in the equation of state of the plasma, Equation (30), satisfies $\gamma = 4/3$ with a maximum error of 0.2%.

ORCID iDs

R. Ruffini https://orcid.org/0000-0003-0829-8318
Y. Wang https://orcid.org/0000-0001-7959-3387
Y. Aimuratov https://orcid.org/0000-0001-5717-6523
U. Barres de Almeida https://orcid.org/0000-0001-7909-588X
C. L. Bianco https://orcid.org/0000-0001-7749-4078
Y. C. Chen https://orcid.org/0000-0002-7543-2727
M. Kovacevic https://orcid.org/0000-0003-4928-4510
R. Moradi https://orcid.org/0000-0002-2516-5894
M. Muccino https://orcid.org/0000-0002-2234-9225
A. V. Penacchioni https://orcid.org/0000-0001-7816-3668
G. B. Pisani https://orcid.org/0000-0003-3452-2491
J. A. Rueda https://orcid.org/0000-0003-4904-0014
G. V. Vereshchagin https://orcid.org/0000-0002-1623-3576

References

Aimuratov, Y., Ruffini, R., Muccino, M., et al. 2017, ApJ, 844, 83
Aksenov, A. G., Ruffini, R., & Vereshchagin, G. V. 2007, PhRvL, 99, 125003

Amati, L., & Della Valle, M. 2013, IJMPD, 22, 30028
Amati, L., Frontera, F., Vietri, M., et al. 2000, Sci, 290, 953
Atwood, W. B., Abdo, A. A., Ackermann, M., et al. 2009, ApJ, 697, 1071
Barraud, C., Olive, J.-F., Lestrade, J. P., et al. 2003, A&A, 400, 1021
Barthelmy, S. D., Baumgartner, W. H., Cummings, J. R., et al. 2013, GCN, 15456, 1
Barthelmy, S. D., Chincarini, G., Burrows, D. N., et al. 2005, Natur, 438, 994
Baumgartner, W. H., Barthelmy, S. D., Cummings, J. R., et al. 2014, GCN, 16127, 1
Becerra, L., Bianco, C. L., Fryer, C. L., Rueda, J. A., & Ruffini, R. 2016, ApJ, 833, 107
Becerra, L., Cipolletta, F., Fryer, C. L., Rueda, J. A., & Ruffini, R. 2015, ApJ, 812, 100
Berger, E. 2014, ARA&A, 52, 43
Bernardini, M. G., Bianco, C. L., Chardonnet, P., et al. 2005, ApJL, 634, L29
Bethe, H. A. 1991, The Road from LOS Alamos (Melville, NY: AIP)
Bianco, C. L., & Ruffini, R. 2004, ApJL, 605, L1
Bianco, C. L., & Ruffini, R. 2005a, ApJL, 620, L23
Bianco, C. L., & Ruffini, R. 2005b, ApJL, 633, L13
Bianco, C. L., & Ruffini, R. 2006, ApJL, 644, L105
Bianco, C. L., Ruffini, R., & Xue, S.-S. 2001, A&A, 368, 377
Blandford, R. D., & McKee, C. F. 1976, PhFl, 19, 1130
Bloom, J. S., Frail, D. A., & Sari, R. 2001, AJ, 121, 2879
Bromberg, O., Nakar, E., Piran, T., & Sari, R. 2013, ApJ, 764, 179
Butler, N., Ricker, G., Atteia, J.-L., et al. 2005, GCN, 3570, 1
Caito, L., Amati, L., Bernardini, M. G., et al. 2010, A&A, 521, A80
Caito, L., Bernardini, M. G., Bianco, C. L., et al. 2009, A&A, 498, 501
Calderone, G., Ghirlanda, G., Ghisellini, G., et al. 2015, MNRAS, 448, 403
Cavallo, G., & Rees, M. J. 1978, MNRAS, 183, 359
Cenko, S. B., Kasliwal, M., Harrison, F. A., et al. 2006, ApJ, 652, 490
Cherubini, C., Geralico, A., Rueda, H. J. A., & Ruffini, R. 2009, PhRvD, 79, 124002
Chester, M. M., Wang, X. Y., Cummings, J. R., et al. 2008, in AIP Conf. Ser. 1000, Gamma-Ray Bursts 2007, ed. M. Galassi, D. Palmer, & E. Fenimore (Melville, NY: AIP), 421
Chincarini, G., Mao, J., Margutti, R., et al. 2010, MNRAS, 406, 2113
Chincarini, G., Moretti, A., Romano, P., et al. 2007, ApJ, 671, 1903
Cleveland, W., & Devlin, S. 1988, J. Am. Stat. Assoc., 83, 596
Cline, T. L., Desai, U. D., Trainor, J., et al. 1979, ApJL, 229, L47
Cobb, B. E. 2007, GCN, 6296, 1
Colella, P., Graves, D. T., Johnson, J. N., et al. 2003, Chombo Software Package for AMR Applications Design Document, Tech. Rep. LBNL-6615E
Colgate, S. A. 1971, ApJ, 163, 221
Costa, E., Frontera, F., Heise, J., et al. 1997, Natur, 387, 783
Cummings, J. R., Barthelmy, S. D., Burrows, D. N., et al. 2007, GCN, 6210, 1
Dai, Z. G., Wang, X. Y., Wu, X. F., & Zhang, B. 2006, Sci, 311, 1127
Damour, T., & Ruffini, R. 1975, PhRvL, 35, 463
D'Avanzo, P., D'Elia, V., & Covino, S. 2008, GCN, 8350, 1
de Pasquale, M., Piro, L., Gendre, B., et al. 2006, A&A, 455, 813
de Ugarte Postigo, A., Fynbo, J. P. U., Thöne, C. C., et al. 2012, A&A, 548, A11
Della Valle, M. 2011, IJMPD, 20, 1745
Dezalay, J.-P., Barat, C., Talon, R., et al. 1992, in AIP Conf. Ser. 265, Gamma-Ray Bursts, ed. W. S. Paciesas & G. J. Fishman (Melville, NY: AIP), 304
Eichler, D., Livio, M., Piran, T., & Schramm, D. N. 1989, Natur, 340, 126
Evans, P. A., Beardmore, A. P., Page, K. L., et al. 2007, A&A, 469, 379
Evans, P. A., Beardmore, A. P., Page, K. L., et al. 2009, MNRAS, 397, 1177
Falcone, A., Barbier, L., Barthelmy, S., et al. 2006, GCN, 4655, 1
Falcone, A. D., Morris, D., Racusin, J., et al. 2007, ApJ, 671, 1921
Fan, Y. Z., Zhang, B., & Proga, D. 2005, ApJL, 635, L129
Fenimore, E. E., Palmer, D., Galassi, M., et al. 2003, in AIP Conf. Ser. 662, Gamma-Ray Burst and Afterglow Astronomy 2001: A Workshop Celebrating the First Year of the HETE Mission, ed. G. R. Ricker & R. K. Vanderspek (Melville, NY: AIP), 491
Fermi, E. 1934, NCim, 11, 1
Frail, D. A., Kulkarni, S. R., Nicastro, L., Feroci, M., & Taylor, G. B. 1997, Natur, 389, 261
Frail, D. A., Kulkarni, S. R., Sari, R., et al. 2001, ApJL, 562, L55
Frey, L. H., Fryer, C. L., & Young, P. A. 2013, ApJL, 773, L7
Frontera, F., Costa, E., Piro, L., et al. 1998, ApJL, 493, L67
Fruchter, A. S., Levan, A. J., Strolger, L., et al. 2006, Natur, 441, 463
Fryer, C., Benz, W., Herant, M., & Colgate, S. A. 1999a, ApJ, 516, 892
Fryer, C. L., Oliveira, F. G., Rueda, J. A., & Ruffini, R. 2015, PhRvL, 115, 231102
Fryer, C. L., Rueda, J. A., & Ruffini, R. 2014, ApJL, 793, L36
Fryer, C. L., Woosley, S. E., & Hartmann, D. H. 1999b, ApJ, 526, 152
Galama, T. J., Vreeswijk, P. M., van Paradijs, J., et al. 1998, Natur, 395 670
Gamow, G., & Schoenberg, M. 1940, PhRv, 58, 1117
Gamow, G., & Schoenberg, M. 1941, PhRv, 59, 539
Gehrels, N., Chipman, E., & Kniffen, D. A. 1993, A&AS, 97, 5
Gehrels, N., Ramirez-Ruiz, E., & Fox, D. B. 2009, ARA&A, 47, 567
Golenetskii, S., Aptekar, R., Frederiks, D., et al. 2013, GCN, 15413, 1
Golenetskii, S., Aptekar, R., Frederiks, D., et al. 2014, GCN, 16134, 1
Golenetskii, S., Aptekar, R., Frederiks, D., et al. 2015, GCN, 18516, 1
Golenetskii, S., Aptekar, R., Mazets, E., et al. 2008, GCN, 7862, 1
Goodman, J. 1986, ApJL, 308, L47
Gursky, H., & Ruffini, R. (ed.) 1975, in Proc. Annual Meeting, Astrophysics and Space Science Library, Vol. 48, Neutron Stars, Black Holes and Binary X-ray Sources (Dordrecht: Reidel), 454
Heisenberg, W. 1943, ZPhy, 120, 513
Hjorth, J., & Bloom, J. S. 2012, in Gamma-Ray Bursts, ed. C. Kouveliotou, R. A. M. J. Wijers, & S. Woosley (Cambridge: Cambridge Univ. Press), 169
Hurley, K., Cline, T., Mazets, E., et al. 2000, ApJL, 534, L23
in 't Zand, J. J. M., Amati, L., Antonelli, L. A., et al. 1998, ApJL, 505, L119
in't Zand, J. J. M., Kuiper, L., Amati, L., et al. 2001, ApJ, 559, 710
Itoh, N., Adachi, T., Nakagawa, M., Kohyama, Y., & Munakata, H. 1989, ApJ, 339, 354
Izzo, L., Ruffini, R., Penacchioni, A. V., et al. 2012, A&A, 543, A10
Jakobsson, P., Fynbo, J. P. U., Vreeswijk, P. M., & de Ugarte Postigo, A. 2008, GCN, 8077, 1
Jaunsen, A. O., Fynbo, J. P. U., Andersen, M. I., & Vreeswijk, P. 2007, GCN, 6216, 1
Jin, Z.-P., Fan, Y.-Z., & Wei, D.-M. 2010, ApJ, 724, 861
Klebesadel, R. W. 1992, in Gamma-Ray Bursts—Observations, Analyses and Theories, ed. C. Ho, R. I. Epstein, & E. E. Fenimore (Cambridge: Cambridge Univ. Press), 161
Klebesadel, R. W., Strong, I. B., & Olson, R. A. 1973, ApJL, 182, L85
Kouveliotou, C., Meegan, C. A., Fishman, G. J., et al. 1993, ApJL, 413, L101
Krimm, H. A., Beardmore, A. P., Brown, P. J., et al. 2008, GCN, 8648, 1
Kruehler, T., Tanvir, N. R., Malesani, D., Xu, D., & Fynbo, J. P. U. 2014, GCN, 15900, 1
Kumar, P., & Zhang, B. 2015, PhR, 561, 1
Landau, L. D., & Lifshitz, E. M. 1980, Statistical Physics. Pt.1 (3rd ed.; Portsmouth, NH: Butterworth-Heinemann)
Ledoux, C., Vreeswijk, P., Smette, A., Jaunsen, A., & Kaufer, A. 2006, GCN, 5237, 1
Lien, A. Y., Barthelmy, S. D., Chester, M. M., et al. 2014, GCN, 15784, 1
Lyman, J. D., Bersier, D., James, P. A., et al. 2016, MNRAS, 457, 328
MacFadyen, A., & Woosley, S. E. 1999, ApJ, 524, 262
Malesani, D., Xu, D., Fynbo, J. P. U., et al. 2014, GCN, 15800, 1
Mangano, V., Cummings, J. R., Cusumano, G., et al. 2008, GCN, 7847, 1
Mao, S., & Yi, I. 1994, ApJL, 424, L131
Margutti, R., Guidorzi, C., Chincarini, G., et al. 2010, MNRAS, 406, 2149
Marisaldi, M., Fuschino, F., Galli, M., et al. 2008, GCN, 7866, 1
Marshall, F. E., Cummings, J. R., Gronwall, C., et al. 2014, GCN, 16118, 1
Maselli, A., D'Ai, A., Lien, A. Y., et al. 2015, GCN, 18478, 1
Masumitsu, T., Negoro, H., Kawai, N., et al. 2015, GCN, 18525, 1
Mazets, E. P., Golenetskii, S. V., Ilinskii, V. N., et al. 1981, Ap&SS, 80, 3
McBreen, S. 2009, GCN, 9415, 1
Mészáros, P. 2002, ARA&A, 40, 137
Mészáros, P. 2006, RPPh, 69, 2259
Meszaros, P., Laguna, P., & Rees, M. J. 1993, ApJ, 415, 181
Mészáros, P., & Rees, M. J. 1997, ApJL, 482, L29
Metzger, M. R., Djorgovski, S. G., Kulkarni, S. R., et al. 1997, Natur, 387, 878
Mignone, A., Zanni, C., Tzeferacos, P., et al. 2011, ApJS, 198, 7
Morgan, A., Grupe, D., Gronwall, C., et al. 2005, GCN, 3577, 1
Munakata, H., Kohyama, Y., & Itoh, N. 1985, ApJ, 296, 197
Narayan, R., Paczynski, B., & Piran, T. 1992, ApJL, 395, L83
Narayan, R., Piran, T., & Shemi, A. 1991, ApJL, 379, L17
Negreiros, R., Ruffini, R., Bianco, C. L., & Rueda, J. A. 2012, A&A, 540, A12
Nousek, J. A., Kouveliotou, C., Grupe, D., et al. 2006, ApJ, 642, 389
Nysewander, M., Reichart, D. E., Crain, J. A., et al. 2009, ApJ, 693, 1417
Oppenheimer, J. R., & Volkoff, G. M. 1939, PhRv, 55, 374
Paczynski, B. 1986, ApJL, 308, L43
Paczyński, B. 1998, ApJL, 494, L45
Pagani, C., Baumgartner, W. H., Chester, M. M., et al. 2008, GCN, 8059, 1
Page, K. L., Barthelmy, S. D., Baumgartner, W. H., et al. 2014, GCNR, 460, 1
Page, K. L., Willingale, R., Bissaldi, E., et al. 2009, MNRAS, 400, 134
Panaitescu, A., & Mészáros, P. 1999, ApJ, 526, 707
Patricelli, B., Bernardini, M. G., Bianco, C. L., et al. 2012, ApJ, 756, 16

Penacchioni, A. V., Ruffini, R., Bianco, C. L., et al. 2013, A&A, 551, A133
Penacchioni, A. V., Ruffini, R., Izzo, L., et al. 2012, A&A, 538, A58
Perley, D. A., Cao, Y., & Cenko, S. B. 2014, GCN, 17228, 1
Perley, D. A., Hillenbrand, L., & Prochaska, J. X. 2015, GCN, 18487, 1
Perley, D. A., Krühler, T., Schulze, S., et al. 2016, ApJ, 817, 7
Piran, T. 1999, PhR, 314, 575
Piran, T. 2004, RvMP, 76, 1143
Piran, T., Shemi, A., & Narayan, R. 1993, MNRAS, 263, 861
Piro, L., De Pasquale, M., Soffitta, P., et al. 2005, ApJ, 623, 314
Pisani, G. B., Izzo, L., Ruffini, R., et al. 2013, A&A, 552, L5
Pisani, G. B., Ruffini, R., Aimuratov, Y., et al. 2016, ApJ, 833, 159
Racusin, J. L., Baumgartner, W. H., Brown, P. J., et al. 2008, GCN, 8344, 1
Rees, M. J., & Meszaros, P. 1992, MNRAS, 258, 41P
Rees, M. J., & Meszaros, P. 1994, ApJL, 430, L93
Romano, P., Campana, S., Chincarini, G., et al. 2006, A&A, 456, 917
Rossi, A., Afonso, P., & Greiner, J. 2009, GCN, 9382, 1
Rowlinson, B. A., Beardmore, A. P., Evans, P. A., et al. 2009, GCN, 9374, 1
Rueda, J. A., Aimuratov, Y., de Almeida, U. B., et al. 2017, IJMPD, 26, 1730016
Rueda, J. A., & Ruffini, R. 2012, ApJL, 758, L7
Ruffini, R. 1998, in Frontiers Science Series 23, Black Holes and High Energy Astrophysics, ed. H. Sato & N. Sugiyama (Tokyo: Universal Academic Press), 167
Ruffini, R. 2015, in Thirteenth Marcel Grossmann Meeting: On Recent Developments in Theoretical and Experimental General Relativity, Astrophysics and Relativistic Field Theories, ed. K. Rosquist (Singapore: World Scientific), 242
Ruffini, R., Bianco, C. L., Chardonnet, P., Fraschetti, F., & Xue, S.-S. 2002, ApJL, 581, L19
Ruffini, R., Bianco, C. L., Fraschetti, F., Xue, S.-S., & Chardonnet, P. 2001a, ApJL, 555, L107
Ruffini, R., Bianco, C. L., Fraschetti, F., Xue, S.-S., & Chardonnet, P. 2001b, ApJL, 555, L113
Ruffini, R., Bianco, C. L., Fraschetti, F., Xue, S.-S., & Chardonnet, P. 2001c, ApJL, 555, L117
Ruffini, R., Izzo, L., Bianco, C. L., et al. 2015a, ARep, 59, 626
Ruffini, R., Muccino, M., Aimuratov, Y., et al. 2016a, ApJ, 831, 178
Ruffini, R., Muccino, M., Bianco, C. L., et al. 2014, A&A, 565, L10
Ruffini, R., Muccino, M., Kovacevic, M., et al. 2015b, ApJ, 808, 190
Ruffini, R., Rueda, J. A., Muccino, M., et al. 2016b, ApJ, 832, 136
Ruffini, R., Salmonson, J. D., Wilson, J. R., & Xue, S. 2000, A&A, 359, 855
Ruffini, R., Salmonson, J. D., Wilson, J. R., & Xue, S.-S. 1999, A&A, 350, 334
Ruffini, R., Song, D. J., & Stella, L. 1983, A&A, 125, 265
Ruffini, R., Vereshchagin, G., & Xue, S. 2010, PhR, 487, 1
Ruffini, R., Wang, Y., Enderli, M., et al. 2015c, ApJ, 798, 10
Ruffini, R., & Wilson, J. 1973, PhRvL, 31, 1362
Sakamoto, T., Barthelmy, S. D., Baumgartner, W. H., et al. 2014, GCN, 15805, 1
Sari, R., Piran, T., & Halpern, J. P. 1999, ApJL, 519, L17
Shemi, A., & Piran, T. 1990, ApJL, 365, L55
Shirasaki, Y., Yoshida, A., Kawai, N., et al. 2008, PASJ, 60, 919
Smith, N. 2014, ARA&A, 52, 487
Smith, N., Li, W., Filippenko, A. V., & Chornock, R. 2011, MNRAS, 412, 1522
Sonbas, E., Cummings, J. R., D'Elia, V., et al. 2014, GCN, 17206, 1
Stamatikos, M., Cummings, J. R., Evans, P. A., et al. 2009, GCN, 9768, 1
Svensson, K. M., Levan, A. J., Tanvir, N. R., Fruchter, A. S., & Strolger, L.-G. 2010, MNRAS, 405, 57
Swenson, C. A., & Roming, P. W. A. 2014, ApJ, 788, 30
Tanvir, N. R., Levan, A. J., Cucchiarra, A., Perley, D., & Cenko, S. B. 2014, GCN, 16125, 1
Tavani, M. 1998, ApJL, 497, L21
Taylor, E. F., & Wheeler, J. A. 1992, Spacetime Physics—Introduction to Special Relativity (2nd ed.; New York: W. H. Freeman & Co.)
Toelge, K., Yu, H. F., & Meegan, C. A. 2015, GCN, 18492, 1
Troja, E., Barthelmy, S. D., Baumgartner, W. H., et al. 2013, GCN, 15402, 1
Troja, E., Piro, L., Vasileiou, V., et al. 2015, ApJ, 803, 10
van Paradijs, J., Groot, P. J., Galama, T., et al. 1997, Natur, 386, 686
von Kienlin, A., & Bhat, P. N. 2014, GCN, 15796, 1
Wheeler, J. A. 1937, PhRv, 52, 1107
Woosley, S. E. 1993, ApJ, 405, 273
Woosley, S. E., & Bloom, J. S. 2006, ARA&A, 44, 507
Xu, D., Fynbo, J. P. U., Jakobsson, P., et al. 2013, GCN, 15407, 1
Yi, S.-X., Wu, X.-F., Wang, F.-Y., & Dai, Z.-G. 2015, ApJ, 807, 92
Yu, H.-F. 2014, GCN, 17216, 1
Yuan, F., Schady, P., Racusin, J. L., et al. 2010, ApJ, 711, 870
Zel'dovich, Y. B., Ivanova, L. N., & Nadezhin, D. K. 1972, SvA, 16 209
Zhang, B., Fan, Y. Z., Dyks, J., et al. 2006, ApJ, 642, 354
Zhang, F.-W., Shao, L., Yan, J.-Z., & Wei, D.-M. 2012, ApJ, 750, 88
Ziaeepour, H. Z., Barthelmy, S. D., Gehrels, N., et al. 2006, GCN, 5233, 1

The Astrophysical Journal, 859:30 (17pp), 2018 May 20 https://doi.org/10.3847/1538-4357/aabee4

On the Rate and on the Gravitational Wave Emission of Short and Long GRBs

R. Ruffini[1,2,3,4], J. Rodriguez[1,2], M. Muccino[1,2], J. A. Rueda[1,2,4], Y. Aimuratov[1,2], U. Barres de Almeida[4,5], L. Becerra[1,2], C. L. Bianco[1,2], C. Cherubini[6,7], S. Filippi[6,7], D. Gizzi[1], M. Kovacevic[1,2,3], R. Moradi[1,2], F. G. Oliveira[1,2,3], G. B. Pisani[1,2], and Y. Wang[1,2]

[1] Dipartimento di Fisica and ICRA, Sapienza Università di Roma, P.le Aldo Moro 5, I-00185 Rome, Italy
[2] ICRANet, P.zza della Repubblica 10, I-65122 Pescara, Italy
[3] Université de Nice Sophia Antipolis, CEDEX 2, Grand Château Parc Valrose, Nice, France
[4] ICRANet-Rio, Centro Brasileiro de Pesquisas Físicas, Rua Dr. Xavier Sigaud 150, 22290-180 Rio de Janeiro, Brazil
[5] Centro Brasileiro de Pesquisas Físicas, Rua Dr. Xavier Sigaud 150, 22290-180 Rio de Janeiro, Brazil
[6] Unit of Nonlinear Physics and Mathematical Modeling, Università Campus Bio-Medico di Roma, Via A. del Portillo 21, I-00128 Rome, Italy
[7] ICRA, Università Campus Bio-Medico di Roma, Via A. del Portillo 21, I-00128 Rome, Italy
Received 2016 October 25; revised 2018 April 6; accepted 2018 April 15; published 2018 May 18

Abstract

On the ground of the large number of gamma-ray bursts (GRBs) detected with cosmological redshift, we classified GRBs in seven subclasses, all with binary progenitors which emit gravitational waves (GWs). Each binary is composed of combinations of carbon–oxygen cores (CO_{core}), neutron stars (NSs), black holes (BHs), and white dwarfs (WDs). The long bursts, traditionally assumed to originate from a BH with an ultrarelativistic jetted emission, not emitting GWs, have been subclassified as (I) X-ray flashes (XRFs), (II) binary-driven hypernovae (BdHNe), and (III) BH–supernovae (BH–SNe). They are framed within the induced gravitational collapse paradigm with a progenitor CO_{core}–NS/BH binary. The SN explosion of the CO_{core} triggers an accretion process onto the NS/BH. If the accretion does not lead the NS to its critical mass, an XRF occurs, while when the BH is present or formed by accretion, a BdHN occurs. When the binaries are not disrupted, XRFs lead to NS–NS and BdHNe lead to NS–BH. The short bursts, originating in NS–NS, are subclassified as (IV) short gamma-ray flashes (S-GRFs) and (V) short GRBs (S-GRBs), the latter when a BH is formed. There are (VI) ultrashort GRBs (U-GRBs) and (VII) gamma-ray flashes (GRFs) formed in NS–BH and NS–WD, respectively. We use the occurrence rate and GW emission of these subclasses to assess their detectability by Advanced LIGO-Virgo, eLISA, and resonant bars. We discuss the consequences of our results in view of the announcement of the LIGO/Virgo Collaboration of the source GW 170817 as being originated by an NS–NS.

Key words: binaries: general – black hole physics – gamma-ray burst: general – gravitational waves – stars: neutron – white dwarfs

1. Introduction

Thanks to the extensive observations carried out by γ-ray telescopes, such as AGILE, BATSE, *BeppoSAX*, *Fermi*, *HETE-II*, *INTEGRAL*, Konus/*WIND*, and *Swift*, our understanding of "long" and "short" gamma-ray burst (GRB) progenitor systems has greatly improved. This has led also to a vast literature devoted to the estimate of their relative occurrence rates, all in general agreement. For long bursts see, e.g., Soderberg et al. (2006b), Guetta & Della Valle (2007), Liang et al. (2007), Virgili et al. (2009), Rangel Lemos et al. (2010), Wanderman & Piran (2010), Guetta et al. (2011), and Kovacevic et al. (2014); for short bursts see, e.g., Virgili et al. (2011) and Wanderman & Piran (2015); and for both long and short bursts see, e.g., Sun et al. (2015) and Ruffini et al. (2016b). The rates of gravitational wave (GW) emission from GRBs have been calculated in the literature at a time in which short GRBs were considered to originate in neutron star–neutron star (NS–NS) binaries, while long GRBs were considered to originate in single events,[8] e.g., *collapsars* (Woosley 1993; MacFadyen & Woosley 1999; MacFadyen et al. 2001; Woosley & Bloom 2006; see, however, Ruffini et al. 2018b) and *magnetars* (Usov 1992; Dai & Lu 1998a, 1998b; Kluźniak & Ruderman 1998; Zhang & Mészáros 2001; see, however, Ruffini et al. 2016b). Thus, only short GRBs have been up to now considered to estimate the simultaneous detection rate of GWs and GRBs. For instance, Wanderman & Piran (2015) used the luminosity function of short GRBs observed by *Swift*; Yonetoku et al. (2014), by BATSE; Patricelli et al. (2016), by *Fermi*; and Ghirlanda et al. (2016), by *Swift* and *Fermi*.

In our recent works (see Ruffini et al. 2016b, and references therein) we have introduced a new classification in which all GRBs, namely, both long and short, originate from merging and/or accreting binary systems, each composed of a different combination of carbon–oxygen cores (CO_{core}), NSs, black holes (BHs), and white dwarfs (WDs). For each system the initial state and the final state are here referred to as "in-state" and "out-state," respectively. This opens an ample new scenario for the role of GWs both as detectable sources and as a determining factor in the coalescence process of the GRB progenitors.

We interpret the traditional long GRBs within the induced gravitational collapse (IGC) paradigm (Ruffini et al. 2006, 2007, 2008, 2015b; Izzo et al. 2012a; Rueda & Ruffini 2012; Fryer et al. 2014) that proposes as in-state a tight binary system composed of a CO_{core} undergoing a supernova (SN) explosion and a companion compact object, e.g., an NS (or a BH). The SN explosion triggers a hypercritical accretion onto the NS companion, whose details have been studied, simulated, and presented in several publications (see, e.g., Fryer et al. 2014, 2015b; Becerra et al. 2015, 2016, and references therein;

[8] With the exception of the binary progenitors proposed in Fryer & Woosley (1998), Fryer et al. (1999a, 1999b), and Belczynski et al. (2002).

Appendix A). Depending on the binary parameters, the hypercritical accretion can lead to three very different outcomes:

I. X-ray flashes (XRFs) with isotropic energy $E_{\rm iso} \lesssim 10^{52}$ erg and rest-frame spectral peak energy $E_{p,i} \lesssim 200$ keV. This class occurs in $CO_{\rm core}$–NS binaries when the hypercritical accretion onto the NS companion is not enough to induce gravitational collapse into a BH (Becerra et al. 2015, 2016). Following this definition, Ruffini et al. (2016b) estimated for the XRF a local observed rate of $\rho_{\rm XRF} = 100^{+45}_{-34}$ Gpc^{-3} yr^{-1} (Ruffini et al. 2016b). This rate is in agreement with that of low-luminosity long GRBs, e.g., 325^{+352}_{-177} Gpc^{-3} yr^{-1} (Liang et al. 2007), $\sim$200 Gpc^{-3} yr^{-1} (Virgili et al. 2009), and 164^{+98}_{-65} Gpc^{-3} yr^{-1} (Sun et al. 2015). After the SN explosion, the binary can either get disrupted or remain bound depending on the mass loss and/or natal kick imparted to the system (see Postnov & Yungelson 2014, references therein; Appendix A.5). In the former case the XRF leads to two runaway NSs, while in the latter one the out-states of XRFs are binaries composed of a newly formed $\sim$1.4–1.5 $M_\odot$ NS (hereafter νNS) born in the SN explosion and a massive NS (MNS) that accreted matter from the SN ejecta. Typical periods of these binaries are $P_{\rm orb} \gtrsim 30$ minutes (Becerra et al. 2016).

II. Binary-driven hypernovae (BdHNe) with $E_{\rm iso} \gtrsim 10^{52}$ erg and $E_{p,i} \gtrsim 200$ keV. BdHNe occur in more compact $CO_{\rm core}$–NS binaries, which leads to a more massive hypercritical accretion onto the NS, hence leading to BH formation. Following this definition, Ruffini et al. (2016b) estimated for the BdHNe a local observed rate $\rho_{\rm BdHN} = 0.77^{+0.09}_{-0.08}$ Gpc^{-3} yr^{-1} (Ruffini et al. 2016b). This rate is in agreement with that for high-luminosity long GRBs, e.g., $1.3^{+0.6}_{-0.7}$ Gpc^{-3} yr^{-1} (Wanderman & Piran 2010) and $0.8^{+0.1}_{-0.1}$ Gpc^{-3} yr^{-1} (Sun et al. 2015). As in the case of XRFs, the SN explosion can disrupt the binary depending on the mass loss and/or natal kick. In the case when the system remains bound, the out-states of BdHNe are νNS–BH binaries (see Fryer et al. 2015b; Appendix A.5). Typical periods of these binaries are 5 minutes $\lesssim P_{\rm orb} \lesssim 30$ minutes (Becerra et al. 2016).

III. BH–SNe with $E_{\rm iso} \gtrsim 10^{54}$ erg and $E_{p,i} \gtrsim 2$ MeV. BH–SNe occur in close $CO_{\rm core}$ (or helium or Wolf-Rayet star)–BH binaries (Ruffini et al. 2001) in which the hypercritical accretion occurs onto a previously formed BH. Such BH–SN systems correspond to the late evolutionary stages of X-ray binaries such as Cyg X-1 (Giacconi & Ruffini 1978; Belczynski et al. 2011) or microquasars (Mirabel & Rodríguez 1998). These systems might be also formed following the binary evolutionary patch leading to scenario XI in Fryer et al. (1999a). Since the estimated rate of BdHNe covers systems with the above $E_{\rm iso}$ and $E_{p,i}$ range, we can adopt the rate of BdHNe as an upper limit to the rate of BH–SNe, i.e., $\rho_{\rm BH\text{–}SN} \lesssim \rho_{\rm BdHN} = 0.77^{+0.09}_{-0.08}$ Gpc^{-3} yr^{-1} (Ruffini et al. 2016b). As in the above cases of XRFs and BdHNe, the SN explosion may disrupt the binary. If the binary survives, then the out-states of BH–SNe can be a νNS–BH or a BH–BH if the SN central remnant directly collapses to a BH. However, the latter scenario is currently ruled out by the observations of pre-SN cores that appear to have masses $\lesssim 18\, M_\odot$, very low to lead to direct BH formation (see, e.g., Smartt 2009, 2015, for details).

In the current literature such a difference between an XRF, a BdHN, and a BH–SN in the evaluation of GWs, here implemented, is still missing.

We turn now to the short bursts. Although their progenitors are still under debate, there is an ample consensus in the scientific community that they originate from NS–NS and/or NS–BH merging binaries (see, e.g., Goodman 1986; Paczynski 1986; Eichler et al. 1989; Narayan et al. 1991; Meszaros & Rees 1997; Rosswog et al. 2003; Lee et al. 2004; Berger 2014). By adopting the same in-states as in the above traditional models, namely, NS–NS and/or NS–BH mergers, they can be divided into three subclasses (Fryer et al. 2015b; Ruffini et al. 2015a, 2016b):

Short gamma-ray flashes (S-GRFs), with $E_{\rm iso} \lesssim 10^{52}$ erg and $E_{p,i} \lesssim 2$ MeV, occur when no BH is formed in the NS–NS merger, i.e., they lead to an MNS. Following this definition, Ruffini et al. (2016b) estimated for the S-GRFs a local observed rate $\rho_{\rm S\text{-}GRF} = 3.6^{+1.4}_{-1.0}$ Gpc^{-3} yr^{-1}.
Authentic short GRBs (S-GRBs), with $E_{\rm iso} \gtrsim 10^{52}$ erg and $E_{p,i} \gtrsim 2$ MeV, occur when a BH is formed in the NS–NS merger (Muccino et al. 2013; Ruffini et al. 2015a, 2016a). Following this definition, Ruffini et al. (2016b) estimated for the S-GRBs a local observed rate $\rho_{\rm S\text{-}GRB} = (1.9^{+1.8}_{-1.1}) \times 10^{-3}$ Gpc^{-3} yr^{-1} (Ruffini et al. 2016b).
Ultrashort GRBs (U-GRBs), a new subclass of short bursts originating from νNS–BH merging binaries. They can originate from BdHNe (see subclass II above) or from BH–SN events (see subclass III above). Since in Fryer et al. (2015b) it was shown that the majority of BdHN out-states remain bound, we can assume as an upper limit of their local density rate $\rho_{\rm U\text{-}GRB} \approx \rho_{\rm BdHN} = 0.77^{+0.09}_{-0.08}$ Gpc^{-3} yr^{-1} (Ruffini et al. 2016b). U-GRBs are yet unobserved/unidentified and present a great challenge not only in the case of high energy but also possibly in the radio band, where they could manifest themselves, prior to the merger phase, as pulsar–BH binaries (see, e.g., Tauris et al. 2015a, and references therein).

It is important to mention that the sum of the occurrence rates of the above short burst subclasses IV–VI is in agreement with the estimates obtained from the whole short burst population reported in the literature (see, e.g., Sun et al. 2015; Wanderman & Piran 2015). It is then clear that what in the current literature are indicated as short GRBs are actually just S-GRFs.

In addition to the above three subclasses of long bursts and three subclasses of short bursts, we recall the existence of a class of bursts occurring in a low-density circumburst medium (CBM), e.g., $n_{\rm CBM} \sim 10^{-3}$ cm^{-3}, which show hybrid properties between short and long bursts in γ-rays. These bursts are not associated with SNe, even at low redshift, where the SN detection would not be precluded (Della Valle et al. 2006). We have called such bursts gamma-ray flashes (GRFs; Ruffini et al. 2016b).

GRFs have 10^{51} erg $\lesssim E_{\rm iso} \lesssim 10^{52}$ erg and 0.2 MeV $\lesssim E_{p,i} \lesssim 2$ MeV. These bursts, which show an extended and softer emission, are thought to originate in NS–WD mergers (Ruffini et al. 2016b). NS–WD binaries are notoriously common astrophysical systems (Cadelano et al. 2015), and possible evolutionary scenarios leading to such mergers have been envisaged (see, e.g., Fryer et al. 1999b; Tauris et al. 2000; Lazarus et al. 2014).[9] GRFs form an MNS and not a BH (see Ruffini et al. 2016b, for details). Following this definition, Ruffini et al. (2016b) estimated for the GRFs a local observed rate $\rho_{\rm GRF} = 1.02^{+0.71}_{-0.46}\,{\rm Gpc}^{-3}\,{\rm yr}^{-1}$ (Ruffini et al. 2016b). This density rate appears to be low with respect to the current number of known NS–WD binaries in the Galaxy (see, e.g., Cadelano et al. 2015). From the GRB side, we note that indeed only one NS–WD merger has been identified (see analysis of GRB 060614 in Caito et al. 2009). The above implies that, very likely, the majority of the expected mergers are under the threshold of the existing X-ray and gamma-ray detectors.

The aforementioned density rates for all GRB subclasses have been estimated in Ruffini et al. (2016b) assuming no beaming. The presence of beaming would require the observation of achromatic jet breaks in the afterglow light curve. In the present case of short bursts such clear achromatic jet breaks have never been observed. Fong et al. (2015) reported four measured jet breaks in a sample of 11 short bursts: GRB 051221A, GRB 090426A, GRB 111020A, and GRB 130603B (see Table 5 there). However:

(1) GRB 051221A: The break is inferred only from the X-ray light curve, while the contemporary optical and radio data do not support such an interpretation (see Soderberg et al. 2006a).

(2) GRB 090426A: The break is inferred from the optical band only, and there are no contemporary observations in other bands (see Nicuesa Guelbenzu et al. 2011).

(3) GRB 111020A: The break is inferred only from the X-ray light curve, but this interpretation is based on a single upper limit by *Chandra* and no data points (see Fong et al. 2012).

(4) GRB 130603B: The break is inferred from the optical band and is compatible with the radio data. However, contemporary X-ray observations are clearly contradicting this interpretation and present no break at all. In fact, the authors invoke the presence of an extra source to justify what they call "late time X-ray excess" (see Fong et al. 2014).

In addition, Aimuratov et al. (2017a) and Ruffini et al. (2018a) have shown that, in all the identified S-GRBs, the GeV emission has been always observed when the source was within the *Fermi*-LAT field of view. This result points as well to no significant presence of beaming in the GeV emission of S-GRBs.

Therefore, all the above points imply that there is still no evidence for the need to assume beaming.

We show in Table 1 a summary of the astrophysical aspects related to the GRB subclasses and their observational properties.

The aim of this article is to use the rate of occurrence of the above GRB subclasses to assess the detectability of their associated GW emission by the ground-based interferometers Advanced LIGO and Advanced Virgo, by the space-based interferometer eLISA, and by the resonant bars, for completeness.

We show in Table 2 a summary of acronyms used in this work.

2. Relevance of the NS Structure and Critical Mass

Having introduced the above seven subclasses of GRBs, the relevance of the NS physics becomes clear, in particular the NS critical mass value, in the definition of subclasses I–II and IV–V.

First, we recall that in our previous works we have adopted an NS critical mass within the range 2.2–3.4 $M_\odot$, depending on the equation of state (EOS) and on the NS angular momentum (Belvedere et al. 2014; Becerra et al. 2015; Cipolletta et al. 2015). These quoted values are for EOSs based on relativistic nuclear mean-field models (in this case the NL3, TM1, and GM1 models) and for an NS angular momentum from $J = 0$ up to $J_{\rm max} \approx 0.7GM^2/c$ (Cipolletta et al. 2015). Hereafter, we adopt the stiffest model, namely, the NL3 EOS, which leads to the largest NS critical mass: from $M_{\rm crit} \approx 2.7\,M_\odot$ at $J = 0$, which, as expected, is lower than the nonrotating critical mass upper limit of 3.2 $M_\odot$ established by Rhoades & Ruffini (1974), to $M_{\rm crit} \approx 3.4\,M_\odot$ at $J_{\rm max}$ (Cipolletta et al. 2015). Our choice of relativistic mean-field theory models is based on the fact that they satisfy important properties such as Lorentz covariance, relativistic self-consistency (hence they do not violate causality), intrinsic inclusion of spin, and a simple mechanism of nuclear matter saturation (see, e.g., Dutra et al. 2014, 2016, for further details on these kinds of models). The above three representative EOSs that we have explored satisfy in addition the astrophysical constraint of leading to an NS critical mass larger than the heaviest massive NS observed, PSR J0348+0432, with $M = 2.01 \pm 0.04\,M_\odot$ (Antoniadis et al. 2013).

As discussed in Ruffini et al. (2016b), the separatrix energy value of $\approx 10^{52}$ erg between subclasses I and II appears as a theoretical estimate of the upper limit to the energy emitted in the hypercritical accretion process onto a $\sim 1.4\,M_\odot$ NS (see, e.g., Becerra et al. 2016) and the aforementioned adopted critical mass. This has been shown to be in agreement with the observations of 20 XRFs and 233 BdHNe (up to the end of 2014). In fact, observationally, the current upper limit for XRFs is $(7.3 \pm 0.7) \times 10^{51}$ erg, and the lower limit for BdHNe is $(9.2 \pm 1.3) \times 10^{51}$ erg (see Ruffini et al. 2016b, for further details). It is clear that the separatrix energy should have some dependence on the initial NS mass undergoing accretion and on the precise value of the nonrotating critical mass. Although the precise value of the latter is yet unknown, it is constrained within the range 2.0–3.2 $M_\odot$, where the lower value is the mass of PSR J0348+0432 and the upper value is the well-established absolute maximum NS mass of Rhoades & Ruffini (1974).

It is clear that similar arguments apply also to the case of subclasses IV and V (Ruffini et al. 2015a), namely, the amount of energy emitted during the NS–NS merger leading to a BH should be $\gtrsim 10^{52}$ erg. Observationally, the current upper limit for S-GRFs is $(7.8 \pm 1.0) \times 10^{51}$ erg, and the lower limit for BdHNe is $(2.44 \pm 0.22) \times 10^{52}$ erg (see Ruffini et al. 2016b, for further details).

The above subclassification is further supported by the fact that GeV emission, expected in the presence of a rotating BH, is indeed observed only in BdHNe (e.g., Ruffini et al. 2015b) and in S-GRBs (e.g., Muccino et al. 2013; Ruffini et al. 2015a,

[9] An additional (but less likely) scenario leading to merging NS–WD systems might occur in an NS–NS approaching the merger phase (Ruffini et al. 2016b). According to Bildsten & Cutler (1992) and Clark & Eardley (1977) (see also references therein), in a very close, NS–NS binary with unequal-mass components, stable mass transfer from the less massive to the more massive NS might occur for appropriate mass ratios in such a way that the donor NS moves outward in the mass-loss process until it reaches the beta-decay instability becoming a low-mass WD.

Table 1
Summary of the Astrophysical Aspects of the Different GRB Subclasses and of Their Observational Properties

	Subclass	In-state	Out-state	$E_{p,i}$ (MeV)	E_{iso} (erg)	$E_{iso,X}$ (erg)	$E_{iso,Gev}$ (erg)	z_{max}	ρ_{GRB} (Gpc^{-3} yr^{-1})
I	XRFs	CO_{core}–NS	νNS–NS	$\lesssim 0.2$	$\sim 10^{48}$–10^{52}	$\sim 10^{48}$–10^{51}	⋯	1.096	100^{+45}_{-34}
II	BdHNe	CO_{core}–NS	νNS–BH	~ 0.2–2	$\sim 10^{52}$–10^{54}	$\sim 10^{51}$–10^{52}	$\lesssim 10^{53}$	9.3	$0.77^{+0.09}_{-0.08}$
III	BH–SN	CO_{core}–BH	νNS–BH	$\gtrsim 2$	$>10^{54}$	$\sim 10^{51}$–10^{52}	$\gtrsim 10^{53}$	9.3	$\lesssim 0.77^{+0.09}_{-0.08}$
IV	S-GRFs	NS–NS	MNS	$\lesssim 2$	$\sim 10^{49}$–10^{52}	$\sim 10^{49}$–10^{51}	⋯	2.609	$3.6^{+1.4}_{-1.0}$
V	S-GRBs	NS–NS	BH	$\gtrsim 2$	$\sim 10^{52}$–10^{53}	$\lesssim 10^{51}$	$\sim 10^{52}$–10^{53}	5.52	$(1.9^{+1.8}_{-1.1}) \times 10^{-3}$
VI	U-GRBs	νNS–BH	BH	$\gtrsim 2$	$>10^{52}$	⋯	⋯	⋯	$\gtrsim 0.77^{+0.09}_{-0.08}$
VII	GRFs	NS–WD	MNS	~ 0.2–2	$\sim 10^{51}$–10^{52}	$\sim 10^{49}$–10^{50}	⋯	2.31	$1.02^{+0.71}_{-0.46}$

Note. In the first four columns we indicate the GRB subclasses and their corresponding in-states and out-states. In the fifth through eighth columns we list the ranges of $E_{p,i}$ and E_{iso} (rest-frame 1–10^4 keV), $E_{iso,X}$ (rest-frame 0.3–10 keV), and $E_{iso,GeV}$ (rest-frame 0.1–100 GeV). The ninth and tenth columns list, for each GRB subclass, the maximum observed redshift and the local observed rate ρ_{GRB} obtained in Ruffini et al. (2016b). We refer the reader to Appendix B for details on the method used to calculate ρ_{GRB}.

Table 2
Acronyms Used in This Work in Alphabetic Order

Extended Wording	Acronym
Binary-driven hypernova	BdHN
Black hole	BH
Carbon–oxygen core	CO_{core}
Gamma-ray burst	GRB
Gamma-ray flash	GRF
Induced gravitational collapse	IGC
Massive neutron star	MNS
Neutron star	NS
New neutron star created in the SN explosion	νNS
Short gamma-ray burst	S-GRB
Short gamma-ray flash	S-GRF
Supernova	SN
Ultrashort gamma-ray burst	U-GRB
White dwarf	WD
X-ray flash	XRF

2016a; Aimuratov et al. 2017b) and absent in XRFs and S-GRFs where no BH is formed (see Figure 10 and the Appendix in Ruffini et al. 2016b, for more details).

Therefore, the direct observation of the separatrix energy between XRFs and BdHNe, as well as between S-GRFs and S-GRBs, and their precise occurrence rate ratio give crucial information on the actual NS critical mass value.

3. Ingredient Setup for the Computation of the GW Emission and Its Detectability

We have recalled in Section 1 that the evolution of the binary progenitors of both short and long GRBs leads to compact binaries that will eventually merge in a characteristic timescale and emit GWs. We turn in the following sections to assessing the detectability of the GW emission by these merging binaries by Advanced LIGO.

In order to do this, we make the following drastic simplified assumptions:

1. Although it is manifest that the release of gravitational energy of the system in the merger phase is dominated by the X-ray, gamma-ray, and GeV emission (see Table 1), we assume that the binary dynamics is only driven by the GW emission.
2. Consistent with the above GW emission dominance assumption, we further assume that the GW waveform is known and thus one can use the matched filtering technique to estimate the signal-to-noise ratio. The actual GW waveform under the realistic conditions of electromagnetic emission dominance is still unknown.
3. To estimate the maximum distance of GW detectability, we adopt optimally oriented sources with respect to the detector.

The above assumptions are made with the only aim of establishing an absolute upper limit to the GW emission and its putative detectability under the most optimistic conditions. Similarly, we assume that the binarity of the system does not compromise the interior structure of the NS (see Section 2).

The minimum GW frequency detectable by the broadband Advanced LIGO interferometer is $f_{min}^{aLIGO} \approx 10$ Hz (LIGO Scientific Collaboration et al. 2015). Since during the binary inspiral the GW frequency is twice the orbital one, the above implies that a binary is inside the Advanced LIGO band for orbital periods $P_{orb} \lesssim 0.2$ s.

3.1. Systems to Be Analyzed

The CO_{core}–NS binaries, in-states of XRFs and BdHNe, and CO_{core}–BH binaries, in-states of BH–SNe, are not detectable by Advanced LIGO since they have orbital periods $P_{orb} \gtrsim$ 5 minutes $\gg 0.2$ s (Becerra et al. 2016). After their corresponding hypercritical accretion processes, it is clear that the out-states of both XRFs and BdHNe can become the in-states of short GRBs, as follows (Becerra et al. 2015; Fryer et al. 2015b; Ruffini et al. 2016b).

First, let us discuss the out-states of XRFs. We have mentioned that XRFs can either get disrupted by the SNe and lead to runaway NSs or, in the case in which the binary remains bound, lead to a νNS–NS system. Since $\rho_{XRF} > \rho_{S\text{-}GRF} + \rho_{S\text{-}GRB}$, such νNS–NS binaries, out-states of XRFs, could be the in-states of S-GRFs (NS–NS mergers leading to an MNS) and/or S-GRBs (NS–NS mergers leading to a BH). By denoting the total rate of short bursts as $\rho_{short} \equiv \rho_{S\text{-}GRF} + \rho_{S\text{-}GRB}$, our estimated rates would imply that the fraction of systems that appear to remain bound as νNS–NS is $(\rho_{short}/\rho_{XRF}) \approx 2\%$–$8\%$, while 92%–98% of XRFs are disrupted by the SN explosion. Interestingly, this is consistent with the fraction of bound NS–NS obtained in population synthesis analyses (see, e.g., Dominik et al. 2012, 2015; Postnov & Yungelson 2014; Fryer et al. 2015a; Belczynski et al. 2016, and references therein; Appendix A.4 and A.5). Therefore, these merging νNS–NS binaries are clearly included in the S-GRF and S-GRB population. Such binaries are at birth undetectable by Advanced LIGO since they have initially $P_{\rm orb} \gtrsim 5$ minutes $\gg 0.2$ s, but their merging can become detectable.

We have already recalled in the Introduction that in Fryer et al. (2015b) it was shown that, contrary to the case of XRFs, most BdHNe are expected to remain bound after the SN explosion in view of their short orbital periods and more massive accretion process. We have argued that those mergers would lead to the new class of short bursts, the U-GRBs (Fryer et al. 2015b), which, however, have still to be electromagnetically identified. The same applies to the νNS–BH systems produced by BH–SN systems, with the only difference being the mass of the BH, which, by definition of this subclass, can be larger than the NS critical mass since this BH is formed from direct collapse of a massive star. All the above merging νNS–BH binaries are, by definition, the U-GRB population. Such binaries are at birth undetectable by Advanced LIGO because their initial orbital periods $P_{\rm orb} \gtrsim 5$ minutes $\gg 0.2$ s, but their merger can become detectable.

In the case of NS–WD binaries, the WD large radius and its very likely tidal disruption by the NS make their GW emission hard to detect (see, e.g., Paschalidis et al. 2009). Thus, we do not consider NS–WD binaries in the following GW discussion.

To summarize, we are going to analyze below the GW emission and detectability of S-GRF and S-GRB, the mergers of νNS–NS produced by XRFs, as well as of U-GRBs, which are the mergers of the νNS–BH produced by BdHNe and BH–SNe.

3.2. Binary Component Masses

For S-GRFs, we consider the simple case of nonspinning, equal-mass NS–NS merging binaries, i.e., $m_1 = m_2 = m$. The precise value of the merging NS masses leading to a BH is still poorly known; thus, we have chosen as an upper limit roughly half the maximum NS critical mass (see Section 2). Thus, we shall explore mass values $m \approx 1$–$1.7\,M_\odot$.

For S-GRBs, we also consider nonspinning, equal-mass NS–NS merging binaries. For self-consistency, we choose a range of component masses starting from the upper edge of the S-GRF one, i.e., $m \approx 1.7\,M_\odot$, up to the maximum nonrotating stable mass, i.e., $m \approx 2.8\,M_\odot$.

For U-GRBs, we adopt in the case of out-states of BdHNe $m_1 = 1.5\,M_\odot$ for the νNS and $m_{\rm BH} = 2.7$–$3.4\,M_\odot$ for the BH (see Section 2). In the case of out-states of BH–SNe, we adopt $m_1 = 1.5\,M_\odot$ for the νNS and $m_{\rm BH} = 3.4$–$10\,M_\odot$ for the BH, consistent with the assumption that the BH in this subclass has been previously formed in the binary evolution and therefore it can have a mass larger than the NS critical mass.

3.3. Signal-to-noise Ratio

We first recall the main ingredients needed to estimate the detectability of the aforementioned merging binaries associated with the different GRB classes. The signal $h(t)$ induced in the detector is

$$h(t) = F_+(\theta, \phi, \psi)h_+(t, \iota, \beta) + F_\times(\theta, \phi, \psi)h_\times(t, \iota, \beta), \quad (1)$$

where h_+ and $h_\times$ are the two polarizations of the GW; ι and β are the polar and azimuthal angles of the unit vector from the source to the detector, relative to a coordinate system centered in the source. The detector pattern functions F_+ and $F_\times$ depend on the localization of the source with respect to the detector, i.e., they depend on the spherical polar angles θ and ϕ of the source relative to a coordinate system centered in the detector. The pattern functions also depend on the polarization angle ψ.

Since the GW signal might be deep inside the noise, the signal-to-noise ratio, denoted hereafter by ρ, is usually computed using the matched filter technique, i.e. (Flanagan & Hughes 1998),

$$\rho^2 = 4\int_0^\infty \frac{|\tilde{h}(f)|^2}{S_n(f)}df, \quad (2)$$

where f is the GW frequency in the detector's frame, $\tilde{h}(f)$ is the Fourier transform of $h(t)$, and $\sqrt{S_n(f)}$ is the one-sided amplitude spectral density (ASD) of the Advanced LIGO noise. We recall that in the detector's frame the GW frequency is redshifted by a factor of $1 + z$ with respect to the one in the source's frame, f_s, i.e., $f = f_s/(1 + z)$.

The exact position of the binary relative to the detector and the orientation of the binary rotation plane are usually unknown; thus, it is a common practice to estimate the signal-to-noise ratio averaging over all the possible locations and orientations, i.e.,

$$\langle\rho^2\rangle = 4\int_0^\infty \frac{\langle|\tilde{h}(f)|^2\rangle}{S_n(f)}df = 4\int_0^\infty \frac{h_c^2(f)}{f^2 S_n(f)}df, \quad (3)$$

with $h_c(f)$ the characteristic strain (Flanagan & Hughes 1998)

$$h_c = \frac{(1 + z)}{\pi d_l}\sqrt{\frac{\langle F_+^2\rangle}{2}\frac{G}{c^3}\frac{dE}{df_s}[(1 + z)f]}, \quad (4)$$

where

$$d_l = \frac{(1 + z)c}{H_0}\int_0^z [\Omega_M(1 + x)^3 + \Omega_\Lambda]^{-1/2}dx \quad (5)$$

is the source luminosity distance and we have used the fact that $\langle F_+^2\rangle = \langle F_\times^2\rangle$ and $\langle F_+ F_\times\rangle = 0$. We recall that $\langle F_+^2\rangle = 1/5$ for an interferometer and $\langle F_+^2\rangle = 4/15$ for a resonant bar (see, e.g., Maggiore 2007). We adopt a ΛCDM cosmology with $H_0 = 71$ km s^{-1} Mpc^{-1}, $\Omega_M = 0.27$, and $\Omega_\Lambda = 0.73$ (Rigault et al. 2015). It is important to recall that, as we have mentioned, we are interested in estimating the GW detectability under the most optimistic conditions. Thus, to estimate the maximum distance of GW detectability, we adopt in Section 3 the ansatz of optimally oriented sources with respect to the detector. The above averaging procedure is here used with the only aim of giving an estimate of the GW strain amplitude, h_c, compared and contrasted below in Section 5 with the detector's strain noise.

4. GW Energy Spectrum

In general, a GW-driven binary system evolves in time through two regimes: the first is the *inspiral regime*, and the second, which we refer hereafter to as the *merger regime*, is composed in the most general case of the final plunge, the merger, and the ringdown (oscillations) of the newly formed object.

4.1. Inspiral Regime

During the inspiral regime, the system evolves describing quasi-circular orbits, and it is well described by the traditional point-like quadrupole approximation (Peters & Mathews 1963; Peters 1964; Rees et al. 1974; Landau & Lifshitz 1975). The GW frequency is twice the orbital frequency ($f_s = 2f_{\rm orb}$) and grows monotonically. The energy spectrum during the inspiral regime is

$$\frac{dE}{df_s} = \frac{1}{3}(\pi G)^{2/3} M_c^{5/3} f_s^{-1/3}, \tag{6}$$

where $M_c = \mu^{3/5} M^{2/5} = \nu^{3/5} M$ is the called *chirp mass*, $M = m_1 + m_2$ is the total binary mass, $\mu = m_1 m_2/M$ is the reduced mass, and $\nu \equiv \mu/M$ is the symmetric mass-ratio parameter. A symmetric binary ($m_1 = m_2$) corresponds to $\nu = 1/4$, and the test-particle limit is $\nu \to 0$. The total energy emitted during this regime can be estimated as the difference of the energy of the binary between infinity and the one at the last circular orbit (LCO). For a test particle in the Schwarzschild background the LCO is located at $r_{\rm LCO} = 6GM/c^2$, its energy is $\sqrt{8/9}\,\mu c^2$, and then

$$\Delta E_{\rm insp} = (1 - \sqrt{8/9})\mu c^2. \tag{7}$$

4.2. Merger Regime

The GW spectrum of the merger regime is characterized by a GW burst (see, e.g., Davis et al. 1971; Shibata & Taniguchi 2011; Bernuzzi et al. 2015). Thus, to estimate whether this part of the signal contributes to the signal-to-noise ratio, it is sufficient to estimate the location of the GW burst in the frequency domain and its energy content. We recall that, in general, the merger regime is composed of plunge+merger+ringdown. The frequency range spanned by the GW burst is $\Delta f = f_{\rm qnm} - f_{\rm merger}$, where $f_{\rm merger}$ is the frequency at which the merger starts and $f_{\rm qnm}$ is the frequency of the ringing modes of the newly formed object after the merger, and the energy emitted is $\Delta E_{\rm merger}$. With these quantities defined, we can estimate the typical value of the merger regime spectrum as

$$\left(\frac{dE}{df_s}\right)_{\rm merger} \sim \frac{\Delta E_{\rm merger}}{\Delta f}. \tag{8}$$

Numerical relativity simulations (e.g., Shibata & Taniguchi 2011; Bernuzzi et al. 2015) show that finite size effects might end the inspiral regime before the LCO. After this point, the GW spectrum damps exponentially. For the case of NS–NS the merger starts in an orbit larger than the LCO, and for the case of an NS–BH, as we will see below, the merger can occur below the LCO, making the spectrum similar to a BH–BH merger. When the merger occurs well before the LCO, there is no plunge. Therefore, the emitted energy will be less than the case when the plunge is present. We can therefore obtain an upper limit to $\Delta E_{\rm merger}$ by adopting the energy emitted during the plunge-merger-ringdown of a BH–BH merger (Detweiler & Szedenits 1979)

$$\Delta E_{\rm merger} \approx 0.5\nu^2 M c^2. \tag{9}$$

To complete the estimate of the merger regime spectrum, we have to estimate the value of Δf in the different cases of interest.

4.2.1. NS–NS Merger

The approach to the merger point, $r = r_{\rm merger}$, depends on the nature of the binary system. Typically, the merger is assumed to start at the point of maximum GW strain (see, e.g., Bernuzzi et al. 2015, and references therein). However, since the transition from a binary system to a single merged object is not sharply definable, different definitions of the merger point in the literature can be found (see, e.g., Kawaguchi et al. 2015). For our purpose it is sufficient to estimate the frequency at "contact," namely, the frequency at a binary separation $r_{\rm contact} \approx r_1 + r_2$, where r_i is the radius of the i-component. This certainly sets a lower limit to the frequency at maximum strain at merger, i.e., $r_{\rm contact} \gtrsim r_{\rm merger}$. Thus, we adopt for these systems

$$f_{\rm merger}^{\rm NS-NS} \approx f_{\rm contact}^{\rm NS-NS} = \frac{1}{\pi}\frac{c^3}{GM}\left[\frac{\mathcal{C}_1\mathcal{C}_2(1+q)}{\mathcal{C}_1 + q\mathcal{C}_2}\right]^{3/2}, \tag{10}$$

where $q = m_2/m_1$ is the mass ratio, which is related to the symmetric mass-ratio parameter by $\nu = q/(1+q)^2$, and $\mathcal{C}_i \equiv Gm_i/c^2 r_i$ is the compactness of the i-component.

For a mass-symmetric NS–NS binary, we have that $f_{\rm contact}^{\rm NS-NS} \approx (1/\pi)(c^3/G)\mathcal{C}_{\rm NS}^{3/2}/M$, where $\mathcal{C}_{\rm NS} \equiv \mathcal{C}_1 = \mathcal{C}_2$ is the compactness parameter of the initial NS. For example, for the NL3 EOS, the NS compactness lies in the range $\mathcal{C}_{\rm NS} \approx 0.14$–$0.3$ for an NS mass 1.4–2.8 $M_\odot$ (see, e.g., Cipolletta et al. 2015). Thus, using the same EOS, we have, for an $M = (1.4 + 1.4)\ M_\odot = 2.8\ M_\odot$ binary, $f_{\rm contact}^{\rm NS-NS} \approx$ 1.34 kHz and, for an $M = (2.0 + 2.0)\ M_\odot = 4.0\ M_\odot$ binary, $f_{\rm contact}^{\rm NS-NS} \approx 1.43$ kHz.

In the merger regime either a BH or an MNS can be formed. If the merger does not lead to a BH, the merger frequency is dominated by the frequency of the quasi-normal modes of the MNS formed. This frequency is of the order of

$$f_{\rm qnm}^{\rm MNS} \approx \frac{1}{\pi}\left(\frac{GM}{R^3}\right)^{1/2} = \frac{1}{\pi}\left(\frac{c^3}{G}\right)\frac{\mathcal{C}_{\rm MNS}^{3/2}}{M}, \tag{11}$$

where R is the radius of the MNS and $\mathcal{C}_{\rm MNS} \equiv GM/(c^2R)$ is its compactness. Thus, in the case of S-GRFs the value of Δf is

$$\Delta f_{\rm S\text{-}GRF} \equiv f_{\rm qnm}^{\rm MNS} - f_{\rm contact}^{\rm NS-NS} \approx (\mathcal{C}_{\rm MNS}^{3/2} - \mathcal{C}_{\rm NS}^{3/2})\frac{c^3}{\pi GM}. \tag{12}$$

If the merger forms a BH, the merger frequency is dominated by the frequency of the quasi-normal modes of the BH formed, namely, the GW-burst spectrum peaks at the frequency (Davis et al. 1971, 1972)

$$f_{\rm qnm}^{\rm BH} \approx \frac{0.32}{2\pi}\frac{c^3}{GM}, \tag{13}$$

i.e., $f_{\rm qnm} \approx 3.4$ kHz for a Schwarzschild BH of 3 $M_\odot$. In the case of a rotating BH, namely, a Kerr BH, the peak frequency shifts to higher values (Detweiler 1980). Thus, the value of $f_{\rm qnm}^{\rm BH}$ given by Equation (13) can be considered as a lower bound to the actual peak frequency. Thus, in the case of

S-GRBs the value of Δf is

$$\Delta f_{\text{S-GRB}} \equiv f_{\text{qnm}}^{\text{BH}} - f_{\text{contact}}^{\text{NS-NS}} \approx (0.16 - \mathcal{C}_{\text{NS}}^{3/2})\frac{c^3}{\pi GM}. \quad (14)$$

In either case of BH or MNS formation, $f_{\text{qnm}} > f_{\text{contact}}$ is satisfied. It can be checked that the above frequency estimates are consistent with values obtained from full numerical relativity simulations (see, e.g., Anninos et al. 1995; Bernuzzi et al. 2015).

4.2.2. NS–BH Merger

For an NS–BH merger, the approach to merger is different since general relativistic effects avoid the objects to go all the way to the "contact" point following circular orbits. For example, let us assume $m_1 = m_{\text{BH}} \approx 3\,M_\odot$ and $m_2 = M_{\text{NS}} \approx 1.5\,M_\odot$, so that $M = 1.5 + 3.0\,M_\odot = 4.5\,M_\odot$. In this case $r_1 = 2Gm_{\text{BH}}/c^2$ (for a Schwarzschild BH) and $r_2 = Gm_2/(c^2\mathcal{C}_2)$, so $r_{\text{contact}} \approx 3.3GM/c^2$. Within the test-particle limit, the LCO around a Schwarzschild BH occurs at $r_{\text{LCO}} = 6Gm_{\text{BH}}/c^2 \approx 6GM/c^2 > r_{\text{contact}}$. Thus, we have that $r_{\text{contact}} < r_{\text{LCO}}$, which suggests that an NS–BH binary, similar to the case of a BH–BH one, can pass from the inspiral regime, to the plunge from $r_{\text{plunge}} = r_{\text{LCO}}$ to merger at $r_{\text{merger}} \approx r_{\text{contact}}$, to the ringing of the newly formed BH. At r_{plunge}, the GW frequency is

$$f_{\text{plunge}}^{\text{NS-BH}} \approx \frac{1}{\pi}\left(\frac{GM}{r_{\text{LCO}}^3}\right)^{1/2} = \frac{1}{\pi 6^{3/2}}\left(\frac{c^3}{GM}\right), \quad (15)$$

and as in the previous case of BH formation from an NS–NS merger, the NS–BH post-merger GW spectrum will be dominated by frequencies given by Equation (13). Namely, for the present example $f_{\text{plunge}}^{\text{NS-BH}} \approx 980$ Hz and $f_{\text{qnm}}^{\text{BH}} \approx 2.3$ kHz.

Thus, in the case of NS–BH merger (U-GRB subclass), the value of Δf is

$$\Delta f_{\text{U-GRB}} \equiv f_{\text{qnm}}^{\text{BH}} - f_{\text{plunge}}^{\text{NS-BH}} \approx 0.092\frac{c^3}{\pi GM}. \quad (16)$$

In the above analysis we have neglected the possibility that the NS can be tidally disrupted by the BH before it reaches $r = r_{\text{LCO}}$. The NS is disrupted by the BH if $r_{\text{LCO}} < r_{\text{td}}$, where r_{td} is the tidal disruption radius. The value of r_{LCO} and r_{td} for an NS–BH system depends both on the binary mass ratio $q \equiv m_2/m_1 \leqslant 1$ and on the NS compactness $\mathcal{C}_{\text{NS}}$, which depends, in turn, on the NS mass and EOS. Numerical simulations of NS–BH binary mergers adopting a polytropic EOS for the NS matter suggest $r_{\text{td}} \approx 2.4q^{-1/3}R_{\text{NS}}$ and $r_{\text{LCO}} \approx 6GM/c^2[1 - 0.44q^{1/4}(1 - 3.54\mathcal{C}_{\text{NS}}]^{-2/3}$ (see Shibata & Taniguchi 2011, and references therein). The ratio $r_{\text{td}}/r_{\text{LCO}}$ is a decreasing function of the BH mass for given NS mass (but always close to unity). If we extrapolate these results to BH masses in the range of 3–10 $M_\odot$ and an NS of 1.5 $M_\odot$ obeying the NL3 EOS, we have $r_{\text{LCO}} < r_{\text{td}}$ for $m_{\text{BH}} \lesssim 6\,M_\odot$ and $r_{\text{LCO}} > r_{\text{td}}$ otherwise. It is clear that the specific range of NS and BH masses for which there is tidal disruption is highly sensitive to the compactness of the NS and hence to the nuclear EOS, and thus more simulations using a wide set of updated nuclear EOSs are needed to assess this issue. If tidal disruption occurs, the inspiral regime will cut off at a GW frequency

$$f_{\text{td}}^{\text{NS-BH}} \approx \frac{1}{\pi}\left(\frac{GM}{r_{\text{td}}^3}\right)^{1/2}. \quad (17)$$

Since r_{td} is near r_{LCO} for our systems, and to not introduce further uncertainties in our estimates, we shall adopt that the inspiral regime of our NS–BH systems ends at the GW frequency given by Equation (15).

5. Characteristic Strain and Detector Sensitivity

From Equations (6) and (8) and with the knowledge of the energy released in GWs (Equation (9)) and the spanned frequencies in the merger regime (see Table 3), we can estimate the characteristic strain given by Equation (4), which can be compared and contrasted with the strain noise of GW detectors.

Figure 1 shows the GW signal ASD produced by S-GRFs, S-GRBs, and U-GRBs, obtained with the aid of Equation (4). In this figure we adopt a (1.4+1.4) $M_\odot$ νNS–NS merger for S-GRFs, a (2.0+2.0) $M_\odot$ νNS–NS merger for S-GRBs, a (1.5+3.0) $M_\odot$ νNS–BH merger for U-GRBs produced by out-states of BdHNe, and a (1.5+10.0) $M_\odot$ νNS–BH merger for U-GRBs produced by out-states of BH–SNe. We have assumed in this plot that these sources are located at the closest luminosity distance d_l at which each subclass has been observed (see Table 3 for details). We show the noise ASD of Advanced LIGO in the current run (O1) and in the expected 2022+ run (Abbott et al. 2016); the expected noise ASD of Advanced Virgo (BNS-optimized; Abbott et al. 2016); the expected noise ASD of the space-based interferometer eLISA for the N2A1, N2A2, and N2A5 configurations (see, e.g., Klein et al. 2016); and the noise ASD of the NAUTILUS bar detector for a 1 ms GW burst (Astone et al. 2006, 2008). Narrowband resonant bar detectors (such as ALLEGRO, AURIGA, EXPLORER, NAUTILUS, and NIOBE) are sensitive within a bandwidth of ∼1–10 Hz around the resonant frequency, which is typically $f_0 \sim 1$ kHz (see, e.g., Table 2 in Camp & Cornish 2004, for a summary of the properties of the bar detectors). The bar detector with the wider bandwidth is NAUTILUS, with a minimum strain spectral noise $\sqrt{S_n} = 10^{-21}\,\text{Hz}^{-1/2}$ at $f_0 = 935$ Hz and $\sqrt{S_n} \leqslant 10^{-20}\,\text{Hz}^{-1/2}$ in a bandwidth of ∼30 Hz around f_0 (Astone et al. 2008). This implies that a 1 ms GW burst would be detected by this instrument if it has a strain amplitude $h \gtrsim 3 \times 10^{-19}$ (Astone et al. 2006, 2008).

From this figure we can conclude the following for the NS–NS and NS–BH binaries associated with S-GRFs, S-GRBs, and U-GRBs:

1. *Before merging:* they transit, during their inspiral regime which spans the frequency range $f < f_{\text{merger}}/(1 + z)$ (see in Table 3 the frequencies and redshift), first the eLISA frequency band and then enter the Advanced LIGO-Virgo ones in the final orbits prior to the merging process (when $P_{\text{orb}} < 0.2$ s). The narrow bandwidth of the bar detectors does not cover these frequencies. For the adopted distances we see that the characteristic strain generated by all these sources is below the sensitivity of eLISA. S-GRFs are below the sensitivity of Advanced LIGO (O1), Advanced Virgo, and NAUTILUS, but inside the sensitivity of Advanced LIGO (2022+). S-GRBs are below the sensitivity of Advanced LIGO (all runs),

Table 3
Properties of the GW Emission of S-GRFs, S-GRBs, and U-GRBs

	$\Delta E_{\rm insp}$ (erg)	$\Delta E_{\rm merger}$ (erg)	$f_{\rm merger}$ (kHz)	$f_{\rm qnm}$ (kHz)	$z_{\rm min}^{\rm obs}$	$d_{l_{\rm min}}$ (Mpc)	$d_{\rm GW}$ (Mpc)		
							O1	O2	2022+
S-GRF	7.17×10^{52}	1.60×10^{53}	1.20	3.84	0.111	508.70	90.51–181.02	181.02–271.52	452.54
S-GRB	1.02×10^{53}	2.28×10^{53}	1.43	2.59	0.903	5841.80	121.84–243.67	243.67–365.51	609.18
U-GRB	1.02×10^{53}	2.03×10^{52}	0.98	2.30	0.169	804.57	126.71–253.43	253.43–380.14	633.57
U-GRB (BH–SN)	1.34×10^{53}	1.35×10^{53}	0.38	0.90	0.169	804.57	197.86–395.71	395.71–593.57	989.28

Note. We have made the Drastic simplified assumption that the binary evolution is only driven by GW emission, although it is manifest that the gravitational energy of the system in the merger phase is dominated by the radio, optical, X-ray, gamma-ray, and GeV emission (see Table 1). This assumption is made with the only aim of establishing an absolute upper limit to the GW emission and its detectability under the most optimistic conditions. Column (1): GRB subclass. Column (2): energy emitted in GWs during the inspiral regime $\Delta E_{\rm insp}$ given by Equation (7). Column (3): energy emitted in GWs during the merger regime (plunge+merger+ringdown) $\Delta E_{\rm merger}$ given by Equation (9). Column (4): GW frequency at merger. Column (5): GW frequency of the ringdown regime. Column (6): lowest cosmological redshift value $z_{\rm min}^{\rm obs}$ at which each subclass has been observed. Column (7): luminosity distance corresponding to $z_{\rm min}^{\rm obs}$, $d_{l_{\rm min}}$, estimated from Equation (5). Columns (8)–(10): GW horizon calculated with the sensitivity of advanced LIGO during the O1 and O2 runs and with the expected final sensitivity including LIGO-India (2022+), respectively. It can be seen that the current GW horizon is much smaller than the observed distances of GRBs, impeding a positive detection by advanced LIGO. Only in the case of U-GRB (BH–SN) is a possible detection foreseen during the run 2022+. See also Table 4. We have used for S-GRFs (1.4+1.4) $M_\odot$, for S-GRBs (2.0+2.0) $M_\odot$, and for U-GRBs (1.5+3.0) $M_\odot$ and (1.5+10.0) $M_\odot$ for the out-states of BdHNe and of BH–SNe, respectively. Even if no U-GRB has yet been identified, we use here the values of $z_{\rm min}^{\rm obs}$ and $d_{l_{\rm min}}$ corresponding to the closest BdHN observed.

Advanced Virgo, and NAUTILUS. U-GRBs from out-states of BdHNe are below the sensitivity of Advanced LIGO (O1), Advanced Virgo, and NAUTILUS, but inside the sensitivity of Advanced LIGO (2022+). U-GRBs from out-states of BH–SNe are below the sensitivity of Advanced LIGO (O1) and NAUTILUS, inside the sensitivity of Advanced LIGO (2022+), and marginally inside the sensitivity of Advanced Virgo.

2. *Merging:* the merging regime, which expands frequencies from $f_{\rm contact}/(1+z)$ to $f_{\rm qnm}/(1+z)$ (see in Table 3 the frequencies and redshift), is outside the eLISA frequency band but inside the Advanced LIGO-Virgo and bar detector ones. The characteristic strain in this final merger phase $h \sim 10^{-24}$ to 10^{-23} is, unfortunately, well below the sensitivity of all of them (see also Kobayashi & Mészáros 2003, for similar conclusions for Advanced LIGO).

From the above it can be seen that the most interesting instrument for the possible detection of the GW emission from binaries associated with GRBs is Advanced LIGO. Therefore, we estimate in the next section the expected detection rates by Advanced LIGO-Virgo (see Figure 2 and Table 4).

6. GW Detection Rate

We assume a threshold for the Advanced LIGO-Virgo single detector $\rho_0 = 8$ (Abbott et al. 2016). This minimum ρ_0 defines a maximum detection distance or GW horizon distance, which is denoted as $d_{\rm GW}$. This horizon corresponds to the most optimistic case when the binary is just above the detector and the binary plane is parallel to the detector plane, i.e., $\theta = \phi = \iota = 0$ (Allen et al. 2012):

$$d_{\rm GW} = \frac{2A}{\rho_0}\left(\int_0^\infty \frac{f^{-7/3}}{S_n(f)}df\right)^{1/2}, \tag{18}$$

where $A = 5/(24\pi^{4/3})^{1/2}(GM_c/c^3)^{5/6}c$. Since not all the sources are optimally aligned with the detector, the number of detected sources inside a sphere of radius $d_{\rm GW}$ will be a fraction $\mathcal{F}^3$ of the total. This fraction determines the so-called "range" of the detector, $\mathcal{R} = \mathcal{F} d_{\rm GW}$, where $\mathcal{F}^{-1} = 2.2627$ (see Finn & Chernoff 1993, for details). In order to give an estimate of the annual number of detectable binaries associated with GRBs, we use the *search volume* as computed in Abbott et al. (2016), $\mathcal{V}_s = V_{\rm max}^{\rm GW}\mathcal{T}$, where $V_{\rm max}^{\rm GW} = (4\pi/3)\mathcal{R}^3$ and $\mathcal{T}$ is the observing time accounting for the detector's duty cycles. We use here the lower and upper values of $\mathcal{R}$ and $\mathcal{V}_s$ for a (1.4+1.4) $M_\odot$ NS binary for the different observational campaigns reported in Abbott et al. (2016): 2015/2016 (O1) with $\mathcal{R} = 40$–80 Mpc, $\mathcal{T} = 3$ months, $\mathcal{V}_S = (0.5$–$(4) \times 10^5$ Mpc^3 yr; 2016/2017 (O2) with $\mathcal{R} = 80$–120 Mpc, $\mathcal{T} = 6$ months, $\mathcal{V}_S = (0.6$–$2) \times 10^6$ Mpc^3 yr; 2017/2018 (O3) with $\mathcal{R} = 120$–170 Mpc, $\mathcal{T} = 9$ months, $\mathcal{V}_S = (3$–$10) \times 10^6$ Mpc^3 yr; and the one by the entire network including LIGO-India at design sensitivity (2022+) with $\mathcal{R} = 200$ Mpc, $\mathcal{T} = 1$ year, $\mathcal{V}_S = 4 \times 10^7$ Mpc^3 yr. We can use the above information for a (1.4+1.4) $M_\odot$ binary and extrapolate it to other binaries with different masses using the property that $d_{\rm GW}$ scales with the chirp mass as $M_c^{5/6}$ (see Equation (18)). We show in Table 3 the GW horizon for a specific value of the binary component masses expected for S-GRFs, S-GRBs, and U-GRBs (see Section 3.2).

From the inferred occurrence rates $\rho_{\rm GRB}$ (not to be confused with signal-to-noise ratio ρ) summarized in Table 1, we show in Figure 2 the expected number of GW detections by Advanced LIGO-Virgo for each observational campaign

$$\dot{N}_{\rm GW} = \rho_{\rm GRB}\mathcal{V}_s \tag{19}$$

for S-GRFs, S-GRBs, and U-GRBs as a function of the binary component masses (see Section 3.2).

We compare and contrast the following in Table 4 for the GRB subclasses: the expected GW detection rate by Advanced LIGO-Virgo given by Equation (19), $\dot{N}_{\rm GW}$; the inferred occurrence rate of GRBs, $\dot{N}_{\rm GRB}$; and the observed GRB rate from γ-ray telescopes (AGILE, BATSE, *BeppoSAX*, *Fermi*, *HETE-II*, *INTEGRAL*, Konus/*WIND*, and *Swift*), simply estimated as $\dot{N}_{\rm GRB}^{\rm obs} = N_{\rm GRB}^{\rm obs}/T_{\rm obs}$, where $N_{\rm GRB}^{\rm obs}$ is the number of GRBs detected in the observing time $T_{\rm obs}$. The rate $\dot{N}_{\rm GRB}$ is obtained from the GRB specific rate through the reconstruction of the GRB luminosity function and the study of its evolution with redshift (for details see Ruffini et al. 2016b; Appendix B).

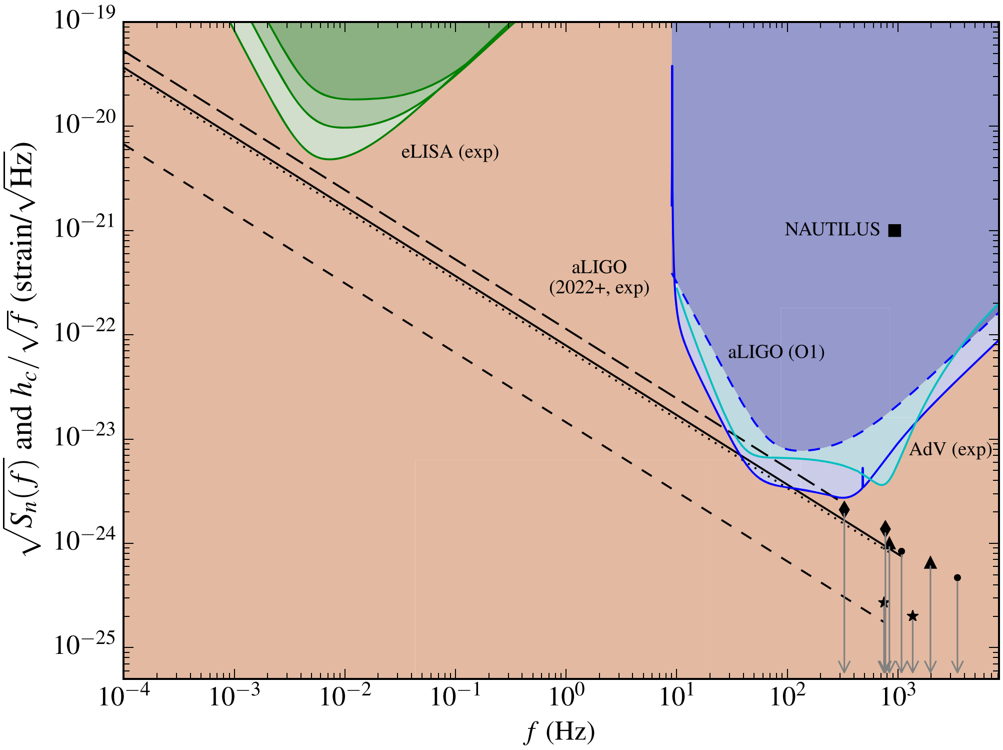

Figure 1. Comparison of the signal's ASD $h_c/\sqrt{f}$ of S-GRFs, S-GRBs, and U-GRBs with the noise's ASD $\sqrt{S_n(f)}$, where S_n is the power spectrum density of the detector's noise of eLISA, of Advanced LIGO (aLIGO), and of the bar detector NAUTILUS. The red lines, from top to bottom, are the expected noise's ASD of the N2A1, N2A2, and N2A5 configurations of eLISA (Klein et al. 2016). The dashed and solid red lines correspond to the noise's ASD of the Advanced LIGO O1 run (2015/2016) and of the expected Advanced LIGO 2022+ run (Abbott et al. 2016), respectively, and the cyan line is the expected noise's ASD of Advanced Virgo (AdV) BNS-optimized (Abbott et al. 2016). The filled square indicates the noise's ASD of the NAUTILUS resonant bar for a 1 ms GW burst (Astone et al. 2006, 2008). The red filled area indicates the region of undetectability by any of the above instruments. We recall that in this plot the GW frequency is redshifted by a factor of $1 + z$ with respect to the source frame value, i.e., $f = f_s/(1 + z)$, for which we use the cosmological redshift and corresponding luminosity distance of the closest observed source of each subclass (see Table 3). The following three curves correspond to the inspiral regime of the coalescence: S-GRFs with (1.4+1.4) $M_\odot$ (solid curve), S-GRBs with (2.0+2.0) $M_\odot$ (short-dashed curve), U-GRB with (1.5+3.0) $M_\odot$ (dotted curve) from out-states of BdHNe, and U-GRB with (1.5+10.0) $M_\odot$ (long-dashed curve) from out-states of BH–SNe. The circle, star, triangle, and diamond correspond to h_c in the merger regime for S-GRFs, S-GRBs, U-GRBs from out-states of BdHNe, and U-GRBs from out-states of BH–SNe, respectively. The first point is located at $f_{\rm merger}/(1 + z)$ and the second at $f_{\rm qnm}/(1 + z)$ (see Table 3). The downward-pointing arrows indicate that these estimates have to be considered as upper limits since we have assumed that all the energy released in the system goes in GWs, which clearly overestimates the GW energy output in view of the dominance of the electromagnetic emission (see Table 4). We have also overestimated the GW energy in the merger regime by using Equation (9), which is the expected GW energy emitted in the plunge+merger+ringdown phases of a BH–BH merger. For binary mergers involving NSs, as we have discussed in Section 4, the energy released in GWs must be necessarily lower than this value.

This estimate, therefore, is larger than $\dot{N}_{\rm GRB}^{\rm obs}$, which is limited to those events beyond the detector sensitivity threshold, falling inside its field of view and within its operational time.

7. Conclusions

Short and long GRBs have been divided into seven subclasses according to their binary nature (Ruffini et al. 2016b). We summarize in Table 1 their main physical properties characterizing the outcome of X-rays, gamma-rays, and high-energy and ultra-high-energy detectors, as well as their occurrence rate. Particularly important for the present work is the specification of the in-states and out-states of the GRB progenitors.

With the knowledge of the nature of the compact-object binaries associated with each GRB subclass and the relevance of the NS structure and critical mass in Section 2, we introduce in Section 3 the main ingredients for the computation of the GW emission and detectability for such systems. We describe in Section 4 the general properties of the GW emission during the inspiral and merger regimes of these binaries. We argue that S-GRFs, S-GRBs, and U-GRBs are the GRB subclasses relevant for the GW analysis. It is manifest that the release of the gravitational energy of the system in the merger phase is dominated by the X-rays, gamma-rays, and GeV emission (see Table 1). In order to evaluate the GW emission, we have made in this work the drastic simplified assumption that the binary evolution is only driven by GW emission. This assumption is of interest, with the only aim of establishing an absolute upper limit and checking the detectability of the GW emission under this most optimistic condition. We compare and contrast in Section 5 the GW characteristic strain amplitude produced by the inspiral and merger regimes with the strain noise of the broadband detectors eLISA and Advanced LIGO-Virgo and of the narrowband resonant bar NAUTILUS. In order to do this, we use the cosmological redshift and corresponding luminosity distance of the closest observed source of each subclass (see Table 3). We show that the inspiral regime is possibly detectable only by Advanced LIGO (see Table 3 and Figure 1) and the merger regime is undetectable by any of these instruments.

Therefore, in Section 6 we assess quantitatively the GW detectability of the inspiral regime of S-GRFs, S-GRBs, and U-GRBs only by Advanced LIGO. We recall that, following

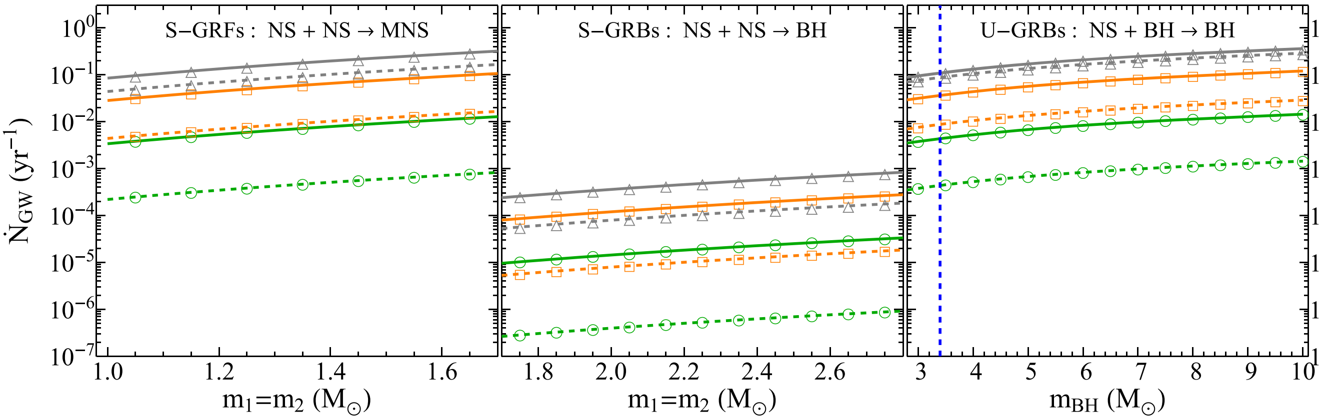

Figure 2. Expected annual GW upper and lower bounds (solid and dashed lines, respectively) for the detections expected from S-GRFs (left panel), S-GRBs (middle panel), and U-GRBs (right panel), for three selected observational campaigns: 2015/2016 (O1; red curves with circles), 2017/2018 (O3; orange curve with squares), and 2022+ (gray curve with triangles). The vertical red dashed line in the plot of U-GRBs separates νNS–BH binaries produced by BdHNe (BH masses equal to the NS critical mass) and BH–SNe (BH masses larger than the NS critical mass).

Table 4
Inferred and Observed Number of GRBs Per Year, and the Corresponding Expected Rate of GW Detections for Each GRB Subclass

GRB Subclass	$\dot{N}_{\rm GRB}$ (yr^{-1})	$\dot{N}_{\rm GRB}^{\rm obs}$ (yr^{-1})	$\dot{N}_{\rm GW}$ (yr^{-1})
XRFs	144–733	1 (1997–2014)	Undetectable
BdHNe	662–1120	14 (1997–2014)	Undetectable
BH–SNe	$\lesssim$662–1120	$\lesssim$14 (1997–2014)	Undetectable
S-GRFs	58–248	3 (2005–2014)	O1: 0.0001–0.002 O2: 0.002–0.01 O3: 0.008–0.05 2022+: 0.1–0.2
S-GRBs	2–8	1 (2006–2014)	O1: (0.1–3.1) $\times 10^{-6}$ O2: (0.1–1.6) $\times 10^{-5}$ O3: (0.6–7.8) $\times 10^{-5}$ 2022+: (0.78–3.12) $\times 10^{-4}$
U-GRBs	662–1120	⋯	O1: (0.9–9) $\times 10^{-4}$ O2: 0.001–0.005 O3: 0.006–0.024 2022+: 0.076–0.094
U-GRBs (BH–SN)	$\lesssim$662–1120	⋯	O1: $\lesssim$0.00036–0.0036 O2: $\lesssim$0.004–0.018 O3: $\lesssim$0.02–0.09 2022+: $\lesssim$0.29–0.36
GRFs	29-153	1 (2005–2014)	Undetectable

Note. Column (1): GRB subclass. Column (2): inferred number of GRBs per year in the entire universe, $\dot{N}_{\rm GRB}$, for each GRB subclass (see also Figure 6 in Ruffini et al. 2016b). Column (3): number of GRBs observed per year, $\dot{N}_{\rm GRB}^{\rm obs}$, obtained from the observations of γ-ray telescopes such as AGILE, BATSE, *BeppoSAX*, *Fermi*, *HETE-II*, *INTEGRAL*, Konus/*WIND*, and *Swift*, in the indicated years of observations (see also Tables 2–6 in Ruffini et al. 2016b). Column (4): expected rate of GW detections by advanced LIGO of all the GRB subclasses, computed for three selected observational campaigns, 2015/2016 (O1), 2016/2017 (O2), and 2017/2018 (O3), and the one by the entire network at design sensitivity including LIGO-India (2022+). The binary component masses used here are the same as in Table 3.

Abbott et al. (2016), we adopt as the threshold for detectability a signal-to-noise ratio equal to 8. We present in Figure 2 and Table 4 the expected detection rate of the GW emission. Four observational campaigns of Advanced LIGO are analyzed: O1 (2015/2016), O2 (2016/2017), O3 (2017/2018), and 2022+, namely the one by the entire network at design sensitivity including LIGO-India. In Table 4 we compare and contrast this rate with the occurrence rate of the GRB subclasses and their rate of observations by γ-ray telescopes.

Keeping the above in mind, we conclude the following for each GRB subclass:

I. XRFs: their νNS–NS out-states transit, during the inspiral regime, which spans the frequency range $f < f_{\rm merger}/(1+z)$ (see Table 3), first the eLISA frequency band and then enter the Advanced LIGO-Virgo ones in the final orbits prior to the merging process (i.e., when $P_{\rm orb} < 0.2$ s). Resonant bar detectors are not sensitive in this inspiral regime frequency range. The characteristic strain generated by these sources in the inspiral regime is below the sensitivity of eLISA. The merger regime, which expands frequencies from $f_{\rm contact}/(1+z)$ to $f_{\rm qnm}/(1+z)$ (see Table 3), is outside the eLISA frequency band but inside the frequency band of Advanced LIGO-Virgo and bar detectors. See Figure 1 for details. These νNS–NS mergers can lead to either S-GRFs or S-GRBs (see in IV and V below the conclusion about their GW detectability).

II. BdHNe: their νNS–BH out-states transit, during the inspiral regime, which spans the frequency range $f < f_{\rm merger}/(1+z)$ (see Table 3), first the eLISA frequency band and then enter the Advanced LIGO-Virgo ones in the final orbits prior to the merging process (i.e., when $P_{\rm orb} < 0.2$ s). Resonant bar detectors are not sensitive in this inspiral regime frequency range. The characteristic strain generated by these sources in the inspiral regime is below the sensitivity of eLISA. The merger regime, which expands frequencies from $f_{\rm contact}/(1+z)$ to $f_{\rm qnm}/(1+z)$ (see Table 3), is outside the eLISA frequency band but inside the frequency band of Advanced LIGO-Virgo and bar detectors. See Figure 1 for details. These νNS–BH mergers lead to U-GRBs (see in VI below the conclusion about their GW detectability).

III. BH–SN: their νNS–BH out-states transit, during the inspiral regime, which spans the frequency range $f < f_{\rm merger}/(1+z)$ (see Table 3), first the eLISA frequency band and then enter the Advanced LIGO-Virgo ones in the final orbits prior to the merging process (i.e., when $P_{\rm orb} < 0.2$ s). Resonant bar detectors are not sensitive in this inspiral regime frequency range. The characteristic strain generated by these sources in the inspiral regime is below the sensitivity of eLISA. The merger regime, which expands frequencies from $f_{\rm contact}/(1+z)$ to $f_{\rm qnm}/(1+z)$ (see Table 3), is outside the eLISA frequency band but inside the frequency band of Advanced LIGO-Virgo and bar detectors. See Figure 1 for details. These νNS–BH mergers lead to U-GRBs (see in VI below the conclusion about their GW detectability).

IV. S-GRFs: the final orbits of the inspiral regime (when $P_{\rm orb} < 0.2$ s) fall inside the frequency band of Advanced LIGO-Virgo and bar detectors. However, the GW energy output in the merger regime leads to a characteristic strain that is not sufficient to be detectable either by any of them. See Figure 1 for details. The inspiral regime is detectable for sources located at distances smaller than 181 Mpc for the O1 Advanced LIGO run and smaller than 452 Mpc for the 2022+ run (see Table 3). The closest S-GRF observed up to now is, however, located at 509 Mpc. See Table 4 for the expected GW detection rate.

V. S-GRBs: the final orbits of the inspiral regime (when $P_{\rm orb} < 0.2$ s) fall inside the frequency band of Advanced LIGO-Virgo and bar detectors. However, the GW energy output in the merger regime leads to a characteristic strain that is not sufficient to be detectable either by any of them. See Figure 1 for details. The inspiral regime is detectable for sources located at distances smaller than 244 Mpc for the O1 Advanced LIGO run and smaller than 609 Mpc for the 2022+ run (see Table 3). The closest S-GRB observed up to now is, however, located at 5842 Mpc. See Table 4 for the expected GW detection rate.

VI. U-GRBs: the final orbits of the inspiral regime (when $P_{\rm orb} < 0.2$ s) fall inside the frequency band of Advanced LIGO-Virgo and bar detectors. However, the GW energy output in the merger regime leads to a characteristic strain that is not sufficient to be detectable either by any of them. See Figure 1 for details. In the case of U-GRBs originating from the BdHN out-states, the inspiral regime is detectable for sources located at distances smaller than 253 Mpc for the O1 Advanced LIGO run and smaller than 634 Mpc for the 2022+ run (see Table 3). In the case of U-GRBs originating from the BH–SN out-states, the inspiral regime is detectable for sources at distances smaller than 396 Mpc for the O1 Advanced LIGO run and smaller than 989 Mpc for the 2022+ run (see Table 3). No U-GRB has yet been electromagnetically identified. The closest distance at which its possible progenitor, namely, a BdHN, is located is 805 Mpc. See Table 4 for the expected GW detection rate.

VII. GRFs: The tidal disruption of the WD by the NS produces an undetectable GW emission (see, e.g., Paschalidis et al. 2009).

We recalled in the Introduction that the simultaneous detection rates of GWs and GRBs have been estimated up to now in the literature only in the case of S-GRFs, in which no BH is formed but instead the merger of the two NSs leads to an MNS. Indeed, it can be seen that the recent GW detection rate estimated by Patricelli et al. (2016) of short bursts at Advanced LIGO design sensitivity (see Table 1 there), 0.04–15 $\rm yr^{-1}$, is consistent with the one of S-GRFs estimated in this work, $\dot{N}_{\rm GW} = 0.1$–$0.2\ \rm yr^{-1}$ (see Table 4). This represents the most favorable case for the possible GW detection by Advanced LIGO-Virgo of NS–NS merger, which, however, does not lead to a BH formation but to an MNS.

We have given in this article, for the first time, a rate for the formation of BHs in both short and long bursts, and this is of clear astrophysical relevance. Among such bursts producing a BH, the most favorable cases for GW detection are those from U-GRBs from BdHNe with $\dot{N}_{\rm GW} = 0.08$–$0.09\ \rm yr^{-1}$ and those from BH–SNe with $\dot{N}_{\rm GW} = 0.3$–$0.4\ \rm yr^{-1}$ (see Table 4). These NS–BH merging binaries were unknown in the literature, and thus their occurrence and GW detection rates are a definite prediction of this work.

Any detection by Advanced LIGO-Virgo of an NS–NS merger or an NS–BH merger will imply a drastic increase of the occurrence rate of events shown here and an examination of the consistency with GRB observations.

We have already given evidence on the unsuitability of the *collapsar* model to explain the GRB observations in Ruffini et al. (2018b). We have published a classification on the ground of the current observations of 480 sources with known redshift (Ruffini et al. 2016b, 2018b), which is both necessary and sufficient, as of today, to cover all GRBs observed. As the number of sources will increase, it is conceivable that the discovery of different systems will be observed, and in that case we will be ready for their inclusion in additional subclasses within our classification scheme.

As we have mentioned, the above are estimates based on the most favorable conditions for GW emission, and realistic $\dot{N}_{\rm GW}$ values will need the assessment of the ratio of GW to electromagnetic energy, which is necessarily smaller than unity from energy conservation.

After the submission of this work, the LIGO-Virgo Collaboration announced the detection of the signal GW 170817 and interpreted it as due to an NS–NS merger (Abbott et al. 2017b). As we have mentioned above, any possible GW detection of an NS–NS merger would imply a revision of its consistency with the inferences from GRB observations. It may then appear that our above conclusions of poor chance of detectability of NS–NS mergers by the Advanced LIGO-Virgo detector network are in tension with the detection of GW 170817 during the O2 run. The association of GW 170817 with GRB 170817A, a weak, short-duration GRB observed by the Gamma-ray Burst Monitor (GBM) on board the *Fermi* satellite (Abbott et al. 2017a; Goldstein et al. 2017) and followed-up in the optical bands (e.g., Cowperthwaite et al. 2017), in the X-rays (e.g., Haggard et al. 2017), and by further gamma-ray facilities (e.g., Savchenko et al. 2017), allows us in the following to make an assessment on this issue.

First, we recall that GRB 170817A, with its isotropic energy emitted in gamma rays of $E_{\rm iso} \approx 5 \times 10^{46}$ erg (Goldstein et al. 2017) and peak luminosity of $(1.7 \pm 0.1) \times 10^{47}\ \rm erg\ s^{-1}$ (Zhang et al. 2017), would belong to the S-GRF subclass if we assume that it is produced in an NS–NS merger. On the other hand, we recall that our estimates of the local density rate of the GRB subclasses (see Table 1), obtained from Ruffini et al. (2016b), are reliable for GRBs with luminosities higher than the lowest GRB luminosity in the subclass sample (see Appendix B for details). In the case of S-GRFs, we had identified GRB 050509B as the source with the lowest energetics, $E_{\rm iso} \approx 8.5 \times 10^{48}$ erg (see Table 4 in Ruffini et al. 2016b), and a peak luminosity of $(1.1 \pm 0.5) \times 10^{51}\,{\rm erg\,s^{-1}}$ (Fox et al. 2005). This implies that our predicted detention rates for the Advanced LIGO-Virgo detectors for S-GRFs are valid for sources with electromagnetic emission over the above values. Even a single observation of a close and underluminous source, such as GRB 170817A, would lead to an increase of the local density rate of this GRB subclass. Indeed, Zhang et al. (2017) have recently estimated the increase in the local density rate when GRB 170817A is included in the sample of short bursts. Following a similar method to the one described in Appendix B, they found that their previously estimated isotropic local density rate of 3.2–5.5 $\rm Gpc^{-3}\,yr^{-1}$, obtained for sources with peak luminosities above $7 \times 10^{49}\,{\rm erg\,s^{-1}}$,[10] increases to a lower limit of 30–630 $\rm Gpc^{-3}\,yr^{-1}$, for sources with peak luminosities above $1.7 \times 10^{47}\,{\rm erg\,s^{-1}}$, i.e., when GW 170817 is included in the sample. The above range implies an increase of the local density rate by a factor of ∼10–100. It is then easy to check, using Table 4, that an increase of such a factor in the S-GRF density rate would imply a detection rate of 0.01–1 $\rm yr^{-1}$ for the O2 observational run, in agreement with the detection of GW 170817.

In fact, the above isotropic density rate inferred by Zhang et al. (2017) is consistent with the NS–NS observed merger rate of 320–4740 $\rm Gpc^{-3}\,yr^{-1}$, inferred by the LIGO Collaboration with the detection of GW 170817 (see Section 5 in Abbott et al. 2017b, for details). This result implies that S-GRFs (or in general all short bursts) are not beamed or, if a beaming is assumed, the jet half-opening angle should be at least as large as 25°–30°.

We thank the referee for suggestions that improved the presentation of our results. M.K. acknowledges the support given by the International Relativistic Astrophysics Erasmus Mundus Joint Doctorate Program under grants 2013–1471, from EACEA of the European Commission. M.M. and J.A.R. acknowledge the partial support of project no. 3101/GF4 IPC-11 and target program F.0679 of the Ministry of Education and Science of the Republic of Kazakhstan. C.C. and S.F. acknowledge INdAM-GNFM for support.

Appendix A
IGC, Hypercritical Accretion, and Long GRBs

We give in this appendix details of the accretion process within the IGC scenario following Fryer et al. (2014, 2015b) and Becerra et al. (2015, 2016).

There are two main physical conditions for which hypercritical (i.e., highly super-Eddington) accretion onto the NS occurs in XRFs and BdHNe. The first is that the photons are trapped within the inflowing material, and the second is that the shocked atmosphere on top of the NS becomes sufficiently hot ($T \sim 10^{10}$ K) and dense ($\rho \gtrsim 10^6\,{\rm g\,cm^{-3}}$) to produce a very efficient neutrino–antineutrino ($\nu\bar{\nu}$) cooling emission. In this way the neutrinos become the main source responsible for releasing the energy gained by accretion, allowing hypercritical accretion to continue.

The first IGC simulations were performed in Fryer et al. (2014), including (1) realistic SN explosions of the $\rm CO_{core}$, (2) the hydrodynamics within the accretion region, and (3) the simulated evolution of the SN ejecta up to their accretion onto the NS. Becerra et al. (2015) then estimated the amount of angular momentum carried by the SN ejecta and how much is transferred to the NS companion by accretion. They showed that the SN ejecta can circularize for a short time and form a disk-like structure surrounding the NS before being accreted. The evolution of the NS central density and rotation angular velocity (the NS is spun up by accretion) was computed from full numerical solutions of the axisymmetric Einstein equations. The unstable limits of the NS are set by the mass-shedding (or Keplerian) limit and the critical point of gravitational collapse given by the secular axisymmetric instability (see, e.g., Becerra et al. 2015, for details).

The accretion rate of the SN ejecta onto the NS is given by

$$\dot{M}_B(t) = \pi\rho_{\rm ej}R_{\rm cap}^2\sqrt{v_{\rm rel}^2 + c_{\rm s,ej}^2},$$
$$R_{\rm cap}(t) = \frac{2GM_{\rm NS}(t)}{v_{\rm rel}^2 + c_{\rm s,ej}^2}, \tag{20}$$

where G is the gravitational constant, $\rho_{\rm ej}$ and $c_{\rm s,ej}$ are the density and sound speed of the ejecta, respectively, $R_{\rm cap}$ and $M_{\rm NS}$ are the NS gravitational capture radius (Bondi–Hoyle radius) and gravitational mass, respectively, and $v_{\rm rel}$ is the ejecta velocity relative to the NS, $\boldsymbol{v}_{\rm rel} = \boldsymbol{v}_{\rm orb} - \boldsymbol{v}_{\rm ej}$, where $|\boldsymbol{v}_{\rm orb}| = \sqrt{G(M_{\rm core} + M_{\rm NS})/a}$ and $\boldsymbol{v}_{\rm ej}$ is the velocity of the SN ejecta (see Figure 3).

Numerical simulations of the SN explosions suggest the adopted homologous expansion of the SN, i.e., $v_{\rm ej}(r, t) = nr/t$, where r is the position of each layer from the SN center and n is the expansion parameter. The density evolves as

$$\rho_{\rm ej}(r, t) = \rho_{\rm ej}^0(r/R_{\rm star}(t), t_0)\frac{M_{\rm env}(t)}{M_{\rm env}(0)}\left(\frac{R_{\rm star}(0)}{R_{\rm star}(t)}\right)^3, \tag{21}$$

where $M_{\rm env}(t)$ is the mass of the $\rm CO_{core}$ envelope, $R_{\rm star}(t)$ is the radius of the outermost layer, and $\rho_{\rm ej}^0$ is the pre-SN $\rm CO_{core}$ density profile, $\rho_{\rm ej}(r, t_0) = \rho_{\rm core}(R_{\rm core}/r)^m$, where $\rho_{\rm core}$, $R_{\rm core}$, and m are the profile parameters obtained from numerical simulations. Typical parameters of the $\rm CO_{core}$ mass are 3.5–9.5 $M_\odot$, corresponding to 15–30 $M_\odot$ zero-age main-sequence progenitors (see Fryer et al. 2014; Becerra et al. 2015, for details). The binary period is limited from below by the request of having no Roche lobe overflow by the $\rm CO_{core}$ before the SN explosion (Fryer et al. 2014). For instance, for a $\rm CO_{core}$ of 9.5 $M_\odot$ forming a binary system with a 2 $M_\odot$ NS, the minimum orbital period allowed by this condition is $P_{\rm min} \approx 5$ minutes. For these typical binary and pre-SN parameters, Equation (20) gives accretion rates of 10^{-4} to $10^{-2}\,M_\odot\,{\rm s^{-1}}$.

We adopt an initially nonrotating NS companion so that its exterior spacetime at time $t = 0$ is described by the Schwarzschild metric. The SN ejecta approach the NS with specific

[10] This rate is consistent with the local density rate $\rho_{\rm S\text{-}GRFs}+\rho_{\rm S\text{-}GRBs} \approx \rho_{\rm S\text{-}GRFs} = (2.6\text{–}5.0)\,{\rm Gpc^{-3}\,yr^{-1}}$ used in the present work; see Table 1 and Ruffini et al. (2016b).

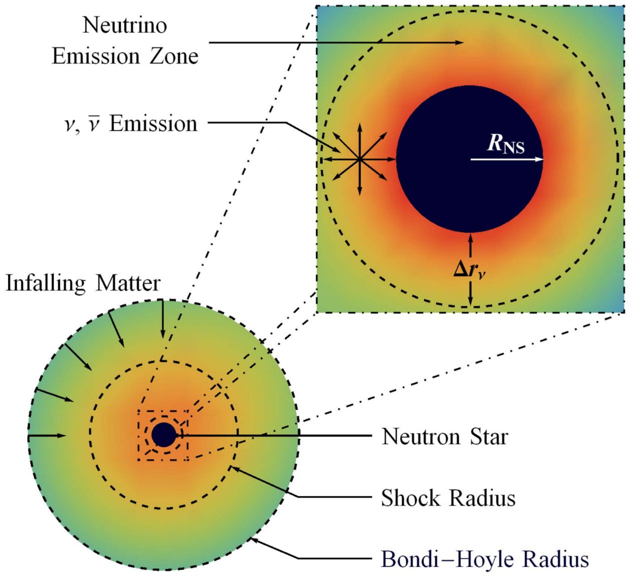

Figure 3. Scheme of the IGC scenario: the CO_{core} undergoes SN explosion, and the NS accretes part of the SN ejecta and then reaches the critical mass for gravitational collapse to a BH, with consequent emission of a GRB. The SN ejecta reach the NS Bondi–Hoyle radius and fall toward the NS surface. The material shocks and decelerates while it piles over the NS surface. At the neutrino emission zone, neutrinos take away most of the gravitational energy gained by the matter infall. The neutrinos are emitted above the NS surface in a region of thickness Δr_ν about half the NS radius, which allows the material to reduce its entropy to be finally incorporated into the NS. For further details and numerical simulations of the above process see Fryer et al. (2014) and Becerra et al. (2015, 2016).

angular momentum, $l_{acc} = \dot{L}_{cap}/\dot{M}_B$, circularizing at a radius $r_{circ} \geqslant r_{lco}$ if $l_{acc} \geqslant l_{lso}$, with r_{lco} the radius of the LCO. For a nonrotating NS $r_{lco} = 6GM_{NS}/c^2$ and $l_{lco} = 2\sqrt{3}\,GM_{NS}/c$. For typical parameters, $r_{circ}/r_{lco} \sim 10$–10^3.

The accretion onto the NS proceeds from the radius r_{in}. The NS mass and angular momentum evolve as (Becerra et al. 2015; Cipolletta et al. 2017)

$$\dot{M}_{NS} = \left(\frac{\partial M_{NS}}{\partial M_b}\right)_{J_{NS}} \dot{M}_b + \left(\frac{\partial M_{NS}}{\partial J_{NS}}\right)_{M_b} \dot{J}_{NS}, \quad \dot{J}_{NS} = \xi\, l(r_{in})\dot{M}_B, \tag{22}$$

where M_b is the NS baryonic mass; $l(r_{in})$ is the specific angular momentum of the accreted material at r_{in}, which corresponds to the angular momentum of the LCO; and $\xi \leqslant 1$ is a parameter that measures the efficiency of angular momentum transfer. In this picture we have $\dot{M}_b = \dot{M}_B$.

For the integration of Equations (20) and (22) we have to supply the values of the two partial derivatives in Equation (22). They are obtained from the relation of the NS gravitational mass, M_{NS}, with M_b and J_{NS}, namely, from the knowledge of the NS binding energy. For this we use the general relativistic calculations of rotating NSs presented in Cipolletta et al. (2015). They show that, independent of the nuclear EOS, the following analytical formula represents the numerical results with sufficient accuracy (error <2%):

$$\frac{M_b}{M_\odot} = \frac{M_{NS}}{M_\odot} + \frac{13}{200}\left(\frac{M_{NS}}{M_\odot}\right)^2\left(1 - \frac{1}{137} j_{NS}^{1.7}\right), \tag{23}$$

where $j_{NS} \equiv cJ_{NS}/(GM_\odot^2)$.

Table 5
Critical NS Mass in the Nonrotating Case and Constants k and p Needed to Compute the NS Critical Mass in the Nonrotating Case Given by Equation (25)

EOS	$M_{crit}^{J=0}$ ($M_\odot$)	p	k
NL3	2.81	1.68	0.006
GM1	2.39	1.69	0.011
TM1	2.20	1.61	0.017

Note. The values are given for the NL3, GM1, and TM1 EOS.

In the accretion process the NS gains angular momentum and therefore spin-up. To evaluate the amount of angular momentum transferred to the NS at any time, we include the dependence of the LCO specific angular momentum as a function of M_{NS} and J_{NS}. For corotating orbits the following relation is valid for the NL3, TM1, and GM1 EOS (Becerra et al. 2015; Cipolletta et al. 2017):

$$l_{lco} = \frac{GM_{NS}}{c}\left[2\sqrt{3} - 0.37\left(\frac{j_{NS}}{M_{NS}/M_\odot}\right)^{0.85}\right]. \tag{24}$$

The NS continues to accrete until an instability limit is reached or up to when all the SN ejecta overcome the NS Bondi–Hoyle region. We take into account the two main instability limits for rotating NSs: the mass-shedding or Keplerian limit and the secular axisymmetric instability limit. The latter defines critical NS mass. For the aforementioned nuclear EOS, the critical mass is approximately given by (Cipolletta et al. 2015)

$$M_{NS}^{crit} = M_{NS}^{J=0}(1 + kj_{NS}^p), \tag{25}$$

where k and p are EOS-dependent parameters (see Table 5). These formulae fit the numerical results with a maximum error of 0.45%.

A.1. Most Recent Simulations of the IGC Process

Additional details and improvements of the hypercritical accretion process leading to XRFs and BdHNe were presented in Becerra et al. (2016). Specifically:

1. The density profile included finite size/thickness effects, and additional CO_{core} progenitors leading to different SN ejecta masses were considered.
2. In Becerra et al. (2015) the maximum orbital period, P_{max}, over which the accretion onto NS companion is not sufficient to bring it to the critical mass, was inferred. Thus, binaries with $P > P_{max}$ lead to XRFs, while the ones with $P \lesssim P_{max}$ lead to BdHNe. Becerra et al. (2016) extended the determination of P_{max} for all the possible initial values of the NS mass. They also examined the outcomes for different values of the angular momentum transfer efficiency parameter.
3. The expected luminosity during the process of hypercritical accretion for a wide range of binary periods covering both XRFs and BdHNe was estimated.
4. It was shown that the presence of the NS companion originates asymmetries in the SN ejecta (see, e.g., Figure 6 in Becerra et al. 2016). The signatures of such asymmetries in the X-ray emission were there shown in the specific example of XRF 060218.

A.2. Hydrodynamics and Neutrino Emission in the Accretion Region

The accretion rate onto the NS can be as high as $\sim 10^{-2}$ to $10^{-1}\,M_\odot\,\mathrm{s}^{-1}$. For such accretion rates:

1. The magnetic pressure is much smaller than the random pressure of the infalling material; therefore, the magnetic field effects on the accretion process are negligible (Fryer et al. 1996; Rueda & Ruffini 2012).
2. The photons are trapped within the infalling matter; hence, the Eddington limit does not apply and hypercritical accretion occurs. The trapping radius is defined by Chevalier (1989): $r_{\mathrm{trapping}} = \min\{\dot{M}_B\kappa/(4\pi c), R_{\mathrm{cap}}\}$, where κ is the opacity. Fryer et al. (2014) estimated a Rosseland mean opacity of $\approx 5\times 10^3\,\mathrm{cm}^2\,\mathrm{g}^{-1}$ for the $\mathrm{CO}_{\mathrm{cores}}$. This, together with our typical accretion rates, leads to $\dot{M}_B\kappa/(4\pi c)\sim 10^{13}$–$10^{19}$ cm. This radius is much bigger than the Bondi–Hoyle radius.
3. The above condition, as well as the temperature–density values reached on top of the NS surface, leads to an efficient neutrino cooling that radiates away the gain of gravitational energy of the infalling material (Zel'dovich et al. 1972; Ruffini & Wilson 1973; Fryer et al. 1996, 2014; Rueda & Ruffini 2012).

A.2.1. Convective Instabilities

The accretion shock moves outward as the material piles onto the NS. Since the post-shock entropy is inversely proportional to the shock radius position, the NS atmosphere is unstable with respect to Rayleigh–Taylor convection at the beginning of the accretion process. Such instabilities might drive high-velocity outflows from the accreting NS (Fryer et al. 2006; Fryer 2009). The entropy at the base of the atmosphere is (Fryer et al. 1996)

$$S_{\mathrm{bubble}} \approx 16\left(\frac{1.4\,M_\odot}{M_{\mathrm{NS}}}\right)^{-7/8}\left(\frac{M_\odot\,\mathrm{s}^{-1}}{\dot{M}_{\mathrm{B}}}\right)^{1/4} \times\left(\frac{10^6\,\mathrm{cm}}{r}\right)^{3/8} k_B/\mathrm{nucleon}. \tag{26}$$

The material expands and cools down adiabatically, i.e., $T^3/\rho = $ constant. In the case of a spherically symmetric expansion, $\rho\propto 1/r^3$ and $k_B T_{\mathrm{bubble}} = 195\,S_{\mathrm{bubble}}^{-1}(10^6\,\mathrm{cm}/r)$ MeV. In the more likely case that the material expands laterally, we have (Fryer 2009) $\rho\propto 1/r^2$, i.e., $T_{\mathrm{bubble}} = T_0(S_{\mathrm{bubble}})(r_0/r)^{2/3}$, where $T_0(S_{\mathrm{bubble}})$ is obtained from the above equation at $r = r_0 \approx R_{\mathrm{NS}}$. This implies a bolometric blackbody flux at the source from the rising bubbles:

$$F_{\mathrm{bubble}} \approx 2\times 10^{40}\left(\frac{M_{\mathrm{NS}}}{1.4\,M_\odot}\right)^{-7/2}\left(\frac{\dot{M}_{\mathrm{B}}}{M_\odot\,\mathrm{s}^{-1}}\right) \times\left(\frac{R_{\mathrm{NS}}}{10^6\,\mathrm{cm}}\right)^{3/2}\left(\frac{r_0}{r}\right)^{8/3}\mathrm{erg\,s^{-1}\,cm^{-2}}, \tag{27}$$

where σ is the Stefan–Boltzmann constant.

The above thermal emission has been shown (Fryer et al. 2014) to be a plausible explanation of the early ($t\lesssim 50$ s) X-ray emission observed in some GRBs. In the specific example of GRB 090618 (Izzo et al. 2012a, 2012b), adopting an accretion rate of $10^{-2}\,M_\odot\,\mathrm{s}^{-1}$, the bubble temperature drops from 50 to 15 keV while expanding from $r\approx 10^9$ cm to 6×10^9 cm.

A.2.2. Neutrino Emission and Effective Accretion Rate

Temperatures $k_B T\sim 1$–10 MeV and densities $\rho\gtrsim 10^6\,\mathrm{g\,cm^{-3}}$ develop near the NS surface during the accretion process. Under these conditions, e^+e^- annihilation into $\nu\bar{\nu}$ pairs becomes the dominant neutrino emission process in the accretion region (see Becerra et al. 2016, for details). The effective accretion rate onto the NS can be estimated as (e.g., Fryer et al. 1996) $\dot{M}_{\mathrm{eff}}\approx \Delta M_\nu(L_\nu/E_\nu)$, where ΔM_ν and L_ν are the mass and neutrino luminosity in the emission region, respectively, and E_ν is half the gravitational potential energy gained by the material falling from infinity to a distance Δr_ν from the NS surface. Δr_ν is the thickness of the neutrino emitting region, which is approximately given by the temperature scale height ($\Delta r_\nu\approx 0.6 R_{\mathrm{NS}}$). Since $L_\nu\approx 2\pi R_{\mathrm{NS}}^2\Delta r_\nu\epsilon_{e^-e^+}$, with $\epsilon_{e^-e^+}$ the e^+e^- pair annihilation process emissivity, and $E_\nu = (1/2)GM_{\mathrm{NS}}\Delta M_\nu/(R_{\mathrm{NS}}+\Delta r_\nu)$, for $M_{\mathrm{NS}} = 1.4\,M_\odot$ one obtains $\dot{M}_{\mathrm{eff}}\approx 10^{-9}$ to $10^{-1}\,M_\odot\,\mathrm{s}^{-1}$ for $k_B T = 1$–10 MeV.

A.3. Accretion Luminosity

The energy release in a time interval dt, when an amount of mass dM_b with angular momentum $l\dot{M}_b$ is accreted, is

$$L_{\mathrm{acc}} = (\dot{M}_b - \dot{M}_{\mathrm{NS}})c^2 = \dot{M}_b c^2 \times\left[1-\left(\frac{\partial M_{\mathrm{NS}}}{\partial J_{\mathrm{NS}}}\right)_{M_b} l - \left(\frac{\partial M_{\mathrm{NS}}}{\partial M_b}\right)_{J_{\mathrm{NS}}}\right]. \tag{28}$$

This is the amount of gravitational energy gained by the matter by infalling to the NS surface that is not spent in NS gravitational binding energy. The total energy release in the time interval from t to $t+dt$, $\Delta E_{\mathrm{acc}}\equiv\int L_{\mathrm{acc}}dt$, is given by the NS binding energy difference between its initial and final state. The typical luminosity is $L_{\mathrm{acc}}\approx\Delta E_{\mathrm{acc}}/\Delta t_{\mathrm{acc}}$, where Δt_{acc} is the duration of the accretion process.

The value of Δt_{acc} is approximately given by the flow time of the slowest layers of the SN ejecta to the NS companion position. If we denote the velocity of these layers by v_{inner}, we have $\Delta t_{\mathrm{acc}}\sim a/v_{\mathrm{inner}}$, where a is the binary separation. For $a\sim 10^{11}$ cm and $v_{\mathrm{inner}}\sim 10^8\,\mathrm{cm\,s^{-1}}$, $\Delta t_{\mathrm{acc}}\sim 10^3$ s. For shorter separations, e.g., $a\sim 10^{10}$ cm ($P\sim 5$ minutes), $\Delta t_{\mathrm{acc}}\sim 10^2$ s. For a binary with $P = 5$ minutes, the NS accretes $\approx 1\,M_\odot$ in $\Delta t_{\mathrm{acc}}\approx 100$ s. From Equation (23) one obtains that the binding energy difference of a $2\,M_\odot$ and a $3\,M_\odot$ NS is $\Delta E_{\mathrm{acc}}\approx 13/200(3^2-2^2)\,M_\odot c^2\approx 0.32\,M_\odot c^2$. This leads to $L_{\mathrm{acc}}\approx 3\times 10{-3}\,M_\odot c^2\approx 0.1\dot{M}_b c^2$. The accretion power can be as high as $L_{\mathrm{acc}}\sim 0.1\dot{M}_b c^2\sim 10^{47}$–$10^{51}\,\mathrm{erg\,s^{-1}}$ for accretion rates in the range $\dot{M}_b\sim 10^{-6}$ to $10^{-2}\,M_\odot\,\mathrm{s}^{-1}$.

A.4. Possible Evolutionary Scenario for CO_{core}–NS Binary Formation

Two independent communities have introduced a new evolutionary scenario for the formation of compact-object binaries (NS–NS or NS–BH). After the collapse of the primary star forming an NS, the binary undergoes mass-transfer episodes, finally leading to the ejection of both the hydrogen and helium shells of the secondary star. These processes lead naturally to a binary composed of a $\mathrm{CO}_{\mathrm{core}}$ and an NS companion. In the X-ray binary and SN communities these systems are called "ultra-stripped" binaries (see, e.g., Tauris et al. 2015b). These systems are expected to compose 0.1%–1% of the total SNe (Tauris et al. 2013).

In the above studies most of the binaries have orbital periods in the range of 3×10^3–3×10^5 s, which are longer than the periods expected in the BdHN scenario. The formation of the CO_{core}–NS binaries leading to BdHNe might be a subset of the ultra-stripped binaries. In such a subset the conditions of the initial orbital separation and CO_{core} mass must be such as to lead to final orbital periods in the range of 100–1000 s. Assuming an SN rate of 2×10^4 Gpc^{-3} yr^{-1} (Guetta & Della Valle 2007), the ultra-stripped binaries would have a rate of 20–200 Gpc^{-3} yr^{-1}, and thus BdHNe, with a rate of $\sim$1 Gpc^{-3} yr^{-1} (see Table 1 and Ruffini et al. 2016b), might be produced by the 0.5%–5% of the ultra-stripped binary population.

A.5. Post-explosion Orbits and NS–BH Binary Formation

The SN explosion leaves as a central remnant the νNS, while the NS companion might lead, for sufficient accretion rates, to the formation of a BH. We examined in Fryer et al. (2015b) the question whether BdHNe can indeed form NS–BH binaries or, on the contrary, they are disrupted by the SN explosion.

Most of the typical binaries become unbound during an SN explosion owing to the amount of mass loss and momentum imparted (kick) to the νNS in the explosion. Assuming an instantaneous explosion, the binary is disrupted if half of the binary mass is lost. For this reason the fraction of massive binaries that can produce double compact-object binaries might be as low as $\sim$0.001%–1% (Fryer et al. 1999a; Dominik et al. 2012; Postnov & Yungelson 2014). Indeed, this is consistent with our estimated GRB local observed rates: we have shown in Section 3.1 that the NS–NS population leading to short bursts can be explained as being descendant from the CO_{core}–NS if $\sim$1% of them remain bound after the SN explosion.

Assuming instantaneous mass loss, the post-explosion semimajor axis is (Hills 1983)

$$\frac{a}{a_0} = \frac{M_0 - \Delta M}{M_0 - 2a_0\Delta M/r}, \tag{29}$$

where a_0 and a are the initial and final semimajor axes, respectively, M_0 is the (initial) binary mass, ΔM is the change of mass (in this case the amount of mass loss), and r is the orbital separation before the explosion. For circular orbits, the system is unbound if it loses half of its mass. For the very tight BdHNe, however, additional effects have to be taken into account to determine the fate of the binary.

The shock front in an SN moves at roughly 10^4 km s^{-1}, but the denser, lower-velocity ejecta can move at velocities as low as 10^2–10^3 km s^{-1} (Fryer et al. 2014). This implies that the SN ejecta overcomes an NS companion in a time 10–1000 s. For wide binaries this time is a small fraction of the orbital period and the "instantaneous" mass-loss assumption is perfectly valid. BdHNe have instead orbital periods as short as 100–1000 s; hence, the instantaneous mass-loss approximation breaks down.

We recall the specific examples studied in Fryer et al. (2015b): close binaries in an initial circular orbit of radius 7×10^9 cm, CO_{core} radii of (1–4) $\times 10^9$ cm with a 2.0 $M_\odot$ NS companion. The CO_{core} leaves a central 1.5 $M_\odot$ NS, ejecting the rest of the core. The NS leads to a BH with a mass equal to the NS critical mass. For these parameters it was there obtained that even if 70% of the mass is lost, the binary remains bound provided that the explosion time is of the order of the orbital period ($P = 180$ s) with semimajor axes of less than 10^{11} cm.

The tight νNS–BH binaries produced by BdHNe will, in due time, merge owing to the emission of GWs. For the above typical parameters the merger time is of the order of 10^4 yr, or even less. We expect little baryonic contamination around such a merger site since this region has been cleaned up by the BdHN. These conditions lead to a new family of sources that we have called ultrashort GRBs, U-GRBs.

Appendix B
Local Density Rate of GRB Subclasses

We recall now the method used in Ruffini et al. (2016b) to estimate, for each GRB subclass, the local observed density rates that we use in this work. This is defined by the convolution of the luminosity function, which tells us the fraction of bursts with isotropic equivalent luminosities in the interval $\log L$ and $\log L + d \log L$, and the cosmic GRB occurrence rate, which tells us the number of sources at different redshifts. These functions depend on a priori assumptions, and some investigations have been carried out in the literature: for long bursts (e.g., Soderberg et al. 2006b; Guetta & Della Valle 2007; Liang et al. 2007; Virgili et al. 2009; Rangel Lemos et al. 2010; Wanderman & Piran 2010; Guetta et al. 2011; Kovacevic et al. 2014), for short bursts (e.g., Virgili et al. 2011; Wanderman & Piran 2015), and for both long and short bursts (e.g., Sun et al. 2015). Additional properties that introduce further uncertainties are the instrumental sensitivity threshold, the field of view Ω_i, and the operational time T_i of the i-detector.

Hereafter we neglect the possible redshift evolution of the luminosity function. For ΔN_i events detected by various detectors in a finite logarithmic luminosity bin from $\log L$ to $\log L + \Delta \log L$, the total local event rate density between observed minimum (L_{min}) and maximum (L_{max}) luminosities is (e.g., Sun et al. 2015)

$$\rho_0 \simeq \sum_i \sum_{\log L_{min}}^{\log L_{max}} \frac{4\pi}{\Omega_i T_i} \frac{1}{\ln 10} \frac{1}{g(L)} \frac{\Delta N_i}{\Delta \log L} \frac{\Delta L}{L}, \tag{30}$$

where

$$g(L) = \int_0^{z_{max}(L)} \frac{f(z)}{1+z} \frac{dV(z)}{dz} dz, \tag{31}$$

and the comoving volume is

$$\frac{dV(z)}{dz} = \frac{c}{H_0} \frac{4\pi d_L^2}{(1+z)^2[\Omega_M(1+z)^3 + \Omega_\Lambda]^{1/2}}, \tag{32}$$

where d_L is the luminosity distance. We set $f(z) = 1$, namely, we do not assume any redshift dependence of the GRB cosmic event rate density. The maximum volume within which the event of luminosity L can be detected is defined by the maximum redshift $z_{max}(L)$. The latter is computed, following Schaefer (2007), from the 1 s bolometric peak luminosity L, k-corrected from the observed detector energy band into the burst cosmological rest-frame energy band 1–10^4 keV, and the corresponding 1 s threshold peak flux f_{th}. This is the limiting peak flux for the burst detection (Band 2003). With this, z_{max} can be defined from

(see, e.g., Zhang et al. 2009; Ruffini et al. 2014)

$$f_{\rm th} = \frac{L}{4\pi d_L^2(z_{\rm max})k}. \tag{33}$$

The possible evolution with the redshift of the GRB density rates has been analyzed in Ruffini et al. (2016b) by separating the bursts into several redshift bins, following the method suggested in Sun et al. (2015). In each redshift interval $z_j \leqslant z \leqslant z_{j+1}$, the integration limits of Equation (31) are replaced by z_j and min $[z_{j+1}, z_{\rm max,j}(L)]$, where $z_{\rm max,j}(L)$ is the maximum redshift for the jth redshift bin. Finally, from Equation (30) an event rate ρ_0^z in each redshift bin around z is obtained.

We adopt the fields of view and operational times for the detectors: *BeppoSAX*, $\Omega_{\rm BS} = 0.25$ sr, $T_{\rm BS} = 7$ yr; BATSE, $\Omega_{\rm B} = \pi$ sr, $T_{\rm B} = 10$ yr, *HETE*-2, $\Omega_{\rm H} = 0.8$ sr, $T_{\rm H} = 7$ yr; *Swift*-BAT, $\Omega_{\rm S} = 1.33$ sr, $T_{\rm S} = 10$ yr; *Fermi*-GBM, $\Omega_{\rm F} = 9.6$ sr, $T_{\rm F} = 7$ yr. We adopt no beaming correction.

ORCID iDs

M. Muccino https://orcid.org/0000-0002-2234-9225
J. A. Rueda https://orcid.org/0000-0002-3455-3063
C. L. Bianco https://orcid.org/0000-0001-7749-4078
M. Kovacevic https://orcid.org/0000-0003-4928-4510
G. B. Pisani https://orcid.org/0000-0003-3452-2491

References

Abbott, B. P., Abbott, R., Abbott, T. D., et al. 2016, LRR, 19, 1
Abbott, B. P., Abbott, R., Abbott, T. D., et al. 2017a, ApJL, 848, L13
Abbott, B. P., Abbott, R., Abbott, T. D., et al. 2017b, PhRvL, 119, 161101
Aimuratov, Y., Ruffini, R., Muccino, M., et al. 2017a, ApJ, 844, 83
Aimuratov, Y., Ruffini, R., Muccino, M., et al. 2017b, arXiv:1704.08179
Allen, B., Anderson, W. G., Brady, P. R., Brown, D. A., & Creighton, J. D. E. 2012, PhRvD, 85, 122006
Anninos, P., Hobill, D., Seidel, E., Smarr, L., & Suen, W.-M. 1995, PhRvD, 52, 2044
Antoniadis, J., Freire, P. C. C., Wex, N., et al. 2013, Sci, 340, 448
Astone, P., Ballantini, R., Babusci, D., et al. 2006, CQGra, 23, S57
Astone, P., Ballantini, R., Babusci, D., et al. 2008, CQGra, 25, 114048
Band, D. L. 2003, ApJ, 588, 945
Becerra, L., Bianco, C. L., Fryer, C. L., Rueda, J. A., & Ruffini, R. 2016, ApJ, 833, 107
Becerra, L., Cipolletta, F., Fryer, C. L., Rueda, J. A., & Ruffini, R. 2015, ApJ, 812, 100
Belczynski, K., Bulik, T., & Bailyn, C. 2011, ApJL, 742, L2
Belczynski, K., Bulik, T., & Rudak, B. 2002, ApJ, 571, 394
Belczynski, K., Repetto, S., Holz, D. E., et al. 2016, ApJ, 819, 108
Belvedere, R., Boshkayev, K., Rueda, J. A., & Ruffini, R. 2014, NuPhA, 921, 33
Berger, E. 2014, ARA&A, 52, 43
Bernuzzi, S., Dietrich, T., & Nagar, A. 2015, PhRvL, 115, 091101
Bildsten, L., & Cutler, C. 1992, ApJ, 400, 175
Cadelano, M., Pallanca, C., Ferraro, F. R., et al. 2015, ApJ, 812, 63
Caito, L., Bernardini, M. G., Bianco, C. L., et al. 2009, A&A, 498, 501
Camp, J. B., & Cornish, N. J. 2004, ARNPS, 54, 525
Chevalier, R. A. 1989, ApJ, 346, 847
Cipolletta, F., Cherubini, C., Filippi, S., Rueda, J. A., & Ruffini, R. 2015, PhRvD, 92, 023007
Cipolletta, F., Cherubini, C., Filippi, S., Rueda, J. A., & Ruffini, R. 2017, PhRvD, 96, 024046
Clark, J. P. A., & Eardley, D. M. 1977, ApJ, 215, 311
Cowperthwaite, P. S., Berger, E., Villar, V. A., et al. 2017, ApJL, 848, L17
Dai, Z. G., & Lu, T. 1998a, A&A, 333, L87
Dai, Z. G., & Lu, T. 1998b, PhRvL, 81, 4301
Davis, M., Ruffini, R., Press, W. H., & Price, R. H. 1971, PhRvL, 27, 1466
Davis, M., Ruffini, R., & Tiomno, J. 1972, PhRvD, 5, 2932
Della Valle, M., Chincarini, G., Panagia, N., et al. 2006, Natur, 444, 1050
Detweiler, S. 1980, ApJ, 239, 292
Detweiler, S. L., & Szedenits, E., Jr. 1979, ApJ, 231, 211
Dominik, M., Belczynski, K., Fryer, C., et al. 2012, ApJ, 759, 52
Dominik, M., Berti, E., O'Shaughnessy, R., et al. 2015, ApJ, 806, 263
Dutra, M., Lourenço, O., Avancini, S. S., et al. 2014, PhRvC, 90, 055203
Dutra, M., Lourenço, O., & Menezes, D. P. 2016, PhRvC, 93, 025806
Eichler, D., Livio, M., Piran, T., & Schramm, D. N. 1989, Natur, 340, 126
Finn, L. S., & Chernoff, D. F. 1993, PhRvD, 47, 2198
Flanagan, É. É., & Hughes, S. A. 1998, PhRvD, 57, 4535
Fong, W., Berger, E., Margutti, R., et al. 2012, ApJ, 756, 189
Fong, W., Berger, E., Margutti, R., & Zauderer, B. A. 2015, ApJ, 815, 102
Fong, W., Berger, E., Metzger, B. D., et al. 2014, ApJ, 780, 118
Fox, D. B., Frail, D. A., Price, P. A., et al. 2005, Natur, 437, 845
Fryer, C. L. 2009, ApJ, 699, 409
Fryer, C. L., Belczynski, K., Ramirez-Ruiz, E., et al. 2015a, ApJ, 812, 24
Fryer, C. L., Benz, W., & Herant, M. 1996, ApJ, 460, 801
Fryer, C. L., Herwig, F., Hungerford, A., & Timmes, F. X. 2006, ApJL, 646, L131
Fryer, C. L., Oliveira, F. G., Rueda, J. A., & Ruffini, R. 2015b, PhRvL, 115, 231102
Fryer, C. L., Rueda, J. A., & Ruffini, R. 2014, ApJ, 793, L36
Fryer, C. L., & Woosley, S. E. 1998, ApJL, 502, L9
Fryer, C. L., Woosley, S. E., & Hartmann, D. H. 1999a, ApJ, 526, 152
Fryer, C. L., Woosley, S. E., Herant, M., & Davies, M. B. 1999b, ApJ, 520, 650
Ghirlanda, G., Salafia, O. S., Pescalli, A., et al. 2016, A&A, 594, A84
Giacconi, R., & Ruffini, R. (ed.) 1978, Physics and Astrophysics of Neutron Stars and Black Holes (Amsterdam: North Holland Publishing Co.)
Goldstein, A., Veres, P., Burns, E., et al. 2017, ApJL, 848, L14
Goodman, J. 1986, ApJL, 308, L47
Guetta, D., & Della Valle, M. 2007, ApJL, 657, L73
Guetta, D., Pian, E., & Waxman, E. 2011, A&A, 525, A53
Haggard, D., Nynka, M., Ruan, J. J., et al. 2017, ApJL, 848, L25
Hills, J. G. 1983, ApJ, 267, 322
Izzo, L., Rueda, J. A., & Ruffini, R. 2012a, A&A, 548, L5
Izzo, L., Ruffini, R., Penacchioni, A. V., et al. 2012b, A&A, 543, A10
Kawaguchi, K., Kyutoku, K., Nakano, H., et al. 2015, PhRvD, 92, 024014
Klein, A., Barausse, E., Sesana, A., et al. 2016, PhRvD, 93, 024003
Kluźniak, W., & Ruderman, M. 1998, ApJL, 505, L113
Kobayashi, S., & Mészáros, P. 2003, ApJ, 589, 861
Kovacevic, M., Izzo, L., Wang, Y., et al. 2014, A&A, 569, A108
Landau, L. D., & Lifshitz, E. M. 1975, The Classical Theory of Fields, Vol. 2 (Oxford: Pergamon)
Lazarus, P., Tauris, T. M., Knispel, B., et al. 2014, MNRAS, 437, 1485
Lee, W. H., Ramirez-Ruiz, E., & Page, D. 2004, ApJL, 608, L5
Liang, E., Zhang, B., Virgili, F., & Dai, Z. G. 2007, ApJ, 662, 1111
LIGO Scientific Collaboration, Aasi, J., Abbott, B. P., et al. 2015, CQGra, 32, 074001
MacFadyen, A. I., & Woosley, S. E. 1999, ApJ, 524, 262
MacFadyen, A. I., Woosley, S. E., & Heger, A. 2001, ApJ, 550, 410
Maggiore, M. 2007, Gravitational Waves, Vol 1: Theory and Experiments (Oxford: Oxford Univ. Press)
Meszaros, P., & Rees, M. J. 1997, ApJL, 482, L29
Mirabel, I. F., & Rodríguez, L. F. 1998, Natur, 392, 673
Muccino, M., Ruffini, R., Bianco, C. L., Izzo, L., & Penacchioni, A. V. 2013, ApJ, 763, 125
Narayan, R., Piran, T., & Shemi, A. 1991, ApJL, 379, L17
Nicuesa Guelbenzu, A., Klose, S., Rossi, A., et al. 2011, A&A, 531, L6
Paczynski, B. 1986, ApJL, 308, L43
Paschalidis, V., MacLeod, M., Baumgarte, T. W., & Shapiro, S. L. 2009, PhRvD, 80, 024006
Patricelli, B., Razzano, M., Cella, G., et al. 2016, JCAP, 11, 056
Peters, P. C. 1964, PhRv, 136, 1224
Peters, P. C., & Mathews, J. 1963, PhRv, 131, 435
Postnov, K. A., & Yungelson, L. R. 2014, LRR, 17, 3
Rangel Lemos, L. J., Bianco, C. L., Mosquera Cuesta, H. J., Rueda, J. A., & Ruffini, R. 2010, in 25th Texas Symp. Relativistic Astrophysics, ed. F. M. Rieger, C. van Eldik, & W. Hofmann (Triste: SISSA), 204
Rees, M., Ruffini, R., & Wheeler, J. A. 1974, Black Holes, Gravitational Waves and Cosmology (New York: Gordon and Breach Science Publishers Inc.)
Rhoades, C. E., & Ruffini, R. 1974, PhRvL, 32, 324
Rigault, M., Aldering, G., Kowalski, M., et al. 2015, ApJ, 802, 20
Rosswog, S., Ramirez-Ruiz, E., & Davies, M. B. 2003, MNRAS, 345, 1077

Rueda, J. A., & Ruffini, R. 2012, ApJL, 758, L7
Ruffini, R., Bernardini, M. G., Bianco, C. L., et al. 2006, in The Tenth Marcel Grossmann Meeting, ed. M. Novello, S. Perez Bergliaffa, & R. Ruffini (Singapore: World Scientific), 369
Ruffini, R., Bernardini, M. G., Bianco, C. L., et al. 2007, in Proc. of the VI INTEGRAL Workshop, The Obscured Universe, ed. S. Grebenev, R. Sunyaev, & C. Winkler (Noordwijk: ESA), 561
Ruffini, R., Bernardini, M. G., Bianco, C. L., et al. 2008, in Proc. of the MG11 Meeting on General Relativity, The Eleventh Marcel Grossmann Meeting On Recent Developments in Theoretical and Experimental General Relativity, Gravitation and Relativistic Field Theories, ed. H. Kleinert, R. T. Jantzen, & R. Ruffini (Singapore: World Scientific), 368
Ruffini, R., Bianco, C. L., Fraschetti, F., Xue, S.-S., & Chardonnet, P. 2001, ApJL, 555, L117
Ruffini, R., Izzo, L., Muccino, M., et al. 2014, A&A, 569, A39
Ruffini, R., Muccino, M., Aimuratov, Y., et al. 2016a, ApJ, 831, 178
Ruffini, R., Muccino, M., Aimuratov, Y., et al. 2018a, arXiv:1802.07552
Ruffini, R., Muccino, M., Kovacevic, M., et al. 2015a, ApJ, 808, 190
Ruffini, R., Rueda, J. A., Muccino, M., et al. 2016b, ApJ, 832, 136
Ruffini, R., Wang, Y., Aimuratov, Y., et al. 2018b, ApJ, 852, 53
Ruffini, R., Wang, Y., Enderli, M., et al. 2015b, ApJ, 798, 10
Ruffini, R., & Wilson, J. 1973, PhRvL, 31, 1362
Savchenko, V., Ferrigno, C., Kuulkers, E., et al. 2017, ApJL, 848, L15
Schaefer, B. E. 2007, ApJ, 660, 16
Shibata, M., & Taniguchi, K. 2011, LRR, 14, 6
Smartt, S. J. 2009, ARA&A, 47, 63
Smartt, S. J. 2015, PASA, 32, e016
Soderberg, A. M., Berger, E., Kasliwal, M., et al. 2006a, ApJ, 650, 261
Soderberg, A. M., Kulkarni, S. R., Nakar, E., et al. 2006b, Natur, 442, 1014
Sun, H., Zhang, B., & Li, Z. 2015, ApJ, 812, 33
Tauris, T. M., Kaspi, V. M., Breton, R. P., et al. 2015a, in Proc. of Advancing Astrophysics with the Square Kilometre Array (AASKA14), Understanding the Neutron Star Population with the SKA (Triste: SISSA), 39
Tauris, T. M., Langer, N., Moriya, T. J., et al. 2013, ApJL, 778, L23
Tauris, T. M., Langer, N., & Podsiadlowski, P. 2015b, MNRAS, 451, 2123
Tauris, T. M., van den Heuvel, E. P. J., & Savonije, G. J. 2000, ApJL, 530, L93
Usov, V. V. 1992, Natur, 357, 472
Virgili, F. J., Liang, E.-W., & Zhang, B. 2009, MNRAS, 392, 91
Virgili, F. J., Zhang, B., O'Brien, P., & Troja, E. 2011, ApJ, 727, 109
Wanderman, D., & Piran, T. 2010, MNRAS, 406, 1944
Wanderman, D., & Piran, T. 2015, MNRAS, 448, 3026
Woosley, S. E. 1993, ApJ, 405, 273
Woosley, S. E., & Bloom, J. S. 2006, ARA&A, 44, 507
Yonetoku, D., Nakamura, T., Sawano, T., Takahashi, K., & Toyanago, A. 2014, ApJ, 789, 65
Zel'dovich, Y. B., Ivanova, L. N., & Nadezhin, D. K. 1972, SvA, 16, 209
Zhang, B., & Mészáros, P. 2001, ApJL, 552, L35
Zhang, B., Zhang, B., Virgili, F. J., et al. 2009, ApJ, 703, 1696
Zhang, B.-B., Zhang, B., Sun, H., et al. 2017, arXiv:1710.05851

Journal of Cosmology and
Astroparticle Physics

GRB 170817A-GW170817-AT 2017gfo and the observations of NS-NS, NS-WD and WD-WD mergers

To cite this article: J.A. Rueda *et al* JCAP10(2018)006

Journal of Cosmology and Astroparticle Physics
An IOP and SISSA journal

GRB 170817A-GW170817-AT 2017gfo and the observations of NS-NS, NS-WD and WD-WD mergers

J.A. Rueda,[a,b,c] **R. Ruffini,**[a,b,c,d] **Y. Wang,**[a,b] **Y. Aimuratov,**[a,b] **U. Barres de Almeida,**[c,e] **C.L. Bianco,**[a,b] **Y.C. Chen,**[a,b] **R.V. Lobato,**[a,b,f] **C. Maia,**[g] **D. Primorac,**[a,b] **R. Moradi**[a,b] **and J.F. Rodriguez**[a,b]

[a]Dipartimento di Fisica and ICRA, Sapienza Università di Roma, P.le Aldo Moro 5, I–00185 Rome, Italy
[b]ICRANet, P.zza della Repubblica 10, I–65122 Pescara, Italy
[c]ICRANet-Rio, Centro Brasileiro de Pesquisas Físicas, Rua Dr. Xavier Sigaud 150, 22290–180 Rio de Janeiro, Brazil
[d]Université de Nice Sophia Antipolis, CEDEX 2, Grand Château Parc Valrose, Nice, France
[e]Centro Brasileiro de Pesquisas Físicas, Rua Dr. Xavier Sigaud 150, 22290–180 Rio de Janeiro, Brazil
[f]Departamento de Física, Instituto Tecnológico de Aeronáutica, ITA, São José dos Campos, 12228-900 SP, Brazil
[g]Instituto de Física, Universidade de Brasília, 70910–900 Brasília, DF, Brazil

E-mail: jorge.rueda@icra.it, ruffini@icra.it

Received February 28, 2018
Revised September 25, 2018
Accepted September 27, 2018
Published October 3, 2018

Abstract. The LIGO-Virgo Collaboration has announced the detection of GW170817 and has associated it with GRB 170817A. These signals have been followed after 11 hours by the optical and infrared emission of AT 2017gfo. The origin of this complex phenomenon has been attributed to a neutron star-neutron star (NS-NS) merger. In order to probe this association we confront our current understanding of the gravitational waves and associated electromagnetic radiation with four observed GRBs originating in binaries composed of different combinations NSs and white dwarfs (WDs). We consider 1) GRB 090510 the prototype of NS-NS merger leading to a black hole (BH); 2) GRB 130603B the prototype of a NS-NS merger leading to massive NS (MNS) with an associated kilonova; 3) GRB 060614 the prototype of a NS-WD merger leading to a MNS with an associated kilonova candidate; 4) GRB

JCAP10(2018)006

 https://doi.org/10.1088/1475-7516/2018/10/006

170817A the prototype of a WD-WD merger leading to massive WD with an associated AT 2017gfo-like emission. None of these systems support the above mentioned association. The clear association between GRB 170817A and AT 2017gfo has led to introduce a new model based on a new subfamily of GRBs originating from WD-WD mergers. We show how this novel model is in agreement with the exceptional observations in the optical, infrared, X- and gamma-rays of GRB 170817A-AT 2017gfo.

Keywords: gamma ray burst experiments, gravitational waves / experiments, gravitational waves / sources, X-rays

ArXiv ePrint: 1802.10027

Contents

1 Introduction

The LIGO-Virgo Collaboration announced the detection of the gravitational-wave signal GW170817, at a luminosity distance of 40^{+8}_{-14} Mpc, as consistent with the merging of a neutron star-neutron star (NS-NS) binary [1]. The best-constrained parameter from the GW170817 data is the binary chirp mass, $\mathcal{M} \equiv (m_1 m_2)^{3/5}/M^{1/5} = 1.188^{+0.004}_{-0.002}\ M_\odot$, where m_1 and m_2 are the binary merging components and $M = m_1 + m_2$ is the binary total mass. The 90% confidence level of the total binary mass leads to the range $M = (2.73\text{–}3.29)\ M_\odot$. The lowest value, i.e. $M = 2.73 M_\odot$, corresponds to the case of equal-mass components, $m_1 = m_2 \equiv m = M/2 = 1.365 M_\odot$.

GW170817 has been associated with a short-duration gamma-ray burst (GRB) observed by the Gamma-ray Burst Monitor (GBM) on board the Fermi-satellite, GRB 170817A [2, 3], as well as with the optical-infrared-ultraviolet "kilonova" emission, AT 2017gfo [4]; see also [5–7].

If the above associations were correct, then they would support the hypothesis that GW170817-GRB 1709817A-AT 2017gfo was produced by a NS-NS merger. The aim of this article is to gain additional insight into the nature of the electromagnetic signal of GRB 170817A by comparing and contrasting it with GRBs associated with four relevant systems: NS-NS mergers leading to a black hole (BH), NS-NS mergers leading to a more massive NS (MNS), NS-WD mergers leading to a MNS and WD-WD leading to a massive WD.

The article is organized as follows. In section 2 we recall the GRB subclasses associated with NS-NS and NS-WD mergers and we have introduced as a new subclass of GRBs originating from WD-WD mergers leading to a massive WD and their observational properties. In section 3 we analyze the gravitational-wave emission of NS-NS, NS-WD and WD-WD mergers. In section 4 we compare and contrast the X-ray and optical isotropic light-curves of GRB 090510A, GRB 130603B, GRB 060614 and GRB 170817A including as well the infrared light-curve. In section 5 we describe a new subclass of GRB originating from WD-WD merger. This model is an alternative mildly-relativistic uncollimated emission as oppose to the NS-NS ultra-relativistic merger. In figure 5 we model the data of AT 2017gfo in the r, V, Ks and i bands following the WD-WD merger model. In section 6 we present the conclusions.

JCAP10(2018)006

2 GRB subclasses and observational properties of NS-NS and NS-WD mergers

Short-duration GRBs are expected to be produced in the mergers of NS-NS and NS-BH binaries (see, e.g., refs. [8–12]). Two different subclasses of short bursts from NS-NS mergers, depending on whether they lead to a MNS or to a BH, have been identified [13–15]:

- *Authentic short GRBs (S-GRBs)*: they occur when the NS-NS merger leads to a BH [14, 16, 17]. These bursts have $E_{\rm iso} \gtrsim 10^{52}$ erg and $E_{p,i} \gtrsim 2\,$MeV, and their electromagnetically inferred isotropic occurrence rate is $\rho_{\rm S-GRB} \approx \left(1.9^{+1.8}_{-1.1}\right) \times 10^{-3}$ Gpc^{-3} yr^{-1} [15, 18]. The distinct signature of the formation of a BH in a NS-NS merger in S-GRBs follows from the observations of the 0.1–100 GeV emission by the *Fermi*-LAT [19], as observed in the best prototype case of GRB 090510. This is supported by the additional information of the following sources: GRB 090227B [17], GRB 140619B [14], GRB 090510 [16] and more recently in GRB 081024B and GRB 140402A [20]. The luminosity of the GeV emission follows a decreasing power-law with index $\gamma = -1.29 \pm 0.06$, when measured in the rest frame of the source [19].

- *Short gamma-ray flashes (S-GRFs)*: they occur when the NS-NS merger leads to a MNS; i.e. there is no BH formation [15, 18]. These bursts have isotropic energy $E_{\rm iso} \lesssim 10^{52}$ erg, peak energy $E_{p,i} \lesssim 2\,$MeV, and their electromagnetically inferred isotropic occurrence rate is $\rho_{\rm S-GRF} \approx 3.6^{+1.4}_{-1.0}$ Gpc^{-3} yr^{-1} [15, 18].

Besides the gamma-ray and X-ray emission, NS-NS mergers are expected to emit a kilonova in the infrared, optical and ultraviolet wavelengths, observable days after the merger [21–24]. This signal comes from the radioactive decay of $\sim 0.01\ M_\odot$ r-process heavy material synthesized in the merger and it is expected to be nearly isotropic (see, e.g., refs. [21, 22]). The first kilonova associated with a short burst was established for GRB 130603B [23, 24]. With $E_{\rm iso} \approx 2 \times 10^{51}$ erg [25], GRB 130603B belongs to the S-GRF subclass. The second association has been claimed for GRB 050709 [26] which, with an $E_{\rm iso} \approx 8 \times 10^{49}$ erg, is also a S-GRF.

In addition to the above short bursts there is a subclass which show hybrid gamma-ray properties between long and short bursts. These gamma-ray flashes (GRFs) occur in a low-density circumburst medium (CBM), e.g. $n_{\rm CBM} \sim 10^{-3}$ cm^{-3}, and are not associated with supernovae (SNe) [15, 27, 28].

- *Gamma-ray flashes (GRFs)*: they are thought to originate in NS-WD mergers, see. e.g., [15, 18]. NS-WD binaries are notoriously common astrophysical systems [29] and possible evolutionary scenarios leading to these mergers have been envisaged (see, e.g., refs. [30–32]). These bursts, which show an extended and softer emission, have $10^{51} \lesssim E_{\rm iso} \lesssim 10^{52}$ erg, peak energy $0.2 \lesssim E_{p,i} \lesssim 2\,$MeV, and their electromagnetically inferred isotropic occurrence rate is $\rho_{\rm GRF} = 1.02^{+0.71}_{-0.46}$ Gpc^{-3} yr^{-1} [15, 18]. This density rate appears to be low with respect to the number of estimated NS-WD binaries [29] which can be of $(0.5–1) \times 10^4$ Gpc^{-3} yr^{-1} [33]. From the GRB side, we note that indeed only one NS-WD merger has been identified (see analysis of GRB 060614, in ref. [28]). This implies that the majority of the expected mergers are under the threshold of the existing X- and gamma-ray detectors. A kilonova has been associated with GRB 060614 [34]. Detail spectral and luminosity analysis has been presented in [33]. GRFs form a more massive NS and not a BH (see [15] and references therein).

JCAP10(2018)006

Finally, the case of GRB 170817A opens a new problematic: both its very low energetic $E_{\rm iso} \approx 5 \times 10^{46}$ erg [1, 3, 35] and the unprecedented details of the optical, infrared, radio and X-ray information of AT 2017gfo (see, e.g., refs. [5–7]) which promise to give most precise information on the Lorentz factor of the different episodes underline the nature of this source. The observational features of GRB 170817A and AT 2017gfo lead us to consider here the possibility of an additional subclass of GRBs produced in WD-WD mergers leading to the formation of a massive WD.

- *WD-WD mergers*: the WD-WD merger rate has been recently estimated to be (1–80) $\times 10^{-13}$ yr^{-1} $M_\odot^{-1}$ (at 2σ) and (5–9) $\times 10^{-13}$ yr^{-1} $M_\odot^{-1}$ (at 1σ) [36, 37]. For a Milky Way-like stellar mass 6.4×10^{10} $M_\odot$ and using an extrapolating factor of Milky Way equivalent galaxies, 0.016 Mpc^{-3} [38], it leads to a local cosmic rate (0.74–5.94) $\times 10^6$ Gpc^{-3} yr^{-1} (2σ) and (3.7–6.7) $\times 10^5$ Gpc^{-3} yr^{-1} (1σ).

  We are interested in WD-WD mergers forming as central remnant a massive ($\sim$ 1.2–1.5 $M_\odot$), highly magnetized (10^9–10^{10} G), fast rotating (P = 1–10 s) WD (see [39] and references therein). Since there is no SN associated with GRB 170817A the merger should not lead to a SN explosion (see e.g. [40] and references therein). This is therefore different, for instance, to the WD-WD mergers considered in [41] where the existence of a SN was explicitly envisaged. The above occurrence rate implies that (12–22)% of WD-WD mergers may explain the entire population of SN Ia. This is consistent with previous estimated rates of WD-WD mergers leading to SNe Ia (see e.g. [42]). The rest of the population is indeed sufficient to explain the population of GRB 170817A-like sources (see section 5).

  We show below in section 5 that the expected observables of these WD-WD mergers in the X- and gamma-rays, and in the optical and in the infrared wavelengths are suitable for the explanation of the GRB 170817A-AT 2017gfo association.

  We recall that the name kilonova was coined in [22] to the optical transient produced in NS-NS mergers in view of their optical luminosity, $\sim 10^{41}$ erg s^{-1}, which is approximately 1000 times the one of novae, $\sim 10^{38}$ erg s^{-1}. The results of this work show that indeed this designation can be extended to the optical transient produced in WD-WD mergers. In this case the kilonova is not powered by the decay of r-process material but by the energy released by accretion onto the new WD formed in the merger (see section 5).

  In addition, it is interesting that the above mentioned physical properties (e.g. mass, rotation period and magnetic field) of the WD formed in the merger process correspond to the ones described by the WD model of soft gamma-repeaters (SGRs) and anomalous X-ray pulsars (AXPs) [39, 43]. Indeed, the WD-WD merger rate is high enough to explain the Galactic population of SGRs/AXPs. Therefore the possible evolution of GRB 170817A-AT 2017gfo into this kind of sources has to be attentively scrutinized in the forthcoming months (see section 5).

3 Gravitational-wave emission of NS-NS, NS-WD and WD-WD mergers

We first compare and contrast the gravitational-wave emission expected from the above GRBs originating from mergers and their observed electromagnetic emissions with the ones associated with GW170817, namely GRB 170817A and AT 2017gfo [1].

We here consider our canonical model of GRBs assuming uncollimated emission, in absence of observational evidence of an achromatic jet break (see [18, 44] and references therein). We understand that a vast literature exists on alternative models based on a large variety of structured beamed emission which we do not consider here in view of the above considerations. A different approach leading to an agreement with the observational data is here proposed.

In figure 1 we show the gravitational-wave source amplitude spectral density (ASD), $h_c(f)/\sqrt{f}$, together with the one-sided ASD of the Advanced LIGO detector's noise, $\sqrt{S_n}$ [45]. The gravitational-wave characteristic strain is $h_c = (1+z)\sqrt{(1/10)(G/c^3)dE/df_s}/d_L(z)$, where $d_L(z)$ is the luminosity distance to the source, $f = f_s/(1+z)$ and f_s are the gravitational-wave frequency in the detector's and in the source's frame and dE/df_s is the gravitational-wave spectrum, respectively. For the luminosity distance we adopt a ΛCDM cosmology with $H_0 = 71$ km s^{-1}, $\Omega_M = 0.73$ and $\Omega_\Lambda = 0.23$ [46]. The spectrum of the binary inspiral can be adopted from the traditional quadrupole formula, $dE/df_s = (2^{1/3}/3)(\pi G)^{2/3}\mathcal{M}^{5/3}f_s^{-1/3}$, where we recall $\mathcal{M} \equiv (m_1 m_2)^{3/5}/M^{1/5}$ and $M = m_1 + m_2$ are, respectively, the chirp mass and total mass of the binary. We cut the gravitational-wave emission of the inspiral at the point where the two stars enter into contact, namely at a distance $r = R_1 + R_2$, where R_1 and R_2 are the stellar radii. For the NS radii we use the mass-radius relation shown in [47] obtained with the GM1 equation of state while, for the WDs, we use the mass-radius relation in [48] obtained with the relativistic Feynman-Metropolis-Teller equation of state.

To represent the emission of a S-GRB we adopt the parameters of GRB 090510A, the first identified NS-NS merger leading to a BH [16]. We thus use $m_1 = m_2 = 1.36\ M_\odot$, consistent with the condition that the merging mass exceeds the NS critical mass in the case of the GM1 nuclear equation of state which, for a non-rotating NS, is $M_{\rm crit} \approx 2.4\ M_\odot$ [47]. We are here neglecting, for simplicity, the angular momentum distribution of the post-merger configuration which would lead to a more complex analysis of the initial merging masses leading to BH formation (Rodriguez, et al., in preparation).

For a S-GRF, we assume a GRB 130603B-like source with $m_1 = m_2 = 1.1\ M_\odot$, consistent with the condition that the merged object is a massive but stable NS, consistent with the adopted NS critical mass value.

For a GRF, we adopt a GRB 060614-like source, namely a NS-WD binary with $m_1 = 1.2\ M_\odot$ and $m_2 = 0.5\ M_\odot$ [28].

To compare and contrast the gravitational-wave emission, we have located all the sources at a distance of $d = 40$ Mpc, as the one of GW170817 [1]. The gravitational-wave emission associated with the inspiral phase of the NS-NS mergers (GRB 090510A-like and GRB 130603B-like) would be consistent, both in the characteristic strain and the spanned frequency range, with the ones of GW170817 (see ref. [1], for details on this source). Instead, the emission of NS-WD and WD-WD mergers is outside the Advanced LIGO frequency band. For details of the gravitational-wave emission from these binaries see [18].

4 Comparison of the prompt, X-rays and optical light-curves of NS-NS and NS-WD mergers

We turn now to the comparison of the electromagnetic emission of all these binaries, namely of S-GRBs, S-GRFs and GRFs, with the ones of GRB 170817A - AT 2017gfo.

JCAP10(2018)006

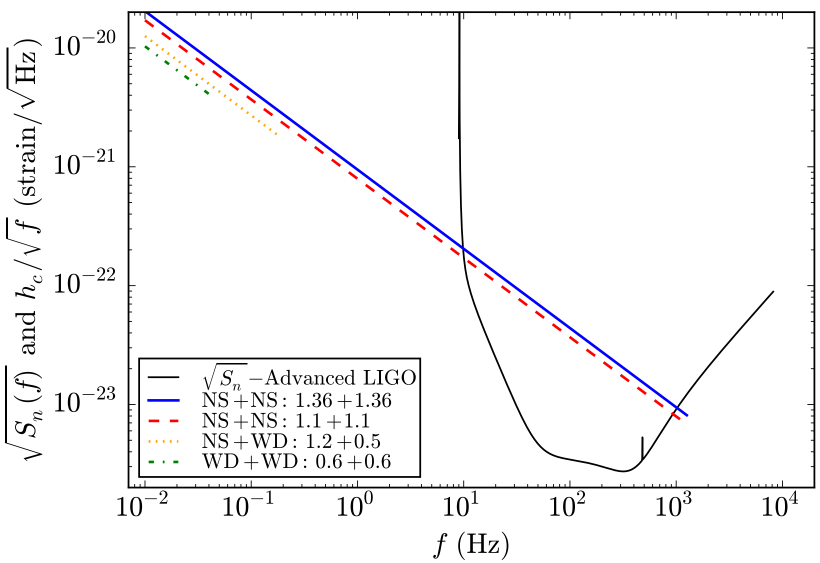

Figure 1. Source ASD, $h_c(f)/\sqrt{f}$, together with the one-sided ASD of the Advanced LIGO detector's noise, $\sqrt{S_n}$, for representative examples of S-GRBs (GRB 090510A-like), S-GRFs (GRB 130603B-like) and GRFs (GRB 060614-like). We have also included the expected ASD for a representative WD-WD binary. For the sake of the comparison all sources have been artificially assumed to be at a luminosity distance of 40 Mpc (cosmological redshift $z \approx 0.009$). For details of the gravitational-wave emission of these binaries see [18].

GeV emission. A first general conclusion can be directly inferred for the absence in GRB 170817A of the GeV emission (see e.g. [49, 50]): we can at once conclude that GRB 170817A is not consistent with a S-GRB, a NS-NS merger leading to a BH formation (see figure 2 and [19]). This conclusion is in agreement with the one obtained from the analysis of the gamma-ray prompt emission and the X-ray emission; see below and figures 3–4 and tables 1–2.

Gamma-ray prompt emission. Figure 3 shows the gamma-ray (10–1000 keV) prompt emission isotropic rest-frame light-curves of GRBs 090510, 130603B, 060614 and 170817A. In table 1 we compare and contrast the isotropic energy, peak luminosity and peak energy of the prompt emission for the same GRBs.

We can conclude that the gamma-ray prompt emission from GRB 170817A is not consistent with the one observed in GRBs 090510A, 130603B and 060614.

X-rays. In addition, we also show in figure 3 the corresponding X-ray isotropic light-curves, in the rest-frame 0.3–10 keV energy band. It can be seen the overlapping of the light-curves at times $t \gtrsim 5000$ s from the BAT trigger [54]. We recall that we had presented a first comparison of the X-ray light-curves of GRBs 090510A and 130603B in [55]. The match of the X-ray light-curves occurs irrespectively of their isotropic energies which differ up to a

JCAP10(2018)006

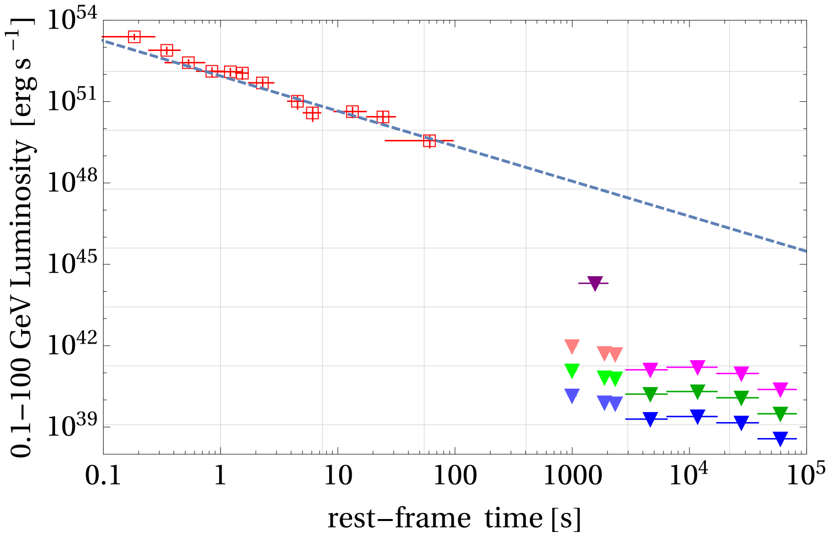

Figure 2. Comparison of the rest-frame, 0.1–100 GeV band light-curve of GRB 090510A (red empty squares) with the corresponding observational upper limits of GRB 170817A (filled triangles). The dashed line indicates the power-law decay with slope index -1.29 ± 0.06, observed in S-GRBs (see [19] for details, and references therein). The purple triangle indicates the upper limit by Fermi-LAT of 9.7×10^{43} erg s^{-1} from 1151 to 2025 s from the Fermi trigger time. AGILE upper limits (pink, green and blue triangles) were calculated through extrapolation to the Fermi-LAT working energy band (0.1–100 GeV). We assume the spectral indices -2.0 (blue triangles), -1.0 (green triangles), -0.1 (pink triangles). The data of GRB 170817A were retrieved from [49, 50].

GRB	$E_{\rm iso}$ (erg)	$L_{\rm peak}$ (erg s^{-1})	$E_{\rm peak}$ (MeV)	Reference
060614	2.17×10^{51}	3×10^{49}	$0.34^{+0.24}_{-0.1}$	GCN Circular 5264 [51]
090510	3.95×10^{52}	9.1×10^{52}	7.89 ± 0.76	[15]
130603B	2.1×10^{51}	4.1×10^{51}	0.90 ± 0.14	GCN Circular 14771 [52]
170817A	3.1×10^{46}	1.2×10^{47}	0.082 ± 0.021	GCN Circular 21520 [53]

Table 1. The isotropic energy, luminosity of the peak and peak energy of GRBs 060614, 090510, 130603B and 170817A in the prompt gamma-ray emission phase.

factor of ≈ 20 for instance in the case of GRB 130603B, $E_{\rm iso} = 2.1 \times 10^{51}$ erg [56] and GRB 090510A, $E_{\rm iso} = 3.95 \times 10^{52}$ erg [16]).

We can see that the X-ray emission from GRB 170817A is not consistent with the one observed in GRBs 090510A, 130603B and 060614.

Optical and infrared. We show in figure 4 the optical (r band) and infrared (H and Ks bands)light-curve of GRB 090510A [57, 58], GRB 130603B [23, 24], GRB 060614 [28, 34], and GRB 170817A (i.e. AT 2017gfo [4–7]).

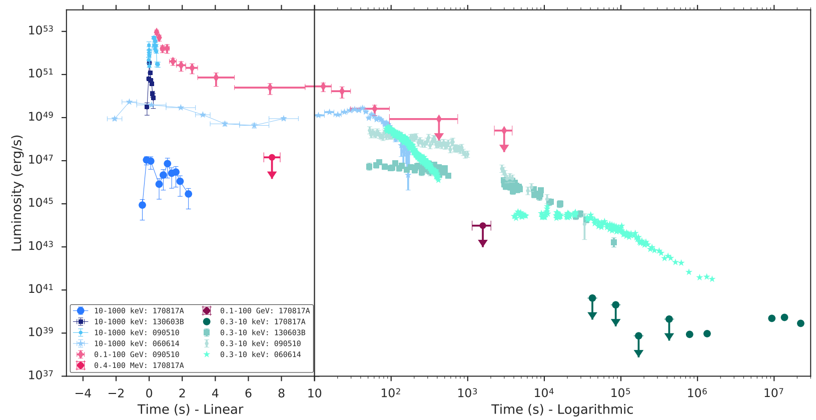

Figure 3. Light-curves of GRBs 060614, 090510A, 130603 and 170817A in the cosmological rest-frame. We show the gamma-ray (10–1000 keV) prompt and the X-ray (0.3–10 keV) emissions. The first 10 seconds are plotted in a linear scale and longer times in the logarithmic scale.

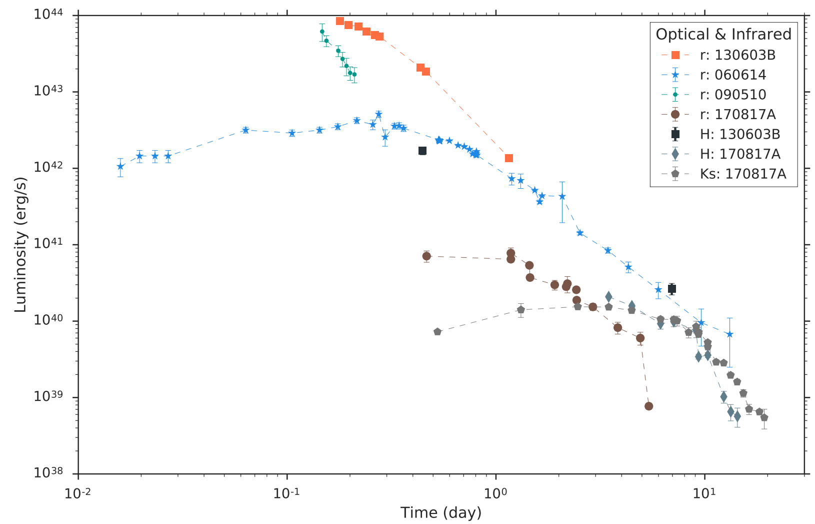

Figure 4. Optical (r band) and infrared (H and Ks bands) light-curves of GRBs 060614, 090510A, 130603 and 170817A in the cosmological rest-frame.

Since a kilonova emission had been associated with GRB 130603B [23], the similarity of this GRB in the X-rays with GRB 090510A boosted us to seek for a kilonova signature in the case GRB 090510A. This appears to be confirmed by figure 4. We can conclude that all of these sources, S-GRFs, S-GRBs and GRFs, can produce a kilonova emission in line with the source AT 2017gfo, the kilonova associated with GRB 170817A.

Some of the above correlations of the electromagnetic emissions clearly originate from the traditional kilonova models based on ultra-relativistic regimes in NS-NS and NS-WD mergers pioneered in [10, 21, 59], following the classical work of [60, 61].

The common asymptotic behavior at late times of the X-ray and optical emission of GRB 090510A [55] and GRB 130603B [23] are a manifestation of a common synchrotron emission as recently outlined in [62]. This approach is also supported by the parallel behavior of the optical and X-ray emission of GRB 060614 (see figures 3 and 4). Similar behavior was already indicated in the case of long GRBs (BdHNe) [63, 64]. In fact, it is interesting to use this similarity to set a lower limit to the mass of the expanding matter by equating the energy emitted in the X-rays, $E_{\rm iso,X}$ (see table 2), to the kinetic energy, $E_{\rm kin} = (\Gamma - 1)Mc^2$., where Γ is the Lorentz factor. By using for instance $\Gamma \sim 1.2$ ($v/c \sim 0.5$), a typical value obtained for the expanding blackbody component in the X-ray afterglow of BdHNe [44], we obtain $9.2 \times 10^{-4}\ M_\odot$, $9.4 \times 10^{-5}\ M_\odot$ and $2.4 \times 10^{-4}\ M_\odot$ for GRBs 090510A, 130603B and 060614. These lower limits are indeed in line with the ejecta mass obtained from an independent analysis of the optical emission (see e.g. [22–24, 26]). The same analysis of the X-ray emission applied to GRB 170817A would lead to a nearly ten orders of magnitude less massive ejecta, giving further support to a possible different nature of this source.

The above contrast of the gamma- and X-rays observational properties of GRB 170817A with respect to GRBs produced by NS-NS and NS-WD mergers has led us to consider the possibility of an additional subclass of GRBs produced by the merger of a still different compact-star binary, a WD-WD merger, leading to a massive WD. We proceed now to discuss the framework of such a model to explain the electromagnetic properties of the association GRB 170817A - AT 2017gfo.

5 WD-WD mergers as an alternative mildly relativistic uncollimated emission for GRB 170817A-AT 2017gfo

The estimated WD-WD merger rate (see section 2) implies that 0.1% of WD-WD mergers can explain the GRB 170817A-like population for which a lower limit of (30–630) $\rm Gpc^{-3}\ yr^{-1}$ has been recently obtained (see [65] for details).

The energy observed in gamma-rays in GRB 170817A, $E_{\rm iso} \approx 3 \times 10^{46}$ erg, can originate from flares owing to the twist and stress of the magnetic field lines during the merger process: a magnetic energy of 2×10^{46} erg is stored in a region of radius 10^9 cm and magnetic field of 10^{10} G [43].

The emission at optical and infrared wavelengths (see figure 5), can be explained from the adiabatic cooling of $10^{-3}\,M_\odot$ ejecta from the merger [66, 67] heated by fallback accretion onto the newly-formed WD [66]. The ejecta becomes transparent at times $t\ \sim 1$ day with a peak bolometric luminosity of $L_{\rm bol} \sim 10^{42}$ erg s^{-1}. The fallback accretion injects to the ejecta 10^{47}–10^{49} erg s^{-1} at early times and fall-off following a power-law behavior (see [66] for details). The kilonovae from WD-WD mergers are therefore powered by a different mechanism with respect to the kilonovae from NS-NS mergers which are powered by the radioactive decay of r-process heavy material.

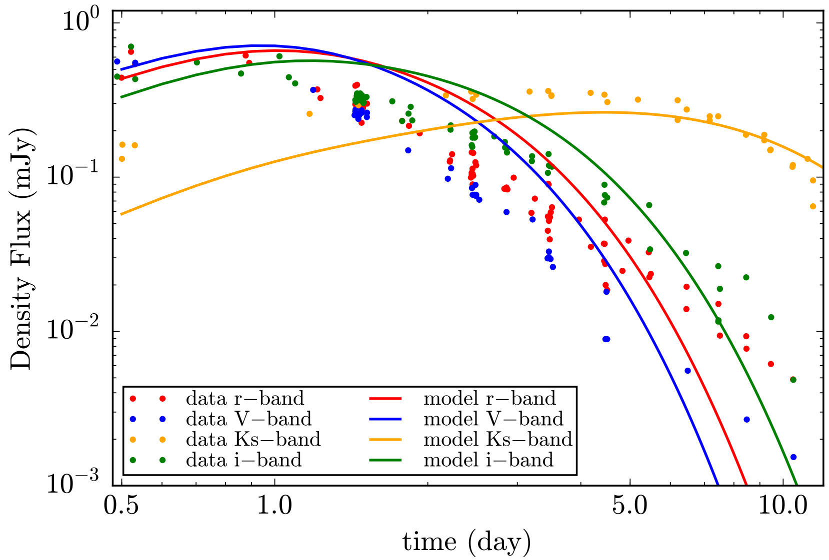

Figure 5. Points: observed optical and infrared density flux of AT 2017gfo [6, 7]. Solid curves: corresponding theoretical expectation from the cooling of $10^{-3}\,M_\odot$ of WD-WD merger ejecta heated by fallback accretion onto the newly-formed central WD.

At times $t \sim 100$–200 day, the ejecta are expected to become transparent to the X-rays leading to a luminosity of $\approx 10^{39}$ erg s^{-1} as the one recently observed in GRB 170817A (see figure 3). At earlier times, the X-rays from fallback accretion are instead absorbed by the ejecta and are mainly transformed into kinetic energy then increasing the expansion velocity of the ejecta, from an initial non-relativistic value 0.01 c typical of the escape velocity from the WD, to a mildly relativistic velocity 0.1 c. This mildly relativistic velocity is also consistent with the value derived from the evolution of blackbody spectra observed from ~ 0.5 day to ~ 7 day. We present the detailed analysis of all the above properties of WD-WD mergers in [68].

As we have mentioned in section 2, the WD formed in the merger can become an SGR/AXP [39, 43]. Thus, there is the possibility that, if a WD-WD merger produced GRB 170817A-AT 2017gfo, an SGR/AXP (a WD-pulsar) will show in this sky position in the near future.

The observational features of these WD-WD mergers in the X- and the gamma-rays as well as in the optical and infrared wavelengths are an important topic by their own. We are going to present elsewhere additional details on the multiwavelength observables of the merger, of the post-merger and of the ejected matter.

6 Discussion and conclusions

In this work we have compared and contrasted the gravitational-wave and the electromagnetic emission of canonical GRBs associated with NS-NS (both S-GRBs and S-GRFs), NS-

Subclass	*In-state* → *Out-state*	T_{90} (s)	$E_{\rm p,i}$ (MeV)	$E_{\rm iso}$ (erg)	$E_{\rm iso,Gev}$ (erg)	$E_{\rm iso,X}$ (erg)	Kilonova	$L_{\rm p,KN}$ (erg s^{-1})	Hz-kHz GW
S-GRFs	NS-NS → MNS	$\lesssim 2$	$\lesssim 2$	10^{49}–10^{52}	—	10^{49}–10^{51}	RPKN	10^{41}	Yes
S-GRBs	NS-NS → BH	$\lesssim 2$	$\gtrsim 2$	10^{52}–10^{53}	10^{52}–10^{53}	$\lesssim 10^{51}$	RPKN	10^{41}	Yes
GRFs	NS-WD → MNS	2–100	0.2–2	10^{51}–10^{52}	—	10^{49}–10^{50}	TBD	10^{41}	No
GR-K	WD-WD → MWD	$\lesssim 1$	$\lesssim 0.1$	$\lesssim 10^{47}$	—	10^{38}–10^{39}	FBKN	10^{41}	No

Table 2. Summary of the GRB subclasses discussed in this article: short gamma-ray flashes (S-GRFs), authentic short GRBs (S-GRBs) and gamma-ray flash kilonovae (GR-K) introduced in this work. See further details in [15, 18, 68] and references therein. The columns indicate the GRB subclass, *in-states* (progenitor) and *out-states* (final outcome), the T_{90} in the rest-frame, the rest-frame spectral peak energy $E_{\rm p,i}$ and $E_{\rm iso}$ (rest-frame 1–10^4 keV), the isotropic energy of the GeV emission $E_{\rm iso,GeV}$ (rest-frame 0.1–100 GeV), the isotropic energy of the X-ray data $E_{\rm iso,X}$ (rest-frame 0.3–10 keV), the presence or not of kilonova and its nature (radioactive-powered kilonova, RPKN; fallback-powered kilonova, FBKN), the typical associated kilonova peak luminosity, and finally the presence or not of Hz-kHz gravitational-wave emission, e.g. as the one detectable by LIGO-Virgo. As for the kilonova from NS-WD mergers we have specified "to be defined (TBD)" since this possibility has not been yet explored in the literature.

WD (GRFs) and WD-WD mergers with the one of the associated sources GRB 170817A-GW170817-AT 2017gfo. We present in table 2 a summary. As a canonical S-GRB we use GRB 090510A, for S-GRF we use GRB 130603B and for GRF we use GRB 060614 and for GRB 170817 a twin WD with component masses $M = 0.6 M_\odot$, see figure 1.

We can conclude:

1. The comparison of the properties of NS-NS (S-GRFs and S-GRBs) and NS-WD (S-GRFs) with GRB 170817A-GW170817-AT 2017gfo shows that all of them may include a kilonova (AT 2017gfo-like). Only in NS-NS there could be the Hz-kHz gravitational-wave emission needed to explain the energetics of GW170817 (see figure 1). However, this solution necessarily implies an X and gamma-ray emission in the prompt phase that is missing in the case of GRB 170817A (see data up to 10 s in figure 3). Indeed, the observational features in gamma- and X-rays of GRB 170817A contrasts with any other GRB associated with the above binary progenitors (see figures 3–4 and tables 1–2). In conclusion, the NS-NS scenario cannot explain the association GRB170817A-GW170817.

2. Indeed, the X-ray and gamma-ray observations of GRB 170817A clearly show that we are in presence of a phenomenon much less energetic than the one observed in any S-GRB, S-GRF, GRF, or BdHN, and perhaps with a substantially larger occurrence rate (see e.g. [65]). These observations have led us to consider a new subclass of GRBs, also with binary progenitors, originating from WD-WD mergers leading to a massive WD. The occurrence rate of these mergers can explain the rate of GRB 170817A-like sources, they produce a gamma- and X-ray emission consistent with the ones observed in GRB 170817A and cannot be associated with GW170817.

3. The optical and infrared emission AT 2017gfo can be powered by a different physical mechanism with respect to the radioactive decay of r-process heavy material synthesized in the much more energetic NS-NS mergers: it can be alternatively explained by the cooling of the ejecta expelled in a WD-WD merger and heated up by fallback accretion onto the newly-formed massive WD, see figure 5. In view of the above difference

we propose to call radioactive-powered kilonovae (RPKNe) the optical transient produced by NS-NS mergers and fallback-powered kilonovae (FBKNe) the one by WD-WD mergers. See table 2.

4. The ejecta from a WD-WD merger are different from the ejecta from a NS-NS merger in that they have a lighter nuclear composition with respect to the one of the ejecta of NS-NS mergers which is made of r-processed heavy nuclei. The spectroscopic identification of atomic species can therefore discriminate between the two scenarios. However, such an identification has not been possible in any of the observed kilonovae since it needs accurate models of atomic spectra, nuclear reaction network, density profile, as well as radiative transport (opacity) that are not yet available.

5. These WD-WD mergers opens the possibility to a new subclass of GRBs with a much less energetic and softer prompt emission whose observation would benefit from a new mission operating in soft X-rays like, e.g., THESEUS [69]. In addition, as we have shown, the outcome of such a GRB, namely a massive, highly magnetized, fast rotating WD, may become in due time observable as SGRs/AXP.

6. Since the early submission of our paper additional observations in the optical and in the X-rays have appeared (see e.g. [70, 71]) which have allowed to strength our conclusions (see e.g. figure 5 and [68]). What we can do at this stage from a theoretical point of view is to formulate what conventional physics can tell us about these events and this has been done in this article.

7. It is clear that the only possibility of a null chance coincidence of GRB 170817A and GW170817 is to assume that one of the events does not exist in reality. If the two events exist then there is non-null chance coincidence by definition and its evaluation has been estimated (see e.g. [2]). The association of these events, from an observational point of view is, in our opinion, not yet sufficiently established to formulate a well-motivated answer. It is auspicable, as soon as the LIGO collaboration releases the templates of the gravitational-wave source GW170817 in the interferometers, to reconstruct the precise chronology of the space-time sequence of events in the LIGO detectors and in the Fermi and Integral satellites, necessary to validate the association between GW170817 and GRB 170817A.

Acknowledgments

We thank P. Lorén-Aguilar for discussions on WD-WD mergers. We thank both the Referee and Scientific Editor for valuable help in optimizing the presentation of our paper as well as for the detailed and constructive discussions.

References

[1] Virgo and LIGO Scientific collaborations, B. Abbott et al., *GW170817: Observation of Gravitational Waves from a Binary Neutron Star Inspiral*, *Phys. Rev. Lett.* **119** (2017) 161101 [arXiv:1710.05832] [inSPIRE].

[2] Virgo, Fermi-GBM, INTEGRAL and LIGO Scientific collaborations, B.P. Abbott et al., *Gravitational Waves and Gamma-rays from a Binary Neutron Star Merger: GW170817 and GRB 170817A*, *Astrophys. J.* **848** (2017) L13 [arXiv:1710.05834] [inSPIRE].

[3] A. Goldstein et al., *An Ordinary Short Gamma-Ray Burst with Extraordinary Implications: Fermi-GBM Detection of GRB 170817A*, Astrophys. J. **848** (2017) L14 [arXiv:1710.05446] [INSPIRE].

[4] D.A. Coulter et al., *Swope Supernova Survey 2017a (SSS17a), the Optical Counterpart to a Gravitational Wave Source*, Science (2017) [arXiv:1710.05452] [INSPIRE].

[5] I. Arcavi et al., *Optical emission from a kilonova following a gravitational-wave-detected neutron-star merger*, Nature **551** (2017) 64 [arXiv:1710.05843] [INSPIRE].

[6] P.S. Cowperthwaite et al., *The Electromagnetic Counterpart of the Binary Neutron Star Merger LIGO/Virgo GW170817. II. UV, Optical and Near-infrared Light Curves and Comparison to Kilonova Models*, Astrophys. J. **848** (2017) L17 [arXiv:1710.05840] [INSPIRE].

[7] M. Nicholl et al., *The Electromagnetic Counterpart of the Binary Neutron Star Merger LIGO/VIRGO GW170817. III. Optical and UV Spectra of a Blue Kilonova From Fast Polar Ejecta*, Astrophys. J. **848** (2017) L18 [arXiv:1710.05456] [INSPIRE].

[8] J. Goodman, *Are gamma-ray bursts optically thick?*, Astrophys. J. **308** (1986) L47 [INSPIRE].

[9] B. Paczynski, *Gamma-ray bursters at cosmological distances*, Astrophys. J. **308** (1986) L43 [INSPIRE].

[10] D. Eichler, M. Livio, T. Piran and D.N. Schramm, *Nucleosynthesis, Neutrino Bursts and Gamma-Rays from Coalescing Neutron Stars*, Nature **340** (1989) 126 [INSPIRE].

[11] R. Narayan, T. Piran and A. Shemi, *Neutron star and black hole binaries in the galaxy*, Astrophys. J. **379** (1991) L17 [INSPIRE].

[12] R. Narayan, B. Paczynski and T. Piran, *Gamma-ray bursts as the death throes of massive binary stars*, Astrophys. J. **395** (1992) L83 [astro-ph/9204001] [INSPIRE].

[13] C.L. Fryer, F.G. Oliveira, J.A. Rueda and R. Ruffini, *On the Neutron Star-Black Hole Binaries Produced by Binary-driven-Hypernovae*, Phys. Rev. Lett. **115** (2015) 231102 [arXiv:1505.02809] [INSPIRE].

[14] R. Ruffini et al., *GRB 140619B: a short GRB from a binary neutron star merger leading to black hole formation*, Astrophys. J. **808** (2015) 190 [arXiv:1412.1018] [INSPIRE].

[15] R. Ruffini et al., *On the classification of GRBs and their occurrence rates*, Astrophys. J. **832** (2016) 136 [arXiv:1602.02732] [INSPIRE].

[16] R. Ruffini et al., *GRB 090510: a genuine short-GRB from a binary neutron star coalescing into a Kerr-Newman black hole*, Astrophys. J. **831** (2016) 178 [arXiv:1607.02400] [INSPIRE].

[17] M. Muccino, R. Ruffini, C.L. Bianco, L. Izzo and A.V. Penacchioni, *GRB 090227B: the missing link between the genuine short and disguised short GRBs*, Astrophys. J. **763** (2013) 125 [arXiv:1205.6600] [INSPIRE].

[18] R. Ruffini et al., *On the rate and on the gravitational wave emission of short and long GRBs*, Astrophys. J. **859** (2018) 30 [arXiv:1602.03545] [INSPIRE].

[19] R. Ruffini et al., *On the Short GRB GeV emission from a Kerr Black hole*, arXiv:1802.07552 [INSPIRE].

[20] Y. Aimuratov et al., *GRB 081024B and GRB 140402A: two additional short GRBs from binary neutron star mergers*, Astrophys. J. **844** (2017) 83 [arXiv:1704.08179] [INSPIRE].

[21] L.-X. Li and B. Paczynski, *Transient events from neutron star mergers*, Astrophys. J. **507** (1998) L59 [astro-ph/9807272] [INSPIRE].

[22] B.D. Metzger et al., *Electromagnetic Counterparts of Compact Object Mergers Powered by the Radioactive Decay of R-process Nuclei*, Mon. Not. Roy. Astron. Soc. **406** (2010) 2650 [arXiv:1001.5029] [INSPIRE].

JCAP10(2018)006

[23] N.R. Tanvir et al., *A "kilonova" associated with short-duration gamma-ray burst 130603B*, Nature **500** (2013) 547 [arXiv:1306.4971] [INSPIRE].

[24] E. Berger, W. Fong and R. Chornock, *An r-process Kilonova Associated with the Short-hard GRB 130603B*, Astrophys. J. **774** (2013) L23 [arXiv:1306.3960] [INSPIRE].

[25] W. Fong et al., *Short GRB 130603B: Discovery of a Jet Break in the Optical and Radio Afterglows and a Mysterious Late-time X-Ray Excess*, Astrophys. J. **780** (2014) 118 [arXiv:1309.7479] [INSPIRE].

[26] Z.-P. Jin et al., *The Macronova in GRB 050709 and the GRB/macronova connection*, Nature Commun. **7** (2016) 12898 [arXiv:1603.07869] [INSPIRE].

[27] M. Della Valle et al., *GRB 060614: An enigmatic long-duration gamma-ray burst not due to a hypernova*, Nature **444** (2006) 1050 [astro-ph/0608322] [INSPIRE].

[28] L. Caito, M.G. Bernardini, C.L. Bianco, M.G. Dainotti, R. Guida and R. Ruffini, *GRB060614: a 'fake' short GRB from a merging binary system*, Astron. Astrophys. **498** (2009) 501 [arXiv:0810.4855] [INSPIRE].

[29] M. Cadelano et al., *Optical Identification of He White Dwarfs Orbiting Four Millisecond Pulsars in the Globular Cluster 47 Tucanae*, Astrophys. J. **812** (2015) 63 [arXiv:1509.01397] [INSPIRE].

[30] C.L. Fryer, S.E. Woosley, M. Herant and M.B. Davies, *Merging white dwarf/black hole binaries and gamma-ray bursts*, Astrophys. J. **520** (1999) 650 [astro-ph/9808094] [INSPIRE].

[31] P. Lazarus et al., *Timing of a Young Mildly Recycled Pulsar with a Massive White Dwarf Companion*, Mon. Not. Roy. Astron. Soc. **437** (2014) 1485 [arXiv:1310.5857] [INSPIRE].

[32] T.M. Tauris, E.P. J. v.d. Heuvel and G.J. Savonije, *Formation of millisecond pulsars with heavy white dwarf companions - extreme mass transfer on sub-thermal timescales*, Astrophys. J. **530** (2000) L93 [astro-ph/0001013] [INSPIRE].

[33] T.A. Thompson, M.D. Kistler and K.Z. Stanek, *A High Rate of White Dwarf-Neutron Star Mergers & Their Transients*, arXiv:0912.0009 [INSPIRE].

[34] B. Yang et al., *A possible Macronova in the late afterglow of the 'long-short' burst GRB 060614*, Nature Commun. **6** (2015) 7323 [arXiv:1503.07761] [INSPIRE].

[35] B.P. Abbott et al., *Multi-messenger Observations of a Binary Neutron Star Merger*, Astrophys. J. **848** (2017) L12 [arXiv:1710.05833] [INSPIRE].

[36] D. Maoz and N. Hallakoun, *The binary fraction, separation distribution and merger rate of white dwarfs from SPY*, Mon. Not. Roy. Astron. Soc. **467** (2017) 1414 [arXiv:1609.02156] [INSPIRE].

[37] D. Maoz, N. Hallakoun and C. Badenes, *The separation distribution and merger rate of double white dwarfs: improved constraints*, Mon. Not. Roy. Astron. Soc. **476** (2018) 2584 [arXiv:1801.04275] [INSPIRE].

[38] V. Kalogera, R. Narayan, D.N. Spergel and J.H. Taylor, *The coalescence rate of double neutron star systems*, Astrophys. J. **556** (2001) 340 [astro-ph/0012038] [INSPIRE].

[39] J.A. Rueda et al., *A white dwarf merger as progenitor of the anomalous X-ray pulsar 4U 0142+61?*, arXiv:1306.5936 [INSPIRE].

[40] L. Becerra, J.A. Rueda, P. Loren-Aguilar and E. Garcia-Berro, *The Spin Evolution of Fast-Rotating, Magnetized Super-Chandrasekhar White Dwarfs in the Aftermath of White Dwarf Mergers*, Astrophys. J. **857** (2018) 134 [arXiv:1804.01275] [INSPIRE].

[41] V.M. Lipunov, *Double O-Ne-Mg white dwarfs merging as the source of the Powerfull Gravitational Waves for LIGO/VIRGO type interferometers*, New Astron. **56** (2017) 84 [arXiv:1703.04000] [INSPIRE].

[42] A.J. Ruiter, K. Belczynski and C.L. Fryer, *Rates and Delay Times of Type Ia Supernovae*, Astrophys. J. **699** (2009) 2026 [arXiv:0904.3108] [INSPIRE].

[43] M. Malheiro, J.A. Rueda and R. Ruffini, *SGRs and AXPs as rotation powered massive white dwarfs*, Publ. Astron. Soc. Jap. **64** (2012) 56 [arXiv:1102.0653] [INSPIRE].

[44] R. Ruffini et al., *Early X-ray Flares in GRBs*, Astrophys. J. **852** (2018) 53 [arXiv:1704.03821] [INSPIRE].

[45] VIRGO, KAGRA and LIGO SCIENTIFIC collaborations, B.P. Abbott et al., *Prospects for Observing and Localizing Gravitational-Wave Transients with Advanced LIGO, Advanced Virgo and KAGRA*, Living Rev. Rel. **21** (2018) 3 [arXiv:1304.0670] [INSPIRE].

[46] M. Rigault et al., *Confirmation of a Star Formation Bias in Type Ia Supernova Distances and its Effect on Measurement of the Hubble Constant*, Astrophys. J. **802** (2015) 20 [arXiv:1412.6501] [INSPIRE].

[47] F. Cipolletta, C. Cherubini, S. Filippi, J.A. Rueda and R. Ruffini, *Fast Rotating Neutron Stars with Realistic Nuclear Matter Equation of State*, Phys. Rev. **D 92** (2015) 023007 [arXiv:1506.05926] [INSPIRE].

[48] M. Rotondo, J.A. Rueda, R. Ruffini and S.-S. Xue, *The relativistic Feynman-Metropolis-Teller theory for white dwarfs in general relativity*, Phys. Rev. **D 84** (2011) 084007 [arXiv:1012.0154] [INSPIRE].

[49] FERMI-LAT collaboration, D. Kocevski, N. Omodei and G. Vianello, *Fermi-LAT observations of the LIGO/Virgo event GW170817*, arXiv:1710.05450 [INSPIRE].

[50] F. Verrecchia et al., *AGILE Observations of the Gravitational-wave Source GW170817: Constraining Gamma-Ray Emission from a NS-NS Coalescence*, Astrophys. J. **850** (2017) L27 [arXiv:1710.05460] [INSPIRE].

[51] S. Golenetskii, R. Aptekar, E. Mazets, V. Pal'Shin, D. Frederiks and T. Cline, *Konus-wind observation of GRB 060614*, GRB Coordinates Network 5264 (2006).

[52] S. Golenetskii et al., *Konus-wind observation of GRB 130603B*, GRB Coordinates Network, Circular Service, No. 14771, #1 (2013).

[53] A. von Kienlin, C. Meegan and A. Goldstein, *GRB 170817A: Fermi GBM detection*, GRB Coordinates Network, Circular Service, No. 21520, #1 (2017).

[54] A. Melandri et al., *GRB 130603B: Swift detection of a bright short burst*, GRB Coordinates Network, Circular Service, No. 14735, #1 (2013).

[55] R. Ruffini et al., *GRB 130603B: analogy with GRB 090510A and possible connection with a supernova*, GRB Coordinates Network, Circular Service, No. 14913, #1 (2013).

[56] D. Frederiks, *GRB 130603B: rest-frame energegics in gamma-rays*, GRB Coordinates Network, Circular Service, No. 14772, #1 (2013).

[57] GBM and FERMI-LAT collaborations, M. De Pasquale et al., *Swift and Fermi observations of the early afterglow of the short Gamma-Ray Burst 090510*, Astrophys. J. **709** (2010) L146 [arXiv:0910.1629] [INSPIRE].

[58] A.N. Guelbenzu et al., *The late-time afterglow of the extremely energetic short burst GRB 090510 revisited*, Astron. Astrophys. **538** (2012) L7 [arXiv:1201.3885] [INSPIRE].

[59] J.M. Lattimer, F. Mackie, D.G. Ravenhall and D.N. Schramm, *The decompression of cold neutron star matter*, Astrophys. J. **213** (1977) 225 [INSPIRE].

[60] W.D. Arnett, *Analytic solutions for light curves of supernovae of Type II*, Astrophys. J. **237** (1980) 541.

[61] W.D. Arnett, *Type I supernovae. I - Analytic solutions for the early part of the light curve*, Astrophys. J. **253** (1982) 785.

[62] R. Ruffini et al., *On a GRB afterglow model consistent with hypernovae observations*, arXiv:1712.05000 [INSPIRE].

[63] R. Ruffini et al., *On Binary Driven Hypernovae and their nested late X-ray emission*, Astron. Astrophys. **565** (2014) L10 [arXiv:1404.3946] [INSPIRE].

[64] R. Ruffini et al., *GRB 130427A and SN 2013cq: A multi-wavelength Analysis of An Induced Gravitational Collapse Event*, Astrophys. J. **798** (2015) 10 [arXiv:1405.5723] [INSPIRE].

[65] B.B. Zhang et al., *A peculiar low-luminosity short gamma-ray burst from a double neutron star merger progenitor*, Nature Commun. **9** (2018) 447 [arXiv:1710.05851] [INSPIRE].

[66] P. Lorén-Aguilar, J. Isern and E. García-Berro, *High-resolution smoothed particle hydrodynamics simulations of the merger of binary white dwarfs*, Astron. Astrophys. **500** (2009) 1193.

[67] M. Dan, S. Rosswog, J. Guillochon and E. Ramirez-Ruiz, *Prelude to a double degenerate merger: the onset of mass transfer and its impact on gravitational waves and surface detonations*, Astrophys. J. **737** (2011) 89 [arXiv:1101.5132] [INSPIRE].

[68] J.A. Rueda et al., *Electromagnetic emission of white dwarf binary mergers*, arXiv:1807.07905 [INSPIRE].

[69] THESEUS collaboration, L. Amati et al., *The THESEUS space mission concept: science case, design and expected performances*, Adv. Space Res. **62** (2018) 191 [arXiv:1710.04638] [INSPIRE].

[70] P. D'Avanzo et al., *The evolution of the X-ray afterglow emission of GW 170817/ GRB 170817A in XMM-Newton observations*, Astron. Astrophys. **613** (2018) L1 [arXiv:1801.06164] [INSPIRE].

[71] J.D. Lyman et al., *The optical afterglow of the short gamma-ray burst associated with GW170817*, Nat. Astron. **2** (2018) 751 [arXiv:1801.02669] [INSPIRE].

JCAP10(2018)006

The Astrophysical Journal, 869:101 (9pp), 2018 December 20 https://doi.org/10.3847/1538-4357/aaeac8

A GRB Afterglow Model Consistent with Hypernova Observations

R. Ruffini[1,2,3,4], M. Karlica[1,2,3], N. Sahakyan[2,5], J. A. Rueda[1,2,4], Y. Wang[1,2], G. J. Mathews[2,6], C. L. Bianco[1,2], and M. Muccino[1,2]

[1] ICRA and Dipartimento di Fisica, Sapienza Università di Roma, P.le Aldo Moro 5, I-00185 Rome, Italy
[2] ICRANet, P.zza della Repubblica 10, I-65122 Pescara, Italy
[3] Université de Nice Sophia Antipolis, CEDEX 2, Grand Château Parc Valrose, Nice, France
[4] ICRANet-Rio, Centro Brasileiro de Pesquisas Físicas, Rua Dr. Xavier Sigaud 150, 22290–180 Rio de Janeiro, Brazil
[5] ICRANet-Armenia, Marshall Baghramian Avenue 24a, Yerevan 0019, Armenia
[6] Center for Astrophysics, Department of Physics, University of Notre Dame, Notre Dame, IN, 46556, USA
Received 2017 December 13; revised 2018 July 16; accepted 2018 October 21; published 2018 December 14

Abstract

We describe the afterglows of the long gamma-ray-burst (GRB) 130427A within the context of a binary-driven hypernova. The afterglows originate from the interaction between a newly born neutron star (νNS), created by an Ic supernova (SN), and a mildly relativistic ejecta of a hypernova (HN). Such an HN in turn results from the impact of the GRB on the original SN Ic. The mildly relativistic expansion velocity of the afterglow ($\Gamma \sim 3$) is determined, using our model-independent approach, from the thermal emission between 196 and 461 s. The power law in the optical and X-ray bands of the afterglow is shown to arise from the synchrotron emission of relativistic electrons in the expanding magnetized HN ejecta. Two components contribute to the injected energy: the kinetic energy of the mildly relativistic expanding HN and the rotational energy of the fast-rotating highly magnetized νNS. We reproduce the afterglow in all wavelengths from the optical (10^{14} Hz) to the X-ray band (10^{19} Hz) over times from 604 s to 5.18×10^6 s relative to the *Fermi*-GBM trigger. Initially, the emission is dominated by the loss of kinetic energy of the HN component. After 10^5 s the emission is dominated by the loss of rotational energy of the νNS, for which we adopt an initial rotation period of 2 ms and a dipole plus quadrupole magnetic field of $\lesssim 7 \times 10^{12}$ G or $\sim 10^{14}$ G. This scenario with a progenitor composed of a CO_{core} and an NS companion differs from the traditional ultra-relativistic-jetted treatments of the afterglows originating from a single black hole.

Key words: binaries: general – black hole physics – gamma-ray burst: general – hydrodynamics – stars: neutron – supernovae: general

1. Introduction

It has been noted for almost two decades (Galama et al. 1998) that many long-duration gamma-ray bursts (GRBs) show the presence of an associated unusually energetic supernova (SN) of type Ic (hypernova, HN) as well as of a long-lasting X-ray afterglow (Costa et al. 1997). Such HNe are unique in their spectral characteristics; they have no hydrogen and helium lines, suggesting that they are members of a binary system (Smartt 2009). Moreover, these are broad-lined HNe suggesting the occurrence of energy injection beyond that of a normal SN Ic (Lyman et al. 2016).

This has led to our suggestion (e.g., Ruffini et al. 2001; Izzo et al. 2012) of a model for long GRBs associated with SNe Ic. In this paradigm, the progenitor is a carbon–oxygen star (CO_{core}) in a tight binary system with a neutron star (NS). As the CO_{core} explodes in an SN Ic it produces a new NS (hereafter νNS) and ejects a remnant of a few solar masses, some of which is accreted onto the companion NS (Rueda & Ruffini 2012). The accretion onto the companion NS is hypercritical, i.e., highly super-Eddington, reaching accretion rates of up to a tenth of solar mass per second, for the most compact binaries with orbital periods of a few minutes (Fryer et al. 2014). The NS gains mass rapidly, reaching the critical mass, within a few seconds. The NS then collapses to a black hole (BH) with the consequent emission of the GRB (Fryer et al. 2015). In this picture the BH formation and the associated GRB occurs some seconds *after* the initiation of the SN. The high temperature and density reached during the hypercritical accretion and the NS collapse lead to a copious emission of $\nu\bar{\nu}$ pairs which form an e^+e^- pair plasma that drives the GRB (see, e.g., Becerra et al. 2015, 2016; Ruffini et al. 2016). The expanding SN remnant is reheated and shocked by the injection of the e^+e^- pair plasma from the GRB explosion (Ruffini et al. 2018a).

The shocked-heated SN, originally expanding at $0.2c$, is transformed into an HN reaching expansion velocities of up to $0.94c$ (see Section 3). A vast number of totally new physical processes are introduced that must be treated within a correct classical and quantum general relativistic approach (see, e.g., Ruffini et al. 2018a, and references therein). The ensemble of these processes, addressing causally disconnected phenomena, each characterized by specific world lines, ultimately leads to a specific Lorentz Γ factor. This ensemble comprises the binary-driven hypernova (BdHN) paradigm (Ruffini et al. 2016).

In this article we extend this novel approach to the analysis of the BdHN afterglows. The existence of regularities in the X-ray luminosity of BdHNe, expressed in the observer cosmological rest frame, has been previously noted leading to the Muccino–Pisani power-law behavior (Pisani et al. 2013; Ruffini et al. 2014). The aim of this article is to now explain the origin of these power-law relations and to understand their physical origin and their energy sources.

The kinetic energy of the mildly relativistic expanding HN at $0.94c$ following the γ-ray flares and the X-ray flares, as well as the overall plateau phase, appears to have a crucial role (Ruffini et al. 2014). The contribution of the rotational energy electromagnetically radiated by the νNS appears to be equally crucial. As we show in this article, the power-law luminosity in the X-rays and in the optical wavelengths, expressed as a function of time in the GRB source rest frame, could not be explained without their fundamental contribution. We assume here that the afterglow originates from the synchrotron emission of relativistic electrons injected into the magnetized plasma of the HN, using both the kinetic energy of expansion and the electromagnetic energy powered by the rotational energy loss of the νNS (see Section 4).

As an example, we apply this new approach to the afterglow of GRB 130427A associated with the SN 2013cq, in view of the excellent data available in X-rays, as well as optical and radio wavelengths. We fit the spectral evolution of the GRB from 604 to 5.18×10^6 s and over the observed frequency bands from 10^9 to 10^{19} Hz. We present our simulations of the afterglow of GRB 130427A suggesting that a total energy of order $\simeq 10^{53}$ erg has been injected into the electrons confined within the expanding magnetized HN. This energy derives from the kinetic energy of the HN and the rotational energy of the νNS with a rotation period of 2 ms, containing a dipole or quadrupole magnetic field of (5–7) $\times 10^{12}$ G or 10^{14} G.

The article is organized as follows. In Section 2 we summarize how the BdHN treatment compares and contrasts with the traditional collapsar-fireball model of the GRB afterglow which is based on a single ultra-relativistic jet. In Section 3 we present the data reduction of GRB 130427A. In Section 4 we examine the basic parameters of the νNS relevant for this analysis such as the rotation period, the mass, the rotational energy, and the magnetic field structure. We introduce in Section 5 the main ingredients and equations relevant for the computation of the synchrotron emission of the relativistic electrons injected in the magnetized HN. In Section 6 we set up the initial/boundary conditions to solve the model equations of Section 5. In Section 7 we compare and contrast the results of the numerical solution of our synchrotron model, the theoretical spectrum and light curve, with the afterglow data of GRB 130427A at early times $10^2\,\mathrm{s} \lesssim t \lesssim 10^6$ s. We also show the role of the νNS in powering the late, $t \gtrsim 10^6$ s, X-ray afterglow. Finally, we present our conclusions in Section 8 outlining some possible further observational predictions of our model.

2. On BdHNe versus the Traditional Collapsar-fireball Approach

In Ruffini et al. (2016) it was established that there exist seven different GRB subclasses, all with binary systems as progenitors composed of various combinations of white dwarfs, CO_{cores}, NSs, and BHs, and that in only three of these subclasses are BHs formed. Far from being just a morphological classification, the identification of these systems and their properties has been made possible by the unprecedented quality and extent of the data ranging from X-ray, to γ-ray, to GeV emission as well as in the optical and in the radio. A comparable effort has been progressing in the theoretical field by introducing new paradigms and consistently developing the theoretical framework.

The main insight gained from the BdHN paradigm, one of the most numerous of the above seven subclasses, has been the successful identification, guided by the observational evidence, of a vast number of independent processes of the GRB. For each process, the corresponding field equations have been integrated, obtaining their Lorentz Γ factors as well as their spacetime evolution. This is precisely what has been done in the recent publications for the ultra-relativistic prompt emission

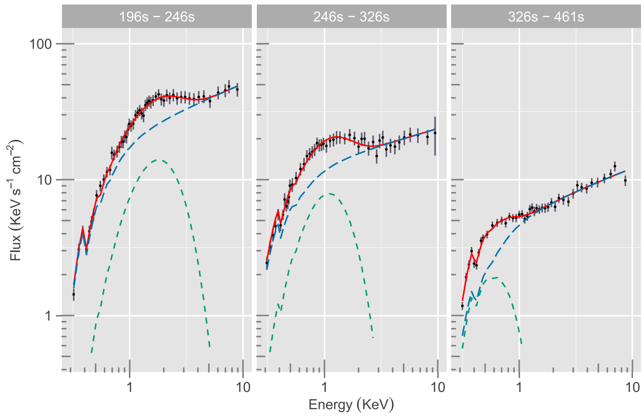

Figure 1. Spectral fitting (Ruffini et al. 2015) of three time intervals (196–246 s, 246–326 s, 326–461 s) in the *Swift*-XRT band (0.3–10 keV). Black points present the spectral data with H absorption, the green dashed line is the fitted thermal component, the blue long-dashed line is the power-law component, and the red line is the sum of two components. Clearly the temperature and the thermal flux drop over time.

(UPE) in the first 10 s with Lorentz factor $\Gamma \sim 500$–1000, the hard X-ray flares with $\Gamma \sim 10$ and for the mildly relativistic soft X-ray flares with $\Gamma \sim 2$–3 (Ruffini et al. 2018a) with the extended thermal X-ray emission (ETE) signaling the transformation of an SN into an HN (Ruffini et al. 2018b).

Here we extend the BdHN model to the study of the afterglow. As a prototype we utilize the data of GRB 130427A. We point out the following for the first time:

1. The role of the hypernova ejecta and of the rotation of the binary system in creating the condition for the occurrence of synchrotron emission, rooted in the pulsar magnetic field (see Section 4).
2. The fundamental role played by the pulsar-like behavior of the νNS (see Figure 6) and its magnetic field to explain the fit of a synchrotron model based on the optical and X-ray data (see Figure 4).
3. To develop a model of the afterglow that is consistent with the mildly relativistic expansion velocity measured in the afterglows following a model-independent procedure (see Equation (1) and Figure 1 in Section 3).

In the current afterglow model (see, e.g., Piran 1999; Mészáros 2002, 2006; Kumar & Zhang 2015, and references therein) it is tacitly assumed that a single ultra-relativistic regime extends all the way from the prompt emission, to the plateau phase, all the way to the GeV emission and to the latest power law of the afterglow. This approach is clearly in contrast with point 3 above.

3. GRB 130427A Data

GRB 130427A is well-known for its high isotropic energy $E_{\mathrm{iso}} \simeq 10^{54}$ erg, SN association, and multiwavelength observations (Ruffini et al. 2015). It triggered *Fermi*-GBM at 07:47:06.42 UT on 2013 April 27 (von Kienlin 2013), when it was within the field of view of *Fermi*-LAT. A long-lasting ($\sim 10^4$ s) burst of ultra high energy (100 MeV–100 GeV) radiation was observed (Ackermann et al. 2014). *Swift* started to follow from 07:47:57.51 UT, 51.1 s after the GBM trigger, observing a soft X-ray (0.3–10 keV) afterglow for more than 100 days (Maselli et al. 2014). NuStar joined the observation during three epochs, approximately ~1.2, 4.8, and 5.4 days after the *Fermi*-GBM trigger, providing rare hard X-ray (3–79 keV) afterglow observations (Kouveliotou et al. 2013). Ultraviolet, optical, infrared, and radio observations were also performed by more than 40 satellites and ground-based telescopes, within which *Gemini-North*, NOT, *William Herschel*, and VLT confirmed the redshift of 0.34 (Flores et al. 2013; Levan et al. 2013; Wiersema et al. 2013; Xu et al. 2013b), and NOT found the associated supernova SN 2013cq (Xu et al. 2013a). We adopt the radio, optical, and the GeV data from various published articles and GCNs (Sonbas et al. 2013; von Kienlin 2013; Xu et al. 2013a; Maselli et al. 2014; Perley et al. 2014; Ruffini et al. 2015). The soft and hard X-rays, which are some of the main subjects of this paper, were analyzed from the original data downloaded from the *Swift* repository[7] and *NuStar* archive.[8] We followed the standard data reduction procedure Heasoft 6.22 with relevant calibration files,[9] and the spectra were generated by XSPEC 12.9 (Evans et al. 2007, 2009). During the data reduction, the pile-up effect in the *Swift*-XRT was corrected for the first five time bins (see Figure 5) before 10^5 s (Romano et al. 2006). The NuStar spectrum at 388,800 s is inferred from the closest first 10,000 s of the *NuStar* third epoch at ~5.4 days, by assuming that the spectra at these two times have the same cutoff power-law shape but different amplitudes. The amplitude at 388,800 s was computed by fitting the *NuStar* light curve. A K-correction was implemented for transferring observational data to the cosmological rest frame (Bloom et al. 2001).

The GRB afterglow emission in the BdHN model originates from a mildly relativistic expanding SN ejecta. This has been confirmed by measuring the expansion velocity $\beta \sim 0.6$–0.9 (corresponding to the Lorentz gamma factor $\Gamma < 5$) within the early hundreds of seconds after the trigger from the observed thermal emission in the soft X-ray. For instance, Ruffini et al. (2014) finds a velocity of $\beta \sim 0.8$ for GRB 090618, and in Ruffini et al. (2018a), GRB 081008 is found to have a velocity $\beta \sim 0.9$. The optical signal at tens of days also implies a mildly relativistic velocity $\beta \sim 0.1$ (Galama et al. 1998; Woosley & Bloom 2006; Cano et al. 2017).

The expanding velocity can be directly inferred from the observable X-ray thermal emission and is summarized from Ruffini et al. (2018a):

$$\frac{\beta^5}{4[\ln(1+\beta)-(1-\beta)\beta]^2}\left(\frac{1+\beta}{1-\beta}\right)^{1/2} = \frac{D_L(z)}{1+z}\frac{1}{t_2-t_1}\left(\sqrt{\frac{F_{\mathrm{bb,obs}}(t_2)}{\sigma T^4_{\mathrm{obs}}(t_2)}}-\sqrt{\frac{F_{\mathrm{bb,obs}}(t_1)}{\sigma T^4_{\mathrm{obs}}(t_1)}}\right), \tag{1}$$

The left term is a function of velocity β, the right term is from observables, and $D_L(z)$ is the luminosity distance for redshift z. From the observed thermal flux $F_{\mathrm{bb,obs}}$ and temperature T_{obs} at times t_1 and t_2, the velocity β can be inferred. This model-independent equation, valid in Newtonian and relativistic regimes, is general. The results inferred do not agree with the ones of the fireball model (Daigne & Mochkovitch 2002; Pe'er et al. 2007), coming from a ultra-relativistic shockwave.

Indeed, GRB 130427A is a well-known example of a GRB associated with SN (Xu et al. 2013a). For this GRB an X-ray thermal emission has been found between 196 and 461 s (Ruffini et al. 2015). The spectral evolution of this source is presented in Figure 1. From the best fit, we obtain a temperature in the observer's frame that drops in time from 0.46 to 0.13 keV. The thermal flux also diminishes over time.

From Equation (1), we obtain a radius in the laboratory frame that increases from $1.67^{+0.43}_{-0.28} \times 10^{13}$ cm to $1.12^{+0.49}_{-0.33} \times 10^{14}$ cm. The velocity inferred from the first and second spectra is $\beta = 0.85^{+0.06}_{-0.10}$, from the second and third spectra increases to $\beta = 0.96^{+0.02}_{-0.03}$. The average velocity of the entire duration of thermal emission is $\beta = 0.94^{+0.03}_{-0.05}$, corresponding to a Lorentz factor $\Gamma = 2.98^{+1.20}_{-0.79}$, at an average radius $3.50^{+1.46}_{-0.97} \times 10^{13}$ cm. At later observer's time around 16.7 days after the GRB trigger, the mildly relativistic velocity ~32,000 km s^{-1} ($\beta \sim 0.1$) of the afterglow is measured from the line of Fe II 5169 (Xu et al. 2013a). Both the mildly relativistic velocities and the small radii are inferred directly from the observations and agree with the required properties of the BdHN model.

The above data are in contrast with the traditional fireball model (e.g., Piran 1999), which involves a shockwave with a high Lorentz factor $\Gamma \sim 500$ continuously expanding and generating the prompt emission at a radius of $\sim 10^{15}$ cm, and then the afterglow at a lab-frame radius of $>10^{16}$ cm. Therefore, any model of the afterglow with ultra-relativistic velocity following after the UPE does not conform to the stringent observational constraints.

One is left, therefore, with the task of developing a consistent afterglow model with a mildly relativistic expansion that is compatible with this clear observational evidence that the afterglow arises from mildly relativistic ejecta. That is the purpose of the present work.

4. Role of the New Fast-rotating NS in the Energetics and Properties of the GRB Afterglow

Angular momentum conservation implies that the νNS should be rapidly rotating. For example, the gravitational collapse of an iron core of radius $R_{\mathrm{Fe}} \sim 5 \times 10^8$ cm of a carbon–oxygen progenitor star leading to an SN Ic, rotating with an initial period of $P \sim 5$ minutes, implies a rotation period $P = (R_{\mathrm{NS}}/R_{\mathrm{Fe}})^2 P_{\mathrm{CO}} \sim 1$ ms for the newly formed neutron star. Thus, one expects the νNS to have a large amount of rotational energy available to power the SN remnant. In order to evaluate such rotational energy we need to know the structure of fast-rotating NSs. This we adopt from Cipolletta et al. (2015).

The structure of NSs in uniform rotation is obtained by numerical integration of the Einstein equations in axial symmetry and the stability sequences are described by two parameters, e.g., the baryonic mass (or the gravitational mass/central density) and the angular momentum (or the angular velocity/polar to equatorial radius ratio). The stability of the star is bounded by (at least) two limiting conditions (see, e.g., Stergioulas 2003, for a review). The first is the mass-shedding or Keplerian limit: for a given mass (or central density) there is a configuration whose angular velocity equals that of a test particle in circular orbit at the stellar equator. Thus, the matter at the stellar surface is marginally bound so that any small perturbation causes mass loss bringing the star back to stability or to a point of dynamical instability. The second is the secular axisymmetric instability: in this limit the star becomes unstable against axially symmetric perturbations and is expected to evolve first quasi-stationarily toward a dynamical instability

[7] http://www.swift.ac.uk
[8] https://heasarc.gsfc.nasa.gov/docs/nustar/nustar_archive.html
[9] http://heasarc.gsfc.nasa.gov/lheasoft/

Table 1
Critical Mass (and Corresponding Radius) Obtained in Cipolletta et al. (2015) for Selected Parameterizations of the Nuclear EOS

EOS	$M_{\rm crit}^{J=0}$ $(M_\odot)$	$R_{\rm crit}^{J=0}$ (km)	$M_{\rm max}^{J\neq 0}$ $(M_\odot)$	$R_{\rm max}^{J\neq 0}$ (km)	a	C	$P_{\rm min}$ (ms)
NL3	2.81	13.49	3.38	17.35	1.68	0.006	0.75
GM1	2.39	12.56	2.84	16.12	1.69	0.011	0.67
TM1	2.20	12.07	2.62	15.98	1.61	0.017	0.71

Note. In the last column we list the rotation period of the fastest possible configuration that corresponds to that of the critical mass configuration (i.e., secularly unstable) that intersects the Keplerian mass-shedding sequence.

point where gravitational collapse ensues. This instability sequence thus leads to the NS critical mass and it can be obtained via the turning-point method by Friedman et al. (1988).

In Cipolletta et al. (2015) the values of the critical mass were obtained for the NL3, GM1, and TM1 equations of state (EOS) and the following fitting formula was found to describe them with a maximum error of 0.45%:

$$M_{\rm NS}^{\rm crit} = M_{\rm crit}^{J=0}(1 + C j_{\rm NS}^{a}), \tag{2}$$

where $j_{\rm NS} \equiv cJ_{\rm NS}/(GM_\odot^2)$ is a dimensionless angular momentum parameter, $J_{\rm NS}$ is the NS angular momentum, C and a are parameters that depend on the nuclear EOS, and $M_{\rm crit}^{J=0}$ is the critical mass in the nonrotating case (see Table 1).

The configurations lying along the Keplerian sequence are also the maximally rotating ones (given a mass or central density). The fastest rotating NS is the configuration at the crossing point between the Keplerian and the secular axisymmetric instability sequences. Figure 2 shows the minimum rotation period and the rotational energy as a function of the NS gravitational mass for the NL3 EOS.

We turn now to the magnetosphere properties. Within the traditional model of pulsars (Goldreich & Julian 1969), in a rotating, highly magnetized NS, a corotating magnetosphere is enforced up to a maximum distance $R_{\rm lc} = c/\Omega = cP/(2\pi)$, where c is the speed of light and Ω is the angular velocity of the star. This defines the so-called light cylinder since corotation at larger distances implies superluminal velocities of the magnetospheric particles. The last B-field line closing within the corotating magnetosphere is located at an angle $\theta_{\rm pc} = \arcsin(\sqrt{R_{\rm NS}/R_{\rm lc}}) \approx \sqrt{R_{\rm NS}/R_{\rm lc}} = \sqrt{R_{\rm NS}\Omega/c} = \sqrt{2\pi R_{\rm NS}/(cP)}$ from the star's pole. The B-field lines that originate in the region between $\theta = 0$ and $\theta = \theta_{\rm pc}$ (referred to as the *magnetic polar caps*) cross the light cylinder and are called "open" field lines. Charged particles leave the star moving along the open field lines and escape from the magnetosphere passing through the light cylinder.

At large distances from the light cylinder the magnetic field lines become radial. Thus, the magnetic field geometry is dominated by the toroidal component, which decreases with the inverse of the distance. For typical pulsar magnetospheres it is expected to be related to the poloidal component of the field at the surface, B_s, as (see Goldreich & Julian 1969 for details)

$$B_t \sim \left(\frac{2\pi R_{\rm NS}}{cP}\right)^2 \left(\frac{R_{\rm NS}}{r}\right) B_s, \tag{3}$$

up to a factor of order unity. Thus, as the SN remnant expands it finds a magnetized medium with a different value of the

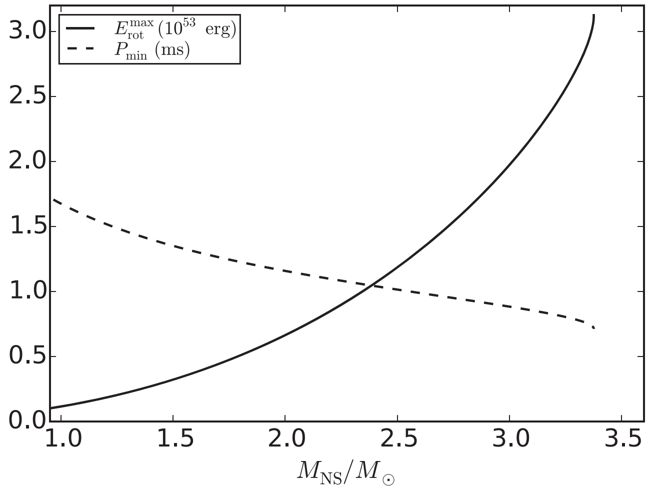

Figure 2. Rotational energy and period of NSs along the Keplerian sequence for the NL3 EOS.

B-field. We adopt a magnetic field of the form

$$B(t) = B_0 \left(\frac{R_0}{r}\right)^{-m}, \tag{4}$$

with $1 \leqslant m \leqslant 2$. We then seek the value of m, which fits the data best (see Sections 5–7).

According to the previous agreement we have found between our model and GRB data (see e.g., Becerra et al. 2016; Ruffini et al. 2018), we shall adopt values for R_0 and the expansion velocity $\dot{R}$ (see below Sections 5–7) and leave the parameter B_0 to be set by the fit of the afterglow data. We then compare and contrast the results with that expected from the NS theory.

5. Model for the Optical and X-Ray Spectrum of the Afterglow

The origin of the observed afterglow emission is interpreted here as due to the synchrotron emission of electrons accelerated in an expanding magnetic HN ejecta.[10] A fraction of the kinetic energy of the ejecta is converted, through a shockwave, to accelerated particles (electrons) above GeV and TeV energies —enough to emit photons up to the X-ray band by synchrotron emission. Depending on the shock speed, number density, magnetic field, etc., different initial energy spectra of particles can be formed. In the most common cases, the accelerated particle distribution function can be described by a power law in the form of

$$Q(\gamma, t) = Q_0(t)\gamma^{-p}\theta(\gamma_{\rm max} - \gamma)\theta(\gamma - \gamma_{\rm min}), \tag{5}$$

where $\gamma = E/mc^2$ is the electron Lorentz factor, $\gamma_{\rm min}$ and $\gamma_{\rm max}$ are the minimum and maximum Lorenz factors, respectively. $Q_0(t)$ is the number of injected particles per second per energy, originating from the remnant impacted by the e^+e^-pair plasma of the GRB.

After the electrons are injected with a spectrum given by Equation (5), the evolution of the particle distribution at a given time can be determined from the solution of the kinetic

[10] We note that synchrotron emission of electrons in the fast cooling regime has been previously applied in GRBs but to explain the prompt emission (see, e.g., Uhm & Zhang 2014).

equation of the electrons taking into account the particle energy losses (Kardashev 1962)

$$\frac{\partial N(\gamma, t)}{\partial t} = \frac{\partial}{\partial \gamma}(\dot{\gamma}(\gamma, t)\, N(\gamma, t)) - \frac{N(\gamma, t)}{\tau} + Q(\gamma, t), \quad (6)$$

where τ is the characteristic escape time and $\dot{\gamma}(\gamma, t)$ is the cooling rate. In the present case the escape time for electrons is much longer than the characteristic cooling timescale (fast cooling regime). The term $\dot{\gamma}(\gamma, t)$ includes various electron energy loss processes, such as synchrotron and inverse-Compton cooling as well as adiabatic losses due to the expansion of the emitting region. For the magnetic field considered here, the dominant cooling process for higher energy electrons is synchrotron emission (the electron cooling timescale due to inverse-Compton scattering is significantly longer) while adiabatic cooling can dominate for the low-energy electrons at later phases. By introducing the expansion velocity of the remnant $\dot{R}(t)$ and its radius $R(t)$, the energy loss rate of electrons can be written as

$$\dot{\gamma}(\gamma, t) = \frac{\dot{R}(t)}{R(t)}\gamma + \frac{4}{3}\frac{\sigma_T}{m_e c}\frac{B(t)^2}{8\pi}\gamma^2, \quad (7)$$

where σ_T is the Thomson cross section and $B(t)$ is the magnetic field strength. From the early X-ray data we find that the initial expansion velocity of GRB 130427A at times $\sim 10^2$ s is $0.8c$ (Ruffini et al. 2015), which then decelerates to $0.1c$ at 10^6 s, as inferred from the SN optical data (Xu et al. 2013a).

SN or hypernova remnants like the one considered here generally evolve through three stages (see Sturner et al. 1997). These are the free expansion phase, the Sedov phase, and the radiative cooling phase. The free expansion phase roughly ends when the total mass of gas swept up by the shock equals the initial SN ejecta mass. During this phase, the shock velocity remains nearly constant at its initial velocity v_0 and the outer radius R of the ejecta evolves linearly in time after the explosion. This phase ends (Sturner et al. 1997) when

$$t \approx 50 \text{ yr} \times \left[\left(\frac{M_{ej}}{5M_\odot}\right) \times \left(\frac{1 \text{ cm}^{-3}}{n_{ISM}}\right) \times \left(\frac{v_0}{0.1\, c}\right)^3\right]^{1/3}, \quad (8)$$

where M_{ej} is the HN ejected mass and n_{ISM} is the hydrogen density in the local interstellar medium. For a mildly relativistic ejecta ($v/c \sim 0.9$, $\Gamma \sim 3$) in a typical ISM of $n_{ISM} \approx 1$ cm^{-3} this phase lasts for 450 years. Even if the ISM is 1000 times more dense due to past mass loss of the progenitor star, this phase still lasts for 45 years. Since we only consider times much less than a year (out to 10^7 s) we are completely justified in treating the expansion as a "ballistic" constant velocity rather than a Sedov expansion.

Nevertheless, we allow for an initial linearly decelerating eject as observed in the thermal component (see Section 3)) until 10^6 s. After which it is allowed to expand with a constant velocity of $0.1c$. Thus, the expansion velocity of the ejecta is written as

$$\dot{R}(t) = \begin{cases} v_0 - a_0\, t & t \leqslant 10^6 \text{ s} \\ v_f & t > 10^6 \text{ s} \end{cases}, \quad (9)$$

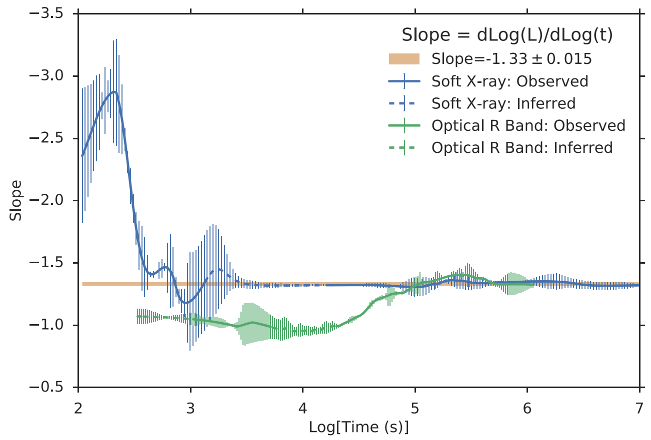

Figure 3. The slope of the afterglow light curve of BdHN 130427A, defined by the logarithmic time derivative of the luminosity: slope $= d\log_{10}(L)/d\log_{10}(t)$. This slope is obtained by fitting the luminosity light curve in the cosmological rest frame, using a machine learning, locally weighted regression (LWR) algorithm. For the corresponding technical details and codes we refer the reader to https://github.com/YWangScience/AstroNeuron. The green line is the slope of the soft X-ray emission, in the 0.3–10 keV range, and the blue line corresponds to the optical R-band, centered at 658 nm.

$$R(t) = \begin{cases} v_0\, t - a_0\, t^2/2 & t \leqslant 10^6 \text{ s} \\ 1.05 \times 10^{16} \text{ cm} + v_f\, t & t > 10^6 \text{ s} \end{cases}, \quad (10)$$

where $v_0 = 2.4 \times 10^{10}$ cm s^{-1}, $a_0 = 2.1 \times 10^4$ cm s^{-2}, and $v_f = 3 \times 10^9$ cm s^{-1}.

Due to the above decelerating expansion of the emitting region, the magnetic field decreases. Therefore we adopt a magnetic field that scales as $B(t) = B_0\left(\frac{R(t)}{R_0}\right)^{-m}$ with $1 \leqslant m \leqslant 2$. We shall show below (see Section 7) that the data are best fit with $m = 1$. This corresponds to conservation of magnetic flux for the longitudinal component.

The initial injection rate of particles, $Q_0(t)$, depends on the energy budget of ejecta and on the efficiency of converting from kinetic to nonthermal energy. This can be defined as

$$L(t) = Q_0(t) m_e c^2 \int_{\gamma_{min}}^{\gamma_{max}} \gamma^{1-p} d\gamma, \quad (11)$$

where it is assumed that $L(t)$ varies over time, based on the recent analyses of BdHNe, which show that the X-ray light curve of GRB 130724A decays in time following a power law of index ~ -1.3 (Ruffini et al. 2015; see Figure 3). In our interpretation, the emission in the optical and X-ray bands is produced from synchrotron emission of electrons: if one assumes the electrons are constantly injected ($L(t) = L$), this will produce a constant synchrotron flux. Thus, we assume that the luminosity of the electrons changes from an initial value L_0 as follows:

$$L(t) = L_0 \times \left(1 + \frac{t}{\tau_0}\right)^{-k}, \quad (12)$$

where the L_0 and k are fixed by the observed afterglow light curve (see Equation (13)) (see details below in Sections 6 and 7).

The kinetic equation given in Equation (6) has been solved numerically. The discretized electron continuity Equation (6) is rewritten in the form of a tridiagonal matrix that is solved using the implementation of the "tridiag" routine in Press et al. (1992). We have carefully tested our code by comparing the numerical results with the analytic solutions given in Kardashev (1962).

The synchrotron luminosity temporal evolution is calculated using $N(\gamma, t)$ with

$$L_{\rm syn}(\nu, t) = \int_1^{\gamma_{\rm max}} N(\gamma, t) P_{\rm syn}(\nu, \gamma, B(t)) d\gamma, \qquad (13)$$

where $P_{\rm syn}(\nu, \gamma, B(t))$ is the synchrotron spectra for a single electron, which is calculated using the parameterization of the emissivity function of synchrotron radiation presented in Aharonian et al. (2010).

6. Initial Conditions for GRB 130724A

In Ruffini et al. (2018a) an analysis was completed for seven subclasses of GRBs including 345 identified BdHNe candidates, one of which is GRB 130724A that was seen in the *Swift*-XRT data and analyzed in detail in Ruffini et al. (2015). From the host-galaxy identification it is known that this burst occurred at a redshift $z = 0.334$. After transforming to the cosmological rest frame of the burst and properly correcting for effects of the cosmological redshift and Lorentz time dilation, one can infer a time duration $t_{90} = 162.8$ s for 90% of the GRB emission. The isotropic energy emission in the range of $1\text{–}10^4$ keV in the cosmological rest frame of the burst is also deduced to be $E_{\rm iso} = (9.3 \pm 1.3) \times 10^{53}$ erg and the total emission in the power-law afterglow can be inferred (Ruffini et al. 2015). This fixes L_0 in Equation (12).

Figure 3 shows the slope of the light curve, defined by the logarithmic time derivative of the luminosity: slope $= d\log_{10}(L)/d\log_{10}(t)$. This slope is obtained by fitting the luminosity light curve in the cosmological rest frame, using a machine learning, locally weighted regression (LWR) algorithm. We have made publicly available the corresponding technical details and codes to perform this calculation at https://github.com/YWangScience/AstroNeuron. The green line is the slope of the soft X-ray emission, in the 0.3–10 keV range, and the blue line corresponds to the optical R-band, centered at 658 nm. The solid line covers the time when the data are well observed, while the dashed line corresponds to an epoch in which observational data are missing. The rapid change of the slope implies variations of the energy injection, different emission mechanisms or different emission phases. The slope of the soft X-ray emission varies dramatically at early times when various complicated GRB components (prompt emission, gamma-ray flare, and X-ray flare) are occurring. Hence, we do not attempt to explain this early part with the synchrotron emission model defined above. We only consider times later than 10^3 s. Also we note that, at times later than 10^5 s, the slopes of the X-ray and R bands reach a common value of -1.33, indicated as a red line.

Furthermore, we are not interested in explaining the GeV emission observed in most of BdHNe (when LAT data are available) with the synchrotron radiation model proposed here. Such emission has been explained in Ruffini et al. (2015) as originating from the further accretion of matter onto the newly formed BH. This explanation is further reinforced by the fact that a similar GeV emission, following the same power-law decay with time, is also observed in the authentic short GRBs (S-GRBs; short bursts with $E_{\rm iso} \gtrsim 10^{52}$ erg; see Ruffini et al. 2016),

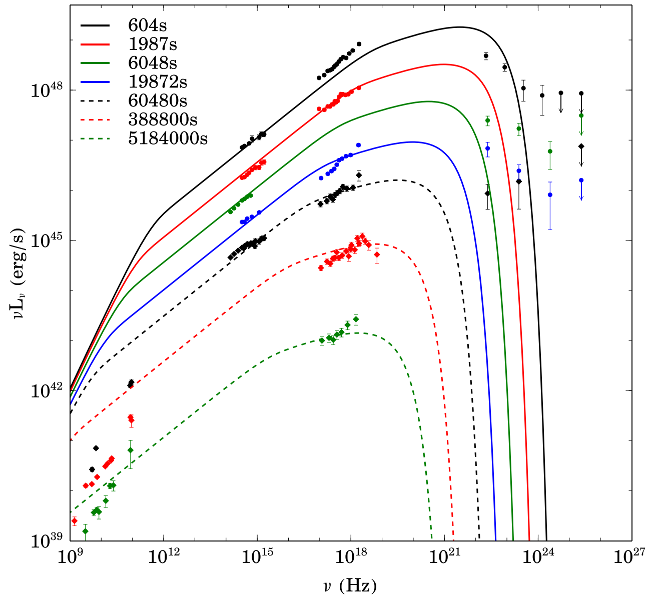

Figure 4. Model evolution (lines) of synchrotron spectral luminosity at various times compared with measurements (points with error bars) in various spectral bands for GRB 130724A.

Table 2
Parameters Used for the Simulation of GRB 130724A

Parameter	Value
B_0	$5.0\ (\pm 1) \times 10^5$ G
R_0	2.4×10^{12} cm
L_0	2.0×10^{51} erg s^{-1}
k	1.58
τ_0	1.0×10^2 s
p	1.5
$\gamma_{\rm min}$	4.0×10^3
$\gamma_{\rm max}$	5.0×10^5

which are expected to be produced in NS–NS mergers leading to BH formation (Ruffini et al. 2016; Y. Aimuratov et al. 2018, in preparation).

Regarding the model parameters, the initial velocity of the expanding ejecta is expected to be $v_0 = 2.4 \times 10^{10}$ cm s^{-1} (Ruffini et al. 2015) from the thermal blackbody emission. Similarly, the radius at the beginning of the X-ray afterglow should be $R_0 \approx 2.4 \times 10^{12}$ cm. This corresponds to an expansion timescale of $t_0 = \tau_0 = 100$ s. These values are consistent with our previous theoretical simulations of BdHNe (Becerra et al. 2016). For our simulation of this burst we include all expected energy losses (synchrotron and adiabatic energy losses). However, the escape timescale was assumed to be large so that its effect could be neglected.

7. Results

Our modeling of the broadband spectral energy distribution of GRB 130724A for different periods is shown in Figure 4. The corresponding parameters are given in Table 2. However, as noted above, the eight parameters in Table 2 are not all "free" and independent. For example, R_0 and $t_0 = \tau_0$ are fixed by the observed thermal component. Also, $\gamma_{\rm min}$ and $\gamma_{\rm max}$ are fixed once B is given. L_0 is fixed by a normalization of the observed source luminosity. The synchrotron index p is not varied, but kept fixed at 1.5 as is typical of synchrotron emission. The parameter k is fixed by the slope of the late time X-ray afterglow. Hence, the only "free parameter" is B_0. This parameter then provides an excellent fit to the observed spectra and light curves over a broad range of wavelengths and timescales for a single plausible value.

The radio emission is due to low-energy electrons that accumulate for longer periods. That is why the radio data are not included in the model. Only the optical and X-ray emissions are interpreted as being due to the synchrotron emission of electrons. Such emission, for instance at 604 s, is produced in a region with a radius of 1.4×10^{14} cm and a magnetic field of $B = 8.3 \times 10^4$ G. For this field strength synchrotron self-absorption can be significant as estimated following Rybicki & Lightman (1979). At the initial phases, when the system is compact and the magnetic field is large, synchrotron self-absorption can be neglected for the photons with frequencies above 10^{14} Hz. Otherwise, it is important. Thus, it is effective in reducing the radio flux predicted by the model, but not the optical and X-ray emission.

The optical and X-ray data can be well fit by a single power-law injection of electrons with $Q \propto \gamma^{-1.5}$ and with initial minimum and maximum energies of $\gamma_{\min} = 4 \times 10^3$ ($E_{\min} = 2.0$ GeV) and $\gamma_{\max} = 5 \times 10^5$ ($E_{\max} = 255.5$ GeV), respectively. Due to the fast synchrotron cooling, the electrons are cooled rapidly, forming a spectrum of $N(\gamma, t) \sim \gamma^{-2}$ for $\gamma \leqslant \gamma_{\min}$ and $N(\gamma, t) \sim \gamma^{-2.5}$ for $\gamma \geqslant \gamma_{\min}$. The slope of the synchrotron emission ($\nu F_\nu \propto \nu^{1-s}$) below the frequency defined by $\gamma_{\min}$ (e.g., $h\nu_{\min} \simeq 3e\ h\ B(t)\ \gamma_{\min}^2 / 4\pi\ m_e\ c$) is $s = (2-1)/2 = 0.5$. This explains well both the optical and X-ray data.

For frequencies above $\nu_{\min}$, the slope is $\nu F_\nu \propto \nu^{0.25}$, which continues up to $h\nu_{\max} \simeq 3e\ h\ B(t)\ \gamma_{\max}^2 / (4\pi m_e c)$. Since $\nu_{\min}$ and $\nu_{\max}$ depend on the magnetic field, they decrease with time, e.g., at $t = 5.2 \times 10^6$ s, $\nu_{\min} \simeq 6.5 \times 10^{14}$ Hz, and $\nu_{\max} \simeq 1.0 \times 10^{19}$ Hz. Due to the changes in the initial particle injection rate and magnetic field, the synchrotron luminosity also decreases. This is evident from Figure 5, where the observed optical and X-ray light curves of GRB 130427A are compared with the theoretical synchrotron emission light curve obtained from Equation (13). In this figure we also show the electron injection power $L(t)$ given by Equation (12). Here, it can be seen how the synchrotron luminosity fits the observed decay of the afterglow luminosity with the correct power-law index -1.3 (see also Figure 3).

The SN ejecta is expected to become transparent to the νNS radiation at around 10^5 s. Thus, we now discuss the pulsar emission that might power the late ($t \gg 10^5$ s) X-ray afterglow light curve.

The late X-ray afterglow also shows a power-law decay of index ~ -1.3 which, as we show below, if powered by the pulsar implies the presence of a quadrupole magnetic field in addition to the traditional dipole one.

Thus, we adopt a dipole+quadrupole magnetic field model (see Pétri 2015, for details). The luminosity from a pure dipole ($l = 1$) is

$$L_{\rm dip} = \frac{2}{3c^3}\Omega^4 B_{\rm dip}^2 R_{\rm NS}^6 \sin^2\chi_1, \tag{14}$$

where $\chi_1 = 0°$ gives the axisymmetric mode $m = 0$ alone whereas $\chi_1 = 90°$ gives the $m = 1$ mode alone. The braking index, following the traditional definition $n \equiv \Omega\ddot{\Omega}/\dot{\Omega}^2$, is in this case $n = 3$.

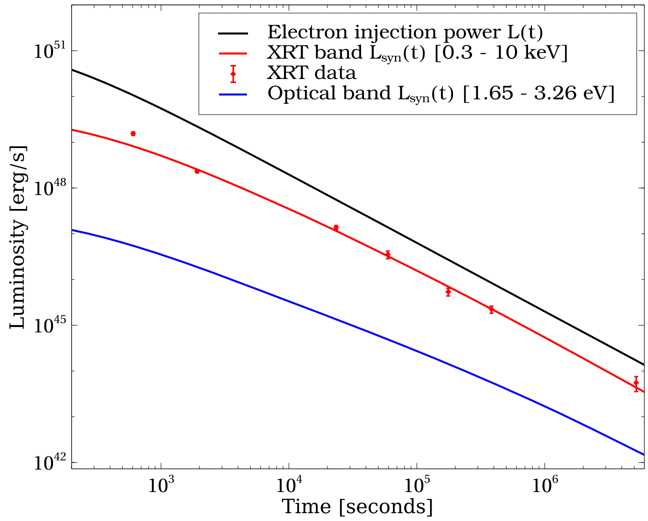

Figure 5. X-ray light curve of GRB 130427A (points with error bars) together with the optical and X-ray theoretical synchrotron light curve (lines) from Equation (13). We also show the electron injection power $L(t)$ given by Equation (12).

On the other hand, the luminosity from a pure quadrupole field ($l = 2$) is

$$L_{\rm quad} = \frac{32}{135c^5}\Omega^6 B_{\rm quad}^2 R_{\rm NS}^8 \sin^2\chi_1(\cos^2\chi_2 + 10\sin^2\chi_2), \tag{15}$$

where the different modes are easily separated by taking $\chi_1 = 0$ and any value of χ_2 for $m = 0$, $(\chi_1, \chi_2) = (90, 0)$ degrees for $m = 1$ and $(\chi_1, \chi_2) = (90, 90)$ degrees for $m = 2$. The braking index in this case is $n = 5$.

Thus, the quadrupole to dipole luminosity ratio is:

$$R_{\rm dip}^{\rm quad} = \eta^2 \frac{16}{45}\frac{R_{\rm NS}^2\Omega^2}{c^2}, \tag{16}$$

where

$$\eta^2 = (\cos^2\chi_2 + 10\sin^2\chi_2)\frac{B_{\rm quad}^2}{B_{\rm dip}^2}. \tag{17}$$

It can be seen that $\eta = B_{\rm quad}/B_{\rm dip}$ for the $m = 1$ mode, and $\eta = 3.16 \times B_{\rm quad}/B_{\rm dip}$ for the $m = 2$ mode. For a 1 ms period νNS, if $B_{\rm quad} = B_{\rm dip}$, the quadrupole emission is about $\sim$10% of the dipole emission, if $B_{\rm quad} = 100 \times B_{\rm dip}$, the quadrupole emission increases to 1000 times the dipole emission; and for a 100 ms pulsar, the quadrupole emission is negligible when $B_{\rm quad} = B_{\rm dip}$, or only $\sim$10% of the dipole emission even when $B_{\rm quad} = 100 \times B_{\rm dip}$. From this result one infers that the quadrupole emission dominates in the early fast rotation phase, then the νNS spins down and the quadrupole emission drops faster than the dipole emission and, after tens of years, the dipole emission becomes the dominant component.

The evolution of the νNS rotation and luminosity are given by

$$\begin{aligned}\frac{dE}{dt} &= -I\Omega\dot{\Omega} = -(L_{\rm dip} + L_{\rm quad})\\ &= -\frac{2}{3c^3}\Omega^4 B_{\rm dip}^2 R_{\rm NS}^6 \sin^2\chi_1\left(1 + \eta^2\frac{16}{45}\frac{R_{\rm NS}^2\Omega^2}{c^2}\right),\end{aligned} \tag{18}$$

where I is the moment of inertia. The solution is

$$t = f(\Omega) - f(\Omega_0) \tag{19}$$

where

$$f(\Omega) = \frac{3Ic\left\{\frac{16}{45}\eta^2 R_{NS}^2\Omega^2\left[2\ln\Omega - \ln\left(c^2 + \frac{16}{45}\eta^2 R_{NS}^2\Omega^2\right)\right] + c^2\right\}}{4B_{dip}^2 \sin^2\chi_1 R_{NS}^6\Omega^2} \tag{20}$$

and

$$f(\Omega_0) = \frac{3Ic\left\{\frac{16}{45}\eta^2 R_{NS}^2\Omega_0^2\left[2\ln\Omega_0 - \ln\left(c^2 + \frac{16}{45}\eta^2 R_{NS}^2\Omega_0^2\right)\right] + c^2\right\}}{4B_{dip}^2 \sin^2\chi_1 R_{NS}^6\Omega_0^2}. \tag{21}$$

The first and the second derivatives of the angular velocity are

$$\dot{\Omega} = -\frac{2B_{dip}^2 \sin^2\chi_1 R_{NS}^6\Omega^3}{3Ic^3}\left(1 + \eta^2\frac{16}{45c^2}R_{NS}^2\Omega^2\right) \tag{22}$$

$$\ddot{\Omega} = -\frac{2B_{dip}^2 \sin^2\chi_1 R_{NS}^6\Omega^2\dot{\Omega}}{Ic^3}\left(1 + \eta^2\frac{16}{27c^2}R_{NS}^2\Omega^2\right). \tag{23}$$

Therefore the braking index is

$$n = \frac{\Omega\ddot{\Omega}}{\dot{\Omega}^2} = \frac{135c^2 + 80\eta^2 R_{NS}^2\Omega^2}{45c^2 + 16\eta^2 R_{NS}^2\Omega^2} \tag{24}$$

that in the present case ranges from 3 to 5. From Equations (19)–(22) we can compute the evolution of total pulsar luminosity as

$$L_{tot}(t) = I\Omega\dot{\Omega}. \tag{25}$$

Figure 6 shows the luminosity obtained from the above model for a 1.5 $M_\odot$ pulsar with a radius of 1.5×10^6 cm, $B_{dip} = 5 \times 10^{12}$ G, an initial rotation period $P_0 = 2$ ms, and for selected values of the parameter η. This figure shows that the theoretical luminosity of the pulsar is close to the soft X-ray luminosity observed in GRB 130427A when η is around 100. This means, if choosing the harmonic mode $m = 2$, the quadrupole magnetic field is about 30 times stronger than the dipole magnetic field. The luminosity of the pulsar before 10^6 s is mainly powered by the quadrupole emission, which is tens of times higher than the dipole emission. At about 10 years the dipole emission starts to surpass the quadrupole emission and continues to dominate thereafter.

It is important to check the self-consistency of the estimated νNS parameters obtained first from the early afterglow via synchrotron emission and then from the late X-ray afterglow via the pulsar luminosity. We can obtain from Equations (4) and (3), via the values of B_0 and R_0 from Table 2 and for $P_0 = 2$ ms, an estimate of the dipole field at the νNS surface from the synchrotron emission powering the early X-ray afterglow, $B_s \approx 6.7 \times 10^{12}$ G. This value is to be compared with the one we have obtained from the pulsar luminosity powering the late afterglow, $B_{dip} = 5 \times 10^{12}$ G. The self-consistency of the two estimates is remarkable. In addition, the initial rotation period $P_0 = 2$ ms for the νNS is consistent with our estimate in Section 4 based upon angular momentum

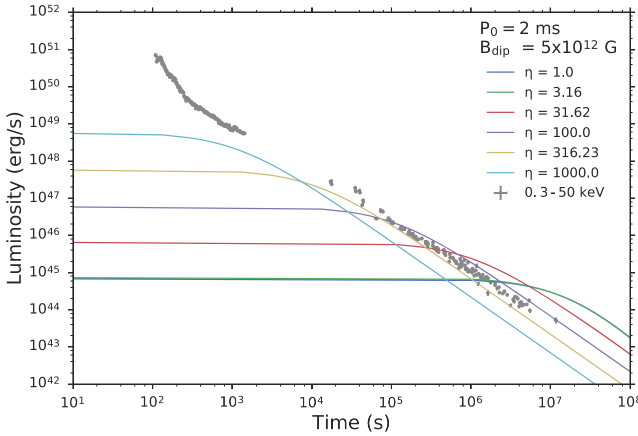

Figure 6. The observed luminosity of GRB 130427A in the 0.3–50 keV band (gray points), and the theoretical luminosity from a pulsar for selected quadrupole to dipole magnetic field ratio and quadrupole angles in color lines. Other parameters of the pulsar are fixed: initial spin period $P_0 = 2$ ms, dipole magnetic field $B_{dip} = 5 \times 10^{12}$ G, inclination angle $\chi_1 = \pi/2$, mass $M = 1.5\,M_\odot$, and radius $R_{NS} = 1.5 \times 10^6$ cm.

conservation during the gravitational collapse of the iron core leading to the νNS. It can also be checked from Figure 2 that P_0 is longer than the minimum period of a 1.5 $M_\odot$ NS, which guarantees the gravitational and rotational stability of the νNS.

8. Conclusions

We have constructed a model for a broad frequency range of the observed spectrum in the afterglow of BdHNe. We have made a specific fit to the BdHN 130427A as a representative example. We find that the parameters of the fit are consistent with the BdHN interpretation for this class of GRBs.

We have shown that the optical and X-ray emission of the early (10^2 s $\lesssim t \lesssim 10^6$ s) afterglow is explained by the synchrotron emission from electrons expanding in the HN threading the magnetic field of the νNS. At later times the HN becomes transparent and the electromagnetic radiation from the νNS dominates the X-ray emission. We have inferred that the νNS possesses an initial rotation period of 2 ms and a dipole magnetic field of (5–7) $\times 10^{12}$ G. It is worth mentioning that we have derived the strength of the magnetic dipole independently by the synchrotron emission model at early times ($t \lesssim 10^6$ s) and by the magnetic braking model powering the late ($t \gtrsim 10^6$ s) X-ray afterglow and show that they are in full agreement.

In this paper we proposed a direct connection between the afterglow of a BdHN and the physics of a newly born fast-rotating NS. This establishes a new self-enhancing understanding both of GRBs and young SNe, which could be of fundamental relevance for the understanding of ultra-energetic cosmic rays and neutrinos as well as new ultra high energy phenomena.

It now appears to be essential to extend our comprehension in three different directions: (1) understanding of the latest phase of the afterglow; (2) the possible connection with historical SNe; and (3) to extend observations from space of the GRB afterglow in the GeV and TeV energy bands. These last observations are clearly additional to the current observations of GRBs and GRB GeV radiation, originating from a Kerr–Newman BH and totally unrelated to the astrophysics of afterglows.

One of the major verifications of our model can come from observing, in still active afterglows of historical GRBs, the pulsar-like emission from the νNS we predict here, and the possible direct relation of the Crab Nebula to a BdHN is now open to further examination.

We acknowledge the continuous support of the MAECI. This work made use of data supplied by the UK Swift Science Data Center at the University of Leicester. M.K. is supported by the Erasmus Mundus Joint Doctorate Program grant N.2014–0707 from EACEA of the European Commission. J. A.R. acknowledges the partial support of the project N. 3101/GF4 IPC-11, and the target program F.0679 0073-6/PTsF of the Ministry of Education and Science of the Republic of Kazakhstan. Work at the University of Notre Dame (G.J.M.) is supported by the U.S. Department of Energy under Nuclear Theory Grant DE-FG02-95-ER40934. N.S. acknowledges the support of the RA MES State Committee of Science, in the frames of the research project No. 18T-1C335.

ORCID iDs

N. Sahakyan https://orcid.org/0000-0003-2011-2731
G. J. Mathews https://orcid.org/0000-0002-2663-0540
C. L. Bianco https://orcid.org/0000-0001-7749-4078
M. Muccino https://orcid.org/0000-0002-2234-9225

References

Ackermann, M., Ajello, M., Asano, K., et al. 2014, Sci, 343, 42
Aharonian, F. A., Kelner, S. R., & Prosekin, A. Y. 2010, PhRvD, 82, 043002
Becerra, L., Bianco, C. L., Fryer, C. L., Rueda, J. A., & Ruffini, R. 2016, ApJ, 833, 107
Becerra, L., Cipolletta, F., Fryer, C. L., Rueda, J. A., & Ruffini, R. 2015, ApJ, 812, 100
Bloom, J. S., Frail, D. A., & Sari, R. 2001, AJ, 121, 2879
Cano, Z., Wang, S.-Q., Dai, Z.-G., & Wu, X.-F. 2017, AdAst, 2017, 8929054
Cipolletta, F., Cherubini, C., Filippi, S., Rueda, J. A., & Ruffini, R. 2015, PhRvD, 92, 023007
Costa, E., Frontera, F., Heise, J., et al. 1997, Natur, 387, 783
Daigne, F., & Mochkovitch, R. 2002, MNRAS, 336, 1271
Evans, P. A., Beardmore, A. P., Page, K. L., et al. 2007, A&A, 469, 379
Evans, P. A., Beardmore, A. P., Page, K. L., et al. 2009, MNRAS, 397, 1177
Flores, H., Covino, S., Xu, D., et al. 2013, GCN, 1, 14491
Friedman, J. L., Ipser, J. R., & Sorkin, R. D. 1988, ApJ, 325, 722
Fryer, C. L., Oliveira, F. G., Rueda, J. A., & Ruffini, R. 2015, PhRvL, 115, 231102
Fryer, C. L., Rueda, J. A., & Ruffini, R. 2014, ApJL, 793, L36
Galama, T. J., Vreeswijk, P. M., van Paradijs, J., et al. 1998, Natur, 395, 670
Goldreich, P., & Julian, W. H. 1969, ApJ, 157, 869
Izzo, L., Rueda, J. A., & Ruffini, R. 2012, A&A, 548, L5
Kardashev, N. S. 1962, SvA, 6, 317
Kouveliotou, C., Granot, J., Racusin, J. L., et al. 2013, ApJL, 779, L1
Kumar, P., & Zhang, B. 2015, PhR, 561, 1
Levan, A. J., Cenko, S. B., Perley, D. A., & Tanvir, N. R. 2013, GCN, 1, 14455
Lyman, J. D., Bersier, D., James, P. A., et al. 2016, MNRAS, 457, 328
Maselli, A., Melandri, A., Nava, L., et al. 2014, Sci, 343, 48
Mészáros, P. 2002, ARA&A, 40, 137
Mészáros, P. 2006, RPPh, 69, 2259
Pe'er, A., Ryde, F., Wijers, R. A. M. J., Mészáros, P., & Rees, M. J. 2007, ApJL, 664, L1
Perley, D. A., Cenko, S. B., Corsi, A., et al. 2014, ApJ, 781, 37
Pétri, J. 2015, MNRAS, 450, 714
Piran, T. 1999, PhR, 314, 575
Pisani, G. B., Izzo, L., Ruffini, R., et al. 2013, A&A, 552, L5
Press, W. H., Teukolsky, S. A., Vetterling, W. T., & Flannery, B. P. 1992, Numerical Recipes in C. The Art of Scientific Computing (2nd ed.; Cambridge: Cambridge Univ. Press)
Romano, P., Campana, S., Chincarini, G., et al. 2006, A&A, 456, 917
Rueda, J. A., & Ruffini, R. 2012, ApJL, 758, L7
Ruffini, R., Aimuratov, Y., Becerra, L., et al. 2018b, ApJ, in press
Ruffini, R., Bianco, C. L., Fraschetti, F., Xue, S.-S., & Chardonnet, P. 2001, ApJL, 555, L117
Ruffini, R., Muccino, M., Bianco, C. L., et al. 2014, A&A, 565, L10
Ruffini, R., Rueda, J. A., Muccino, M., et al. 2016, ApJ, 832, 136
Ruffini, R., Wang, Y., Aimuratov, Y., et al. 2018a, ApJ, 852, 53
Ruffini, R., Wang, Y., Enderli, M., et al. 2015, ApJ, 798, 10
Rybicki, G. B., & Lightman, A. P. 1979, Radiative Processes in Astrophysics (New York: Wiley)
Smartt, S. J. 2009, ARA&A, 47, 63
Sonbas, E., Guver, T., Gogus, E., & Kirbiyik, H. 2013, GCN, 1, 14475
Stergioulas, N. 2003, LRR, 6, 3
Sturner, S. J., Skibo, J. G., Dermer, C. D., & Mattox, J. R. 1997, ApJ, 490, 619
Uhm, Z. L., & Zhang, B. 2014, NatPh, 10, 351
von Kienlin, A. 2013, GCN, 1, 14473
Wiersema, K., Vaduvescu, O., Tanvir, N., Levan, A., & Hartoog, O. 2013, GCN, 1, 14617
Woosley, S. E., & Bloom, J. S. 2006, ARA&A, 44, 507
Xu, D., de Ugarte Postigo, A., Leloudas, G., et al. 2013a, ApJ, 776, 98
Xu, D., de Ugarte Postigo, A., Schulze, S., et al. 2013b, GCN, 1, 14478

The Astrophysical Journal, 869:151 (15pp), 2018 December 20 https://doi.org/10.3847/1538-4357/aaee68

On the Ultra-relativistic Prompt Emission, the Hard and Soft X-Ray Flares, and the Extended Thermal Emission in GRB 151027A

R. Ruffini[1,2,3,4], L. Becerra[1,2], C. L. Bianco[1,2], Y. C. Chen[1,2], M. Karlica[1,2,3], M. Kovačević[1,2,3], J. D. Melon Fuksman[1,2], R. Moradi[1,2], M. Muccino[1,2], G. B. Pisani[1,2], D. Primorac[1,2], J. A. Rueda[1,2,4], G. V. Vereshchagin[1,2], Y. Wang[1,2], and S. S. Xue[1,2]

[1] ICRA and Dipartimento di Fisica, Sapienza Università di Roma, P.le Aldo Moro 5, I-00185 Rome, Italy
[2] ICRANet, P.zza della Repubblica 10, I-65122 Pescara, Italy
[3] Université de Nice Sophia Antipolis, CEDEX 2, Grand Château Parc Valrose, Nice, France
[4] ICRANet-Rio, Centro Brasileiro de Pesquisas Físicas, Rua Dr. Xavier Sigaud 150, 22290–180 Rio de Janeiro, Brazil; ruffini@icra.it
Received 2017 December 13; revised 2018 November 2; accepted 2018 November 3; published 2018 December 20

Abstract

We analyze GRB 151027A within the binary-driven hypernova approach, with a progenitor of a carbon–oxygen core on the verge of a supernova (SN) explosion and a binary companion neutron star (NS). The hypercritical accretion of the SN ejecta onto the NS leads to its gravitational collapse into a black hole (BH), to the emission of the gamma-ray burst (GRB), and to a copious e^+e^- plasma. The impact of this e^+e^- plasma on the SN ejecta explains the early soft X-ray flare observed in long GRBs. Here, we apply this approach to the ultra-relativistic prompt emission (UPE) and to the hard X-ray flares. We use GRB 151027A as a prototype. From the time-integrated and the time-resolved analysis, we identify a double component in the UPE and confirm its ultra-relativistic nature. We confirm the mildly relativistic nature of the soft X-ray flare, of the hard X-ray flare, and of the extended thermal emission (ETE). We show that the ETE identifies the transition from an SN to a hypernova (HN). We then address the theoretical justification of these observations by integrating the hydrodynamical propagation equations of the e^+e^- into the SN ejecta, with the latter independently obtained from 3D smoothed particle hydrodynamics simulations. We conclude that the UPE, the hard X-ray flare, and the soft X-ray flare do not form a causally connected sequence. Within our model, they are the manifestation of the same physical process of the BH formation as seen through different viewing angles, implied by the morphology and the ~300 s rotation period of the HN ejecta.

Key words: binaries: general – black hole physics – gamma-ray burst: general – hydrodynamics – stars: neutron – supernovae: general

1. Introduction

Gamma-ray bursts (GRBs) are traditionally classified in short GRBs with a total duration of $\lesssim$2 s, and as long GRBs lasting $\gtrsim$2 s (Mazets et al. 1981; Dezalay et al. 1992; Klebesadel 1992; Kouveliotou et al. 1993; Tavani 1998). A large majority of long bursts are spatially correlated with bright star-forming regions in their host galaxies (Fruchter et al. 2006; Svensson et al. 2010). For this reason, the long GRBs have been traditionally associated with the collapse of the core of a single massive star to a black hole (BH), surrounded by a thick massive accretion disk: the collapsar (Woosley 1993; Paczyński 1998; MacFadyen & Woosley 1999; Piran 2004; Bromberg et al. 2013). In this traditional picture, the GRB dynamics follows the "fireball" model, which assumes the existence of a single ultra-relativistic collimated jet (see e.g., Blandford & McKee 1976; Shemi & Piran 1990; Meszaros et al. 1993; Piran et al. 1993; Mao & Yi 1994). The structures of long GRBs were described either by internal or external shocks (see Rees & Meszaros 1992, 1994). The emission processes were linked to the occurrence of a synchrotron and/or inverse-Compton radiation coming from the single ultra-relativistic jetted structure, characterized by Lorentz factors $\Gamma \sim 10^2$–10^3.

Such a collapsar model does not address some observational facts: (1) most massive stars are found in binary systems (Smith 2014), (2) most SNe Ib/c occur in binary systems (Smith et al. 2011), and (3) the SNe associated with long GRBs are indeed of type Ib/c (Della Valle 2011). These facts motivated us to develop the binary-driven hypernova (BdHN) model.

Recently, we have found evidence for multiple components in long GRB emissions, indicating the presence of a sequence of astrophysical processes (Izzo et al. 2012; Penacchioni et al. 2012), which have led us to formulate, in precise terms, the sequence of events in the Induced Gravitational Collapse (IGC) paradigm (Ruffini et al. 2001a, 2007a; Rueda & Ruffini 2012; Fryer et al. 2014), making explicit the role of binary systems as progenitors of the long GRBs.

Within the IGC scenario, the long bursts originate in tight binary systems composed of a carbon–oxygen core (CO_{core}) undergoing an SN explosion and a companion neutron star (NS; Becerra et al. 2015, 2016, 2018). The SN explosion triggers a hypercritical accretion process onto the companion NS; photons are trapped in the infalling material, and the gravitational energy gained by accretion is carried out through an efficient neutrino emission (Zel'dovich et al. 1972; Ruffini & Wilson 1973; Fryer et al. 2014). Depending on the CO_{core}–NS binary separation/period, two outcomes may occur. For widely separated ($a \gtrsim 10^{11}$ cm) CO_{core}–NS binaries, the hypercritical accretion rate is $<10^{-2}\, M_\odot\, s^{-1}$, and it is insufficient to induce the gravitational collapse of the NS to a BH. Instead, the NS just increases its mass, becoming a massive NS. This process leads to the emission of the so-called X-ray flashes (XRFs) with a typical X-ray emission of $\lesssim 10^{52}$ erg.

For more tightly bound ($a \lesssim 10^{11}$ cm) CO_{core}–NS binaries, the hypercritical accretion rate of the SN ejecta can be as large as $\gtrsim 10^{-2}$–$10^{-1}\, M_\odot\, s^{-1}$, leading the companion NS to collapse into a BH. This process leads to the occurrence of the BdHN, which exhibits a more complex structure than XRFs and an emission of $\gtrsim 10^{52}$ erg (Ruffini et al. 2016b).

The opportunity of introducing the BdHN model, based on binary progenitors, which exhibits a large number of new physical process and admits a theoretical treatment by detailed equations whose corresponding solutions are in agreement with the observations, has been presented in a large number of publications and was recently summarized in Ruffini et al. (2018c). There, we performed an extensive analysis using 421 BdHN, all with measured redshift and observed until the end of 2016, and described in their cosmological rest frame (Pisani et al. 2016).

The large variety of spectra and light curves has allowed the introduction of seven different GRBs subclasses (see e.g., Ruffini et al. 2016b, 2018b).

We recalled that since 2001, we fit the ultra-relativistic prompt emission (UPE) light curve and spectra, solving the equations of the dynamics of the e^+e^- baryon plasma and of its slowing down due to the interaction with the circumburst medium (CBM; see e.g., Ruffini et al. 1999, 2000, 2002). This treatment allows us to evaluate the ultra-relativistic gamma factor of the UPE exhibited in hundreds of short and long GRBs. Some under-luminous GRBs may well have a non-ultrarelativistic prompt emission (J. A. Rueda et al. 2018, in preparation).

Attention was then directed to examine the flare plateau afterglow (FPA) phase following the UPE.

Among the BdHNe, we identified all of the ones with a soft X-ray flare in the 0.3–10 keV rest-frame energy range in the FPA phase. In view of the excellent data and complete light curves, we could identify a thermal component in them (see Figure 32 and Table 7 in Ruffini et al. 2018c), which is essential in measuring the mildly relativistic expansion velocity of $v = c\beta \sim 0.8c$ (see Section 9 in Ruffini et al. 2018c).

In addition we then followed, through a hydrodynamical description, the propagation and the slowing down inside the SN ejecta of the e^+e^- plasma generated in the BH formation, in order to explain the mildly relativistic nature of the soft X-ray flares expansion velocity (see Section 10 in Ruffini et al. 2018c).

Obviously, these considerations cannot be repeated here.

We only recall a few points of the conclusions of Ruffini et al. (2018c); e.g., (a) the data of the soft X-ray flare have determined its mildly relativistic expansion velocity already $\sim$100 s after the UPE, in contrast to the traditional approach; (b) the role of the interaction of the e^+e^- GRB emission in SN ejecta in order to explain the astrophysical origin of soft X-ray flare; (c) the determination of the density profile of the SN ejecta derived from the simulation of the IGC paradigm.

In this article, we apply our model to study a multiple component in the UPE phase observed in the range of 10–1000 keV as well as the hard X-ray flares observed in the range of 0.3–150 keV, the extended thermal emission (ETE), and finally the soft X-ray flare observed in the range of 0.3–10 keV using GRB 151027A as a prototype. The aim is to identify the crucial role of the SN and of its binary NS companion in the BdHN model, to analyze the interaction of the e^+e^- plasma generating the GRB with the SN ejecta via 3D simulations, and to compare and contrast the observational support of the BdHN model with the other traditional approaches. To facilitate the reader, we have made a special effort in referencing to the current works, in indicating new developments and their observational verifications, and finally in giving references for the technical details in the text.

In Section 2, we outline the new results motivating our paper: (1) three thermal emissions processes in GRBs, compared and contrasted. The relativistic treatment that relates the velocity of expansion of the hard X-ray flare, of the soft X-ray flare and of the ETE to the observed fluxes and temperatures is particularly relevant for our work. (2) The 3D simulations of the hypercritical accretion in a BdHN, which are essential for obtaining the density profiles of the SN ejecta recently submitted for publication in Becerra et al. (2018). (3) The generalization of the spacetime representation of the BdHN. These are some useful conceptual tools needed to create a viable GRB model.

In Section 3, we refer to GRB 151027A as a prototype example of high-quality data, enabling the detailed time-resolved analysis for the UPE phase, with its thermal component, as well as the first high-quality data for studying the hard X-ray flare and especially for the clear evolution of the ETE. We perform the time-integrated analysis for the UPE, further analyze the two ultra-relativistic gamma-ray spikes in the UPE, and apply the fireshell model to the first spike. We identify the proper GRB (P-GRB), the baryon load $B = (1.92 \pm 0.35) \times 10^{-3}$; and an average CBM density of $(7.46 \pm 1.2)\,\mathrm{cm}^{-3}$, which are consistent with our numerical simulation presented in Section 6. We determine an initial Lorentz factor of the UPE $\Gamma_0 = 503 \pm 76$, confirming the clearly observed ultra-relativistic nature of the UPE.

In Section 4, we perform the time-resolved analysis for the hard X-ray flare and the soft X-ray flare, comparing and contrasting our results with the ones in the literature by Nappo et al. (2017). The hard X-ray flare is divided into eight time intervals, and we find a high significant thermal component existing in all time intervals (see Figure 8). We report the results of our time-resolved spectral analysis in the first five columns of Table 2. Using the best-fit model for a nonthermal component in the time interval 95–130 s, we determine a Lorentz factor $\Gamma = 3.28 \pm 0.84$ for the hard X-ray flare duration. The soft X-ray flare is analyzed in 4 time intervals, in which spectra are best fitted by a single power-law (PL).

In Section 5, we turn to the thermal component evolving across the hard X-ray flare by adopting the description in the GRB laboratory frame. Following our recent works (Ruffini et al. 2018c), we determine the expansion velocity evidencing the transition from an initial velocity $\approx 0.38c$ and increasing up to $0.98c$ in the late part; see column 6 of Table 2. This is the first relativistic treatment of the hard X-ray flare and its associated thermal emission clearly evidences the transition from an SN to an HN, which was first identified in GRB 151027A. We compare and contrast our results with the current ones in the literature.

In Section 6, we proceed to the hard X-ray flare and the soft X-ray flare theoretical explanation from the analysis of the e^+e^- plasma propagating and slowing down within the SN ejecta. The simulated velocity and radius of the hard X-ray flare and the soft X-ray flare are consistent with the observations. We visualize all these results by direct comparison of the observational data by *Swift*, the *International Gamma-ray Astrophysics Laboratory* (*INTEGRAL*), *Fermi,* and *Agile*, in addition to the optical observations, with the theoretical understanding of the 3D dynamics of the SN recently jointly performed by our group in collaboration with the Los Alamos National Laboratory (Becerra et al. 2018). This visualization is particularly helpful in order to appreciate the novel results made possible by the BdHN paradigm and also by allowing the visualization of a phenomena observed today but occurred 10 billion light years away in our past light cone. The impact of the e^+e^- plasma on the entire SN ejecta gives origin to the thermal emission from the external surface of the SN ejecta and, equally, we can therefore conclude that the UPE, the hard X-ray flare, and the soft X-ray flare are not a causally connected sequence (see Figures 14–17 and Table 2). Within our model, they are the manifestation of the same physical process of the BH formation as seen through different viewing angles, implied by the morphology and by the ∼300 s rotation period of the HN ejecta.

In Section 7, we proceed to the summary, discussion, and conclusions:

1. In the summary, we have recalled the derived Lorentz gamma factor and the detailed time-resolved analysis of the light curves and spectra of UPE, hard X-ray flare, ETE, and soft X-ray flare. We mention a double spike structure in the UPE and in the FPA, which promises to be directly linked to the process of the BH formation. We have equally recalled our relativistic treatment of the ETE, which, for the first time, has allowed us to observe the transition of an SN into an HN—the main result of this paper.
2. WE have recalled in the discussions, using specific examples in this article, that our data analysis is performed within a consistent relativistic field-theoretical treatment. In order to be astrophysically significant, it needs the identification of the observed astrophysical components, including: the binary nature of the progenitor system, the presence of an SN component, and it also needs a 3D simulation of the process of hypercritical accretion in the binary progenitors. We have also recalled the special role of the rotation by which phenomena, traditionally considered different, are actually the same phenomenon as seen from different viewing angles.
3. Looking forward in the conclusions, three main implications follow from the BdHN model, which are now open to further scrutiny: (1) only 10% of the BdHNe whose line of sight lies in the equatorial plane of the progenitor binary system are actually detectable; in the other 90%, the UPE is not detectable due to the morphology of the SN ejecta (see Figure 2) and therefore the *Fermi* and *Swift* instruments are not triggered; (2) the $E_{\rm iso}$, traditionally based on a spherically symmetric equivalent emission, has to be replaced by an $E_{\rm tot}$, duly taking into account the contributions of the UPE, hard X-ray flare, ETE, and soft X-ray flare; (3) when the BdHNe are observed normally to the orbital plane, the GeV emission from the newly formed BH becomes observable, and this additional energy should also be accounted for.

We summarize in Table 1 the list of acronyms introduced in the present paper.

2. Recent Progress on BdHNe

We address three progresses obtained in the last year in the theory of BdHNe: (1) the identification of three different thermal emission processes, (2) the visualization of the IGC paradigm, and (3) an extended spacetime diagram of the BdHN with a viewing angle in the equatorial plane of the binary progenitors.

Table 1
Alphabetic Ordered List of the Acronyms Used in This Work

Extended Wording	Acronym
Binary-driven hypernova	BdHN
Black hole	BH
Carbon–oxygen core	$CO_{\rm core}$
Circumburst medium	CBM
Extended thermal emission	ETE
Flare plateau afterglow	FPA
Gamma-ray burst	GRB
Gamma-ray flash	GRF
Induced gravitational collapse	IGC
Massive neutron star	MNS
Neutron star	NS
New neutron star	νNS
Ultra-relativistic prompt emission	UPE
Proper gamma-ray burst	P-GRB
Short gamma-ray burst	S-GRB
Short gamma-ray flash	S-GRF
Supernova	SN
Ultrashort gamma-ray burst	U-GRB
White dwarf	WD
X-ray flash	XRF

One of the first examples of a thermal emission has been identified in the early seconds after the trigger of some long GRBs (Ryde 2004; Ryde et al. 2006; Ryde & Pe'er 2009). This emission has been later identified in the BdHN model with the soft X-ray emission occurring in the photosphere of convective outflows in the hypercritical accretion process from the newly born SN into the NS binary companion. Additional examples have been given in BdHNe (Fryer et al. 2014) and in XRFs (Becerra et al. 2016). These process are practically Newtonian in character with the velocity of expansions of the order of 10^8–10^9 cm s^{-1} (see e.g., Izzo et al. 2012, for the case of GRB 090618).

A second thermal emission process has been identified in the acceleration process of GRBs, when the self-accelerating optically thick e^+e^- plasma reaches transparency and a thermal emission with very high Lorentz factor $\Gamma \sim 10^2$–10^3 is observed. This has been computed both in the fireball model (Piran 1999; Daigne & Mochkovitch 2002; Pe'er et al. 2007) and in the fireshell model (Ruffini 1999; Ruffini et al. 2000). The difference consists in the description of the equations of motion of the fireball assumed in the literature and instead is explicitly evaluated in the fireshell model from the integration of classical and quantum magnetohydrodynamic process (see also Ruffini et al. 2007b, and references therein). The moment of transparency leads to a thermal emission whose relativistic effect has been evaluated, leading to the concept of the equitemporal surface (EQTS; Bianco & Ruffini 2005a). This derivation has also been successfully applied to short GRBs (Ruffini et al. 2015, 2016a; Aimuratov et al. 2017) and is here applied in Section 3 to the UPE.

There is finally a third additional ETE observed in BdHNe and in the X-ray flares (Ruffini et al. 2018c). This ETE has allowed the determination of the velocity of expansion and the Lorentz gamma factor of the thermal emission based on the variation in time of the observed radius and temperature of the thermal emission (see the equation in Figure 1) under the assumption of uncollimated emission and considering only the radiation coming

$$\underbrace{\frac{C\beta^5}{4[\ln(1+\beta)-(1-\beta)\beta]^2}\left(\frac{1+\beta}{1-\beta}\right)^{1/2}}_{\text{Derived Velocity Parameter}} = \underbrace{\frac{D_L(z)}{1+z}\frac{1}{t^d_{a,2}-t^d_{a,1}}\left(\sqrt{\frac{F_{\rm bb,obs}(t^d_{a,2})}{\sigma T^4_{\rm obs}(t^d_{a,2})}}-\sqrt{\frac{F_{\rm bb,obs}(t^d_{a,1})}{\sigma T^4_{\rm obs}(t^d_{a,1})}}\right)}_{\text{Observable}}$$

Figure 1. Equation to compute the velocity from the thermal component. This equation is summarized from Ruffini et al. (2018c). The left-hand side term is only a function of velocity β, and the right-hand side term is only of the observables. $D_L(z)$ is the luminosity distance for redshift z. From the observed thermal flux, $F_{\rm bb,obs}$, and the temperature, $T_{\rm obs}$, at arrival times of the detector $t^d_{a,1}$ and $t^d_{a,2}$, the velocity and the corresponding Lorentz factor can be computed. This equation assumes uncollimated emission and considers only the radiation coming from the line of sight. The computed velocity is instantaneous, and there is no reliance on the expansion history.

from the line of sight. The left-hand side term is only a function of the velocity, β, the right-hand side term is only function of the observables, and $D_L(z)$ is the luminosity distance for redshift z. Therefore, from the observed thermal flux, $F_{\rm bb,obs}$, and the temperature, $T_{\rm obs}$, at times t_1 and t_2, we can compute the velocity, β. This highly nonlinear equation is not straightforwardly solvable analytically, so in the present paper, we solve it numerically after verifying the monotonically increasing behavior of the left-hand side term as a function of β (see, e.g., C. L. Bianco et al. 2018, in preparation).

The second progress has been presented in Becerra et al. (2016) and more recently in Becerra et al. (2018). The first 3D smoothed particle hydrodynamics (SPH) simulations of the IGC leading to a BdHN are there presented. We simulate the SN explosion of a $\rm CO_{core}$ forming a binary system with a NS companion. We follow the evolution of the SN ejecta, including their morphological structure, subjected to the gravitational field of both the new NS (νNS), formed at the center of the SN, and the one of the NS companion. We compute the accretion rate of the SN ejecta onto the NS companion as well as onto the νNS from SN matter fallback. We determine the fate of the binary system for a wide parameter space, including different $\rm CO_{core}$ masses, orbital periods ($\sim$300 s), and SN explosion geometry and energies. We evaluate, for selected NS equations of state, if the accretion process leads the NS either to the mass-shedding limit or to the secular asymmetric instability for the gravitational collapse to a BH or to a more massive, fast rotating but stable NS. We also assess whether the binary keeps or is not gravitationally bound after the SN explosion, hence exploring the space of the binary and SN explosion parameters leading to the formation of νNS–NS or νNS–BH binaries. The consequences of our results for the modeling of GRBs via the IGC scenario are discussed in Becerra et al. (2018). The relevance of these simulations for GRB 151027A, which is subject of this paper, will be illustrated below (see Figure 2).

Finally, we present an update of the BdHN spacetime diagram (see Figure 3) that clearly evidences the large number of episodes and physical processes, each with observationally computed time-varying Lorentz Γ factors, which require the systematic use of the four different time coordinates, as already indicated in Ruffini et al. (2001a). The diagram illustrates departures from the traditional collapsar-fireball description of a GRB. The diagram shows how the sequence of events of the UPE, of the hard X-ray flare, and of the soft X-ray flare occur in a sequence only when parameterized in the arrival time and when they are not, in fact, causally related.

We recall that, within our model, the line of sight of the prototypical GRB 151027A lies in the equatorial plane of the progenitor binary system. The more general case of an arbitrary viewing angle has been explored in Ruffini et al. (2018a), and some specific additional characteristic features common to the collapsar model have been manifested in this more general case.

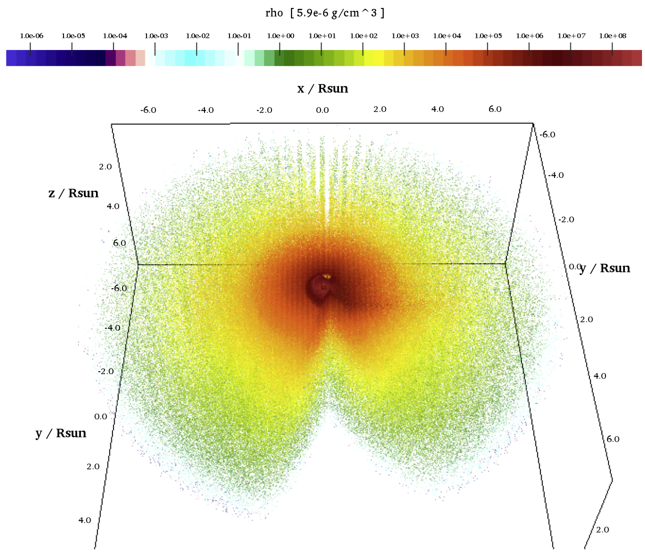

Figure 2. A 3D, half-hemisphere view of the density distribution of the SN ejecta at the moment of BH formation in a BdHN. The simulation is performed with an SPH code that follows the SN ejecta expansion under the influence of the gravitational field of both the νNS formed at the center of the SN and of the NS companion. It includes the effects of the orbital motion and the changes in the NS gravitational mass by the hypercritical accretion process (see Becerra et al. 2016, for additional details). The binary parameters of this simulation are: the NS companion has an initial mass of 2.0 $M_\odot$; the $\rm CO_{core}$, obtained from a progenitor with ZAMS mass, $M_{\rm ZAMS} = 30\,M_\odot$, which leads to a total ejecta mass of 7.94 $M_\odot$ and to a 1.5 $M_\odot$ νNS, and the orbital period is $P \approx 5$ min (binary separation $a \approx 1.5 \times 10^{10}$ cm). Only the sources, whose ultra-relativistic emission lies within the allowed cone of $\sim 10°$ with low baryon contamination, will trigger the gamma-ray instrument (e.g., *Fermi*/GBM or *Swift*/BAT).

3. UPE

GRB 151027A was detected and located by the *Swift* Burst Alert Telescope (BAT; Maselli et al. 2015). It was also detected by the *Fermi* Gamma-ray Burst Monitor (GBM; Toelge et al. 2015), Monitor of All-sky X-ray Image (MAXI; Masumitsu et al. 2015), and by *Konus*-Wind (Golenetskii et al. 2015). The *Swift* X-Ray Telescope (XRT) started its observation 87 s after the burst trigger (Goad et al. 2015). The redshift of the source, measured through the Mg II doublet in absorption from the Keck/High Resolution Echelle Spectrometer (HIRES) spectrum, is $z = 0.81$ (Perley et al. 2015). The Large Area Telescope (LAT) boresight of the source was 10° at the time of the trigger, there are no associated high-energy photons; an upper limit of observed count flux is computed as 9.24×10^{-6} photons $\rm cm^{-2}\,s^{-1}$ following the standard *Fermi*-LAT likelihood analysis. The BAT light curve shows a complex peaked structure lasting at least 83 s. XRT began observing the field 48 s after the BAT trigger. The GBM light curve consists of various pulses with a duration of about 68 s in the 50–300 keV

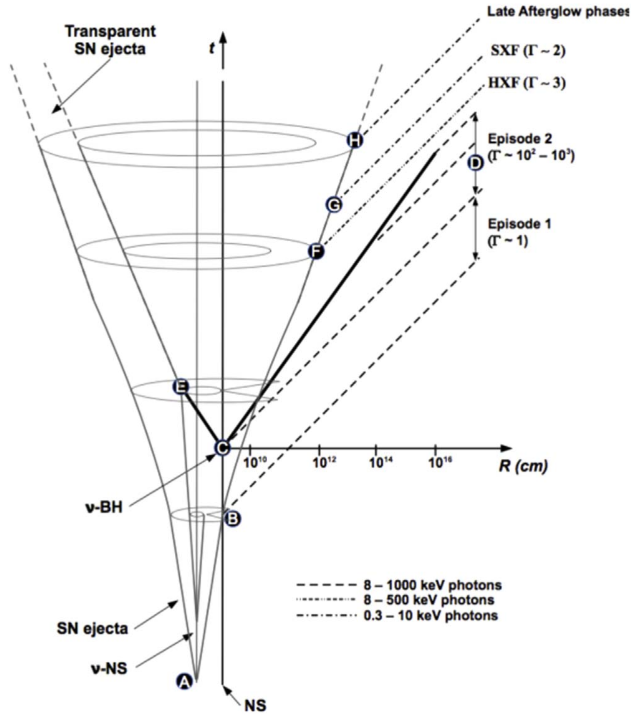

Figure 3. Spacetime diagram (not in scale) of BdHNe. The CO_{core} explodes as an SN at point A and forms a νNS. The companion NS (bottom right line) accretes the SN ejecta starting from point B, giving rise to the nonrelativistic Episode 1 emission (with Lorentz factor $\Gamma \approx 1$). At point C, the NS companion collapses into a BH, and an e^+e^- plasma—the dyadosphere—is formed (Ruffini 1999). The following self-acceleration process occurs in a spherically symmetric manner (thick black lines). A large portion of plasma propagates in the direction of the line of sight, where the environment is cleaned up by the previous accretion into the NS companion, finding a baryon load of $B \lesssim 10^{-2}$ and leading to the GRB UPE gamma-ray spikes (Episode 2, point D) with $\Gamma \sim 10^2$–10^3. The remaining part of the plasma impacts with the high-density portion of the SN ejecta (point E), propagates inside the ejecta encountering a baryon load of $B \sim 10^1$–10^2, and finally reaches transparency, leading to the hard X-ray flare emission (point F) in gamma-rays with an effective Lorentz factor of $\Gamma \lesssim 10$ and to soft X-ray flare emission (point G) with an effective $\Gamma \lesssim 4$, which are then followed by the late afterglow phases (point H). For simplicity, this diagram is 2D and static and does not attempt to show the 3D rotation of the ejecta.

band. The *Konus*-Wind light curve consists of various pulses with a total duration of ∼66 s. The MAXI detection is not significant, but the flux is consistent with the interpolation from the *Swift*/XRT light curve. The first 25 s (rest frame 14 s) corresponds to the UPE. It encompasses two spikes of duration of ≈8.5 s and ≈7.5 s, respectively, with a separation between two peaks of ≈17 s (see Figure 4 (a)). The rest-frame 1–10^4 keV isotropic equivalent energies computed from the time-integrated spectra of these two spikes (see Figures 4 (b) and (c)) are $E_{\rm iso,1} = (7.26 \pm 0.36) \times 10^{51}$ erg and $E_{\rm iso,2} = (4.99 \pm 0.60) \times 10^{51}$ erg, respectively.

A similar analysis was performed by Nappo et al. (2017). They describe the two spikes of the UPE by a single light curve with a "Fast Rise and Exponential Decay" (FRED) shape.

We analyze the first spike (see Figure 5) as the traditional UPE of a long GRB within the fireshell model (see, e.g., Ruffini et al. 2003, for a review).

Thanks to the wide energy range of the *Fermi*-GBM instrument (8–1000 keV), it has been possible to perform a time-resolved analysis within the UPE phase to search for the typical P-GRB emission at the transparency of the e^+e^-–baryon

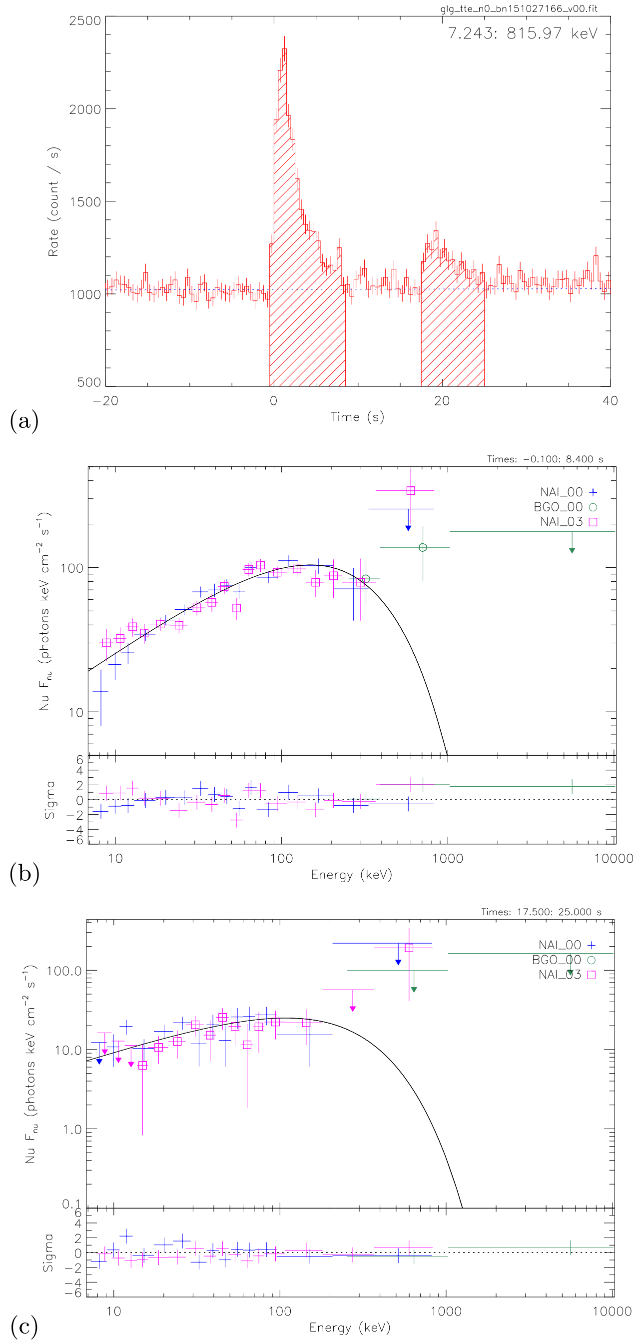

Figure 4. (a) *Fermi*-GBM light curve from the Na I-n0 detector (≈8–800 keV) of the UPE of GRB 151027A. The dotted horizontal line corresponds to the γ-ray background. (b) Time-integrated νF_ν spectrum of the first spike. (c) Time-integrated νF_ν spectrum of the second spike.

plasma (Ruffini 1999; Ruffini et al. 2000, 2001b). Indeed, we find this thermal spectral feature in the time interval $T_0 - 0.1$–$T_0 + 0.9$ s (with respect to the *Fermi*-GBM trigger time T_0). The best-fit model of this emission is a composition of a blackbody (BB) spectrum and a cutoff power-law model (CPL, see Figure 5(a)). The BB component has an observed temperature of $kT = (36.6 \pm 5.2)$ keV and an energy of $E_{\rm BB} = (0.074 \pm 0.038) \times E_{\rm iso,1} = (5.3 \pm 2.7) \times 10^{50}$ erg. These values are in agreement with an initial e^+e^- plasma of energy, $E_{\rm iso,1}$, with a baryon load of $B = (1.92 \pm 0.35) \times 10^{-3}$, and a Lorentz factor

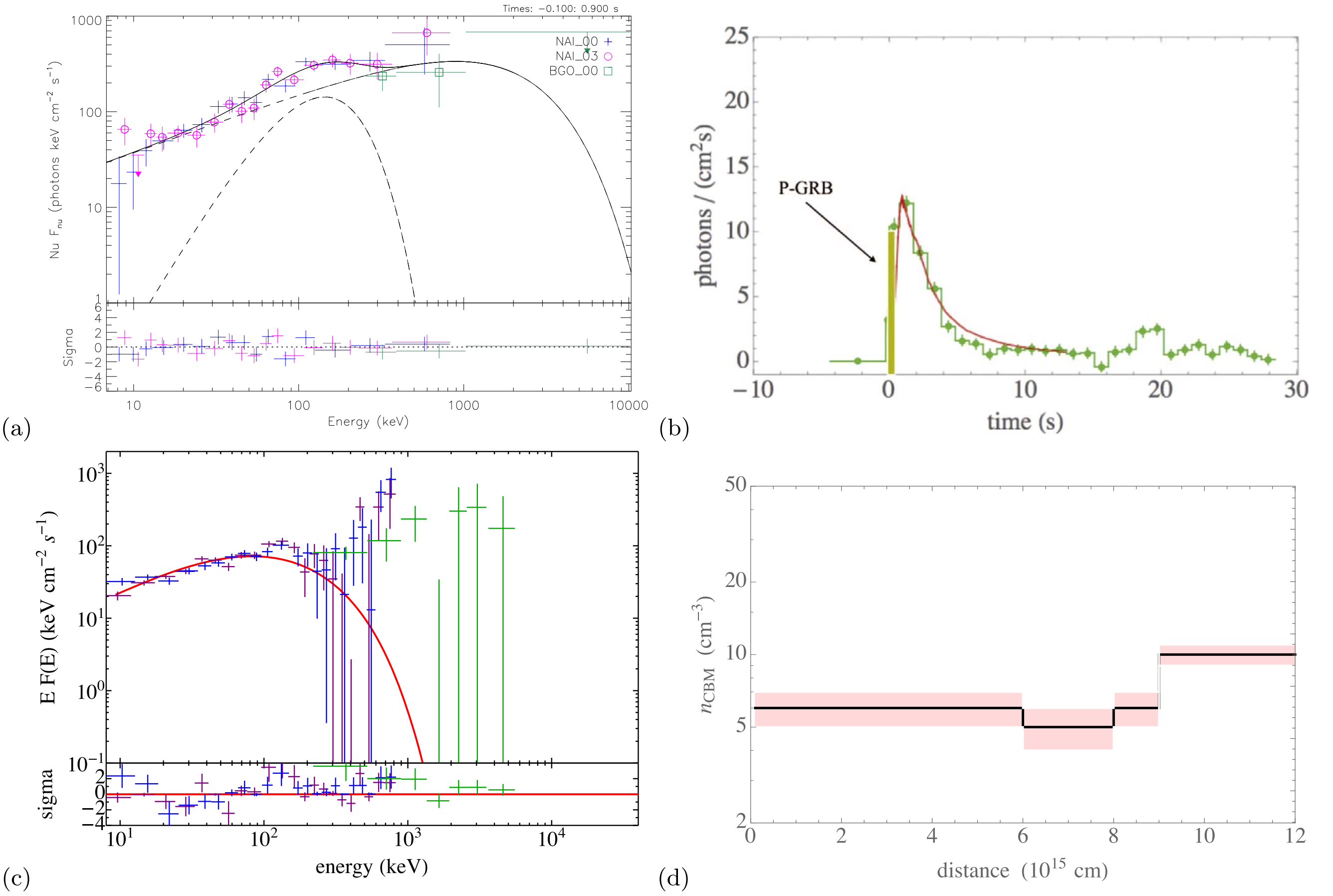

Figure 5. Ultra-relativistic prompt emission (UPE). (a) The combined Na I-n0, n3+BGO-b0 νF_ν spectrum of the P-GRB in the time interval $T_0 - 0.1$–$T_0 + 0.9$ s. The best-fit model is CPL+BB. (b) The comparison between the background subtracted 10–1000 keV *Fermi*-GBM light curve (green) and the simulation with the fireshell model (red curve) in the time interval $T_0 + 0.9$–$T_0 + 9.6$ s. (c) The comparison between the Na I-n0 (purple squares), n3 (blue diamonds), and the BGO-b0 (green circles) νF_ν data in the time interval, $T_0 + 0.9$–$T_0 + 9.6$ s, and the simulated fireshell spectrum (red curve). (d) The radial density of the CBM clouds used for the above UPE light curve and spectrum simulations.

and a radius at the transparency condition of $\Gamma_0 = 503 \pm 76$ and $r_{\rm tr} = (1.92 \pm 0.17) \times 10^{13}$ cm, respectively.

We turn now to the simulation of the remaining part of the first spike of the UPE (from $T_0 + 0.9$ s to $T_0 + 9.6$ s). In the fireshell model, this emission occurs after the P-GRB, and results from the slowing down of the accelerated baryons are due to their interaction with the CBM (Ruffini et al. 2002, 2006; Patricelli et al. 2012). To simulate the UPE light curve and its corresponding spectrum, we need to derive the number density of the CBM clouds surrounding the burst site. The agreement between the observations and the simulated light curve (see Figure 5(b)) and the corresponding spectrum (see Figure 5(c)) is obtained for an average CBM density of (7.46 ± 1.2) cm^{-3} (see Figure 5(d)), consistent with the typical value of the long-burst host galaxies at radii $\simeq 10^{16}$ cm. By contras,t the second spike of the UPE appears to be featureless.

The general conclusion of the UPE is the following: from the morphological 3D simulation, the SN ejecta is distorted by the binary accretion. A cone of very low baryon contamination is formed along the direction from the SN center pointing to the newly born BH (see Figure 2). A portion of e^+e^- plasma generated from the BH formation propagates through this cone and engulfs a low baryon load of $B = (1.92 \pm 0.35) \times 10^{-3}$ and reaches a Lorentz gamma factor of $\Gamma_0 = 503 \pm 76$. The e^+e^- plasma self-accelerates and expands ultra-relativistically until reaching transparency (Ruffini 1998; Aksenov et al. 2007; Ruffini et al. 2010), when a short-duration (<1 s) thermal emission occurs: the P-GRB. The ultra-relativistic associated baryons then interact with the CBM clouds. The dynamics of the plasma has been integrated by the classical hydrodynamics equations and by the equation of annihilation-creation rate (Bianco et al. 2001; Bianco & Ruffini 2004, 2005a, 2005b, 2006). It enables us to simulate the structure of spikes in the prompt emission, and it has been applied to the case of BdHNe (see, e.g., Ruffini et al. 2002, 2016a; Bernardini et al. 2005; Izzo et al. 2012; Penacchioni et al. 2012, 2013). For a typical baryon load for the cone direction, $10^{-4} \lesssim B \lesssim 10^{-2}$, a Lorentz factor of $\Gamma \approx 10^2$–10^3, characteristic of the prompt emission occurs in a distance $\approx 10^{15}$–10^{17} cm from the BH (Ruffini et al. 2016b).

1. A double emission is clearly manifested by presence of the two spikes at the time interval of the 17 s (rest frame 9 s). We are currently examining the possibility that this double emission is an imprinting of the process of the BH formation.
2. When we take into account the rotation period of the binary $\sim$300 s, we see that UPE occurs in a cone centered in the BH of 10°.

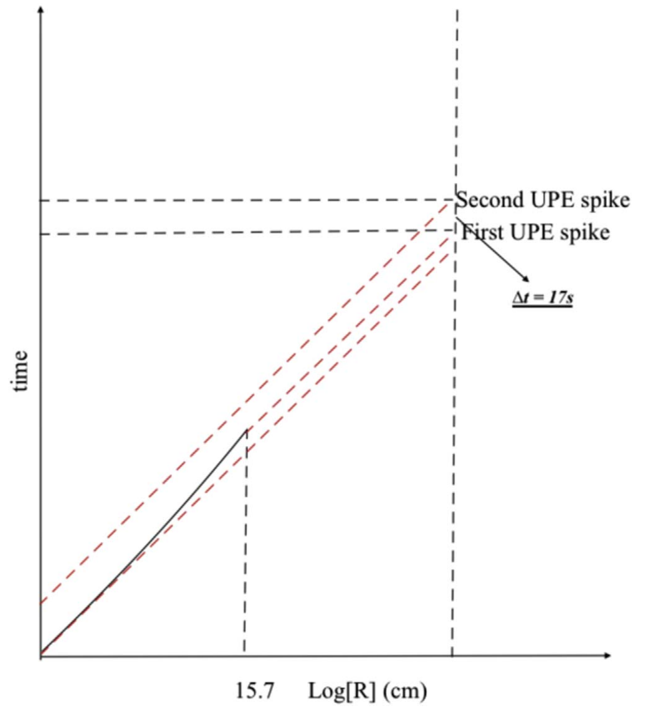

Figure 6. Spacetime diagram of the UPE. The initial e^+e^- plasma self-accelerates in the small-density cone until it reaches transparency (curved black line), producing the first of the two ultra-relativistic UPE spikes (bottom solid red line). The second one is produced by a latter emission from the BH formation, with a difference in the observed time of $\sim$17 s (rest frame of $\sim$9.4 s, top solid red line).

3. This conical region is endowed with a very low density determined by the P-GRB and the inferred CBM medium density of (7.46 ± 1.2) cm^{-3} up to 10^{16} cm from BH along the cone (see Figure 5(d)).

This conceptual framework can, in principle, explain the featureless nature of the second spike, which propagates along the region that has already been swept by the first spike (see Figure 6).

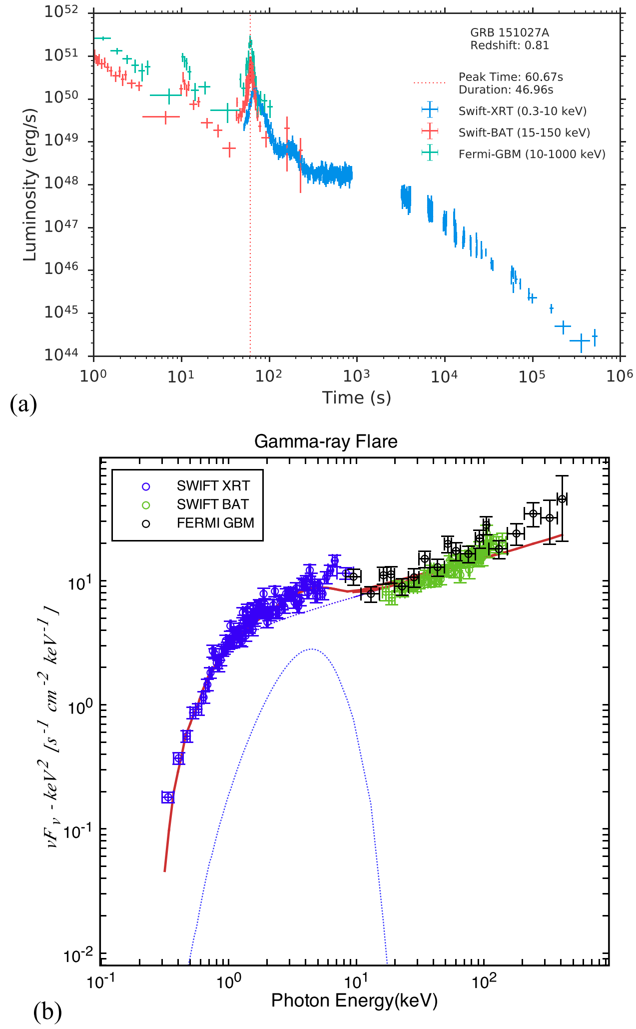

Figure 7. (a) Luminosity light curves in the rest-frame energy bands: 10–1000 keV for *Fermi*-GBM (green), 15–150 keV for *Swift*-BAT (red), and 0.3–10 keV for *Swift*-XRT (blue). The red dotted line marks the position of the hard X-ray flare. (b) Time-integrated νF_ν spectrum of the hard X-ray flare and the PL+BB model (solid red curve) that best fit the data.

4. Hard and Soft X-Ray Flare

4.1. Hard X-Ray Flare

We turn now to the hard X-ray flare and the soft X-ray flare. The hard X-ray flare is observed in the time interval 94–180 s (corresponding to the rest-frame time interval 52–99 s; see Figure 7 (a)). The luminosity light curves in the rest-frame energy bands of 10–1000 keV for *Fermi*-GBM (green), 15–150 keV for *Swift*-BAT (red), and 0.3–10 keV for *Swift*-XRT (blue) are displayed. The total isotropic energy of the hard X-ray flare is $E_\gamma = (3.28 \pm 0.13) \times 10^{52}$ erg. The overall spectrum is best fit by a superposition of a PL function with an index of -1.69 ± 0.01 and a BB model with a temperature of $kT = 1.13 \pm 0.08$ keV (see Figure 7 (b)).

We perform a more detailed analysis by dividing the whole hard X-ray flare duration (94–180 s) into eight intervals (indicated with Δt_a^d in Table 2). Among these time intervals, the first six have both BAT and XRT data (total energy range 0.3–150 keV), while the last two fits involve XRT data only (an energy range of 0.3–10 keV). The XRT data were extremely piled up, and corrections have been performed in a conservative way to ascertain that the BB is not due to pileup effects (Romano et al. 2006). The absorption of the spectrum below 2 keV has been also taken into due account. Here, we use the following spectral energy distributions to fit the data: power law (PL), cutoff power law (CPL), PL+BB, and CPL+BB, PL+BB, and CPL+BB. An extra BB component is always preferred to the simple PL models and, only in the sixth interval, to the CPL model whose cutoff energy may be constrained within a 90% significance. The results of the time-resolved analysis are shown in Figure 8 and summarized in Table 2. The BB parameters and errors in Table 2 correspond, respectively, to the main values and the 90% probability interval errors with respect to the central values, both obtained from the Markov Chain-Monte Carlo method applied in XSpec with 10^5 steps (excluding first 10^4). The values are in line with the ones corresponding to minimum χ^2 and with errors to the ones corresponding to intervals obtained from the difference $\Delta\chi^2 = 2.706$ from the minimum χ^2 value. The only exception is the first time bin where $\chi^2_{\rm min}$ value is almost two times lower than the main value. It is useful to infer the bulk Lorentz factor of the hard X-ray flare emission

Table 2
Hard X-Ray Flare: Parameters of the Time-resolved Spectral Analysis

Δt_a^d (s)	Model	α	$E_{\rm p}$ (keV)	$kT_{\rm obs}$ (keV)	$A_{\rm BB}$ (ph cm^{-2}s^{-1})	ϕ_0 (10^{12} cm)	β	Γ	R (10^{12} cm)
94–100	BB+PL	$1.349^{+0.024}_{-0.036}$		$2.2^{+1.1}_{-1.1}$	$0.052^{+0.043}_{-0.034}$	$0.065^{+0.070}_{-0.064}$	$0.38^{+0.19}_{-0.31}$	$1.079^{+0.138}_{-0.077}$	$0.10^{+0.11}_{-0.10}$
100–110	BB+PL	$1.293^{+0.029}_{-0.031}$		$2.57^{+0.43}_{-0.50}$	$0.206^{+0.083}_{-0.084}$	$0.094^{+0.037}_{-0.041}$	$0.606^{+0.042}_{-0.049}$	$1.257^{+0.057}_{-0.053}$	$0.194^{+0.077}_{-0.086}$
110–120	BB+PL	$1.392^{+0.028}_{-0.033}$		$2.17^{+0.22}_{-0.26}$	$0.62^{+0.14}_{-0.15}$	$0.229^{+0.053}_{-0.062}$	$0.852^{+0.035}_{-0.052}$	$1.91^{+0.26}_{-0.24}$	$0.80^{+0.21}_{-0.25}$
120–130	BB+PL	$1.732^{+0.049}_{-0.057}$		$1.10^{+0.14}_{-0.12}$	$0.592^{+0.077}_{-0.073}$	$0.87^{+0.23}_{-0.20}$	$0.957^{+0.014}_{-0.028}$	$3.46^{+0.78}_{-0.76}$	$5.7^{+1.8}_{-2.3}$
130–140	BB+PL	$1.82^{+0.11}_{-0.14}$		$0.617^{+0.046}_{-0.043}$	$0.247^{+0.037}_{-0.038}$	$1.79^{+0.30}_{-0.28}$	$0.983^{+0.0046}_{-0.0079}$	$5.6^{+1.0}_{-1.0}$	$19.1^{+4.2}_{-5.6}$
140–150	CPL+PL	$1.65^{+0.15}_{-0.16}$	$7.3^{+66.3}_{-4.6}$	$0.469^{+0.065}_{-0.064}$	$0.102^{+0.028}_{-0.027}$	$1.99^{+0.61}_{-0.61}$	$0.919^{+0.054}_{-0.560}$	$2.5^{+1.8}_{-1.5}$	$9.5^{+4.4}_{-9.5}$
150–160	BB+PL	$2.40^{+0.45}_{-0.34}$		$0.386^{+0.061}_{-0.061}$	$0.046^{+0.016}_{-0.015}$	$1.97^{+0.71}_{-0.70}$	$0.935^{+0.048}_{-0.934}$	$2.8^{+2.7}_{-1.8}$	$10.5^{+5.5}_{-10.5}$
160–180	BB+PL	$2.15^{+0.29}_{-0.34}$		$0.193^{+0.032}_{-0.030}$	$0.020^{+0.011}_{-0.013}$	$5.2^{+2.3}_{-2.3}$	$0.953^{+0.042}_{-0.952}$	$3.3^{+7.0}_{-2.3}$	32^{+21}_{-32}

Note. Columns list, respectively, the time interval of the spectral analysis; the PL or CPL Index α; the CPL peak energy $E_{\rm p}$ when present; the BB observed temperature, $kT_{\rm obs}$; and normalization $A_{\rm BB}$, fitted from Section 4 . The quantity, ϕ_0; the expansion velocity, β; the Lorentz factor, Γ; and the effective thermal emitter radius in the laboratory frame, R, inferred from Section 5.

from the nonthermal component of the spectrum. Using the *Fermi* data, the best-fit model for this nonthermal component in the time interval 95–130 s is a CPL with a spectral cutoff energy, $E_c = 926 \pm 238$ keV. Such a cutoff can be caused by $\gamma\gamma$ absorption, for which the target photon's energy is comparable to E_c, i.e., $E_c \gtrsim [\Gamma m_e c^2/(1+z)]^2/E_c$ and, therefore, the Lorentz factor can be deduced by

$$\Gamma \approx \frac{E_c}{m_e c^2}(1+z), \tag{1}$$

where m_e is the electron mass. From the above value of E_c, we infer $\Gamma = 3.28 \pm 0.84$, which represents an average over the hard X-ray flare duration. It is in the range of the ones observed in thermal component (see the first five columns of the Table 2), coinciding in turn with the numerical simulation of the interaction of the e^+e^- plasma with the SN ejecta described in the Section 6.

4.2. Soft X-Ray Flare

The soft X-ray flare, which has been discussed in Ruffini et al. (2018c), peaks at a rest-frame time of $t_p = (184 \pm 16)$ s, has a duration of $\Delta t = (164 \pm 30)$ s, a peak luminosity of $L_p = (7.1 \pm 1.8) \times 10^{48}$ erg s^{-1}, and a total energy in the rest-frame 0.3–10 keV energy range of $E_X = (4.4 \pm 2.9) \times 10^{51}$ erg. The overall spectrum within its duration, Δt, is best-fit by a PL model with a PL index of -2.24 ± 0.03 (see Figure 9).

Here, we also perform a time-resolved analysis of the soft X-ray flare. We divide the total interval Δt into four subintervals, i.e., 235–300 s, 300–365 s, 365–435 s, and 435–500 s in the observer frame (see Figure 10). The best-fits of each of these four time intervals are PL models with indexes ranging from -2.3 to -2.1, which are consistent with the typical values inferred in Ruffini et al. (2018c).

The complete spacetime diagram, showing UPE, hard X-ray flare, and soft X-ray flare, is represented in Figure 11.

5. Evolution of Thermal Component around the Hard X-Ray Flare

Following Figure 1, it is possible to infer the expansion velocity β (i.e., the velocity in units of the velocity of light c). We assume that the blackbody emitter has spherical symmetry and expands with a constant Lorentz gamma factor. Therefore, the expansion velocity β is also constant during the emission. The relations between the comoving time, $t_{\rm com}$; the laboratory time, t; the arrival time, t_a; and the arrival time, t_a^d, at the detector (see Bianco et al. 2001; Ruffini et al. 2001c, 2002; Bianco & Ruffini 2005a) in this case become:

$$\begin{aligned} t_a^d &= t_a(1+z) = t(1-\beta\cos\vartheta)(1+z) \\ &= \Gamma t_{\rm com}(1-\beta\cos\vartheta)(1+z). \end{aligned} \tag{2}$$

We can infer an effective radius R of the blackbody emitter from: (1) the observed blackbody temperature, $T_{\rm obs}$, which comes from the spectral fit of the data; (2) the observed bolometric blackbody flux, $F_{\rm bb,obs}$, computed from $T_{\rm obs}$ and the normalization of the blackbody spectral fit; and (3) the cosmological redshift z of the source (see also Izzo et al. 2012). We recall that $F_{\rm bb,obs,}$ by definition, is given by

$$F_{\rm bb,obs} = \frac{L}{4\pi D_L(z)^2}, \tag{3}$$

where $D_L(z)$ is the luminosity distance of the source, which in turn is a function of the cosmological redshift z, and L is the source bolometric luminosity (i.e., the total emitted energy per unit time). L is Lorentz invariant, so we can compute it in the comoving frame of the emitter using the usual blackbody expression:

$$L = 4\pi {R_{\rm com}}^2 \sigma {T_{\rm com}}^4, \tag{4}$$

where $R_{\rm com}$ and $T_{\rm com}$ are the comoving radius and the comoving temperature of the emitter, respectively, and σ is the Stefan–Boltzmann constant. We recall that $T_{\rm com}$ is constant over the entire shell due to our assumption of spherical symmetry. From Equations (3) to (4), we then have

$$F_{\rm bb,obs} = \frac{{R_{\rm com}}^2 \sigma {T_{\rm com}}^4}{D_L(z)^2}. \tag{5}$$

We now need the relation between $T_{\rm com}$ and the observed blackbody temperature, $T_{\rm obs}$. Considering both the cosmological redshift and the Doppler effect due to the velocity of the emitting surface, we have:

$$\begin{aligned} T_{\rm obs}(T_{\rm com}, z, \Gamma, \cos\vartheta) &= \frac{T_{\rm com}}{(1+z)\Gamma(1-\beta\cos\vartheta)} \\ &= \frac{T_{\rm com}\mathcal{D}(\cos\vartheta)}{1+z}, \end{aligned} \tag{6}$$

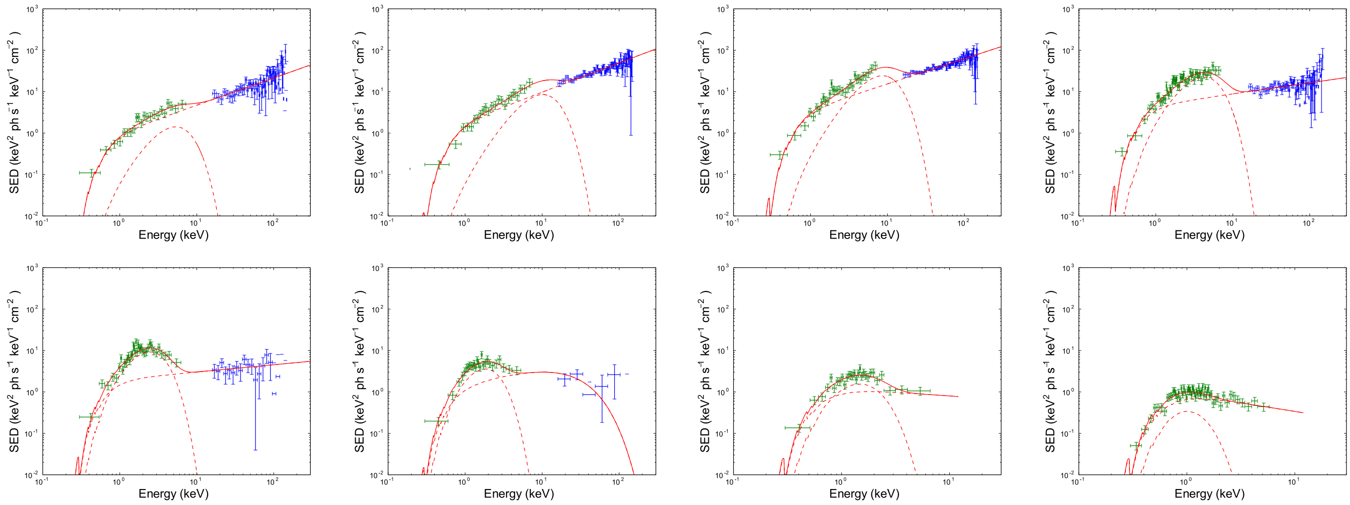

Figure 8. Hard X-ray flare: time-resolved νF_ν spectra of the eight time intervals in Table 2 (from the top left to the right, and from the bottom left to the right). XRT data are displayed in green and BAT data are in blue; BAT data points with no vertical lines corresponds to upper limits. Plots correspond to parameters obtained from minimum χ^2 fit.

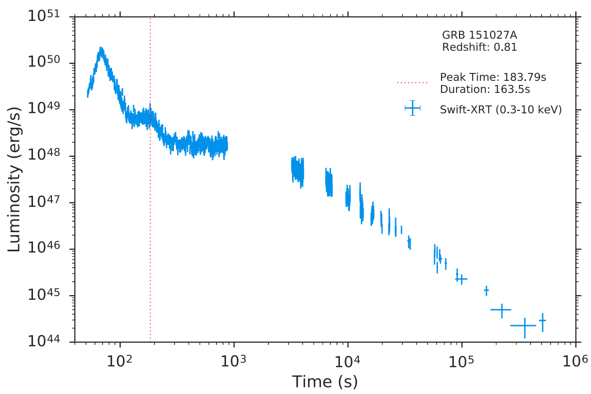

(a)

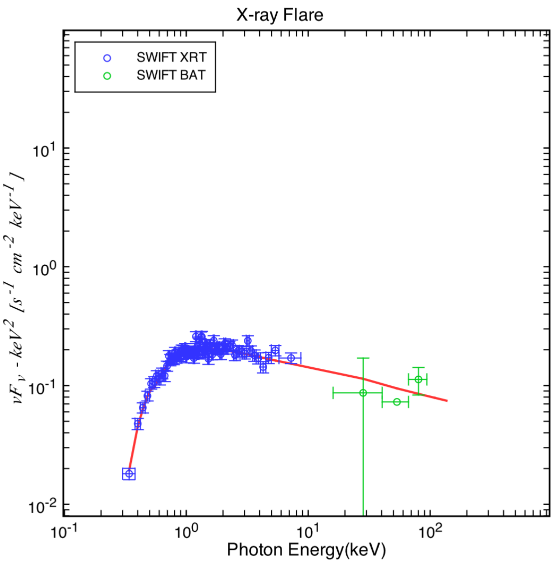

(b)

Figure 9. (a) Rest-frame 0.3–10 keV luminosity light curve of GRB 151027A. The red dotted line marks the position of the soft X-ray flare. (b) Time-integrated νF_ν spectrum of the X-ray flare and the PL model (solid red curve) that best fits the data.

where we have defined the Doppler factor $\mathcal{D}(\cos\vartheta)$ as

$$\mathcal{D}(\cos\vartheta) \equiv \frac{1}{\Gamma(1-\beta\cos\vartheta)}. \tag{7}$$

Equation (6) gives us the observed blackbody temperature of the radiation coming from different points of the emitter surface, corresponding to different values of $\cos\vartheta$. However, since the emitter is at a cosmological distance, we are not able to resolve spatially the source with our detectors. Therefore, the temperature that we actually observe corresponds to an average of Equation (6) computed over the emitter surface:

$$\begin{aligned} T_{\rm obs}(T_{\rm com}, z, \Gamma) &= \frac{1}{1+z}\frac{\int_\beta^1 \mathcal{D}(\cos\vartheta) T_{\rm com}\cos\vartheta d\cos\vartheta}{\int_\beta^1 \cos\vartheta d\cos\vartheta} \\ &= \frac{2}{1+z}\frac{\beta(\beta-1)+\ln(1+\beta)}{\Gamma\beta^2(1-\beta^2)}T_{\rm com} \\ &= \Theta(\beta)\frac{\Gamma}{1+z}T_{\rm com}, \end{aligned} \tag{8}$$

where we defined

$$\Theta(\beta) \equiv 2\,\frac{\beta(\beta-1)+\ln(1+\beta)}{\beta^2}. \tag{9}$$

We have used the fact that due to relativistic beaming, we observe only a portion of the surface of the emitter defined by

$$\beta \leqslant \cos\vartheta \leqslant 1, \tag{10}$$

and we used the definition of Γ given above. Therefore, inverting Equation (8), the comoving blackbody temperature, $T_{\rm com}$, can be computed from the observed blackbody temperature, $T_{\rm obs}$, the source cosmological redshift, z, and the emitter Lorentz gamma factor in the following way:

$$T_{\rm com}(T_{\rm obs}, z, \Gamma) = \frac{1+z}{\Theta(\beta)\Gamma}T_{\rm obs}. \tag{11}$$

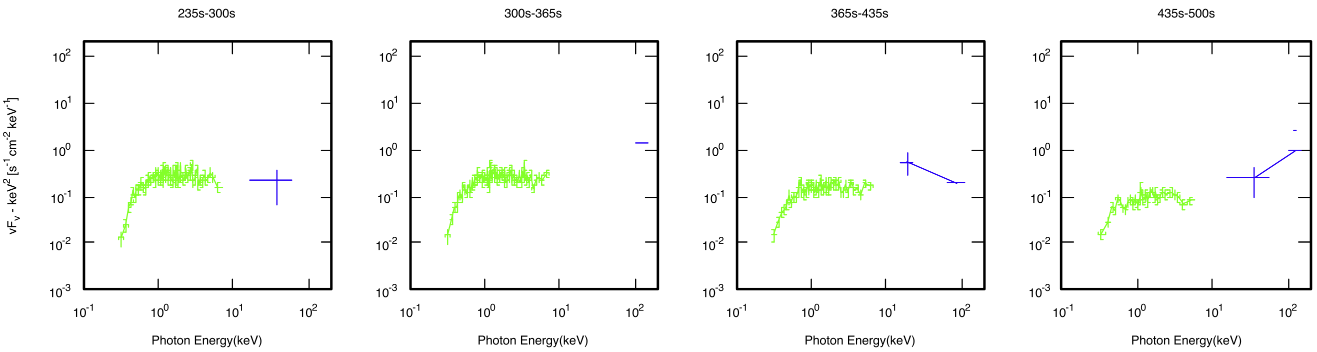

Figure 10. Soft X-ray flare: time-resolved BAT (blue) and XRT (green) νF_ν spectra of the soft X-ray flare in the indicated time intervals.

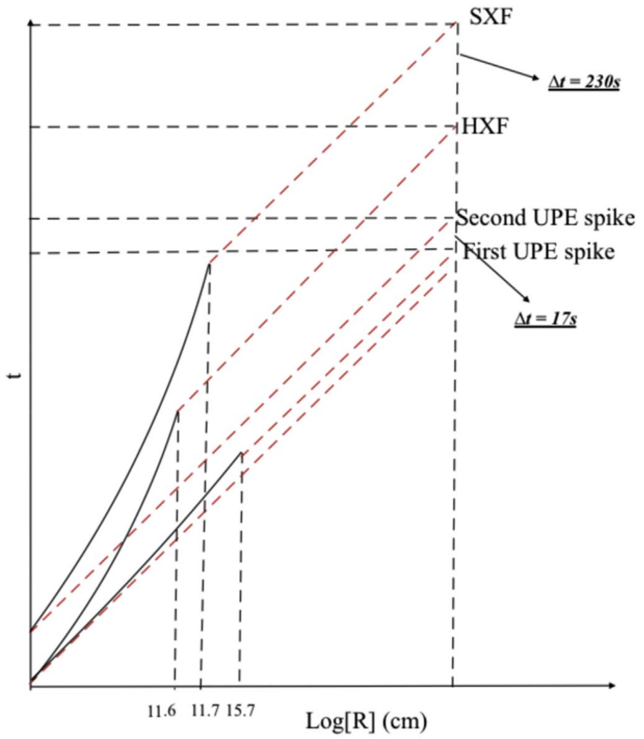

Figure 11. Same as Figure 6, but also showing the position of the plasma shock within the SN ejecta (dashed black lines) for each of the components of the UPE, until the breakout. The first spike originates as the hard X-ray flare, and the second spike originates as the soft X-ray flare. The photon wordlines (solid red lines) of the hard X-ray flare and the soft X-ray flare are observed with a time difference of ∼230 s (rest frame of ∼130 s) due to the differential deceleration of the two UPE components within the SN ejecta.

We can now insert Equation (11) into Equation (5) to obtain

$$F_{\mathrm{bb,obs}} = \frac{{R_{\mathrm{com}}}^2}{D_L(z)^2}\sigma T_{\mathrm{com}}^4 = \frac{{R_{\mathrm{com}}}^2}{D_L(z)^2}\sigma\left[\frac{1+z}{\Theta(\beta)\Gamma}T_{\mathrm{obs}}\right]^4. \quad (12)$$

Since the radius, R, of the emitter in the laboratory frame is related to R_{com} by

$$R_{\mathrm{com}} = \Gamma R, \quad (13)$$

we can insert Equation (13) into Equation (12) and obtain

$$F_{\mathrm{bb,obs}} = \frac{(1+z)^4}{\Gamma^2}\left(\frac{R}{D_L(z)}\right)^2\sigma\left[\frac{T_{\mathrm{obs}}}{\Theta(\beta)}\right]^4. \quad (14)$$

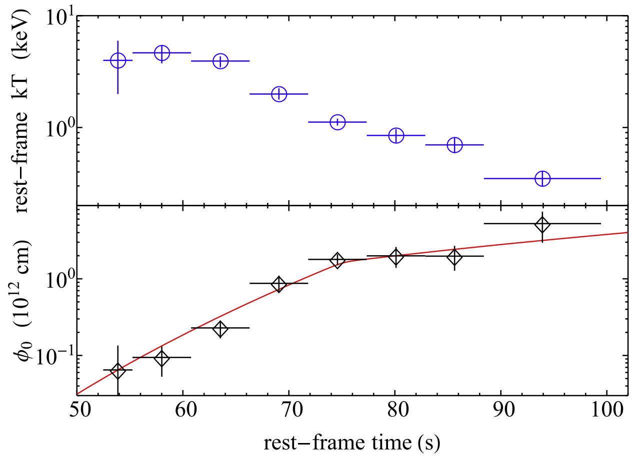

Figure 12. Cosmological rest-frame evolution of kT (top panel) and ϕ_0 (bottom panel) of the thermal emitter in the hard X-ray flare of GRB 151027A. The ϕ_0 interpolation (red line) is obtained using two smoothly joined PL segments.

Solving Equation (14) for R, we finally obtain the thermal emitter effective radius in the laboratory frame:

$$R = \Theta(\beta)^2\Gamma\frac{D_L(z)}{(1+z)^2}\sqrt{\frac{F_{\mathrm{bb,obs}}}{\sigma T_{\mathrm{obs}}^4}} = \Theta(\beta)^2\Gamma\phi_0, \quad (15)$$

where we have defined ϕ_0 as

$$\phi_0 \equiv \frac{D_L(z)}{(1+z)^2}\sqrt{\frac{F_{\mathrm{bb,obs}}}{\sigma T_{\mathrm{obs}}^4}}. \quad (16)$$

The evolutions of the rest-frame temperature and ϕ_0 are shown in Figure 12. In astronomy, the quantity ϕ_0 is usually identified with the radius of the emitter. However, in relativistic astrophysics, this identity cannot be straightforwardly applied, because the estimate of the effective emitter radius R in Equation (15) crucially depends on the knowledge of its expansion velocity β (and, correspondingly, of Γ).

It must be noted that Equation (15) above gives the correct value of R for all values of $0 \leqslant \beta \leqslant 1$ by taking all of the relativistic transformations properly into account. In the nonrelativistic limit ($\beta \rightarrow 0$), we have, respectively:

$$\Theta \underset{\beta\to 0}{\longrightarrow} 1,\ \Theta^2 \underset{\beta\to 0}{\longrightarrow} 1, \quad (17)$$

$$T_{\mathrm{com}} \underset{\beta\to 0}{\longrightarrow} T_{\mathrm{obs}}(1+z),\ R \underset{\beta\to 0}{\longrightarrow} \phi_0, \quad (18)$$

as expected. Analogously, in the ultra-relativistic limit ($\beta \to 1$), we have

$$\Theta \underset{\beta \to 1}{\longrightarrow} 1.39,\ \Theta^2 \underset{\beta \to 1}{\longrightarrow} 1.92, \tag{19}$$

$$T_{\rm com} \underset{\beta \to 1}{\longrightarrow} \frac{0.72}{\Gamma} T_{\rm obs}(1+z),\ R \underset{\beta \to 1}{\longrightarrow} 1.92\Gamma\phi_0. \tag{20}$$

It must also be noted that the numerical coefficient in Equation (15) is computed as a function of β using Equation (9) above, and it is different from the constant values proposed by Pe'er et al. (2007) and by Ghirlanda et al. (2013).

An estimate of the expansion velocity, β, can be deduced from the ratio between the variation of the emitter effective radius, ΔR, and the emission duration in laboratory frame, Δt, i.e.,

$$\beta = \frac{\Delta R}{c\Delta t} = \Theta(\beta)^2\Gamma(1-\beta\cos\vartheta)(1+z)\frac{\Delta\phi_0}{c\Delta t_a^d}, \tag{21}$$

where we used Equation (15), the relation between Δt and Δt_a^d given in Equation (2), we used the definition of Γ given above. and ϑ is the displacement angle of the considered photon emission point on the surface from the line of sight. In the following, we only consider the case $\cos\vartheta = 1$. In this case, using Equation (9), Equation (21) assumes the form presented in Figure 1. It allows us to estimate the expansion velocity, β, of the emitter using only the observed blackbody flux, temperature, photon arrival time, and cosmological redshift, assuming uncollimated emission and only considering the radiation coming from the line of sight. We can explain the observed blackbody emission in GRB 151027A without introducing the "reborn fireball" scenario (see Ghisellini et al. 2007; Nappo et al. 2017).

To infer β, we fit the evolution of ϕ_0 (see Figure 12 and Table 2) using two smoothly joined PL segments. It allows us to estimate the ratio $\Delta\phi_0/(c\Delta t_a^d)$ in Equation (21) and, therefore, the values of β and Γ, assuming that they are constant in each time interval (see Figure 13, top and middle panels). Consequently, we can estimate the evolution of the radius, R, of the emitter in the laboratory frame by taking into account the relativistic transformations described in Equations (2), (15), and (16) (see bottom panel of Figure 13). The results are also summarized in Table 2.

6. On the Nature of the Hard X-Ray Flare and the Soft X-Ray Flare

Following the procedure described in Section 10 of Ruffini et al. (2018c), we interpret the thermal emission observed in the hard X-ray flare as the observational feature arising from the early interaction between the expanding SN ejecta and the e^+e^- plasma. In order to test the consistency of this model with the data, we have performed a series of numerical simulations, whose details we summarize as follows.

(a) Our treatment of the problem is based on an implementation of the 1D relativistic hydrodynamical module included in the PLUTO code[5] (Mignone et al. 2011). In the spherically symmetric case considered, only the radial coordinate is used, and consequently the code integrates a system of partial differential equations in only two coordinates:

[5] http://plutocode.ph.unito.it/

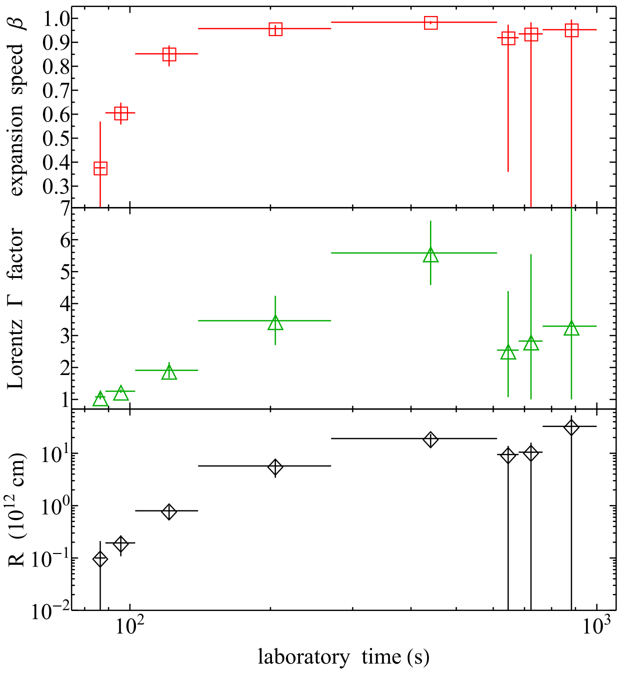

Figure 13. Evolution in the laboratory frame of β, Γ, and R of the thermal emitter from the time intervals in Table 2.

the radius and the time. This permits the study of the evolution of the plasma along one selected radial direction at a time. The aforementioned equations are those of an ideal relativistic fluid, which can be written as follows:

$$\frac{\partial(\rho\Gamma)}{\partial t} + \nabla.(\rho\Gamma\boldsymbol{v}) = 0, \tag{22}$$

$$\frac{\partial m_r}{\partial t} + \nabla.(m_r\boldsymbol{v}) + \frac{\partial p}{\partial r} = 0, \tag{23}$$

$$\frac{\partial\mathcal{E}}{\partial t} + \nabla.(\boldsymbol{m} - \rho\Gamma\boldsymbol{v}) = 0, \tag{24}$$

where ρ and p are the comoving fluid density and pressure, $\boldsymbol{v}$ is the coordinate velocity in natural units ($c = 1$), $\Gamma = (1 - \boldsymbol{v}^2)^{-\frac{1}{2}}$ is the Lorentz gamma factor, $\boldsymbol{m} = h\Gamma^2\boldsymbol{v}$ is the fluid momentum, m_r is the radial component, $\mathcal{E}$ is the internal energy density measured in the comoving frame, and h is the comoving enthalpy density, which is defined by $h = \rho + \epsilon + p$. We define $\mathcal{E}$ as follows:

$$\mathcal{E} = h\Gamma^2 - p - \rho\Gamma. \tag{25}$$

The first two terms on the right-hand side of this equation coincide with the T^{00} component of the fluid energy-momentum, and the last one is the mass density in the laboratory frame.

Under the conditions discussed in Ruffini et al. (2018c), the plasma satisfies the equation of state of an ideal relativistic gas, which can be expressed in terms of its enthalpy as

$$h = \rho + \frac{\gamma p}{\gamma - 1}, \tag{26}$$

with $\gamma = 4/3$. Imposing this equation of state closes and completely defines the system of equations, leaving as the only remaining freedom the choice as the matter density profile and the boundary conditions. To compute the evolution of these

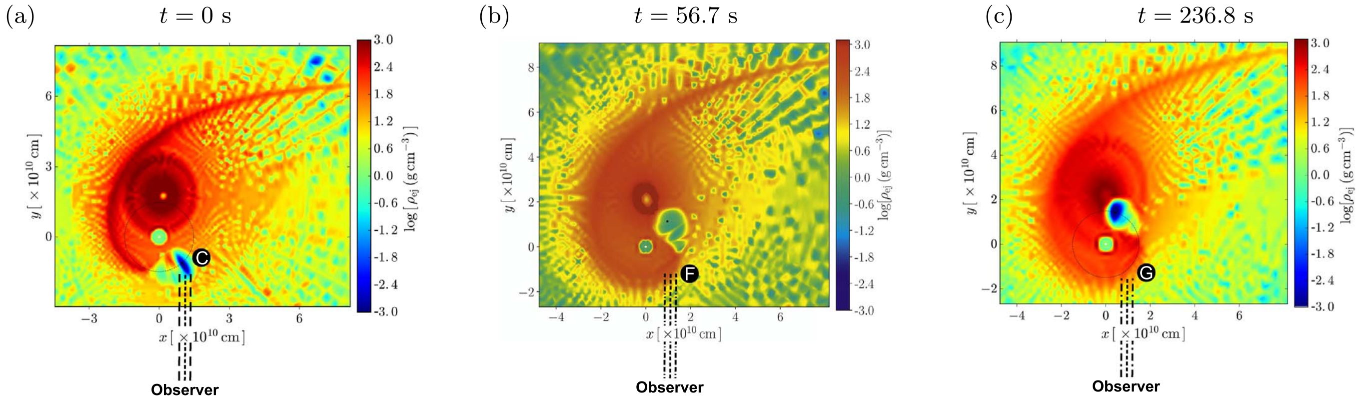

Figure 14. Three snapshots of the density distribution of the SN ejecta in the equatorial plane of the progenitor binary system. The time $t = 0$ indicates the instant when the NS companion reaches, by accretion, the critical mass and leads to the formation of a BH (black dot). As evidenced in panel (a), the location of the black hole formation is widely separated from the central position represented by the SN explosion, it is actually located in the white conical region in Figure 2. The binary parameters of this simulations are: the NS companion has an initial mass of 2.0 $M_\odot$; the CO_{core}, obtained from a progenitor with a ZAMS mass of $M_{ZAMS} = 30\,M_\odot$, leads to a total ejecta mass of 7.94 $M_\odot$ and to a 1.5 $M_\odot$ νNS (white dot); and the orbital period is $P \approx 5$ minutes, i.e., a binary separation of $a \approx 1.5 \times 10^{10}$ cm.

quantities in the chosen setup, the code uses the HLLC Riemann solver for relativistic fluids (see Mignone et al. 2011). The time evolution is performed by means of a second-order Runge–Kutta integration, and a second-order total variation diminishing scheme is used for the spatial interpolation. An adaptive mesh refinement algorithm is implemented as well, provided by the CHOMBO library (Colella et al. 2003). We turn now to the determination of the SN ejecta.

(b) The initially ultra-relativistic e^+e^- plasma expands through the SN ejecta matter, slowing down to mildly relativistic velocities. The SN density and velocity profiles are taken from the 3D SPH simulation of the SN ejecta expansion under the influence of the νNS and the NS companion gravitational field. In our simulations, we include the NS orbital motion and the NS gravitational-mass changes due to the accretion process modeled with the Bondi–Hoyle formalism (see Becerra et al. 2016, for more details). We set the SN ejecta initial conditions, adopting a homologous velocity distribution in free expansion, and the SN matter was modeled with 16 million point-like particles. Each SN layer is initially populated following a PL density profile of the CO_{core}, as obtained from low-metallicity progenitors evolved with the *Kepler* stellar evolution code (Woosley et al. 2002). Here, we take the simulation of an initial binary system formed by a 2.0 $M_\odot$ NS and a CO_{core} produced by an $M_{ZAMS} = 30\,M_\odot$ progenitor as a reference model. This leads to a total ejecta with a mass of 7.94 $M_\odot$ and a νNS of 1.5 $M_\odot$. The orbital period of the binary is $P \approx 5$ minutes, i.e., a binary separation of $a \approx 1.5 \times 10^{10}$ cm. The density profile exhibiting the evolution of the SN ejecta and the companion star is shown in Figure 14. Figure 15 shows the SN ejecta mass enclosed within a cone of 5° of the semi-aperture angle with the vertex at the position of the BH at the moment of its formation. The cone axis stands along the θ direction measured counterclockwise with respect to the line of sight. We simulate the interaction of the e^+e^- plasma with such ejecta from a radius $\approx 10^{10}$ cm all the way to $\approx 10^{12}$ cm where transparency is reached. We have recently run new 3D SPH simulations of this process in Becerra et al. (2018) using the SNSPH code (Fryer et al. 2006). These new simulations have allowed for a wide exploration of the binary parameter space and have confirmed the results and the physical picture presented in Becerra et al. (2016). On the basis of these new simulations, we have determined the value of the baryon loads both for the hard X-ray flares and the soft X-ray flares.

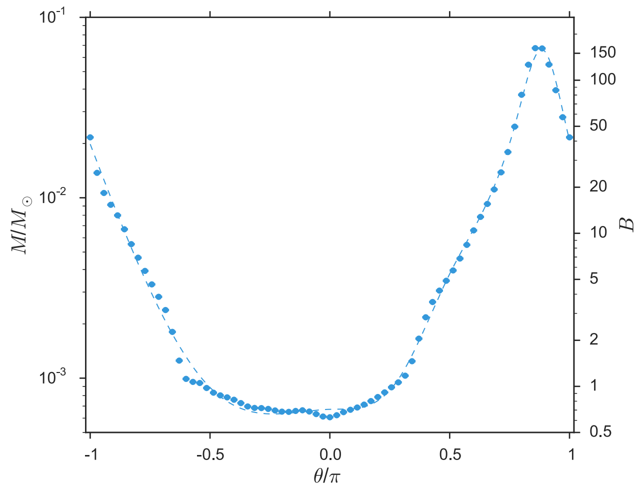

Figure 15. SN ejecta mass enclosed within a cone of 5° of semi-aperture angle and vertex centered on the SN and positioned to an angle θ, measured counterclockwise, with respect to the line of sight (which passes through the νNS and BH at the moment of its formation; see Conclusions). The binary parameters of this simulations are: the NS has an initial mass of 2.0 $M_\odot$; the CO_{core} obtained from a progenitor with ZAMS mass $M_{ZAMS} = 30\,M_\odot$, leads to a total ejecta mass 7.94 $M_\odot$, the orbital period is $P \approx 5$ min, i.e., a binary separation $a \approx 1.5 \times 10^{10}$ cm. The right-side vertical axis gives, as an example, the corresponding value of the baryon load, B, assuming a plasma energy of $E_{e^+e^-} = 1 \times 10^{53}$ erg. It is appropriate to mention that the above values of the baryon load are computed using an averaging procedure, which is performed centered on the SN explosion and produces larger values than the one centered around the BH with a specific value of the baryon load $B \sim 1.9 \times 10^{-3}$ (see Figure 14(a)).

(c) For the simulation of the hard X-ray flare, we set a total energy of the plasma equal to that of the hard X-ray flare, i.e., $E_\gamma = 3.28 \times 10^{52}$ erg, and a baryon load of $B = 79$, corresponding to a baryonic mass of $M_B = 1.45\,M_\odot$. We obtain a radius of the transparency $R_{ph} = 4.26 \times 10^{11}$ cm, a Lorentz factor at transparency $\Gamma = 2.86$, and an arrival time of the corresponding radiation in the cosmological rest frame $t_a = 56.7$ s (see Figure 16). This time is in agreement with

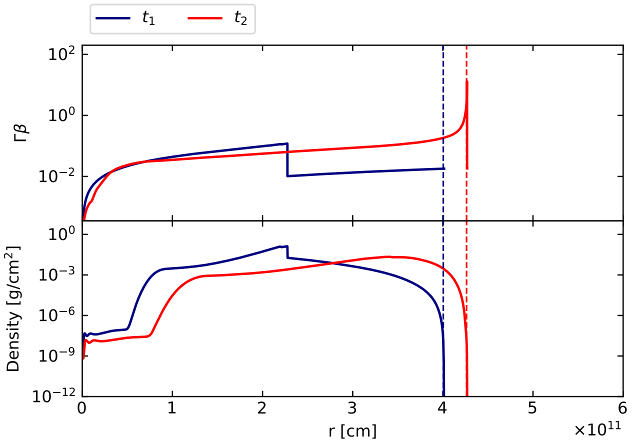

Figure 16. Numerical simulation of the hard X-ray flare. We set a total energy of the plasma as $E_\gamma = 3.28 \times 10^{52}$ erg and a baryon load as $B = 79$, corresponding to a baryonic mass of $M_B = 1.45\ M_\odot$. Top: distribution of the velocity inside the SN ejecta at the two fixed values of the laboratory time t_1 (before the plasma reaches the external surface of the ejecta) and t_2 (the moment at which the plasma, after crossing the entire SN ejecta, reaches the external surface). We plotted the quantity $\Gamma\beta$, recalling that we have $\Gamma\beta \sim \beta$ when $\beta < 1$ and $\Gamma\beta \sim \Gamma$ when $\beta \sim 1$. Bottom: corresponding distribution of the mass density of the SN ejecta in the laboratory frame $\rho_{\rm lab}$. We obtain a radius of the transparency of $R_{\rm ph} = 4.26 \times 10^{11}$ cm, a Lorentz factor at transparency $\Gamma = 2.86$, and an arrival time of the corresponding radiation in the cosmological rest frame of $t_a = 56.7$ s.

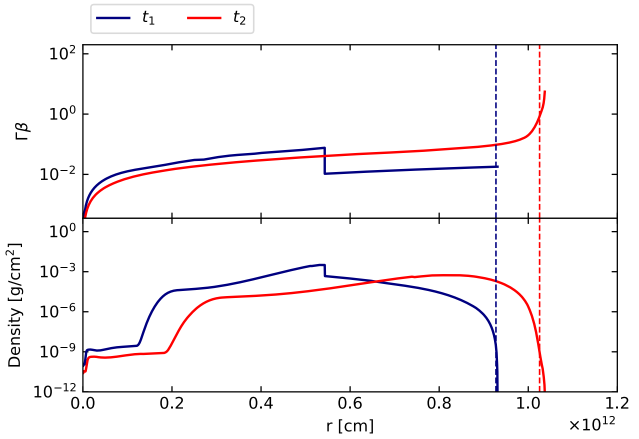

Figure 17. Numerical simulation of the soft X-ray flare. We set a total energy of the plasma as $E_X = 4.39 \times 10^{51}$ erg and a baryon load *as* $B = 207$, corresponding to a baryonic mass of $M_B = 0.51\ M_\odot$. The plotted quantities are the same as in Figure 16. We obtain a radius of the transparency of $R_{\rm ph} = 1.01 \times 10^{12}$ cm, a Lorentz factor at transparency $\Gamma = 1.15$, and an arrival time of the corresponding radiation in the cosmological rest frame of $t_a = 236.8$ s.

the starting time of the hard X-ray flare in the source rest frame (see Section 3).

For the simulation of the soft X-ray flare, we set the energy $E_X = 4.39 \times 10^{51}$ erg as the total energy of the plasma and a baryon load as $B = 207$, which corresponds to a baryonic mass of $M_B = 0.51\ M_\odot$. We obtain a radius of the transparency of $R_{\rm ph} = 1.01 \times 10^{12}$ cm, a Lorentz gamma factor at transparency $\Gamma = 1.15$, and an arrival time of the corresponding radiation in the cosmological rest frame of $t_a = 236.8$ s (see Figure 17). This time is in agreement with the above time t_p at which the soft X-ray flare peaks in the rest frame.

7. Summary, Discussion, and Conclusions

7.1. Summary

It is by now clear that seven different subclass of GRBs with different progenitors exist (Ruffini et al. 2016b). Each GRB subclass is itself composed of different episodes, each one characterized by specific observational data that make their firm identification possible (see e.g., Ruffini et al. 2018c, and references therein). Here, we evidence how, within the BdHN subclass, a further differentiation follows by selecting special viewing angles. We have applied our recent treatment (Ruffini et al. 2018c) to the UPE phase and the hard X-ray flare using the specific case of GRB 151027A as a prototype in view of the excellent available data.

We recall three results:

1. We have confirmed the ultra-relativistic nature of the UPE, which appears to be composed of a double spike (see Figures 4(a) and 5(b)). This double spike structure appears to be also present in other systems, such as GRB 140206A and GRB 160509A (R. Ruffini et al. 2018, in preparation). From the analysis of the P-GRB of the first spike, we derived an ultra-relativistic Lorentz factor of $\Gamma_0 = 503 \pm 76$, a baryon load of $B = (1.92 \pm 0.35) \times 10^{-3}$, and a structure in the CBM with the density (7.46 ± 1.2) cm^{-3} extending to dimensions of 10^{16} cm (see Figure 5(d)). The second spike of energy, $E_{\rm iso,2} = (4.99 \pm 0.60) \times 10^{51}$ erg, after a cosmological rest-frame time of 9 s following the first spike of energy, $E_{\rm iso,1} = (7.26 \pm 0.36) \times 10^{51}$ erg (see Figures 4(b) and (c)), appear to be featureless. We are currently examining the possibility that the nature of these two spikes and their morphology could be directly connected to the formation process of the BH.
2. A double spikes appears to occur also in the FPA phase (see Figure 7(a)); the first component is the hard X-ray flare, and the second is the soft X-ray flare. The energy of the hard X-ray flare is $E_\gamma = (3.28 \pm 0.13) \times 10^{52}$ erg (Figure 7), and the energy of the soft X-ray flare is $E_X = (4.4 \pm 2.9) \times 10^{51}$ erg (Figure 9). We have analyzed both flares with our usual approach of the hydrodynamical equations describing the interaction of the e^+e^- plasma with the SN ejecta (see Figure 16 for the hard X-ray flare and Figure 17 for the soft X-ray flare). The baryon loads of the two flares are different: $B = 79$ for the hard X-ray flare, and $B = 207$ for the soft X-ray flare. This is visualized in Figure 11 as well as in our 3D simulations (see the three snapshots shown in Figure 14). Both the hard X-ray flare and the soft X-ray flare show mildly relativistic regimes, as already observed in Ruffini et al. (2018c), namely a Lorentz factor at transparency of $\Gamma \sim 5$ for the hard X-ray flare and a Lorentz factor of $\Gamma \sim 2$ for the soft X-ray flare.
3. We studied the ETE associated to the hard X-ray flare. We have measured its expansion velocity derived from the relativistic treatment described in Section 5, following the formula in Figure 1 (see also Ruffini et al. 2018c). We have identified the transition from an SN, with an initial computed velocity of $0.38c$, to an HN, with a computed velocity of $0.98c$ (see Figure 13 and Table 2). These results are in good agreement with observations of both SNe and HNe (see e.g., Table 3 and Figure 20 in Nicholl et al. 2015).

Table 3
Parameters of the Sequence of Astrophysical Processes that Characterize the BdHNe: The Columns List, Respectively, the Name of Each Process, the Radius of Transparency, the Lorentz Gamma Factor (Γ) and the Baryon Load, Starting Time of the Process, the Duration, and, Finally, the Best-fit Model of the Spectrum

	Name	Radius(cm)	Γ	Baryon Load	$t_{\mathrm{start}}(s)$	Duration(s)	Spectrum
UPE	First spike (P-GRB)	$\sim 10^{13}$	$\sim 10^2$–10^3	$\sim 10^{-4}$–10^{-2}	$\sim T_0$	~ 1	CPL+BB
	First spike (rest)	$\sim 10^{15}$–10^{17}	$\sim 10^2$–10^3	$\sim 10^{-4}$–10^{-2}	$\sim T_0+1$	~ 5	Band
	Second spike	$\sim 10^{15}$–10^{17}	$\gtrsim 10^3$	$\lesssim 10^{-4}$	$\sim T_0+15$	~ 5	Band
	hard X-ray flare	$\sim 10^{11}$–10^{12}	$\lesssim 10$	$\sim 10^2$	$\sim T_0+50$	$\sim 10^2$	PL+BB
	soft X-ray flare	$\sim 10^{12}$–10^{13}	$\lesssim 4$	$\sim 10^3$	$\sim T_0+10^2$	~ 150	PL(+BB)
	Late afterglow	$\gtrsim 10^{13}$	$\lesssim 2$	–	$\gtrsim T_0+10^2$	$\gtrsim 10^6$	PL
	SN optical emission	$\sim 10^{15}$	~ 1	–	$\sim T_0+10^6$	$\gtrsim 10^6$	PL
	GeV emission	–	–	–	$\sim T_0+1$	$\sim 10^4$	PL

Note. T_0 is the *Fermi*-GBM trigger time.

The above observational analysis, as already presented in Pisani et al. (2013, 2016), set the ensemble of the data that any viable model of GRBs has to conform. In the last 30 years, the enormous number of high-quality data obtained (e.g., by *Beppo-SAX*, *Swift*, *Agile,* and *Fermi*) further extended by specific optical, radio, and ultrahigh-energy data offered the possibility to test the viable models that conform to these data. We have shown that the BdHN model can explain the above observational features.

7.2. Discussion

1. By to adopting the BdHN approach, we discovered the existence of four different process: a double feature in the UPE phase, the hard X-ray flares, the soft X-ray flares, and the ETE phase. Each one of these processes is generated by a different e^+e^- injection occurring in a different baryon load medium. Using the binary nature of the progenitor system in BDHN, especially the presence of an incipient SN and a companion NS, together with an appropriate theoretical treatment and an ample program of numerical simulations (Becerra et al. 2018), we have been able to determine the nature of these processes. Clear observational predictions have followed, including (the major one) the coincidence of the numerical value of the velocity of expansion at the end of the ETE phase with the observed expansion velocity of the HN, confirmed in additional BdHN and currently being observationally addressed in additional cases. A clear temporal sequence in the occurrence of these processes, as well as the specific sequence in the values of the Lorentz gamma factors, has been established.
2. For the first time, the rotation of the binary system, of the order of 400 s, has been essential in order to untangle the sequence of events discovered and explained in this article, recognizing their a-causal nature and their modulation by the rotation of the progenitor binary system.
3. The above different processes, including the double spiky structure of the UPE phase, the hard and soft X-ray flares, and the ETE phase are actually different appearances of the same physical process: the black hole formation, as seen from different viewing angles due to the rotation of the SN ejecta in the binary system (see Figure 14) and the consequent angular dependence of the baryon load (see Figure 15).

7.3. Conclusions

1. A clear prediction that will soon be submitted, following our paper, is that of all of the BdHNe occurring with a line of sight in the orbital plane of the binary, with only a fraction of approximately 10% being actually detectable. They correspond to the sources whose ultra-relativistic emission lies within the allowed cone of $\sim 10°$ of low baryon contamination (see Figure 2 and Figure 15). They are the only ones able to trigger the gamma-ray instruments (e.g., the *Fermi*/GBM or *Swift*/BAT detectors). The remaining 90% will not be detectable by current satellites and will possibly need a new mission operating in soft X-rays (like e.g., THESEUS; see Amati et al. 2018).
2. The E_{iso}, traditionally defined using an underlying assumption of isotropy of the BH emission, has to be modified by considering an anisotropic emission process. A total energy, E_{tot}, summing the energies of the UPE, of the hard X-ray flare, of the ETE, and of the soft X-ray flare, has to be considered for sources seen in the equatorial plane. It is not surprising that the energy of the hard X-ray flare in GRB 151027A is larger than the one of the UPE, pointing to an anisotropic emission from the BH.
3. When the inclination of the viewing angle is less that 60° from the normal to the plane of the binary system, the GeV radiation becomes detectable, and its energy, which has been related to the BH rotational energy, will need to be taken into account (Ruffini et al. 2018a).

We acknowledge the referee's comments, which have significantly helped us in formulating a clearer, logically motivated and well-balanced presentation of our results.

Software: PLUTO (Mignone et al. 2011), CHOMBO (Colella et al. 2003), SNSPH (Fryer et al. 2006).

ORCID iDs

C. L. Bianco https://orcid.org/0000-0001-7749-4078
M. Muccino https://orcid.org/0000-0002-2234-9225
G. B. Pisani https://orcid.org/0000-0003-3452-2491

References

Aimuratov, Y., Ruffini, R., Muccino, M., et al. 2017, ApJ, 844, 83
Aksenov, A. G., Ruffini, R., & Vereshchagin, G. V. 2007, PhRvL, 99, 125003

Amati, L., O'Brien, P., Goetz, D., et al. 2018, AdSpR, 62, 191
Becerra, L., Bianco, C. L., Fryer, C. L., Rueda, J. A., & Ruffini, R. 2016, ApJ, 833, 107
Becerra, L., Cipolletta, F., Fryer, C. L., Rueda, J. A., & Ruffini, R. 2015, ApJ, 812, 100
Becerra, L., Ellinger, C. L., Fryer, C. L., Rueda, J. A., & Ruffini, R. 2018, ApJ, in press (arXiv:1803.04356)
Bernardini, M. G., Bianco, C. L., Chardonnet, P., et al. 2005, ApJL, 634, L29
Bianco, C. L., & Ruffini, R. 2004, ApJL, 605, L1
Bianco, C. L., & Ruffini, R. 2005a, ApJL, 620, L23
Bianco, C. L., & Ruffini, R. 2005b, ApJL, 633, L13
Bianco, C. L., & Ruffini, R. 2006, ApJL, 644, L105
Bianco, C. L., Ruffini, R., & Xue, S.-S. 2001, A&A, 368, 377
Blandford, R. D., & McKee, C. F. 1976, PhFl, 19, 1130
Bromberg, O., Nakar, E., Piran, T., & Sari, R. 2013, ApJ, 764, 179
Colella, P., Graves, D. T., Johnson, J. N., et al. 2003, Chombo Software Package for AMR Applications Design Document Tech. Rep. LBNL-6615E
Daigne, F., & Mochkovitch, R. 2002, MNRAS, 336, 1271
Della Valle, M. 2011, IJMPD, 20, 1745
Dezalay, J.-P., Barat, C., Talon, R., et al. 1992, in AIP Conf. Ser. 265, Gamma-ray bursts, ed. W. S. Paciesas & G. J. Fishman (Melville, NY: AIP), 304
Fruchter, A. S., Levan, A. J., Strolger, L., et al. 2006, Natur, 441, 463
Fryer, C. L., Rockefeller, G., & Warren, M. S. 2006, ApJ, 643, 292
Fryer, C. L., Rueda, J. A., & Ruffini, R. 2014, ApJL, 793, L36
Ghirlanda, G., Pescalli, A., & Ghisellini, G. 2013, MNRAS, 432, 3237
Ghisellini, G., Celotti, A., Ghirlanda, G., Firmani, C., & Nava, L. 2007, MNRAS, 382, L72
Goad, M. R., Osborne, J. P., Beardmore, A. P., & Evans, P. A. 2015, GCN, 18482
Golenetskii, S., Aptekar, R., Frederiks, D., et al. 2015, GCN, 18516
Izzo, L., Ruffini, R., Penacchioni, A. V., et al. 2012, A&A, 543, A10
Klebesadel, R. W. 1992, in The Durations of Gamma-ray Bursts, ed. C. Ho, R. I. Epstein, & E. E. Fenimore (Cambridge: Cambridge Univ. Press), 161
Kouveliotou, C., Meegan, C. A., Fishman, G. J., et al. 1993, ApJL, 413, L101
MacFadyen, A. I., & Woosley, S. E. 1999, ApJ, 524, 262
Mao, S., & Yi, I. 1994, ApJL, 424, L131
Maselli, A., D'Ai, A., Lien, A. Y., et al. 2015, GCN, 18478
Masumitsu, T., Negoro, H., Kawai, N., et al. 2015, GCN, 18525
Mazets, E. P., Golenetskii, S. V., Ilinskii, V. N., et al. 1981, Ap&SS, 80, 3
Meszaros, P., Laguna, P., & Rees, M. J. 1993, ApJ, 415, 181
Mignone, A., Zanni, C., Tzeferacos, P., et al. 2011, ApJS, 198, 7
Nappo, F., Pescalli, A., Oganesyan, G., et al. 2017, A&A, 598, A23
Nicholl, M., Smartt, S. J., Jerkstrand, A., et al. 2015, MNRAS, 452, 3869
Paczyński, B. 1998, ApJL, 494, L45
Patricelli, B., Bernardini, M. G., Bianco, C. L., et al. 2012, ApJ, 756, 16
Pe'er, A., Ryde, F., Wijers, R. A. M. J., Mészáros, P., & Rees, M. J. 2007, ApJL, 664, L1
Penacchioni, A. V., Ruffini, R., Bianco, C. L., et al. 2013, A&A, 551, A133
Penacchioni, A. V., Ruffini, R., Izzo, L., et al. 2012, A&A, 538, A58
Perley, D. A., Hillenbrand, L., & Prochaska, J. X. 2015, GCN, 18487
Piran, T. 1999, PhR, 314, 575
Piran, T. 2004, RvMP, 76, 1143
Piran, T., Shemi, A., & Narayan, R. 1993, MNRAS, 263, 861
Pisani, G. B., Izzo, L., Ruffini, R., et al. 2013, A&A, 552, L5
Pisani, G. B., Ruffini, R., Aimuratov, Y., et al. 2016, ApJ, 833, 159
Rees, M. J., & Meszaros, P. 1992, MNRAS, 258, 41P
Rees, M. J., & Meszaros, P. 1994, ApJL, 430, L93
Romano, P., Campana, S., Chincarini, G., et al. 2006, A&A, 456, 917
Rueda, J. A., & Ruffini, R. 2012, ApJL, 758, L7
Ruffini, R. 1998, in Frontiers Science Series 23, Black Holes and High Energy Astrophysics, ed. H. Sato & N. Sugiyama (Kyoto: Universal Academic Press), 167
Ruffini, R. 1999, A&A, 138, 513
Ruffini, R., Bernardini, M. G., Bianco, C. L., et al. 2006, in AIP Conf. Ser. 836, Gamma-Ray Bursts in the Swift Era, ed. S. S. Holt, N. Gehrels, & J. A. Nousek (Melville, NY: AIP), 103
Ruffini, R., Bernardini, M. G., Bianco, C. L., et al. 2007a, in ESA Spec. Publ. 622, The Obscured Universe, ed. S. Grebenev, R. Sunyaev, & C. Winkler (Noordwijk: ESA), 561
Ruffini, R., Bianco, C. L., Chardonnet, P., Fraschetti, F., & Xue, S.-S. 2002, ApJL, 581, L19
Ruffini, R., Bianco, C. L., Fraschetti, F., Xue, S.-S., & Chardonnet, P. 2001a, ApJL, 555, L117
Ruffini, R., Bianco, C. L., Fraschetti, F., Xue, S.-S., & Chardonnet, P. 2001b, ApJL, 555, L113
Ruffini, R., Bianco, C. L., Fraschetti, F., Xue, S.-S., & Chardonnet, P. 2001c, ApJL, 555, L107
Ruffini, R., Bianco, C. L., Vereshchagin, G., & Xue, S.-S. 2007b, in Proc. Relativistic Astrophysics Legacy and Cosmology Conf., Einstein's Legacy, ed. B. Aschenbach et al. (Berlin: Springer), 402
Ruffini, R., Moradi, R., Wang, Y., et al. 2018a, ApJ, submitted (arXiv:1803.05476)
Ruffini, R., Muccino, M., Aimuratov, Y., et al. 2016a, ApJ, 831, 178
Ruffini, R., Muccino, M., Kovacevic, M., et al. 2015, ApJ, 808, 190
Ruffini, R., Rodriguez, J., Muccino, M., et al. 2018b, ApJ, 859, 30
Ruffini, R., Rueda, J. A., Muccino, M., et al. 2016b, ApJ, 832, 136
Ruffini, R., Salmonson, J. D., Wilson, J. R., & Xue, S.-S. 1999, A&A, 350, 334
Ruffini, R., Salmonson, J. D., Wilson, J. R., & Xue, S.-S. 2000, A&A, 359, 855
Ruffini, R., Vereshchagin, G., & Xue, S. 2010, PhR, 487, 1
Ruffini, R., Vitagliano, L., & Xue, S. 2003, PhLB, 573, 33
Ruffini, R., Wang, Y., Aimuratov, Y., et al. 2018c, ApJ, 852, 53
Ruffini, R., & Wilson, J. 1973, PhRvL, 31, 1362
Ryde, F. 2004, ApJ, 614, 827
Ryde, F., Björnsson, C.-I., Kaneko, Y., et al. 2006, ApJ, 652, 1400
Ryde, F., & Pe'er, A. 2009, ApJ, 702, 1211
Shemi, A., & Piran, T. 1990, ApJL, 365, L55
Smith, N. 2014, ARA&A, 52, 487
Smith, N., Li, W., Filippenko, A. V., & Chornock, R. 2011, MNRAS, 412, 1522
Svensson, K. M., Levan, A. J., Tanvir, N. R., Fruchter, A. S., & Strolger, L.-G. 2010, MNRAS, 405, 57
Tavani, M. 1998, ApJL, 497, L21
Toelge, K., Yu, H.-F., & Meegan, C. A. 2015, GCN, 18492
Woosley, S. E. 1993, ApJ, 405, 273
Woosley, S. E., Heger, A., & Weaver, T. A. 2002, RvMP, 74, 1015
Zel'dovich, Y. B., Ivanova, L. N., & Nadezhin, D. K. 1972, SvA, 16, 209

ISSN 1063-7729, Astronomy Reports, 2018, Vol. 62, No. 12, pp. 905–910. © Pleiades Publishing, Ltd., 2018.

Relativistic Behavior and Equitemporal Surfaces in Ultra-Relativistic Prompt Emission Phase of Gamma-Ray Bursts*♯

R. Moradi[1,2], R. Ruffini[1,2], C. L. Bianco[1,2], Y.-C. Chen[1,2], M. Karlica[1,2], J. D. Melon Fuksman[1,2], D. Primorac[1,2], J. A. Rueda[1,2], S. Shakeri[3], Y. Wang[1,2], and S. S. Xue[1,2]**

[1] *ICRANet, Pescara, Italy*

[2] *ICRA and University of Rome "Sapienza", Physics Department, Rome, Italy*

[3] *School of Astronomy, Institute for Research in Fundamental Sciences (IPM), Tehran, Iran*

Received August 1, 2018; in final form, August 25, 2018

Abstract—In this work we study a role of baryon load and interstellar medium density to explain the nature of peaks in the ultra-relativistic prompt emission (UPE) phase of Gamma-ray Bursts (GRBs). We study the behavior of their Γ Lorenz factor from the moment of transparency all the way up to interstellar medium. We finally study the characteristic of equitemporal surfaces in the UPE phase.

DOI: 10.1134/S1063772918120259

1. INTRODUCTION

After launch of Compton satellite and the observations by the BATSE, Gamma-Ray-Bursts (GRBs) were phenomenologically categorized into two groups: long GRBs with $T_{90} > 2$ s, and short GRBs with $T_{90} < 2$ s [1–5]. Long bursts are known to be connected with the regions in the host galaxies in which very bright stars are forming [6, 7]. Therefore, the idea of explaining the long GRBs with a core collapse of a single massive star to a black hole (BH) is developed [8–12].

Recently the possibility of multiple components in long GRB emissions has been discussed in [13, 14], indicating the presence of several astrophysical processes [15, 16], which has led to formulation of a sequence of non-causally related events in the Induced Gravitational Collapse (IGC) paradigm [17–20]. This paradigm presents the explicit role of binary systems as progenitors of the long GRBs which is in agreement with the fact that many collapsing objects are associated with multiple stars orbiting together, with the binary situation representing the most common ones [21].

The concept of IGC was introduced for explaining two sub-families of long GRBs associated with type Ic supernovae (SN) that we have called binary-driven hypernovae (BdHNe) ($E_{\rm iso} > 10^{52}$) and X-ray flashes ($E_{\rm iso} < 10^{52}$) [13]. Within this paradigm, a SN explosion and a GRB occur in the following time sequence taking place in a binary system composed of a carbon–oxygen (CO) core and a neutron star (NS) companion: (a) explosion of the CO core; (b) hypercritical accretion onto the NS ; (c) NS gravitational collapse to a black hole in BdHNe and massive neutron star (MNS) in XRFs; d) emission of the GRB.

The case of short duration GRBs following the observational and theoretical evidences [see, e.g., 22–24] is confirmed to be from NS–NS (or NS–BH) binaries.

In this paper we use IGC scenario to study the behavior of the ultra-relativistic prompt emission phase of BdHNe 151027A. In Section 1 the BdHNe model is briefly introduced then we discuss the role of thermal component in this model. In Section 2 we introduce the simple model to explain how double peak in the ultra-relativistic prompt emission phase are formed and how their Γ Lorentz factor will evolve in time. Finally, we present the conclusion.

---

*The article is published in the original.

**E-mail: r.moradi9@gmail.com

♯Paper presented at the Third Zeldovich meeting, an international conference in honor of Ya.B. Zeldovich held in Minsk, Belarus on April 23–27, 2018. Published by the recommendation of the special editors: S.Ya. Kilin, R. Ruffini, and G.V. Vereshchagin.

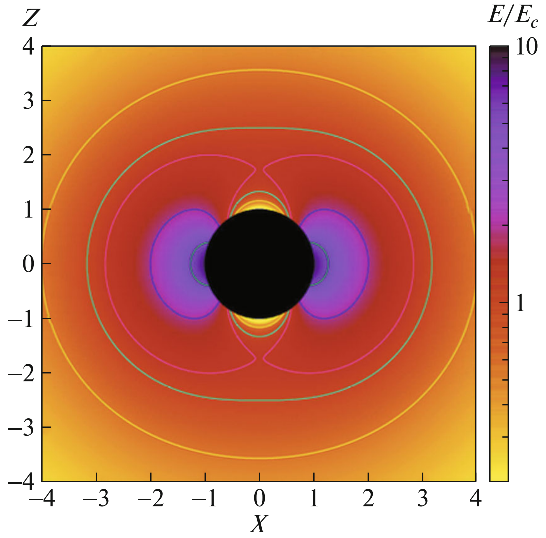

Fig. 1. The structure of overcritical field around the Kerr BH.

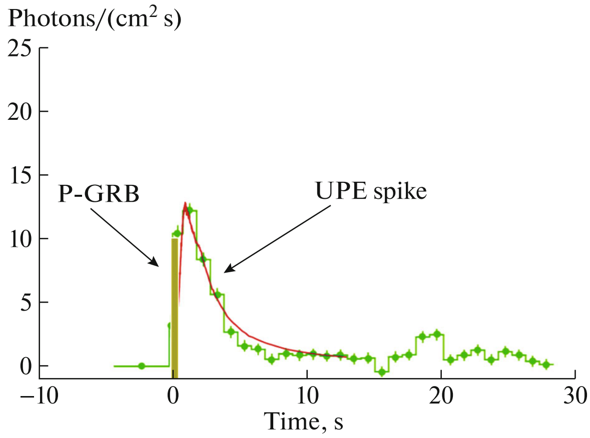

Fig. 2. Simulation of the P-GRB and spike structure in UPE phase for GRB 151027A. $kT_{\rm PGRB} = 36.6$ and $E_{\rm PGRB} = 5.3 \times 10^{50}$ erg. Data and plot are taken from [48].

2. FIRESHELL MODEL IN IGC SCENARIO

For explaining the GRB emission, considering relativistic magneto-hydrodynamical effects, quantum-electrodynamical process and relativistic space-time transformations is necessary. The fireshell scenario [see, e.g., 17, 25, 26] is introduced to model the GRB when a black hole is formed during the gravitational collapse [27].

Ruffini and Wilson [28] have studied for the first time the effect of magneto-hydrodynamics in the gravitational collapse of a neutral magnetized plasma into a Kerr BH. The separation of a local charge on the horizon, during a globally neutral accretion process, leads to the formation of an overcritical electric fields. Producing the overcritical fields in the accretion process and consequently creation of an e^+e^- plasma, have been explained in [27, 29] (see Fig. 1).

A sequence of physical and astrophysical events plays a crucial role in the GRB phenomenon:

(1) An optically thick fireshell of e^+e^- plasma of total energy $E^{\rm tot}_{e^+e^-}$. Its expansion and self-acceleration due to internal pressure has been described in [30]. Dynamics of the fireshell due to the effect of baryonic matter (the remnant of the collapsed object) has been considered in [31]. In the latter work authors have shown that even after the sweeping of a baryonic mass M_B, the fireshell remains optically thick and expands due to its self-acceleration up to ultra-relativistic velocities ($\Gamma \sim 500$ in the case of long GRBs) [32, 33].

(2) The transparency of the e^+e^- plasma. When the fireshell becomes transparent, a thermal radiation, proper-GRB (P-GRB) is emitted [30, 31]. The dynamics of the fireshell up to the transparency condition is fully described by $E^{\rm tot}_{e^+e^-}$ and B ($B = M_Bc^2/E^{\rm tot}_{e^+e^-}$): solutions with $B \leq 10^{-2}$ are characterized by regular relativistic expansion; for $B > 10^{-2}$ turbulence and instabilities occur [31], see Fig. 2.

(3) Sweeping cloud of interstellar medium (ISM) with e^+e^- plasma after transparency. The thermal P-GRB is followed by the prompt emission [25]. The prompt emission stem from collisions of baryons left over after transparency, with high Lorentz factor $\Gamma \approx 100-1000$, with ISM [34–36] (see Fig. 2). It has been shown that these interactions produce a quasi-blackbody spectrum in the co-moving frame [37]. The observed spectrum can be found by taking into account the role of constant arrival time effects in the EQuiTemporal Surfaces (EQTS) [38, 39]. As it is expected, the convolution of a large number of modified thermal spectra with different Lorentz factors and temperatures, therefore this spectrum is non-thermal.

In [37] it has been shown that to simulate the light curve and spectra of prompt emission, three additional parameters related to the properties of the circumbust medium (CBM) are needed: the CBM density profile $n_{\rm CBM}$, the filling factor $\mathcal{R}$ which represents the size of the effective emitting area, and a power-law index α of the modified black body spectrum. These parameters are obtained by running a trial-and-error simulation of the observed prompt emission light curves and spectra. In running procedure all the characteristic of the UPE phase must fit with data, namely, temperature, duration of burst, isotropic energy, spectrum, and light curve.

To obtain the dynamics of e^+e^--baryon-plasma from the BH magnetosphere at $\sim 10^6$ cm all the way up to $\sim 10^{17}$ cm, both in the P-GRB and the prompt emission, the relativistic formulation and spacetime transformations has been discussed in [26]. The equations and transformations relating to the comoving, laboratory, arrival time at the detector corrected by the cosmological redshift is given in [see also 38–41], where in the next section we summarize them. The evolution of a baryon-loaded pair plasma, is generally described in terms of $E^{\rm tot}_{e^+e^-}$ and B and it is independent of the way the pair plasma is created.

3. SIMULATION OF GRB 151027A IN UPE PHASE

GRB 151027A was detected and located by the *Swift* Burst Alert Telescope (BAT) [42]. It was also detected by the *Fermi* Gamma-ray Burst Monitor (GBM) [43], MAXI [44], and by *Konus*-Wind [45]. The *Swift* X-Ray Telescope (XRT) started its observation 87 s after the burst trigger [46]. The redshift of the source, measured through the MgII doublet in absorption from the Keck/HIRES spectrum, is $z = 0.81$ [47].

The rest-frame $1{-}10^4$ keV isotropic equivalent energies computed from the spectra of two spikes in UPE phase of GRB 151027A are $E_{\rm iso,1} = (7.26 \pm 0.36) \times 10^{51}$ erg and $E_{\rm iso,2} = (4.99 \pm 0.60) \times 10^{51}$ erg, respectively (see Fig. 3).

There are two spikes in UPE phase of GRB 151027A with corresponding time difference of arrival $\sim$15 s and unknown emitting time difference of ΔT_e [48], see Figs. 3 and 4.

For the explanation of the first spike we consider the e^+e^- plasma is expanding till reaching the transparency in which P-GRB happens. Then the e^+e^- plasma expands through the interstellar medium (ISM) and produces the first UPE peak.The second peak we consider is featureless and moves with very high Γ factor. In arrival time the time difference of the peak of two spikes is $\Delta T_a \simeq 15$ s (rest-frame time $\simeq$8 s).

Therefore, in the starting point the emitting time difference must be $\Delta T_e = (15 + \Delta t_1)$, in which Δt_1 is the delay time due to the decelerating e^+e^- from $R_1 = 1.92 \times 10^{13}$ cm to the radius of the first peak $R_2 = 4.7 \times 10^{15}$ cm (these values are obtained from the run-trial simulation from [48]). According to our simulation of the expanding e^+e^- plasma, after the emission of P-GRB, the e^+e^- plasma decelerates through the interstellar medium (ISM) of the average number density $n = (15.9 \pm 3.2)$ cm^{-3}. The Lorentz gamma factor decreases from $\Gamma = 503$ at $R = 1.92 \times 10^{13}$ cm to $\Gamma = 370$ at $R = 4.7 \times 10^{15}$ cm, which leads to the $\Delta t_1 = 0.373$ s.

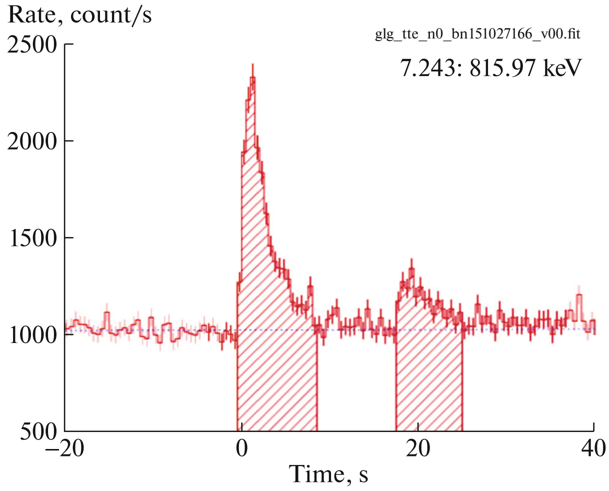

Fig. 3. Two spikes in UPE phase of GRB 151027A. Time difference of arrival is $\sim$15 s. Isotropic energy of the first spike is $E_{\rm iso,1} = (7.26 \pm 0.36) \times 10^{51}$ erg and the second one is $E_{\rm iso,2} = (4.99 \pm 0.60) \times 10^{51}$ erg. Data are retrieved from Fermi-GBM.

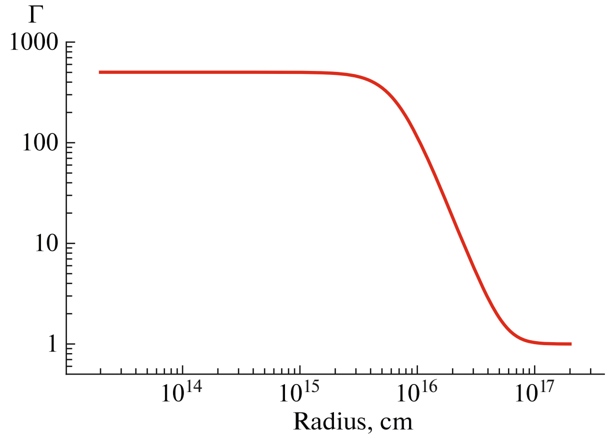

Fig. 4. Equitemporal surfaces in UPE phase of GRB 151027A, with arrival time $T_0 + 1$ and $T_0 + 10$, respectively (T_0 is Fermi trigger time).

4. ANALYTIC SOLUTION

When photon (or an object with ultraleratívistic motion, $\Gamma > 500$ in our case) and an object with velocity v start moving from the same position with time difference of ΔT_e, the difference of arrival time from R_1 to R_2 can be calculated as follows

$$\Delta T_a = \Delta T_e - \Delta t_1$$
$$= \Delta T_e - \left(\int_{R_1}^{R_2} \frac{dr}{v(r)} - \int_{R_1}^{R_2} \frac{dr}{c} \right). \qquad (1)$$

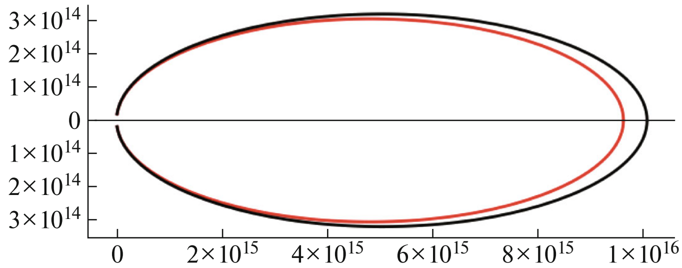

Fig. 5. The Lorentz gamma factor decreases from $\Gamma \simeq 500$ at $R \simeq 10^{13}$ cm to $\Gamma \simeq 1.0001$ at $R \simeq 10^{17}$ cm through the CBM.

If one considers the relativistic motion, the Lorentz gamma factor is

$$\Gamma = \frac{1}{\sqrt{1-\frac{v^2}{c^2}}}, \tag{2}$$

therefore,

$$\frac{1}{v} = \frac{1}{c\sqrt{1-\frac{1}{\Gamma^2}}}. \tag{3}$$

If $\Gamma = const$ and $\Gamma \gg 1$

$$\frac{1}{v} \simeq 1 + \frac{1}{2c\Gamma^2}, \tag{4}$$

therefore, the Eq. (1) reduces to

$$\Delta t_1 \simeq \frac{\Delta R}{2c\Gamma^2}, \tag{5}$$

if Γ is a function of r, i.e., $\Gamma = \Gamma(r)$,

$$\Delta t_1 = \int\limits_{R_1}^{R_2} \frac{dr}{c\sqrt{1-\frac{1}{\Gamma(r)^2}}} - \int\limits_{R_1}^{R_2} \frac{dr}{c}. \tag{6}$$

By having Γ as a function of r one can obtain the time difference of arrival. In this work we assume head-on emission, i.e., $\vartheta = 0$, where $\vartheta = \vartheta(r)$ corresponds to an arrival time t_a of the photons at the detector and represents an angle between the radial expansion velocity of a point on its surface and the line of sight:

$$c\Delta t_a = c\Delta t\,(r) - \Delta r \cos\vartheta. \tag{7}$$

A specific arrival time is related to emission from a surface which can be characterized by $\vartheta(r)$, for GRB 151027A this equitemporal surfaces are shown in Fig. 5.

4.1. Energy and Momentum Conservation

In order to determine Lorentz Γ factor, one needs to solve the set of energy and momentum conservation equations for a e^+e^--baryon plasma when it goes through the ISM is:

$$\begin{cases} dE_{\text{int}} = (\Gamma - 1)\, dM_{\text{ism}} c^2 \\ d\Gamma = -\frac{\Gamma^2-1}{M} dM_{\text{ism}} \\ dM = \frac{1-\varepsilon}{c^2} dE_{\text{int}} + dM_{\text{ism}} \\ dM_{\text{ism}} = 4\pi m_p n_{\text{ism}} r^2 dr, \end{cases} \tag{8}$$

Γ, E_{int}, and M are the pulse Lorentz gamma factor, internal energy, and mass-energy, respectively, n_{ism} is the ISM number density, m_p is the proton mass, ε is the emitted fraction of the energy developed in the collision with the ISM. M_{ism} is the amount of ISM mass swept up within the radius r.

Assuming the case of fully radiative regime one can have the analytic solution of $\Gamma(r)$ [29]:

$$\Gamma(r) = \frac{1 + (M_{\text{ism}}/M_B)\left(1+\Gamma_\circ^{-1}\right)[1 + (1/2)(M_{\text{ism}}/M_B)]}{\Gamma_\circ^{-1} + (M_{\text{ism}}/M_B)\left(1+\Gamma_\circ^{-1}\right)[1 + (1/2)(M_{\text{ism}}/M_B)]}, \tag{9}$$

where $\Gamma_\circ$ and M_B are, respectively, the values of the Lorentz gamma factor and of the mass of the accelerated baryons at the beginning of the afterglow phase. M_{ism} is the amount of ISM mass swept up within the radius r:

$$M_{\text{ism}} = m_p n_{\text{ism}} \frac{4\pi}{3}\left(r^3 - {R_1}^3\right), \tag{10}$$

where R_1 is the starting radius of the shock front which here we assume $R_1 = 1.92 \times 10^{13}$ cm (emission of P-GRB), n_{ism} is the ISM number density, m_p is the proton mass. The behavior of Γ in UPE phase of GRB 151027A is shown in Fig. 4.

The first UPE spikes happens at $R = 4.7 \times$

10^{15} cm with $\Gamma = 365$ which gives the $\Delta t_1 = 0.371$ s, which is very similar to the one directly calculated from the simulation. Therefore, the initial time difference of the two peaks is $\Delta t_a + 0.37 \simeq 15.37$ in which $\Delta t_a \simeq 15$ s is the observational time difference between two peaks. These spikes are believed to occur in the Kerr black hole in which rotation and evolving horizon of the BH play an important role [21, 49–51], this is the subject of upcoming works.

5. CONCLUSION

In this paper we have used the fireshell model to explain the propagation of e^+e^- plasma through the interstellar medium in GRB 151027A. Two spikes in GRB 151027A are from the same origin but emitting with time difference (when considering far enough from BH) of 15.4 s which in arrival time we measure this time difference as 15 s. Presenting a simple model we showed that our results are fully in agreement with relativistic formulations. We also showed that in order to decelerate such an ultra-relativistic plasma, which is endowed with baryon contamination, through the interstellar medium it must reaches the distance of order of $\sim 10^{17}$ cm which shows that the origin of early afterglow (corresponding to radius of order of $\sim 10^{12}$ cm) in GRB 151027A is different from UPE phase. We also studied the EQuiTemporal Surfaces in UPE phase of GRB 151027A which emit in different radius and time but arriving at the same time to the detector.

REFERENCES

1. E. P. Mazets, S. V. Golenetskii, V. N. Ilinskii, V. N. Panov, R. L. Aptekar, I. A. Gurian, M. P. Proskura, I. A. Sokolov, Z. I. Sokolova, and T. V. Kharitonova, Astrophys. Space Sci. **80**, 3 (1981).
2. J.-P. Dezalay, C. Barat, R. Talon, R. Syunyaev, O. Terekhov, and A. Kuznetsov, AIP Conf. Ser. **265**, 304 (1992).
3. R. W. Klebesadel, in *Gamma-Ray Bursts: Observations, Analyses and Theory,* Ed. by C. Ho, R. I. Epstein, and E. E. Fenimore (Cambridge Univ. Press, Cambridge, 1992), p. 161.
4. C. Kouveliotou, C. A. Meegan, G. J. Fishman, N. P. Bhat, M. S. Briggs, T. M. Koshut, W. S. Paciesas, and G. N. Pendleton, Astrophys. J. Lett. **413**, L101 (1993).
5. M. Tavani, Astrophys. J. Lett. **497**, L21 (1998), arXiv:astro-ph/9802192.
6. A. S. Fruchter, A. J. Levan, L. Strolger, P. M. Vreeswijk, S. E. Thorsett, D. Bersier, I. Burud, J. M. Castro Cerón, A. J. Castro-Tirado, C. Conselice, et al., Nature (London, U.K.) **441**, 463 (2006); arXiv:astro-ph/0603537.
7. K. M. Svensson, A. J. Levan, N. R. Tanvir, A. S. Fruchter, and L.-G. Strolger, Mon. Not. R. Astron. Soc. **405**, 57 (2010); arXiv:1001.5042.
8. S. E. Woosley, Astrophys. J. **405**, 273 (1993).
9. B. Paczyński, Astrophys. J. Lett. **494**, L45 (1998); astro-ph/9710086.
10. A. I. MacFadyen and S. E. Woosley, Astrophys. J. **524**, 262 (1999); astro-ph/9810274.
11. T. Piran, Rev. Mod. Phys. **76**, 1143 (2004); astro-ph/0405503.
12. O. Bromberg, E. Nakar, T. Piran, and R. Sari, Astrophys. J. **764**, 179 (2013); 1210.0068.
13. R. Ruffini, J. A. Rueda, M. Muccino, Y. Aimuratov, L. M. Becerra, C. L. Bianco, M. Kovacevic, R. Moradi, F. G. Oliveira, G. B. Pisani, et al., Astrophys. J. **832**, 136 (2016); arXiv:1602.02732.
14. R. Ruffini, Y. Wang, Y. Aimuratov, U. Barres de Almeida, L. Becerra, C. L. Bianco, Y. C. Chen, M. Karlica, M. Kovacevic, L. Li, et al., Astrophys. J. **852**, 53 (2018); arXiv:1704.03821.
15. L. Izzo, R. Ruffini, A. V. Penacchioni, C. L. Bianco, L. Caito, S. K. Chakrabarti, J. A. Rueda, A. Nandi, and B. Patricelli, Astron. Astrophys. **543**, A10 (2012); arXiv:1202.4374.
16. A. V. Penacchioni, R. Ruffini, L. Izzo, M. Muccino, C. L. Bianco, L. Caito, B. Patricelli, and L. Amati, Astron. Astrophys. **538**, A58 (2012); arXiv:1112.2970.
17. R. Ruffini, C. L. Bianco, F. Fraschetti, S.-S. Xue, and P. Chardonnet, Astrophys. J. Lett. **555**, L117 (2001); arXiv:astro-ph/0106534.
18. R. Ruffini, M. G. Bernardini, C. L. Bianco, L. Caito, P. Chardonnet, M. G. Dainotti, R. Fraschetti, R. Guida, G. Vereshchagin, and S. Xue, in ESA Specl. Publ. **622**, 561 (2007); arXiv: 0705.2456.
19. J. A. Rueda and R. Ruffini, Astrophys. J. Lett. **758**, L7 (2012); arXiv: 1206.1684.
20. C. L. Fryer, J. A. Rueda, and R. Ruffini, Astrophys. J. Lett. **793**, L36 (2014); arXiv: 1409.1473.
21. C. Cherubini, S. Filippi, A. Loppini, R. Moradi, R. Ruffini, Y. Wang, and S.-S. Xue, Phys. Rev. D **97**, 064038 (2018).
22. J. Goodman, Astrophys. J. Lett. **308**, L47 (1986).
23. B. Paczynski, Astrophys. J. Lett. **308**, L43 (1986).
24. R. Narayan, B. Paczynski, and T. Piran, Astrophys. J. Lett. **395**, L83 (1992); arXiv:astro-ph/9204001.
25. R. Ruffini, C. L. Bianco, F. Fraschetti, S.-S. Xue, and P. Chardonnet, Astrophys. J. Lett. **555**, L113 (2001); arXiv:astro-ph/0106532.
26. C. L. Bianco, R. Ruffini, and S.-S. Xue, Astron. Astrophys. **368**, 377 (2001); astro-ph/0102060.
27. T. Damour and R. Ruffini, Phys. Rev. Lett. **35**, 463 (1975).
28. R. Ruffini and J. R. Wilson, Phys. Rev. D **12**, 2959 (1975).
29. C. Cherubini, A. Geralico, H. J. A. Rueda, and R. Ruffini, Phys. Rev. D **79**, 124002 (2009); arXiv: 0905.3274.
30. R. Ruffini, Astron. Astrophys. **138**, 513 (1999); arXiv: astro-ph/9905072.
31. R. Ruffini, J. D. Salmonson, J. R. Wilson, and S. Xue, Astron. Astrophys. **359**, 855 (2000); arXiv:astro-ph/0004257.

32. A. G. Aksenov, R. Ruffini, and G. V. Vereshchagin, Phys. Rev. Lett. **99**, 125003 (2007); arXiv: 0707.3250.
33. A. G. Aksenov, R. Ruffini, and G. V. Vereshchagin, Phys. Rev. D **79**, 043008 (2009); arXiv: 0901.4837.
34. R. Ruffini, C. L. Bianco, P. Chardonnet, F. Fraschetti, and S. Xue, Astrophys. J. Lett. **581**, L19 (2002); astro-ph/0210648.
35. R. Ruffini, C. L. Bianco, S.-S. Xue, P. Chardonnet, F. Fraschetti, and V. Gurzadyan, Int. J. Mod. Phys. D **13**, 843 (2004); arXiv: astro-ph/0405284.
36. R. Ruffini, M. G. Bernardini, C. L. Bianco, P. Chardonnet, F. Fraschetti, V. Gurzadyan, L. Vitagliano, and S.-S. Xue, in *Proceedings of the 11th Brazilian School of Cosmology and Gravitation,* Ed. by M. Novello and S. E. Perez Bergliaffa, AIP Conf. Proc. **782**, 42 (2005); arXiv: astro-ph/0503476.
37. B. Patricelli, M. G. Bernardini, C. L. Bianco, L. Caito, G. de Barros, L. Izzo, R. Ruffini, and G. V. Vereshchagin, Astrophys. J. **756**, 16 (2012); arXiv: 1206.5605.
38. C. L. Bianco and R. Ruffini, Astrophys. J. Lett. **633**, L13 (2005); astro-ph/0509621.
39. C. L. Bianco and R. Ruffini, Astrophys. J. Lett. **620**, L23 (2005); astro-ph/0501390.
40. C. L. Bianco and R. Ruffini, Astrophys. J. Lett. **605**, L1 (2004); astro-ph/0403379.
41. C. L. Bianco and R. Ruffini, Astrophys. J. Lett. **644**, L105 (2006); astro-ph/0605332.
42. A. Maselli, A. D'Ai, A. Y. Lien, D. M. Palmer, B. Sbarufatti, M. H. Siegel, M. Stamatikos, and T. N. Ukwatta, GRB Coord. Network, No. 18478 (2015).
43. K. Toelge, H.-F. Yu, and C. A. Meegan, GRB Coord. Network, No. 18492 (2015).
44. T. Masumitsu, H. Negoro, N. Kawai, T. Sakamoto, S. Ueno, H. Tomida, S. Nakahira, M. Kimura, M. Ishikawa, Y. E. Nakagawa, et al., GRB Coord. Network, Circ. Service, No. 18525, 1 (2015).
45. S. Golenetskii, R. Aptekar, D. Frederiks, V. Pal'shin, P. Oleynik, M. Ulanov, D. Svinkin, A. Tsvetkova, A. Lysenko, A. Kozlova, et al., GRB Coord. Network, No. 18516 (2015).
46. M. R. Goad, J. P. Osborne, A. P. Beardmore, and P. A. Evans, GRB Coord. Network, No. 18482 (2015).
47. D. A. Perley, L. Hillenbrand, and J. X. Prochaska, GRB Coord. Network, No. 18487 (2015).
48. R. Ruffini et al., arXiv: 1712.05001 (2017).
49. J. T. Firouzjaee and R. Mansouri, Gen. Rel. Grav. **42**, 2431 (2010); arXiv: 0812.5108.
50. R. Moradi, J. T. Firouzjaee, and R. Mansouri, Class. Quant. Grav. **32**, 215001 (2015); arXiv: 1504.04746.
51. R. Moradi, C. Stahl, J. Firouzjaee, and S.-S. Xue, Phys. Rev. D **96**, 104007 (2017); arXiv: 1705.04168.

ISSN 1063-7729, Astronomy Reports, 2018, Vol. 62, No. 12, pp. 933–939. © Pleiades Publishing, Ltd., 2018.

Structure of the Prompt Emission of GRB 151027A Within the Fireshell Model*♯

D. Primorac[1,2], M. Muccino[1,2], R. Moradi[1,2], Y. Wang[1,2], J. D. Melon Fuksman[1,2], R. Ruffini[1,2], C. L. Bianco[1,2], and J. A. Rueda[1,2]**

[1] *ICRANet, Pescara, Italy*

[2] *ICRA and University of Rome "Sapienza", Physics Department, Rome, Italy*

Received August 1, 2018; in final form, August 25, 2018

Abstract—Long gamma-ray burst GRB 151027A was observed by all three detectors onboard the *Swift* spacecraft, and many more, including MAXI, *Konus*-Wind and *Fermi* GBM/LAT instruments. This revealed a complex structure of the prompt and afterglow emission, consisting of a double-peak gamma-ray prompt with a quiescent period and a HRF/SXF within the X-ray afterglow, together with multiple BB components seen within the time-resolved spectral analysis. These features, within the fireshell model, are interpreted as the manifestation of the same physical process viewed at different angles with respect to the HN ejecta. Here we present the time-resolved and time-integrated spectral analysis used to determine the energy of the e^-e^+ plasma $E_{\rm tot}$ and the baryon load B. These quantities describe the dynamics of the fireshell up to the transparency point. We proceed with the light-curve simulation from which CBM density values and its inhomogeneities are deduced. We also investigate the properties of GRB 140206A, whose prompt emission exhibits a similar structure.

DOI: 10.1134/S1063772918120296

1. INTRODUCTION

Gamma-ray bursts (GRBs) are powerful explosions in distant galaxies, having isotropic equivalent energies $E_{\rm iso}$ ranging from 10^{49}–10^{54} erg. The duration of these transient sources in gamma-rays spans from ms up to a few minutes, with few GRBs lasting up to thousands of seconds (see, e.g., [1, 2]). The burst duration parameter T_{90} is measured as the time interval over which 90% of the total background-subtracted counts are observed, starting when the burst emits 5% of its total measured counts. Bimodality of the T_{90} distribution observed by CGRO/BATSE suggested that different emission mechanisms take place for the two observed distributions. The duration was found to be correlated to the hardness ratio for the entire set of the BATSE data, but not correlated at all for either of the two observed classes of GRBs. Since then, there has been a phenomenological classification of GRBs into long and short ones, with the separation at about 2 seconds [3]. The division was still present if one inquired into their rest frame properties, thanks to the X-ray and optical observations of the GRB afterglows (e.g., see [4]). Today it is generally accepted that the origin of the short GRBs are compact star binary merges [5, 6]. Long GRBs on the other hand are associated with the core-collapse of massive stars. This firm connection is based on the observed spectroscopic supernova (SN) signatures that emerge days later within the optical afterglow light-curve (see, e.g., [7]). GRB localization within their host galaxies further supports this division. Some nearby short GRBs are found in the early-type, low star formation rate galaxies or in the low star formation rate regions of the star-forming galaxies, with a large offset from the host. Long GRBs, on the contrary, are commonly found in the typically irregular galaxies with intense star formation. Thus, long GRBs became traditionally associated with the collapse of a single massive star to a black hole (BH) [8]. Here, the existence of a single ultra-relativistic collimated jet is assumed, where internal or external shocks have a role in the prompt phase emission (the *fireball model*, see, e.g., [9]). However, there are still doubts regarding the central engine (e.g., see [10] for the millisecond magnetar model, and [11] for energetic arguments).

*The article is published in the original.

**E-mail: daracparacldv@hotmail.com

♯Paper presented at the Third Zeldovich meeting, an international conference in honor of Ya.B. Zeldovich held in Minsk, Belarus on April 23–27, 2018. Published by the recommendation of the special editors: S.Ya. Kilin, R. Ruffini, and G.V. Vereshchagin.

Although the existence of the two classes is by now well established, GRB classification based solely on T_{90} may not be sufficient. Firstly, there is a large overlap in the two duration distributions (e.g., [12]). Furthermore, Zhao et al. [13] showed that T_{50} distribution is still bimodal, but with ≈3% of GRBs exchanging classes, where short GRBs are becoming the long ones and vice versa. While for the short GRBs this is due to the boundary effect, the long ones mostly have an unsuitably fitted background. These ones also have the hardness ratio closer to the short bursts. Ideally, the GRB classification method should be free from the potential biases introduced by data analysis, detector sensitivity, redshift measurements and many more. Often that is not the case and prompt emission quantites are very sensitive to the instrument's detection threshold [14]. For example, due to the difference in the covered energy range and the sensitivity, long bursts observed by *Fermi* Gamma-ray Burst Monitor (GBM) have a much longer duration when observed with *Swift* Burst Alert Telescope (BAT) [15]. The opposite happens in the case of short GRBs. This can affect the derivation of the isotropic energy. Shahmoradi & Nemiroff [16] found that the ratio of the observed spectral peak energy $E_{\rm p}$ to the T_{90} is the least-biased GRB classification method into two classes. Others find that the ratio of isotropic gamma-ray energy ($E_{\rm iso}$) and the rest-frame peak spectral energy ($E_{\rm p,\,RF}$) is a more suited parameter to distinguish between the Type I and the Type II GRBs, where TypeI/II is a new, physically motivated classification scheme based on origin [17]. Hints of a third peak within the T_{90} distribution were reported in various papers, suggesting a separate, intermediate class of GRBs. Still, finding out that additional parameters added to a nested model result in a better fit does not mean that the improvement is statistically significant (see, e.g., [18]). In addition to this intermediate class, it was proposed that ultra-long GRBs, lasting for hours, may form a distinct population with a blue supergiant as its progenitor (see, e.g., [19]). Also, there is an open question regarding the X-ray afterglow and whether it should, based on its connection to the central engine, be included in the prompt duration and isotropic energy calculation [20]. In that case, the duration distribution of GRBs should be recalculated. Therefore, there is still an ongoing discussion in the scientific community regarding the GRB classification and its central engine.

In this work, we analyze GRB 151027A prompt emission phase within the Induced Gravitational Collapse (IGC) paradigm. In contrast to the standard fireball/collapsar model, the IGC approach takes into account that SNe Ib/c, associated with long GRBs, mostly occur in double systems [21]. It investigates the impact of the SNe remnant and its role in the prompt emission formation. The starting point of the IGC scenario is a binary system composed of a neutron star (NS) and a carbon–oxygen (CO) core undergoing a SN explosion. From here, a well-determined time sequence is implied, with each stage having distinctive observational properties. This approach then also addresses the multiple components often found with the time-resolved analysis of long GRBs.

After the SN explosion, hypercritical accretion onto a NS takes place thanks to a very efficient neutrino emission, which acts as the main energy sink [22]. A thermal emission often observed in the early seconds of some long GRBs [23] is here interpreted as the soft X-ray emission occurring in the photosphere of the convective outflows (see, e.g., [24]). This will trigger the NS to collapse to a BH, if the accretion rate is high enough ($\gtrsim 10^{-2}$–$10^{-1} M_\odot$ s^{-1}). If the accretion effectiveness is under $10^{-2} M_\odot$ s^{-1}, the NS will only gain mass. The accretion rate is separation/period dependent, where the separation of $a > 10^{11}$ cm is expected to lead to the creation of a massive NS (MNS). GRBs generated in this fashion are expected to differ in properties. A MNS scenario is expected to produce less energetic GRBs ($\lesssim 10^{52}$ erg), so-called X-ray flashes (XRFs) . On the other hand, interactions of more tightly bound systems that result in the BH creation produce more energetic GRBs ($\gtrsim 10^{52}$ erg) [25], having a distinct afterglow decay [26] and a possible high energy GeV emission associated with the BH formation. Although, the detection of the latter should depend on the inclination of the viewing angle [27]. We address this subclass as binary-driven hypernovae (BdHNe).

In the BdHNe case scenario, optically thick e^+e^- plasma of energy $E^{\rm tot}$ is formed (*the fireshell*). It self-accelerates due to the e^+e^- annihilation, similar as in the fireball model [9]. Upon reaching transparency, a second thermal emission (the P-GRB) can be observed with high Lorentz factor of $\Gamma \sim 10^2$–10^3, in contrast to the previous thermal emission which is almost Newtonian. A shell of baryons, now optically thin, collides with the circumburst medium (CBM), giving rise to the ultra-relativistic prompt emission (UPE). However, this is true only for a small cone opening of ≈10°, defined by the remnant morphology [28]. The system is dynamical. Because of its rotation (∼300 s period), viewing angle with respect to the SN remnant changes. Other areas have much higher particle density due to the remnant. This gives rise to the hard (HXF) and soft (SXF) X-ray flares and the associated, final, extended thermal emission (ETE), which analysis confirms the mildly-relativistic

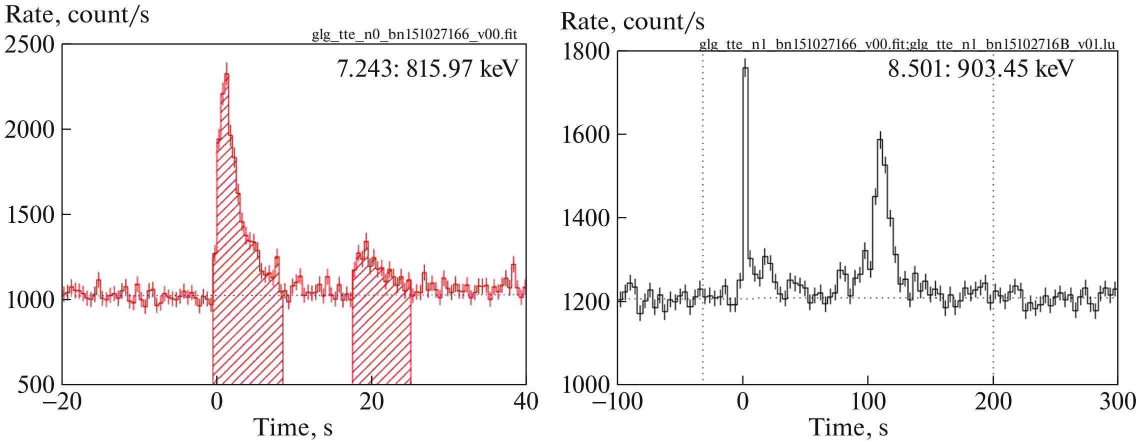

Fig. 1. GRB 151027A GBM-NaI (8–900 keV) light-curve. Two peaks of the UPE phase analyzed in this work are shown on the left, with ≈17 s separation. The entire observed gamma-ray emission is showed on the right, with the HXF starting at 94 s.

regime of this episode. Relativistic treatment shows that the ETE identifies the SN to hypernova (HN) transition. Therefore, these events do not form a causally connected sequence. For more detailed description of each stage, relativistic treatment, numerical simulation results and the comparison between the expected and the obtained properties of such systems, see the recent reviews [25, 29] and references within.

GRB 151027A was detected by multiple observatories and has a vast number of follow-up observations. Thus, it is a good candidate for applying the BdHNe approach, considering the models dependence on the time-resolved and multi-wavelength analysis. As said, here we concentrate on the multiple components in the UPE phase. We perform a P-GRB search through the time-resolved analysis and use simulation of the e^+e^- plasma propagation in order to determine the Lorentz factor and CBM density associated with the UPE. We also investigate the similarities between GRB 151027A and GRB 140206A.

2. TIME-INTEGRATED AND TIME-RESOLVED ANALYSIS OF *FERMI*/GBM DATA

At 3:58:24 UT, the *Swift*/BAT triggered and located GRB 151027A (GCN 18478). The observed light-curve shows two main episodes separated by a quiescent period. The estimated T_{90} in the (15–350 keV) band was 130 seconds. Similar duration, although a bit shorter, was reported by *Konus*-Wind (GCN 18516) and *Fermi*/GBM (GCN 18492). Even though the *Fermi*/LAT (Large Area Telescope) boresight of the source was 10°, there was no detection of high energy photons, suggesting that the line of sight lies in the equatorial plane of the binary system. *Swift* X-ray telescope (XRT) began observing the field 87 s after the trigger, reporting a classiclal FPA light-curve. The first 25 seconds in gamma-rays correspond to the UPE phase in the BdHNe approach. The two peaks, about 8 s in duration (Fig. 1 on the left), are thought to be directly connected to the central engine activity. This activity is again visible later in X-rays, in the form of the HXF (Fig. 1 on the right) and the SXF.

The time-integrated and the time-resolved spectral analysis was performed using the software package RMFIT[1] (version 4.3.2). Both peaks in the UPE phase are best fitted by Compton, as reported by the *Fermi* team, with parameters for the first peak: $E_{\text{p, 1}} = 172.5(\pm 19.3)$ keV and $\alpha_1 = -1.296(\pm 0.056)$. Second peak parameters are similar, with $E_{\text{p, 2}} = 147.4(\pm 46.2)$ keV and $\alpha_2 = -1.356(\pm 0.162)$. We calculate isotropic energy using

$$E_{\text{iso}} = \frac{4\pi d_l^2}{(1+z)} S_{\text{bol}}, \tag{1}$$

where d_l^2 is the luminosity distance, $(1+z)$ is the correction factor for the cosmic time dilatation, and S_{bol} is the bolometric fluence in the $1/(1+z)$ keV to $10^4/(1+z)$ keV frame. We determine S_{bol} from a given detection band (E_{min}, E_{max}) using

$$S_{\text{bol}} = S_{\text{obs}} \frac{\int_{1/(1+z)}^{10^4/(1+z)} E\phi(E)dE}{\int_{E_{\text{min}}}^{E_{\text{max}}} E\phi(E)dE}. \tag{2}$$

[1] RMFIT for GBM and LAT analysis was developed by the GBM Team and is publicly available at fermi.gsfc.nasa.gov/ssc/data/analysis

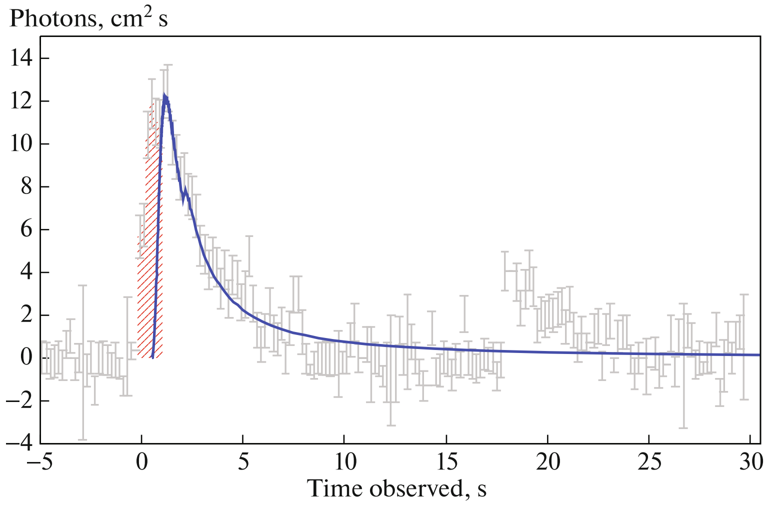

Fig. 2. The observed and the simulated light-curve for the $T_0 + 0.9 - T_0 + 9.44$ s interval of GRB 151027A. The dashed red area marks the P-GRB interval.

Here, ϕ is the Compton model obtained from the spectral fit and $S_{\mathrm{obs}} = \Delta t F_{\mathrm{obs}}$, where F_{obs} is the mean energy flux during the time interval Δt over which the spectral fit was derived. Considering the reported redshift of $z = 0.81$ (GCN 18487), isotropic energies of the two peaks are: $E_{\mathrm{iso,\,1}} = 7.26(\pm 0.36) \times 10^{51}$ and $E_{\mathrm{iso,\,2}} = 4.99(\pm 0.60) \times 10^{51}$.

Finally, we perform a time-resolved analysis on the two peaks. While the second peak appears to be featureless, we find an extra black body (BB) component in the first second of the first peak, superimposed on the previous Compton model. This corresponds to the P-GRB emission, when the e^+e^- plasma reaches the transparency point [30]. The best fit model for the $T - 0.1 - T_0 + 0.9$ s time interval was therefore a Compton+BB, with $kT = 36.6(\pm 5.2)$ keV and an energy $E_{\mathrm{BB}} = 0.074(\pm 0.038) E_{\mathrm{iso,\,1}}$.

3. LIGHT-CURVE AND SPECTRA SIMULATION

Having calculated $E_{\mathrm{iso,\,1}}$ and the P-GRB energy, we could proceed to simulate the UPE light-curve and spectra. This is done by solving the equations of the dynamics of the e^+e^- baryon plasma and its interaction with the CBM [31]. By doing this, we can evaluate the ultra-relativistic gamma factor of the UPE at the transparency point and the CBM distribution. Assuming that the initial e^+e^- energy E^{tot} is equal to $E_{\mathrm{iso,\,1}}$, for the observed P-GRB temperature we obtain the baryon load $B = 1.92(\pm 0.35) \times 10^{-3}$ and the transparency radius of $r_{\mathrm{tr}} = 1.92(\pm 0.17) \times 10^{13}$ cm with Lorenz factor $\Gamma_0 = 503(\pm 76)$. Fitting the UPE light-curve is done by varying the CBM density at different distances. In the IGC paradigm, it is assumed that this emission results from the interaction of the accelerated baryons with the CBM. Agreement with the observed light-curve ($T_0 + 0.9 - T_0 + 9.44$ s, see Fig. 2) and spectra (Fig. 3) was achieved for the average CBM density of $7.46(\pm 1.2)$ cm^{-3}. This is consistent with the typical value of the long GRB host galaxies 10^{16} cm at radii.

4. OBSERVATIONS OF GRB 140206A

Similar to GRB 151027A, GRB 140206A was observed by multiple detectors on various spacecrafts including *INTEGRAL* (GCN 15785), *Swift*/BAT (GCN 15784), and *Fermi*/GBM (GCN 15796). Redshift was reported to be $z = 2.73$ (GCN 15800). Unfortunately, *INTEGRAL* observations encountered technical difficulties. The detection time coincided with the very beginning of the *INTEGRAL* orbit, just outside the radiation belts, making the data polluted by a high particle background. *Fermi*/GBM didn't have more luck. Only the second peak of the GRB has been detected in the GBM data because, during the first peak, the source was occulted by Earth. Therefore, a joined BAT/GBM analysis is needed in the future in order to repeat the procedure as for GRB 151027A. The angle from the *Fermi* LAT boresight was 123 degrees, too far for a meaningful detection of high energy photons.

Nevertheless, BAT observed a multi-peaked structure with a duration of about 90 seconds (Fig. 4). The first pulse duration starts at $\sim T_0 - 15$ and ends at $\sim T_0 + 25$ seconds, and consists of roughly three to four peaks. The second one starts at $\sim T_0 + 50$

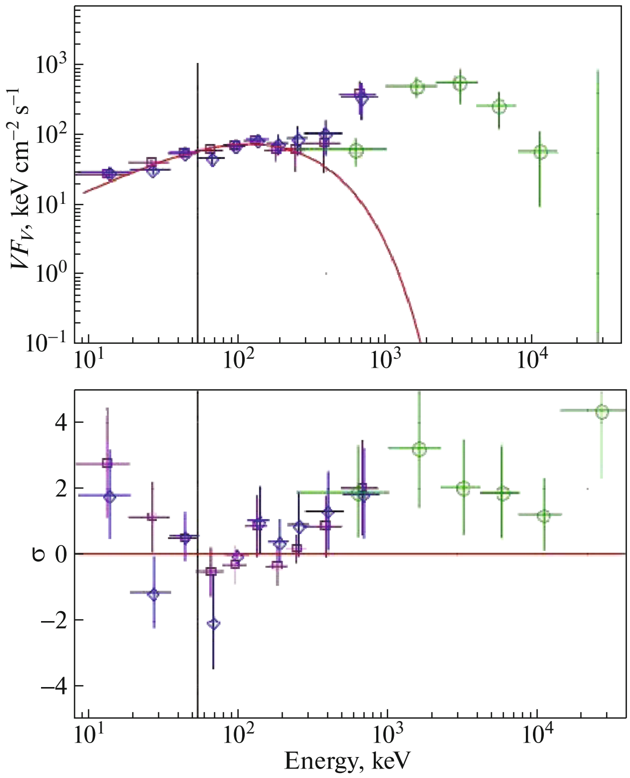

Fig. 3. Simulated spectra of GRB 151027A, superimposed to the observed *Fermi/GBM spectra*. The interval of the time-resolved analysis corresponds to the simulated UPE phase ($T_0 + 0.9 - T_0 + 9.44$ s). There is an agreement between the observed peak spectral energies, where $E_{\rm p,\,obs} = 122.8$ keV and $E_{\rm p,\,sim} = 121.9$ keV.

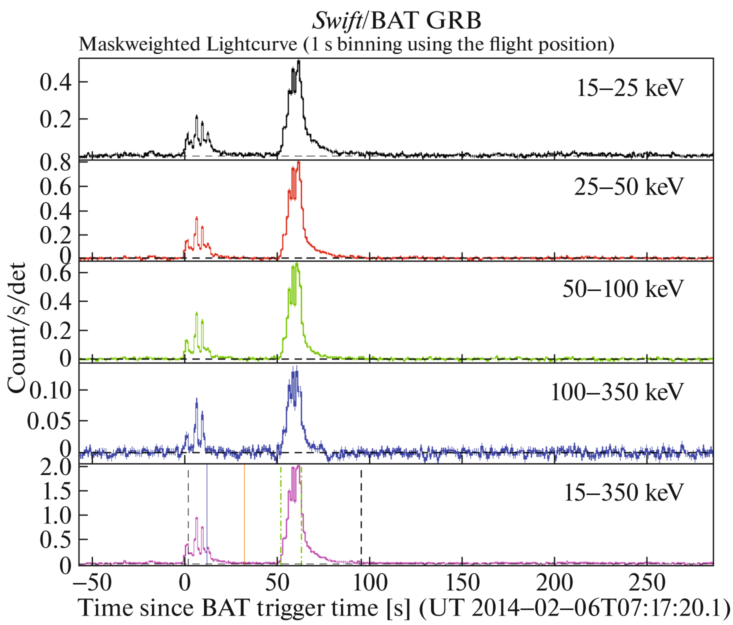

Fig. 4. *Swift*/BAT light-curve in different energy bands of GRB 140206A. Two pulses with the separation of ≈50 s are visible.

and ends at $\sim T_0 + 90$ seconds. There is also a third, weaker pulse peaking at $\sim T_0 + 210$ seconds.

XRT began observations 44 s after the BAT trigger. Light-curve has an initial flaring activity con-

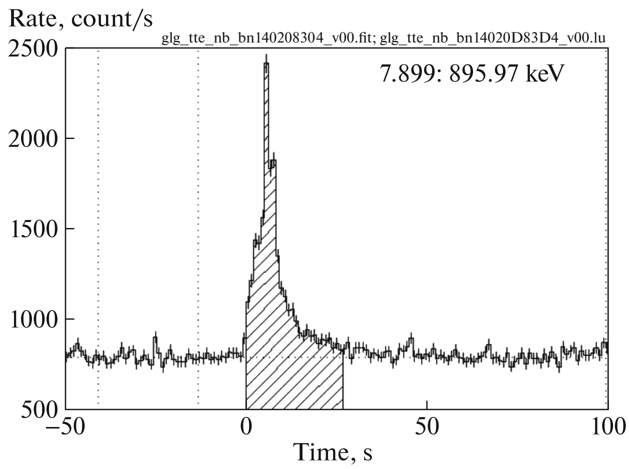

Fig. 5. GBM-NaI light-curve of GRB 140206A. Only second spike is visible. Time interval fitted on different models is showed dashed.

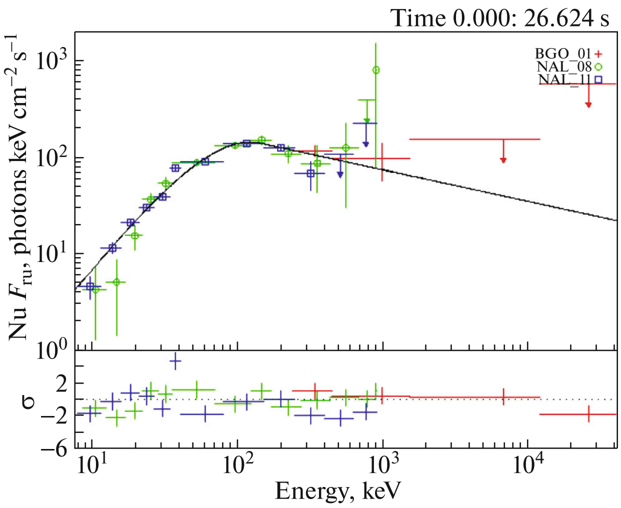

Fig. 6. Best fitted spectral model (Band) for the GRB 140206A T_{90} interval. See the text for parameter values.

sisting of two spikes at about 61 s and 223 s after the trigger. These flares coincide with the second and the third observed gamma-ray spike. This shows that the so-called classical prompt emission and the X-ray afterglow can't always be easily distinguished, and that redefining the duration and E_{iso} parameters should be considered.

A parallel can be drawn between GRB 140206A and GRB 151027A. The first, occulted spike should correspond to the double peak in GRB 151027A, making it an UPE phase of GRB 140206A. The second two peaks, also observed by XRT, should be regarded as the HXF and the SXF within thee BdHNe model. We decided to perform a time-resolved analysis on the second spike using RMFIT package (Fig. 5). We don't find a BB component. Additional analysis of the XRT data should be conducted to investigate the possibility of a thermal signature at lower energies. Band model was the best fitting one (Fig. 6), with $E_{\text{p}} = 123.4(\pm 6.42)$ keV, $\alpha = -0.075(\pm 0.097)$, and $\beta = -2.328(\pm 0.082)$. *Fermi* team reported similar analysis results (GCN 15796).

5. CONCLUSION AND FUTURE WORK

There is still an ongoing discussion regarding the GRB classification and the central engine activity that powers them. In the IGC paradigm, the different observational properties of long GRBs are a direct consequence of the initial binary system separation and the SN ejecta geometry. Based on the NS outcome state, they are divided into the XRF and the BdHNe, where the two are also separated by their energetics and X-ray afterglow light-curves. In this work we analyzed the GRB 151027A UPE phase and confirmed its ultra-relativistic nature, deriving the CBM density that surrounds the ejecta in the process. The UPE, the HXF, and the SXF are the result of the same physical process of the BH formation and they do not form a casually connected sequence. The time difference between the UPE double component and the flares observed in X-rays is then determined by the propagation of the e^+e^- plasma through the SN ejecta and the rotational period of the system.

ACKNOWLEDGMENTS

This work made use of data supplied by the UK Swift Science Data Center at the University of Leicester.

REFERENCES

1. G. Stratta, B. Gendre, J. L. Atteia, M. Boër, et al., Astrophys. J. **779**, 66 (2013); arXiv: 1306.1699.
2. V. Connaughton, Astrophys. J. **567**, 1028 (2002); astro-ph/0111564.
3. C. Kouveliotou, C. A. Meegan, G. J. Fishman, N. P. Bhat, M. S. Briggs, T. M. Koshut, W. S. Paciesas, and G. N. Pendleton, Astrophys. J. Lett. **413**, L101 (1993).
4. L. Amati, C. Guidorzi, F. Frontera, M. Della Valle, et al., Mon. Not. R. Astron. Soc. **391**, 577 (2008); arXiv: 0805.0377.
5. B. P. Abbott, R. Abbott, T. D. Abbott, F. Acernese, K. Ackley, C. Adams, T. Adams, P. Addesso, R. X. Adhikari, V. B. Adya, et al., Astrophys. J. Lett. **848**, L13 (2017); arXiv: 1710.05834.
6. A. Goldstein, P. Veres, E. Burns, M. S. Briggs, et al., Astrophys. J. Lett. **848**, L14 (2017); arXiv: 1710.05446.
7. M. Della Valle, Int. J. Mod. Phys. D **20**, 1745 (2011).
8. S. E. Woosley, Astrophys. J. **405**, 273 (1993).
9. T. Piran, Phys. Rep. **314**, 575 (1999); astro-ph/9810256.
10. H.-J. Lü and B. Zhang, Astrophys. J. **785**, 74 (2014); arXiv: 1401.1562.
11. A. Maselli, A. Melandri, L. Nava, C. G. Mundell, et al., Science (Washington, DC, U. S.) **343**, 48 (2014); arXiv: 1311.5254.
12. H.-J. Lü, E.-W. Liang, B.-B. Zhang, and B. Zhang, Astrophys. J. **725**, 1965 (2010); arXiv: 1001.0598.
13. X.-H. Zhao, Y.-P. Qin, Y.-M. Dong, and Z.-Y. Peng, Chin. J. Astron. Astrophys. **4**, 349 (2004).
14. N. R. Butler, J. S. Bloom, and D. Poznanski, Astrophys. J. **711**, 495 (2010); arXiv: 0910.3341.
15. F. J. Virgili, Y. Qin, B. Zhang, and E. Liang, Mon. Not. R. Astron. Soc. **424**, 2821 (2012); arXiv: 1112.4363.
16. A. Shahmoradi and R. J. Nemiroff, Mon. Not. R. Astron. Soc. **451**, 126 (2015); arXiv: 1412.5630.
17. B. Zhang, Nature (London, U.K.) **444**, 1010 (2006); astro-ph/0612614.
18. M. Tarnopolski, Astrophys. Space Sci. **361**, 125 (2016); arXiv: 1602.02363.
19. A. J. Levan, N. R. Tanvir, R. L. C. Starling, et al., Astrophys. J. **781**, 13 (2014); arXiv: 1302.2352.
20. G. Ghisellini, G. Ghirlanda, L. Nava, and C. Firmani, Astrophys. J. Lett. **658**, L75 (2007); astro-ph/0701430.
21. N. Smith, W. Li, A. V. Filippenko, and R. Chornock, Mon. Not. R. Astron. Soc. **412**, 1522 (2011); arXiv: 1006.3899.
22. Y. B. Zel'dovich, L. N. Ivanova, and D. K. Nadezhin, Sov. Astron. **16**, 209 (1972).
23. F. Ryde, Astrophys. J. **614**, 827 (2004); astro-ph/0406674.
24. C. L. Fryer, J. A. Rueda, and R. Ruffini, Astrophys. J. Lett. **793**, L36 (2014); arXiv: 1409.1473.
25. R. Ruffini, J. A. Rueda, M. Muccino, Y. Aimuratov, L. M. Becerra, C. L. Bianco, M. Kovacevic, R. Moradi, F. G. Oliveira, G. B. Pisani, et al., Astrophys. J. **832**, 136 (2016); arXiv: 1602.02732.
26. G. B. Pisani, L. Izzo, R. Ruffini, C. L. Bianco, M. Muccino, A. V. Penacchioni, J. A. Rueda, and Y. Wang, Astron. Astrophys. **552**, L5 (2013); arXiv: 1304.1764.
27. R. Ruffini, R. Moradi, Y. Wang, Y. Aimuratov, M. Amiri, L. Becerra, C. L. Bianco, Y.-C. Chen, B. Eslam Panah, G. J. Mathews, et al., arXiv: 1803.05476 (2018).
28. L. Becerra, C. L. Bianco, C. L. Fryer, J. A. Rueda, and R. Ruffini, Astrophys. J. **833**, 107 (2016); arXiv: 1606.02523.
29. R. Ruffini, Y. Wang, Y. Aimuratov, U. Barres de Almeida, et al., Astrophys. J. **852**, 53 (2018); arXiv: 1704.03821.
30. R. Ruffini, Astron. and Astrophys. Suppl. **138**, 513 (1999); astro-ph/9905072.
31. R. Ruffini, J. D. Salmonson, J. R. Wilson, and S.-S. Xue, Astron. Astrophys. **350**, 334 (1999); astro-ph/9907030.

EPJ Web of Conferences **168**, 01006 (2018) https://doi.org/10.1051/epjconf/201816801006
Joint International Conference of ICGAC-XIII and IK-15 on Gravitation, Astrophysics and Cosmology

The binary progenitors of short and long GRBs and their gravitational-wave emission

J. A. Rueda[1,2,3,⋆], *R.* Ruffini[1,2,3,4], *J. F.* Rodriguez[1,2], *M.* Muccino[1,2], *Y.* Aimuratov[1,2], *U.* Barres de Almeida[3], *L.* Becerra[1,2], *C. L.* Bianco[1,2], *C.* Cherubini[5,6], *S.* Filippi[5,6], *M.* Kovacevic[1,2], *R.* Moradi[1,2], *G. B.* Pisani[1,2], and *Y.* Wang[1,2]

[1] *Dipartimento di Fisica and ICRA, Sapienza Università di Roma, P.le Aldo Moro 5, I–00185 Rome, Italy*
[2] *ICRANet, P.zza della Repubblica 10, I–65122 Pescara, Italy*
[3] *ICRANet-Rio, Centro Brasileiro de Pesquisas Físicas, Rua Dr. Xavier Sigaud 150, 22290–180 Rio de Janeiro, Brazil*
[4] *Université de Nice Sophia Antipolis, CEDEX 2, Grand Château Parc Valrose, Nice,*
[5] *Unit of Nonlinear Physics and Mathematical Modeling, Università Campus Bio-Medico di Roma, Via A. del Portillo 21, I–00128 Rome, Italy*
[6] *ICRA, Università Campus Bio-Medico di Roma, Via A. del Portillo 21, I–00128 Rome, Italy*

Abstract. We have sub-classified short and long-duration gamma-ray bursts (GRBs) into seven families according to the binary nature of their progenitors. Short GRBs are produced in mergers of neutron-star binaries (NS-NS) or neutron star-black hole binaries (NS-BH). Long GRBs are produced via the induced gravitational collapse (IGC) scenario occurring in a tight binary system composed of a carbon-oxygen core (CO_{core}) and a NS companion. The CO_{core} explodes as type Ic supernova (SN) leading to a hypercritical accretion process onto the NS: if the accretion is sufficiently high the NS reaches the critical mass and collapses forming a BH, otherwise a massive NS is formed. Therefore long GRBs can lead either to NS-BH or to NS-NS binaries depending on the entity of the accretion. We discuss for the above compact-object binaries: 1) the role of the NS structure and the nuclear equation of state; 2) the occurrence rates obtained from X and gamma-rays observations; 3) the predicted annual number of detections by the Advanced LIGO interferometer of their gravitational-wave emission.

1 Introduction

There has been a traditional phenomenological classification of gamma-ray bursts (GRBs) based on the observed prompt duration, T_{90}: long GRBs for $T_{90} > 2$ s and short GRBs for $T_{90} < 2$ s[1–5]. Progress has been made in the meantime in the understanding of the nature of both long and short GRBs leading to a physical, instead of empirical, classification of GRBs based on the progenitor systems [6–8].

⋆e-mail: jorge.rueda@icra.it

1.1 Long GRBs

In the case of long GRBs we stand on the induced gravitational collapse (IGC) scenario that introduces as their progenitors short-period binaries composed of a carbon-oxygen core (CO_{core}) with a NS companion [9–15]. The core-collapse of the CO_{core}, which forms a NS as central remnant (hereafter νNS), leads also to a SN explosion that triggers a massive, hypercritical accretion process onto the NS companion. The parameters of the *in-state*, i.e. of the CO_{core}-NS binary, lead to two sub-classes of long GRBs with corresponding *out-states* [6]:

- *X-ray flashes (XRFs).* Long bursts with $E_{\rm iso} \lesssim 10^{52}$ erg are produced by CO_{core}-NS binaries with relatively large binary separations ($a \gtrsim 10^{11}$ cm). The accretion rate of the SN ejecta onto the NS in these systems is not high enough to bring the NS mass to the critical value $M_{\rm crit}$, hence no BH is formed. The out-state of this GRB sub-class can be either a νNS-NS binary if the system keeps bound after the SN explosion, or two runaway NSs if the binary system is disrupted.
- *Binary driven hypernovae (BdHNe).* Long bursts with $E_{\rm iso} \gtrsim 10^{52}$ erg are instead produced by more compact CO_{core}-NS binaries ($a \lesssim 10^{11}$ cm, see e.g., Refs. [13, 15]). In this case the SN triggers a larger accretion rate onto the NS companion, e.g. $\gtrsim 10^{-2}$–10^{-1} $M_\odot$ s^{-1}, bringing the NS to its critical mass $M_{\rm crit}$,[11–13] namely to the point of gravitational collapse with consequent formation of a BH. Remarkably, in Ref. [14] it was recently shown that the large majority of BdHNe leads naturally to NS-BH binaries owing to the high compactness of the binary that avoids the disruption of it even in cases of very high mass loss exceeding 50% of the total mass of the initial CO_{core}-NS binary.

In addition, it exists the possibility of *BH-SNe*.[6] Long burst with $E_{\rm iso} \gtrsim 10^{54}$ erg occurring in close CO_{core}-BH binaries in which the hypercritical accretion produces, as *out-states*, a more massive BH and a νNS. These systems have been considered in Ref. [6] as a subset of the BdHNe but no specific example have been yet observationally identified.

1.2 Short GRBs

There is the consensus within the GRB community that the progenitors of short GRBs are mergers of NS-NS and/or NS-BH binaries (see, e.g., Refs. [16–19], and Ref. [20], for a recent review). Similarly to the case of long GRBs, in Ref. [6] short GRBs have been split into different sub-classes:

- *Short gamma-ray flashes (S-GRFs).* Short bursts with energies $E_{\rm iso} \lesssim 10^{52}$ erg, produced when the post-merger core do not surpass the NS critical mass $M_{\rm crit}$, hence there is no BH formation. Thus these systems left as byproduct a massive NS and possibly, due to the energy and angular momentum conservation, orbiting material in a disk-like structure or a low-mass binary companion.
- *Authentic short gamma-ray bursts (S-GRBs).* Short bursts with $E_{\rm iso} \gtrsim 10^{52}$ erg, produced when the post-merger core reaches or overcome $M_{\rm crit}$, hence forming a Kerr or Kerr-Newman BH,[8] and also in this case possibly orbiting material.
- *Ultra-short GRBs (U-GRBs).* A new sub-class of short bursts originating from νNS-BH merging binaries. They can originate from BdHNe (see Ref. [14]) or from BH-SNe.

In addition, it exists the possibility of *gamma-ray flashes (GRFs).* These are bursts with hybrid properties between short and long, they have $10^{51} \lesssim E_{\rm iso} \lesssim 10^{52}$ erg. This sub-class of sources originates in NS-WD mergers.[6]

We focus here on the physical properties of the above progenitors, as well as on the main properties of NSs that play a relevant role in the dynamics of these systems and that lead to the above different GRB sub-classes. We shall discuss as well recent estimates of the rates of occurrence on all the above subclasses based on X and gamma-ray observations, and also elaborate on the possibility of detecting the gravitational wave (GW) emission originated in these systems.

2 IGC, Hypercritical Accretion, and Long GRBs

We turn now to the details of the accretion process within the IGC scenario. Realistic simulations of the IGC process were performed in Ref. [12], including: 1) detailed SN explosions of the CO_{core}; 2) the hydrodynamic details of the hypercritical accretion process; 3) the evolution of the SN ejecta material entering the Bondi-Hoyle region all the way up to its incorporation into the NS. Here the concept of hypercritical accretion refers to the fact the accretion rates are highly super-Eddington. The accretion process in the IGC scenario is allowed to exceed the Eddington limit mainly for two reasons: i) the photons are trapped within the infalling material impeding them to transfer momentum; ii) the accreting material creates a very hot NS atmosphere ($T \sim 10^{10}$ K) that triggers a very efficient neutrino emission which become the main energy sink of these systems unlike photons.

The hypercritical accretion process in the above simulations was computed within a spherically symmetric approximation. A further step was given in Ref. [13] by estimating the angular momentum that the SN ejecta carries and transfer to the NS via accretion, and how it affects the evolution and fate of the system. The calculations are as follows: first the accretion rate onto the NS is computed adopting an homologous expansion of the SN ejecta and introducing the pre-SN density profile of the CO_{core} envelope from numerical simulations. Then, it is estimated the angular momentum that the SN material might transfer to the NS: it comes out that the ejecta have enough angular momentum to circularize for a short time and form a disc around the NS. Finally, the evolution of the NS central density and rotation angular velocity (spin-up) is followed computing the equilibrium configurations from the numerical solution of the axisymmetric Einstein equations in full rotation, until the critical point of collapse of the NS to a BH taking into due account the equilibrium limits given by mass-shedding and the secular axisymmetric instability.

Now we enter into the details of each of the above steps. The accretion rate of the SN ejecta onto the NS can be estimated via the Bondi-Hoyle-Lyttleton accretion formula:

$$\dot{M}_B(t) = \pi \rho_{\rm ej} R_{\rm cap}^2 \sqrt{v_{\rm rel}^2 + c_{\rm s,ej}^2}, \qquad R_{\rm cap}(t) = \frac{2GM_{\rm NS}(t)}{v_{\rm rel}^2 + c_{\rm s,ej}^2}, \tag{1}$$

where G is the gravitational constant, $\rho_{\rm ej}$ and $c_{\rm s,ej}$ are the density and sound speed of the SN ejecta, $R_{\rm cap}$ is the NS gravitational capture radius (Bondi-Hoyle radius), $M_{\rm NS}$, the NS mass, and $v_{\rm rel}$ the ejecta velocity relative to the NS: $\vec{v}_{\rm rel} = \vec{v}_{\rm orb} - \vec{v}_{\rm ej}$, with $|\vec{v}_{\rm orb}| = \sqrt{G(M_{\rm core} + M_{\rm NS})/a}$, the module of the NS orbital velocity around the CO_{core}, and $\vec{v}_{\rm ej}$ the velocity of the supernova ejecta (see Fig. 1).

Extrapolating the results for the accretion process from stellar wind accretion in binary systems, the angular momentum per unit time that crosses the NS capture region can be approximated by:$\dot{L}_{\rm cap} = (\pi/2)\left(\epsilon_\rho/2 - 3\epsilon_v\right)\rho_{\rm ej}(a,t) v_{\rm rel}^2(a,t) R_{\rm cap}^4(a,t)$, where ϵ_ρ and ϵ_v are parameters measuring the inhomogeneity of the flow (see Ref. [13] for details).

In order to simulate the hypercritical accretion it is adopted an homologous expansion of the SN ejecta, i.e. the ejecta velocity evolves as $v_{\rm ej}(r,t) = nr/t$, where r is the position of every ejecta layer from the SN center and n is called expansion parameter. The ejecta density is given by $\rho_{\rm ej}(r,t) = \rho_{\rm ej}^0(r/R_{\rm star}(t), t_0)\frac{M_{\rm env}(t)}{M_{\rm env}(0)}\left(\frac{R_{\rm star}(0)}{R_{\rm star}(t)}\right)^3$, where $M_{\rm env}(t)$ the mass of the CO_{core} envelope, namely the mass of the ejected material in the SN explosion and available to be accreted by the NS, $R_{\rm star}(t)$ is the position of the outermost layer of the ejected material, and $\rho_{\rm ej}^0$ is the pre-SN density profile. The latter can be approximated with a power law: $\rho_{\rm ej}(r,t_0) = \rho_{\rm core}(R_{\rm core}/r)^m$, where $\rho_{\rm core}$, $R_{\rm core}$ and m are the profile parameters which are fixed by fitting the pre-SN profiles obtained from numerical simulations.

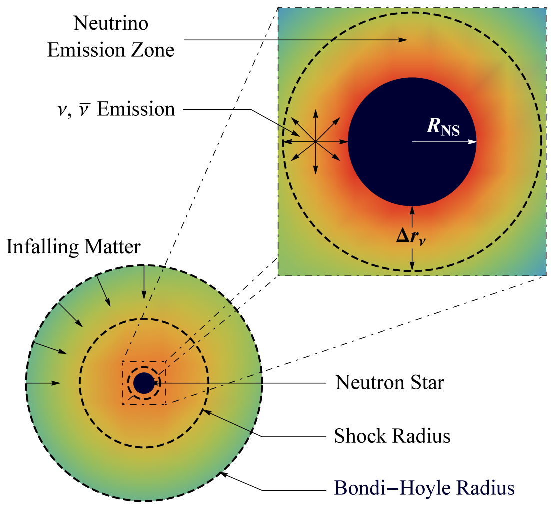

Figure 1. Scheme of the IGC scenario: the CO_{core} undergoes SN explosion, the NS accretes part of the SN ejecta and then reaches the critical mass for gravitational collapse to a BH, with consequent emission of a GRB. The SN ejecta reach the NS Bondi-Hoyle radius and fall toward the NS surface. The material shocks and decelerates as it piles over the NS surface. At the neutrino emission zone, neutrinos take away most of the infalling matter gravitational energy gain. The neutrinos are emitted above the NS surface in a region of thickness Δr_ν about half the NS radius that allow the material to reduce its entropy to be finally incorporated to the NS. The image is not to scale. For further details and numerical simulations of the above process see Refs. [12, 13, 15].

For the typical parameters of pre-SN CO_{core} and assuming a velocity of the outermost SN layer $v_{sn}(R_{star}, t_0) \sim 10^9$ cm s^{-1} and a free expansion $n = 1$ (for details of typical initial conditions of the binary system see Refs. [12] and [13]), Eq. (1) gives accretion rates around the order of $10^{-4} - 10^{-2} M_\odot$ s^{-1}, and an angular momentum per unit time crossing the capture region $\dot{L}_{cap} \sim 10^{46}$–$10^{49}$ g cm^2 s^{-2}.

We consider the NS companion of the CO_{core} initially as non-rotating, thus at the beginning the NS exterior spacetime is described by the Schwarzschild metric. The SN ejecta approach the NS with specific angular momentum, $l_{acc} = \dot{L}_{cap}/\dot{M}_B$, thus they will circularize at a radius r_{st} if they have enough angular momentum. What does the word "enough" means here? The last stable circular orbit (LSO) around a non-rotating NS is located at a distance $r_{lso} = 6GM_{NS}/c^2$ and has an angular momentum per unit mass $l_{lso} = 2\sqrt{3}GM_{NS}/c$. The radius r_{lso} is larger than the NS radius for masses larger than 1.67 $M_\odot$, 1.71 $M_\odot$, and 1.78 $M_\odot$ for the GM1, TM1, and NL3 nuclear equation of state (EOS).[13] If $l_{acc} \geq l_{lso}$ the material circularizes around the NS at locations $r_{st} \geq r_{lso}$. For the values of the IGC systems under discussion here, $r_{st}/r_{lso} \sim 10 - 10^3$, thus the SN ejecta have enough angular momentum to form a sort of disc around the NS. Even in this case, the viscous forces and other angular momentum losses that act on the disk will allow the matter in the disk to reach the inner boundary at $r_{in} \sim r_{lso}$, to then be accreted by the NS.

Within this picture, the NS accretes the material from r_{in} and the NS mass and angular angular momentum evolve as:

$$\dot{M}_{NS} = \left(\frac{\partial M_{NS}}{\partial M_b}\right)_{J_{NS}} \dot{M}_b + \left(\frac{\partial M_{NS}}{\partial J_{NS}}\right)_{M_b} \dot{J}_{NS}, \qquad \dot{J}_{NS} = \xi\, l(r_{in})\dot{M}_B, \tag{2}$$

where M_b is the NS baryonic mass, $l(r_{in})$ is the specific angular momentum of the accreted material at r_{in}, which corresponds to the angular momentum of the LSO, and $\xi \leq 1$ is a parameter that measures the efficiency of angular momentum transfer. We assume in our simulations $\dot{M}_b = \dot{M}_B$. The baryonic and gravitational mass are related by [21]:

$$\frac{M_b}{M_\odot} = \frac{M_{NS}}{M_\odot} + \frac{13}{200}\left(\frac{M_{NS}}{M_\odot}\right)^2 \left(1 - \frac{1}{137} j_{NS}^{1.7}\right), \tag{3}$$

where $j_{NS} \equiv cJ_{NS}/(GM_\odot^2)$. In addition, since the NS will spin up with accretion, we need information of the dependence of the specific angular momentum of the LSO as a function of both the NS mass

Table 1. Critical NS mass in the non-rotating case and constants k and p needed to compute the NS critical mass in the non-rotating case given by Eq. (5). The values are given for the NL3, GM1 and TM1 EOS.

EOS	$M_{\rm crit}^{J=0}$ $(M_\odot)$	p	k
NL3	2.81	1.68	0.006
GM1	2.39	1.69	0.011
TM1	2.20	1.61	0.017

and angular momentum. For corotating orbits the following relation is valid for all the aforementioned EOS:[13]

$$l_{\rm lso} = \frac{G M_{\rm NS}}{c}\left[2\sqrt{3} - 0.37\left(\frac{j_{\rm NS}}{M_{\rm NS}/M_\odot}\right)^{0.85}\right]. \tag{4}$$

The NS accretes mass until it reaches a region of instability. There are two main instability limits for rotating NSs: mass-shedding or Keplerian limit and the secular axisymmetric instability. The critical NS mass along the secular instability line is approximately given by:[21]

$$M_{\rm NS}^{\rm crit} = M_{\rm NS}^{J=0}(1 + k j_{\rm NS}^{p}), \tag{5}$$

where the parameters k and p depends of the nuclear EOS (see Table 1). These formulas fit the numerical results with a maximum error of 0.45%.

2.1 Most recent simulations of the IGC process

Additional details and improvements of the hypercritical accretion process leading to XRFs and BdHNe have been recently presented in Ref. [15]. In particular:

1. It was there improved the accretion rate estimate including the density profile finite size/thickness and additional $CO_{\rm core}$ progenitors leading to different SN ejecta masses were also considered.

2. It was shown in Ref. [13] the existence of a maximum orbital period, $P_{\rm max}$, over which the accretion onto NS companion is not high enough to bring it to the critical mass for gravitational collapse to a BH. Therefore, $CO_{\rm core}$-NS binaries with $P > P_{\rm max}$ lead to XRFs while the ones with $P \lesssim P_{\rm max}$ lead to BdHNe. In Ref. [15] the determination of $P_{\rm max}$ was extended to all the possible initial values of the mass of the NS companion and the angular momentum transfer efficiency parameter was also allowed to vary.

3. It was computed the expected luminosity during the hypercritical accretion process for a wide range of binary periods covering XRFs and BdHNe.

4. It was there shown that the presence of the NS companion originates large asymmetries (see, e.g., simulation in Fig. 2) in the SN ejecta leading to observable signatures in the X-rays.

Fig. 2 shows a simulation of an IGC process presented in Ref. [15]. We considered the effects of the gravitational field of the NS on the SN ejecta including the orbital motion as well as the changes in the NS gravitational mass owing to the accretion process via the Bondi formalism. The supernova matter was described as formed by point-like particles whose trajectory was computed by solving the Newtonian equation of motion. The initial conditions of the SN ejecta are computed assuming an homologous velocity distribution in free expansion. The initial power-law density profile of the CO

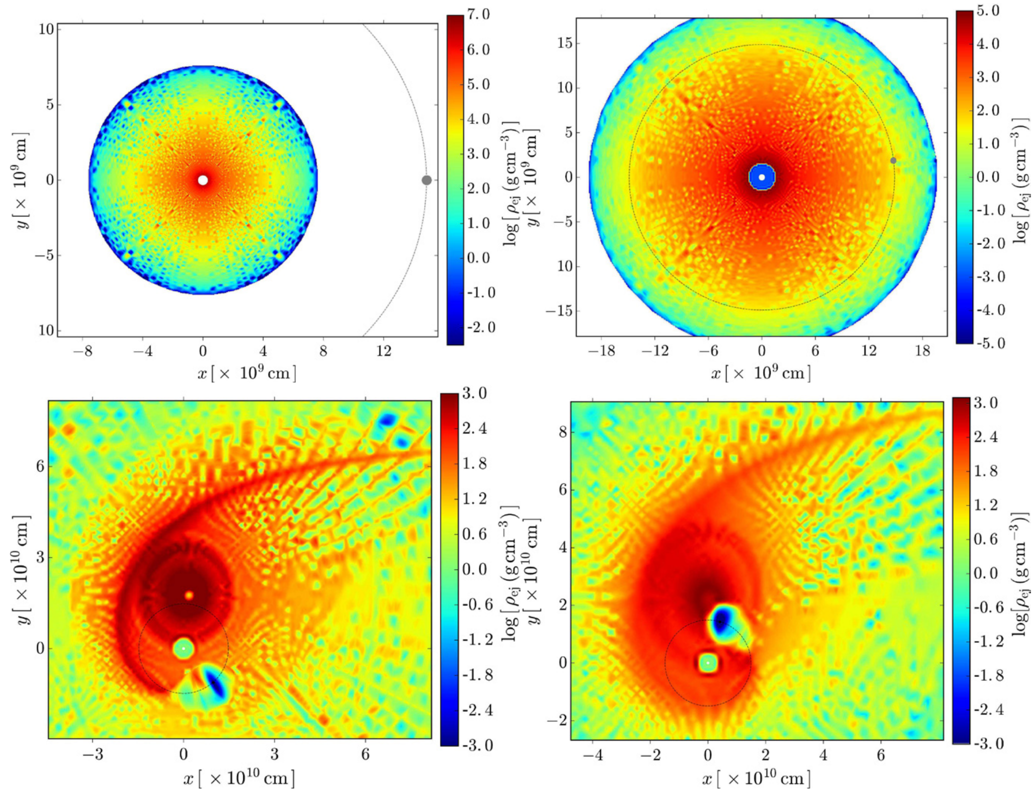

Figure 2. Hypercritical accretion process in the IGC binary system at selected evolution times. In this example the $CO_{\rm core}$ has a total mass of 9.44 $M_\odot$ divided in an ejecta mass of 7.94 $M_\odot$ and a νNS of 1.5 $M_\odot$ formed by the collapsed high density core. The supernova ejecta evolve homologously with outermost layer velocity $v_{0,\rm star} = 2 \times 10^9$ cm s^{-1}. The NS binary companion has an initial mass of 2.0 $M_\odot$. The binary period is $P \approx 5$ min, which corresponds to a binary separation $a \approx 1.5 \times 10^{10}$ cm. The system of coordinates is centered on the νNS represented by the white-filled circle at $(0, 0)$. The NS binary companion, represented by the gray-filled circle, orbits counterclockwise following the thin-dashed circular trajectory. The colorbar indicates values of ejecta density in logarithmic scale. *Left upper panel:* initial time of the process. The supernova ejecta expand radially outward and the NS binary companion is at $(a, 0)$. *Right upper panel:* the accretion process starts when the first supernova layers reach the Bondi-Hoyle region. This happens at $t = t_{\rm acc,0} \approx a/v_{0,\rm star} \approx 7.7$ s. *Left lower panel:* the NS binary companion reaches the critical mass by accreting matter from the SN with consequent collapse to a BH. This happens at $t = t_{\rm coll} \approx 254$ s $\approx 0.85\,P$. The newly-formed BH of mass $M_{\rm BH} = M_{\rm crit} \approx 3\,M_\odot$ is represented by the black-filled circle. It is here evident the asymmetry of the supernova ejecta induced by the presence of the accreting NS companion at close distance. *Right lower panel:* $t = t_{\rm coll} + 100$ s $= 354$ s $\approx 1.2P$, namely 100 s after the BH formation. It appears here the new binary system composed of the νNS and the newly-formed BH.

envelope is simulated by populating the inner layers with more particles. For the $M_{\rm ZAMS} = 30\,M_\odot$ progenitor which gives a $CO_{\rm core}$ with envelope profile $\rho^0_{\rm ej} \approx 3.1 \times 10^8 (8.3 \times 10^7/r)^{2.8}$ g cm^{-3}, we adopt for the simulation a total number of $N = 10^6$ particles. We assume that particles crossing the Bondi-Hoyle radius are captured and accreted by the NS so we removed them from the system as they reach that region. We removed these particles according to the results obtained from the numerical integration explained above. Fig. 2 shows the orbital plane of an IGC binary at selected times of its evolution. The NS has an initial mass of 2.0 $M_\odot$; the $CO_{\rm core}$ leads to a total ejecta mass 7.94 $M_\odot$ and a νNS of 1.5 $M_\odot$. The orbital period of the binary is $P \approx 5$ min, i.e. a binary separation $a \approx 1.5\times10^{10}$ cm. For these parameters the NS reaches the critical mass and collapses to form a BH.

2.2 Post-Explosion Orbits and Formation of NS-BH Binaries

We have seen how in BdHNe the accretion process can lead to BH formation in a time-interval as short as the orbital period. We here deepen this analysis to study the effect of the SN explosion in such a scenario following Ref. [14]. As the ejecta timescale becomes a fraction of the orbital one, the fate of the post-explosion binary is altered. For these models, we assumed tight binaries in circular orbit with an initial orbital separation of 7×10^9 cm. With $CO_{\rm core}$ radii of 1–4×10^9 cm, such a separation is small, but achievable. The binary consists of a $CO_{\rm core}$ and a 2.0 $M_\odot$ NS companion. When the $CO_{\rm core}$ collapses, it forms a 1.5 $M_\odot$ NS, ejecting the rest of the core. We then vary the ejecta mass and time required for most of the ejected matter to move out of the binary. Ref. [14] showed that even if 70% of the mass is lost from the system (in the 8 $M_\odot$ ejecta case), the system remains bound as long as the explosion time is just above the orbital time ($T_{\rm orbit} = 180$ s) with semi-major axes of less than 10^{11} cm.

The tight compact binaries produced in these explosions will emit GWs driving the system to merge. For typical massive star binaries, the merger time is many Myr. For BdHNe, the merger time is typically 10^4 yr, or less [14]. Since the merger should occur within the radius swept clean by the BdHN we expect a small baryonic contamination around the merger site which might lead to a new family of events which we term ultrashort GRBs, U-GRBs, to this new family of events.

3 NS-NS/NS-BH mergers and Short GRBs

Let us turn to short GRBs. We first proceed to estimate the mass and the angular momentum of the post-merger core via baryonic mass and angular momentum conservation of the system. We adopt for simplicity that non-rotating binary components. We first compute the total baryonic mass of the NS-NS binary $M_b = M_{b_1} + M_{b_2}$ using the relation between the gravitational mass M_i and the baryonic mass M_{b_i} ($i = 1, 2$) recently obtained in Ref. [21] and given in Eq. (3) assuming $j_{\rm NS} = cJ_{\rm NS}/(GM_\odot^2) = 0$. The post-merger core will have approximately the entire baryonic mass of the initial binary, i.e. $M_{b,\rm core} \approx M_b$, since little mass is expected to be ejected during the coalescence process. However, the gravitational mass of the post-merger core cannot be estimated using again the above formula since, even assuming non-rotating binary components, the post-merger core will necessarily acquire a fraction $\eta \leq 1$ of the binary angular momentum at the merger point. One expects a value of η smaller than unity since, during the coalesce, angular momentum is loss e.g. by gravitational wave emission and it can be also redistributed e.g. into a surrounding disk.

To obtain the gravitational mass of the post-merger core, we can use again Eq. (3) relating the baryonic mass $M_{b,\rm NS}$ and the gravitational mass $M_{\rm NS}$ in this case with $j_{\rm NS} \neq 0$. The mass and angular momentum of the post-merger core, respectively $M_{\rm core}$ and $J_{\rm core}$, are therefore obtained from baryon mass and angular momentum conservation, i.e.: $M_{\rm core} = M_{\rm NS}$, $M_{b,\rm core} = M_{b,\rm NS} = M_{b_1} + M_{b_2}$, $J_{\rm core} = J_{\rm NS} = \eta J_{\rm merger}$, where $J_{\rm merger}$ is the system angular momentum at the merger point. The value of $J_{\rm merger}$ is approximately given by $J_{\rm merger} = \mu r_{\rm merger}^2 \Omega_{\rm merger}$, where $\mu = M_1 M_2/M$ is the binary reduced mass, $M = M_1 + M_2$ is the total binary mass, and $r_{\rm merger}$ and $\Omega_{\rm merger}$ are the binary separation and angular velocity at the merger point. If we adopt the merger point where the two stars enter into contact we have $r_{\rm merger} = R_1 + R_2$, where R_i is the radius (which depend on the EOS) of the i-component of the binary.

Given the parameters of the merging binary, the above equations lead to the merged core properties. For the sake of exemplifying, let us assume a mass-symmetric binary, $M_1 = M_2 = M/2$. In this case the above equations lead to the angular momentum of the merged core $J_{\rm core} = (\eta/4)(GM^2/c)C^{-1/2}$, where $C \equiv GM_1/(c^2R_1) = GM_2/(c^2R_2)$ is the compactness of the merging binary components. Therefore, if we adopt $M_1 = 1.4\ M_\odot$ and $C = 0.15$, $M_{\rm core} = (2.61, 2.65)\ M_\odot$ for

$\eta = (0, 1)$, i.e. for a dimensionless angular momentum of the merged core $j_{\rm core} = (0, 5.06)$. Whether or not these pairs $(M_{\rm core}, j_{\rm core})$ correspond to stable NSs depend on the nuclear EOS. A similar analysis can be done for any other pair of binary masses.

4 Detectability of GWs produced by the GRB progenitors

Having established the nature of the progenitors of each GRB sub-class, we turn now to briefly discuss the detectability of their associated GW emission. The minimum GW frequency detectable by the broadband aLIGO interferometer is $f_{\rm min}^{\rm aLIGO} \approx 10$ Hz.[35] Since during the binary inspiral the GW frequency is twice the orbital one, this implies that a binary enters the aLIGO band for orbital periods $P_{\rm orb} \lesssim 0.2$ s. Thus, $CO_{\rm core}$-NS binaries, *in-states* of XRFs and BdHNe, and $CO_{\rm core}$-BH binaries, *in-states* of BH-SN, are not detectable by aLIGO since they have orbital periods $P_{\rm orb} \gtrsim 5$ min $\gg 0.2$ s. Concerning their *out-states* after the corresponding hypercritical accretion processes, namely νNS-NS, *out-states* of XRFs, and νNS-BH, *out-states* of BdHNe and BH-SNe, they are not detectable by aLIGO at their birth but only when approaching the merger. Clearly, the analysis of the νNS-NS mergers is included in the analysis of the S-GRFs and S-GRBs and, likewise, the merger of νNS-BH binaries is included in the analysis of U-GRBs. In the case of NS-WD binaries the WD is tidally disrupted by the NS making their GW emission hard to be detected (see, e.g., Ref. [36]).

A coalescing binary evolves first through the *inspiral regime* to then pass over a *merger regime*, the latter composed by the plunge leading to the merger itself and by the ringdown (oscillations) of the newly formed object. During the inspiral regime the system evolves through quasi-circular orbits and is well described by the traditional point-like quadrupole approximation.[37–39] The GW frequency is twice the orbital frequency ($f_s = 2f_{\rm orb}$) and grows monotonically. The energy spectrum during the inspiral regime is: $dE/df_s = (1/3)(\pi G)^{2/3} M_c^{5/3} f_s^{-1/3}$, where $M_c = \mu^{3/5} M^{2/5} = \nu^{3/5} M$ is the so-called *chirp mass* and $\nu \equiv \mu/M$ is the symmetric mass-ratio parameter. A symmetric binary ($m_1 = m_2$) corresponds to $\nu = 1/4$ and the test-particle limit is $\nu \to 0$. The GW spectrum of the merger regime is characterized by a GW burst.[40] Thus, one can estimate the contribution of this regime to the signal-to-noise ratio with the knowledge of the location of the GW burst in the frequency domain and of the energy content. The frequency range spanned by the GW burst is $\Delta f = f_{\rm qnm} - f_{\rm merger}$, where $f_{\rm merger}$ is the frequency at which the merger starts and $f_{\rm qnm}$ is the frequency of the ringing modes of the newly formed object after the merger, and the energy emitted is $\Delta E_{\rm merger}$. With these quantities defined, one can estimate the typical value of the merger regime spectrum as: $dE/df_s \approx \Delta E_{\rm merger}/\Delta f$. Unfortunately, the frequencies and energy content of the merger regime of the above merging binaries are such that it is undetectable by LIGO.[41].

Since the GW signal is deep inside the detector noise, the signal-to-noise ratio (ρ) is usually estimated using the matched filter technique.[42] The exact position of the binary relative to the detector and the orientation of the binary rotation plane are usually unknown, thus it is a common practice to average over all the possible locations and orientations, i.e.:[42] $\langle\rho^2\rangle = 4\int_0^\infty \langle|\tilde{h}(f)|^2\rangle/S_n(f)df = 4\int_0^\infty h_c^2(f)/[f^2 S_n(f)]df$, where f is the GW frequency in the detector frame, $\tilde{h}(f)$ is the Fourier transform of $h(t)$, and $\sqrt{S_n(f)}$ is the one-sided amplitude spectral density of the detector noise, and $h_c(f)$ is the characteristic strain, $h_c = (1+z)/(\pi d_l)\sqrt{(1/10)(G/c^3)(dE/df_s)}$. We recall that in the detector frame the GW frequency is redshifted by a factor $1+z$ with respect to the one in the source frame, f_s, i.e. $f = f_s/(1+z)$ and d_l is the luminosity distance to the source. We adopt a ΛCDM cosmology with $H_0 = 71$ km s^{-1} Mpc^{-1}, $\Omega_M = 0.27$ and $\Omega_\Lambda = 0.73$.[43]

A threshold $\rho_0 = 8$ in a single detector is adopted by LIGO.[44] This minimum ρ_0 defines a maximum detection distance or GW horizon distance, say $d_{\rm GW}$, that corresponds to the most optimistic case when the binary is just above the detector and the binary plane is parallel to the detector plane.

In order to give an estimate the annual number of merging binaries associated with the above GRB sub-classes detectable by aLIGO we can use the lower and upper values of the aLIGO *search volume* defined by $\mathcal{V}_s = V_{\rm max}^{\rm GW}\mathcal{T}$, where $V_{\rm max}^{\rm GW} = (4\pi/3)\mathcal{R}^3$, where $\mathcal{T}$ is the observing time and $\mathcal{R}$ is the so-called *detector range* defined by $\mathcal{R} = \mathcal{F}\, d_{\rm GW}$, with $\mathcal{F}^{-1} = 2.2627$ (see, Ref. [44, 45], for details). For a (1.4+1.4) $M_\odot$ NS binary and the three following different observational campaigns we have:[44] 2015/2016 (O1; $\mathcal{T}$ = 3 months) $\mathcal{V}_S$ = (0.5–4) $\times$ 10^5 Mpc^3 yr, 2017/2018 (O3; $\mathcal{T}$ = 9 months) $\mathcal{V}_S$ = (3–10)$\times 10^6$ Mpc^3 yr, and the entire network including LIGO-India at design sensitivity (2022+; $\mathcal{T}$ = 1 yr) $\mathcal{V}_S = 2 \times 10^7$ Mpc^3 yr. The maximum possible sensitivity reachable in 2022+ leads to $d_{\rm GW} \approx 0.2$ Gpc, hence $V_{\rm max}^{\rm GW} \approx 0.033$ Gpc^3, for such a binary. One can use this information for other binaries with different masses taking advantage of the fact that $d_{\rm GW}$ scales with the binary chirp mass as $M_c^{5/6}$. The expected GW detection rate by aLIGO can be thus estimated as: $\dot{N}_{\rm GW} \equiv \rho_{\rm GRB} V_{\rm max}^{\rm GRB}$, where $\rho_{\rm GRB}$ is the inferred occurrence rate of GRBs computed in Ref. [6]. Bearing the above in mind it is easy to check that there is a low probability for aLIGO to detect the GW signals associated with the GRB binary progenitors: indeed in the best case of the 2022+ observing rung one obtains, respectively, $\sim$ 1 detection every 3 and 5 yr for U-GRBs and S-GRFs.

References

[1] E.P. Mazets, S.V. Golenetskii, V.N. Ilinskii, V.N. Panov, R.L. Aptekar, I.A. Gurian, M.P. Proskura, I.A. Sokolov, Z.I. Sokolova, T.V. Kharitonova, Ap&SS**80**, 3 (1981)

[2] R.W. Klebesadel, *The durations of gamma-ray bursts*, in *Gamma-Ray Bursts - Observations, Analyses and Theories*, edited by C. Ho, R.I. Epstein, E.E. Fenimore (Cambridge University Press, 1992), pp. 161–168

[3] J.P. Dezalay, C. Barat, R. Talon, R. Syunyaev, O. Terekhov, A. Kuznetsov, *Short cosmic events - A subset of classical GRBs?*, in *American Institute of Physics Conference Series*, edited by W. S. Paciesas & G. J. Fishman (1992), Vol. 265 of *American Institute of Physics Conference Series*, pp. 304–309

[4] C. Kouveliotou, C.A. Meegan, G.J. Fishman, N.P. Bhat, M.S. Briggs, T.M. Koshut, W.S. Paciesas, G.N. Pendleton, ApJ**413**, L101 (1993)

[5] M. Tavani, ApJ**497**, L21 (1998), `arXiv:astro-ph/9802192`

[6] R. Ruffini, J.A. Rueda, M. Muccino, Y. Aimuratov, L.M. Becerra, C.L. Bianco, M. Kovacevic, R. Moradi, F.G. Oliveira, G.B. Pisani et al., ApJ**832**, 136 (2016), `1602.02732`

[7] R. Ruffini, Y. Wang, M. Enderli, M. Muccino, M. Kovacevic, C.L. Bianco, A.V. Penacchioni, G.B. Pisani, J.A. Rueda, ApJ**798**, 10 (2015), `1405.5723`

[8] R. Ruffini, M. Muccino, M. Kovacevic, F.G. Oliveira, J.A. Rueda, C.L. Bianco, M. Enderli, A.V. Penacchioni, G.B. Pisani, Y. Wang et al., ApJ**808**, 190 (2015), `1412.1018`

[9] R. Ruffini, M.G. Bernardini, C.L. Bianco, L. Vitagliano, S.S. Xue, P. Chardonnet, F. Fraschetti, V. Gurzadyan, *Black Hole Physics and Astrophysics: The GRB-Supernova Connection and URCA-1 - URCA-2*, in *The Tenth Marcel Grossmann Meeting*, edited by M. Novello, S. Perez Bergliaffa, R. Ruffini (Singapore: World Scientific, 2006), p. 369, `astro-ph/0503475`

[10] L. Izzo, J.A. Rueda, R. Ruffini, A&A**548**, L5 (2012), `1206.2887`

[11] J.A. Rueda, R. Ruffini, ApJ**758**, L7 (2012), `1206.1684`

[12] C.L. Fryer, J.A. Rueda, R. Ruffini, ApJ**793**, L36 (2014), `1409.1473`

[13] L. Becerra, F. Cipolletta, C.L. Fryer, J.A. Rueda, R. Ruffini, ApJ**812**, 100 (2015), `1505.07580`

[14] C.L. Fryer, F.G. Oliveira, J.A. Rueda, R. Ruffini, Physical Review Letters **115**, 231102 (2015), `1505.02809`

[15] L. Becerra, C.L. Bianco, C.L. Fryer, J.A. Rueda, R. Ruffini, ApJ**833**, 107 (2016), `1606.02523`

[16] J. Goodman, ApJ**308**, L47 (1986)
[17] B. Paczynski, ApJ**308**, L43 (1986)
[18] D. Eichler, M. Livio, T. Piran, D.N. Schramm, Nature**340**, 126 (1989)
[19] R. Narayan, T. Piran, A. Shemi, ApJ**379**, L17 (1991)
[20] E. Berger, ARAA**52**, 43 (2014), `1311.2603`
[21] F. Cipolletta, C. Cherubini, S. Filippi, J.A. Rueda, R. Ruffini, Phys. Rev. D**92**, 023007 (2015), `1506.05926`
[22] C.L. Fryer, W. Benz, M. Herant, ApJ**460**, 801 (1996), `astro-ph/9509144`
[23] R.A. Chevalier, ApJ**346**, 847 (1989)
[24] Y.B. Zel'dovich, L.N. Ivanova, D.K. Nadezhin, Soviet Astronomy **16**, 209 (1972)
[25] R. Ruffini, J. Wilson, Physical Review Letters **31**, 1362 (1973)
[26] C.L. Fryer, F. Herwig, A. Hungerford, F.X. Timmes, ApJ**646**, L131 (2006), `astro-ph/0606450`
[27] C.L. Fryer, ApJ**699**, 409 (2009), `0711.0551`
[28] L. Izzo, R. Ruffini, A.V. Penacchioni, C.L. Bianco, L. Caito, S.K. Chakrabarti, J.A. Rueda, A. Nandi, B. Patricelli, A&A**543**, A10 (2012)
[29] N.R. Tanvir, A.J. Levan, A.S. Fruchter, J. Hjorth, R.A. Hounsell, K. Wiersema, R.L. Tunnicliffe, Nature**500**, 547 (2013), `1306.4971`
[30] N.R. Sibgatullin, R.A. Sunyaev, Astronomy Letters **26**, 772 (2000), `astro-ph/0011344`
[31] C.L. Fryer, S.E. Woosley, D.H. Hartmann, ApJ**526**, 152 (1999), `astro-ph/9904122`
[32] M. Dominik, K. Belczynski, C. Fryer, D.E. Holz, E. Berti, T. Bulik, I. Mandel, R. O'Shaughnessy, ApJ**759**, 52 (2012), `1202.4901`
[33] K.A. Postnov, L.R. Yungelson, Living Reviews in Relativity **17**, 3 (2014), `1403.4754`
[34] J.G. Hills, ApJ**267**, 322 (1983)
[35] LIGO Scientific Collaboration, J. Aasi, B.P. Abbott, R. Abbott, T. Abbott, M.R. Abernathy, K. Ackley, C. Adams, T. Adams, P. Addesso et al., Classical and Quantum Gravity **32**, 074001 (2015), `1411.4547`
[36] V. Paschalidis, M. MacLeod, T.W. Baumgarte, S.L. Shapiro, Phys. Rev. D**80**, 024006 (2009)
[37] P.C. Peters, J. Mathews, Phys. Rev. **131**, 435 (1963)
[38] P.C. Peters, Phys. Rev. **136**, 1224 (1964)
[39] M. Rees, R. Ruffini, J.A. Wheeler, *Black holes, gravitational waves and cosmology* (Gordon and Breach Science Publishers Inc., New York, 1974)
[40] M. Davis, R. Ruffini, W.H. Press, R.H. Price, Phys. Rev. Lett. **27**, 1466 (1971)
[41] R. Ruffini, J. Rodriguez, M. Muccino, J.A. Rueda, Y. Aimuratov, U. Barres de Almeida, L. Becerra, C.L. Bianco, C. Cherubini, S. Filippi et al., ArXiv:1602.03545 (2016), `1602.03545`
[42] É.É. Flanagan, S.A. Hughes, Phys. Rev. D**57**, 4535 (1998), `gr-qc/9701039`
[43] M. Rigault, G. Aldering, M. Kowalski, Y. Copin, P. Antilogus, C. Aragon, S. Bailey, C. Baltay, D. Baugh, S. Bongard et al., ApJ**802**, 20 (2015), `1412.6501`
[44] B.P. Abbott, R. Abbott, T.D. Abbott, M.R. Abernathy, F. Acernese, K. Ackley, C. Adams, T. Adams, P. Addesso, R.X. Adhikari et al., Living Reviews in Relativity **19** (2016), `1304.0670`
[45] L.S. Finn, D.F. Chernoff, Phys. Rev. D**47**, 2198 (1993)

What can we learn from GRBs?

Marco Muccino[1,2,⋆], *Remo* Ruffini[1,2,3,4], *Yerlan* Aimuratov[1,3], *Laura M.* Becerra[1,2], *Carlo L.* Bianco[1,2], *Mile* Karlica[1,3], *Milos* Kovacevic[1,3], *Julio D.* Melon Fuksman[1,2], *Rahim* Moradi[1,2], *Ana V.* Penacchioni[5,6], *Giovanni B.* Pisani[1,2], *Daria* Primorac[1,2], *Jorge A.* Rueda[1,2,4], *Soroush* Shakeri[2,7], *Gregory V.* Vereshchagin[1,2], *She-Sheng* Xue[1,2], and *Yu* Wang[1,2]

[1] *Dip. di Fisica, Sapienza Università di Roma, Piazzale Aldo Moro 5, I-00185 Rome, Italy*
[2] *ICRANet-Pescara, Piazza della Repubblica 10, I-65122 Pescara, Italy*
[3] *Université de Nice Sophia-Antipolis, Grand Château Parc Valrose, Nice, CEDEX 2, France*
[4] *ICRANet-Rio, Centro Brasileiro de Pesquisas Fisicas, Rua Dr. Xavier Sigaud 150, Rio de Janeiro, RJ, 22290-180, Brazil*
[5] *University of Siena, Dept. of Physical Sciences, Earth and Environment, Via Roma 56, I-53100 Siena, Italy*
[6] *ASI Science Data Center, via del Politecnico s.n.c., I-00133 Rome Italy*
[7] *Department of Physics, Isfahan University of Technology, 84156-83111, Iran*

Abstract. We review our recent results on the classification of long and short gamma-ray bursts (GRBs) in different subclasses. We provide observational evidences for the binary nature of GRB progenitors. For long bursts the induced gravitational collapse (IGC) paradigm proposes as progenitor a tight binary system composed of a carbon-oxygen core (CO_{core}) and a neutron star (NS) companion; the supernova (SN) explosion of the CO_{core} triggers a hypercritical accretion process onto the companion NS. For short bursts a NS–NS merger is traditionally adopted as the progenitor. We also indicate additional sub-classes originating from different progenitors: (CO_{core})–black hole (BH), BH–NS, and white dwarf–NS binaries. We also show how the outcomes of the further evolution of some of these sub-classes may become the progenitor systems of other sub-classes.

1 Introduction

Gamma-ray bursts (GRBs) are traditionally classified based on their duration [1–5]: short GRBs last $\lesssim 2$ s, while long GRBs last $\gtrsim 2$ s.

Thanks to the extensive data collected by γ-ray telescopes, such as AGILE, BATSE, BeppoSAX, *Fermi*, *HETE-II*, *INTEGRAL*, Konus/WIND and *Swift*, to more sofisticated time-resolved spectral analyses, and to the theoretical treatment of the *fireshell* model [6–8] it has become evident that both long and short bursts originate from binary progenitors and that they can be further subdivided into a variety of sub-classes, depending on the evolution of these binary systems [9–11].

Short bursts are associated to NS-NS or BH-NS mergers [12–22]: their host galaxies are of both early- and late-type, their localization with respect to the host galaxy often indicates a large offset [23–29] or a location of minimal star-forming activity with typical circumburst medium (CBM) densities of $\sim 10^{-5}$–10^{-4} cm^{-3}, and no supernovae (SNe) have ever been associated to them.

Long bursts have been traditionally associated to the death of single massive stars [30]. The large majority of long bursts is related to SNe and are spatially correlated with bright star-forming regions in their host galaxies [31, 32] with a typical CBM density of ~ 1 cm^{-3} [33, 34]. However, the above single progenitor model contrasts with the fact that most massive stars are found in binary systems [35], that most type Ib/c SNe occur in binary systems [36] and that SNe associated to long GRBs are indeed of type Ib/c [37]. Indeed, recently we have found evindence for multiple components in long GRB emissions evidencing the presence of a precise sequence of different astrophysical processes [33, 34], which led to the formulation of the Induced Gravitational Collapse (IGC) paradigm [6, 38–40] expliciting the role of binary systems as progenitors of the long GRBs. The IGC paradigm explains the GRB-SN connection by proposing as progenitors (or *in-state*) a tight binary system composed of a carbon-oxygen core (CO_{core}) undergoing a SN explosion and a companion neutron star (NS) [39–41]. The SN explosion triggers hypercritical accretion onto the companion NS [39, 40, 42].

Recent observations of a prolonged 0.1–100 GeV high energy emission by the *Fermi*-LAT instrument evidenced its correlation with both long [9] and short bursts [10] with isotropic energy $E_{\rm iso} \gtrsim 10^{52}$ erg. On the basis of this correlation in such systems with different progenitors, we have identified the onset of the GeV emission with the moment of the formation of a black hole (BH) [9, 10]. This implies that systems with energy $E_{\rm iso} \lesssim 10^{52}$ erg, which do not exhibit GeV emission, do not form BHs.

Indeed, we proposed the following classification scheme. Long GRBs, according to the IGC paradigm [9], are classified into two sub-classes [42]:

⋆e-mail: marco.muccino@icranet.it

- X-ray flashes (XRFs) with $E_{\rm iso} \lesssim 10^{52}$ erg and rest-frame spectral peak energy $E_{p,i} \lesssim 200$ keV. These systems, already pioneered in a different context [43–45], originate in widely separated $CO_{\rm core}$–NS binaries with an orbital separation $a > 10^{11}$ cm [41], therefore the hypercritical accretion onto the NS companion is insufficient to induce gravitational collapse to a BH [39–41] and, therefore, as expected in our theory no GeV emission is observed. The outcomes (or *out-states*) of XRFs are binaries composed of a new NS (νNS) produced from the SN explosion, and a massive NS (MNS) which accreted matter from the SN ejecta. Their occurrence rate is $\rho_{\rm XRF} = 100^{+45}_{-34}$ Gpc^{-3}yr^{-1} [42] (see figure 1).
- Binary-driven hypernovae (BdHNe) with $E_{\rm iso} \gtrsim 10^{52}$ erg and $E_{p,i} \gtrsim 200$ keV. BdHNe occur in tighter binaries ($a < 10^{11}$ cm), where the hypercritical accretion onto the companion NS leads to the formation of a BH [41] and, therefore, to the emission of the associated prolonged GeV emission (observable when inside the LAT field of view). Specific constant power-law behaviors are observed in their high energy GeV and X-rays luminosity light curves [9, 46, 47]. The out-states of BdHNe are νNS-BH binaries [41, 42, 48, 49]. The BdHN occurrence rate is $\rho_{\rm BdHN} = 0.77^{+0.09}_{-0.08}$ Gpc^{-3}yr^{-1} [42] (see figure 1).

For progenitor system composed of a $CO_{\rm core}$ in binary with an already formed BH [8, 42], leading to bursts with $E_{\rm iso} \gtrsim 10^{54}$ erg and $E_{p,i} \gtrsim 2$ MeV, the observational identification is still pending. In these systems, which correspond to the late evolutionary stages of X-ray binaries as Cyg X-1 and Cyg X-3 [50], or microquasars [51], the hypercritical accretion produces, as *out-states*, a more massive BH and a νNS. Their occurrence rate can contribute to that of BdHNe, being $CO_{\rm core}$–BH a particular case of BdHN progenitors (see figure 1).

In total analogy, the formation of a BH can occur in short bursts, depending whether or not the mass of the merged core of the binary system exceeds the NS critical mass. For NS–NS binaries, which are the outcomes of XRFs, we have [10, 42, 48]:

- Short gamma-ray flashes (S-GRFs), with $E_{\rm iso} \lesssim 10^{52}$ erg and $E_{p,i} \lesssim 2$ MeV. They occur when the merged core does not exceed the NS critical mass and does not collapse into a BH, but still remains as a MNS with some additional orbiting material to guarantee the angular momentum conservation. As a consequence, no GeV emission is expected from these systems and, indeed, is not observed. The S-GRF occurrence rate is $\rho_{\rm S-GRF} = 3.6^{+1.4}_{-1.0}$ Gpc^{-3} y^{-1} [42] (see figure 1).
- Authentic short GRBs (S-GRBs) with $E_{\rm iso} \gtrsim 10^{52}$ erg and $E_{p,i} \gtrsim 2$ MeV. They occur when a BH is formed in the NS–NS merger. Thus, these systems exhibit GeV emission. Their occurrence rate is $\rho_{\rm S-GRB} = \left(1.9^{+1.8}_{-1.1}\right) \times 10^{-3}$ Gpc^{-3} y^{-1} [42] (see figure 1).

We have recently proposed the existence of ultra-short GRBs (U-GRBs), a new hybrid sub-class of (yet unobserved) short bursts originating from the BdHNe out-states (νNS–BH binaries), which remain bound nearly in 100% of the cases [48]. These systems represent a yet unaccounted family of merging NS-BH binaries in the current standard population synthesis analyses [48], therefore, including other possible channels of formation for NS-BH binaries, the lower limit of the U-GRB occurrence rate can be assumed equal to the BdHN rate, i.e., $\rho_{\rm U-GRB} \gtrsim 0.77^{+0.09}_{-0.08}$ Gpc^{-3}yr^{-1} [42] (see figure 1).

Finally, we proposed another sub-class of sources originating in NS–WD mergers: gamma-ray flashes (GRFs), a class of long GRBs occurring in a CBM environment with low density, e.g., $\sim 10^{-3}$ cm^{-3}, typical of the halos of the GRB host galaxies [42, 52, 53], not associated with SNe [54], and characterized by the presence of a macronova emission in the optical afterglow [55]. GRFs have $10^{51} \lesssim E_{\rm iso} \lesssim 10^{52}$ erg and $0.2 \lesssim E_{p,i} \lesssim 2$ MeV and, therefore, the NS–WD merger forms a MNS and not a BH [42]. NS–WD binaries, are notoriously very common astrophysical systems [56] and their possible formation channels have been studied [57, 58]; as proposed in Ref. [42], another less likely but yet possible channel of formation is the merger of a NS–WD binary produced from an S-GRF. The GRF rate of occurrence is $\rho_{\rm GRF} = 1.02^{+0.71}_{-0.46}$ Gpc^{-3} y^{-1} [42] (see figure 1).

In all the above systems, the 10^{52} erg limit is clearly a function of the yet unknown precise value of the NS critical mass. As already pointed out in Ref. [42] the direct observation of the separatrix energy between S-GRFs and S-GRBs, and also between BdHNe and XRFs, gives fundamental informations for the determination of the actual value of maximum NS mass and for the minimum mass of the newly-formed BH.

In this paper we review the latest observational and theoretical results which led to above burst classification scheme. In Section 2, we briefly summarize the fireshell model. In Section 3, we describe the observational properties of XRFs and BdHNe and their interpretation within the IGC paradism. In Section 4, we focus on the S-GRBs and specially on the theoretical interpretation of their GeV emission. In Section 4, we summarize our Conclusions.

2 The fireshell model

Before going into details in the observational and theoretical description of XRFs, BdHNe, S-GRFs and S-GRBs, we briefly summarize the fireshell model which is at the basis for the above classification of all bursts.

In the fireshell model [6–8], the GRB emission originate from an optically thick e^+e^- plasma of total energy $E^{\rm tot}_{e^+e^-}$ – the fireshell. Its expansion and self-acceleration is due to the gradual e^+e^- annihilation [59]. Even after engulfing the baryonic mass M_B left over by the progenitor system, quantified by the baryon load $B = M_B c^2/E^{\rm tot}_{e^+e^-}$ [60], the fireshell remains still optically thick and continues its self-acceleration up to ultrarelativistic velocities [61, 62]. When the fireshell reaches the transparency condition, a first flash of radiation, the P-GRB, is emitted [7, 59, 60]. The spectrum of the P-GRB is determined by the geometry of the pair-creation region: in the case of the spherically symmetric dyadosphere, the P-GRB spectrum is generally described by a single thermal component

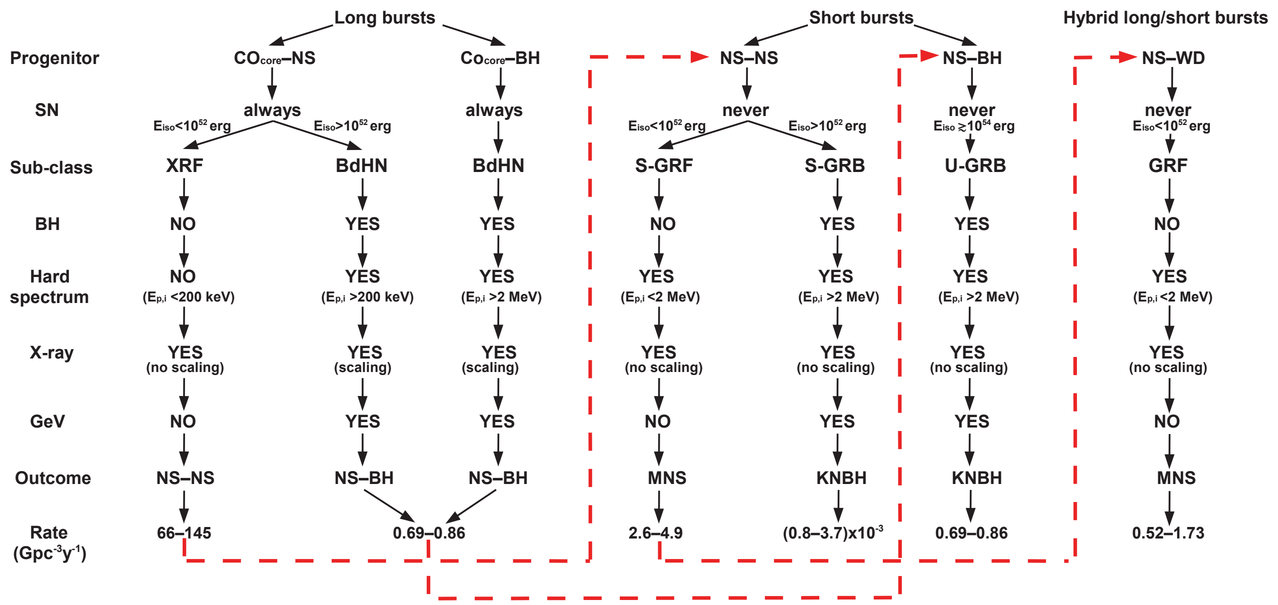

Figure 1. Summary of the properties of the burst sub-classes discussed in the Introduction. The red dashed lines indicate the evolutionary tracks linking out-states and in-states of some of the sub-classes. Additional details can be found in Ref. [42].

[10, 63]; in the case of an axially symmetric dyadotorus, the resulting P-GRB spectrum is a convolution of thermal spectra of different temperatures which resembles more a power-law spectral energy distribution with an exponential cutoff [64, 65].

After transparency, the accelerated baryons propagate through and interact in fully radiative regime with the CBM, giving rise to the prompt emission [7]. The structures observed in the prompt emission of a GRB depend on the CBM density n_{CBM} and its inhomogeneities [66–68]. In both long and short bursts the CBM clouds have similar masses (10^{22}–10^{24} g), sizes ($\approx 10^{15}$–10^{16} cm), and typical distances from the BH ($\approx 10^{16}$–10^{17} cm) [10, 33]. The observed prompt emission spectrum results from the convolution of a large number of comoving spectra with decreasing temperatures and Lorentz and Doppler factors, due to each collision with the CBM, over the surfaces of constant arrival time for photons at the detector [69, 70] over the entire observation time.

To conclude, the evolution of an optically thick baryon-loaded pair plasma, is generally described in terms of $E^{tot}_{e^+e^-}$ and B and it is independent of the way the pair plasma is created. This general formalism can also be applied to any optically thick e^+e^- plasma, like the one created via $\nu\bar{\nu} \leftrightarrow e^+e^-$ mechanism in a NS merger as described in [17, 71, 72].

3 XRFs and BdHNe in the IGC paradigm

We here focus on the comparison between XRF and BdHN sub-classes within the IGC paradigm, giving a special attention to the latest theoretical results on the BdHNe.

In the IGC scenario, both XRFs and BdHNe originate in the hypercritical accretion process of the SN ejecta onto the NS binary companion. In this phenomenon photons are trapped in the accreting material and the accretion energy is lost through a large associated neutrino emission [39, 40, 73, 74]. In the XRFs, the CO$_{core}$-NS binary is widely separated ($a \gtrsim 10^{11}$ cm), thus the accretion rate $< 10^{-2}\, M_\odot\, s^{-1}$ can only push the binary companion NS to become a MNS. The resulting emission, dubbed *Episode 1*, lasts $\sim 10^2$–10^4 s. Its spectrum is characterized by: 1) a thermal component spectrum with temperatures in the range of 0.1–2 keV and corresponding radii of 10^{10}–10^{12} cm (see figure 2, left-panel), possibly originating from the outflow within the NS atmosphere driven out by Rayleigh-Taylor convection instabilities [40], and 2) a power-law component, possibly related to the excess of angular momentum of the system which necessarily leads to a jetted emission [41]. The long lasting X-ray emission does not exhibit any specific common late power-law behavior (see figure 2, right panel) and can be explained by the emission of the SN ejecta shocked by the hypercritical accretion emission of the XRF. This energy injection into the SN ejecta leads to the occurrence of a broad-lined SN Ic [75] with a kinetic energy larger than that of the traditional SNe Ic [42]. The absence of GeV emissions is implicit in the nature of the hypercritical accretion process not leading to a BH. Of course, all XRFs at redshift $z \lesssim 1$ exhibit an optical SN with a luminosity similar to the one of SN 1998bw [76], which occurs after 10–15 days in the source cosmological rest-frame.

In the IGC paradigm, the shorter the CO$_{core}$-NS binary period, the larger the accretion rate and the values of E_{iso} and $E_{p,i}$, and correspondingly the shorter the prompt emission duration [41]. Indeed, in BdHNe the CO$_{core}$-NS binary is more tightly bound ($a \lesssim 10^{11}$ cm) and the accretion rates of the SN ejecta can be $\gtrsim 10^{-2}$–$10^{-1}\, M_\odot\, s^{-1}$, leading the companion NS to collapse to a BH [40, 41]. For

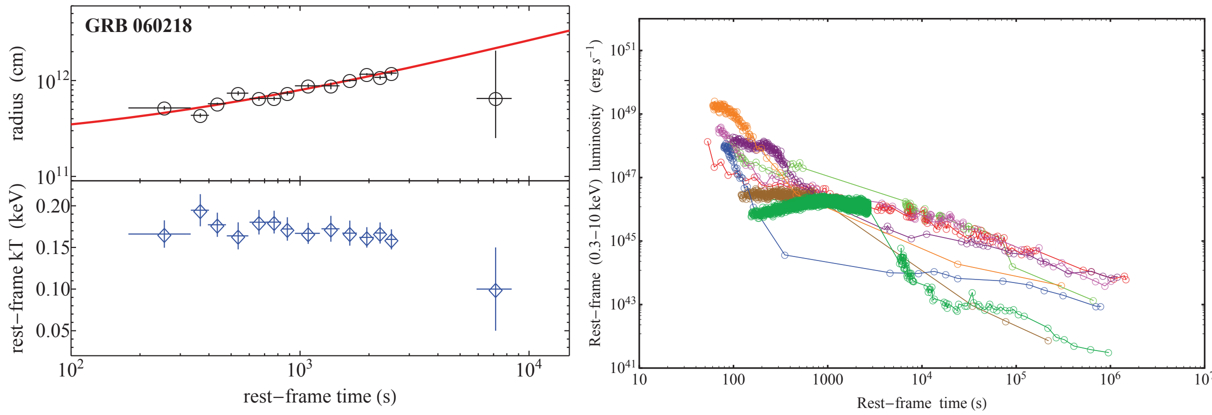

Figure 2. Left panel: the evolution of the radius of the thermal component detected in GRB 060218 (black circles) and its linear fit (solid red curve) and of the corresponding rest-frame temperature (blue diamonds). Reproduced from Ref. [77]. Right panel: rest-frame X-ray 0.3–10 keV luminosity light curves of selected XRFs: 050416A (red), 060218 (dark green), 070419A (orange), 081007 (magenta), 100316D (brown), 101219B (purple), and 130831A (green).

this reason BdHNe exhibit a more complex structure than XRFs composed of distinct Episodes.

- *Episode 1* in BdHNe, like in the case of XRFs, also originates in the hypercritical accretion process. The corresponding spectrum again exhibits: 1) an expanding thermal component with a decreasing temperature, typical radii of 10^9–10^{10} cm and an average expansion speed of $\sim 10^8$–10^9 cm s^{-1} (see figure 3 (a)), and b) a power-law function [33, 34, 78].
- *Episode 2* corresponds to the γ-ray prompt emission of an authentic long GRB (see figure 3 (b)), stemming from the collapse of the companion NS to a BH and leading to the vacuum polarization process and the creation of an e^+e^- plasma. The analysis of the P-GRB emission indicates that BdHNe have a baryon load of $B \approx 10^{-4}$–10^{-2} and at transparency they reach a Lorentz factor of $\Gamma = 10^2$–10^3. The prompt emission is produced by the interaction of the fireshell with the CBM clouds located at $\sim 10^{16}$–10^{17} cm from the burst site with average number density of ~ 1 cm^{-3} [33, 78].
- *Episode 3* occurs after the prompt emission in the X-rays. It composed of a steep decay characterized by the presence of an early X-ray flare, a plateau and a late power-law decay which we refer as to the afterglow. These three components are dubbed flare-plateau-afterglow (FPA) phase [79]. During the early X-ray flare phase (typically at a rest-frame time of $\sim 10^2$ s) an expanding thermal component has been observed in its spectrum [9, 47, 79]. The inferred radii are typically $\sim 10^{12}$–10^{13} cm and they expand at mildly relativistic speed with $\Gamma \lesssim 4$ [9, 47, 78, 79]. The size of the corresponding emitting region is clearly incompatible with the radii inferred from Episodes 1 and 2. When computed in the source cosmological rest-frame, the plateau and the late power-law decay exhibit new features (see figure 3 (c)): 1) the overlapping of the afterglow phases, which have typical slopes of $-1.7 \lesssim \alpha \lesssim -1.3$ and show a characteristic common power-law behavior [46]; the nested property, which shows that the duration (the luminosity) of the plateau phase is inversely (directly) proportional to the energy of the GRB emission, i.e., the more energetic the source, the smaller (higher) the duration (the luminosity) of the plateau [47]. The use of the overlapping of the afterglows as a distance indicator has been explored by inferring the redshifts of GRB 101023 [34], and has been applied to predict the occurrence of the SN associated to GRB 130427A before its discovery [80], later confirmed by the observations [81–84]. In the IGC scenario, the FPA originates from the SN ejecta [9, 79]. In BdHNe the SN ejecta experiences an energy injection from GRB emission leading to the occurrence of a broad-lined SN Ic [75] with a kinetic energy larger than that of the traditional SNe Ic. This energy injection results in an isotropic energy emission of 10^{51}–10^{52} erg for the FPA phase. In particular, the X-ray flare can be modeled by considering the impact of the GRB on the SN ejecta and the propagation of the optically thick e^+e^- plasma into a medium largely baryon-contaminated ($B \approx 10$–10^2). A numerical integration starting at 10^{10} cm all the way to 10^{12} cm, where the transparency is reached, gives a perfect agreement between the radius of the emitter at transparency and the observations, as well a coincidence of the observed time of the peak emission of the flare [79]. The plateau and the afterglow phases are still under study (M. Karlica et al., in preparation).
- *Episode 4* corresponds to the optical SN emission observable in all BdHNe at $z \lesssim 1$ after $\approx$ 10–15 days in the cosmological rest-frame. All these SNe have a standard luminosity similar to the one of SN 1998bw [76].
- *Episode 5* is identified with the distinctive long-lived GeV emission, observed in the majority of BdHNe when within the LAT field of view. Though this emission follows a precise power-law behavior with index ≈ -1.2 [42, 85] (see figure 3 (d)), this emission is conceptually distinct in its underlying physical process from that of Episode 3: it originate, in facts, in the further accretion of matter onto the newly-formed BH and it is ob-

servable only after the transparency emission, i.e., the P-GRB [42].

4 The S-GRBs in the NS–NS merger paradigm

In Section 1 we discussed the rates of S-GRFs and S-GRBs, showing that S-GRFs are the most frequent events among the short bursts. This result is also in good agreement with the NS–NS binaries observed within our Galaxy: only a subset of them has a total mass larger than the NS critical mass $M_{\rm crit}^{\rm NS}$ and can form a BH in their merging process [10] if we assume that $M_{\rm crit}^{\rm NS} = 2.67 M_{\odot}$ for a non-rotating, globally neutral NS within the NL3 nuclear model [87]. In this light S-GRBs are very important for inferring constraints on $M_{\rm crit}^{\rm NS}$, on the NS equation of state, and on the minimum mass of the newly-formed BH.

To date, within the fireshell model we have analized five authentic S-GRBs: 090227B [63], 140619B [10], GRB 090510 [64], 081024B and 140402A [65]. The analyses of the P-GRB emission and the correlation between the spikes of the prompt emission and CBM inhomogeneities gave the most successful test for the fireshell model. S-GRBs share some remarkable analogies but also some differences with BdHNe in view of the simplicity of the underlying physical system of S-GRBs, which unlike the BdHNe, do not exhibit any of the extremely complex activities related to the SN (see Section 3).

- *Episode 1* here is related to the NS–NS merger activity before the gravitational collapse into a BH and possibly corresponds to faint precursors observed in some short bursts [64, 88]. Because of the compactness of the systems this process at times is not observable.
- *Episode 2* corresponds to the GRB emission from the NS-NS merger. Within the fireshell model it is composed of the P-GRB, which occur before the onset of the GeV emission, and the prompt emission (see figure 4, left panel). From the analysis of their P-GRB emission, all S-GRBs have a standard values of the baryon load ($B \approx 5 \times 10^{-5}$), which is consistent with the crustal masses of NS-NS mergers [10, 89], and of the Lorentz factors at the transparency $\Gamma \approx 10^4$ [10, 63–65]. From the fit of the prompt emission (see figure 4, right panel), it came out that S-GRBs occur in a standard CBM with average density $\langle n_{\rm CBM} \rangle \approx 10^{-5}$ cm^{-3} [10, 63–65], which is typical of galactic halos where NS–NS mergers migrate, owing to natal kicks imparted to the binaries at birth [22].
- *Episode 3*, which corresponds to the traditional X-ray afterglow, differs from that of BdHNe which results from the interaction between the GRB and the SN ejecta. Work on this topic is still ongoing.
- *Episode 4*, identified with the optical emission of a SN, is here missing.
- *Episode 5* coincides with the GeV emission turning on soon after the P-GRB and being coeval with the prompt emission. With the exception of GRB 090227B, which was outside the nominal *Fermi*-LAT field of view [86], all S-GRBs consistently exhibit this emission, which appears to be strictly correlated to that observed in the BdHNe. Since the presence of a BH is the only commonality between BdHNe and S-GRBs, by analogy we assume that the GeV emission originate from the activity of the newly-born BH produced in the merger [10]. The rest-frame 0.1–100 GeV luminosity light curves of all S-GRBs with LAT data follow a common power-law behavior with the rest-frame time which goes as $t^{-1.29\pm0.06}$ (see dashed black line in figure 5).

Table 1 lists the redshift, $E_{p,i}$, E_{iso} (in the rest-frame energy band 1–10000 keV), and the GeV isotropic emission energy E_{LAT} (in the rest-frame energy band 0.1–100 GeV) of all S-GRBs. The values of E_{LAT} represent lower limits to the actual GeV isotropic emission energies, since at late times the observations of GeV emission could be prevented due to instrumental threshold of the LAT. Using the maximum GeV photon observed energy $E_{\rm GeV}^{\rm max}$ listed in table 1, we derive a lower limit on the Lorentz factor of the GeV emission $\Gamma_{\rm GeV}^{\rm min}$ by requiring the optically thin condition to the high energy photons [90]. For each S-GRB we estimate lower limits in each time interval of the GeV luminosity light curves in figure 5. Then, $\Gamma_{\rm GeV}^{\rm min}$ for each S-GRB has been then determined as the largest among the inferred lower limits. It follows that the GeV emission is produced by an ultrarelativistic outflows with $\Gamma_{\rm GeV}^{\rm min} \gtrsim 300$ (see table 1).

We propose that the GeV emission in S-GRBs is produced by accretion onto the new-born BH of a certain amount of mass that remains bound to it because of the conservation of energy and angular momentum from the merger moment to the BH birth [64]. Lower limits on the amount of accreted mass can be attained by considering the accretion process onto a maximally rotating Kerr BH. Depending whether the infalling material is in co- or counter-rotating orbit with the spinning BH, the maximum efficiency of the conversion of gravitational energy into radiation is $\eta_+ = 42.3\%$ or $\eta_- = 3.8\%$, respectively [91] and, therefore, $E_{\rm LAT}$ can be expressed as

$$E_{\rm LAT} = f_{\rm b}^{-1} \eta_{\pm} M_{\rm acc}^{\eta_{\pm}} c^2 , \quad (1)$$

where $f_{\rm b}$ is the beaming factor which depends on the geometry of the GeV emission, and $M_{\rm acc}^{\eta_{\pm}}$ is the amount of accreted mass depending on the choice of the efficiency. The observational evidence that the totality of S-GRBs exhibit GeV emission and that its absence is due instrumental absence of alignment between the LAT and the source at the time of the GRB emission suggest no significant beaming. Therefore, in the following we set $f_{\rm b} \equiv 1$. The corresponding estimates of $M_{\rm acc}^{\eta_{\pm}}$ in our sample of S-GRBs are listed in table 1.

5 Conclusions

Remarkable progresses in the understanding of GRBs have been made possible thanks to the great amount X- and γ-rays and high energy data and to a deeper theoretical understanding of WD [92], NS [87, 89] and BH [93], leading to a new paradigm purporting the role of binary systems as progenitors of GRBs: $\rm CO_{core}$–NS binaries for long

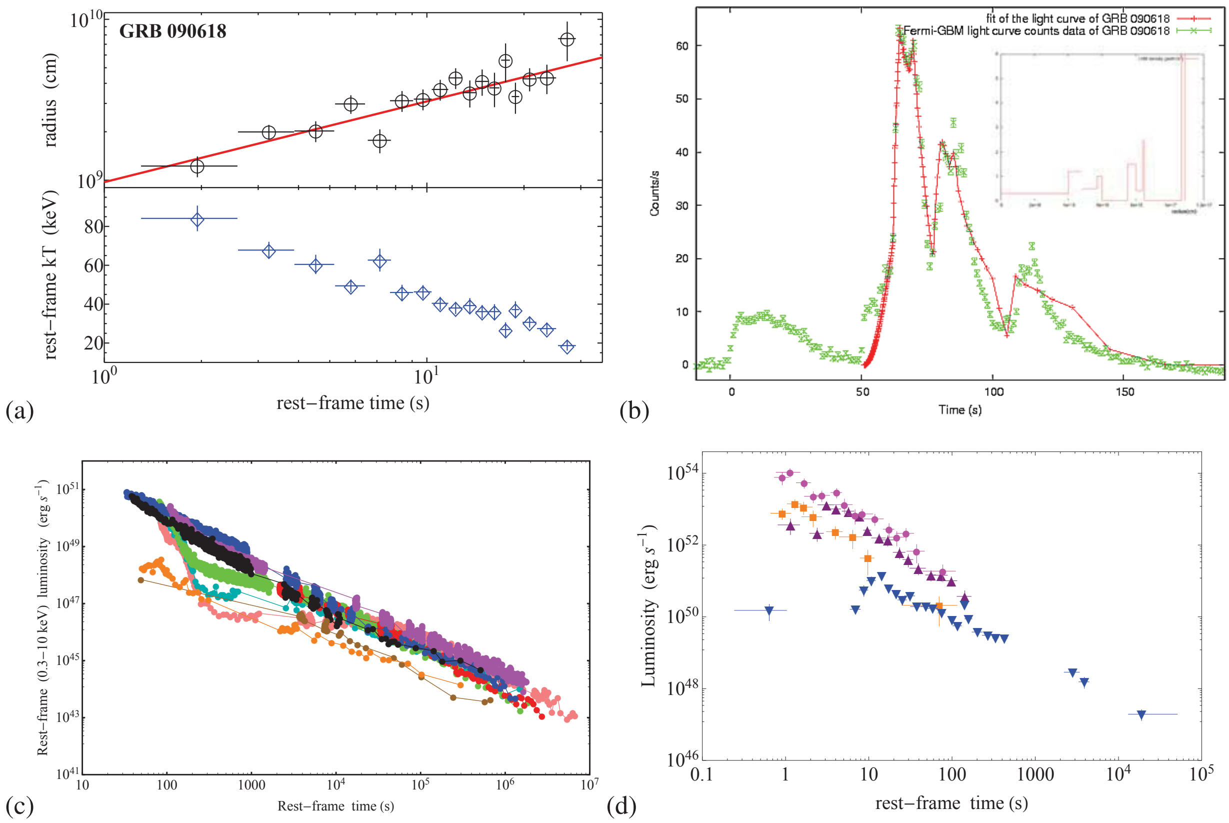

Figure 3. (a) The evolution of the radius of the thermal component detected in the Episode 1 of GRB 090618 (black circles) and its linear fit (solid red curve), and the decay of the corresponding rest-frame temperature (blue diamonds). (b) The fireshell simulation (red line) of the light curve of Episode 2 of the prototype GRB 090618 (green data). The small inset reproduces the CBM profile required for the simulation. Reproduced from Ref. [33]. (c) The rest-frame 0.3–10 keV luminosity light curves of selected BdHNe: 050525 (brown), 060729 (pink), 061007 (black), 080319B (blue), 090618 (green), 091127 (red), 100816A (orange), 111228A (light blue), and 130427A (purple) [79]. (d) The rest-frame 0.1–100 GeV luminosity light curves [86] of selected BdHNe: GRB 080916C (magenta circles), GRB 090902B (purple triangles), GRB 110731A (orange squares), GRB 130427A (blue reversed triangles).

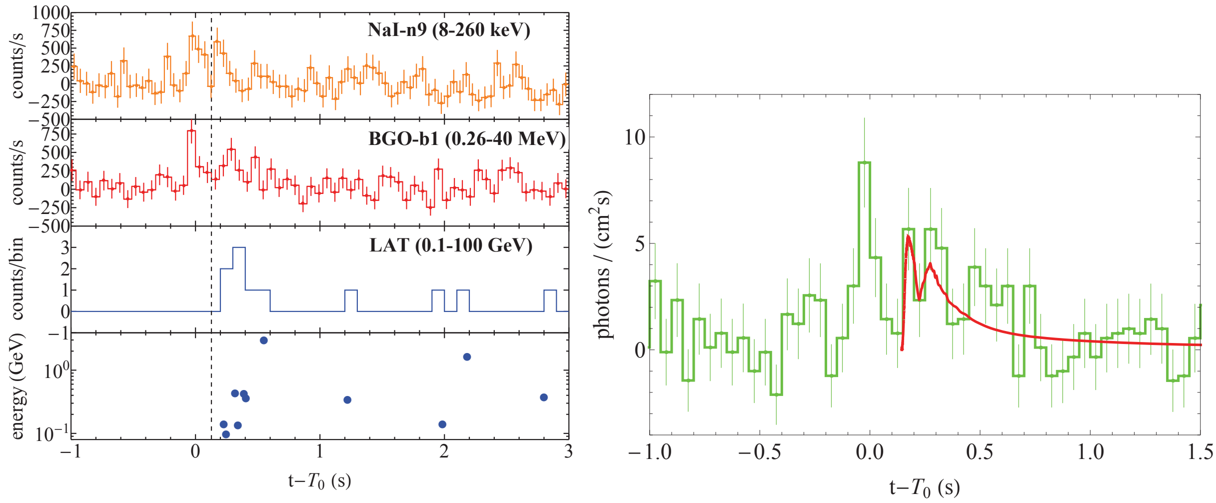

Figure 4. Left panel: background subtracted 50 ms binned data from the NaI-n9 (8 – 260 keV, top panel) and BGO-b1 (0.26 – 40 MeV, second panel) detectors, the 100 ms binned high energy data (0.1 – 100 GeV, third panel, without error bars), and the high energy photons detected by the of the *Fermi*-LAT (bottom panel) for the S-GRB 081024B; the vertical dashed line marks the on-set of the LAT light curve. Right panel: the NaI-n9 light curve of the prompt emission of the S-GRB 081024B (green data) and the simulation within the fireshell model (red curve). All plots are reproduced from Ref. [65].

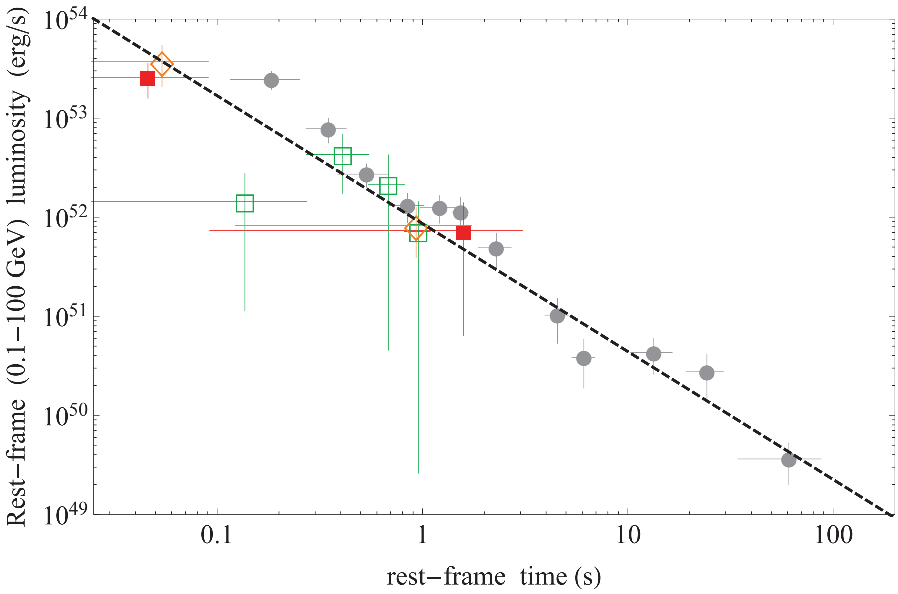

Figure 5. The rest-frame 0.1–100 GeV isotropic luminosities of the S-GRBs: 081024B (orange empty diamonds), 090510 (gray filled circles), 140402A (red filled squares), and 140619B (green empty squares). All the light curves start after the P-GRB emission. The dashed black line marks the common behavior of all the S-GRB light curves which goes as $t^{-1.29\pm0.06}$. Reproduced from Ref. [65].

GRB	z	$E_{\rm p,i}$ (MeV)	$E_{\rm iso}$ (10^{52} erg)	$E^{\rm max}_{\rm GeV}$ (GeV)	$\Gamma^{\rm min}_{\rm GeV}$	$E_{\rm LAT}$ (10^{52} erg)	$M^{\eta+}_{\rm acc}$ ($M_\odot$)	$M^{\eta-}_{\rm acc}$ ($M_\odot$)
081024B	3.12 ± 1.82	9.56 ± 4.94	2.64 ± 1.00	3	$\gtrsim 779$	$\gtrsim 2.79 \pm 0.98$	$\gtrsim 0.04$	$\gtrsim 0.41$
090227B	1.61 ± 0.14	5.89 ± 0.30	28.3 ± 1.5	–	–	–	–	–
090510	0.903 ± 0.003	7.89 ± 0.76	3.95 ± 0.21	31	$\gtrsim 551$	$\gtrsim 5.78 \pm 0.60$	$\gtrsim 0.08$	$\gtrsim 0.86$
140402A	5.52 ± 0.93	6.1 ± 1.6	4.7 ± 1.1	3.7	$\gtrsim 354$	$\gtrsim 4.5 \pm 2.2$	$\gtrsim 0.06$	$\gtrsim 0.66$
140619B	2.67 ± 0.37	5.34 ± 0.79	6.03 ± 0.79	24	$\gtrsim 471$	$\gtrsim 2.34 \pm 0.91$	$\gtrsim 0.03$	$\gtrsim 0.35$

Table 1. S-GRB properties: z, $E_{\rm p,i}$, the maximum GeV photon observed energy $E^{\rm max}_{\rm GeV}$, the minimum Lorentz factor of the GeV emission $\Gamma^{\rm min}_{\rm GeV}$, E_{iso}, $E_{\rm LAT}$, and the amount of infalling accreting mass co-rotating (counter-rotating) with the BH $M^{\eta+}_{\rm acc}$ ($M^{\eta-}_{\rm acc}$), needed to explaing $E_{\rm LAT}$.

bursts within the IGC paradigm [6, 38–40], and NS–NS (or NS-BH) binaries for short bursts, as widely accepted and confirmed by strong observational and theoretical evidences [12–22]. These paradigms have led to the classification of GRBs in seven different sub-classes (see figure 1). We here focus our attention on the sub-classes of XRFS, BdHNe, S-GRFs and S-GRBs.

In Section 2, we review the fireshell model for GRBs [6–8] and its essential role in order to disentangle the various emission episodes characterizing each of the above sub-classes.

In Section 3, we summarize the commonalities and the differences between the observational properties of XRFs and BdHNe and provide their theoretical interpretation within the IGC paradigm, namely, whether or not the hypercritical accretion process leads to the formation of a BH.

In Section 4, we outline the properties S-GRFs and S-GRBs originating in NS–NS mergers leading to a MNS and the formation of a BH, respectively. Then, we focus on S-GRBs and on the key role of the P-GRB identification for their description, as well as the analysis of the GeV emission. We finally discuss in details the GeV emission uniquely observed in both BdHNe and S-GRBs, when within the Fermi-LAT FoV. In both cases it starts after the P-GRB emission and it is coeval with the occurrence of the prompt emission [42]. Moreover, the rest-frame 0.1–100 GeV luminosities in BdHNe and S-GRBs share a common luminosity pattern, a precise power-law behavior with time $\propto t^{-1.2}$ [9, 10, 42, 65, 85]. These commonalities, in such different systems, as well as their energy requirements are naturally explained if we assume that the GeV emission originates by accretion processes in the newly-born BH [9, 10]. In all the identified S-GRBs, within the Fermi-LAT FoV, GeV photons are always observed [42, 64]. This implies that no intrinsic beaming is necessary to explain the S-GRB GeV emission. Within the hypothesis of isotropic emission, in the case of S-GRBs we point out how the total energy of the GeV emission can attained from the gravitational binding energy of mass accretion of $M \gtrsim 0.03$–$0.08 M_\odot$ or $M \gtrsim 0.35$–$0.86 M_\odot$ for co- or counter-rotating orbits with a maximally rotating BH, respectively (see table 1). A lower limit on the Lorentz factor of the GeV emission of $\Gamma^{\rm min}_{\rm GeV} \gtrsim 300$ can be obtained by requiring the optically thin condition to the high energy photons [90].

From the above consideration and the proposed classification scheme some considerations follow.

- The knowledge of the separatrix energy of 10^{52} erg, which discriminates between systems forming or not BHs and on which our classification scheme of GRBs is based, represents an observational constraints on the value of the NS critical mass $M_{\rm crit}$, certainly in the range of 2.2–2.7 $M_\odot$ for a non-rotating NS depending on the equations of state [87], and the minimum mass of a BH. This value is consistent and can be derived in BdHNe by considering the hypercritical accretion process onto a NS leading to an energy release in form of neutrinos and photons, given by the gain of gravitational potential energy of the matter accreted in the NS. This includes the change of binding energy of the NS while accreting both matter and angular momentum [42].
- Most noteworthy, the existence of a precise common power-law behavior in the rest-frame 0.1–100 GeV luminosities of S-GRBs (see figure 5), following the BH formation, points to a commonality in the mass and spin of the newly-formed BH. This result is explainable with the expected mass of the merging NSs, each one of mass $M \approx 1.3$–$1.5 M_\odot$ [94], and the above expected range of the non-rotating NS critical mass, leading to a standard value of the BH mass and of its Kerr parameter [10].
- Finally, we discuss the gravitational wave (GW) detectability by advanced LIGO (aLIGO) from S-GRBs. We have already shown that binaries in which each NS has a mass $M_{\rm NS} = 1.34\ M_\odot = 0.5 M_{\rm crit}^{\rm NS}$ produce GW signals which are well below the signal to noise ratio S/N= 8 needed for a positive detection by aLIGO: a positive GW detection may occur only for sources located at $z \lesssim 0.14$ for the aLIGO 2022+ run, a redshift well above that of GRB 090510, to date the closest S-GRB located at $z = 0.903$ [10, 95, 96].

M. M. and J. A. R. acknowledge the partial support of the project N 3101/GF4 IPC-11, and the target program F.0679 0073-6/PTsF of the Ministry of Education and Science of the Republic of Kazakhstan.

References

[1] E.P. Mazets, S.V. Golenetskii, V.N. Ilinskii, V.N. Panov, R.L. Aptekar, I.A. Gurian, M.P. Proskura, I.A. Sokolov, Z.I. Sokolova, T.V. Kharitonova, Astrophysics and Space Science **80**, 3 (1981)

[2] J.P. Dezalay, C. Barat, R. Talon, R. Syunyaev, O. Terekhov, A. Kuznetsov, *Short cosmic events - A subset of classical GRBs?*, in *American Institute of Physics Conference Series*, edited by W. S. Paciesas & G. J. Fishman (1992), Vol. 265 of *American Institute of Physics Conference Series*, pp. 304–309

[3] R.W. Klebesadel, *The durations of gamma-ray bursts*, in *Gamma-Ray Bursts - Observations, Analyses and Theories*, edited by C. Ho, R.I. Epstein, E.E. Fenimore (Cambridge University Press, 1992), pp. 161–168

[4] C. Kouveliotou, C.A. Meegan, G.J. Fishman, N.P. Bhat, M.S. Briggs, T.M. Koshut, W.S. Paciesas, G.N. Pendleton, ApJ Letters **413**, L101 (1993)

[5] M. Tavani, ApJ Letters **497**, L21 (1998), `arXiv:astro-ph/9802192`

[6] R. Ruffini, C.L. Bianco, F. Fraschetti, S.S. Xue, P. Chardonnet, ApJ Letters **555**, L117 (2001), `arXiv:astro-ph/0106534`

[7] R. Ruffini, C.L. Bianco, F. Fraschetti, S.S. Xue, P. Chardonnet, ApJ Letters **555**, L113 (2001), `arXiv:astro-ph/0106532`

[8] R. Ruffini, C.L. Bianco, F. Fraschetti, S.S. Xue, P. Chardonnet, ApJ Letters **555**, L107 (2001), `arXiv:astro-ph/0106531`

[9] R. Ruffini, Y. Wang, M. Enderli, M. Muccino, M. Kovacevic, C.L. Bianco, A.V. Penacchioni, G.B. Pisani, J.A. Rueda, ApJ **798**, 10 (2015), `1405.5723`

[10] R. Ruffini, M. Muccino, M. Kovacevic, F.G. Oliveira, J.A. Rueda, C.L. Bianco, M. Enderli, A.V. Penacchioni, G.B. Pisani, Y. Wang et al., ApJ **808**, 190 (2015), `1412.1018`

[11] R. Ruffini, J.A. Rueda, M. Muccino, G.B. Pisani, Y. Wang, L.M. Becerra, M. Kovacevic, F.G. Oliveira, Y. Aimuratov, C.L. Bianco et al., ArXiv e-prints (2016), `1602.02732`

[12] J. Goodman, ApJ Letters **308**, L47 (1986)

[13] B. Paczynski, ApJ Letters **308**, L43 (1986)

[14] D. Eichler, M. Livio, T. Piran, D.N. Schramm, Nature **340**, 126 (1989)

[15] R. Narayan, T. Piran, A. Shemi, ApJ Letters **379**, L17 (1991)

[16] P. Meszaros, M.J. Rees, ApJ Letters **482**, L29 (1997), `astro-ph/9609065`

[17] S. Rosswog, E. Ramirez-Ruiz, M.B. Davies, MNRAS **345**, 1077 (2003), `astro-ph/0110180`

[18] W.H. Lee, E. Ramirez-Ruiz, D. Page, ApJ Letters **608**, L5 (2004), `astro-ph/0404566`

[19] E. Nakar, Physics Reports **442**, 166 (2007), `astro-ph/0701748`

[20] A. Endrizzi, R. Ciolfi, B. Giacomazzo, W. Kastaun, T. Kawamura, ArXiv e-prints (2016), `1604.03445`

[21] M. Ruiz, R.N. Lang, V. Paschalidis, S.L. Shapiro, ApJ Letters **824**, L6 (2016), `1604.02455`

[22] E. Berger, Annual Review of A&A **52**, 43 (2014), `1311.2603`

[23] K.C. Sahu, M. Livio, L. Petro, F.D. Macchetto, J. van Paradijs, C. Kouveliotou, G.J. Fishman, C.A. Meegan, P.J. Groot, T. Galama, Nature **387**, 476 (1997), `arXiv:astro-ph/9705184`

[24] J. van Paradijs, P.J. Groot, T. Galama, C. Kouveliotou, R.G. Strom, J. Telting, R.G.M. Rutten, G.J. Fishman, C.A. Meegan, M. Pettini et al., Nature **386**, 686 (1997)

[25] J.S. Bloom, J.X. Prochaska, D. Pooley, C.H. Blake, R.J. Foley, S. Jha, E. Ramirez-Ruiz, J. Granot, A.V. Filippenko, S. Sigurdsson et al., ApJ **638**, 354 (2006), `arXiv:astro-ph/0505480`

[26] E. Troja, A.R. King, P.T. O'Brien, N. Lyons, G. Cusumano, MNRAS **385**, L10 (2008), 0711.3034
[27] W. Fong, E. Berger, D.B. Fox, ApJ **708**, 9 (2010), 0909.1804
[28] E. Berger, New Astron. Rev. **55**, 1 (2011), 1005.1068
[29] D. Kopač, P. D'Avanzo, A. Melandri, S. Campana, A. Gomboc, J. Japelj, M.G. Bernardini, S. Covino, S.D. Vergani, R. Salvaterra et al., MNRAS **424**, 2392 (2012), 1203.1864
[30] S.E. Woosley, J.S. Bloom, Annual Review of A&A **44**, 507 (2006), astro-ph/0609142
[31] A.S. Fruchter, A.J. Levan, L. Strolger, P.M. Vreeswijk, S.E. Thorsett, D. Bersier, I. Burud, J.M. Castro Cerón, A.J. Castro-Tirado, C. Conselice et al., Nature **441**, 463 (2006), arXiv:astro-ph/0603537
[32] K.M. Svensson, A.J. Levan, N.R. Tanvir, A.S. Fruchter, L.G. Strolger, MNRAS **405**, 57 (2010), 1001.5042
[33] L. Izzo, R. Ruffini, A.V. Penacchioni, C.L. Bianco, L. Caito, S.K. Chakrabarti, J.A. Rueda, A. Nandi, B. Patricelli, A&A **543**, A10 (2012), 1202.4374
[34] A.V. Penacchioni, R. Ruffini, L. Izzo, M. Muccino, C.L. Bianco, L. Caito, B. Patricelli, L. Amati, A&A **538**, A58 (2012), 1112.2970
[35] N. Smith, Annual Review of A&A **52**, 487 (2014), 1402.1237
[36] N. Smith, W. Li, A.V. Filippenko, R. Chornock, MNRAS **412**, 1522 (2011), 1006.3899
[37] M. Della Valle, International Journal of Modern Physics D **20**, 1745 (2011)
[38] R. Ruffini, M.G. Bernardini, C.L. Bianco, L. Caito, P. Chardonnet, M.G. Dainotti, R. Fraschetti, R. Guida, G. Vereshchagin, S. Xue, *The Role of GRB 031203 in Clarifying the Astrophysical GRB Scenario*, in *ESA Special Publication* (2007), Vol. 622 of *ESA Special Publication*, p. 561, 0705.2456
[39] J.A. Rueda, R. Ruffini, ApJ **758**, L7 (2012)
[40] C.L. Fryer, J.A. Rueda, R. Ruffini, ApJ Letters **793**, L36 (2014), 1409.1473
[41] L. Becerra, F. Cipolletta, C.L. Fryer, J.A. Rueda, R. Ruffini, ApJ **812**, 100 (2015), 1505.07580
[42] R. Ruffini, J.A. Rueda, M. Muccino, Y. Aimuratov, L.M. Becerra, C.L. Bianco, M. Kovacevic, R. Moradi, F.G. Oliveira, G.B. Pisani et al., ApJ **832**, 136 (2016), 1602.02732
[43] J. Heise, *X-Ray Flashes and X-Ray Counterparts of Gamm-Ray Bursts*, in *Gamma-Ray Burst and Afterglow Astronomy 2001: A Workshop Celebrating the First Year of the HETE Mission*, edited by G.R. Ricker, R.K. Vanderspek (2003), Vol. 662 of *American Institute of Physics Conference Series*, pp. 229–236, astro-ph/0111246
[44] L. Amati, F. Frontera, J.J.M. in't Zand, M. Capalbi, R. Landi, P. Soffitta, L. Vetere, L.A. Antonelli, E. Costa, S. Del Sordo et al., A&A **426**, 415 (2004), astro-ph/0407166
[45] A.M. Soderberg, S.R. Kulkarni, E. Nakar, E. Berger, P.B. Cameron, D.B. Fox, D. Frail, A. Gal-Yam, R. Sari, S.B. Cenko et al., Nature **442**, 1014 (2006), astro-ph/0604389
[46] G.B. Pisani, L. Izzo, R. Ruffini, C.L. Bianco, M. Muccino, A.V. Penacchioni, J.A. Rueda, Y. Wang, A&A **552**, L5 (2013), 1304.1764
[47] R. Ruffini, M. Muccino, C.L. Bianco, M. Enderli, L. Izzo, M. Kovacevic, A.V. Penacchioni, G.B. Pisani, J.A. Rueda, Y. Wang, A&A **565**, L10 (2014), 1404.3946
[48] C.L. Fryer, F.G. Oliveira, J.A. Rueda, R. Ruffini, Physical Review Letters **115**, 231102 (2015), 1505.02809
[49] L. Becerra, C.L. Bianco, C.L. Fryer, J.A. Rueda, R. Ruffini, ApJ **833**, 107 (2016), 1606.02523
[50] R. Giacconi, R. Ruffini, *Physics and astrophysics of neutron stars and black holes* (1978)
[51] I.F. Mirabel, L.F. Rodríguez, Nature **392**, 673 (1998)
[52] L. Caito, M.G. Bernardini, C.L. Bianco, M.G. Dainotti, R. Guida, R. Ruffini, A&A **498**, 501 (2009), 0810.4855
[53] L. Caito, L. Amati, M.G. Bernardini, C.L. Bianco, G. de Barros, L. Izzo, B. Patricelli, R. Ruffini, A&A **521**, A80+ (2010), 1006.4842
[54] M. Della Valle, G. Chincarini, N. Panagia, G. Tagliaferri, D. Malesani, V. Testa, D. Fugazza, S. Campana, S. Covino, V. Mangano et al., Nature **444**, 1050 (2006), arXiv:astro-ph/0608322
[55] Z.P. Jin, X. Li, Z. Cano, S. Covino, Y.Z. Fan, D.M. Wei, ApJ Letters **811**, L22 (2015), 1507.07206
[56] M. Cadelano, C. Pallanca, F.R. Ferraro, M. Salaris, E. Dalessandro, B. Lanzoni, P.C.C. Freire, ApJ **812**, 63 (2015), 1509.01397
[57] T.M. Tauris, E.P.J. van den Heuvel, G.J. Savonije, ApJ Letters **530**, L93 (2000), astro-ph/0001013
[58] P. Lazarus, T.M. Tauris, B. Knispel, P.C.C. Freire, J.S. Deneva, V.M. Kaspi, B. Allen, S. Bogdanov, S. Chatterjee, I.H. Stairs et al., MNRAS **437**, 1485 (2014), 1310.5857
[59] R. Ruffini, J.D. Salmonson, J.R. Wilson, S.S. Xue, A&A **350**, 334 (1999), arXiv:astro-ph/9907030
[60] R. Ruffini, J.D. Salmonson, J.R. Wilson, S. Xue, A&A **359**, 855 (2000), arXiv:astro-ph/0004257
[61] A.G. Aksenov, R. Ruffini, G.V. Vereshchagin, Physical Review Letters **99**, 125003 (2007), 0707.3250
[62] A.G. Aksenov, R. Ruffini, G.V. Vereshchagin, Physical Review D **79**, 043008 (2009), 0901.4837
[63] M. Muccino, R. Ruffini, C.L. Bianco, L. Izzo, A.V. Penacchioni, ApJ **763**, 125 (2013), 1205.6600
[64] R. Ruffini, M. Muccino, Y. Aimuratov, C.L. Bianco, C. Cherubini, M. Enderli, M. Kovacevic, R. Moradi, A.V. Penacchioni, G.B. Pisani et al., ApJ **831**, 178 (2016), 1607.02400
[65] Y. Aimuratov, R. Ruffini, M. Muccino, C.L. Bianco, A.V. Penacchioni, G.B. Pisani, D. Primorac, J.A. Rueda, Y. Wang, ApJ **844**, 83 (2017), 1704.08179

[66] R. Ruffini, C.L. Bianco, P. Chardonnet, F. Fraschetti, S. Xue, ApJ Letters **581**, L19 (2002), `arXiv:astro-ph/0210648`

[67] R. Ruffini, C.L. Bianco, S.S. Xue, P. Chardonnet, F. Fraschetti, V. Gurzadyan, International Journal of Modern Physics D **13**, 843 (2004), `arXiv:astro-ph/0405284`

[68] R. Ruffini, M.G. Bernardini, C.L. Bianco, P. Chardonnet, F. Fraschetti, V. Gurzadyan, L. Vitagliano, S.S. Xue, *The Blackholic energy: long and short Gamma-Ray Bursts (New perspectives in physics and astrophysics from the theoretical understanding of Gamma-Ray Bursts, II)*, in *XIth Brazilian School of Cosmology and Gravitation*, edited by M. Novello & S. E. Perez Bergliaffa (2005), Vol. 782 of *American Institute of Physics Conference Series*, p. 42, `arXiv:astro-ph/0503476`

[69] C.L. Bianco, R. Ruffini, ApJ Letters **633**, L13 (2005), `arXiv:astro-ph/0509621`

[70] C.L. Bianco, R. Ruffini, ApJ Letters **620**, L23 (2005), `arXiv:astro-ph/0501390`

[71] R. Narayan, B. Paczynski, T. Piran, ApJ Letters **395**, L83 (1992), `arXiv:astro-ph/9204001`

[72] J.D. Salmonson, J.R. Wilson, ApJ **578**, 310 (2002), `astro-ph/0203349`

[73] Y.B. Zel'dovich, L.N. Ivanova, D.K. Nadezhin, Soviet Astronomy **16**, 209 (1972)

[74] R. Ruffini, J. Wilson, Physical Review Letters **31**, 1362 (1973)

[75] K. Maeda, K. Nomoto, ApJ **598**, 1163 (2003), `astro-ph/0304172`

[76] T.J. Galama, P.M. Vreeswijk, J. van Paradijs et al., Nature **395**, 670 (1998)

[77] S. Campana, V. Mangano, A.J. Blustin, P. Brown, D.N. Burrows, G. Chincarini, J.R. Cummings, G. Cusumano, M. Della Valle, D. Malesani et al., Nature **442**, 1008 (2006), `arXiv:astro-ph/0603279`

[78] R. Ruffini, *Black Holes, Supernovae and Gamma Ray Bursts*, in *Thirteenth Marcel Grossmann Meeting: On Recent Developments in Theoretical and Experimental General Relativity, Astrophysics and Relativistic Field Theories*, edited by K. Rosquist (2015), pp. 242–314

[79] R. Ruffini, Y. Wang, Y. Aimuratov, L. Becerra, C.L. Bianco, M. Karlica, M. Kovacevic, L. Li, J.D. Melon Fuksman, R. Moradi et al., ArXiv e-prints (2017), `1704.03821`

[80] R. Ruffini, C.L. Bianco, M. Enderli, M. Muccino, A.V. Penacchioni, G.B. Pisani, J.A. Rueda, N. Sahakyan, Y. Wang, L. Izzo, GRB Coordinates Network **14526**, 1 (2013)

[81] A. de Ugarte Postigo, D. Xu, G. Leloudas, T. Kruehler, D. Malesani, J. Gorosabel, C.C. Thoene, R. Sanchez-Ramirez, S. Schulze, J.P. Fynbo et al., GRB Coordinates Network **14646**, 1 (2013)

[82] A.J. Levan, A.S. Fruchter, J. Graham, N.R. Tanvir, J. Hjorth, J. Fynbo, D. Perley, S.B. Cenko, E. Pian, Z. Cano et al., GRB Coordinates Network **14686**, 1 (2013)

[83] A.M. Watson, N. Butler, A. Kutyrev, W.H. Lee, M.G. Richer, C. Klein, O. Fox, J.X. Prochaska, J. Bloom, A. Cucchiara et al., GRB Coordinates Network **14666**, 1 (2013)

[84] D. Xu, A. de Ugarte Postigo, T. Kruehler, D. Malesani, G. Leloudas, J.P.U. Fynbo, J. Hjorth, S. Schulze, P. Jakobsson, Z. Cano et al., GRB Coordinates Network **14597**, 1 (2013)

[85] L. Nava, G. Vianello, N. Omodei, G. Ghisellini, G. Ghirlanda, A. Celotti, F. Longo, R. Desiante, R. Barniol Duran, MNRAS **443**, 3578 (2014), `1406.6693`

[86] M. Ackermann, M. Ajello, K. Asano, M. Axelsson, L. Baldini, J. Ballet, G. Barbiellini, D. Bastieri, K. Bechtol, R. Bellazzini et al., ApJ Supplement **209**, 11 (2013), `1303.2908`

[87] F. Cipolletta, C. Cherubini, S. Filippi, J.A. Rueda, R. Ruffini, Physical Review D **92**, 023007 (2015), `1506.05926`

[88] E. Troja, S. Rosswog, N. Gehrels, ApJ **723**, 1711 (2010), `1009.1385`

[89] R. Belvedere, J.A. Rueda, R. Ruffini, Journal of Korean Physical Society **65**, 897 (2014)

[90] Y. Lithwick, R. Sari, ApJ **555**, 540 (2001)

[91] L.D. Landau, E.M. Lifshitz, *The classical theory of fields* (Course of theoretical physics - Pergamon International Library of Science, Technology, Engineering and Social Studies, Oxford: Pergamon Press, 4th rev.engl.ed., 1975)

[92] K. Boshkayev, J.A. Rueda, R. Ruffini, I. Siutsou, ApJ **762**, 117 (2013), `1204.2070`

[93] R. Ruffini, G. Vereshchagin, S. Xue, Physics Reports **487**, 1 (2010), `0910.0974`

[94] F. Özel, P. Freire, Annual Review of A&A **54**, 401 (2016), `1603.02698`

[95] F.G. Oliveira, J.A. Rueda, R. Ruffini, ApJ **787**, 150 (2014)

[96] R. Ruffini, J. Rodriguez, M. Muccino, J.A. Rueda, Y. Aimuratov, U. Barres de Almeida, L. Becerra, C.L. Bianco, C. Cherubini, S. Filippi et al., ArXiv e-prints (2016), `1602.03545`

EPJ Web of Conferences **168**, 02005 (2018) https://doi.org/10.1051/epjconf/201816802005
Joint International Conference of ICGAC-XIII and IK-15 on Gravitation, Astrophysics and Cosmology

On the Induced Gravitational Collapse

Laura M. Becerra[1,2,⋆], *Carlo* Bianco[1,2], *Chris* Fryer[4], *Jorge* Rueda[1,2,3], and *Remo* Ruffini[1,2,3]

[1] *Dipartimento di Fisica and ICRA, Sapienza Università di Roma, P.le Aldo Moro 5, I–00185 Rome, Italy*
[2] *ICRANet, P.zza della Repubblica 10, I–65122 Pescara, Italy*
[3] *ICRANet-Rio, Centro Brasileiro de Pesquisas Físicas, Rua Dr. Xavier Sigaud 150, 22290–180 Rio de Janeiro, Brazil*
[4] *CCS-2, Los Alamos National Laboratory, Los Alamos, NM 87545*

Abstract. The induced gravitational collapse (IGC) paradigm has been applied to explain the long gamma ray burst (GRB) associated with type Ic supernova, and recently the X-ray flashes (XRFs). The progenitor is a binary systems of a carbon-oxygen core (CO) and a neutron star (NS). The CO core collapses and undergoes a supernova explosion which triggers the hypercritical accretion onto the NS companion (up to $10^{-2}\,M_{\odot}s^{-1}$). For the binary driven hypernova (BdHNe), the binary system is enough bound, the NS reach its critical mass, and collapse to a black hole (BH) with a GRB emission characterized by an isotropic energy $E_{iso} > 10^{52}$ erg . Otherwise, for binary systems with larger binary separations, the hypercritical accretion onto the NS is not sufficient to induced its gravitational collapse, a X-ray flash is produced with $E_{\rm iso} < 10^{52}$ erg. We're going to focus in identify the binary parameters that limits the BdHNe systems with the XRFs systems.

1 Introduction

In [1], the progenitors of long gamma-ray bursts (GRBs) have been explained within the Induced Gravitational Collapse (IGC) paradigm. The initial configuration is a compact binary system, formed by a Carbon-Oxygen (CO) core, a star that has lost its helium and hydrogen layers, with a neutron star (NS). The CO-core collapses and produces a supernova explosion that triggers an hypercritical accretion onto the NS companion. If the hypercritical accretion on the NS is not enough to make it to reach the critical mass for gravitational collapse, a first scenario takes place characterized by a x-ray flash (XRF) emission. The final system will be a NS-NS binary, formed by the ν-NS, the remnant from the collapse of the CO-core, and a more massive NS. This kind of events are characterized by isotropic energies of $E_{\rm iso} \lesssim 10^{52}$ erg, peak energies between $4 < E_{\rm p,i} < 200$ keV and a prompt emission duration of about $\sim 10^2 - 10^4$ s. Otherwise if the system is enough compact, the NS companion reaches by accretion the critical mass and collapses to a black hole (BH). These systems have been called binary-driven hypernovae (BdHNe) and has been deeply studied in [1–5, 10, 11] . The BdHNe events are characterized by isotropic energies $E_{\rm iso} \gtrsim 10^{52}$ erg, spectral peak energy in $0.2 < E_{\rm p,i} < 2$ MeV and prompt emission with durations of up to 100 s. The final system is a νNS-BH binary [6].

In this proceedings, we will identify the principal parameters of the initial binary configurations that can leave either to XRFs or BdHNe. In section 2, we estimate the accretion rate on the NS and

⋆e-mail: laura.maarcela@icranet.com

follow its mass and angular momentum evolution in order to establish critical binary initial parameters that determined the final fate of the system after the supernova explosion. In section 3, we model the light-curve of the XRF 060218 with the IGC scenario and finally in section 4 we resume our results.

2 Hypercritical Accretion process

Following the Bondy-Hoyle-Lyttleton formalism [7–9], an estimation of the accretion rate of the ejected material onto the NS is given by:

$$\dot{M}_B = \pi \rho_{\rm ej} R_{\rm cap}^2 \sqrt{v_{\rm ej}^2 + v_{\rm orb}^2 + c_{\rm s,ej}^2}, \quad \text{with} \quad R_{\rm cap} = \frac{2GM_{\rm NS}}{v_{\rm ej}^2 + v_{\rm orb}^2 + c_{\rm s,ej}^2} \tag{1}$$

where $R_{\rm cap}$ is the NS gravitational capture radius, G is the gravitational constant, $\rho_{\rm ej}$ and $\vec{v}_{\rm ej}$ the density and velocity of the supernova ejecta, $M_{\rm NS}$ the NS mass, $v_{\rm orb} = \sqrt{G\left(M_{\rm NS} + M_{\rm CO}\right)/a}$ is the orbital velocity of the binary system, with a the binary separation, and $M_{\rm CO} = M_{\rm env} + M_{\rm Fe}$ the total mass of the CO core which consist of the envelope mass $M_{\rm env}$ that will be ejected in the SN explosion and the central iron core mass, $M_{\rm Fe}$. In order to integrate equation (1), we have fitted the pre-supernova density profile of the CO envelope with a power-law, $\rho_{\rm ej} \propto r^{-m}$ with $m < 3.0$, and adopted an homologous explosion model for the supernova expansion (see [10, 11] for details). The left panel of figure 1 shows the evolution of the mass accretion rate onto the NS. We have used, as our canonical model, an initial binary system of a $2\,M_\odot$ NS and the CO-core of a $30\,M_{\rm zams}$ progenitor, that ejects $M_{\rm env} = 7.94\,M_\odot$ in the SN explosion and leaves an iron core of $M_{\rm Fe} = 1.5\,M_\odot$. The accretion on the NS can be as high as $\sim\ 10^{-1}\,M_\odot\,s^{-1}$. For these high accretions, the photons would be trapped in the accretion flow and the gain of gravitational energy of the accreted material is mainly radiated via neutrino emission, specifically, by the e^+e^- pair annihilation process [12–14].

2.1 Mass and angular momentum evolution of the NS companion during the hypercritical accretion

If we want to discriminate the binary parameters of the systems in which the NS can reach, by accretion, its critical mass ($M_{\rm crit}$) and consequently collapse to a BH, from the systems in which the

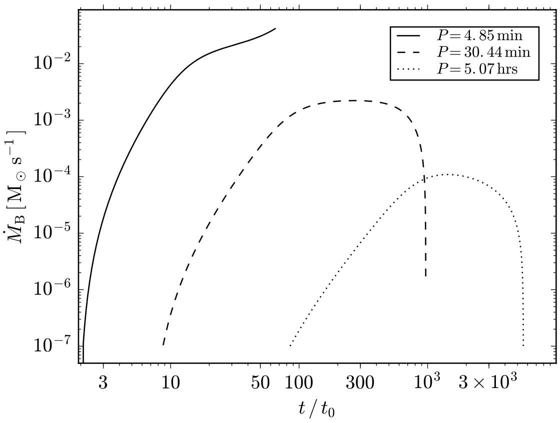

(a)

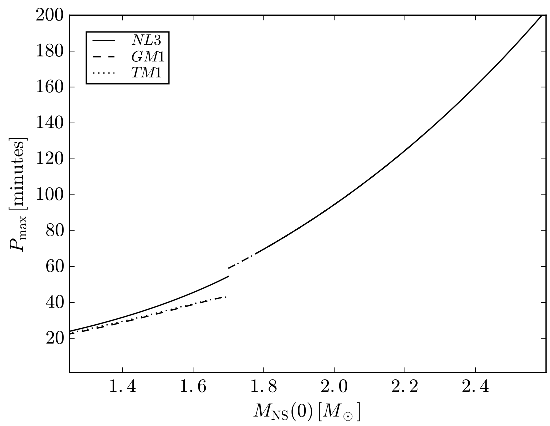

(b)

Figure 1. Left: Evolution of the mass accretion rate on the NS companion calculated with the Bondy-Hoyle-Lyttleton accretion formalism for three selected orbital period. The initial binary system is formed by a $2\,M_\odot$ NS and the CO-core of a $30\,M_{\rm zamns}$ progenitor. Right: Maximum orbital period for which the NS reaches its critical mass by the accretion of material from the SN ejecta and collapse in a BH.

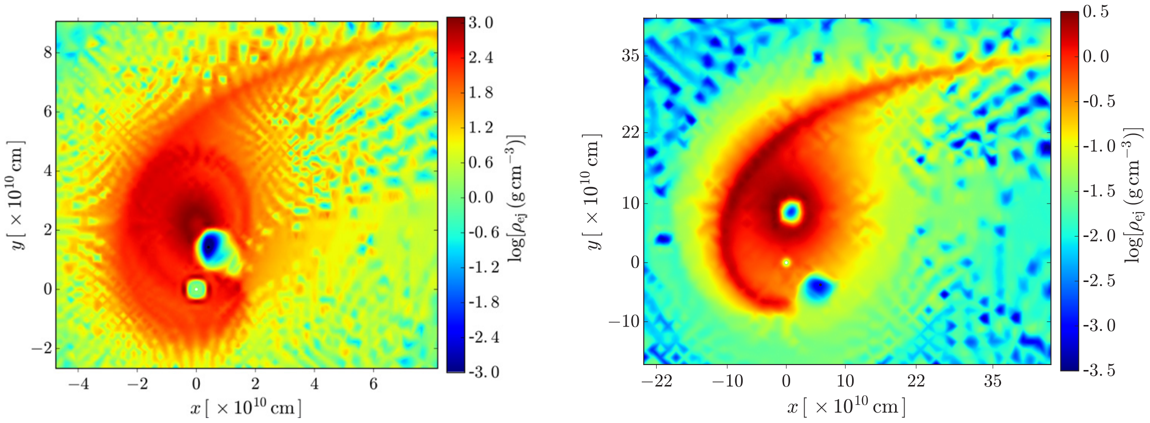

(a) (b)

Figure 2. Snapshots of the supernova ejecta density on the binary equatorial plane in the IGC scenario. We used the binary parameter of our canonical model. The left panel corresponds to a binary initial period of $P_{\rm orb} = 5$ min and the picture is made at 100 s after the collapse of the NS. The right panel corresponds to a period of $P_{\rm orb} = 50$ min. In this case the NS does not collapse and the snapshot is at $t \approx 44$ min.

accretion is not sufficient to induce such a collapse, we need to determine how the NS evolves during the accretion process. In general, the accretion of baryonic mass, M_b, as well as the accretion of angular momentum $J_{\rm NS}$, will modify the NS gravitational mass, $M_{\rm NS}$ in the following way:

$$\dot{M}_{\rm NS}(t) = \frac{\partial M_{\rm NS}}{\partial M_b}\dot{M}_b + \frac{\partial M_{\rm NS}}{\partial J_{\rm NS}}\dot{J}_{\rm NS}, \tag{2}$$

In [10] it was demonstrated that the supernova ejecta material has enough angular momentum to circularize around the NS and form a disk-like structure. Then, the NS angular momentum evolution is dictated by the disk accretion torque: $\dot{J}_{\rm NS} = \xi l(R_{\rm in})\dot{M}_B$, with $l(R_{\rm in})$ the angular momentum per unit mass of the material located at $r = R_{\rm in}$, the disk inner boundary radius, that will be the maximum between the radius of the last stable circular orbit, $r_{\rm lso}$, and the NS radius, $R_{\rm NS}$. We have also introduced a parameter $\xi \leq 1$ that accounts for the efficiency of the angular momentum transfer. Additionally, if we assume that all the mass entering the NS capture region will be accreted by the NS as baryonic mass: $M_b(t) = M_b(t_0) + M_B(t)$, then $\dot{M}_b = \dot{M}_B$, we can integrate equation (2) to follow the evolution of the NS during the accretion process. We have used the fitting formulas obtained in [15, 16] for the relations between the NS gravitational mass with its baryonic mass and angular momentum as well as the angular momentum of the last stable orbit.

Thus, a NS with initial mass $M_{\rm NS}(t_0)$ can reach $M_{\rm crit}$ if it accretes an amount of mass $\Delta M_{\rm acc} = M_{\rm crit} - M_{\rm NS}(t_0)$ from the supernova ejecta. This critical mass will depend, in general, on the EoS consider to model the NS matter and, in the case of a rotating NS, n the star angular momentum [15]. Therefore, given the initial NS mass, the CO core mass, and the supernova ejecta profile and its velocity, the accretion rate increases for shorter orbital periods. Therefore, there exists a maximum orbital period, $P_{\rm max}$, up to which, given $M_{\rm NS}(t_0)$ (and all the other binary parameters), the NS can accreate this precise amount of mass, $\Delta M_{\rm acc}$. The right panel of figure 1 shows $P_{\rm max}$ as a function of the NS initial mass, for a CO core progenitor of 30 $M_{\rm zmans}$.

3 SN-asymmetries induced by the NS companion presence

For supernova explosions occurring in close binaries with compact companions such as NSs or BHs, like the case of the IGC scenario, the supernova ejecta is subjected to a strong gravitational field

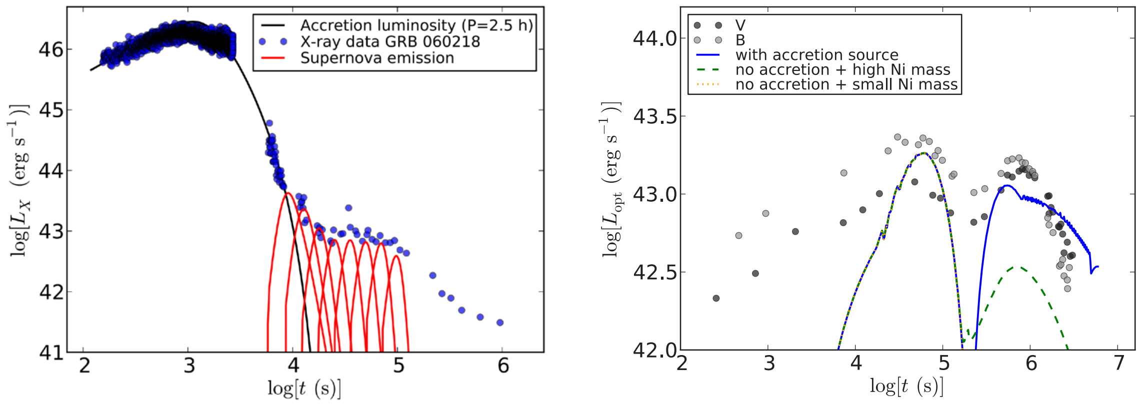

(a) (b)

Figure 3. Left: Comparison of the accretion and the supernova luminosity with the observed X-ray luminosity of XRF 060218. The binary system has the following parameters: supernova velocity $v_{\rm star,0} = 2 \times 10^9$ cm s^{-1}, a pre-supernova core obtained from the $M_{\rm ZAMS} = 20\ M_\odot$ evolution, initial NS mass $M_{\rm NS}(t_0) = 1.4\ M_\odot$, and orbital period of 2.5 h. Right: Optical and UV luminosity of XRF 060218 [18]. The red dotted curve shows the supernova optical emission without either ^{56}Ni decay or accretion energy. The blue solid curve includes the energy deposition from the accretion onto the NS. The dashed green curve increases the total ^{56}Ni yield but cannot explain the observational data.

which produces a deformation of the supernova fronts closer to the accreting companion. In order to visualize this, we have simulated the evolution of the supernova layers in the binary system by dividing the SN ejecta in N particles of different mass and following its three-dimensional motion under the action of the gravitational field of the orbiting NS. We have varied the NS gravitational mass with equations (1) and (2) and also, we have removed from the simulation the particles that are crossing the Bondi-Hoyle radius. Figure 2 shows the surface density on the equatorial plane for the canonical initial binary system parameters. The left panel corresponds to an orbital period of about $P \approx 5$ min and its made at 100 s after the collapse of the NS companion and the formation of the BH . It can be seen the increasing asymmetry of the supernova ejecta around the orbital plane. Even for longer binary periods, from which the accretion does not lead to the collapse of the NS, the asymmetries can still be formed, as in shown in the right panel of figure 2. This system corresponds to a orbital period of about $P \approx 50$ min.

In order to validate the IGC scenario, we have to contrast it with the observations. In the left panel of figure 3 we present the observed X-ray luminosity of XRF 060218. The early part of the light-curve ($t \lesssim 10^3$ s) has been fitted with the luminosity expected from the accretion process on the NS companion, that was estimated as: $L_{\rm acc} = (\dot{M}_b - \dot{M}_{\rm NS})c^2$, the amount of gravitational energy gained by the accreted matter by falling to the NS surface and which is not spent in changing the gravitational binding energy of the NS.

For the long-lasting X-ray plateau in the afterglow (at times $t \sim 10^3$–10^6 s) we need to analyze the emission of the supernova at early stages. We have calculated the shock breakout luminosity using the light-curve code described in [17]. To simulate the energy that the hypercritical accretion process onto the NS adds to the ejecta, we injected it as an energy source at the base of the explosion and to mimic the asymmetries in the SN ejecta, caused by the NS companion presence (see figures 2), we have modeled a series of spherical explosions with different densities. For XRF 060218, we assume an initial explosion energy of 2×10^{51} erg, ranging the spherical equivalent-mass from 0.05–4 $M_\odot$. Figure 3 shows light-curves rising quickly at $t \lesssim 10^4$ s for the lowest mass to $\sim 10^5$ s for the 4 $M_\odot$

explosion. The observed emission would come from the sum of this full range of explosions (see [11] for details).

Finally, the right panel of figure 3 shows the V and B band light-curves for XRF 060218 [18]. The light-curve has two peaks: near 50,000 s and at 500,000 s. Using our 1 $M_\odot$ 1D model from our X-ray emission, we simulate the V and B band light-curves. Without either ^{56}Ni decay or accretion energy, the supernova explosion only explains the first peak. However, if we include the energy deposition from the accretion onto the NS (for our energy deposition, we use 4×10^{46} erg s^{-1} over a 2500 s duration), our simulations produce a second peak at roughly 500,000 s (see [11] for details).

4 Conclusions

We have studied the IGC paradigm to explain the nature of BdHNe and XRFs. We have followed the accretion onto the NS and computed the binary period, $P_{\rm max}$, over which the NS does not accrete sufficient matter to reach the critical mass and produce a BH. We have shown that the presence of the NS in very compact orbit produces large asymmetries in the supernova ejecta around the orbital plane due to the accretion and the action of the NS gravitational field on the supernova layers. These asymmetries lead to observable effects in the supernova emission. We have analyzed the light curve of XRF 060218 and explained its prompt emission ($t \lesssim 10^3$ s) with the accretion luminosity. We have shown that the observed long-lasting ($t > 10^3$ s) afterglow X-ray emission can be powered by a sequence of shock breakouts in different directions: the more massive directions produce later shock breakouts. Finally, we have simulated the optical emission of the supernova and compared our theoretical expectation with the optical luminosity of XRF 060218 which shows a peculiar double-peaked shape. We demonstrated that the source of energy given by the hypercritical accretion onto the NS provides a double-peaked light-curve consistent with the observational data.

References

[1] Ruffini, R., Rueda, J. A., Muccino, M., et al., ApJ **832**, 136 (2016)
[2] Ruffini, R., Bernardini, M. G., Bianco, C. L., et al. *Proceedings of the MG10 Meeting* (Singapore: World Scientific Publishing, Rio de Janeiro, Brazil, 2003) 369
[3] Izzo, L., Rueda, J. A., & Ruffini, R., A&A **548**, L5 (2012)
[4] Rueda, J. A., & Ruffini, R., ApJL, **758**, L7 (2012)
[5] Fryer, C. L. and Rueda, J. A. and Ruffini, R., ApJL, **793**, L36 (2014)
[6] Fryer, C. L. and Oliveira, F. G. and Rueda, J. A. and Ruffini, R., PhRvL, **115**, 231102 (2015)
[7] Hoyle, F., & Lyttleton, R. A., Proceedings of the Cambridge Philosophical Society **35**, 405 (1939)
[8] Bondi, H., & Hoyle, F., MNRAS **104**, 273 (1944)
[9] Bondi, H., MNRAS **112**, 195 (1952)
[10] Becerra, L., Cipolletta, F., Fryer, C. L., Rueda, J. A., & Ruffini, R., ApJ **812**, 100 (2015)
[11] Becerra, L., Bianco, C., Fryer, C. L., Rueda, J. A., & Ruffini, R., ApJ **833**, 107 (2016)
[12] Zel'dovich, Y. B., Ivanova, L. N., & Nadezhin, D. K., Soviet Ast **16**, 209 (1972)
[13] Chevalier, R. A., ApJ **346**, 847 (1989)
[14] Fryer, C. L., Benz, W., & Herant, M., ApJ **460**, 801 (1996)
[15] Cipolletta, F., Cherubini, C., Filippi, S., Rueda, J. A., & Ruffini, R., PhRvD **92**, 023007 (2015)
[16] Cipolletta, F. and Cherubini, C. and Filippi, S. and Rueda, J. A., & Ruffini, R., PhRvD **96**, 024046 (2017)
[17] Bayless, A. J., Even, W., Frey, L. H., et al., ApJ **805**, 98 (2015)
[18] Pian, E., Mazzali, P. A., Masetti, N., et al. 2006, Nature **442**, 1011 (2006)

EPJ Web of Conferences **168**, 04002 (2018) https://doi.org/10.1051/epjconf/201816804002
Joint International Conference of ICGAC-XIII and IK-15 on Gravitation, Astrophysics and Cosmology

THE FIRST ICRANET CATALOG OF BINARY-DRIVEN HYPERNOVAE

G. B. Pisani[1,2], R. Ruffini[1,2,3,4], Y. Aimuratov[1,2,3], C. L. Bianco[1,2], M. Karlica[1,2,3], M. Kovacevic[1,2,3], R. Moradi[1,2], M. Muccino[1,2], A. V. Penacchioni[5,6], D. Primorac[1,2], J. A. Rueda[1,2,4], Y. Wang[1,2]

Draft version September 18, 2017

ABSTRACT

In a series of recent publications, scientists from ICRANet, led by professor Remo Ruffini, have reached a novel comprehensive picture of gamma-ray bursts (GRBs) thanks to their development of a series of new theoretical approaches. Among those, the induced gravitational collapse (IGC) paradigm explains a class of energetic, long-duration GRBs associated with Ib/c supernovae (SN), recently named binary-driven hypernovae (BdHNe).
BdHNe have a well defined set of observational features which allow to identify them. Among them, the main two are: 1) long duration of the GRB explosion, namely larger than 2 s in the rest frame; 2) a total energy, released in all directions by the GRB explosion, larger than 10^{52} ergs.
A striking result is the observation, in the BdHNe sources, of a universal late time power-law decay in the X-rays luminosity after 10^4 s, with typical decaying slope of ~ 1.5. This leads to the possible establishment of a new distance indicator having redshift up to $z \sim 8$.
Thanks to this novel theoretical and observational understanding, it was possible for ICRANet scientists to build the firstst BdHNe catalog, composed by the 345 BdHNe identified up to the end of 2016.

Keywords: supernovae: general — binaries: general — gamma-ray burst: general — stars: neutron

1. TOWARDS A FIRST CATALOG OF BINARY-DRIVEN HYPERNOVAE

The first observations by the BATSE instrument on board the Compton γ-ray Observatory satellite have evidenced what has later become known as the prompt radiation of GRBs. On the basis of their hardness as well as their duration, GRBs were initially classified into short and long in an epoch when their cosmological nature was still being debated (Mazets et al. 1981; Klebesadel 1992; Dezalay et al. 1992; Kouveliotou et al. 1993; Tavani 1998).

The advent of the *BeppoSAX* satellite (Boella et al. 1997) introduced a new approach to GRBs by introducing joint observations in the X-rays and γ-rays thanks to its instruments: the Gamma-ray Burst Monitor (40–700 keV), the Wide Field Cameras (2–26 keV), and the Narrow Field Instruments (2-10 keV). The unexpected discovery of a well separate component in the GRB soon appeared: the afterglow, namely a radiation lasting up to 10^5–10^6 s after the emission of the prompt radiation (see Costa et al. 1997a,b; Frontera et al. 1998, 2000; de Pasquale et al. 2006). Beppo-SAX clearly indicated the existence of a power law behavior in the late X-ray emission (LXRE).

The coming of the *Swift* satellite (Gehrels et al. 2004; Evans et al. 2007, 2010), significantly extending the observation energy band to the X-ray band thanks to its X-ray Telescope (XRT band: 0.3–10 keV), has allowed us for the first time to uncover the unexplored region between the end of the prompt radiation and the power-law late X-ray behavior discovered by *BeppoSAX*: in some long GRBs, a steep decay phase was observed leading to a plateau followed then by a typical LXRE power law behavior (Evans et al. 2007, 2010).

Recently, Pisani et al. (2013) noticed the unexpected result that the LXREs of a “golden sample” (GS) of six long, closeby ($z \lesssim 1$), energetic ($E_{iso} > 10^{52}$ erg) GRBs, when moved in the rest-frame of the sources, were showing a common power-law behavior (see Fig. 1), independently from the isotropic energy E_{iso} coming from the GRB prompt radiation (see Fig 2). More unexpected was the fact that the plateau luminosity and duration before merging in the common LXRE power-law behavior were clearly functions of the E_{iso} (see Fig. 2, and Ruffini et al. 2014c), while the late power-law remains independent from the E_{iso} of the prompt emission (see Fig. 1–2, and Pisani et al. 2013; Ruffini et al. 2014c). For this reason, this striking scaling law has been used as a distance indicator to independently estimate the cosmological redshift of some long GRBs by imposing the overlap of their LXRE (see, e.g., Penacchioni et al. 2012, 2013; Ruffini et al. 2013b,c, 2014a), and also to predict, ten days in advance, the observation of the typical optical signature of the supernova SN 2013cq, associated with GRB 130427A (Ruffini et al. 2015, 2013a; de Ugarte Postigo et al. 2013; Levan et al. 2013).

All these analyses are based on the paradigms introduced in Ruffini et al. (2001a) for the space-time parametrization of the GRB phenomena, in Ruffini et al. (2001b) for the interpretation of the structure of the GRB prompt radiation, and in Ruffini et al. (2001c) for the induced gravitational collapse (IGC) mechanism, further

[1] Dipartimento di Fisica, Sapienza Università di Roma and ICRA, Piazzale Aldo Moro 5, I-00185 Roma, Italy
[2] International Center for Relativistic Astrophysics Network (ICRANet), Piazza della Repubblica 10, I-65122 Pescara, Italy
[3] Université de Nice Sophia-Antipolis, Grand Château Parc Valrose, Nice, CEDEX 2, France
[4] ICRANet-Rio, Centro Brasileiro de Pesquisas Fisicas, Rua Dr. Xavier Sigaud 150, Rio de Janeiro, RJ, 22290-180, Brazil
[5] University of Siena, Department of Physical Sciences, Earth and Environment, Via Roma 56, I-53100 Siena, Italy
[6] ASI Science Data Center, via del Politecnico s.n.c., I-00133 Rome Italy

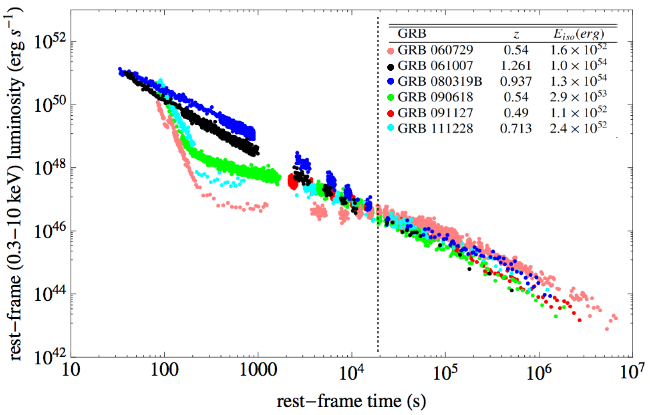

Figure 1. Scaling law found in the isotropic X-ray late times luminosity within the GS by Pisani et al. (2013). Despite the different early behavior, the different light curves join all together the same power law after a rest-frame time of $t_{rf} \sim 2 \times 10^4$ s.

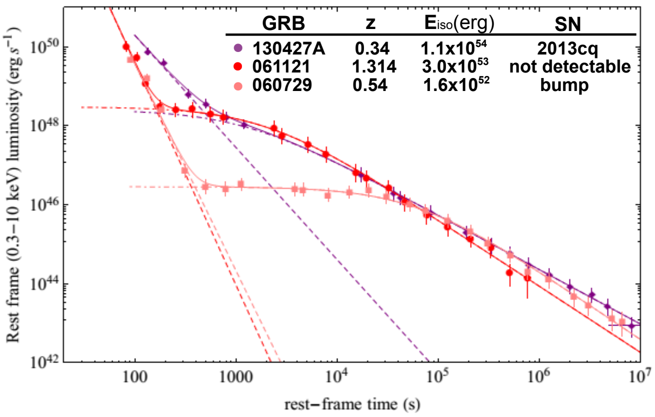

Figure 2. Nested structure of the isotropic X-ray luminosity of the BdHNe. This includes the previously mentioned scaling law of the late power law and leads to an inverse proportionality between the luminosity of the plateau and the rest-frame time delimiting its end and the beginning of the late power law decay Ruffini et al. (2014c).

developed in Ruffini et al. (2007),Rueda & Ruffini (2012), Fryer et al. (2014), and Ruffini et al. (2016). In the present case, the phenomenon points to an IGC occurring when a tight binary system composed of a carbon-oxygen core (CO_{core}) undergoes a supernova (SN) explosion in the presence of a binary neutron star (NS) companion (Ruffini et al. 2001b, 2007; Izzo et al. 2012; Rueda & Ruffini 2012; Fryer et al. 2014; Ruffini et al. 2015). When the IGC leads the NS to accrete enough matter and therefore to collapse to a black hole (BH), the GRB shows a long duration, and its prompt emission overtakes the treshold value of 10^{52} ergs. The overall observed phenomenon is called binary-driven hypernova (BdHN; Fryer et al. 2014; Ruffini et al. 2015, 2016).

A decisive further step has been the identification as a BdHN of GRB 090423 (Ruffini et al. 2014b) at the extremely high redshift of $z = 8.2$ (Salvaterra et al. 2009; Tanvir et al. 2009). On top of that, the LXRE of GRB 090423 overlaps entirely with the ones of the GS (see Fig. 3), extending such a scaling law up to extreme cosmological distances. This result led to the necessity of checking such an common behavior of the LXREs in BdHNe at redshifts larger than $z \sim 1$.

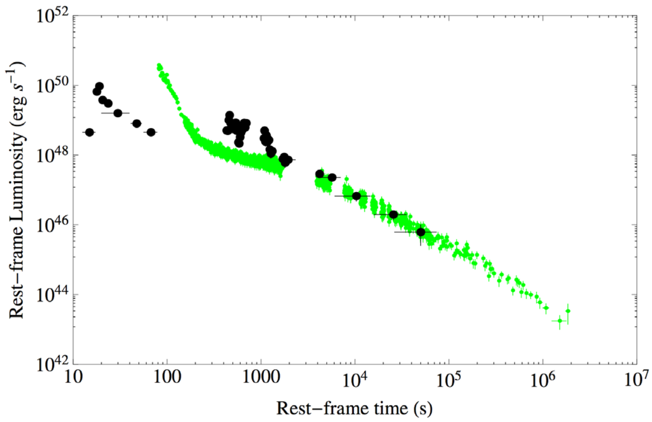

Figure 3. X-ray luminosity of GRB 090423 (black points) compared with the one of GRB 090618 (green points), the prototype BdHN, by Ruffini et al. (2014b).

In Pisani et al. (2016), we present an "enlarged sample" (ES) of 161 BdHNe observed up to the end of 2015. In this work we analysed the signatures contained in the LXREs at $t_{rf} \gtrsim 10^4$ s, where t_{rf} is the rest-frame time after the initial GRB explosion. In particular, we probed a further improvement for the presence of such an LXRE universal behavior of BdHNe by the introduction of a collimation effect within the emission mechanism.

In our recent work (Ruffini et al. 2017), we focused on analyzing the early X-Ray Flares in the GRB flare-plateau-afterglow (FPA) phase observed by Swift/XRT. The FPA occurs only in the BdHNe while is not present in the other subclasses of GRBs, for details see Ruffini et al. (2016). The sample presented in Table 9 of Ruffini et al. (2017), namely an updated version of the ES up to the end of 2016, together with the BdHNe lacking LXRE data and the ones from the pre-Swift-era, counts 345 BdHNe in total. This represents the current BdHNe catalog from ICRANet.

In the following, we present various insightful results which ICRANet scientists gained from this catalog: in Sections 2, 3, and 4, we describe how we built the ES and we study the LXRE features within it; finally, in Section 5 we refer to our up-to-date catalog of BdHNe and we draw our perspectives.

2. THE FIRST ENLARGED SAMPLE OF BDHN

Starting from the GS originally presented in Pisani et al. (2013), in Pisani et al. (2016) we have built a new sample of BdHNe, which we called "enlarged sample" (ES), under the following selection criteria:

- measured redshift z;
- GRB rest-frame duration larger than 2 s;
- isotropic energy E_{iso} larger than 10^{52} erg; and
- presence of associated *Swift*/XRT data lasting at least up to $t_{rf} = 10^4$ s.

We collected 161 sources, satisfying our criteria, which cover 11 years of *Swift*/XRT observations, up to the end of 2015, see Table 2 of Pisani et al. (2016). The E_{iso} of each source has been estimated using the observed redshift z together with the best-fit parameters of the

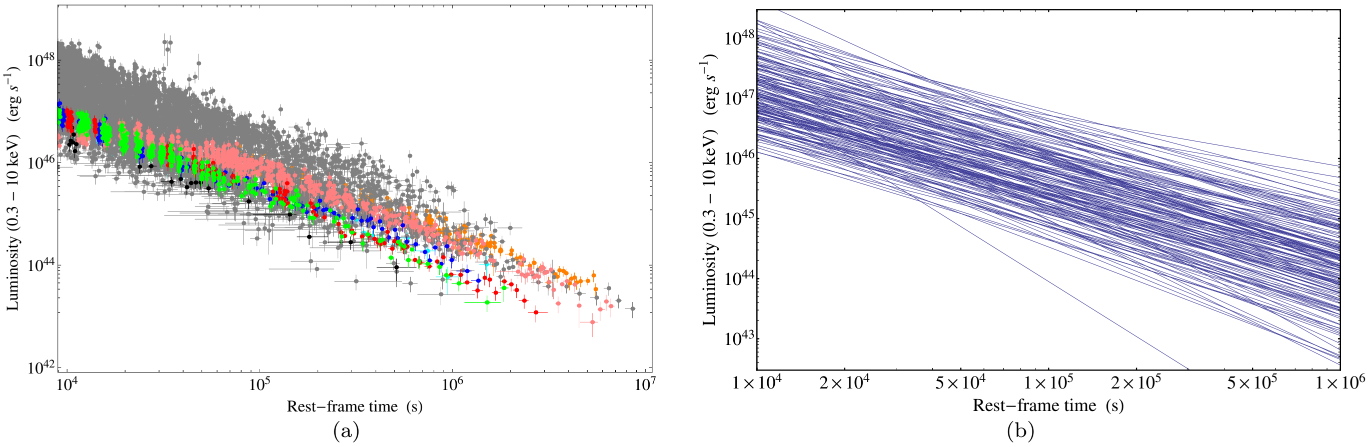

Figure 4. Panel (a): LXRE luminosity light curves of all 161 sources of the ES (gray) compared with the ones of the GS: GRB 060729 (pink), GRB 061007 (black), GRB 080913B (blue), GRB 090618 (green), GRB 091127 (red), and GRB 111228 (cyan), plus GRB 130427A (orange; from Pisani et al. 2016). Panel (b): power laws which best fit the luminosity light curves of the X-ray emissions of all 161 sources of the ES (from Pisani et al. 2016).

γ-ray spectrum published in the GCN circular archive[7]. Most of of the ES sources, 102 out of 161, have γ-ray data observed by *Fermi*/GBM and Konus-WIND, which, with their energy bands being 10–1000 keV and 20–2000 keV, respectively, lead to a solid estimate of the E_{iso}, computed in the "bolometric" 1–10^4 keV band (Bloom et al. 2001). The remaining sources of the ES have had their γ-ray emission provided by *Swift*/BAT only, with the unique exception of one source observed by HETE. The energy bands of these two detectors, being 15–150 keV and 8–400 keV, respectively, lead to an estimate of E_{iso} by extrapolation in the "bolometric" 1–10^4 keV band (Bloom et al. 2001).

3. GOING TO THE REST-FRAME

We compare the *Swift*/XRT isotropic luminosity light curve $L_{iso}(t_{rf})$ for 161 GRBs of the ES in the common rest-frame energy range of $0.3-10$ keV. We initially adjust the observed *Swift*/XRT flux f_{obs} as if it had been observed in the $0.3-10$ keV rest-frame energy range. In the detector frame, the $0.3-10$ keV rest-frame energy band becomes $[0.3/(1+z)]-[10/(1+z)]$ keV, where z is the measured redshift of the GRB. We assume a simple power-law as the best fit for the spectral energy distribution of the *Swift*/XRT data[8]:

$$\frac{dN}{dA\,dt\,dE} \propto E^{-\gamma}\,. \tag{1}$$

Hence, we can calculate the flux light curve in the $0.3-10$ keV rest-frame energy band, f_{rf}, multiplying the observed one, f_{obs}, by the k-correctionr:

$$f_{rf} = f_{obs}\frac{\int_{\frac{0.3\,keV}{1+z}}^{\frac{10\,keV}{1+z}} E^{1-\gamma}dE}{\int_{0.3\,keV}^{10\,keV} E^{1-\gamma}dE} = f_{obs}(1+z)^{\gamma-2}\,. \tag{2}$$

Then, to calculate the isotropic X-ray luminosity L_{iso}, we need to multiply f_{rf} by the spherical surface having the luminosity distance as radius

$$L_{iso} = 4\,\pi\, d_l^2(z) f_{rf}\,, \tag{3}$$

where we assume a standard cosmological ΛCDM model, namely $\Omega_m = 0.27$ and $\Omega_\Lambda = 0.73$. In the end, we convert the observed times into rest-frame times t_{rf}:

$$t_{rf} = \frac{t_{obs}}{1+z}\,. \tag{4}$$

After, we fit the isotropic luminosity light-curve late phase with a decaying power-law function defined as:

$$L_{iso}(t_{rf}) = L_0\; t_{rf}^{-\alpha}\,, \tag{5}$$

where α, the power law index, is a positive number, and L_0 is the luminosity at a fixed time $t_{rf} = t_0$ after the GRB initial explosion in the rest-frame of the source. All the power-laws are shown in Fig. 4b. Fig. 5a shows the distribution of the α indexes within the ES. This distribution follows a Gaussian behavior having a mean value of $\mu_\alpha = 1.48$ and a standard deviation of $\sigma_\alpha = 0.32$. The LXRE luminosity light curves of the ES in the 0.3–10 keV rest-frame energy range are plotted in Fig. 4a, together with the curves of the GS. Fig. 4a shows that the power-laws within the ES span around two orders of magnitude in luminosity. The spread of the LXRE light curves in the ES is better shown off by Fig. 5b which display the distribution within the ES of the LXRE integrated energies E_{LT} defined as:

$$E_{LT} \equiv \int_{10^4 s}^{10^6 s} L_{iso}(t_{rf})\,\mathrm{d}t_{rf}\,. \tag{6}$$

The solid red line in Fig. 5b is the Gaussian function that best fits the late integrated energies E_{LT} in logarithmic scale. Its mean value is $\mu_{\mathrm{Log}_{10}(E_{LT})} = 51.40$, and its standard deviation is $\sigma_{\mathrm{Log}_{10}(E_{LT})} = 0.47$.

The LXRE power-law spread, given approximately by $2\sigma_{\mathrm{Log}_{10}(E_{LT})} = 0.94$, is larger than the one of the previous work of Pisani et al. (2013), which results as $2\sigma_{\mathrm{Log}_{10}(E_{LT})} = 0.56$. This is certainly due to the important growth of the number of BdHNe composing the ES (161) in respect to the ones of the GS (6).

Moreover, there is no evidence for a correlation between the LXRE power-law behavior and the isotropic energy radiated by the source during the GRB prompt radiation (for details, see Pisani et al. 2016).

[7] http://gcn.gsfc.nasa.gov/gcn3_archive.html
[8] http://www.swift.ac.uk/

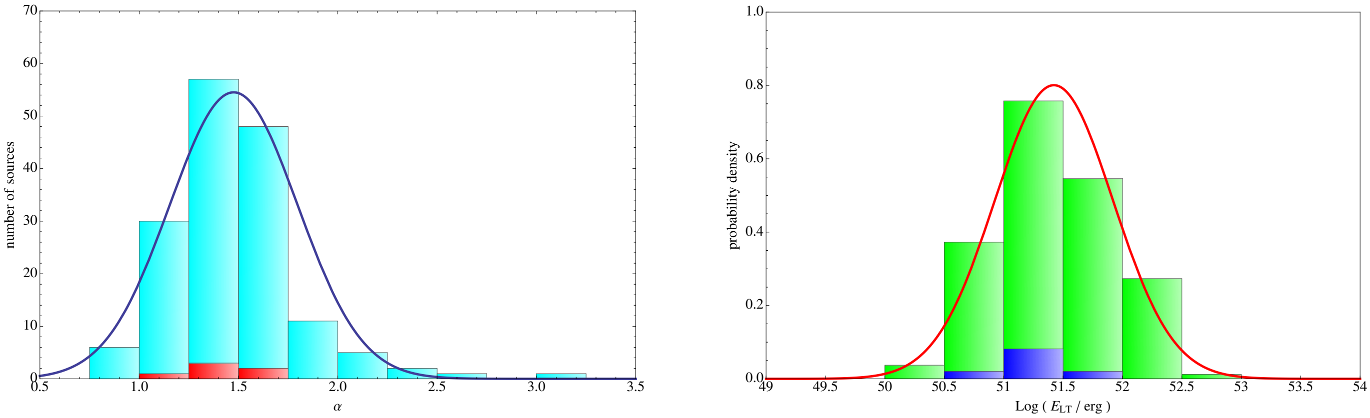

Figure 5. Panel (a): distribution of the LXRE power law indexes α within the ES (cyan) compared to the one of the GS (red). Such a distribution follows a Gaussian behavior (blue line) with a mean value of $\mu_\alpha = 1.48$ and a standard deviation of $\sigma_\alpha = 0.32$ (from Pisani et al. 2016). Panel (b): probability distribution of the LXRE integrated energies within the time interval 10^4–10^6 s in the rest-frame after the initial GRB trigger for all the sources of the ES (in green) compared with the GS (in blue). The solid red line represents the Gaussian function which best fits the ES data in logarithmic scale. Its mean value is $\mu_{\mathrm{Log}_{10}(E_{LT})} = 51.40$, while its standard deviation is $\sigma_{\mathrm{Log}_{10}(E_{LT})} = 0.47$ (from Pisani et al. 2016).

4. COLLIMATION

In Pisani et al. (2016), we also proposed to reduce the spread of the LXRE power laws within the ES by introducing a collimation effect in the emission mechanism. In fact, if such a process is not isotropic, our estimates for the LXRE luminosities are actually overestimations of the intrinsic ones. By introducing a collimation effect, namely assuming that the LXREs are not radiated isotropically but inside a double-cone region having half-opening angle θ, we can compute the intrinsic LXRE luminosity $L_{intr}(t_{rf})$ from the isotropic $L_{iso}(t_{rf})$:

$$L_{intr}(t_{rf}) = L_{iso}(t_{rf})\,(1-\cos\theta)\,. \tag{7}$$

From Eq. 7, an angle θ can be computed for each source of the ES if an intrinsec universal LXRE light curve $L_{intr}(t_{rf})$ is given. By assuming GRB 050525A, which has the lowest luminosity within the ES, as our sole "isotropic" LXRE source, we obtain the probability distribution of the half-opening angle θ within the ES showed in Fig. 6a. The blue solid line represents a logarithmic normal distribution, which best fits the data. This distribution has a mode of $Mo_\theta = 17.62°$, a mean of $\mu_\theta = 30.05°$, a median of $Me_\theta = 25.15°$, and a standard deviation of $\sigma_\theta = 19.65°$. In addition, it is possible to verify that, by adjusting the $L_{iso}(t_{rf})$ light curve of each ES source for its corresponding θ, an overlap of the LXRE luminosity light curves as good as the one seen in the GS by Pisani et al. (2013) shown in Fig. 1 is obtained. Since the LXRE follows a power-law behavior, we can evaluate the tightness of the LXREs overlap estimating the correlation coefficient ρ between all the luminosity light-curve data points of the ES sources in log-log scale. Considering the data points of the LXRE power laws within the 10^4–10^6 s time interval (the time interval where we defined E_{LT}), we obtain $\rho = -0.94$ for the GS, $\rho = -0.84$ for the ES before the collimation effect correction, and $\rho = -0.97$ after the collimation correction. Therefore, assuming the collimation not only let the spread of the LXREs within the ES decrease, but makes the LXREs overlap even tighter than the one previously observed in the GS. This leads to the possible establishment of a new distance indicator, eventually useful to test the standard cosmological ΛCDM model.

5. THE CURRENT BDHNE CATALOG

Thanks to the tremendous amount of work from ICRANet scientists in the past years (Ruffini et al. 2001a,b,c, 2007; Rueda & Ruffini 2012; Izzo et al. 2012; Fryer et al. 2014; Ruffini et al. 2015, 2016), today we know that all the observed GRBs having long duration and isotropic energy E_{iso} larger than 10^{52} erg are the observational result of a BdHN phenomenon. Therefore, these two signatures are necessary and sufficient to identify a BdHN source. This holds also in the case it was not possible to observe the other typical features of the BdHNe following the GRB explosion, like: the FPA structure in the X-rays; the LXRE in the X-rays; and the associated Ib/c SN in the optical rays. In our recent work (Ruffini et al. 2017), in order to focus our analysis on the early X-Ray Flares in the FPA phase, we collected all the BdHNe ever observed till the end of 2016, collecting all the GRBs which satisfies the following criteria:

- measured redshift z;
- GRB rest-frame duration larger than 2 s;
- isotropic energy E_{iso} larger than 10^{52} erg.

The updated list presented in Table 9 of (Ruffini et al. 2017) is composed by 345 BdHNe, and represents the current ICRANet catalog of BdHNe. The ES, updated to the end of 2016, counts 182 BdHNe having *Swift*/XRT data up to at least 10^4 s in the rest-frame after the initial GRB explosion. It composes $\sim 53\%$ of the total BdHNe catalog. Since the *Swift* satellite is operating since 2005, we have an average of ~ 15 BdHNe per year having good LXRE observations. Consequently, this representes the expected rate of BdHNe which, in the near future, will be useful to test the standard cosmological ΛCDM model at redshifts up to $z \sim 8$.

This work made use of data supplied by the UK Swift Science Data Center at the University of Leices-

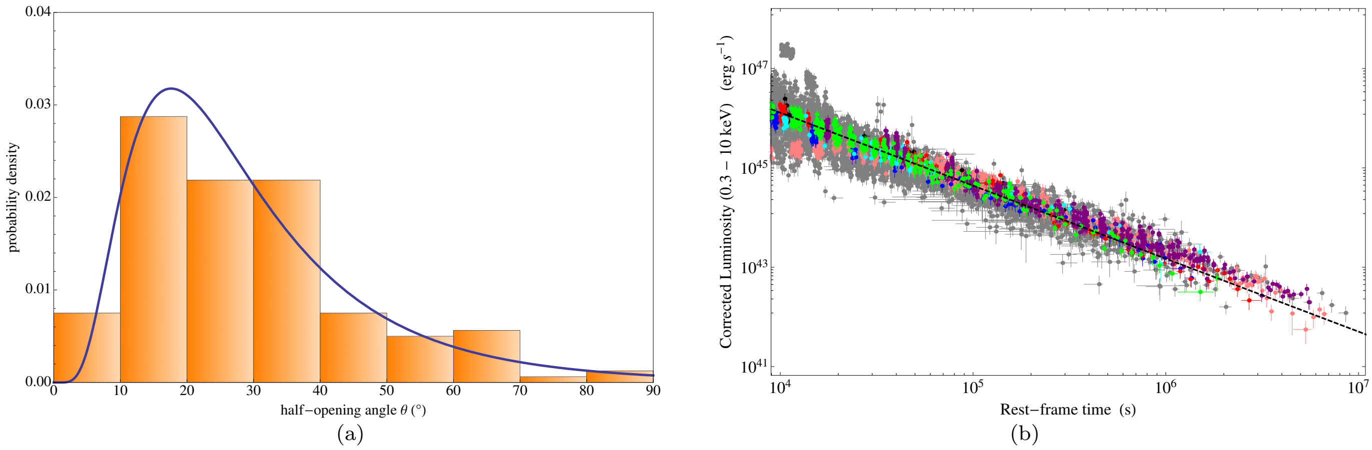

Figure 6. Left panel (a): probability distribution of the half-opening angle θ within the ES. The blue solid line represents a logarithmic normal distribution, which best fits the data. This distribution has a mode of $Mo_\theta = 17.62°$, a mean of $\mu_\theta = 30.05°$, a median of $Me_\theta = 25.15°$, and a standard deviation of $\sigma_\theta = 19.65°$ (from Pisani et al. 2016). Right panel (b): corrected LXRE luminosity light curves of all 161 sources of the ES (gray) compared to the ones of the GS: GRB 060729 (pink), GRB 061007 (black), GRB 080913B (blue), GRB 090618 (green), GRB 091127 (red), and GRB 111228 (cyan), plus GRB 130427A (purple; Pisani et al. 2013; Ruffini et al. 2015). The black dotted line represents the universal LXRE power law, namely the linear fit of the late emission of GRB 050525A (from Pisani et al. 2016).

ter. J. A. R. acknowledges the support by the International Cooperation Program CAPES-ICRANet financed by CAPES-Brazilian Federal Agency for Support and Evaluation of Graduate Education within the Ministry of Education of Brazil. M. M. acknowledges the partial support of the project No. 3101/GF4 IPC-11/2015, and the target program of the Ministry of Education and Science of the Republic of Kazakhstan.

REFERENCES

Bloom, J. S., Frail, D. A., & Sari, R. 2001, AJ, 121, 2879
Boella, G., Butler, R. C., Perola, G. C., et al. 1997, A&AS, 122, 299
Costa, E., Frontera, F., Heise, J., et al. 1997a, Nature, 387, 783
Costa, E., Feroci, M., Piro, L., et al. 1997b, IAU Circ., 6576
de Pasquale, M., Piro, L., Gendre, B., et al. 2006, A&A, 455, 813
de Ugarte Postigo, A., Xu, D., Leloudas, G., et al. 2013, GCN Circ., 14646, 1
Dezalay, J.-P., Barat, C., Talon, R., et al. 1992, in American Institute of Physics Conference Series, Vol. 265, American Institute of Physics Conference Series, ed. W. S. Paciesas & G. J. Fishman, 304–309
Evans, P. A., Beardmore, A. P., Page, K. L., et al. 2007, A&A, 469, 379
Evans, P. A., Willingale, R., Osborne, J. P., et al. 2010, A&A, 519, A102
Frontera, F., Costa, E., Piro, L., et al. 1998, ApJ, 493, L67
Frontera, F., Amati, L., Costa, E., et al. 2000, ApJSS, 127, 59
Fryer, C. L., Rueda, J. A., & Ruffini, R. 2014, ApJ, 793, L36
Gehrels, N., Chincarini, G., Giommi, P., et al. 2004, ApJ, 611, 1005
Izzo, L., Rueda, J. A., & Ruffini, R. 2012, A&A, 548, L5
Klebesadel, R. W. 1992, in Gamma-Ray Bursts - Observations, Analyses and Theories, ed. C. Ho, R. I. Epstein, & E. E. Fenimore (Cambridge University Press), 161–168
Kouveliotou, C., Meegan, C. A., Fishman, G. J., et al. 1993, ApJ, 413, L101
Levan, A. J., Fruchter, A. S., Graham, J., et al. 2013, GCN Circ., 14686, 1
Mazets, E. P., Golenetskii, S. V., Ilinskii, V. N., et al. 1981, Ap&SS, 80, 3
Penacchioni, A. V., Ruffini, R., Bianco, C. L., et al. 2013, A&A, 551, A133
Penacchioni, A. V., Ruffini, R., Izzo, L., et al. 2012, A&A, 538, A58
Pisani, G. B., Izzo, L., Ruffini, R., et al. 2013, A&A, 552, L5
Pisani, G. B., Ruffini, R., Aimuratov, Y., et al. 2016, ApJ, 833, 159
Rueda, J. A., & Ruffini, R. 2012, ApJ, 758, L7
Ruffini, R., Bianco, C. L., Chardonnet, P., Fraschetti, F., & Xue, S.-S. 2001a, ApJ, 555, L107
—. 2001b, ApJ, 555, L113
—. 2001c, ApJ, 555, L117
Ruffini, R., Bernardini, M. G., Bianco, C. L., et al. 2007, ESA SP, 622, 561
Ruffini, R., Bianco, C. L., Enderli, M., et al. 2013a, GCN Circ., 14526, 1
—. 2013b, GRB Coordinates Network, 14888
—. 2013c, GRB Coordinates Network, 15576
—. 2014a, GRB Coordinates Network, 15707
Ruffini, R., Izzo, L., Muccino, M., et al. 2014b, A&A, 569, A39
Ruffini, R., Muccino, M., Bianco, C. L., et al. 2014c, A&A, 565, L10
Ruffini, R., Wang, Y., Enderli, M., et al. 2015, ApJ, 798, 10
Ruffini, R., Rueda, J. A., Muccino, M., et al. 2016, ApJ, 832, 136
Ruffini, R., Wang, Y., Aimuratov, Y., et al. 2017, ArXiv e-prints
Salvaterra, R., Della Valle, M., Campana, S., et al. 2009, Nature, 461, 1258
Tanvir, N. R., Fox, D. B., Levan, A. J., et al. 2009, Nature, 461, 1254
Tavani, M. 1998, ApJ, 497, L21

GRB 110731A within the IGC paradigm

Daria Primorac[1,2,⋆], *Remo* Ruffini[1,2,3,4,⋆⋆], *Giovanni Battista* Pisani[1,2,⋆⋆⋆], *Yerlan* Aimuratov[1,2,3], *Carlo Luciano* Bianco[1,2], *Mile* Karlica[1,2,3], *Julio David* Melon Fuksman[1,2], *Rahim* Moradi[1,2], *Marco* Muccino[1,2], *Ana Virginia* Penacchioni[5,6], *Jorge Armando* Rueda[1,2,4], and *Yu* Wang[1,2]

[1] *Dipartimento di Fisica and ICRA, Sapienza Università di Roma, Piazzale Aldo Moro 5, I–00185 Rome, Italy*
[2] *ICRANet, Piazza della Repubblica 10, I–65122 Pescara, Italy*
[3] *Université de Nice Sophia Antipolis, CEDEX 2, Grand Château Parc Valrose, Nice, France*
[4] *ICRANet-Rio, Centro Brasileiro de Pesquisas Físicas, Rua Dr. Xavier Sigaud 150, 22290–180 Rio de Janeiro, Brazil*
[5] *ASI Science Data Center, Via del Politecnico s.n.c., I-00133 Rome, Italy*
[6] *Dept. of Physical Sciences, Earth and Environment, University of Siena, Via Roma 56, I-53100 Siena, Italy*

Abstract. Bright gamma-ray burst (GRB) 110731A was simultaneously observed by *Fermi* and *Swift* observatories, with a follow up optical observation which inferred the redshift of z = 2.83. Thus, available data are spanning from optical to high energy (GeV) emission. We analyze these data within the induced gravitational collapse (IGC) paradigm, recently introduced to explain temporal coincidence of some long GRBs with type Ic supernovae. The case of binary-driven hypernova (BdHN) assumes a close system, which starts as an evolved core - neutron star binary. After the core-collapse event, the new NS - black hole system is formed, emitting the GRB in the process. We performed the time-resolved and time-integrated analysis of the *Fermi* data. Preliminary results gave isotropic energy $E_{\rm iso} = 6.05\times10^{53}$ erg and the total P-GRB energy of $E_{\rm P-GRB} = 3.7\times10^{52}$ erg. At transparency point we found a Lorentz factor $\Gamma \sim 2.17 \times 10^3$, laboratory radius of 8.33×10^{13} cm, P-GRB observed temperature of 168 keV and a baryon load $B = 4.35 \times 10^{-4}$. Simulated light-curve and prompt emission spectra showed the average circum burst medium density to be $n \sim 0.03$ particles per cm^3. We reproduced the X-ray light-curve within the rest-frame of the source, finding the common late power-law behavior, with $\alpha = -1.22$. Considering these results, we interpret GRB 110731A as a member of a BdHNe group.

1 Introduction

Gamma-ray bursts (GRBs) are known to be the most luminous events in the universe. The data provided by CGRO/BATSE observations showed that the T_{90} distribution of the observed bursts is bimodal in structure [1]. Since then, GRBs are traditionally divided into long/soft and short/hard bursts with the separation of about 2 seconds in the observed frame [2]. This division came prior to the redshift measurements. Once X-ray observations provided more accurate positions, optical telescopes could determine the distance at which the GRBs occurred, confirming their cosmological origin. Thanks to their extreme brightness, GRBs are detectable up to redshift $z \approx 9$ (see, e.g., [3]). With redshifts available, correlations between burst observables could facilitate the use of GRBs as standard candles, constraining the expansion history of the universe. The separation in long and short GRBs was still present when one inquired into their rest-frame properties. For example, the $E_{iso} - E_p$ dependence for long bursts follows Amati relation [4, 5], where E_{iso} is the burst isotropic energy and E_p is the rest-frame peak energy in the $\nu F(\nu)$ spectrum. The short GRBs on the other hand follow a different relation (see, e.g., [6–8]). Therefore, it is generally accepted that long and short GRBs have different progenitors, where the first are the result of a gravitational collapse event (see [9, 10]) while the latter originate from compact mergers [11, 12]. However, there are still doubts regarding the dominant mechanism of long GRBs.

Connection between some long GRBs and type Ib/c supernovae (SNe) has been known since GRB 980425/SN 1998bw observations [13]. The induced gravitational collapse (IGC) paradigm has been introduced in the past years to explain this temporal coincidence in the case of binary-driven hypernovae (BdHNe): long, extremely energetic bursts ($E_{iso} > 10^{52}$ erg) with high rest-frame peak energies ($E_p > 200$ keV) up to some MeV. The model invokes a close binary system consisting of a neutron star (NS) and a carbon-oxygen (CO) core close to a core-collapse event (see, e.g., [14–16]). A well-determined time sequence is implied, where each stage is expected to have distinctive observational properties:

Hypercritical accretion. After the CO core SN explosion, the companion NS gains mass via hypercritical accretion of the ejected material. Spectrum is described with an expanding thermal component ($\sim10^{9-10}$ cm) plus an ex-

⋆e-mail: Daria.Primorac@icranet.org
⋆⋆e-mail: ruffini@icra.it
⋆⋆⋆e-mail: giovanni.b.pisani@gmail.com

tra power-law (PL). The black body (BB) temperature decreases with time following a broken PL [17].

BH formation and the P-GRB. The companion NS reaches critical mass and collapses into a BH. This leads to a formation of an optically thick e^+e^- plasma – the *fireshell* of total energy $E^{\rm tot}$ [18, 19]. The fireshell expands and self-accelerates due to the e^+e^- annihilation up to ultra-relativistic velocities, until the transparency condition has been reached. The dynamics of the fireshell up to this point are fully described with $E^{\rm tot}$ and the baryon load $B = M_B c^2/E^{\rm tot}$, where M_B is the mass of the baryons engulfed by the plasma. In the case of long GRBs, it is characterized by $10^{-4} \lesssim B < 10^{-2}$. The proper-GRB (P-GRB) is then emitted, with a spectrum defined by the geometry of the pair-creation region. PL with an exponential cutoff is expected in the case of axial symmetry. After the transparency has been achieved, evidence of a BH formation is seen in form of high energy photons (up to few GeV). The BdHN scenario invokes the BH formation. X-ray flashes (XRFs) are less energetic sub-class of long GRBs, where the NS only gains mass, and there is no BH formation.

Canonical GRB emission. After the transparency emission, the optically thin shell of baryons collides with a circum burst medium (CBM) of density n_{CBM}, giving rise to the prompt emission. The CBM is modeled by the filling factor, which takes into account filamentary structures of the medium, $R = A_{eff}/A_{vis}$. Here, A_{eff} is the area covered by the CBM clouds while A_{vis} is the total observable area [8, 15]. The prompt emission occurs at $\sim 10^{15-17}$ cm [17].

X-ray afterglow. Rest-frame X-ray light-curves show precise behavior consisting of three PL segments: starting at the endpoint of the prompt emission, followed by a plateau phase, and ending by a late constant PL decay [20, 21]. While plateau shrinks as a function of the increasing E_{iso}, the late PL decay is common to all sources after $\approx 10^4$ s in the rest-frame, with typical slopes of $-1.7 \lesssim a_x \lesssim -1.3$ [22, 23]. In the case of XRFs, light-curves are less energetic and more chaotic, not exhibiting these properties. The emitting region inferred for some BdHNe sources suggested that the origin of the X-ray emission has the initial size of $\sim 10^{12}$, meaning that the place of origin is SN ejecta, not the GRB.

SN remnant detection in optical. Optical SN emission due to the ^{56}Ni decay is expected after ∼10 – 15 days in the source rest-frame, and it is currently detectable only up to $z \lesssim 1$. In the end, system that began as a CO core - NS binary now consists of a newly born NS (ν-NS) and a BH.

In this work we shortly summarize relevant observations of the energetic GRB 110731A. We use these data to search for the BdHN scenario signatures described above. We perform time-integrated and time-resolved spectral analysis and study the results within the IGC model. From this we derive the baryon load, Lorentz factor at transparency point and P-GRB energy. We proceed to simulate the light-curve and spectra to obtain the average densities of CBM.

2 Analysis of *Fermi/GBM* data

Gamma-Ray Burst Monitor (GBM, [24]) onboard *Fermi* observatory was specially designed for GRB studies. Having 12 sodium iodide (NaI) detectors (8 keV–1 MeV) and 2 bismuth germanate detectors (250 keV–40 MeV), it covers the energy range of 8 keV – 40MeV. Large Area Telescope (LAT, [25]) is the second instrument onboard *Fermi*, able to detect photons with energies up to more than 300 GeV. GRB 110731A triggered the GBM [26] at 11:09:29.94 (UT) on 2011 July 31 (T_0). The GRB was already in the LAT field of view (≈ 3°), so both instruments observed the burst from early on. Using LAT data burst was preliminarily localized at (R.A., J2000)=−280°.39, (decl., J2000)=−28°.53. We downloaded the time-tagged event (TTE) data of the triggering detectors NaI-n0 & NaI-n3, and of the corresponding BGO-b0 detector, from the NASA Fermi Web site[1]. Software package RMFIT[2] was used to perform the time-integrated and time-resolved spectral analysis of the TTE data. Data preparation included subtracting the background by fitting it to a low order polynomial and excluding the overflow channels. We reproduced the LAT and GBM (background subtracted) light-curves in various energy bands (see figure 1) using the TTE data (GBM) and 'P8R2_TRANSIENT020'-class events (LAT). The light-curve, starting around $T_0 - 0.4$s can be described as a complex single-peak structure lasting up to ≈10 s, with a sudden decrease after ≈7.3 s.

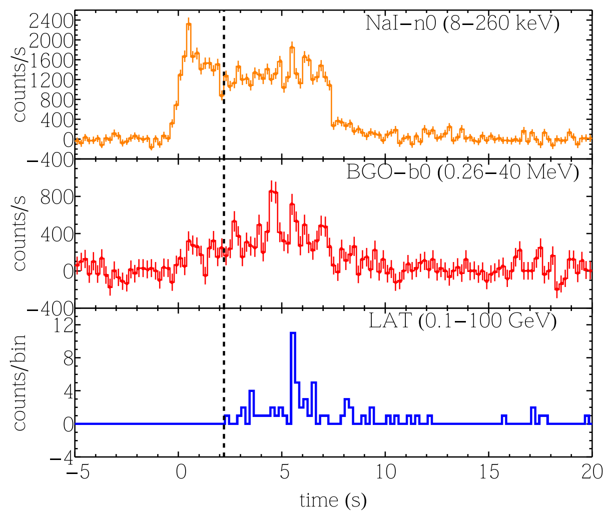

Figure 1. LAT and GBM (NaI & BGO, background subtracted) light-curves of GRB 110731A. Top two panels show NaI-n0 (8–260 keV, top panel) and BGO-b0 (0.26–40 MeV, middle panel) data with 0.2 s binning. The vertical dashed line at $T_0 \sim 2.4$ s indicates the onset of high energy emission observed by LAT (bottom panel, 0.5 s binning).

We performed a time-integrated analysis using the GBM energy range (8 keV – 40 MeV) and approximate GBM-T_{90} interval [0.19 s, 7.9 s]. Three different empirical models were tested: a simple power-law (PL), a

[1] ftp://legacy.gsfc.nasa.gov/fermi/data/gbm/bursts/
[2] fermi.gsfc.nasa.gov/ssc/data/analysis

Table 1. Best-fit parameters of models used for the time-integrated ([0.19 s, 7.9 s]) spectral analysis. The reference energy is fixed to 100 keV. The energy flux is evaluated for the 10–1000 keV range.

Model	E_p (keV)	α	β	Γ_{PL}	F (erg cm^{-2}s^{-1})	C-STAT/DOF
PL	-	-	-	-1.51 ± 0.01	$(2.600 \pm 0.026) \times 10^{-6}$	1921.9/362
Compt	344.5 ± 12.8	-0.86 ± 0.03	-	-	$(2.815 \pm 0.045) \times 10^{-6}$	618.4/361
BAND	324.1 ± 17.3	-0.85 ± 0.03	-2.50 ± 0.15	-	$(2.803 \pm 0.040) \times 10^{-6}$	612.9/360

power-law with the exponential cutoff (Compton) and the Band function [27]. The goodness of the fit was measured using C-statistic [28], requiring an improvement by ΔC-stat=9 for every degree of freedom (DOF). Compton-fit showed a significant improvement over the power-law fit. Band function, having one parameter more, improved the fit by ΔC-stat≈6. The Compton was therefore considered the best-fit model with parameter values of E_p = 344.5(±12.8) keV and $\alpha = -0.86(\pm 0.03)$ (see table 1). In order to calculate the isotropic energy E_iso, we fitted the Band function using the entire observed emission interval [-0.38 s, 10.56 s]. This avoids flux underestimation due to the Compton model and detector sensitivity (see, e.g., [29]). The best-fit parameters were: $\alpha = -0.91^{+0.03}_{-0.03}$, $\beta = 2.19^{+0.07}_{-0.09}$, with $E_\mathrm{p} = 319.4^{+18.9}_{-16.8}$ keV. E_iso was obtained using

$$E_\mathrm{iso} = \frac{4\pi d_\mathrm{l}^2}{(1+z)} S_\mathrm{bol}, \tag{1}$$

where d_l^2 is the luminosity distance, z is the redshift and S_bol is the bolometric fluence in the $1/(1+z)$ keV to $10^4/(1+z)$ keV frame:

$$S_\mathrm{bol} = S_\mathrm{obs} \frac{\int_{1/(1+z)}^{10^4/(1+z)} E\phi(E)dE}{\int_{E_\mathrm{min}}^{E_\mathrm{max}} E\phi(E)dE}. \tag{2}$$

Here, ϕ is the Band model obtained from the spectral fit and $S_\mathrm{obs} = \Delta t F_\mathrm{obs}$, where F_obs is the mean energy flux in the $(E_\mathrm{min}, E_\mathrm{max})$ detection band and Δt is the time interval of the spectral fit. We find the value of E_iso = $6.05(\pm 0.09) \times 10^{53}$ erg.

We proceed to the time-resolved spectral analysis and P-GRB identification. P-GRB is expected in the form of the first flash of thermal radiation , once the e^+e^- plasma reaches transparency point. This takes place before the evidence of the BH formation, and thus, before the high energy emission (∼2.4 *s*). Expected spectra is thermal (spherically symmetric case) or Compton, produced by a convolution of many instantaneous co-moving spectra with different temperatures (axially symmetric case). Therefore, in order to identify the P-GRB, we selected the times before the high energy emission using a time binning criteria of $S/N = 15$, and fitted six different models to each bin: power-law, Compton, Band and the same three empirical models with added black body (BB) component. We adopted the same criteria of ΔC-stat=9 for every degree of freedom. For every time bin Compton was showed to be the best-fit model (similar as [30], see table 2).

The effective temperature was calculated using $kT = E_\mathrm{p}/3.92$, or $kT^\mathrm{RF} = E_\mathrm{p}(1+z)/3.92$ for the rest-frame value. We identified the P-GRB as the emission up to T_0 + 0.68 s, at which point the temperature starts to drop (see figure 2). This coincides with the light-curve maximum. The Compton-fit parameters of this interval are: E_p = 171.9(±17.1) keV, $\alpha = -1.08(\pm 0.08)$ and A = 0.0631(±0.0077) p/s cm^2 keV, where A is the amplitude. They were used to obtain the P-GRB energy $E_\mathrm{P-GRB} = 3.7 \times 10^{52}$ erg and the rest-frame temperature kT^RF = 167.9 keV.

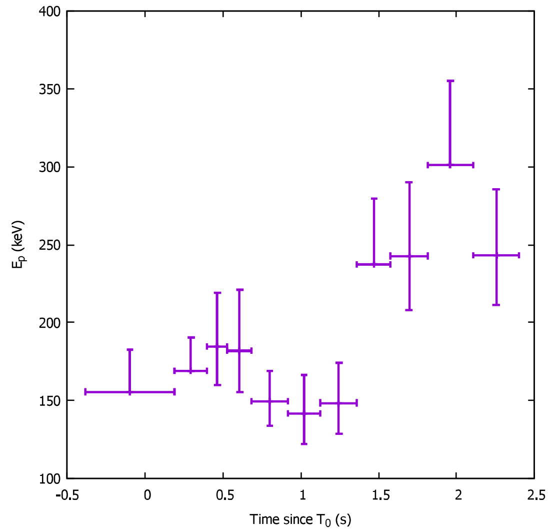

Figure 2. Temporal evolution of the E_p spectral parameter within the Compton model. Bars represent $\pm 1\sigma$ error intervals. Time is given in the observer frame with the binning criteria of S/N=15.

2.1 Light-curve and spectra simulation

The obtained energy values for E_iso and $E_\mathrm{P-GRB}$ served as an input in our numerical code . Calculated value of the baryon load was $B = 4.35 \times 10^{-4}$. At the transparency point, the laboratory radius was 8.33×10^{13} cm and the P-GRB observed temperature 168 keV, with Lorentz factor $\Gamma \sim 2.17 \times 10^3$. We simulated the light-curve and the prompt emission spectrum (see figure 3 and figure 4). The resulting average CBM value was $n \sim 0.03$ particles cm^3.

3 *Swift/XRT* observations

In addition to *Fermi*, GRB 110731A triggered many other observatories, including the burst alert telescope (BAT) onboard *Swift* [31]. Besides BAT, *Swift* spacecraft [32]

Table 2. C-STAT values of 6 models used in the time-resolved spectral analysis, with bin duration given in the first column. E_p value of the best fitting Compton model is given in the second column.

Time bins (s)	Best-fit Compt		C-STAT/DOF other models				
	E_p (keV)	C-STAT/DOF	PL	PL+BB	Compt+BB	Band	Band+BB
$[-0.38, 0.19]$	$155.7^{+26.9}_{-0.0}$	413.2/361	429.7/362	413.8/360	412.5/359	413.2/360	413.1/358
$[0.19, 0.40]$	$168.9^{+21.6}_{-0.0}$	368.3/361	403.0/362	366.7/360	361.9/359	368.3/360	-NaN/358
$[0.40, 0.53]$	$184.7^{+34.5}_{-24.6}$	319.1/361	361.8/362	332.7/360	314.9/359	319.0/360	315.1/358
$[0.53, 0.67]$	$181.9^{+38.9}_{-26.9}$	331.6/361	359.8/362	332.4/360	331.1/359	330.0/360	329.8/358
$[0.67, 0.92]$	$149.3^{+19.8}_{-15.3}$	362.3/361	421.3/362	364.5/360	362.2/359	361.7/360	360.1/358
$[0.92, 1.13]$	$141.7^{+24.8}_{-19.7}$	373.7/361	425.8/362	369.1/360	361.4/359	362.0/360	361.2/358
$[1.13, 1.36]$	$148.5^{+25.8}_{-19.5}$	357.7/361	393.2/362	359.3/360	357.2/359	358.1/360	358.7/358
$[1.36, 1.58]$	$237.3^{+42.3}_{-0.0}$	365.1/361	391.8/362	368.9/360	363.4/359	364.4/360	363.9/358
$[1.58, 1.81]$	$242.8^{+47.3}_{-34.5}$	366.9/361	429.5/362	380.3/360	361.6/359	365.0/360	361.5/358
$[1.81, 2.11]$	$301.0^{+54.2}_{-0.0}$	431.8/361	455.8/362	433.8/360	425.9/359	430.2/360	424.1/358
$[2.11, 2.40]$	$243.2^{+42.4}_{-31.6}$	421.6/361	487.5/362	419.6/360	418.7/359	421.8/360	418.6/358

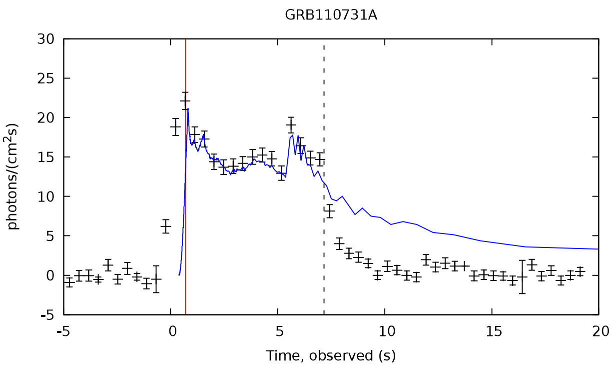

Figure 3. Simulated and NaI-n3 detector (0.2 s binning) light-curve of GRB 110731A. Red vertical line at 0.69 s marks the end of the P-GRB. The dashed line marks the end of the simulation for the spectra.

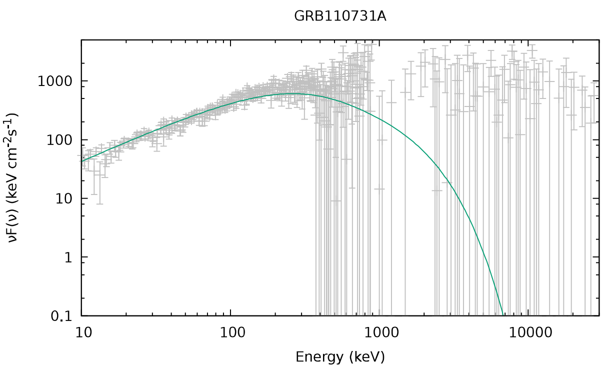

Figure 4. Simulated $\nu F(\nu)$ spectra of the prompt emission, superimposed on the joined NaI-n0, n3 & BGO-b0 observed spectra.

harbors X-ray (XRT) and UV/optical (UVOT) telescopes, intended for the afterglow observations. Available multi-wavelength data make this burst a good candidate to investigate the IGC paradigm. The XRT began observations 56 s after the BAT trigger, where first 8 s were taken while *Swift* was still slewing. The GBM and LAT localizations are consistent with the position provided by *Swift*. Redshift z=2.83 was provided by spectroscopic observations done by GMOS-N [33]. This enabled the XRT light-curve to be transformed to the 0.3–10 keV rest-frame energy range, plotted as a function of the rest-frame time (see figure 5). The GRB 110731A light-curve is superimposed on the X-ray luminosity light-curves of other BdHNe for comparison of the common late power-law behavior, typical for BdHNe. Non-existence of the plateau phase is in agreement with the high E_{iso} of this burst. Furthermore, the PL index $\alpha = -1.22$ is within the limits presented in [22, 23].

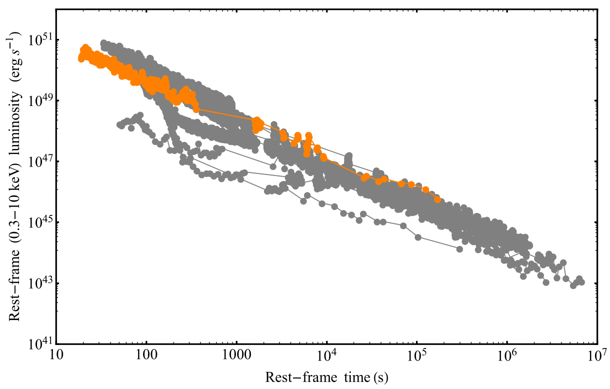

Figure 5. Rest-frame luminosity light-curve of GRB 110731A in the 0.3–10 keV range (orange), superimposed on other BdHNe light-curves (grey): 050525, 060729, 061007, 080319B, 090618, 091127, 100816A, 111228A, 130427A [34]. All GRBs have known redshift.

4 Conclusion and future perspectives

The mechanism responsible for the prompt emission of GRBs is still a debated issue. The origin of the GRB prompt emission in a BdHNe scenario is a consequence of a well-determined sequence of a binary system interaction. Being observed by multiple observatories, GRB

110731A makes a good candidate for investigation of the expected BdHNe signatures. The light-curve showed no evidence of the hypercritical accretion phase, which possibly remains under the detection level, considering the large distance of this GRB ($z = 2.83$). Calculated isotropic energy $E_{\rm iso} = 6.05\times10^{53}$ erg is well above the BdHNe lower limit of $\sim 10^{52}$ erg. Using the calculated $E_{\rm iso}$ and P-GRB identified via time-resolved spectral analysis, we inferred the baryon load of $B = 4.35\times10^{-4}$, which is within the expected limits for long GRBs. LAT detected a high energy emission $\sim$ 2.4 s after the the GBM trigger, expected in the BdHNe case as a signature of a BH formation. X-ray rest-frame luminosity light-curve showed typical late PL behavior, shared between the other members within the BdHNe group.

This preliminary analysis showed that GRB 110731A is a strong BdHN candidate. Still, in our ongoing analysis we will check the influence of the background selection, bad channels and different binning on the obtained parameters. We will investigate the use of different models and compare these results with the rest of the BdHNe sample.

References

[1] Meegan, C. A., Fishman, G. J., Wilson, R. B., Horack, J. M., Brock, M. N., Paciesas, W. S., Pendleton, G. N., & Kouveliotou, C., Nature **355**, 143 (1992)

[2] Kouveliotou, C., Meegan, C. A., Fishman, G. J., et al., ApJL (413), L101 (1993)

[3] Cucchiara, A., Levan, A. J., Fox, D. B., et al., ApJ (736), 7 (2011)

[4] Amati, L., et al., A&A **390**, 81 (2002)

[5] Amati, L., Guidorzi, C., Frontera, F., Della Valle, M., Finelli, F., Landi, R., & Montanari, E., MNRAS **391**, 577 (2008)

[6] Zhang, F. W., Shao, L., Yan, J. Z., & Wei, D. M., ApJ **750**, 88 (2012)

[7] Calderone, G., Ghirlanda, G., Ghisellini, G., et al. 2015, MNRAS, 448, 403.

[8] Ruffini, R., Rueda, J. A., Muccino, M., et al., ApJ **832**, 136 (2016)

[9] Damour, T., & Ruffini, R., Physical Review Letters **35**, 463 (1975)

[10] Piran, T., Reviews of Modern Physics **76**, 1143 (2004)

[11] Narayan, R., Piran, T., & Shemi, A., ApJL **379**, L17 (1991)

[12] Lee, W. H., Ramirez-Ruiz, E., & Page, D., ApJL **608**, L5 (2004)

[13] Galama, T. J., Vreeswijk, P. M., van Paradijs, J., et al., Nature **395**, 670 (1998)

[14] Fryer, C. L., Rueda, J. A., & Ruffini, R., ApJL **793**, L36 (2014)

[15] Ruffini, R., Bianco, C. L., Fraschetti, F., Xue, S.-S., & Chardonnet, P., ApJ **555**, L117 (2001)

[16] Rueda, J. A., & Ruffini, R., ApJL **758**, L7 (2012)

[17] Izzo, L., Ruffini, R., Penacchioni, A. V., et al., A&A **543**, A10 (2012)

[18] Ruffini, R., Salmonson, J. D., Wilson, J. R., & Xue, S.-S., A&A **350**, 334 (1999)

[19] Ruffini, R., Salmonson, J. D., Wilson, J. R., & Xue, S.-S., A&A **359**, 855 (2000)

[20] Nousek, J. A., Kouveliotou, C., Grupe, D., et al., ApJ **642**, 389 (2006)

[21] Zhang, B., Fan, Y. Z., Dyks, J., et al., ApJ **642**, 354 (2006)

[22] Pisani, G. B., Izzo, L., Ruffini, R., et al., A&A **552**, L5 (2013)

[23] Ruffini, R., Muccino, M., Bianco, C. L., et al., 2014, A&A, 565, L10 (2014)

[24] Meegan, C., Lichti, G., Bhat, P. N., et al., ApJ **702**, 791 (2009)

[25] Atwood, W. B., Abdo, A. A., Ackermann, M., et al., ApJ **679**, 1071 (2009)

[26] Gruber, D., GRB Coordinates Network, 12221 (2011)

[27] Band, D., Matteson, J., Ford, L., et al., ApJ **413**, 281 (1993)

[28] Cash, W., ApJ **228**, 939 (1979)

[29] Virgili, F. J., Qin, Y., Zhang, B., & Liang, E., MNRAS **424**, 2821 (2012)

[30] Ackermann, M., et al., ApJ **763**, 71 (2013)

[31] Oates, S. R., Beardmore, A. P., et al., GRB Coordinates Network, 12215 (2011)

[32] Gehrels, N., et al., ApJ **611**, 1005 (2004)

[33] Tanvir, N. R., Wiersema, K., et al., GRB Coordinates Network, 12225 (2011)

[34] Ruffini, R., Wang, Y., Aimuratov, Y., et al., arXiv:170403821 (2017)

EPJ Web of Conferences **168**, 04009 (2018) https://doi.org/10.1051/epjconf/201816804009
Joint International Conference of ICGAC-XIII and IK-15 on Gravitation, Astrophysics and Cosmology

Evolution of an electron-positron plasma produced by induced gravitational collapse in binary-driven hypernovae

J. D. Melon Fuksman[1,2,⋆], *L.* Becerra[1,2], *C. L.* Bianco[1,2], *M.* Karlica[1,2,3], *M.* Kovacevic[1,2,3], *R.* Moradi[1,2], *M.* Muccino[1,2], *G. B.* Pisani[1,2], *D.* Primorac[1,2], *J. A.* Rueda[1,2,4], *R.* Ruffini[1,2,3,4], *G. V.* Vereshchagin[1,2], and *Y.* Wang[1,2]

[1] *Dipartimento di Fisica, Sapienza Università di Roma, Piazzale Aldo Moro 5, 00185 Rome, Italy*
[2] *ICRANet, Piazza della Repubblica 10, 65122 Pescara, Italy*
[3] *Université de Nice Sophia Antipolis, CEDEX 2, Grand Château Parc Valrose, Nice, France*
[4] *ICRANet-Rio, Centro Brasileiro de Pesquisas Físicas, Rua Dr. Xavier Sigaud 150, 22290–180 Rio de Janeiro, Brazil*

Abstract. The binary-driven hypernova (BdHN) model has been introduced in the past years, to explain a subfamily of gamma-ray bursts (GRBs) with energies $E_{iso} \geq 10^{52}$ erg associated with type Ic supernovae. Such BdHNe have as progenitor a tight binary system composed of a carbon-oxigen (CO) core and a neutron star undergoing an induced gravitational collapse to a black hole, triggered by the CO core explosion as a supernova (SN). This collapse produces an optically-thick e^+e^- plasma, which expands and impacts onto the SN ejecta. This process is here considered as a candidate for the production of X-ray flares, which are frequently observed following the prompt emission of GRBs. In this work we follow the evolution of the e^+e^- plasma as it interacts with the SN ejecta, by solving the equations of relativistic hydrodynamics numerically. Our results are compatible with the Lorentz factors estimated for the sources that produce the flares, of typically $\Gamma \lesssim 4$.

1 Introduction

The *induced gravitational collapse* (IGC) (see, e.g., [1], [2], [3]) has been proposed in the past years, as a way to explain a sub-class of long gamma-ray bursts (GRBs) called binary-driven hypernovae (BdHNe), characterised by an isotropic energy $E_{iso} \geq 10^{52}$ erg and a rest-frame spectral peak energy between 0.2 and 2 MeV. The model considers a binary system formed by a carbon-oxygen (CO) core and a neutron star (NS), which undergo a tight orbit. If the core-collapse of the CO star produces a supernova explosion, the ejected material may trigger an hypercritical accretion process onto the NS, due to a copious neutrino emission and the trapping of photons within the accretion flow. This process can cause the NS to collapse as well, thus forming a black hole (BH). It has been proposed in [4] and, e.g., [5], that such collapse can lead to the formation of an e^+e^- plasma, that later expands and interacts with the SN ejecta, finally producing a GRB.

In this scenario, the major portion of the optically thick e^+e^--baryon plasma originating from the collapse expands away from the supernova (SN), giving rise to the canonical GRB *prompt emission*. This emission occurs at approximately 10^{15}-10^{17} cm from the BH, and is measured to come from material that expands at Lorentz factors $\Gamma \sim 10^2$-10^3 (see e.g. [5]). Right after this first stage, that can last up to $\sim$ 100 s, *X-ray flares* are frequently observed, followed by the so-called "plateau" and finally by the late decay of the X-ray afterglow [6]. By studying the time evolution of the thermal component of the X-ray flares, it can be inferred that they originate from regions which move at roughly $\Gamma \lesssim 4$, as pointed out in [6].

These differences in the features of the prompt emission and the flares can be explained in terms of the IGC model. In it, the prompt emission is produced after the interaction of the e^+e^- with the SN ejecta, in a direction that corresponds to lower overall densities along the line of sight of an external observer (see [7] and Fig. 1). On the other hand, as the binary system keeps spinning, the mass density profile along that line changes. If a bigger amount of mass gets between the BH and the observer (see [8] and Fig. 1), an X-ray flare is emitted at the moment the plasma escapes the outermost regions of the SN ejecta, namely, at the shock *breakout*. Due to the deceleration of the shock by its interaction with the surrounding material, the Lorentz factors measured for the flares will be smaller than for the prompt emission.

In this work we describe numerically the evolution of the plasma along different directions, and study the compatibility of the IGC model with some of the abovementioned observational features.

2 Equations and numerical scheme

We have modeled the evolution of the e^+e^- plasma and the SN ejecta following a single-fluid approach, where all the involved particle species, in this case baryons, photons, electrons and positrons, coming either from the plasma or the SN, are in *local thermodynamic equilibrium* (LTE).

⋆e-mail: david.melon@icranet.org

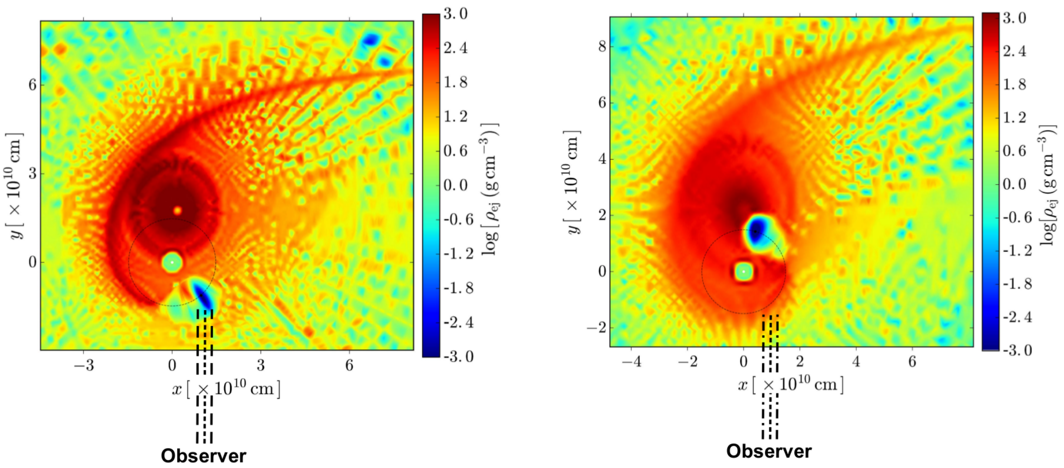

Figure 1. Density profiles calculated in [8] corresponding to the SN ejecta at (left) the moment of the collapse and (right) 100 s later. The line of sight of an observer that sees the initial prompt emission is indicated, to point out the change of the mass profile along it.

Under this assumption, the dynamics of the resulting fluid is governed by the equations of relativistic hydrodynamics (RHD). Throughout this work, we have numerically solved the one-dimensional RHD equations with the additional assumption of spherical symmetry, considering only a dependence of the intensive variables on the radial spherical coordinate. This allows us to study the evolution of the plasma along one selected radial direction at a time, thus to consider the different density distributions as seen through each direction. In the absence of gravity, the resulting equations of motion can be written as follows:

$$\frac{\partial(\rho\Gamma)}{\partial t} + \nabla.(\rho\Gamma\mathbf{v}) = 0, \tag{1}$$

$$\frac{\partial m_r}{\partial t} + \nabla.(m_r\mathbf{v}) + \frac{\partial p}{\partial r} = 0, \tag{2}$$

$$\frac{\partial \mathcal{E}}{\partial t} + \nabla.(\mathbf{m} - \rho\Gamma\mathbf{v}) = 0, \tag{3}$$

where ρ is the comoving mass density, $\mathbf{v}$ is the fluid velocity (natural units where $c = 1$ are used), $\Gamma = (1-\mathbf{v}^2)^{-\frac{1}{2}}$ is the Lorentz factor, $\mathbf{m}$ the total momentum density, and the subscript r indicates the radial component of a vector. The momentum density $\mathbf{m}$ is defined as $\mathbf{m} = h\Gamma^2\mathbf{v}$, where h is the comoving enthalpy density, given by $h = \rho + \epsilon + p$, where p is the gas pressure and ϵ its internal energy density, both measured in the comoving frame. Finally, we denote by $\mathcal{E}$ the value of ϵ in the laboratory (or coordinate) frame. In the above formulation of these equations, we compute this energy density by substracting the coordinate mass density $\rho\Gamma$ to the $(0,0)$ component of the fluid's energy-momentum tensor $T^{\mu\nu}$, as

$$\begin{aligned}\mathcal{E} &= T^{00} - \rho\Gamma \\ &= h\Gamma^2 - p - \rho\Gamma\,.\end{aligned} \tag{4}$$

Whenever the LTE condition holds, an equation of state relating ϵ, p and ρ can be obtained, thus closing the system defined by equations (1) to (4). In this work, we have used the equation of state of an ideal relativistic gas, which can be expressed in terms of its enthalpy as:

$$h = \rho + \frac{\gamma p}{\gamma - 1}, \tag{5}$$

with $\gamma = 4/3$. Considering the contributions of all the involved particles to the total density, mass and energy, we have verified that equation (5) holds in the full range of parameters used in our simulations, with a value of γ that deviates from $4/3$ with a maximum error of 0.2%. The details of this calculation can be found in [6].

To integrate the above-defined system of equations, we have used the one-dimensional RHD module included in the PLUTO code [9]. The code works by making use of Godunov-type Riemann solvers, of which we have chosen an extension of the HLLC scheme to the equations of RHD (see [10] for the complete details). Among the possible configurations included in PLUTO, we have used a second-order total variation diminishing scheme for spatial reconstruction, and second-order Runge Kutta integration for time evolution. On each time step, the grid was updated in order to better follow total energy density gradients, by means of an adaptive mesh refinement algorithm provided by the CHOMBO library [11].

3 Simulations

3.1 Low density directions

As a verification of this scheme's applicability to our system, we have performed similar simulations to those in [7], which account for the evolution of the plasma in the lower density regions (see Fig. 1). To be more precise about this, we define the *baryon load* as $B = M_B c^2/E_{e^+e^-}$, where M_B is the total integrated mass considering the assumed spherically symmetric distribution, and $E_{e^+e^-}$ is the initial internal energy of the plasma. Namely, B works as an indicator of the mass-to-energy ratio along each direction.

In this part, we will only consider density distributions such that $B < 10^{-2}$. As it is explained in detail in [7], in that case the plasma forms a slab that expands while

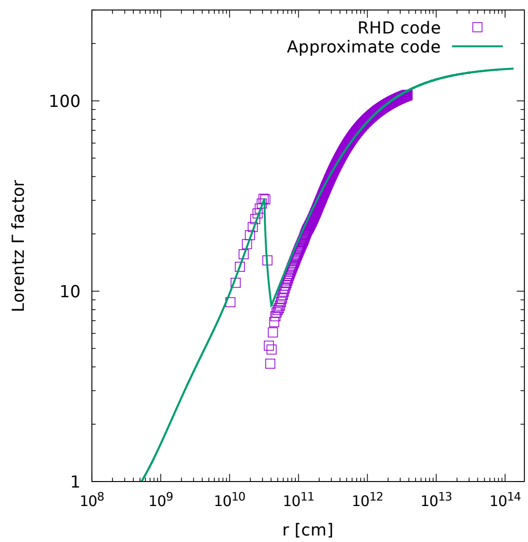

Figure 2. Lorentz factor Γ computed in with the PLUTO code, compared with the one computed with the semi-analytic approximate code. For this plot, the values $E_{e^+e^-} = 1.0 \times 10^{53}$ erg and $B = 6.61 \times 10^{-3}$ have been chosen. Similar good agreement is found for other values of $E_{e^+e^-}$ and B as long as $B < 10^{-2}$. Reproduced from [6].

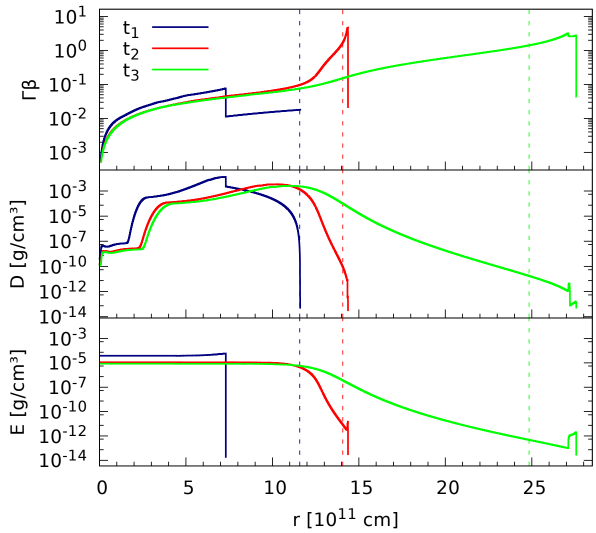

Figure 3. Profiles of $\Gamma v/c$ (up), $D = \rho\Gamma$ (center) and plasma internal energy $\mathcal{E}$ (down) for $B = 200$ at three different times, labeled as t_1 (before the breakout), t_2 (at the breakout) and t_3 (after the breakout). The factor $\Gamma v/c$ is approximately equal to v/c when $v \ll c$, and to Γ when $v \sim c$. Contributions to $\mathcal{E}$ due to the density have been neglected, in order to substract the baryon's kinetic energy, and show the position of the shock. The vertical dashed lines indicate the position of R_{ph} at each time. See also [6].

accelerating, until it reaches a constant Lorentz factor of roughly $\Gamma \sim 1/B$. During its evolution, and still under the condition $B < 10^{-2}$, the slab's width remains constant when measured in the laboratory frame. This process is studied in [7] using an approximate semi-analytic code that assumes this feature, and allows to predict average intensive quantities by means of conservation equations.

In Fig. 2 we show the comparison between the Lorentz factors computed with both the semi-analytic code and PLUTO, for one particular value of $E_{e^+e^-}$ and B. The simulations run with PLUTO show the formation of a slab of constant width, that accelerates accordingly to what is expected from the semi-analytic code. This is in turn consistent with the treatment done in [7], and therefore, the analysis done so far for the prompt emission remains unchanged.

3.2 High density directions

Having applied the current scheme to the already-known region of the parameter space, we proceed to study the case $B > 10^{-2}$, which corresponds to the interaction of the e^+e^- plasma with the SN remnant along the higher density directions, and the subsequent emission of the flares. To this end, we have chosen for each simulation an initial density profile that matches the ones obtained in [8] (see Fig. 1). Hence, all the considered profiles were set in the following way:

$$\rho \propto (R_0 - r)^{\alpha}\,, \tag{6}$$

where R_0 and α, with $2 < \alpha < 3$, are fitting parameters. Each profile of this kind has a single baryon load, that corresponds to the evolution of the fluid along one particular direction. Similarly, we have taken the velocity to depend on the radius as $v_r \propto r$, in order to set an initial profile that corresponds to the homologous expansion of the SN ejecta. Lastly, the plasma is initially contained within a radius of order $10^8 - 10^9$ cm, and has an uniform energy density.

Once the system is let to evolve from these initial conditions, the plasma expands and forms a shock that reaches the outermost part of the SN ejecta. Instead of forming a thin shell with an almost uniform Lorentz factor, the plasma evolves in such a way that the shock is followed by smooth energy and velocity distributions, where the module of the last may differ in several orders of magnitude from one point to another, as it is shown in Fig. 3.

After an initial expansion where Γ may reach values of several tenths, the shock rapidly elgulfs enough mass to decelerate and reach a non relativistic velocity distribution, typically in $t < 1$ s. This is maintained through the whole time the plasma is contained within the SN ejecta, until the breakout, in which the sudden decrease of the density causes the closest areas to the shock to reach relativistic velocities, as it can be seen in Fig. 3. From then on, the matter pushed by the shock -and no longer in homologous expansion- keeps expanding while cooling down.

As the shock propagates inside of the SN ejecta, photons are trapped inside the region occupied by the plasma, since their diffusion timescale is much longer than the dynamical times. Since characteristic equilibrium times are much shorter than both scales (see e.g. [12]), LTE is maintained during the whole evolution of the plasma within the SN material. However, at the breakout, the plasma reaches

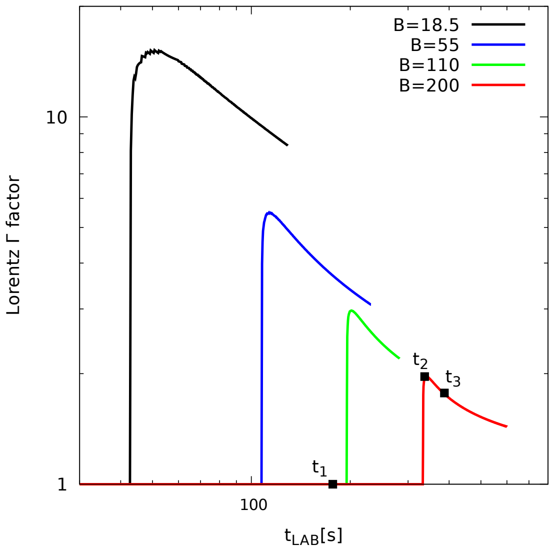

Figure 4. Lorentz gamma at the photospheric radius, calculated for different values of the baryon load, corresponding to different considered directions along the SN ejecta. The three times considered for $B = 200$ in Fig. 3 are indicated. Reproduced from [6].

the *photosphere*, which is an optically thin area located in the outermost regions of the SN ejecta. When this happens, photons begin to escape, and produce what is later observed as a flare.

To perform a comparison between these results and the observed Γ factors, we firstly recall from [13] that, before reaching an external observer, most of the photons are lastly scattered from a region peaked at $\tau \sim 1$, where τ is the optical depth calculated from the observer's line of sight. We hence define the transparency -or photospheric-radius R_{ph} as the value of the r coordinate that satisfies $\tau(R_{ph}) = 1$. Finally, we can give an estimation of the observed Γ by computing its value at $r = R_{ph}$.

Since τ is a Lorentz invariant when the total photon cross section is constant, which we assume as a first approximation, it can be calculated in laboratory coordinates as

$$\tau = \int_{R_{ph}}^{\infty} \mathrm{d}r\, \sigma_T\, n_{e^-}(r), \qquad (7)$$

where we set the cross section to $\sigma_T = 6.65 \times 10^{-25}$ cm^2, i.e., the one corresponding to Thomson scattering by electrons. Moreover, we compute the electron density as $n_{e^-} = \rho\Gamma/m_P$, where m_P is the proton mass. In doing so, we neglect the mass of the electrons, and we assume to have an average of one electron per nucleon.

Fig. 4, already shown in [6], shows the time evolution of $\Gamma(R_{ph})$, calculated for four different baryon loads that correspond to four different high-density directions along the SN ejecta. For a high enough B, it can be seen that, indeed, $\Gamma(R_{ph}) \lesssim 4$.

4 Final remarks and future work

The performed simulations of the evolution of an e^+e^- plasma inside of a SN ejecta show as a result the formation, expansion and breakout of a shock. Within the IGC model's parameters, the Lorentz factor at the photospheric radius verifies $\Gamma \lesssim 4$ for a high enough integrated mass across the observer's line of sight. This is consistent with the existence of a thermal emitter expanding at such a Lorentz factor, as it is inferred from the thermal component observed in the X-ray flares.

We have said that RHD holds as long as LTE is granted. However, this is not the case for the thin region close to the shock, from where photons can escape. If this is taken into account, the pressure radiation, which is the dominant one, should be actually smaller, and consequently we should expect the actual Lorentz factors to be even smaller. Therefore, the results of this work must be taken as a superior limit for Γ. To take this effect into account, we are currently working on a scheme that evolves radiation and massive particles separately, which would allow to compute the emitted luminosity as well.

References

[1] Rueda, J. A., & Ruffini, R., ApJL, **758**, L7 (2012)
[2] Izzo, L., Rueda, J. A., & Ruffini, R., A&A, **548**, L5 (2012)
[3] Fryer, C. L., Rueda, J. A., & Ruffini, R., ApJL, **793**, L36 (2014)
[4] Damour, T., Ruffini, R., APS, **35, 7**, 463 (1975)
[5] Ruffini, R., Rueda, J. A., Muccino, M., et al., **832**, 136 (2016)
[6] Ruffini, R., Wang Y. et al, https://arxiv.org/abs/1704.03821, submitted to ApJ (2017)
[7] Ruffini, R., Salmonson, J. D., Wilson, J. R., Xue, S., A&A, **359**, 855 (2000)
[8] Becerra L., Bianco C. L., Fryer C. L., Rueda J. A., Ruffini R., ApJ **833**, 107 (2016)
[9] Mignone, A., Zanni, C., Tzeferacos, P., et al., The Astrophysical Journal Supplement Series, **198**, 7 (2011)
[10] Mignone, A., Bodo, G., Mon. Not. R. Astron. Soc., **364**, 126 (2005)
[11] Colella, P., Graves, D. T., Johnson, J. N., et al., *Chombo software package for AMR applications design document*, Tech. Rep. LBNL-6615E (2003)
[12] Aksenov A. G. , Ruffini R., Vereshchagin G. V., Phys. Rev. D **79**, 043008 (2009)
[13] Pe'er A., ApJ, **682**, 463 (2008)